Methods to simulate photo-excited properties of aromatic molecules

by

Marcus Peter Taylor

UNIVERSITY OF BIRMINGHAM

A thesis submitted to

the University of Birmingham

for the examination of

DOCTOR OF PHILOSOPHY

School of Chemistry
University of Birmingham
2018

Abstract

The study of ultrafast dynamics is crucial for understanding the photophysics of many chemical and fundamental processes. Theoretical models have become vital for providing the rationale for experimental observations. These models require solving the time-dependent Schrödinger equation (TDSE). An efficient way for solving the TDSE is the MCTDH method, an algorithm for efficient propagation of wavepackets. A pre-requisite for performing quantum dynamics is the construction of potential energy surfaces (PES), which often require expensive electronic structure calculations, and are further complicated by non-adiabatic features such as conical intersections.

In this thesis, the photo-excited properties of a range of aromatic molecules are studied, including chromophores of fluorescent proteins, the most renowned being the green fluorescent protein (GFP). Much focus is therefore given to the photochemistry of GFP and its corresponding chromophore, HBDI.

The stability of the HBDI anion and its photoelectron spectrum was understood through considering its molecular components, imidazolide and phenoxide, as well as the totally symmetric analogues bis-imidazoloxy and bis-phenoxy. A vibronic coupling Hamiltonian was developed for each molecule to calculate the photoelectron spectrum. Good agreement with experimental data was achieved, indicating the fitted surfaces provide accurate PES. From the results, the contribution of the phenoxide and imidazolide ring to the photophysics of HBDI was determined.

A simple linear vibronic coupling Hamiltonian has been developed to calculate the photoelectron spectra for the two lowest bands of phenol. The obtained spectra were in good agreement with experiment, however an alternative assignment of the vibrational fine structure is proposed. The existence of a conical intersection between D_0 and D_1 was found and its effect on the photodynamics determined from

diabatic state populations. The ion surfaces, along with those for the excited states, are necessary for modelling time-resolved photoelectron spectra to complement experimental data. To ensure accuracy of the S_1 and S_2 surfaces, the absorption spectrum of phenol was also calculated.

Two alternative methods for calculating PESs are then investigated. The first uses gradients and second derivatives from Hessian calculations to express the potentials for all normal modes as displaced harmonic potentials. This methodology was applied to calculating the absorption and emission spectra for a range of anthracene derivatives and linear polyacenes. The success and limitations of the model are evaluated. The second is the recently developed DD-vMCG method, where Gaussian wavepackets are propagated on PES calculated "on-the-fly". Using this approach, the excited state proton transfer in GFP is studied and the mechanism elucidated. Despite the dynamics not being fully completed, preliminary results provide details on the mechanism, in support of previous studies.

"No fair! You changed the outcome by measuring it!"

Professor Hubert J. Farnsworth

The Luck of the Fryrish

Futurama, Season 3, Episode 36, Fox Television, March 11, 2001

Acknowledgements

A PhD thesis is not easily accomplished by an individual reliant only on himself. It requires a dedicated supervisor, a supportive group, a loving family and a group of crazy, yet wonderful friends. These last four years have been hard graft, but have also presented me with numerous opportunities to develop as a scientist, but also much more. I am lucky to have been to Paris several times for workshops and visited many cities across the country for conferences. It's funny to think that at one point I was perfectly content with only three years of undergraduate chemistry and here I am now having done many more years.

Firstly, a massive thank you to my supervisor, Graham, for his guidance, knowledge and enthusiasm. Your generosity with your time, as well as many a pint of beer, has always kept me encouraged and determined over the last few years. The Worth group, which despite undergoing a few personnel changes, have always been friendly, willing to help and have made for some great group outings, conferences and pub "group meetings".

One faces many challenges during a PhD, although one that is more unusual is your group and supervisor moving down to London. Luckily, I was taken in by the Johnston Group and all of office 204D, to whom I am very grateful for adopting me and providing an ample supply of laughs and serious discussions about everything, but science. In return, I enlightened you with lots of long group presentations and brilliantly crafted witticisms! Thank you to my surrogate supervisors at Birmingham, Roy and Sarah. Roy for his patience whilst I explain what I've been doing and Sarah for always taking the time to talk to me. You have both provided a lot of positive and constructive advice and feedback.

As for Hydra and the other computers residing in the server room - I hate you all! Many, many hours have been spent managing, fixing and occasionally hitting you.

I am relieved to finally relinquish all administrative, network and security duties! Good luck to you Chris!

For all their love and support, I am deeply indebted to Mum and Dad. I know that the majority of this thesis will seem like inane jargon to you, but hopefully you will enjoy the figures and those "*weird, funny looking things*," I call molecules! It is with great sadness that Grandma did not see the completion of this thesis, as I know she would have been so proud and would have thoroughly enjoyed perusing through. Your kindness was deeply appreciated.

Thank you to all the friends, both new and old, who have helped me through the last few years and kept me sane (or least matched my sanity!).

The importance of living somewhere you can relax and feel at ease cannot be overstated, nor can living with friends you can laugh with, rant at and build the occasional igloo. For this reason, I am especially grateful to Phil and Alex. From the walks to and from University, to many late night games, it has always been great fun. Being on a first floor flat, was never going to prevent us growing windowsill fruit and herbs. Thank you also Rupert for being there to listen and talk whenever times were tough. During those moments of self-doubt, you encouraged me to believe in myself and carry on. Your continued support is greatly appreciated.

This thesis and the work described in it are entirely my own, except where I have acknowledged *either* help from a named person *or* a reference is given to a published source or a thesis. Text taken from another source will be enclosed in quotation marks and a reference will be given.

May 26, 2019

List of Publications

M. P. Taylor and G. A. Worth, "*Vibronic coupling model to calculate the photoelectron spectum of phenol*", Chemical Physics, **515**, 719 (2018)

O. J. Daubney, M. P. Taylor, C. Soto and G. A. Worth, "*Expanding the Spectroscopic Toolbox - Efficient Emission Prediction of Small Polyaromatic Hydrocarbons*", Manuscript in Preparation.

G. Christopoulou, J. Woodhouse, M. P. Taylor, G. A. Worth and H. H. Fielding "*TR-PES of phenol*", Manuscript in Preparation.

Contents

List of Figures

List of Tables

Glossary

ADLA Adiabatic local density approximation

AnCA anthracene-9-carboxylic acid

AnCHO anthracene-9-carbaldehyde

AnMe 9-methyl anthracene

AnMeOH 9-hydroxymethyl anthracene

aug-cc-pVNZ augmented correlation-consistent polarisation valence N-zeta basis

BOA Born-Oppenheimer approximation

CASPT2 Complete active space with second-order perturbation

CASSCF Complete active space self-consistent field

CC Coupled Cluster

CCD Coupled Cluster singles

CCSD Coupled Cluster singles and doubles

CGFs Contracted Gaussian functions

CI Configuration interaction

CoI Conical Intersection

CSF Configuration State Functions

DD-vMCG Direct dynamics variational multi-configurational Gaussian

DFT Density functional theory

DOF Degrees of Freedom

DVR Discrete variable representation

EOM Equations of motion

EOM-CC Equation of motion coupled cluster

EOM-EA-CCSD Equation of motion - electron affinity - coupled cluster singles and doubles

EOM-IP-CCSD Equation of motion - ionisation potential - coupled cluster singles and doubles

ESIPT Excited state intramolecular proton transfer

ESPT Excited state proton transfer

FBR Finite basis representation

FC Franck-Condon

GFP Green Fluorescent Protein

GGA Generalised gradient approximation

GTOs Gaussian-type orbitals

GWP Gaussian wavepacket

HBDI *p*-hydroxybenzylidene-2,3-dimethylimidazolinone

HF Hartree-Fock

HK

HOMO Highest occupied molecular orbital

HP Hartree Product

IC Internal Conversion

ISC Intersystem Crossing

LCAOs Linear Combination of Atomic Orbitals

LDA Local density approximation

LHA Local Harmonic approximation

LR-TDDFT Linear response time dependent density functional

LUMO Lowest unoccupied molecular orbital

MBPT Many-body perturbation theory

MCSCF Multi-configurational self-consistent field

MCTDH Multi-configuration time dependent Hartree

MP2 Møller Plesset second-order perturbation theory

MPPT Møller Plesset perturbation theory

MRCI Multi-reference configuration interaction

PECs Potential Energy Curves

PES Potential Energy Surface

SCF Self-consistent field

SPFs Single particle functions

STOs Slater-type orbitals

TD Time dependent

TDDFT Time Dependent Density Functional Theory

TDH Time dependent Hartree

TDSE Time dependent Schrödinger equation

TISE Time independent Schrödinger equation

TR-PES Time Resolved Photoelectron Spectrum

vMCG variational multi-configurational Gaussian

wtGFP Wild Type Green Fluorescent Protein

Chapter 1

Introduction

The effect of light on daily life has been known for millenia. For many, such influences have come from the main source of light for us, the sun. Some of the earliest applications of light were the sun bleaching of fabrics - on bleachfields. The interaction of light with atoms and molecules was first reported in the 17$^{\text{th}}$ Century, when the influence of light on silver salts was noted. Johann Heinrich Schulze observed the photosensitivity of silver nitrate crystals, which turned dark upon exposure to sunlight. Soon after, Jean Hellot discovered that silver solutions in *aqua fortis* made ink invisible, only to reappear when exposed to sunlight [1]. The ability of light to affect, or even initiate, chemical reactions was first noted in the 18$^{\text{th}}$ Century. The first organic photochemical reaction is often attributed to Trommsdorf [2]. Around this time, von Grotthus determined that phosphorescent light was of different wavelength to the absorbed light [3], whilst Draper stated that only light rays that are absorbed can produce a chemical reaction, with the rate of reaction proportional to the intensity of the light [4]. These two observations led to the 1st law of photochemistry: light must be absorbed by a molecule for a photo-chemical reaction to occur.

The early 20$^{\text{th}}$ Century saw the beginning of a quantitative approach to the interaction of light and matter. The emission of light of different frequencies from hydrogen had already been noted by Balmer [5]. In fact, the radiation of light by

any hot body *i.e.* blackbody radiation, was confounding physicists. From classical physics, the Rayleigh-Jeans law predicted that, regardless of temperature, the total energy radiated from a blackbody was infinite. This was clearly an absurd outcome. The now famous solution was proposed by Planck, who suggested the energy of electromagnetic radiation to be quantised [6]. This energy was proportional to the frequency, with a proportionality constant, h.

This concept was fundamental to the emergence of quantum mechanics and was also used by Einstein to explain the photoelectric effect. This phenomenon was related to the emission of electrons from metal surfaces. Such emission, however, occurred regardless of the intensity, but depended on the frequency of incoming light. Indeed, emission was only observed when the frequency exceeded a threshold value. Einstein's theory proposed that the electromagnetic field was quantised and consisted of packets of energy, later to be named photons [7, 8].

Since that time, the branch of photochemistry - interaction of light with molecules - has developed rapidly. Its application can be found in all areas of chemistry, from organic reactions to activating initiators for polymerisation, from the development of light emitting devices to biomedical probes, and many more.

One important area devoted to the interaction of light with molecules is spectroscopy. The word spectroscopy is a combination of the Latin "spectrum" meaning apparition or image, and the ancient Greek "skopa" meaning to see. Molecular spectroscopy has numerous forms, allowing a range of properties to be probed. Most of these techniques begin with molecules in the ground state, before subsequently being excited to higher energy electronic states. The majority of Chemistry is concerned only with the ground electronic state and related properties such as conformations, transition states, vibrational frequencies and bonding. The importance of molecular dynamics and excited state chemistry cannot however be overlooked and is vital in explaining experimental observations.

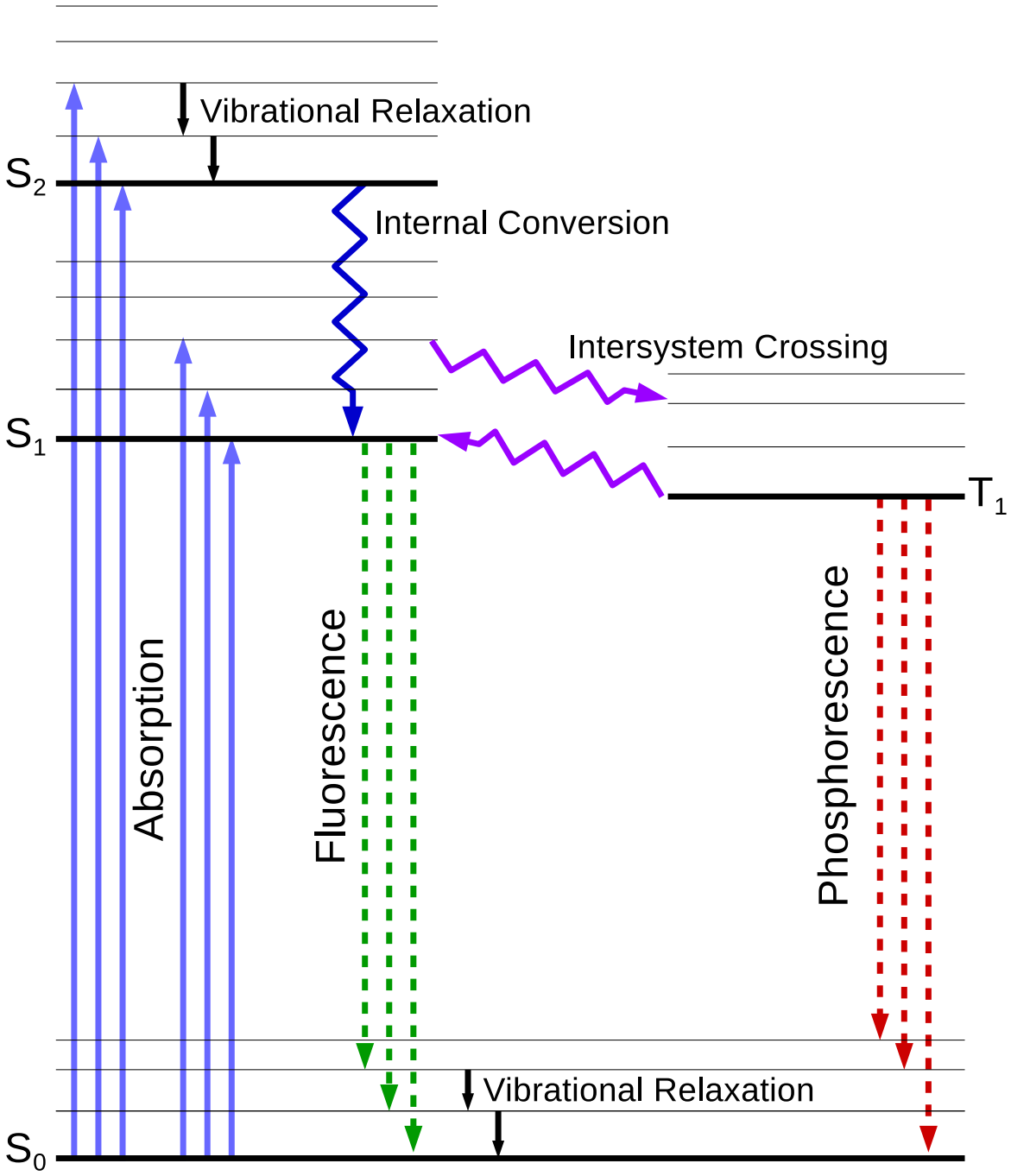

Fig. 1.1: A Jablonski diagram illustrating the various photodynamic processes that can occur following excitation with light. S_0 is the ground electronic state, S_1 and S_2 are excited singlet states and T_1 is the lowest triplet state.

Upon excitation, numerous pathways become available, allowing transitions between different electronic states of the molecule. The various photodynamics processes that can occur are illustrated in the Jablonski diagram, Figure 1.1. One form of excitation is through absorption of a photon and subsequent promotion of an electron into an unoccupied orbital. This excess energy can then be dissipated through radiative and non-radiative processes. Vibrational relaxation is the dissipation of this excess energy through vibrational motion of the molecule itself or energy transfer to its surroundings. This relaxes the excited state to its lowest vibrational level. Overlap between vibrational levels of different electronic states, but having the same spin multiplicity, results in internal conversion (IC), another non-radiative transition. IC is illustrated in Figure 1.1 between the S_2 and S_1 states. Both of these processes are rapid, on the scale of femtoseconds.

Relaxation can also occur through fluorescence, a radiative process with emission of a photon. In general, photoemission usually only occurs in appreciable yield from the lowest excited state of a given multiplicity. This is known as Kasha's rule [9].

Transitions to states of different multiplicity are also possible. This is known as intersystem crossing (ISC) and is another non-radiative process. For molecules with large spin-orbit coupling, intersystem crossing is more likely to occur. The rate of ISC is also increased if the transition involves a change in orbital type *e.g.* $^1\pi\pi^* \rightarrow {}^3n$, an effect known as El Sayed's rule [10, 11]. Following ISC, relaxation to the ground state can occur via two radiative processes as shown in Figure 1.1. The first is phosphorescence, where photoemission results in direct relaxation to the ground state. The other is delayed fluorescence, where a transition back to the lowest singlet excited state precedes photoemission.

Other photodynamic processes include transitions to unbound states, leading to dissociation or photofragmentation [12]. Fast radiationless relaxation can also occur when two potential energy surfaces (PES) cross. This is a conical intersection (CoI)

and is an important feature in photochemistry and throughout this thesis [13].

One class of molecules that often exhibit rich and varied photochemistry is aromatic molecules. There is no strict or concise definition of aromaticity. For many, Hückel's rule provides a good guide as to whether a molecule is aromatic, although proton NMR perhaps provides the strongest evidence. Hückel's rule states that a system can be considered aromatic if it is a planar, fully conjugated monocycle containing $4n + 2$ π-electrons.

The earliest and most renowned example of aromaticity is benzene. The π-molecular orbitals for benzene are shown in Figure 1.2(a). Using six p-orbitals, one centred on each carbon, results in six molecular π-orbitals, three bonding and three anti-bonding. The lowest energy, and most stable, is the all in-phase combination. The HOMO for benzene is a pair of degenerate π-molecular orbitals containing one nodal plane. The lowest anti-bonding molecular orbital (LUMOs) consist of another pair of degenerate π-orbitals with two nodal planes. The least stable orbital is the all out-of-phase combination, with three nodal planes. The six π-electrons completely fill the three bonding orbitals leading to a closed shell configuration and giving benzene maximum stability. The electron density of these π-orbitals is distributed over the entire ring system and the electrons are said to be delocalised.

Typically, molecules composed of multiple benzene rings fused together are also aromatic. This includes the linear fusing of two benzene rings (naphthalene), three benzene rings (anthracene) and so on. Non-linear combinations such as phenanthrene, pyrene and coronene are aromatic too.

Ring systems containing heteroatoms can also be aromatic. Imidazole, a 5-membered ring containing two nitrogens satisfies Hückel's rules and is therefore aromatic. The 2p π-orbitals for imidazole are shown in Figure 1.2(b). The nitrogen bound to a proton is not π-bonded, but contributes its lone pair into the system. This gives imidazole 6 π-electrons and fulfills Hückel's rules. The lone pair of the

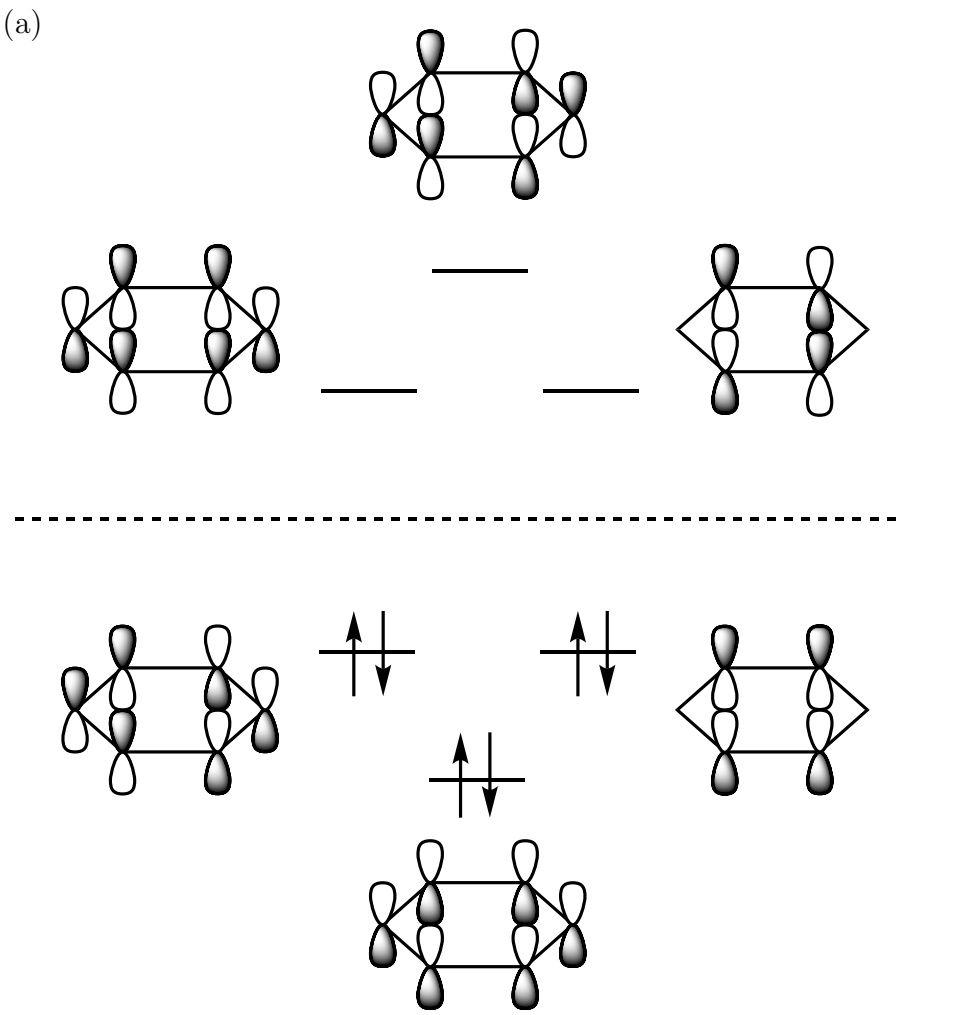

Fig. 1.2: A diagram showing the molecular orbitals of (a) benzene and (b) imidazole. For benzene, the lowest energy bonding orbitals are all in-phase and hence delocalised around the ring. The diagram for imidazole shows how the lone pair for one of the nitrogens is delocalised, whilst for the other nitrogen the lone pair lies in the plane.

other nitrogen resides in the plane of the ring, and hence is not involved in the delocalisation.

Benzene exhibits rich and varied photochemistry and for this reason has been extensively studied. Upon excitation, benzene can undergo several different competing relaxation pathways back to the ground state. At low excess energy, excitation to the S_1 state results in appreciable fluorescence (channel 1) or decay through ISC to low lying triplet states (channel 2) [14, 15]. At higher excess energies, the loss of fluorescence [16, 17] was observed, resulting from the onset of a new photodynamic process (channel 3). Explanations for this attributed the process to a CoI leading to population of a dark state [18]. In addition to the variety of radiative and non-radiative decay, photochemical rearrangements can also occur to form the isomers fulvene, benzvalene and Dewar benzene [19–21].

Combined experimental and quantum dynamic studies have shown the channel 3 decay process to involve competition between two ultrafast processes, IC and ISC, that occur on similar timescales. The near degeneracy of the S_1 and T_2 states allows for efficient ISC, despite benzene having weak spin orbit coupling [22, 23].

Azulene, an isomer of naphthalene, is another planar aromatic system that exhibits unusual photochemistry. In violation of Kasha's rule, emission is observed from the S_2 state rather than S_1, an observation first reported by Beer and Longuet-Higgins [24]. This behaviour is usually attributed to the large S_1-S_2 gap that is assumed to make IC relatively slow. Fluorescence from the S_1 state has been observed, although it is extremely weak with a quantum yield, $\Phi_f = 10^{-6}$ [25]. The lifetime of the S_1 state was found to be very short, with decay through non-radiative decay to the ground state taking place in under 1 ps [26–28].

Using semi-classical models, Bearpark *et al.* proposed that non-radiative decay occurs via a conical intersection within a femtosecond time scale [29]. The simulation also indicated the decay to take place before a single oscillation through the crossing

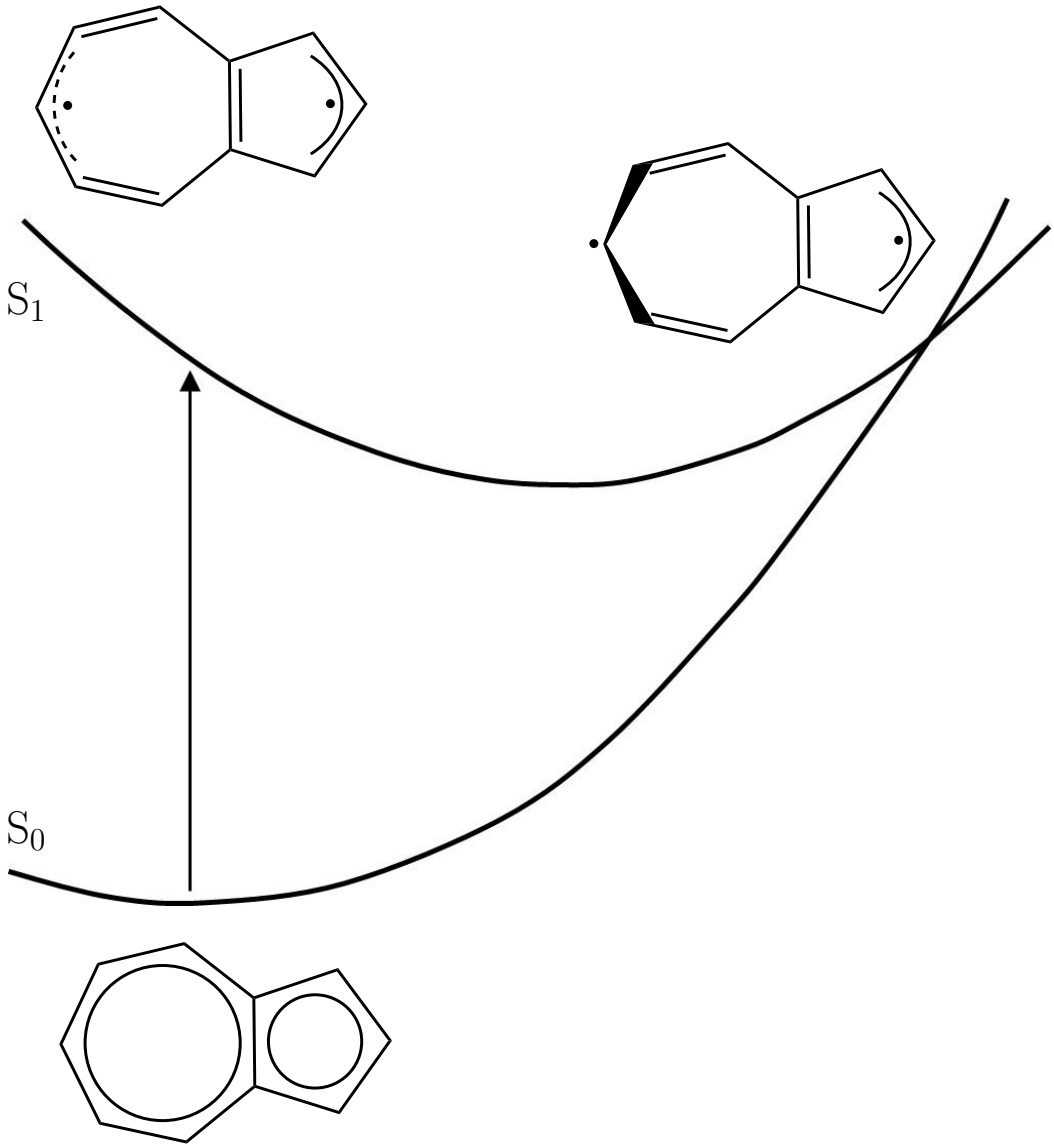

Fig. 1.3: Potential energy surface for azulene showing the conical intersection between the S_0 and S_1 states. Changes to the ground state structure in the S_1 state and approaching the intersection are also shown.

is completed. The PESs for the S_1 and S_0 states leading to the intersection are shown in Figure 1.3. The change to the ground state geometry in the excited state and at the intersection are also shown. Amatatsu and Komura investigated the reaction coordinate leading to this intersection [30]. Upon excitation to the S_1 state, the planar, aromatic structure of azulene is seen to change. The transannular bond increases its double bond character and there is a decrease in aromaticity of the peripheral bonds. At the intersection, the geometry distorts to become non-planar, but upon decay to the ground state rapidly recovers its planar, aromatic form. Fluorescence, and phosphorescence, from higher excited states is not unique to azulene and has been observed for a range of organic molecules [31].

Delocalisation is also present for systems with a series of overlapping p-orbitals over which the π-electrons can extend. Such systems are said to be conjugated. Typically conjugated systems are formed from alternating single and multiple bonds, and can incorporate aromatic molecules. Chromophores are molecules, or part of a molecule, that are highly conjugated and where absorption of light occurs. They are the primary location of photodynamic activity, typically seen as changes in geometry and are responsible for the colour of the molecule. Chromophores are extensively found in biomolecules where they are embedded in protein matrices.

Retinal is the chromophore found within rhodospin, the molecule responsible for vision. The primary photochemistry is the conversion from 11-*cis* retinal to its all *trans* form [33]. This reactivity is attributed to a conical intersection between the ground (S_0) and S_1 states [34,35]. The PES along the *cis-trans* isomerisation for the S_0 and S_1 states of retinal are shown in Figure 1.4.

Absorption of light excites the 11-*cis* isomer to the S_1 excited state. Within 80 fs, the conical intersection is reached, by which point the molecule is highly strained [36]. From here, the majority of the photoproduct is the *trans* isomer, thus completing the isomerisation [32]. A small minority of the *cis*-isomer is also formed.

Some chromophore containing proteins are described by the colour of their fluorescence, the most famous being the Green Fluorescent Protein (GFP). GFP was first isolated from the *Aequorea victoria* jellyfish (in conjunction with a separate fluorescent protein, aequorin) and reported in 1962 by Shimomura [37], who subsequently published its emission spectrum [38]. Properties of the aequorin protein were detailed towards the end of the decade [39]. The emission spectra from GFP showed a peak centred at 508 nm, whilst the co-protein aequorin, which displayed blue luminescence, had a peak around 470 nm. This value was noted to be close to one of the GFP excited peaks, leading to a hypothesis that the GFP could convert the blue emission of the aequorin into the characteristic green colour.

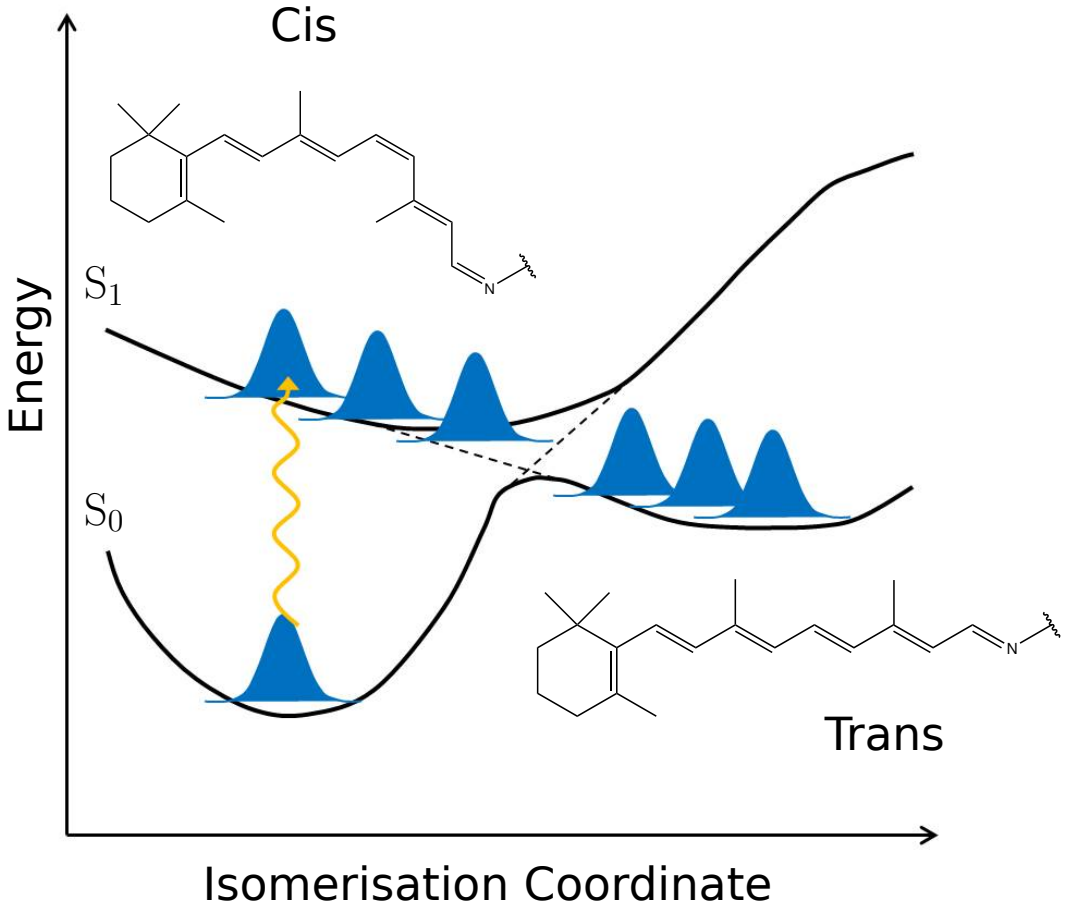

Fig. 1.4: Potential energy surface along the *cis-trans* isomerisation coordinate showing the conversion from 11-*cis* retinal to *trans* retinal as mediated by a conical intersection between the S_0 and S_1 states. Figure adapted from [32].

Morise *et al.* [40] managed to purify, crystallise and partially characterise GFP. It was known that the jellyfish, *Aequorea victoria*, emitted green light whereas the protein extracted from it, aequorin, emitted blue light in the presence of Ca^{+} ions, a phenomenon reported to occur in other bioluminescent marine organisms by Morin [41]. Morise, therefore, postulated that an *in vitro* energy transfer takes place from the blue emitting aequorin to GFP, resulting in the trade-mark green fluorescence.

The so called 'GFP revolution' is usually described as having started in the 1990s, when the cover of an issue of Science, containing the work of Chalfie *et al.* [42], displayed the striking green glow of the sensory neurons in *Caenorhabditis elegans*. The work itself was a breakthrough in cell biology, but also in GFP research as it showed that it was possible to clone GFP and express it in other organisms. This work was verified by Tsuji who also reported the expression gene and fluorescence of GFP [43]. Earlier work had been carried out by Prasher *et al.*, who reported the expression and cloning of the aequorin protein [44] and later detailed the primary structure of wild-type GFP (wtGFP) [45].

The 3D crystal structure of GFP was resolved by two different groups in quick succession. Ormo *et al.* published the structure of the Thr^{65} variant of GFP at 1.9 Å resolution [46]. In a separate study, the structure of wtGFP was also resolved to the same resolution by Yang *et al.* and was shown to exhibit a new type of protein fold, coined beta-can [47]. These crystal structures helped to elucidate the position of the chromophore central to the bio-luminescent properties of GFP. A representation of the structure is shown in Figure 1.5. The work in the discovery, expression and development of GFP culminated in the 2008 Nobel Prize for Chemistry being shared by Chalfie, Osamu and Tsien [48].

The identification and structure of the chromophore was first proposed by Shimomura [49] who suggested it comprises a phenoxy moiety attached to an imidazole ring by an ethylene bridge. Later work by Cody *et al.* characterised the chromophore

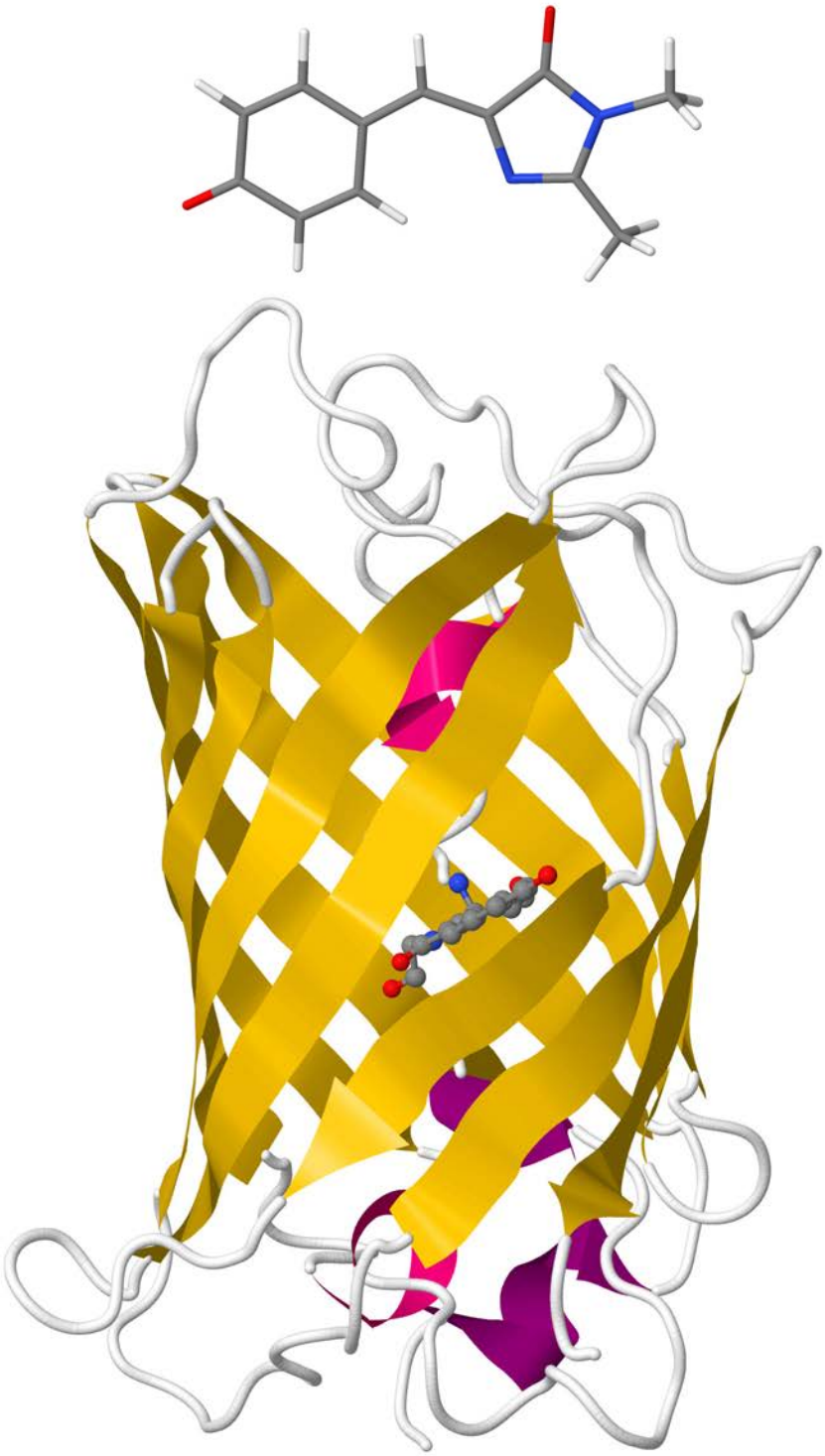

Fig. 1.5: Structure of GFP drawn in cartoon style showing the beta can conformation. The chromophore can be seen residing inside the protein. The actual structure of the HBDI chromophore is shown top. (Taken from the PDB: 1EMA as deposited by Ormo and Remington [46]).

when released as a hexapeptide after papain digestion of GFP. The proposed structure [50] differed from Shimomura's through the amino acid residues attached at the 1- and 2- position of the imidazole ring, although the core structure of phenoxy and imidazole moieties remained. Further work undertaken by Niwa *et al.* determined the structure to contain 4-hydroxybenzylidene-imidazolinone. It was also noted how the environment and conformation of this chromophore had a substantial impact on its fluorescence.

Structure elucidation showed the chromophore, *p*-hydroxybenzylidene-imidazolinone (*p*-HBDI), to be an essential component of the protein backbone. Furthermore, the central localisation of the chromophore completely protects it from the bulk solvent and has also been attributed to the high quantum yield of fluorescence by preventing O_2 from quenching the excited state [46]. Perhaps most remarkable is that excitation of the chromophore results in an excited state proton transfer (ESPT) and deprotonation of the chromophore's phenol group. This conversion of HBDI from the neutral to anion form is crucial as it is the anion that gives rise to the eponymous fluorescence in GFP. A biosynthetic scheme for the formation of HBDI from the protein's own sequence was postulated and reported by Heim [51] and subsequently showed that the final formation step requires O_2 and is a time-gated procedure; negating the use of any enzymes in the procedure. Since then, there have been numerous studies of the structure of GFP and HBDI [52–56].

The photophysics of GFP has been extensively studied both experimentally and computationally, and yet the exact mechanism by which the fluorescence operates is still the subject of uncertainty and debate [57–59]. What is unusual about GFP's photophysics, is that both HBDI itself, and the denatured form of GFP, do not fluoresce [60–63], with quantum yield measurements reported as being 2×10^{-4}. This itself seems to correlate well with other fluorescent proteins [64–66], however, it is all the more striking considering that the quantum yield of GFP itself is over

0.8 [67]. This emphasises the role of the protein matrix and indeed the environment on the chromophore.

ESPT has been found to occur for similar fluorescent proteins, for which structures are shown in Figure 1.6. Using electronic structure calculations, Wu *et al.* reported excited-state intramolecular proton transfer (ESIPT) in the blue fluorescent protein, which also resulted in dual emission [68]. The ESIPT was determined to occur within 18 ps, much longer than GFP, with an associated barrier of 0.26 eV. Upon excitation to S_1, the system initially relaxed to a local minimum. Following this, two competitive relaxation pathways were possible. The first was the ESIPT and the second was photoisomerisation, converting the structure from planar to the rings being perpendicular. ESPT was also seen for the red fluorescent protein, LSSmKate1, and used to explain its large Stokes shift. Using molecular dynamics

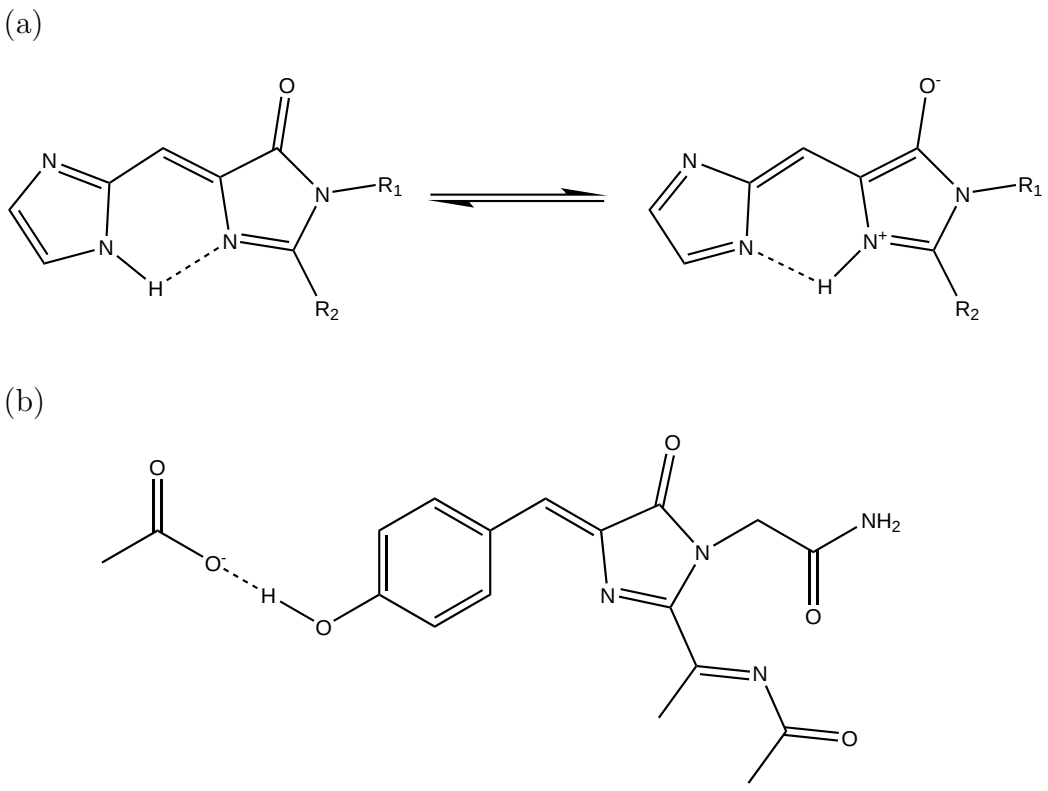

Fig. 1.6: Structures of other fluorescent proteins for which excited proton transfer occurs. Shown is (a) the blue fluorescent protein and (b) the red fluorescent protein, LSSmKate1.

and quantum chemistry calculations, Chen *et al.* deduced that excitation to S_1 leads to migration of electrons from the phenol ring to the N-acylimine, enhancing the acidity of the phenolic proton [69]. Eventually, deprotonation of this group leaves an anionic intermediate from which the experimental fluorescence is observed. A further conformation change, similar to that seen in GFP, was reported to be very slow.

As well as proteins, ESPT has also been reported for other biologically important molecules. ESIPT has been observed in several fluorescent nucleobases and nucleoside analogues [70]. To study the N-H to N hydrogen bonding between nucleobases in DNA, Horke *et al.* used ammonia dimers as a model to study the ESPT [71]. Using photoelectron spectroscopy imaging studies, it was determined that exciting the ammonia dimer populates the A'' state. In this state, proton transfer takes place within 130 fs to form NH_4NH_2. From here, two decay processes are possible: non-adiabatic crossing to the A' state through a conical intersection within 50 fs followed by charge transfer and reverse proton transfer to form the ground state dimer; or dissociation into NH_2 and NH_4.

The transfer of a proton along a wire of hydrogen bonded molecules has also been observed in other systems. Georgieva *et al.* studied the ESPT of 7-hydroxy-4-methyl coumarin along a hydrogen-bonded water wire consisting of three water molecules (shown in Figure 1.7(a)) [72]. The waters bridge between the proton donating O-H and the proton accepting carbonyl group. Liu *et al.* instead studied the ESPT dynamics of a hydrogen-bonded wire comprising acetic acid molecules [73]. For 6-hydroxyquinoline, it was found that at least three acetic acid molecules were needed to establish a proton wire between the proton accepting and donating groups (Figure 1.7(b)). The results showed that transfer begins with protonation of the nitrogen, with a negligible barrier, and concludes with deprotonation of the phenol. Further investigation of the effect of the number of water molecules on the ESPT mechanism

was studied by Tang *et al.* for 2,6-diazaindole$(H_2O)_n$ clusters [74]. They found that no mechanism for ESPT was possible with two waters but did exist for three and four waters. The adopted conformations are shown in Figure 1.7(c). The mechanisms in both of these proton wires start with movement of the proton from the N-H to the water and occurs in a concerted manner, with an energy barrier of 0.14 eV. Solvent dependency on the ESPT leading to dissociation in hydroxyaryls has been reported by Agmon [75].

There has been much attention given to finding applications for molecules that

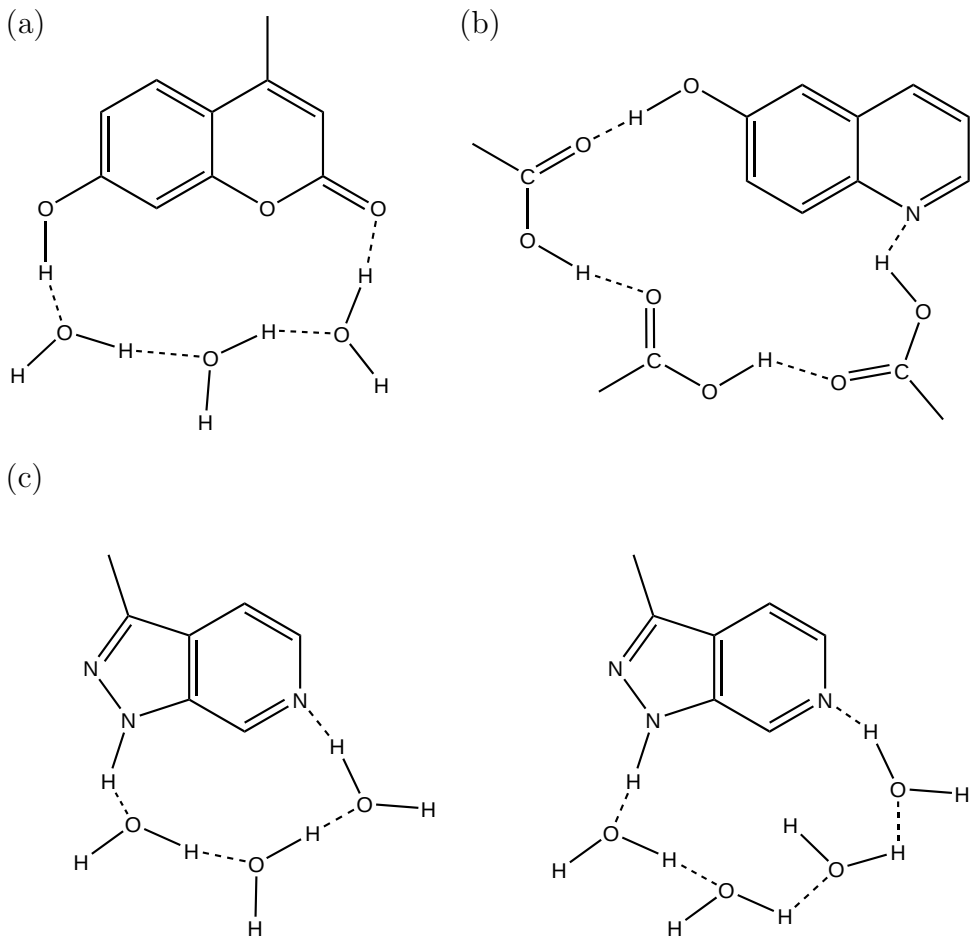

Fig. 1.7: Structures for molecules that undergo excited state proton transfer through a proton wire consisting of hydrogen bonded molecules. (a) shows 7-hydroxy-4-methylcoumarin with a three water proton wire and (b) shows 6-hydroxyquinoline with a three acetic acid wire. (c) is 2,6-diazaindole.$(H_2O)_n$ clusters for n = 3 and 4.

undergo ESPT. One of the earliest and most fascinating uses 3-hydroxyflavone as a laser dye. In this molecule, the process of ESPT and reverse proton transfer in the ground state creates a four state system similar to how lasers operate, as shown in Figure 1.8 [76]. A large population inversion is achieved creating a photoinduced molecular laser.

A range of molecules that undergo ESIPT have been touted for use as fluorescent probes or in organic optoelectronics [77, 78]. These generally involve aromatic containing molecules that undergo conversion from the enol to keto form through intramolecular proton transfer. It has been possible to control the rate of ESPT by changing the groups bonded to the aromatic ring (R) and the nitrogen (R′) [79]. When R and R′ are both hydrogens, no ESPT is observed. For R′= CN and R = H or CH_3, slow ESPT occurs. When, however, R is a tosyl group and R′ = H or CN, then ultrafast proton transfer takes place.

A review into ESPT and elucidating their mechanism has been recently detailed by Zhou and Han using *ab initio* methods [80]. Despite the breadth of theoretical work, they note that further work is needed in locating and discerning transition states in the mechanism.

In this thesis, the photodynamic properties of aromatic molecules are studied. Particular attention is also given to the chromophore found in GFP, HBDI. In Chapter 4, the photoelectron spectrum of HBDI is discussed and its spectrum and electronic structure investigated by considering its components: imidazolide and phenoxide. The totally symmetric analogues, bis-imidazoloxy and bis-phenoxy are also studied and their relation to the stability and photoelectron spectrum of HBDI discussed. Chapter 5, focuses on the aromatic molecule, phenol, which like benzene has interesting photochemistry. The excited states along the O-H stretch mode have received much attention due to the presence of several conical intersections, leading to photodissociation of the hydroxy proton. Conversely, the ionised states of phenol

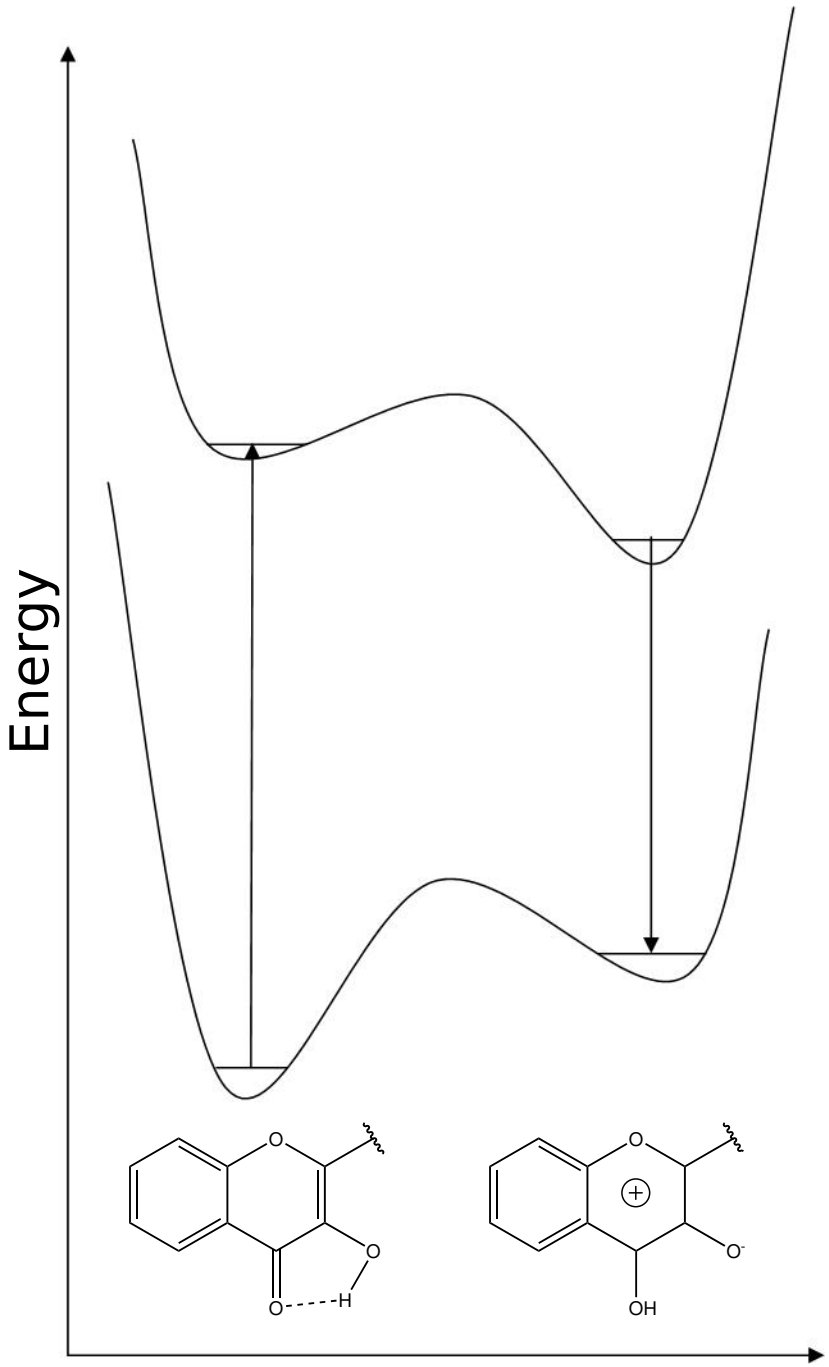

Fig. 1.8: A schematic showing the potential energy surfaces along the tautomerism pathway of 3-hydroxyflavone. This creates a four state system facilitating the large population inverse necessary for laser operation.

have received less attention. Here, the two lowest ion states of phenol are studied and the photoelectron spectrum calculated. In addition, surfaces for the S_1 state are obtained and the absorption spectrum calculated.

In Chapter 6, the absorption and emission spectra for a range of aromatic molecules, the linear polyacenes and anthracene derivatives, are calculated using a simple, automated procedure. This method constructs simple models of the PESs in the form of shifted Harmonic potentials. The molecules studied highlight the successes and limitations of this methodology and also the accuracy of electronic structure methods for calculating excited states of aromatic systems. Finally, Chapter 7 details the proposed mechanism for the ESPT in GFP and construction of a model system to study and elucidate the mechanism. In this work, the DD-vMCG method, where the PES is calculated "on-the-fly", as opposed to being pre-calculated and fitted, is introduced. The preliminary results are discussed and their support for previous experimental and theoretical studies.

Chapter 2

Theory

The models used to study physical systems are built upon theoretical frameworks governed by a set of mathematical principles. This chapter outlines the key theories pertinent to this thesis. The theories underpinning the computational techniques are described in Chapter 3.

2.1 The nuclear Schrödinger equation

As with any quantum mechanical study, the core equation to be solved is the non-relativistic, time-dependent Schrödinger equation (TDSE):

$$i\hbar\frac{\partial\Psi(\mathbf{r},t)}{\partial t} = \hat{H}\Psi(\mathbf{r},t) \tag{2.1}$$

from which one can obtain a range of properties for the system under consideration. The function $\Psi(\mathbf{r},t)$ is known as the wavefunction and contains a full description of the physical system; $\hat{H}$ is the molecular Hamiltonian. The full Hamiltonian for the nuclei and electrons can be written as:

$$\hat{H}(\mathbf{R},\mathbf{r}) = \hat{T}_n(\mathbf{R}) + \hat{T}_e(\mathbf{r}) + \hat{U}(\mathbf{R},\mathbf{r}) \tag{2.2}$$

Here the first and second terms equate to the kinetic energy operators of the nuclei and electrons, respectively. The final term describes the potential energy and is a function dependent on both the nuclei and the electrons.

This Hamiltonian can be partitioned into two terms: the nuclear kinetic energy and an electronic Hamiltonian, $\hat{H}_{el}$, containing the remaining terms:

$$\hat{H}(\mathbf{R},\mathbf{r}) = \hat{T}_n(\mathbf{R}) + \hat{H}_{el}(\mathbf{R},\mathbf{r}) \tag{2.3a}$$

$$\hat{H}_{el}(\mathbf{R},\mathbf{r}) = \hat{T}_e(\mathbf{r}) + \hat{U}(\mathbf{R},\mathbf{r}) \tag{2.3b}$$

Within the electronic Hamiltonian (equation (2.3b)) the nuclear coordinate becomes parameterised and so for any value of $\mathbf{R}$ a set of eigenfunctions and eigenvalues can be determined, as shown in equation (2.4a). These eigenfunctions can then be used as a basis to expand the wavefunction to solve the Schrödinger equation [81, 82]:

$$\hat{H}_{el}\Phi(\mathbf{R},\mathbf{r}) = V_i(\mathbf{R})\Psi_i(\mathbf{r};\mathbf{R}) \tag{2.4a}$$

$$\Psi(\mathbf{R},\mathbf{r}) = \sum_i \chi_i(\mathbf{R})\Phi_i(\mathbf{r};\mathbf{R}) \tag{2.4b}$$

Insertion of equation (2.4b) into equation (2.1) and multiplication by $\langle\Phi_j|$ results in a set of coupled equations for the nuclear functions, χ:

$$\Big[\hat{T}_n + V_j\Big]\chi_j - \sum \hat{\Lambda}_{ji}\chi_i = i\hbar\frac{\partial}{\partial t}\chi_j \tag{2.5}$$

with $\hat{\Lambda}_{ji}$ being a non-adiabatic coupling operator of the form:

$$\hat{\Lambda}_{ji} = \delta_{ji}\hat{T}_n - \langle\Phi_j|\hat{T}_n|\Phi_i\rangle \tag{2.6}$$

These operate in the space of the nuclear coordinates and detail the dynamical interaction between nuclear and electron motion.

By adopting rectilinear coordinates and atomic units, plus a suitable reduced mass scale, the kinetic energy operator can be formulated as:

$$\hat{T}_n = -\frac{1}{2M}\nabla^2 \tag{2.7}$$

from which the non-adiabatic coupling operator can be defined as:

$$\hat{\Lambda}_{ji} = \frac{1}{2M}\Big(2\mathbf{F}_{ij}.\nabla + G_{ij}\Big) \tag{2.8}$$

where $\mathbf{F_{ij}}$ is a derivative coupling vector and G_{ij} a scalar second-derivative coupling term:

$$\mathbf{F_{ij}} = \langle\phi_i|\boldsymbol{\nabla}\phi_j\rangle \tag{2.9a}$$

$$G_{ij} = \langle\phi_i|\nabla^2\phi_j\rangle \tag{2.9b}$$

Within this framework, the nuclear Schrödinger equation can be re-written as the following [83]:

$$\Big[-\frac{1}{2M}\big(\boldsymbol{\nabla} + \boldsymbol{F}\big)^2 + \mathbf{V}\Big]\chi = i\hbar\frac{\partial}{\partial t}\chi_j \tag{2.10}$$

The Schrödinger equation, as given in equation (2.10), contains the complete and infinite set of adiabatic electronic states. This, however, renders it impractical and so its utility is facilitated by approximations, which make it manageable.

2.2 Born-Oppenheimer and Adiabatic approximations

Given the infinite nature of the full Schrödinger equation as described above, it is inevitable that approximations are required to make it wieldable. Historically, initial approximations rested on the separation of nuclear and electronic motion. Early attempts focused on expanding the solutions of the Schrödinger equation in powers of some small quantity, κ, a ratio between the electronic and nuclear masses. In 1927, Born and Oppenheimer [84] published their seminal paper, using perturbation theory to determine the index of κ to be:

$$\kappa = \frac{1}{M}^{1/4} \tag{2.11}$$

This was used to justify representing the wavefunction as a single product:

$$\Psi(\mathbf{R}, \mathbf{r}) = \chi(\mathbf{R})\Phi(\mathbf{r}; \mathbf{R}) \tag{2.12}$$

Using this to solve the Schrödinger equation yields an alternative, but equivalent, form of equation (2.5):

$$\left[\hat{T}_n + V - \hat{\Lambda}\right]\chi = i\hbar\frac{\partial}{\partial t}\chi \tag{2.13}$$

and $\hat{\Lambda} = \hat{\Lambda}_{ii}$ *i.e.* the non-adiabatic coupling operator for the state of interest only contains non-zero terms on the diagonal.

Ignoring $\hat{\Lambda}$ altogether, and hence the non-adiabatic coupling, results in the adiabatic approximation:

$$\left[\hat{T}_n + V\right]\chi = i\hbar\frac{\partial}{\partial t}\chi \tag{2.14}$$

Within this approximation all states are decoupled and the nuclei return to being parametric over PESs formed by the electrons. In other words, the electronic energy is sufficient to provide the potential surface for nuclear motion.

An alternate approach, yet one that yields the same results as above, can be derived from the context of non-adiabatic coupling. Whilst the Schrödinger equation contains the infinite set of adiabatic electronic states, only those close in energy contribute significant non-adiabatic coupling. The logical approach therefore is to truncate the set of states to include only those of relevance. This, now finite, set of states are then decoupled from the other adiabatic states. The Schrödinger equation is no longer the full version but now takes on the same form as in equation (2.13). Here it is referred to as the group Born-Oppenheimer approximation [83], where the dimensions of $\hat{\Lambda}$ equates to the number of states in the set.

Taking the limit of the set containing a single state results in the Born-Oppenheimer approximation (BOA), whilst ignoring non-adiabatic coupling completely leads to equation (2.14), the adiabatic approximation.

It can be seen, therefore, that the separability of electronic and nuclear motion

is made possible due to the large mass ratio between the nuclei and electrons. This is clearly evident in the non-adiabatic coupling operator, equation (2.8), with the $1/2M$ pre-factor indicating dependence on the mass. Thus, a large mass will reduce the magnitude of the coupling.

It is crucial to note that the non-adiabatic coupling operator, $\hat{\Lambda}$, also has a dependency on the derivative coupling, $\mathbf{F}$. Applying the gradient operator ∇ to the electronic Schrödinger equation (equation (2.3b)) and utilising the definition for $\mathbf{F}$ as outlined in equation (2.9a) provides a useful expression for the derivative couplings in an off-diagonal form of the Hellmann-Feynman theorem:

$$F_{ij} = \frac{\langle \Phi_i | (\nabla \hat{H}_{el}) | \Phi_j \rangle}{V_j - V_i} \qquad \text{for} \quad i \neq j \tag{2.15}$$

Noting the denominator, it is evident that states with a large energetic separation will have small coupling.

From this argument, it is possible to truncate the Schrödinger equation by ignoring any non-adiabatic coupling between weakly coupled states (those with large energetic separation). The result is the group BOA:

$$\Big[-\frac{1}{2M} \big(\boldsymbol{\nabla} + \boldsymbol{F}^{(g)} \big)^2 + \mathbf{W}^{(\mathbf{g})} \Big] \chi^{(g)} = i\hbar \frac{\partial}{\partial t} \chi^{(g)} \tag{2.16}$$

where the (g) index emphasises the inclusion of only a subset of states. Unfortunately, the operator still includes coupling to states outside the specified subset. This can be seen in the "dressed potential energy" matrix elements of $\mathbf{W}$, where the index of summation, $k \notin g$, runs over states outside the selected group:

$$W_{ij}^{(g)} = V_i \delta_{ij} + \frac{1}{2M} \sum_{k \notin g} \langle \nabla \Phi_i | \Phi_k \rangle \langle \Phi_k | \nabla \Phi_j \rangle \tag{2.17}$$

Under the assumptions that the mass is large and the coupling to states outside of {g} is small, then the sum in W can be ignored to arrive at the group adiabatic

approximation:

$$\Big[-\frac{1}{2M}\big(\boldsymbol{\nabla} + \boldsymbol{F^{(g)}}\big)^2 + \mathbf{V^{(g)}}\Big]\chi^{(g)} = i\hbar\frac{\partial}{\partial t}\chi^{(g)} \tag{2.18}$$

Inspection of equations (2.16) and (2.18) illustrate the differing conditions upon which each approximation holds. The BOA rests on being able to separate nuclear and electronic motion, whilst the adiabatic approximation is conditional on the size of the derivative coupling between states. As such, the BOA is valid only when the adiabatic approximation holds true.

From this argument, one can return to the non-adiabatic operator, $\hat{\Lambda}_{ij}$, which has been shown to depend inversely upon the mass of the system and the derivative coupling vector, $\mathbf{F_{ij}}$. The derivative coupling vector itself depends inversely on the energy gap between surfaces and can be neglected for large energetic separations. As states become closer in energy the coupling will increase and surpass the mass factor. The effect is the coupling of nuclear motion on different surfaces. At the point the two surfaces become degenerate *i.e.* $i = j$, the coupling becomes infinite and the adiabatic approximation breaks down. These points of degeneracies and their implications are discussed in Section 2.4. This scenario can be resolved by moving from an adiabatic framework to using diabatic states.

2.3 The Diabatic Representation

Solving the group adiabatic approximation, equation (2.18), is very difficult due to the terms present in $\boldsymbol{F}.\boldsymbol{\nabla}$. Complications in this non-local operator arise through its description of coupling between electronic states by nuclear momentum and the occurrence of singularities at crossing points. In order to render the group adiabatic approximation practical, it is desirable to implement a diabatic basis [85–89].

The choice of basis set is a matter of preference. In the previous section the choice of basis set was the eigenfunctions of the electronic Hamiltonian (equation

(2.4a)). These basis functions can be transformed to a new basis set, Φ_i, by a unitary transformation, $\mathbf{U}$:

$$\mathbf{U}\mathbf{U}^\dagger = 1 \tag{2.19}$$

This implies the nuclear wavefunction has also been transformed as:

$$\tilde{\boldsymbol{\chi}} = \mathbf{U}^\dagger \boldsymbol{\chi} \tag{2.20}$$

due to the invariance of the total wavefunction, $\Psi(\mathbf{R}, \mathbf{r})$, as in equation (2.4b). The question that remains is whether such invariance of the wavefunction is applicable to the group BOA with a set of (g) states:

$$\Big[-\frac{1}{2M}\big(\nabla + \mathbf{F}^{(\mathbf{g})}\big)^2 + \mathbf{W}^{(\mathbf{g})} \Big] \chi^{(g)} = i\hbar \frac{\partial}{\partial t} \chi^{(g)} \tag{2.21}$$

A unitary transformation of the electronic basis set:

$$\hat{\Phi} = \mathbf{S}(\mathbf{R})\Phi \tag{2.22}$$

results in the following transformation of the group BOA:

$$\Big[-\frac{1}{2M}\big(\nabla + \tilde{\mathbf{F}}\big)^2 + \tilde{\mathbf{W}} \Big] \chi = i\hbar \frac{\partial}{\partial t} \chi \tag{2.23}$$

with $\tilde{\mathbf{W}}$ the transformed dressed potential matrix and $\tilde{\mathbf{F}}$ the transformed derivative coupling matrix:

$$\tilde{\mathbf{W}} = \mathbf{S}^\dagger \mathbf{W} \mathbf{S} \tag{2.24a}$$

$$\tilde{\mathbf{F}} = \mathbf{S}^\dagger \mathbf{F} \mathbf{S} + \mathbf{S}^\dagger (\nabla \mathbf{S}) \tag{2.24b}$$

Comparison of equations (2.21) and (2.23) shows the group BOA is invariant to a local gauge transformation. An example of such a transformation is given in Appendix A.1.

A further point of consideration is whether there exists a local gauge transformation that negates non-adiabatic couplings. Inspection of the transformed derivative

coupling matrix (equation (2.24b)) shows that the non-adiabatic coupling can be negated if the following can be solved:

$$\mathbf{FS} + (\nabla \mathbf{S}) = 0 \tag{2.25}$$

leading to the Schrödinger equation in diabatic form:

$$\Big[-\frac{1}{2M}(\boldsymbol{\nabla}^{\mathbf{2}}\mathbf{1} + \tilde{\mathbf{W}}) \Big] \chi = i\hbar \frac{\partial}{\partial t} \chi \tag{2.26}$$

This form comprises a diagonal kinetic energy operator with the couplings between electronic states housed within the potential energy matrix.

An issue of extreme importance, and one so far bypassed within this theoretical framework, concerns the legitimacy of strictly diabatic states [90]. A number of different methodologies have been formulated in the construction of diabatic states [91]. One simple approach is outlined in Appendix A.2.

Strictly diabatic states are possible, so long as the derivative coupling between states inside the group to those outside can be ignored. This is only the case for a one-dimensional problem, *i.e.* consideration of one degree of freedom, such as diatomic molecules. For polyatomics, only quasi-diabatic bases can be achieved through a transformation aimed at minimising the non-adiabatic operator.

2.4 Conical Intersections

Since the derivative coupling vector depends upon the energetic separation between two electronic states, i and j, then as the states become closer in energy a point of degeneracy is reached when $i = j$. At this point the adiabatic and BOA break down as nuclear and electronic motion becomes coupled. This degeneracy is indicative of points at which the potential energy surfaces of i and j cross. Such a crossing is denoted a conical intersection (CoI). CoIs are observed throughout this thesis, particularly in the study of the photoelectron spectrum of phenol (Chapter 5). A

major accomplishment of this study was the discovery of a previously unreported CoI between the D_0 and D_1 states. It is therefore necessary to outline the theory used in this thesis to describe CoIs. The occurrence of crossing points was first proved by von Neumann and Wigner in 1929 [13] and their importance in explaining ultra-fast radiationless processes was established as early as 1937 by Teller [92].

The use of diabatic states, as outlined in the previous section, are vital in providing a theoretical framework of CoIs. Expanding the potential matrix elements of the diabatic potential operator, $\mathbf{W}$, as a Taylor expansion around some point R_0 leads to:

$$\mathbf{W}(\mathbf{R}) = \mathbf{W}^{(0)} + \mathbf{W}^{(1)} + \mathbf{W}^{(2)} + \dots \tag{2.27}$$

Making use of a unitary transformation allows the diabatic basis at R_0 to be taken as equal to the adiabatic basis. Now, the adiabatic potential surfaces become the eigenvalues of the diabatic potential matrices:

$$\mathbf{V} = \mathbf{S}\mathbf{W}\mathbf{S}^{\dagger} \tag{2.28}$$

For a two state system the adiabatic surfaces are thus given as:

$$V_{\pm} = \Sigma \pm \sqrt{\Delta^2 + W_{12}^2} \tag{2.29}$$

where

$$\Sigma = \tfrac{1}{2}(W_{11} + W_{22}); \quad \Delta = \tfrac{1}{2}(W_{22} - W_{11}) \tag{2.30}$$

The first-order terms can be expressed as:

$$W_{11}^{(1)} = \boldsymbol{\kappa}^{(1)}.\mathbf{R}; \quad W_{22}^{(1)} = \boldsymbol{\kappa}^{(2)}.\mathbf{R} \tag{2.31}$$

and

$$\tfrac{1}{2}(W_{22}^{(1)} - W_{11}^{(1)}) = \boldsymbol{\delta}.\mathbf{R}; \quad W_{12}^{(1)} = \boldsymbol{\lambda}.\mathbf{R} \tag{2.32}$$

where $\boldsymbol{\delta}$ is a gradient difference vector and $\boldsymbol{\lambda}$ a linear coupling vector.

Taking R_0 to now be the point of degeneracy demands that Δ^2 and W_{12}^2 in equation (2.29) equal zero. This can only occur when the two vectors are independent functions of different coordinates. Since near the degeneracy $\Delta \approx \boldsymbol{\delta}.\mathbf{R}$ and $W_{12} \approx \boldsymbol{\lambda}.\mathbf{R}$, then to first-order (linearly) the energetic degeneracy is lifted in the space spanned by the vectors δ and λ. This is a consequence of the von Neumann-Wigner theorem [13, 93]. This manifests itself, with respect to the potential energy surfaces, as a double cone with a meeting point corresponding to the point of degeneracy.

Consideration of symmetry is also useful for understanding and explaining CoIs. The terms in equation (2.32), the gradient difference and linear coupling vectors, are only non-zero if:

$$\Gamma_s \otimes \Gamma_{s'} \otimes \Gamma_\alpha \supset A \tag{2.33}$$

hence the products of the symmetries for the two electronic states and the nuclear coordinate contain the totally-symmetric mode. As a result, should the states have different symmetry then the gradient difference will only occur along totally symmetric modes, whereas the first-order linear coupling terms will be non-zero for non-totally symmetric modes. Situations also arise where the states are degenerate *i.e.* have non-Abelian symmetry such as T or E. This results in the Jahn-Teller effect. The Jahn-Teller theorem states that asymmetrically filled degenerate orbitals will bring about a geometric distortion that lifts the degeneracy [94, 95]. This distortion will occur along a non-totally symmetric vibration [96, 97]. Detailed analysis using group theory has lead to different classifications of Jahn-Teller degeneracies [98]. The application of symmetry in molecular photochemistry is discussed more in Section 2.5.

Whilst the application of symmetry is useful in deciding whether a CoI can exist, it provides no information on whether it actually does and it is by no means essential for one to form. It is possible for CoIs to occur between states of the

same symmetry or in molecules with no symmetry at all. This is known as an accidental CoI. Symmetry-allowed accidental CoIs have been observed in H_2S. In C_s symmetry, the two lowest singlet excited states have the same symmetry. However, when transformed into C_{2v} symmetry the two states in question obtain different symmetries and the crossing is allowed [99, 100].

For many years it was widely accepted that the non-crossing rule, which applied to diatomics (that states with the same symmetry avoid each other), also held for tri- and polyatomic systems. It has since been shown though that states of the same symmetry can indeed cross in polyatomics [101–103] such as in methyl mercaptan [104].

2.5 Photochemistry

2.5.1 Group Theory and Symmetry

The use of symmetry and group theory in chemistry has become a vital tool in being able to rationalise spectroscopy, orbitals and dynamics of molecules. Its application to molecular spectroscopy was first published in a series of books by Herzberg [105–107]. The standard approach to using group theory for molecules firstly requires one to identify the point group to which the molecule belongs. The point group defines the unique set of symmetry elements and operations and has a corresponding character table from which a range of molecular properties can be extracted. An example of a character table for the T_d point group is shown in Table 2.1. Further character tables used throughout this thesis can be found in Appendix B. Of particular importance is the first symmetry species in the character table, *e.g.* A_1, A_{1g}, which corresponds to the totally-symmetric representation. Its significance will be outlined later.

The role of symmetry in CoIs has already been illustrated and again plays a crucial part in vibrational, electronic and vibronic spectroscopy. It can aid the

Table 2.1: The character table for the T_d point group.

	E	$8C_3$	$3C_2$	$6S_4$	$6\sigma_d$	linear, rotations	quadratic
A_1	1	1	1	1	1		x^2, y^2, z^2
A_2	1	1	1	-1	-1		
E	2	-1	2	0	0		$x^2 - y^2$
T_1	3	0	-1	1	-1	R_x, R_y, R_z	
T_2	3	0	-1	-1	1	x,y,z	xy, xz, yz

explanation of what is present (or even absent) in spectra and the observed fine structure. Finally, utilising symmetry arguments in theoretical models can help to reduce the number of matrix elements that need to be considered, as many become zero and can therefore be ignored.

2.5.2 Franck-Condon Principle

In an attempt to explain the distribution in various intensities of vibronic transitions, Franck argued qualitatively that an electronic transition proceeds much quicker than a vibrational one, so for a vibronic transition the positions and velocity of the nuclei are roughly the same *before and after* the transition [108]. This idea of the nuclei having the same geometry before and after the transition gives rise to the concept of a vertical transition, as shown in Figure 2.1. This is in contrast to the adiabatic energy, the difference between the minima of the involved electronic states.

In his attempt to explain the same phenomenon, Condon treated vibronic transitions with quantum mechanics and determined the intensity of a vibronic transition, I_{vt}, to be proportional to the square of some term [109, 110]:

$$I_{vt} \propto |\mathbf{R}_{ev}|^2 \tag{2.34}$$

where:

$$\mathbf{R}_{ev} = \int \Psi'^{*}_{ev} \boldsymbol{\mu} \Psi''_{ev} \mathrm{d}\tau_{ev} \tag{2.35}$$

Here, $\boldsymbol{\mu}$ is the electric dipole moment operator and the integral is over both

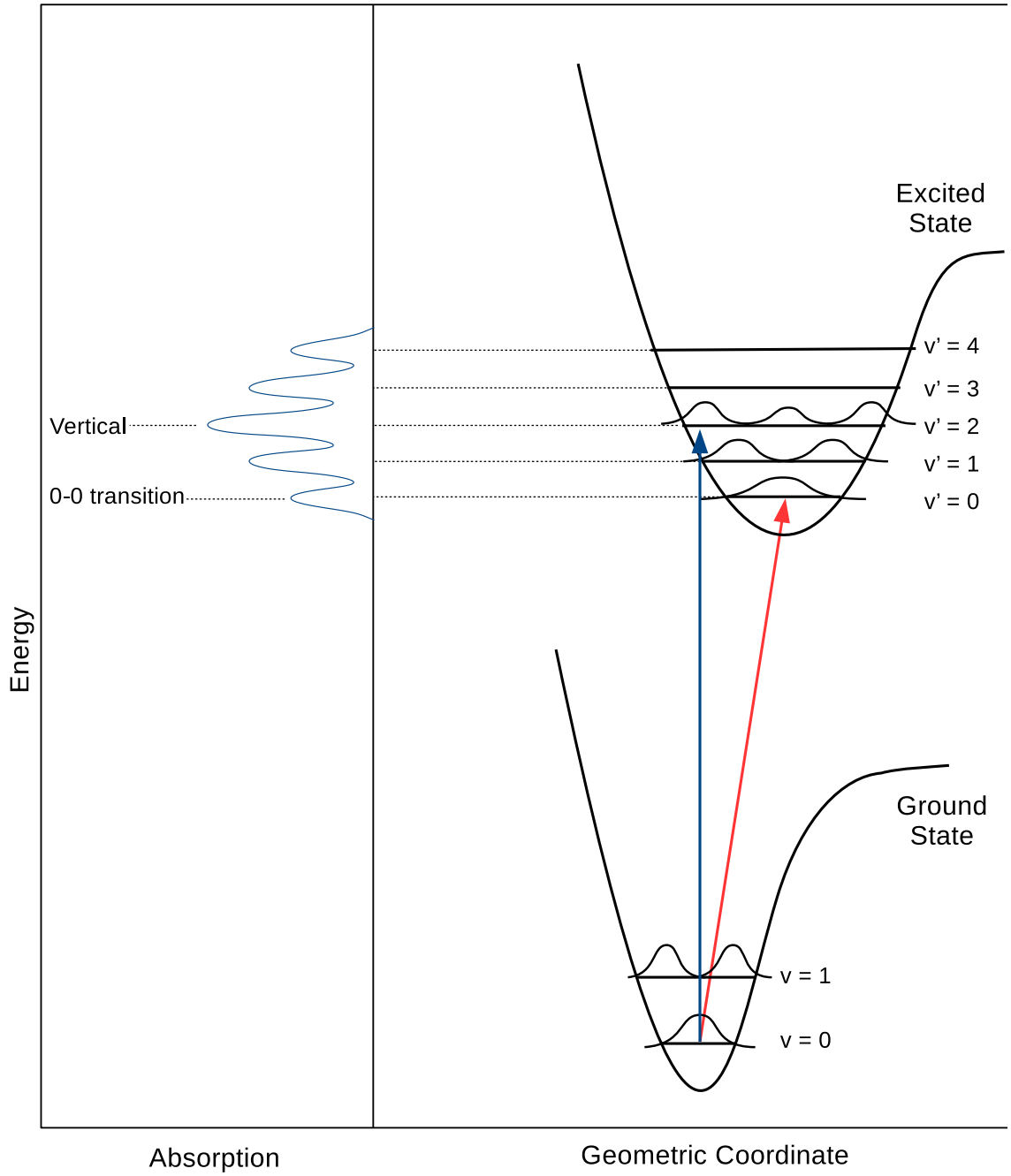

Fig. 2.1: A diagram illustrating a photo-induced transition between two electronic states, with associated vibrational levels and the corresponding spectrum produced. The blue arrow indicates a vertical transition. Here the vibrational overlap integral is greatest giving rise to the most intense peak in the spectrum. The red arrow indicates the adiabatic transition between the ground state vibrational level of both electronic states. This transition is still present in the spectrum but is lower in intensity. The displacement seen in the excited state along the geometric coordinate abscissa is indicative of a geometry change in the excited state that gives rise to the progression in the spectrum.

the electronic and vibrational coordinates. Assuming the BOA holds, then Ψ_{ev} can be separated into individual terms for the electronic and vibrational wavefunction, $\Psi_e\Psi_v$ and the above equation can now be written as:

$$\mathbf{R}_{ev} = \int\int \Psi_e'^{*}\Psi_v'^{*}\boldsymbol{\mu}\Psi_e''\Psi_v''\mathrm{d}\tau_{ev} \tag{2.36}$$

Integrating over the electronic coordinates, τ_e, returns the equation:

$$\mathbf{R}_{ev} = \int \Psi_v'^{*}\mathbf{R}_e\Psi_v''\mathrm{d}r \tag{2.37}$$

where $\mathbf{R}_e$ is the electronic transition moment:

$$\mathbf{R}_e = \int \Psi_e'^{*}\boldsymbol{\mu}\Psi_e''\mathrm{d}\tau_e \tag{2.38}$$

Referring back again to the BOA, the nuclei can be regarded as stationary allowing $\mathbf{R}_e$ to be taken outside the integral and treated as a constant. This results in:

$$\mathbf{R}_{ev} = \mathbf{R}_e \int \underbrace{\Psi_v'^{*}\Psi_v''\mathrm{d}r}_{\substack{\text{Vibrational} \\ \text{Overlap Integral}}} \tag{2.39}$$

where the square of the vibrational overlap integral is the Franck-Condon factor:

$$\left|\int \Psi_v'^{*}\Psi_v''\mathrm{d}r\right|^2 \tag{2.40}$$

2.5.3 Selection Rules

By combining the equations for transition intensities with arguments from symmetry and group theory, one can derive a series of selection rules for determining whether a transition is allowed or forbidden. These selection rules provide theoretical support for explaining the intensities of experimental spectra such as infra-red, photo-absorption, emission and photo-electron. Selection rules can be derived for electronic, vibrational and vibronic transitions and whilst the focus here will be on

electronic and vibronic transitions, analogous rules can easily be derived for vibrations.

Electronic transitions involve the interaction of a molecule (or indeed an atom) with the electronic component of electromagnetic radiation. The selection rules describing these transitions are referred to as electric dipole selection rules. An analogous relationship from equation (2.34) can be determined for an electronic transition, I_{et}, that shows:

$$I_{et} \propto |\mathbf{R}_e|^2 \tag{2.41}$$

where $|\mathbf{R}_e|^2$ is given by equation (2.38). For an allowed transition, $|\mathbf{R}_e| \neq 0$ with the symmetry requirements that:

$$\Gamma(\Psi'_e) \times \Gamma(\boldsymbol{\mu}) \times \Gamma(\Psi''_e) \supset A \tag{2.42}$$

with Γ the irreducible representation. As the components of $\mathbf{R}_e$ along the Cartesian axes are:

$$\mathbf{R}_{e,x} = \int \Psi'^{*}_e \boldsymbol{\mu}_x \Psi''_e \mathrm{d}\tau_e \tag{2.43a}$$

$$\mathbf{R}_{e,y} = \int \Psi'^{*}_e \boldsymbol{\mu}_y \Psi''_e \mathrm{d}\tau_e \tag{2.43b}$$

$$\mathbf{R}_{e,z} = \int \Psi'^{*}_e \boldsymbol{\mu}_z \Psi''_e \mathrm{d}\tau_e \tag{2.43c}$$

then since:

$$|\mathbf{R}_e|^2 = (R_{e,x})^2 + (R_{e,y})^2 + (R_{e,z})^2 \tag{2.44}$$

an electronic transition is allowed so long as:

$$\left.\begin{matrix} R_{e,x} \\ R_{e,y} \\ R_{e,z} \end{matrix}\right\} \neq 0$$

hence for a transition to be allowed the following symmetry rules must be obeyed:

$$\Gamma(\Psi'_e) \times \Gamma(T_x) \times \Gamma(\Psi''_e) \supset A \tag{2.45a}$$

$$\Gamma(\Psi'_e) \times \Gamma(T_y) \times \Gamma(\Psi''_e) \supset A \tag{2.45b}$$

$$\Gamma(\Psi'_e) \times \Gamma(T_z) \times \Gamma(\Psi''_e) \supset A \tag{2.45c}$$

If the lower electronic state is a closed shell ground state then Ψ''_e is totally symmetric and since the product of two species with the same symmetry equals the totally symmetric species, then the symmetry rules for an allowed transition can be simplified to:

$$\Gamma(\Psi'_e) = \Gamma(T_x) \quad \text{and/or} \quad \Gamma(T_y) \quad \text{and/or} \quad \Gamma(T_z) \tag{2.46}$$

If during an electronic transition the vibrational states are also excited then one needs to consider a vibronic transition. The intensity of a vibronic transition and the corresponding vibronic transition moment, $\mathbf{R}_{ev}$, has already been stated in equations (2.34) and (2.35).

Similarly to electronic transitions, the symmetry arguments for a vibronic transition are as follows:

$$\Gamma(\Psi'_{ev}) \times \Gamma(\Psi''_{ev}) = \Gamma(T_x) \quad \text{and/or} \quad \Gamma(T_y) \quad \text{and/or} \quad \Gamma(T_z) \tag{2.47}$$

Since, the general case, $\Gamma(\Psi_{ev}) = \Gamma(\Psi_e) \times \Gamma(\Psi_v)$, then the above can be rewritten as:

$$\Gamma(\Psi'_e) \times \Gamma(\Psi'_v) \times \Gamma(\Psi''_e) \times \Gamma(\Psi''_v) = \Gamma(T_x) \text{ and/or } \Gamma(T_y) \text{ and/or } \Gamma(T_z) \tag{2.48}$$

If the same vibration is excited in both states then $\Psi'_v = \Psi''_v$ and one arrives back at the electronic selection rules.

2.5.4 Vibrational Structure

The involvement of totally symmetric vibrations in a vibronic transition causes a spectrum to contain a progression of peaks. This progression results from a geometry change along one of the normal mode coordinates when going from the lower to upper electronic state. The length of this progression corresponds to the size of the geometry change. For example, in the electronic transition to the S_1 state of formaldehyde there is substantial lengthening of the CO bond. Thus the vibration corresponding to the CO stretch appears in the spectrum as a long progression [111, 112]. This is illustrated in Figure 2.2.

The standard nomenclature when assigning spectra in electronic spectroscopy is of the form $N_{v''}^{v'}$, where N refers to the particular vibration involved and v' and v'' denote the quanta in the upper and lower state, respectively. The pure electronic transition is denoted as 0_0^0 and is usually seen when the transition is allowed, based on electric dipole rules. It is, nevertheless, possible for progressions to arise from non-totally symmetric vibrations. For example, in chlorobenzene the electronic transition $\tilde{A}\,^1B_2 \leftarrow \tilde{X}\,^1A_1$ is allowed as B_2 corresponds to $\Gamma(T_y)$ in the character table and is polarised along the y-axis. The spectrum however shows a vibronic transition from a single quantum of a b_2 vibration [113–115]. Using the selection rules derived above and substituting the irreps for the electronic states and vibrations, the symmetry species for the vibronic transition is:

$$\begin{aligned}\Gamma(\Psi_e') \times \Gamma(\Psi_v') \times \Gamma(\Psi_e'') \times \Gamma(\Psi_v'') &= B_2 \times B_2 \times A_1 \times A_1 \\ &= A_1 = \Gamma(T_z)\end{aligned} \tag{2.49}$$

hence the transition $(b_2)_0^1$ is allowed and polarised along the z-axis. Despite being symmetry allowed, vibronic transitions are often found to have no intensity. Where a vibronic transition does have significant intensity, the Herzberg-Teller theorem can be used to explain why [116]. This theorem is outlined as follows.

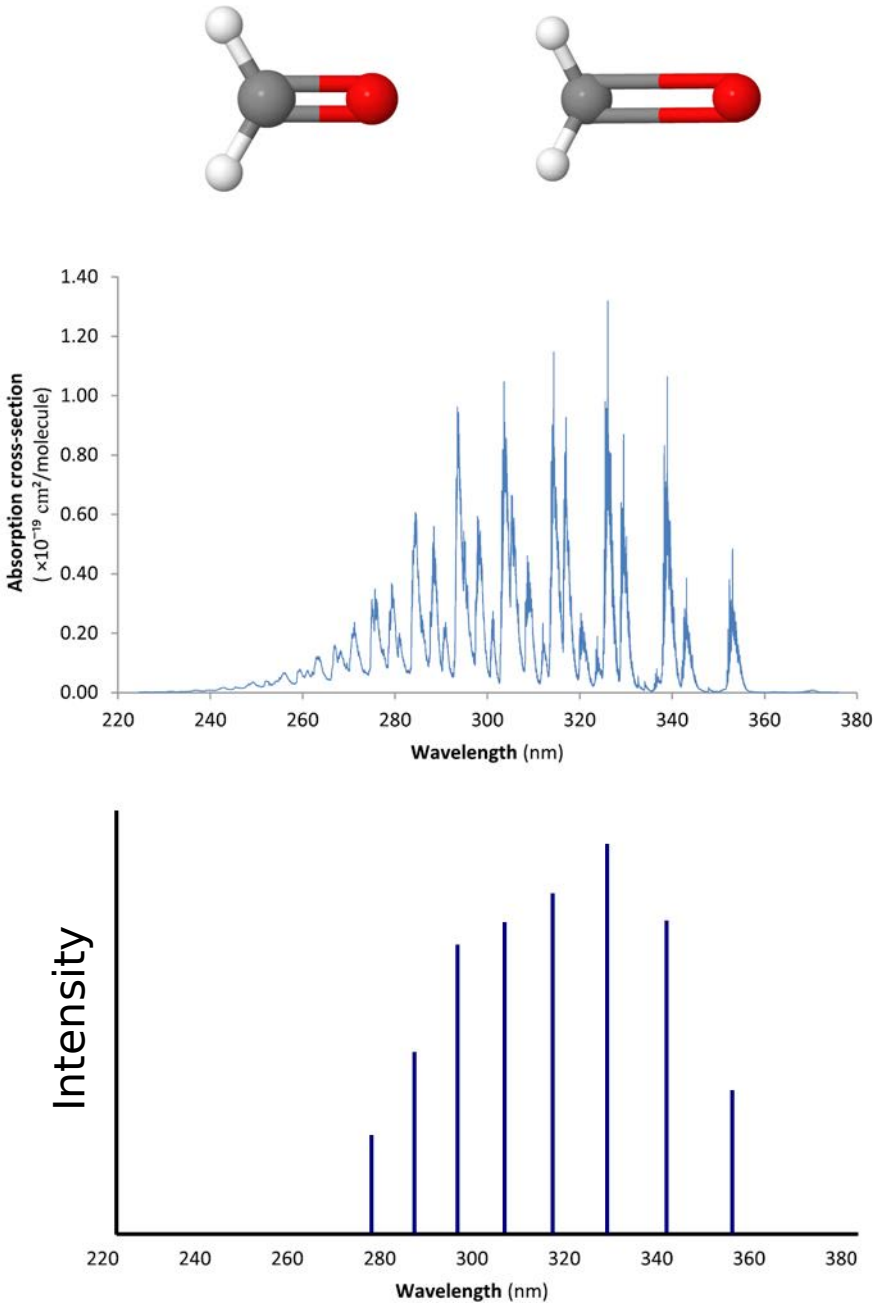

Fig. 2.2: The experimental ultra-violet absorption spectrum of formaldehyde. The top spectrum is the recorded absorption spectrum measured by Davenport *et al.* [117], showing it to be rich in vibrational structure. Below is a simplified cartoon spectrum showing only the peaks formed from the C-O stretching mode. This highlights the long progression that results from the large increase in the CO bond length.

The Franck-Condon (FC) approximation, as stated above, relies upon the electronic transition occurring very rapidly compared to the nuclear motion, with the transition moment for vibronic transitions given by:

$$\mathbf{R}_{ev} = \mathbf{R}_e \int \Psi_v'^* \Psi_v'' \mathrm{d}Q \tag{2.50}$$

with Q being a general vibrational coordinate. In the Herzberg-Teller theorem, the excitation of a non-totally symmetric vibration causes a breakdown of the FC approximation, which would state the transition moment for excitation of this vibration to be zero. To address this, the electronic transition moment, $\mathbf{R}_e$, can be expanded as a Taylor series including only the first two terms:

$$\mathbf{R}_e \simeq (\mathbf{R}_e)_{\mathrm{eq}} + \sum_i \left(\frac{\partial \mathbf{R}_e}{\partial Q_i}\right)_{\mathrm{eq}} Q_i \tag{2.51}$$

By inserting equation (2.50) into equation (2.51) one arrives at:

$$\mathbf{R}_{ev} = \int \Psi_v'^* \left[(\mathbf{R}_e)_{\mathrm{eq}} + \sum_i \left(\frac{\partial \mathbf{R}_e}{\partial Q_i}\right)_{\mathrm{eq}} Q_i\right] \Psi_v'' \mathrm{d}Q_i \tag{2.52}$$

Integrating each term separately leads to the final expression for the Herzberg-Teller theorem:

$$\mathbf{R}_{ev} = (\mathbf{R}_e)_{\mathrm{eq}} \int \Psi_v'^* \Psi_v'' \mathrm{d}Q_i + \sum_i \left(\frac{\partial \mathbf{R}_e}{\partial Q_i}\right)_{\mathrm{eq}} \int \Psi_v'^* Q_i \Psi_v'' \mathrm{d}Q_i \tag{2.53}$$

Here the first term is the same as the FC approximation and is zero when an electronic transition is forbidden. The second term however may be non-zero for a particular non-totally symmetric mode and explains the intensity for certain vibronic transitions. The intensity is then obtained from a transition to another electronic state that is symmetry allowed. This is known as "intensity borrowing".

One of the most studied examples of a vibronic transition is the absorption spectrum of benzene. The transition to the first excited state, $\tilde{A}\,^1B_{2\mathrm{u}} \leftarrow \tilde{X}\,^1A_{1\mathrm{g}}$,

is electronically forbidden and therefore $(\mathbf{R}_e)_{\text{eq}}$ in equation (2.53) is zero, and thus the 0_0^0 band is not observed [16]. The spectrum, however, shows a clear progression with a series of shoulder peaks that have been assigned to the totally symmetric a_{1g} ring breathing mode and a pair of degenerate, non-totally symmetric e_{2g} vibrations. The intensities of these peaks can be explained by the non-zero value of $\left(\frac{\partial \mathbf{R}_e}{\partial Q_i}\right)_{\text{eq}}$ in the Herzberg-Teller equation.

A final point of note is best illustrated by the absorption spectrum of formaldehyde. Whilst the $\tilde{A}\,^1A_2 \leftarrow \tilde{X}\,^1A_1$ transition is electronically forbidden by selection rules, the 0_0^0 transition is observed very weakly in the spectrum. This is because the transition is allowed by magnetic dipole selection rules [118], although typically these are insufficiently intense to be observed.

2.6 Vibronic Coupling Hamiltonian

To describe the photodynamics and features such as CoIs discussed so far, the potential energy functions are often required to be computed. The method used exclusively in this thesis to accomplish this is the vibronic coupling model Hamiltonian.

The vibronic coupling Hamiltonian, as described by Cederbaum, Koppel *et al.* [119, 120], is the diabatic expression of a potential, in terms of dimensionless (mass-frequency scaled) normal modes, $\mathbf{Q_0}$, around a reference point of interest. The Hamiltonian, $\mathbf{H}$, can therefore be written as the sum of the zeroth-order Hamiltonian and a set of diabatic coupling matrices, $\mathbf{W}$, based on a Taylor expansion series:

$$\mathbf{H} = \mathbf{H}^{(0)} + \mathbf{W}^{(0)} + \mathbf{W}^{(1)} + \dots \tag{2.54}$$

The zeroth-order Hamiltonian $\mathbf{H}^{(0)}$ is expressed as the ground state Harmonic oscillator:

$$H^{(0)} = \sum_{\alpha} \frac{\omega_\alpha}{2} \left(\frac{\delta^2}{\delta Q_\alpha^2} + Q_\alpha^2 \right) \tag{2.55}$$

where ω_α is the frequency of mode Q_α.

The zeroth-order coupling potential, $\mathbf{W}^{(0)}$, corresponds to the ground state Harmonic oscillator vertically displaced to the excitation energy, E_i:

$$W_{ij}^{(0)} = E_i \delta_{ij} \tag{2.56}$$

At the point of expansion *i.e.* FC point, it is assumed that the adiabatic potential surface is equal to that of the diabatic surface and hence $\mathbf{W}^{(0)}$ is diagonal.

The first-order potentials can be written as:

$$W_{ii}^{(1)} = \sum_{\alpha} \kappa_{\alpha}^{(i)} Q_{\alpha} \tag{2.57}$$

$$W_{ij}^{(1)} = \sum_{\alpha} \lambda_{\alpha}^{(i,j)} Q_{\alpha} \tag{2.58}$$

where the on-diagonal first-order terms, κ, expresses the distance the excited state minimum is displaced compared with the ground state minimum. The on-diagonal terms, κ, are related to the gradients of the adiabatic potential with respect to the nuclear coordinates. The off-diagonal first-order parameter, λ, defines the coupling between the electronic states:

$$\kappa_{\alpha}^{(i)} = \left\langle \phi_i \left| \frac{\delta H_{el}}{\delta Q_{\alpha}} \right| \phi_i \right\rangle \tag{2.59a}$$

$$\lambda_{\alpha}^{(i,j)} = \left\langle \phi_i \left| \frac{\delta H_{el}}{\delta Q_{\alpha}} \right| \phi_j \right\rangle \tag{2.59b}$$

Second order potentials can also be defined as:

$$W_{ii}^{(2)} = \frac{1}{2} \sum_{\alpha\beta} \gamma_{\alpha\beta}^{(i)} Q_{\alpha} Q_{\beta} \tag{2.60}$$

$$W_{ij}^{(2)} = \frac{1}{2} \sum_{\alpha\beta} \mu_{\alpha\beta}^{(i,j)} Q_{\alpha} Q_{\beta} \tag{2.61}$$

Here, the bilinear on-diagonal second-order term, $\gamma_{\alpha\beta}$, couple vibrational motion between the degrees of freedom and $\mu_{\alpha\beta}^{(i,j)}$ are second-order coupling derivatives.

For a more accurate fitting of the potential, third and fourth order terms can be included. The third order, ι, and fourth order terms, ϵ, have the following form:

$$W_{ii}^{(3)} = \frac{1}{6}\sum_{\alpha\beta\gamma} \iota_{\alpha\beta\gamma}^{(i)} Q_\alpha Q_\beta Q_\gamma \tag{2.62}$$

$$W_{ii}^{(4)} = \frac{1}{24}\sum_{\alpha\beta\gamma\delta} \epsilon_{\alpha\beta\gamma\delta}^{(i)} Q_\alpha Q_\beta Q_\gamma Q_\delta \tag{2.63}$$

Truncated forms of these terms can be expressed as:

$$W_{ii}^{(3)} = \frac{1}{6}\sum_{\alpha\beta} \iota_{\alpha\beta}^{(i)} Q_\alpha Q_\beta^2 \tag{2.64}$$

$$W_{ii}^{(4)} = \frac{1}{24}\sum_{\alpha\beta} \epsilon_{\alpha\beta}^{(i)} Q_\alpha^2 Q_\beta^2 \tag{2.65}$$

$$W_{ii}^{(4)} = \frac{1}{24}\sum_{\alpha} \epsilon_{\alpha}^{(i)} Q_\alpha^4 \tag{2.66}$$

Modes that exhibit anharmonicity can be fitted as a Morse potential of the form:

$$V(r) = D_e \left(1 - \exp[-a(r - r_e)]\right)^2 \tag{2.67}$$

One can take advantage of any symmetry present in the molecule to make certain terms in the coupling matrices vanish. These symmetry arguments can be applied to first and second-order terms, resulting in the following restrictions:

$$\kappa_i^{(\alpha)} \neq 0, \Gamma_i \supset \Gamma_A \tag{2.68a}$$

$$\lambda_i^{(\alpha\beta)} \neq 0, \Gamma_\alpha \otimes \Gamma_i \otimes \Gamma_\beta \supset \Gamma_A \tag{2.68b}$$

$$\gamma_{ij}^{(\alpha\beta)} \neq 0, \Gamma_\alpha \otimes \Gamma_\beta \otimes \Gamma_i \otimes \Gamma_j \supset \Gamma_A \tag{2.68c}$$

where Γ_α and Γ_β are the symmetries of the states and Γ_i the symmetry of the mode. Of particular interest is the symmetry restriction for κ, which implies there are only non-zero values for totally-symmetric modes. Similar restrictions also occur for λ, so that if Ψ_i and Ψ_j have different symmetries, then λ is only non-zero for non-totally symmetric modes of the correct symmetry.

Chapter 3

Quantum Calculations

Having outlined the theoretical and mathematical constructs used in modelling physical systems, attention must now be given towards methods for calculating them. Throughout this thesis, two methods were used. The first are electronic structure methods, where the non-relativistic time independent Schrödinger equation (TISE) is solved to provide the PES. The second, describes the evolution of a wavepacket across the PES and involves solving the TDSE.

3.1 Many-electron wavefunction

The basis for many electronic structure calculations originate from Hartree-Fock (HF) theory and extensions thereof. Indeed, several of the methods utilised in this thesis project initially require molecular orbitals as constructed in the HF scheme. It is therefore useful and necessary to summarise the formulation and derivation of the HF equations for many-electron wavefunctions and operators.

The overall aim of HF theory is to find approximate solutions to the TISE:

$$H\Psi = E\Psi \tag{3.1}$$

Here, H is the Hamiltonian operator for a system of N-electrons and M-nuclei with the form:

$$H = -\sum_{i=1}^{N} \frac{1}{2}\nabla_i^2 - \sum_{A=1}^{M} \frac{1}{2M_A}\nabla_A^2 - \sum_{i=1}^{N}\sum_{A=1}^{M} \frac{Z_A}{r_{iA}} + \sum_{i=1}^{N}\sum_{j>i}^{N} \frac{1}{r_{ij}} + \sum_{A=1}^{M}\sum_{B>A}^{M} \frac{Z_A Z_B}{R_{AB}} \quad (3.2)$$

Invoking the BOA [84] results in the electronic Hamiltonian, whereby the motion of the electrons depend explicitly on the electronic coordinates but only parametrically on the nuclear coordinates. As a result, one can neglect the second term in equation (3.2), the kinetic energy term for the nuclei, whilst the last term, the nuclear repulsion, becomes constant for a particular molecular geometry. From the electronic Hamiltonian:

$$H = -\sum_{i=1}^{N} \frac{1}{2}\nabla_i^2 - \sum_{i=1}^{N}\sum_{A=1}^{M} \frac{Z_A}{r_{iA}} + \sum_{i=1}^{N}\sum_{j>i}^{N} \frac{1}{r_{ij}} \quad (3.3)$$

solutions to the electronic Schrödinger equation:

$$H_{\text{elec}}\Psi_{\text{elec}} = E_{\text{elec}}\Psi_{\text{elec}} \quad (3.4)$$

can be found in the form of an electronic wavefunction that depends explicitly on electron position, but only parametrically on the nuclei. The description of an electron however not only requires three spatial coordinates, r, but also a spin coordinate, ω, which can either be spin up, $\alpha(\omega)$ or spin down, $\beta(\omega)$. This description of an electron is denoted as: $x = \{r, \omega\}$, comprising a spatial *and* a spin component. From this, one can construct a wavefunction for an N-electron system, as a function of $x_1, x_2, \ldots x_N$, such as:

$$\Psi(x_1, x_2, \ldots x_N) \quad (3.5)$$

It is vital also that any wavefunction be anti-symmetric with respect to interchanging the coordinates of any two electrons:

$$\Psi(x_1, \ldots, x_i, \ldots, x_j \ldots, x_N) = -\Psi(x_1, \ldots, x_j, \ldots, x_i \ldots, x_N) \quad (3.6)$$

Enforcing this condition also ensures, by extension, that the Pauli exclusion prin-

ciple is obeyed. From here, a many electron wavefunction can be built, where the wavefunction for each electron is described by a spin orbital, χ, that encompasses both spatial distribution and spin. For each spatial orbital, $\Psi(r)$, two spin orbitals can be formed:

$$\chi(x) = \quad \Psi(r)\alpha(\omega) \quad \text{or} \quad \Psi(r)\beta(\omega) \tag{3.7}$$

So, from a given set of K spatial orbitals $2K$ spin orbitals can be formed.

Considering a simple system, where the electron-electron repulsion is treated in an average way, the wavefunction can be written as a product of spin orbitals. This is termed a Hartree product (HP):

$$H\Psi^{\mathrm{HP}} = E\Psi^{\mathrm{HP}} \tag{3.8a}$$

$$\Psi^{\mathrm{HP}}(x_1, x_2, \ldots, x_N) = \chi_i(x_1)\chi_j(x_2)\ldots,\chi_k(x_N) \tag{3.8b}$$

Whilst this form is convenient and relatively easy to evaluate, it suffers from a major drawback of not satisfying the anti-symmetry principle, furthermore, it is an uncorrelated wavefunction. The wavefunction can be made anti-symmetric though by taking linear combinations of the HPs, which for a two electron system has the following form:

$$\Psi(x_1, x_2) = \frac{1}{\sqrt{2}}\Big[(\chi_i(x_1)\chi_j(x_2)) - (\chi_j(x_1)\chi_i(x_2))\Big] \tag{3.9}$$

and hence:

$$\Psi(x_1, x_2) = -\Psi(x_2, x_1) \tag{3.10}$$

Equation (3.9) can be re-written as a Slater determinant [121]:

$$\Psi(x_1, x_2) = \frac{1}{\sqrt{2}}\begin{vmatrix}\chi_i(x_1) & \chi_j(x_1)\\ \chi_i(x_2) & \chi_j(x_2)\end{vmatrix} \tag{3.11}$$

which for a N-electron system can be generalised to:

$$\Psi(x_1, x_2) = \frac{1}{\sqrt{N}} \begin{vmatrix} \chi_i(x_1) & \chi_j(x_1) & \cdots & \chi_k(x_1) \\ \chi_i(x_2) & \chi_j(x_2) & \cdots & \chi_k(x_2) \\ \vdots & \vdots & \ddots & \vdots \\ \chi_i(x_N) & \chi_j(x_N) & \cdots & \chi_k(x_N) \end{vmatrix} \tag{3.12}$$

Through the use of determinants, not only can the use of HPs ensure an anti-symmetric wavefunction, but the exchange correlation between the motion of two electrons with parallel spin can also be captured. It does not account for the motion between electrons of opposite spin which remains uncorrelated; a failing carried forward into HF theory.

3.2 Hartree Fock

As the TISE cannot be solved exactly, it is approximated by applying a guess wavefunction, such that:

$$\langle \Psi_{\text{guess}} | H | \Psi_{\text{guess}} \rangle = E_{\text{guess}} \tag{3.13}$$

The simplest anti-symmetric wavefunction can be constructed using a single Slater determinant. If, as is often the case, the guess wavefunction is not a true eigenfunction, then a variation principle is applied. By minimising the Rayleigh ratio:

$$\mathscr{E} = \frac{\langle \Psi^* | H | \Psi \rangle}{\langle \Psi^* | \Psi \rangle} \tag{3.14}$$

the spin orbitals that produce the 'best' form of the wavefunction (the lowest possible energy) can be found.

By minimising E_{guess}, with respect to the choice of spin orbitals, one can derive the HF equation:

$$f(i)\chi(x_i) = \varepsilon\chi(x_i) \tag{3.15}$$

with f being the Fock operator, an effective one electron operator of the following

form:

$$\hat{f} = h_1 + \sum_m J_m - K_m \tag{3.16}$$

This operator comprises an effective one electron core Hamiltonian, (h_1), to which is added a summation of the Coulomb, (J_m), and exchange, (K_m), operators:

$$h_1 = -\frac{1}{2}\nabla_i^2 - \sum_A \frac{Z_A}{r_A} \tag{3.17a}$$

$$J_m(1)\chi_a(1) = \int d\tau \chi_m^*(2)\frac{1}{r_{12}}\chi_m(2)\chi_a(1) \tag{3.17b}$$

$$K_m(1)\chi_a(1) = \int d\tau \chi_m^*(2)\frac{1}{r_{12}}\chi_m(2)\chi_a(2) \tag{3.17c}$$

The Coulomb operator is a classical term describing the repulsion between electrons, whilst the exchange operator is a quantum term arising from the anti-symmetric nature of the Slater determinant that incorporates the interaction between electrons of parallel spins. The equations above can be rewritten using "chemist's" notation to represent the electron integrals over spin orbitals. In this form:

$$J = (ii|jj)$$

$$K = (ij|ji)$$

$$h_1 = (a|h|a)$$

which leads to the energy of the ground state HF as:

$$E_0 = \sum_a^N (a|h|a) + \frac{1}{2}\sum_a^N \sum_b^N (aa|bb) - (ab|ba) \tag{3.18}$$

In order to solve equation (3.15) one might like to adopt a numerical approach, however no practical procedure exists to do so. A solution to this problem was proposed by Roothaan [122] through the introduction of a set of known basis functions

in which the molecular orbitals are expanded. By using a set of K known basis functions, the molecular orbitals can be expanded as a linear combination of atomic orbitals (LCAOs):

$$\chi_i = \sum_{\nu=1}^{K} C_{\nu i}\phi_{\nu u} \tag{3.19}$$

Equation (3.19) converts the problem of calculating the HF molecular orbitals into one of determining the expansion coefficients, $C_{\nu i}$. Substitution of equation (3.19) into the HF equations yields:

$$f(1)\sum_{\nu} C_{\nu i}\phi_{\nu}(1) = \varepsilon_i \sum_{\nu} C_{\nu i}\phi_{\nu}(1) \tag{3.20}$$

which can be re-written in matrix form as:

$$\boldsymbol{FC} = \boldsymbol{SC\varepsilon} \tag{3.21}$$

where $\boldsymbol{F}$ is the Fock matrix and $\boldsymbol{S}$ the overlap matrix:

$$F_{ba} = \langle\chi_b|\hat{f}|\chi_a\rangle \qquad \text{and} \qquad S_{ba} = \langle\chi_b|\chi_a\rangle \tag{3.22}$$

Solving this eigenvalue equation by diagonalising $\boldsymbol{F}$ should be straightforward. Nevertheless, with $\boldsymbol{F}$ depending on its own solutions, $\boldsymbol{C}$, through the orbitals, then the solution must be determined iteratively using the *self-consistent-field* (SCF) procedure.

The SCF procedure involves calculating the integrals prior to making an initial guess for the coefficients, $\boldsymbol{C}$, which may typically be generated from a simple approach such as extended Hückel theory. From this, $\boldsymbol{F}$ can be formed and then diagonalised to determine values for ε and $\boldsymbol{C}^{\mathbf{new}}$, which then allows $\boldsymbol{C}$ to be calculated. This procedure is then checked for convergence within a specific threshold. If not converged, $\boldsymbol{C}^{\mathbf{new}}$ is used to generate $\boldsymbol{F}$ and the process is continually repeated until either the convergence criteria is met or the number of maximum iterations is

reached and the SCF has failed to converge.

The formal scaling of HF is N^4, where N is the number of basis functions, although in practice this can be reduced to N^2. This low computational cost makes HF calculations quick to perform. However, whilst HF gives reasonable descriptions of molecules around their equilibrium geometry, it predicts qualitatively wrong ionisation energies (Koopman's theorem), in addition to describing dissociative processes very poorly. This major shortcoming results from neglecting electron correlation, which results from the single-determinant form used for the wavefunction.

The electron correlation energy is generally defined as the difference between the HF energy and the exact energy *i.e.*:

$$E_{\text{corr}} = \mathscr{E}_0 - E_0 \tag{3.23}$$

and is commonly attributed to the exclusion of any correlation between electrons of opposite spin. This incorrect treatment of motion between electrons of opposite spins can also be referred to as Coulomb correlation and arises from the r_{ij}^{-1} term in the electronic Schrödinger equation. By considering the electron density, this Coulomb correlation can be thought of as a region around each electron where the probability of finding another electron is reduced. This Coulomb hole (or Fermi hole for electrons of parallel spin) is important for preventing electrons from coming too close to each other. This concept of holes is discussed in more detail within the constructs of density functional theory, Section 3.9.1. Needless to say, it is this lack of Coulomb hole in HF that results in an underestimation of the inter-electronic distances. This culminates in an increase in repulsion energy and hence an increase in the total energy of the system.

The correlation energy can also be classed as either dynamic or static. Dynamic correlation operates over a short range and accounts for the instantaneous repulsion of electrons, which is particularly true of electrons in the same spatial orbital. Static

correlation is longer range and arises where there is a mixing of near degenerate wavefunctions *i.e.* the electronic wavefunction is not dominated by a single electronic configuration. Here, the use of a single Slater determinant form for the wavefunction, like that used in HF, is not adequate to describe the system. Improvements to HF theory mainly focus on recovering this electron correlation.

Where the HF determinant is satisfactory, thus static correlation is small, post-HF methods focus on recovering the dynamic correlation. Being based on HF as a reference determinant, these methods are often also called single-reference methods and include configuration interaction, perturbation theory and coupled cluster theories. Where there is significant static correlation it becomes necessary to employ multi-reference determinants, *e.g.* multi-configurational self-consistent field, MCSCF. These methods however will not account for dynamic correlation as easily. It is possible to treat static and dynamic correlation simultaneously though through the complete active space with second-order perturbation (CASPT2) and multi-reference configuration interaction (MRCI) methods.

All calculations in this thesis used theories designed to recover the electron correlation. The aims in choosing these methods are to provide accurate excited state energies and more reliable PESs. An outline of configuration interaction provides a good starting point for introducing post-HF theories and is also useful for understanding the CASSCF method outlined in Section 3.7 and used in the Chapter 5.

3.3 Configuration Interaction

By solving Roothaan's equation in a finite basis set we obtain $2K$ spin orbitals, $\{\chi_i\}$. In HF, a single determinant is formed from the N-lowest spin orbitals representative of the ground state, $|\Psi_0\rangle$.

From these $2K$ spin orbitals, however, can be constructed many more deter-

Table 3.1: The structure of the full CI matrix with matrix elements between different determinants. This matrix will extend up to N-tuply excited determinant. Shown underneath are the explicit forms for the matrix elements and their relation to the symbolic form.

$$
\begin{array}{c}
 \\
 \\
\langle\Psi_0| \\
\langle S| \\
\langle D| \\
\langle T| \\
\langle Q| \\
\vdots
\end{array}
\begin{array}{c}
\begin{array}{cccccc}
|\Psi_0\rangle & |\Psi_a^r\rangle & |\Psi_{ab}^{rs}\rangle & |\Psi_{abc}^{rst}\rangle & |\Psi_{abcd}^{rstu}\rangle & \dots \\
 & |S\rangle & |D\rangle & |T\rangle & |Q\rangle & \dots
\end{array} \\
\left[\begin{array}{cccccc}
\langle\Psi_0|\mathscr{H}|\Psi_0\rangle & 0 & \langle\Psi_0|\mathscr{H}|D\rangle & 0 & 0 & \dots \\
0 & \langle S|\mathscr{H}|S\rangle & \langle S|\mathscr{H}|D\rangle & \langle S|\mathscr{H}|T\rangle & 0 & \dots \\
\langle D|\mathscr{H}|\Psi_0\rangle & \langle D|\mathscr{H}|S\rangle & \langle D|\mathscr{H}|D\rangle & \langle D|\mathscr{H}|T\rangle & \langle D|\mathscr{H}|Q\rangle & \dots \\
0 & \langle T|\mathscr{H}|S\rangle & \langle T|\mathscr{H}|D\rangle & \langle T|\mathscr{H}|T\rangle & \langle T|\mathscr{H}|Q\rangle & \dots \\
0 & 0 & \langle Q|\mathscr{H}|D\rangle & \langle Q|\mathscr{H}|T\rangle & \langle Q|\mathscr{H}|Q\rangle & \dots \\
\vdots & \vdots & \vdots & \vdots & \vdots & \vdots
\end{array}\right]
\end{array}
$$

$$\langle S|\mathscr{H}|T\rangle \leftrightarrow \langle\Psi_a^r|\mathscr{H}|\Psi_{cde}^{tuv}\rangle$$

$$\langle D|\mathscr{H}|D\rangle \leftrightarrow \langle\Psi_{ab}^{rs}|\mathscr{H}|\Psi_{cd}^{tu}\rangle$$

minants, up to and including N-tuply excited determinants (*i.e.* singly, doubly, triply...*etc.*). From this, the exact wavefunction can be constructed as linear combinations of all these determinants:

$$\Psi = c_0\Psi_0 + \sum_{a,r} C_a^r|\Psi_a^r\rangle + \sum_{\substack{a<b\\r<s}} c_{ab}^{rs}|\Psi_{ab}^{rs}\rangle + \sum_{\substack{a<b<c\\r<s<t}} c_{acb}^{rst}|\Psi_{abc}^{rst}\rangle + \dots \tag{3.24}$$

This is the full configuration interaction (CI) wavefunction. Equation (3.24) can be simplified into a more symbolic form with the structure:

$$\Psi = c_0\Psi_0 + c_S|S\rangle + c_D|D\rangle + c_T|T\rangle + c_Q|Q\rangle + \cdots \tag{3.25a}$$

$$\Psi^{\mathrm{CI}} = (1 + C_1 + C_2 + C_3 + \dots)\Psi^{\mathrm{HF}} \tag{3.25b}$$

Using this notation, the full CI matrix is expressed in Table 3.1

From Table 3.1 one can extract important rules when calculating the elements of the CI matrix. Firstly, the coupling between the HF ground state and single

excitations is zero, this is a result of Brillouin's theorem [123]. Double excitations mix directly with $|\Psi_0\rangle$ and since singles can interact with doubles, singles can interact indirectly with $|\Psi_0\rangle$. The matrix elements between Slater determinants that differ by more than two spin orbitals are also zero, thus singles do not mix with quadruples and so on.

It quickly becomes apparent that calculating the full CI of a system is unfeasible save for very small molecules due to the vast number of possible determinants. As such, CI is usually truncated at single/double excitations, but even this can be very computationally expensive, with formal scaling of N^6.

3.4 Møller-Plesset Perturbation Theory

Another way through which electron correlation can be recovered is by applying many-body perturbation theory, MBPT. This method was used in Chapter 5 to calculate the optimised structure of phenol. The analytical functions available for this method also made it ideal for calculating derivatives and Hessians.

A quantum theory for time-independent perturbation was derived by Schrödinger, who himself based it upon earlier work by Lord Rayleigh, and so is commonly referred to as Rayleigh-Schrödinger perturbation theory [124, 125]. The derivation of MBPT is shown in Appendix C.1. This, however, only describes the general many-body perturbation theory. The next step is to apply this in electronic structure theories. Møller and Plesset suggested using HF as the starting point [126]. Within Møller-Plesset perturbation theory (MPPT), the Hamiltonian is partitioned as:

$$\hat{H} = \hat{H}_0 + \hat{V} \tag{3.27}$$

with the zeroth-order Hamiltonian being that of the Fock operator $\hat{F}$:

$$H_0 = \sum_i \hat{F}(i) = \sum_i \hat{h}(i) + \sum_{ij} \hat{J}_i - \hat{K}_{ij} \tag{3.28}$$

which is just equation (3.16) with J and K given by equations (3.17b) and (3.17c).

Zeroth-Order

At the zeroth-order, the wavefunction is just that of the HF single determinant, Φ_0 and so the zeroth-order energy is provided by the sum of the occupied (occ) orbital energies:

$$E_0^0 = \sum_i^{\text{occ}} \varepsilon_i \tag{3.29}$$

First-Order

The perturbation operator $\hat{V}$ can be expressed as $\hat{H} - H^0$ which is given by:

$$\hat{H} - H^0 = \sum_{i>j} \frac{1}{r_{ij}} - \sum_{ij} \hat{J}_i - \hat{K}_{ij} \tag{3.30}$$

From here, the first-order correction to the energy is the expectation value of the HF determinant over the perturbation operator:

$$E_0^{(1)} = \langle \Phi_0 | \hat{V} | \Phi_0 \rangle \tag{3.31}$$

$$= -\frac{1}{2} \sum_{a,b}^{\text{occ}} (aa|bb) - (ab|ba) \tag{3.32}$$

Summing the zeroth and first-order of the energy leads to:

$$\begin{aligned} E_n &= E_n^{(0)} + E_n^{(1)} \\ &= \sum_i^{\text{occ}} \varepsilon_i - \frac{1}{2} \sum_{ab} (aa|bb) - (ab|ba) \\ &= \sum_a^{\text{occ}} \left(h_{aa} + \sum_b^{\text{occ}} (aa|bb) - (ab|ba) \right) - \frac{1}{2} \sum_{a,b}^{\text{occ}} (aa|bb) - (ab|ba) \\ &= \sum_a^{\text{occ}} h_{aa} + \frac{1}{2} \sum_{a,b}^{\text{occ}} (aa|bb) - (ab|ba) \\ &= E_{\text{HF}} \end{aligned} \tag{3.33}$$

This important result shows that within MPPT, the first correction to the energy simply yields the HF energy *i.e.* $E(\text{MP1}) = E(\text{HF})$, an occurrence also noted by Møller and Plesset [126].

Second-Order

The revelation that the first-order energy correction returns the HF energy indicates that it is only from the second-order onwards that corrections to HF are obtained. This second-order correction, denoted MP2, is the most widely used class of MPPT in quantum chemical calculations. Referring back to MBPT in Appendix C.1, the second-order correction to the energy is provided by equation (C.12) and requires knowledge of the first-order correction to the wavefunction. This can be calculated by using the following expansion of the wavefunction:

$$\Psi_n^{(1)} = \sum_{\substack{a>b \\ r>s}} C_{n,abrs}^{(1)} \Psi_{ab}^{rs} \tag{3.34}$$

where the coefficients, C, are evaluated through:

$$C_{n,abrs}^{(1)} \langle \Psi_{ab}^{rs} | \Psi_n^{(1)} \rangle = \sum_{\substack{a>b \\ r>s}} \frac{\langle \Psi_{ab}^{rs} | \Psi_n^{(0)} \rangle}{\epsilon_a + \epsilon_b - \epsilon_r - \epsilon_s} \tag{3.35}$$

Substituting this into the second-order energy equation, provides the second-order correction to the energy:

$$E_0^{(2)} = -\frac{1}{4} \sum_{abrs} \frac{|\langle ab||rs\rangle|^2}{\epsilon_a + \epsilon_b - \epsilon_r - \epsilon_s} \tag{3.36}$$

hence the total MP2 energy is given as: $\text{E(MP2)} = \text{E(HF)} + \text{E}_\text{c}\text{(MP2)}$. It is important to note however that MP2 energy is not variational, unlike the HF energy. It is possible to continue to higher order corrections and implement third-order corrections (MP3) [127], fourth-order corrections (MP4) [128] and up to n-order corrections. At this point though the computational intensity far outweighs the

magnitude of the correction. For example, the third-order correction to the energy has the following form:

$$\begin{aligned} E_0^{(3)} = \frac{1}{8}\sum_{a,b,c,d}^{\text{occ}}\sum_{r.s}^{\text{vir}} \frac{\langle ab||rs\rangle\langle rs||cd\rangle\langle cd||ab\rangle}{(\epsilon_r+\epsilon_s-\epsilon_a-\epsilon_b)(\epsilon_r+\epsilon_s-\epsilon_c-\epsilon_d)} \\ +\frac{1}{8}\sum_{a,b}^{\text{occ}}\sum_{r.s,t,u}^{\text{vir}} \frac{\langle ab||rs\rangle\langle rs||tu\rangle\langle tu||ab\rangle}{(\epsilon_r+\epsilon_s-\epsilon_a-\epsilon_b)(\epsilon_t+\epsilon_u-\epsilon_a-\epsilon_b)} \\ +\sum_{a,b,c}^{\text{occ}}\sum_{r.s,t}^{\text{vir}} \frac{\langle ab||rs\rangle\langle cs||tb\rangle\langle rt||ac\rangle}{(\epsilon_r+\epsilon_s-\epsilon_a-\epsilon_b)(\epsilon_r+\epsilon_t-\epsilon_a-\epsilon_c)} \end{aligned} \tag{3.37}$$

The use of MP2 is a popular post-HF method, mainly a result of its relatively low computational cost, which is formally N^5, but in practice can be reduced. It does suffer however from the same drawbacks as HF, perhaps not surprising as the perturbation is itself acting on the HF determinant. The main approach to perturbation theory usually requires that the perturbation itself is very small and so the use of MP2 for situations where the perturbation is large, such as dissociation, render it a poor choice of method. A review on Møller-Plesset theory further outlines its successes and failings [129].

3.5 Coupled Cluster Theory

Coupled cluster (CC) theory is another post-HF method through which the electron correlation can be recovered. This method is known to yield highly accurate results but has the forfeit of high scaling and increased computational effort. The formal scaling for CC ranges from N^8 to N^6 depending on the variant used. The high accuracy of this method made it ideal for the excited state and ionisation calculations in Chapter 4. Even where different methods were employed, such as in Chapters 5 and 6, CC methods were still provided benchmark calculations to compare the results of other methods with. The lack of analytical Hessians and high computational cost, however, rendered it useful for single point energy calculations only.

The initial concept of CC theory is rooted in physics and was introduced by Coester and Kümmel as a way to calculate nuclear binding energies [130, 131]. The transition of the theory to electrons and electronic structure theory was formulated firstly by Čížek and then by Paldus *et al.* [132–134]. From here, development and program implementation of the CC equations was overseen by Bartlett and Purvis [135], Pople *et al.* [136] and then again by Purvis and Bartlett [137].

The concept of CC is compared to that of MBPT (see Section 3.4) in particular MPPT [127]. Perturbative methods will typically include all terms, but only to a given a order *i.e.* to second-order only results in MP2, third-order MP3 and so forth [138, 139]. The CC approach however includes corrections of a given type to infinite order [140]. Similarities and equivalences to CI methods can also be shown.

The starting point of CC theory is to consider an excitation operator, $\mathbf{T}$:

$$\mathbf{T} = \mathbf{T_1} + \mathbf{T_2} + \mathbf{T_3} + \ldots + \mathbf{T}_{\mathbf{N}_{\text{elec}}} \tag{3.38}$$

Within this scheme, $\mathbf{T_i}$ is an operator that acts on the HF reference wavefunction such that all the i^{th} excited Slater determinants are generated. The equations below show, by way of an example, $\mathbf{T_1}$ and $\mathbf{T_2}$ which will generate all the singly and doubly excited states, respectively:

$$T_1\Phi_0 = \sum_{i}^{\text{occ}} \sum_{a}^{\text{vir}} t_i^a \Phi_i^a \tag{3.39a}$$

$$T_2\Phi_0 = \sum_{i<j}^{\text{occ}} \sum_{a<b}^{\text{vir}} t_{ij}^{ab} \Phi_{ij}^{ab} \tag{3.39b}$$

Here the expansion coefficients, t, are known as amplitudes. In contrast to CI methods, CC methods use an exponential wavefunction, which has the direct advantage of ensuring the method is size extensive:

$$\Psi_{\text{cc}} = \mathrm{e}^{\mathbf{T}}\Phi_0 \tag{3.40a}$$

$$e^{\mathbf{T}} = \mathbf{1} + \mathbf{T} + \frac{1}{2}\mathbf{T^2} + \frac{1}{6}\mathbf{T^3} + \ldots = \sum_{k=0}^{\infty} \frac{1}{K!}\mathbf{T^K} \tag{3.40b}$$

Combining equations (3.38) and (3.40b) results in the exponential operator being rewritten as:

$$\begin{aligned} e^{\mathbf{T}} = \mathbf{1} + \mathbf{T_1} + \left(\mathbf{T_2} + \frac{1}{2}\mathbf{T_1^2}\right) + \left(\mathbf{T_3} + \mathbf{T_2 T_1} + \frac{1}{6}\mathbf{T_1^3}\right) \\ + \left(\mathbf{T_4} + \mathbf{T_3 T_1} + \frac{1}{2}\mathbf{T_2 T_1^2} + \frac{1}{24}\mathbf{T_1^4}\right) \end{aligned} \tag{3.41}$$

where, $\mathbf{1}$ generates the HF reference state and $\mathbf{T_1}$ is the operator generating all singly excited states. The first parenthesised term highlights the two possible ways for doubly excited states to be formed. These can either be connected (also known as pure) doubles, $\mathbf{T_2}$ or disconnected (also known as product) doubles, $\mathbf{T_1^2}$. The physical meaning of these two forms can be represented (using quadruples as an example) as the connected type, $\mathbf{T_4}$, being four electrons interacting simultaneously, while the disconnected form, such as $\mathbf{T_2^2}$, can be viewed as two non-interacting pairs of interacting electrons.

Using equation (3.40) the Schrödinger equation now has the form:

$$\hat{H} e^{\mathbf{T}} \Phi_0 = E e^{\mathbf{T}} \Phi_0 \tag{3.42}$$

Following the approach taken for Hartree-Fock and other methods, the next logical step would be to use the expectation value of the wavefunction to calculate the energy and apply the variational principle to obtain the amplitudes:

$$E_{\mathrm{CC}}^{\mathrm{var}} = \frac{\langle \Psi_{\mathrm{CC}} | \hat{H} | \Psi_{\mathrm{CC}} \rangle}{\langle \Psi_{\mathrm{CC}} | \Psi_{\mathrm{CC}} \rangle} = \frac{\langle e^{\mathbf{T}} \Phi_0 | \hat{H} | e^{\mathbf{T}} \Phi_0 \rangle}{\langle e^{\mathbf{T}} \Phi_0 | e^{\mathbf{T}} \Phi_0 \rangle} \tag{3.43a}$$

$$E_{\mathrm{CC}}^{\mathrm{var}} = \frac{\langle (\mathbf{1} + \mathbf{T} + \frac{1}{2}\mathbf{T^2} \cdots \frac{1}{N!}\mathbf{T^N}) \Phi_0 | \hat{H} | (\mathbf{1} + \mathbf{T} + \frac{1}{2}\mathbf{T^2} \cdots \frac{1}{N!}\mathbf{T^N}) \Phi_0 \rangle}{\langle (\mathbf{1} + \mathbf{T} + \frac{1}{2}\mathbf{T^2} \cdots \frac{1}{N!}\mathbf{T^N}) \Phi_0 | (\mathbf{1} + \mathbf{T} + \frac{1}{2}\mathbf{T^2} \cdots \frac{1}{N!}\mathbf{T^N}) \Phi_0 \rangle} \tag{3.43b}$$

Expansion of these equations results in a series of non-vanishing terms up to $\mathrm{N_{elec}}$ which makes the variational CC approach unwieldy [141].

Instead the standard procedure involves projecting the CC equation onto the reference wavefunction, multiplying on the left by Φ_0 and integrating:

$$\begin{aligned}\langle\Phi_0|\hat{H}\mathrm{e}^{\mathbf{T}}|\Phi_0\rangle &= E_{\mathrm{CC}}\langle\Phi_0|\mathrm{e}^{\mathbf{T}}\Phi_0\rangle \\ \langle\Phi_0|\hat{H}\mathrm{e}^{\mathbf{T}}|\Phi_0\rangle &= E_{\mathrm{CC}}\langle\Phi_0|(\mathbf{1}+\mathbf{T_1}+\mathbf{T_2}+\ldots)\Phi_0\rangle \\ E_{\mathrm{CC}} &= \langle\Phi_0|\hat{H}\mathrm{e}^{\mathbf{T}}|\Phi_0\rangle\end{aligned} \tag{3.44}$$

Expanding out the exponential operator as done above, with the knowledge the Hamiltonian contains only one and two electron operators, leads to the following equation for the CC energy:

$$\begin{aligned}E_{\mathrm{CC}} &= \langle\Phi_0|\hat{H}\left(\mathbf{1}+\mathbf{T_1}+\mathbf{T_2}+\frac{1}{2\mathbf{T_1^2}}\right)|\Phi_0\rangle \\ E_{\mathrm{CC}} &= \langle\Phi_0|\hat{H}|\Phi_0\rangle + \langle\Phi_0|\hat{H}|\mathbf{T_1}\Phi_0\rangle + \langle\Phi_0|\hat{H}|\mathbf{T_2}\Phi_0\rangle + \frac{1}{2}\langle\Phi_0|\hat{H}|\mathbf{T_1^2}\Phi_0\rangle \\ E_{\mathrm{CC}} &= E_0 + \sum_i^{\mathrm{occ}}\sum_a^{\mathrm{vir}} t_i^a\langle\Phi_0|\hat{H}|\Phi_i^a\rangle + \sum_{i<j}^{\mathrm{occ}}\sum_{a<b}^{\mathrm{vir}}(t_{ij}^{ab}+t_i^a t_j^b - t_i^b t_j^a)\langle\Phi_0|\hat{H}|\Phi_{ij}^{ab}\rangle\end{aligned} \tag{3.45}$$

Firstly, one notices that the once infinite expansion of the exponential operator now terminates at $\mathbf{T_2}$. Taking the orbitals used to construct the Slater determinant as the HF orbitals, then the first matrix elements in equation (3.45) are zero due to Brillouin's theorem. This also results in the second matrix elements being the two electron integrals over the MOs:

$$E_{\mathrm{CC}} = E_0\sum_{i<j}^{\mathrm{occ}}\sum_{a<b}^{\mathrm{vir}}(t_{ij}^{ab}+t_i^a t_j^b - t_i^b t_j^a)(\langle\phi_i\phi_j|\phi_a\phi_b\rangle - \langle\phi_i\phi_j|\phi_a\phi_b\rangle) \tag{3.46}$$

The end result is that the CC correlation energy can be obtained using only the two electron integrals and the singles and doubles amplitudes. All that remains are equations for determining the amplitudes. The approach taken is initially similar to that for the energy, namely projecting the Schrödinger equation onto the space of (singly, doubly, triply and so forth) excited Slater determinants. From here, however, a similarity transformation of the Hamiltonian is carried out by multiplying on the

left by a de-excitation operator, $e^{-\mathbf{T}}$:

$$e^{-\mathbf{T}}\hat{H}e^{\mathbf{T}}\Phi_0 = E_{\mathrm{CC}}\Phi_0 \tag{3.47}$$

From here, the energy equation can be easily obtained through multiplying on the left with Φ_0^* and integrating:

$$E_{\mathrm{CC}} = \langle\Phi_0^*|e^{-\mathbf{T}}\hat{H}e^{\mathbf{T}}|\Phi_0\rangle \tag{3.48}$$

The action of the de-excitation operator on the reference Φ_0^* is not physically possible and so the above equation becomes identical to equation (3.44). The amplitudes themselves are obtained by multiplying with an excited state:

$$\begin{aligned}\langle\Phi_m^e|e^{-\mathbf{T}}\hat{H}e^{\mathbf{T}}|\Phi_0\rangle &= 0\\ \langle\Phi_{mn}^{ef}|e^{-\mathbf{T}}\hat{H}e^{\mathbf{T}}|\Phi_0\rangle &= 0\\ \langle\Phi_{mnl}^{efg}|e^{-\mathbf{T}}\hat{H}e^{\mathbf{T}}|\Phi_0\rangle &= 0\end{aligned} \tag{3.49}$$

The first equation results from multiplying with a singly excited state, Φ_m^e. This time, the action of the de-excitation operator on Φ_m^e simply produces the reference wavefunction, in addition to the excitation operator, which produces the singly excited state:

$$\begin{aligned}\langle\Phi_m^e|e^{-\mathbf{T}}\hat{H}e^{\mathbf{T}}|\Phi_0\rangle &= 0\\ \langle\Phi_m^e(\mathbf{1}-\mathbf{T_1})|\hat{H}|\mathbf{1}+\mathbf{T_1}+\left(\mathbf{T_2}+\frac{1}{2}\mathbf{T_1^2}\right)+\left(\mathbf{T_3}+\mathbf{T_2T_1}+\frac{1}{6}\mathbf{T_1^3}\right)\Phi_0\rangle &= 0\end{aligned} \tag{3.50}$$

The terms in equation (3.50) are all that remain in the expansion when applying Brillouin's theorem and making use of a Hamiltonian containing only one and two electron integrals. A similar approach, whereby $e^{-\mathbf{T}}$ acts upon Φ_{mn}^{ef}, generates another set of coupled equations.

It is important to note that thus far the formulation of CC methods have been exact. The inclusion of all cluster operators up to, and including $\mathbf{T_N}$, is equivalent

to full CI, an outcome that is unfeasible for use in most molecular systems. This demands truncation of the cluster operator to some excitation level. Any truncation, however, will render the amplitude equations as non-exact, hence making both the amplitudes and the energy approximate. The level of this approximation is dependent on the number of terms included in the cluster operator.

Inclusion of only the $\mathbf{T_1}$ operator offers no improvement over HF, mainly due to the zero matrix elements between the HF determinant and singly excited state. The simplest level of approximation therefore is to take the cluster operator as being $\mathbf{T} = \mathbf{T_2}$, the coupled cluster doubles (CCD) theory. Including both single and double excitations *i.e.* $\mathbf{T} = \mathbf{T_1} + \mathbf{T_2}$ results in the coupled cluster singles and doubles theory (CCSD), the most commonly used form in electronic structure calculations. It is possible to continue further and add triples ($\mathbf{T} = \mathbf{T_1} + \mathbf{T_2} + \mathbf{T_3}$) to the CCSDT model [142–147]. By this point though, the model exceeds the computational expenses of the analogous CISDT model.

3.5.1 Equation of Motion - Coupled Cluster

An extension of the CC model allows one to calculate the excited states of a system. This made it the method of choice for use in Chapter 4 and also as a standard to compare the excited state energies of other methods against in Chapter 5 and 6.

The formulation of equation of motion coupled cluster, (EOM-CC) is generally outlined as follows [148, 149]. One can form the excited state wavefunction Ψ_K as:

$$\Psi_K = R_K \mathrm{e}^T |\phi_0\rangle \tag{3.51}$$

where R_K and T are operators defining the relation between the reference function (ϕ_0) and a set of determinants:

$$\{\mathbf{\Phi}\} = \{\Phi_1, \Phi_2, \ldots, \Phi_n\} \tag{3.52a}$$

$$T|\Phi_0\rangle = \sum_{i=1}^{n} t_i|\Phi_i\rangle \qquad R|\Phi_0\rangle = \sum_{i=0}^{n} r_i|\Phi_i\rangle \tag{3.52b}$$

One can then re-write the Schrödinger equation for the K^{th} excited state:

$$\bar{H}R_K|\Phi_0\rangle = E_K R_K|\Phi_0\rangle \tag{3.53}$$

where, $\bar{H}$ is the similarity transformed Hamiltonian, which is constructed from a set of non-linear CC equations:

$$\langle\Phi_i|\bar{H}|\Phi_0\rangle = 0 \tag{3.54}$$

From the diagonalisation of equation (3.53), the eigenvalues and eigenvectors can be obtained, hence equation (3.53) then becomes an eigenvalue problem:

$$\bar{\boldsymbol{H}}\boldsymbol{R_K} = E_K R_K \tag{3.55}$$

which can be transformed so the eigenvalues become energies of excitations from the reference state: $\omega_{\mathbf{K}} = \mathbf{E_K} - \mathbf{E_0}$:

$$(\bar{H} - 1E_0)R_K = \omega_R R_K \tag{3.56}$$

Simplified equations, with reduced computational cost that make use of partitioning methods have also been derived [150]. These produce excitation energies with a small error compared with full EOM-CCSD.

The EOM-CCSD method, in addition to obtaining excited states, has also been developed to allow calculation of ionisation potentials, EOM-IP-CCSD [151–153] and electron attachment, EOM-EA-CCSD [154].

3.6 Multi-Configurational Self Consistent Field

The single determinant nature of HF and the post-HF methods discussed so far do not account for static correlation. For systems where more than one reference determinant is required, the need for multi-configurational methods becomes cru-

cial. This was found to be the case for the singlet excited states and ionised states in phenol (Chapter 5) and required the use of a multi-determinant method. The following outlines the commonly used theories.

One can consider a multi-determinant wavefunction containing a small number of configurations that have been specifically selected. To construct these configurations, orbitals that minimise the energy need to be used. This is the basis of the multi-configurational self-consistent field (MCSCF) method [155].

In MCSCF, the wavefunction is the truncated CI expansion:

$$|\Psi_{\mathrm{MCSCF}}\rangle = \sum_I c_I |\Psi_I\rangle \tag{3.57}$$

where the coefficients (c_I) and the orbitals are *both* optimised. This allows for more accurate calculations with a small number of configuration state functions (CSF). CSFs are linear combinations of excited determinants that are eigenfunctions of the spin $\hat{S}^2$ operator.

Taking the CI approach, but using a multi-determinant reference state, gives rise to the multi-reference configuration interaction (MRCI) method. Here the excitations are no longer from a single determinant (in comparison with standard CI with a HF reference single determinant) but are from all the determinants in the MCSCF wavefunction. This method however scales rapidly by a factor related to the number of configurations included. This means that even MRCI with single and double excitations can be very computationally expensive, making it impractical for use on the molecules studied in this thesis.

A welcome solution would be to choose a subset of orbitals from the multi-determinant reference state upon which a CI can be performed. A common method using this concept is the complete active space self consistent field (CASSCF) approach, which was the method used in Chapter 5 for studying phenol.

3.7 Complete Active Space

In the CASSCF scheme [156], a subset of molecular orbitals are chosen, defined as the active space, from which configurations are built. A full CI is then performed within the active space. The spin orbitals are split into three classes, as shown in Figure 3.1.

Inactive Orbitals: Lower energy orbitals, not involved in the active space and are doubly occupied in each Slater determinant.

Active Orbitals: The selected orbitals which are involved in the CSFs and from which all possible configurations are constructed. Their occupation varies during the calculation.

Virtual Orbitals: The remaining orbitals within orbital space as defined from the basis set. They remain unoccupied throughout the CAS calculation.

The selection of the active space is crucial in the accuracy of the calculation, but considerations of computational efficiency also need to be included. This leads to the question of how to select the appropriate active space.

The active space should include all orbitals where the occupation number changes significantly or differs greatly from either two or zero. Typically the selection will include valence orbitals that are excited and subsequent virtual orbitals that are likely to become populated.

However, since the number of CSFs scales largely with the number of active orbitals [157] the selection has to be relatively small (typically $\sim 15 - 16$ active orbitals at most), so selecting the right orbitals is vital. Such a restriction made this method unsuitable for calculating the large aromatic molecules in Chapter 4 and 6, where a large active space was needed.

One major shortcoming of the CASSCF method is its failure sometimes to properly account for dynamic correlation. This depends upon the orbitals chosen, or

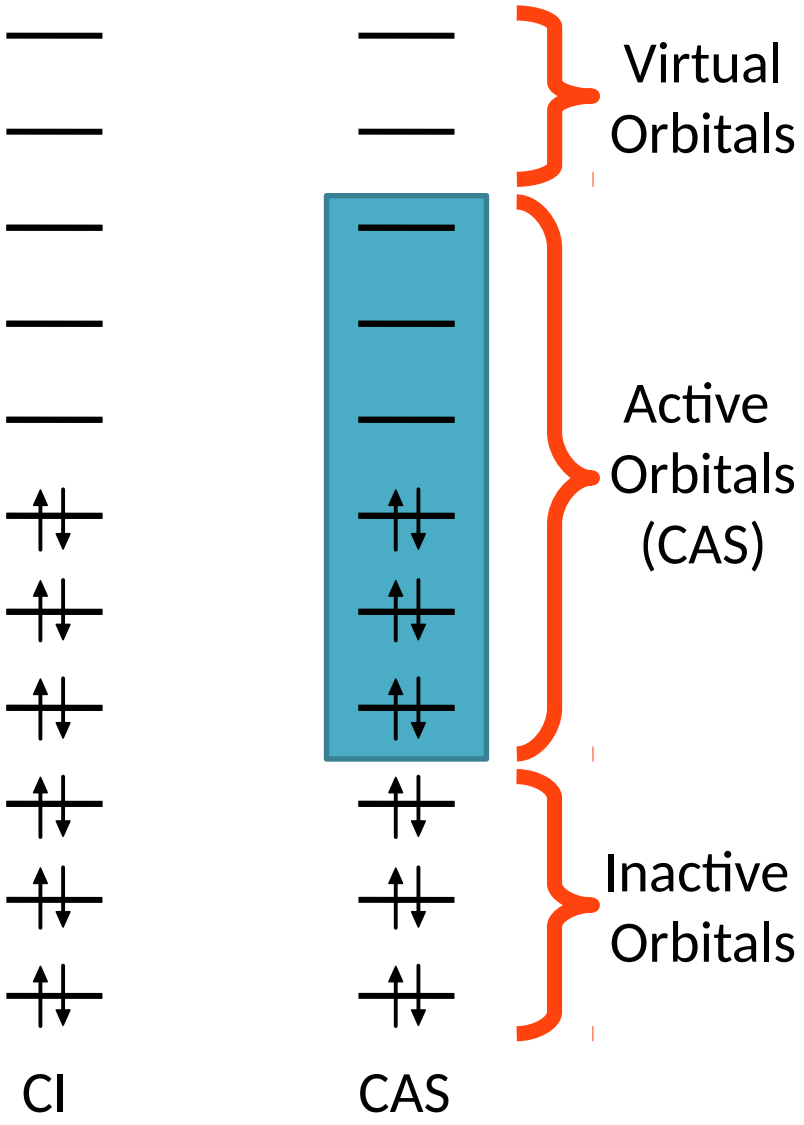

Fig. 3.1: A schematic illustrating the partitioning of orbitals within the complete active space (CAS) method. The orbitals contained within the blue box highlight the choice of active space, comprising three occupied and three unoccupied orbitals. Occupied orbitals not included within the CAS are referred to as inactive orbitals, whilst any unoccupied orbitals outside the CAS are the virtual orbitals. A comparison with configuration interaction (CI), whereby excitations from *all* orbitals are included, is shown left.

neglected, from the active space. A more complete description is therefore needed to address this failing.

Complete Active Space Perturbation Theory Second-Order

An extension to CASSCF that improves upon the accuracy of the calculation, by including dynamic correlation, is complete active space perturbation theory second-order, (CASPT2) [158]. The formulation of this method can be found in Appendix C.2. CASPT2 provides a good description of excited states, at reasonable computational expense.

3.8 Basis Set

For any quantum chemical calculation, the use of a basis set is paramount as a means to construct the molecular orbitals through a set of functions combined in a linear fashion, as described in Section 3.1. Generally these functions are located on the atom centres. In principle, this expansion of MOs as a set of functions is *exact* if the basis set is complete. A complete basis set however contains an infinite number of functions, so one is forced to consider only using a set of finite functions. The size of the basis set used directly influences the quality of the wavefunction and hence the accuracy of the wavefunction [159]. All calculations used throughout this thesis included a basis set, with several variations used depending upon the system being studied. An outline of the different basis sets and extensions are therefore given.

Two types of basis functions are commonly used. Initially, Slater-type orbitals (STOs) were employed mainly due to their similarity to the 1s orbital of hydrogen and are of the form [160]:

$$\mathrm{S}^{\zeta}_{nlm}(r,\theta,\varphi) = \mathrm{N} r^{n-1} \mathrm{e}^{-\zeta r} \mathrm{Y}^{m}_{l}(\theta,\varphi) \tag{3.58}$$

where N is a normalisation constant and $\mathrm{Y}^{m}_{l}(\theta,\varphi)$ are spherical harmonics. Whilst

this form provides a physically meaningful description for MOs, the computational cost of calculating the required integrals is incredibly large.

The second type are Gaussian-type orbitals (GTOs) with the following forms for different coordinates [161]:

$$\text{Polar}: \quad \mathrm{G}^{\zeta}_{nlm}(r,\theta,\varphi) = \mathrm{N}\mathrm{Y}^{m}_{l}(\theta,\varphi) r^{2n-2-l} \mathrm{e}^{-\zeta r^2} \tag{3.59}$$

$$\text{Cartesian}: \quad \mathrm{G}^{\zeta}_{l_x,l_y,l_z}(x,y,z) = \mathrm{N} x^{l_x} y^{l_y} z^{l_z} \mathrm{e}^{-\zeta r^2} \tag{3.60}$$

Compared to STOs, GTOs do not have a "cusp" at the nucleus and also suffer from poor long range description, however calculating the two electron integrals for GTOs is very rapid, with the added advantage of the product of Gaussians being another Gaussian. Ideally, one would like to use STOs to properly describe the behaviour of the orbitals (in this case the hydrogen 1s) but have the efficiency of working with GTOs. The compromise is to use fixed linear combinations of primitive Gaussian functions. These linear combinations are known as contractions and give rise to contracted Gaussian functions (CGFs).

Using this approach, one can reproduce a STO as a linear combination of CGFs. This is known as the STO-nG approach [162], for which Figure 3.2 shows the best fit results from using three CGFs resulting in the STO-3G basis set. This basis is known as the minimum basis with a single basis function being used for each orbital. The next stage in basis set development is to simply double the number of basis functions per orbital leading to the double zeta (DZ) basis set. One can then continue in a systematic way, adding more functions per orbitals leading to triple zeta (TZ) basis sets and quadruple zeta (QZ) basis sets that utilise three and four basis functions per orbital, respectively. One can also consider doubling only the number of functions for the valence orbitals. This results in a split-valence basis, denoted as VDZ.

A different advancement emerged through a progressive series of basis sets pro-

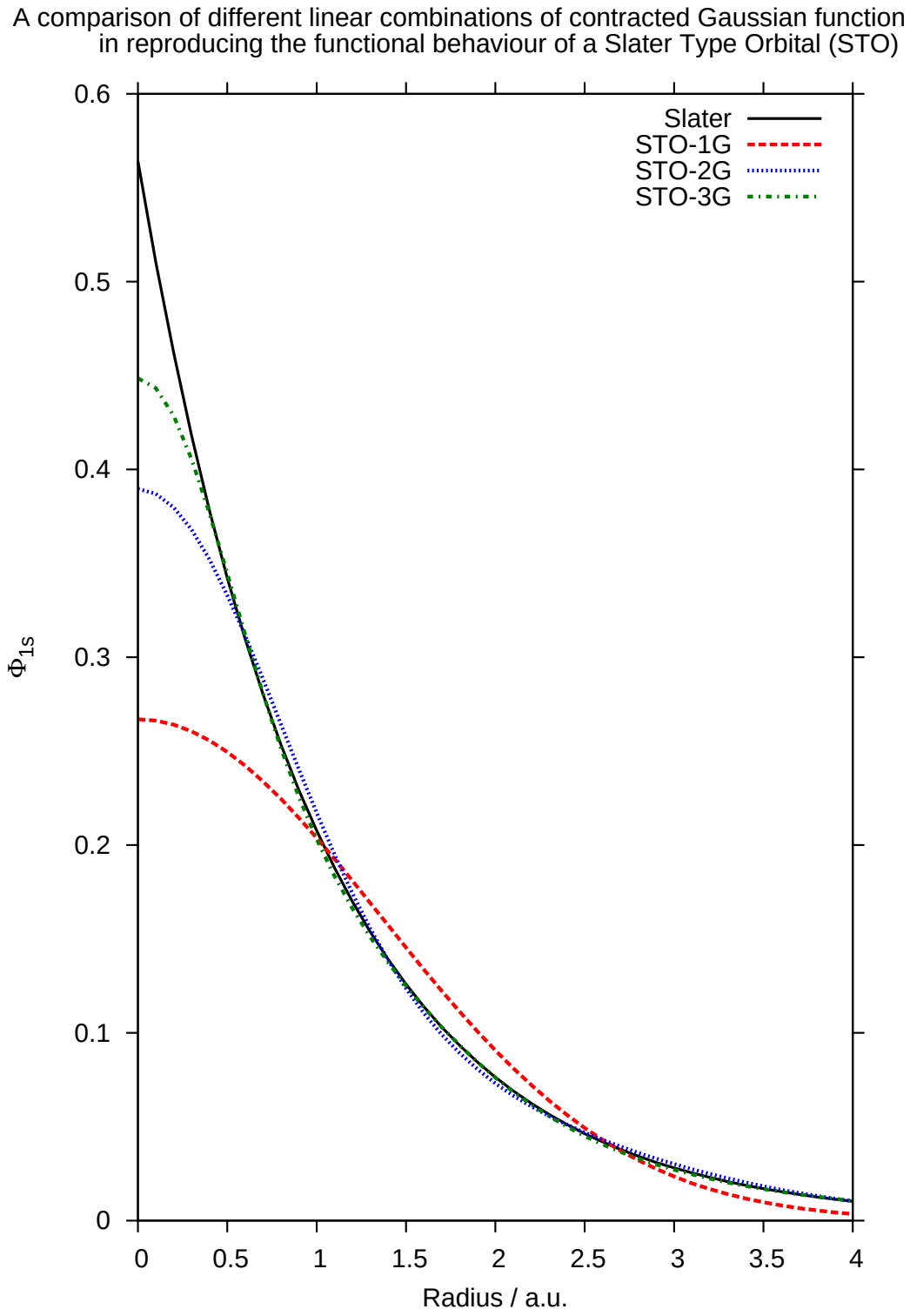

Fig. 3.2: Comparison of fitted functions with a Slater orbital of the 1s orbital for hydrogen with increasing numbers of linear combination of contracted Gaussian functions. The Slater function is shown by the black line whilst the various contracted Gaussian functions are: one Gaussian, STO-1G (red, dashed line); two Gaussians, STO-2G (blue, dotted line) and three Gaussians, STO-3G (green, dotted-dashed line).

duced from the group of Pople *et al.* which unsurprisingly are referred to as Pople-style basis sets [163]. These basis sets have the form:

$$K-nlmG$$

where K is the number of primitive GTOs used for the core orbitals and nlm refers to the number of functions describing the s and p-orbitals of the valence electrons, assuming first or second row atoms only. The functions for these valence electrons are split to describe the inner and outer parts of the orbitals, leading to them being labelled also as split-valence basis sets. The coefficients used in each of these basis sets are optimised at the HF level. An example of one widely used Pople-style split-valence basis set is 6-31G [164], which is used throughout this thesis. Using this as an example, the composition of this basis set can be identified as containing six CGFs for the core orbitals with the valence orbitals being split between three CGFs for the inner part, and a single CGF for the outer part.

These basis sets produce MOs that are very rigid and offer no flexibility. Within molecules however, the presence of other atoms will distort the spherical symmetry and polarise the orbitals. Addition of orbitals with higher angular momentum allows the mixing of orbitals, thus offering them the flexibility to distort. For example, the inclusion of d-orbitals to a basis set with valence p-orbitals allows these p-orbitals to polarise. Such polarised functions have been added to Pople's basis sets and are commonly denoted by * (for heavy atoms) and ** (for inclusion on hydrogen). This results in basis sets such as 6-31G* [165, 166].

As well as polarisation functions, it is sometimes necessary to include diffuse functions. These are functions that decay slowly from the nucleus and are vital where the electron is held far away from the nucleus. This makes them essential for anions, Rydberg states and very electronegative atoms, such as the molecules studied in Chapter 4, which all have anionic ground states. These have also been

incorporated into Pople basis sets and are denoted by + (for heavy atoms) and ++ (for inclusion on hydrogen), giving rise to basis sets such as 6-31+G [167].

Correlation consistent basis sets

As mentioned previously, the coefficients for Pople style basis sets are optimised at the HF level of theory. The question that emerges concerns the quality of calculations using these basis sets for correlated levels of theory. Dunning's correlation consistent basis sets have been optimised using CI wavefunctions [168]. These correlation consistent (cc) basis sets generally have the form:

$$cc{-}pVNZ$$

The p indicates the inclusion of polarisation functions, the V indicates these basis sets are for valence orbitals only and NZ denotes the nth zeta variant is employed, *e.g.* DZ refers to double-zeta. These basis sets can also be augmented with diffuse functions [169], giving rise to basis sets of the form, aug-cc-pVNZ.

3.9 Density Functional Theory (DFT)

The sections covered so far have illustrated an approach to quantum chemistry based solely on the wavefunction and various schemes to approximate it. The wavefunction, however, is difficult to solve for and so an alternative method was sought. One such method rested on whether it was possible to replace the complicated many electron wavefunction by the electron density. This method is known as density functional theory (DFT).

Many of the molecules studied in this thesis are of a size where post-HF methods are computationally expensive and result in time-consuming calculations. This is especially true when high-scaling methods such as CCSD or large CASs are used. Calculating derivatives and Hessians using post-HF methods for these molecules are

also computationally expensive, notably when analytical functions are not available.

For the large polycyclic molecules in Chapter 6, DFT was chosen for its low scaling (formally N^3) and computational cost. It was also the ideal method for the large model system used in Chapter 7. The calculation of the Hessians using post-HF methods was unfeasible, whereas DFT was more suitable. The formal theory of DFT is therefore outlined.

It is well established that in wavefunction theories, the square of the wavefunction corresponds to physical observables *i.e.*:

$$|\Psi(\mathbf{x_1}, \mathbf{x_2} \ldots \mathbf{x_N})|^2 \mathrm{d}\mathbf{x_1}, \mathrm{d}\mathbf{x_2} \ldots, \mathrm{d}\mathbf{x_N} \tag{3.61}$$

From this, one can consider the electron density, $\rho(\mathbf{r})$, defined as:

$$\rho(\mathbf{r}) = N \int \cdots \int |\Psi(\mathbf{x_1}, \mathbf{x_2} \ldots \mathbf{x_N})|^2 \mathrm{d}\mathbf{s_1}, \mathrm{d}\mathbf{x_2} \ldots \mathrm{d}\mathbf{x_N} \tag{3.62}$$

The meaning of $\rho(\mathbf{r})$ is the probability of finding any of the N-electrons within the volume element $\mathrm{d}\mathbf{r_1}$, whilst the other $N-1$ electrons are in arbitrary positions. From this, $\rho(\mathbf{r})$ is formally a probability density, but is often referred to as the electron density. The indistinguishability of electrons however results in the probability of finding any electron at position $\mathrm{d}\mathbf{r_1}$ as simply N multiplied by the probability for one particular electron. The properties of $\rho(\mathbf{r})$ are that it vanishes at infinity and integrates to the total number of electrons:

$$\rho(\mathbf{r} \longrightarrow \infty) = 0 \tag{3.63a}$$

$$\int \rho(\mathbf{r}) \mathrm{d}\mathbf{r_1} = N \tag{3.63b}$$

The great advantage of the electron density is it can be observed directly, unlike the wavefunction. An important feature of the electron density is that at the position of an atom, $\rho(\mathbf{r})$ has a maximum, finite value. At this point, the gradient density exhibits a discontinuity and a cusp results.

3.9.1 Pair Density

Moving forward, one can now consider the probability of finding a pair of electrons, with different spins, simultaneously contained within volume elements, $\mathrm{d}\mathbf{r_1}$, $\mathrm{d}\mathbf{r_2}$. Again, the remaining $N-2$ electrons occupy arbitrary positions. The probability value, known as the pair density $\rho_2(\mathbf{x_1}, \mathbf{x_2})$ can be defined:

$$\rho_2(\mathbf{x_1}, \mathbf{x_2}) = N(N-1) \int \cdots \int |\Psi(\mathbf{x_1}, \mathbf{x_2} \ldots \mathbf{x_N})|^2 \mathrm{d}\mathbf{x_3}, \ldots, \mathrm{d}\mathbf{x_N} \tag{3.64}$$

This quantity also contains information about the correlation of electrons, and is normalised to the total number of non-distinct pairs *i.e.* $N(N-1)$ [170].

As noted previously, a many-electron wavefunction is required to be anti-symmetric, and this needs to be included in the pair density framework. This can be done through introducing a reduced density matrix for two electrons, where the diagonal elements of this matrix represent the pair density, $\rho_2(\mathbf{x_1}, \mathbf{x_2})$. For the case of $\mathbf{x_1} = \mathbf{x_2}$, the probability of finding two electrons with the same spin, in the same volume element, yields:

$$\rho_2(\mathbf{x_1}, \mathbf{x_2}) = -\rho_2(\mathbf{x_1}, \mathbf{x_2}) \tag{3.65}$$

which is only valid when $\rho_2(\mathbf{x_1}, \mathbf{x_2}) = 0$ and thus the probability of finding two electrons with the same spin, in the same point in space, is exactly zero. Consequently, electrons of like spin do not move independently from each other and have correlated motion. This result is none other than the exchange correlation or Fermi energy, as incorporated via the anti-symmetric Slater determinant in HF, equation (3.11).

There is also the electrostatic repulsion to consider. This term prevents the electrons from coming too close together and is therefore known as Coulomb correlation. It is neglected in HF theory, where the repulsion is treated averagely, but can be included in the pair density. One can introduce a condition probability, $\Omega(\mathbf{x_2}; \mathbf{x_1})$, which defines the probability of finding an electron at $\mathbf{x_2}$, should there already be one

known at $\mathbf{x_1}$. As expected, the integral of this quantity equates to $N-1$ electrons:

$$\Omega(\mathbf{x_2};\mathbf{x_1}) = \frac{\rho_2(\mathbf{x_1},\mathbf{x_2})}{\rho(\mathbf{x_1})} \tag{3.66a}$$

$$\int \Omega(\mathbf{x_2};\mathbf{x_1})\mathrm{d}\mathbf{x_2} = N-1 \tag{3.66b}$$

The difference between, $\Omega(\mathbf{x_2};\mathbf{x_1})$ and the uncorrelated probability of finding an electron at $\mathbf{x_2}$ can be determined by:

$$h_{xc}(\mathbf{x_2};\mathbf{x_1}) = \frac{\rho_2(\mathbf{x_1},\mathbf{x_2})}{\rho(\mathbf{x_1})} - \rho(\mathbf{x_2}) \tag{3.67}$$

where h_{xc} is the exchange-correlation hole. This correlation represents depletion of the electron density at $\mathbf{x_2}$ compared to the independent particle system. The value of this exchange-correlation is always negative and has the property of integrating to -1, thus the exchange-correlation hole contains the *exact* charge of one electron. This concept is widely used throughout DFT formulations. By analogy, a way of understanding this concept is to regard the electron as "digging" a hole around itself, thereby diminishing the probability of finding another electron nearby. The exchange-correlation hole can be split into two terms: Fermi (h_x) and Coulomb (h_c), allowing one to write:

$$h_\mathrm{xc}(\mathbf{r_1};\mathbf{r_2}) = h_\mathrm{x}^{\sigma_1=\sigma_2}(\mathbf{r_1};\mathbf{r_2}) + h_\mathrm{c}^{\sigma_1,\sigma_2}(\mathbf{r_1},\mathbf{r_2}) \tag{3.68}$$

Here, the Fermi hole results from the Pauli principle and hence applies only to electrons of the same spin, similar to the single Slater determinant form in HF. The Coulomb hole, however, results from the $\frac{1}{r_{12}}$ electrostatic interaction.

One final point to be addressed, is the role of self-interaction and its inclusion within DFT. In HF the energy is given through:

$$\begin{aligned} E_\mathrm{HF} &= \langle\Phi_\mathrm{SD}|\hat{H}|\Phi_\mathrm{SD}\rangle \\ &= \sum_i^N (i|\hat{h}|i) + \frac{1}{2}\sum_i^N\sum_j^N (ii|jj) - (ij|ji) \end{aligned} \tag{3.69}$$

The double sum present in this expression allows for i=j which yields the following Coulomb term:

$$(ii|jj) = \iint |\chi_i(\mathbf{x_1})|^2 \frac{1}{r_{12}} |\chi_i(\mathbf{x_2})|^2 \mathrm{d}\mathbf{x_1}\mathrm{d}\mathbf{x_2} \tag{3.70}$$

This describes the unphysical interaction of a single electron with itself, denoted self-interaction and is complete nonsense. Fortunately, HF corrects for this self-interaction through the exchange term, which when i=j, is identical to the Coulomb term but of opposite sign and hence cancels the effect out. Unfortunately, such cancellations do not occur in DFT and self-interaction errors become an inherent problem.

3.9.2 Hohenberg-Kohn Theorems

A formal and physically meaningful rationale behind using the electron density to determine the Hamiltonian and system properties was provided by Hohenberg and Kohn in 1964. Their paper outlined two fundamental theorems that underpins the theoretical framework of DFT.

The first Hohenberg-Kohn (HK), theorem, which is discussed in more detail in Appendix D.1, states that [171]:

"$V_{\mathrm{ext}}(\mathbf{r})$ *is (to within a constant) a unique functional of* $\rho(\mathbf{r})$*; since, in turn* $V_{\mathrm{ext}}(\mathbf{r})$ *fixes* $\hat{H}$ *we see that the full many-particle ground state is a unique functional of* $\rho(\mathbf{r})$."

From the first HK theorem, a functional form for the energy, based on the electron density, was derived:

$$E_0[\rho_0] = T[\rho_0] + E_{\mathrm{ee}}[\rho_0] + E_{\mathrm{Ne}}[\rho_0] \tag{3.71}$$

This form contains terms for the kinetic energy, electron-electron repulsion and the potential for the nuclear-electron attraction. If the explicit forms of these terms were

known exactly, then the Schrödinger equation could be solved exactly. However, explicit forms for both $T[\rho]$ and $E_{\text{ee}}[\rho]$ are not known. Only the explicit form for the Coulomb interaction, $J[\rho]$, is known and can hence be extracted out from $E_{\text{ee}}[\rho]$. Finding explicit forms for the remaining terms have been the major hurdle for DFTs.

The second HK theorem seeks to apply a variational principle:

$$E_0 \quad \leq \quad E[\tilde{\rho}] = T[\tilde{\rho}] + E_{\text{ee}}[\tilde{\rho}] + E_{\text{Ne}}[\tilde{\rho}] \tag{3.72}$$

So, for any trial density, the energy obtained will be an upper bound to the true ground state energy E_0. Any trial density will also define its own Hamiltonian and hence its own wavefunction. In principle, knowing the correct ground state density leads to information about the ground state wavefunction, however, it is important to stress that DFT has *no wavefunction*! The variational principle as employed here applies only to the exact functionals and so require caution when approximations to these are used. The end result are energies that may be lower than the exact. Formulating DFT calculations to mimic those of HF *i.e.* use of a Slater determinant, can relieve this problem.

Finally, whilst the HK theorems justify the use of the density to calculate the energy, they provide no insight into the structure of these functionals. The resulting challenge lies in obtaining expressions for each form.

3.9.3 Kohn-Sham Theory

The HK scheme showed the crux in calculating the ground state energy revolves around solving the following functional:

$$\text{F}_{\text{HK}}[\rho(\mathbf{r})] = T[\rho(\mathbf{r})] + J[\rho(\mathbf{r})] + E_{\text{ncl}}[\rho(\mathbf{r})] \tag{3.73}$$

where the Coulombic term is the only functional for which an explicit form is known. It had been noted that similar approaches to calculate properties using the electron

density had failed dramatically owing to the functional form given to the kinetic energy [172, 173]. Kohn and Sham's approach [174] to the kinetic energy initially considered a HF scheme with a single Slater determinant representing the exact wavefunction of a fictitious, non-interacting system of N-electrons. The kinetic energy of this system can be determined exactly through:

$$\mathrm{T_{HF}} = -\frac{1}{2}\sum_{i}^{N}\langle\chi_i|\nabla^2|\chi_j\rangle \tag{3.74}$$

where χ are the usual spin orbitals. One can also consider a non-interacting reference system with a Hamiltonian that contains no electron-electron interactions and an effective, local potential:

$$\hat{H}_s = -\frac{1}{2}\sum_{i}^{N}\nabla_i^2 + \sum_{i}^{N}V_s(\mathbf{r}) \tag{3.75}$$

Utilising the same process as in HF, the ground state wavefunction can be represented as Slater determinant and the spin orbitals determined via the iterative Fock-like equation. Similarly, this scheme also contains a one electron operator denoted the Kohn-Sham operator, $\hat{f}^{KS}$, with orbitals that are referred to as Kohn-Sham orbitals, the validity of which are discussed in Appendix D.2:

$$\hat{f}^{\mathrm{KS}}\varphi_i = \varepsilon\varphi_i \tag{3.76a}$$

$$\hat{f}^{\mathrm{KS}} = -\frac{1}{2}\sum_{i}^{N}\nabla_i^2 + V_s(\mathbf{r}) \tag{3.76b}$$

Using this, Kohn and Sham's solution to calculating the kinetic energy centres around a non-interacting reference system with the same density as the real one. For this system, the exact kinetic energy can be obtained as:

$$\mathrm{T_S} = -\frac{1}{2}\sum_{i}^{N}\langle\chi_i|\nabla^2|\chi_j\rangle \tag{3.77}$$

nevertheless, this energy does not represent the real kinetic energy of the interacting system. This problem was resolved by re-writing the HK functional, equation (D.6), and expressing it as:

$$\mathrm{E}[\rho(\mathbf{r})] = T_s[\rho(\mathbf{r})] + J[\rho(\mathbf{r})] + E_{\mathrm{xc}}[\rho(\mathbf{r})] \tag{3.78}$$

In this structure, the functional containing all the non-classic contributions has been converted to $E_{\mathrm{xc}}[\rho(\mathbf{r})]$ where all the unknown terms are now contained. This includes contributions from self-interaction correction, exchange, correlation and, crucially, the remaining portion of the kinetic energy absent in the non-interacting system. These terms are referred to as the exchange-correlation functional.

This approach still leaves two outstanding issues. Firstly, the expression for the kinetic energy is still not dependent on the density, instead relying on the Kohn-Sham orbitals. This raises the question of how to determine these orbitals for the non-interacting reference system.

Making use of the separation stated in equation (3.76), the energy of the real, interacting system can be expressed as:

$$\mathrm{E}[\rho(\mathbf{r})] = T_s[\rho(\mathbf{r})] + J[\rho(\mathbf{r})] + E_{\mathrm{xc}}[\rho(\mathbf{r})] + E_{\mathrm{Ne}}[\rho(\mathbf{r})] \tag{3.79a}$$

$$\begin{aligned} &= T_s[\rho(\mathbf{r})] + \frac{1}{2}\iint \frac{\rho(\mathbf{r_1})\rho(\mathbf{r_2})}{r_{12}}\mathrm{d}(\mathbf{r_1})\mathrm{d}(\mathbf{r_2}) \\ &\quad + E_{\mathrm{xc}}[\rho(\mathbf{r})] + \int V_{\mathrm{Ne}}\rho(\mathbf{r})\mathrm{d}\mathbf{r} \end{aligned} \tag{3.79b}$$

$$\begin{aligned} &= -\frac{1}{2}\sum_i^N \langle\varphi_i|\nabla^2|\varphi_i\rangle + \frac{1}{2}\sum_i^N\sum_j^N \iint |\varphi_i\mathbf{r_1}|^2 \frac{1}{r_{12}} |\varphi_j\mathbf{r_2}|^2 \mathrm{d}\mathbf{r_1}\mathrm{d}\mathbf{r_2} \\ &\quad + \mathrm{E_{xc}}|\rho(\mathbf{r})| - \sum_i^N \int \sum_A^M \frac{Z_A}{r_{1A}} |\varphi_i\mathbf{r_1}|^2 \mathrm{d}\mathbf{r_1} \end{aligned} \tag{3.79c}$$

The end result shows explicit forms for all components save the exchange-correlation, $\mathrm{E_{xc}}$. Drawing from the HF procedure, a variational principle is applied and the

orbitals $\{\varphi_i\}$ constructed such to ensure the energy can be minimised. This leads to a set of equations:

$$\left(-\frac{1}{2}\nabla^2 + \left[\int \frac{\rho(\mathbf{r_2})}{r_{12}}\mathrm{d}\mathbf{r_2} + \mathrm{V_{XC}}(\mathbf{r_1}) - \sum_A^M \frac{Z_A}{r_{1A}}\right]\right)\varphi_i \\ = \left(-\frac{1}{2}\nabla^2 + \mathrm{V_{eff}}(\mathbf{r_1})\right)\varphi_i = \varepsilon_i\varphi_i \tag{3.80}$$

that are comparable to those for the one-particle non-interacting reference system, equation (3.76), which are required to be solved iteratively. Collating all the above, the procedure summarising the Kohn-Sham approach is as follows: once all the components for equation (3.80) have been determined the one-particle equations to provide the orbitals can be solved. From these orbitals, the ground state density can be obtained and inserted into equation (3.79a) to yield the ground state energy. There is still one major hurdle however - the second outstanding issue to be discussed - the exchange-correlation functional. In equation (3.80) there is no explicit expression for $\mathrm{V_{xc}}$, the potential resulting from $\mathrm{E_{xc}}$. All that can be defined is the following relation:

$$\mathrm{V_{xc}} = \frac{\delta \mathrm{E_{xc}}}{\delta \rho} \tag{3.81}$$

In principle the Kohn-Sham approach is exact. Knowing the exact forms of $\mathrm{V_{xc}}$ and $\mathrm{E_{xc}}$ would lead to the exact energy, but in practice these are unknown and so approximations are required. The utility of DFT rests on finding the best approximation for the exchange-correlation functional.

The Kohn-Sham approach was a pivotal moment in the development of DFT, although there are several additional points of discussion that emerge from this framework that are worth mentioning. For the sake of brevity, however, these are relegated to Appendix D.2.

3.9.4 Approximations for the exchange-correlation functional

Emerging from the Kohn-Sham approach was the pressing need to determine a form for the exchange-correlation functional. In trying to obtain an explicit form, several classes of approximations have developed.

Local Density Approximation (LDA)

The simplest and basic approach is to consider a uniform electron gas. From the outset, one can see the major drawback with this approximation, namely that atoms and molecules possess densities that rapidly vary. The benefits of this model are the good forms available for the exchange and correlation functionals. The exchange-correlation functional, known as the local density approximation (LDA), can be expressed as:

$$\mathrm{E}_{\mathrm{xc}}^{\mathrm{LDA}}[\rho] = \int \rho(\mathbf{r})\varepsilon_{\mathrm{xc}}(\rho(\mathbf{r}))\mathrm{d}\mathbf{r} \tag{3.82}$$

Another benefit of this scheme is $\varepsilon_{\mathrm{XC}}$ can be separated into the individual exchange and correlation contributions:

$$\varepsilon_{\mathrm{xc}}(\rho(\mathbf{r})) = \varepsilon_{\mathrm{x}}(\rho(\mathbf{r})) + \varepsilon_{\mathrm{c}}(\rho(\mathbf{r})) \tag{3.83}$$

The exchange-correlation is determined from the exchange energy of the uniform electron gas, for which the form was devised by Dirac and Bloch in the late 1920s [175, 176]:

$$\varepsilon_{\mathrm{x}} = -\frac{3}{4}\sqrt[3]{\frac{3\rho(\mathbf{r})}{\pi}} \tag{3.84}$$

There is no explicit form known for the correlation part, however an analytical form has been interpolated from high level quantum Monte Carlo simulations of the homogeneous electron gas [177]. Despite the obvious flaw in describing molecular systems through a constant density approximation, the LDA approach is surprisingly successful. This success is two fold, a combination of satisfying a number of

properties for describing the exchange-correlation hole and a fortuitous cancellation of errors. Achieving a better description of the electron density surrounding molecules involves improvements and extensions to the LDA.

Generalised Gradient Approximation (GGA)

The obvious expansion to the LDA is inclusion of the gradient of the charge density, $\nabla\rho(\mathbf{r})$, to allow for the inhomogeneity of the electron density. This functional should also preserve the properties of the exchange-correlation hole that are satisfied within the LDA. These type of functionals are referred to as generalised gradient approximations (GGA) and have the following form:

$$\mathrm{E}_{\mathrm{xc}}^{\mathrm{GGA}}[\rho_\alpha, \rho_\beta] = \int f(\rho_\alpha, \rho_\beta, \nabla\rho_\alpha, \nabla\rho_\beta)\mathrm{d}\mathbf{r} \tag{3.85}$$

Here, f indicates some function within the integrand that has a dependency on both the density, and the density gradient. It is useful to split $\mathrm{E}_{\mathrm{xc}}^{\mathrm{GGA}}$ into its exchange and correlation components:

$$\mathrm{E}_{\mathrm{xc}}^{\mathrm{GGA}} = \mathrm{E}_{\mathrm{x}}^{\mathrm{GGA}} + \mathrm{E}_{\mathrm{c}}^{\mathrm{GGA}} \tag{3.86}$$

The exchange contribution can be expressed in the following form:

$$\mathrm{E}_{\mathrm{x}}^{\mathrm{GGA}} = \mathrm{E}_{\mathrm{x}}^{\mathrm{LDA}} - \sum_\sigma \int F(S_\sigma)\rho_\sigma^{4/3}(\mathbf{r})\mathrm{d}\mathbf{r} \tag{3.87}$$

where S_σ is the reduced density gradient, essentially a local inhomogeneity parameter:

$$S_\sigma(\mathbf{r}) = \frac{\nabla\rho_\sigma(\mathbf{r})}{\rho_\sigma^{4/3}(\mathbf{r})} \tag{3.88}$$

Several different families of the function, F have been suggested. One series are based upon a function developed by Becke and contain terms that are empirically fitted [178]. Examples of these functionals include B (from Becke) [178] and O (Handy's modification of Becke's) [179]. Another set are based on rational functions

of the reduced density gradient and contain no empirically determined parameters. Examples of these type of exchange functionals include B86 [180] and PBE [181].

Gradient corrected correlation functions also exist, however their analytical forms and theoretical rationale are extensive and complicated. Popular examples include P86 [182] and LYP [183]. Other commonly used GGAs combine the exchange functional from Becke (B) and the correlation functional from either Perdew (P) or Lee, Yang and Parr (LYP) to form BP86 and BLYP [184], respectively.

In addition, one could also include the second derivative of the electron density, the Laplacian, $\nabla_n^2(\mathbf{r})$, forming meta-GGA functionals [185].

Hybrid Functionals

Referring back, again, to the familiar HF and analogous Kohn-Sham scheme, it has been extensively noted that, through the use of a Slater determinant, the exchange energy can be computed exactly. From this, a logical step to formulate the exchange-correlation functional is to compute the exact exchange component and use approximations only for the correlation. This methodology performs well for atoms, but poorly for molecules, due mainly to the abysmal properties of the exchange-correlation hole produced. Using the adiabatic connection [186, 187], however, provided a way to incorporate the exact exchange energy. Further detail regarding the adiabatic connection is outlined in Appendix D.3. An adiabatic connection formula for the exchange-correlation energy can be expressed as:

$$\mathrm{E_{xc}} = \int_0^1 \mathrm{E}_{ncl}^{\lambda} \mathrm{d}\lambda \tag{3.89}$$

The term λ can be thought of as a parameter that "turns on" the electron-electron interaction. At the limit of $\lambda = 0$, there is no interaction between the electrons and hence no correlation energy. The exact exchange energy can be obtained from a single Slater determinant analogous to the HF *ansatz*. At the upper limit, $\lambda = 1$, the

system is fully interacting and one of the functionals from the range of classes are required to obtain a good approximation. From this, an approximation for equation (3.89) can be constructed as a weighted sum of these two limits:

$$E_{\mathrm{xc}} = aE_{\mathrm{FOCK}} + bE_{\mathrm{xc}} \tag{3.90}$$

The initial approach was to split the contributions in half, using the exact exchange energy for the non-interacting system and an LDA functional to approximate $\mathrm{E_{xc}}$ in the fully interacting system [188]. This combination form the half-and-half methods:

$$\mathrm{E_{xc}^{H+H}} = \frac{1}{2}\mathrm{E_x^{EXACT}} + \frac{1}{2}\left(\mathrm{E_x^{LSDA}} + \mathrm{E_c^{LSDA}}\right) \tag{3.91}$$

This approach can be extended to implement the better approximations afforded by GGA functionals. In this scheme, the exchange energy is a combination of exact exchange, LDA exchange and a gradient correction component. The correlation energy also appends a similar gradient correction term into it. Using this, Becke then added semi-empirical coefficients to weight the components in his scheme, thus forming a three parameter hybrid functional [189]:

$$\mathrm{E_{xc}^{B3}} = \mathrm{E_{xc}^{LDA}} + a(\mathrm{E_{FOCK}} - \mathrm{E_x^{LDA}}) + b\mathrm{E_x^B} + c\mathrm{E_c^{PW91}} \tag{3.92}$$

Numerous hybrid functionals are now in existence [190–192], including the popular and renowned B3LYP. This functional, devised by Stephens *et al.*, is similar to Becke's original three parameter hybrid but with the PW91 functional substituted with LYP [193]:

$$\begin{aligned}\mathrm{E_{xc}^{B3LYP}} = (1-a)\mathrm{E_x^{LSDA}} + a\mathrm{E_{FOCK}} + b\mathrm{E_x^B} + c\mathrm{E_c^{LYP}} + (1-c)\mathrm{E_c^{LDA}} \\ a = 0.2, \quad b = 0.72 \quad \text{and} \quad c = 0.81\end{aligned} \tag{3.93}$$

The success of B3LYP has made it a popular functional for use in DFT calculations and is used in Chapters 4 and 6. Even so, it is important to note that it is still

an approximation to the true exchange-correlation functional and contains semi-empirically derived parameters, thus despite its overwhelming performance, it is not a black box functional and different functionals may perform better for the system in question. This highlighted in Chapter 7, where a different hybrid functional was employed to account for long range interactions.

3.10 Time Dependent Density Functional Theory

In its standard formulation, DFT (also known as static DFT) is applicable to calculation of ground state properties only. An extension to DFT allows one to consider the dynamics of a non-stationary system, allowing the extraction of properties such as excitation energies. This extension is known as time dependent density functional theory, TDDFT and was used exclusively for excited state calculations in Chapter 6 and 7. The framework for understanding and applying TDDFT is briefly outlined in Appendix D.4. The framework outlined is necessary for the application and understanding of the derivation of TDDFT. As with static DFT, a formal justification is required to show that the density can be employed to calculate the time dependent properties of a system.

3.10.1 Runge-Gross Theorem

Within the context of the TDSE, each external potential, $\nu(\mathbf{r},t)$, produces a time dependent wavefunction, $\Psi(t)$ from an initial given state Ψ_0. From each $\Psi(t)$ a density, $n(\mathbf{r},t)$, is generated:

$$\nu(\mathbf{r},t) \xrightarrow[\text{Fixed } \Psi_0]{i\frac{\partial\Psi}{\partial t} = \hat{H}(t)\Psi} \Psi(t) \xrightarrow{\langle\Psi(t)|\hat{n}|\Psi(t)\rangle} n(\mathbf{r},t) \tag{3.94}$$

This schematic illustrates how the TD potential, as determined via the Schrödinger equation, can be used to determine the dynamics. The core concept within TDDFT

aims to construct the reverse argument of equation (3.94), whereby the TD density, $n(\mathbf{r}, t)$, can be employed as a means to realise the dynamics of a system. For this concept to be valid, a unique one-to-one mapping between the time dependent densities and potentials needs to be shown to exist. Such a correspondence was established by Runge and Gross [194] and is the key theorem to TDDFT, analogous to the HK theorems for static DFT (Section 3.9.2). The implication of this is that two different TD potentials[a], $\nu(\mathbf{r}, t)$ and $\nu'(\mathbf{r}, t)$ affecting a fixed initial state will *always* cause two different time dependent densities, $n(\mathbf{r}, t)$ and $n'(\mathbf{r}, t)$. Here, a condition is imposed that the TD potentials can be expanded in a Taylor series:

$$\nu(\mathbf{r}, t) = \sum_{k=0}^{\infty} \frac{1}{k!} \nu_k(\mathbf{r})(t - t_o)^k \tag{3.95}$$

with a similar expansion also for $\nu(\mathbf{r}, t)$ with ν'_k. From this, the condition that the two potentials differ by more than a functional, $c(t)$, indicates there is a smallest integer value of k, with $k > 0$, for which the following expression holds:

$$\nu_k(\mathbf{r}) - \nu'_k(\mathbf{r}) \neq \text{constant} \tag{3.96}$$

The proof of the Runge-Gross theorem is detailed in Appendix D.5. The theorem showed that different current densities give rise to different densities, therefore two densities subjected to two different potentials will differ immediately after t_0. This implies the external potential is a unique functional of the TD density, similar to the HK theorems. Again, if explicit forms for the terms were known, the many-body Hamiltonian and the wavefunction could be solved exactly.

Formally, within the context of TDDFT, all that is needed to determine any observable is the TD density. In practice, a strategy analogous to the of Kohn-Sham for static DFT is required to determine the TD densities, whilst avoiding any approach needing solutions to the many-body Schrödinger equation.

[a] Assuming these two potentials differ by more than some function: $\nu(\mathbf{r}, t) - \nu'(\mathbf{r}, t) \neq c(t)$

3.10.2 Time-Dependent Kohn Sham Theory

As discussed in Section 3.9.3, the major progress allowing practical use of static DFT was the ability to represent a fully interacting system by a non-interacting equivalent that produces the same density. Given this, a logical, and convenient, approach towards using TDDFT asks whether a similar concept can be applied, namely can the time dependent density of a fully interacting system, be reproduced by a non-interacting system. The van Leeuwen theorem [195] showed this approach to be valid and ensured that a TD density of a fully interacting system (evolving from an initial state being subject to an external potential) can be duplicated through a non-interacting reference system. From here, one can formulate a TD Kohn-Sham equation.

A non-interacting reference system evolving under an effective potential has the form:

$$v_s[n, \Psi_0, \Phi_0](\mathbf{r}, t) \tag{3.97}$$

where:

n is the time dependent density,

Ψ_0 is the initial many-body state,

Φ_0 is the initial state of a non-interacting system.

A system evolving from its ground state at t_0 due to a TD external potential can be expressed as:

$$v(\mathbf{r}, t) = v_0(\mathbf{r}) + v_1(\mathbf{r}, t)\theta(t - t_0) \tag{3.98}$$

Making use of static DFT, the initial states and wavefunctions, Ψ_0 and Φ_0, are simply functionals of the ground state density. Thus, the effective potential simplifies to:

$$v_s[n](\mathbf{r}, t) \tag{3.99}$$

An infinitesimal time after t_0 the TD potential, $v_1(\mathbf{r}, t)$ acts upon the system. Here,

the TD density is:

$$n(\mathbf{r},t) = \sum_{j=1}^{N} |\varphi_j(\mathbf{r},t)|^2 \tag{3.100}$$

The single particle orbitals, $\varphi_j(\mathbf{r},t)$ are determined from the TD Kohn-Sham equation:

$$\left[-\frac{\nabla^2}{2} + v_s[n](\mathbf{r},r)\right]\varphi_j(\mathbf{r},t) = i\frac{\partial}{\partial t}(\mathbf{r},t) \tag{3.101}$$

where the effective potential is given by:

$$v_s[n](\mathbf{r},t) = v(\mathbf{r},t) + \int \mathrm{d}^3r' \frac{n(\mathbf{r}',t)}{|r-r'|} + v_{\mathrm{xc}}[n](\mathbf{r},t) \tag{3.102}$$

Imposing the condition that $\varphi_j(\mathbf{r},t_0) = \varphi_j^0(\mathbf{r})$ ensures that only the occupied Kohn-Sham orbitals evolve in time.

Whilst the above equations pertain to the *exact* TD density of a system evolving through an external potential, the enforcement of several approximations are needed to make the equations tractable. The first of these approximations is for the exchange-correlation potential, $v_{\mathrm{xc}}^0[n_0](\mathbf{r})$ used in static DFT to solve the Kohn-Sham equation for the initial state of the system. A second approximation is also needed for the TD exchange-correlation potential, $v_{\mathrm{xc}}[n_0](\mathbf{r},t)$, the most common of which - the adiabatic connection - is outlined in Appendix D.6. It is important also to ensure that at t_0 the static and TD exchange-correlation are the same *i.e.* $V_{\mathrm{xc}}[n_0](\mathbf{r},t) = V_{\mathrm{xc}}^0[n_0](\mathbf{r})$.

3.10.3 Linear Response TDDFT

In practice, solutions to the full TD Kohn-Sham equations are not necessary as the system is usually subjected to a small perturbation only. It is therefore convenient and simpler to consider only the response to the perturbation. Calculating the response to first-order only is known as linear response, which when applied to TDDFT culminates in linear-response TDDFT or LR-TDDFT. The general formulism for linear response theory and its use in TDDFT is outlined in Appendix

D.7, whilst more detailed derivatives can be found in [196]. LR-TDDFT is the method most frequently implemented for TDDFT calculations in quantum chemical programs.

3.11 Multi-Configuration Time-Dependent Hartree

From electrons to nuclei

Nearly all the methods discussed so far involve solving the TISE, which within the BOA, reduces to nuclei being parametric over PESs formed by the electrons. There are, nevertheless, instances where one needs to move towards solving the time-dependent Schrödinger equation and explicitly consider the motion of the nuclei. This is the case for calculating electronic spectra, reaction dynamics and where non-adiabaticity is important, particularly where a CoI is involved. These phenomena are integral to the research throughout this thesis and required a method for calculating nuclear quantum dynamics. This section outlines the development of the MCTDH scheme used in Chapter 4, 5 and 6. An extension to this method, which is used in Chapter 7, is also detailed in Section 3.12.

3.11.1 Time Dependent Hartree

For quantum dynamics one is required to solve the TDSE:

$$i\hbar\frac{\partial\Psi(\mathbf{x},t)}{\partial t} = \hat{H}\Psi(\mathbf{x},t) \tag{3.103}$$

where the use of atomic units in which $\hbar = 1$, is often implemented.

The use of time-dependent methods for quantum dynamics evolved in the mid-1970s when a technique for Gaussian wavepacket propagation was published [197]. These methods were strengthened by new numerical techniques for solving the TDSE, such as split operator [198], Chebyshev [199], and Lanczos [200].

Solving the TDSE typically involves propagating a wavepacket represented in a TD basis set:

$$\Psi(Q_1,\ldots,Q_f,t)=\sum_{j_1=1}^{N_1}\cdots\sum_{j_f=1}^{N_f}C_{j_1}\cdots C_{j_f}(t)\prod_{\kappa=1}^{f}\chi_{j\kappa}^{(\kappa)}(Q_\kappa) \tag{3.104}$$

where f is the number of degrees of freedom (DOF), Q_1 are the nuclear coordinates, C_{j1} are the TD expansion coefficients and χ_j is the time-independent basis for the degree of freedom, κ. From the Dirac-Frenkel variational principle [175, 201]:

$$\langle\delta\Psi|H-i\delta_t|\Psi\rangle \tag{3.105}$$

equations of motion for C_{j1} can be derived:

$$i\dot{C}_J=\sum_L H_{JL}C_L \tag{3.106}$$

This approach however scales exponentially with the number of DOF and so restricts inclusion to only five or six. Combatting these exponential scaling problems requires approximations. The most popular of these is the time dependent Hartree (TDH) method [175,202]. In this approximation the wavefunction is written as (considering only two degrees of freedom):

$$\Psi(x,y,t)=a(t)\varphi_1(x,t)\varphi_2(y,t) \tag{3.107}$$

The product $\varphi_1\varphi_2$ is known as a Hartree Product. Again, applying the Dirac-Frenkel variational principle provides EOMs for $a(t)$, $\varphi_1(t)$ and $\varphi_2(t)$. This approach allows one to consider many more DOF - typically up to 100 [203–205].

3.11.2 Multi-Configuration Time-Dependent Hartree

The performance of TDH is quite often subpar and, in similar style to that for electronic structure theory, a multi-configuration approach substantially improves this method. By extending this method to include numerous configurations, one

arrives at the multi-configuration time-dependent Hartree (MCTDH) method used predominantly in this thesis.

In the MCTDH scheme the wavefunction *ansatz* is written as a linear combination of Hartree products [206–210]:

$$\begin{aligned}\Psi(q_1,\ldots,q_f,t) &= \sum_{j_1=1}^{n_1}\cdots\sum_{j_f=1}^{n_f} A_{j_1\ldots j_f}(t)\prod_{\kappa=1}^{f}\varphi_{j_\kappa}^{(\kappa)}(q_\kappa,t) \\ &= \sum_{J} A_J\Phi_J\end{aligned} \tag{3.108}$$

where f indicates the number of DOF, $q_1 \ldots q_f$ are nuclear coordinates, $A_{j_1\ldots j_f}$ are expansion coefficients and $\varphi_{j_\kappa}^{(\kappa)}$ are the time dependent basis functions known as single particle functions (SPFs), which are variationally optimised to allow for efficient convergence.

Within this *ansatz*, the case for $n_1 = n_f = 1$ returns the TDH wavefunction, while systematically increasing n will eventually result in the exact TDSE, equation (3.104).

It is necessary to implement constraints to ensure any propagation is uniquely defined. These constraints are the following:

$$\langle\varphi_j^{(\kappa)}(0)|\varphi_l^{(\kappa)}(0)\rangle = \delta_{jl} \tag{3.109}$$

$$\langle\varphi_j^{(\kappa)}(t)|\dot{\varphi}_l^{(\kappa)}(t)\rangle = -i\langle\varphi_j^{(\kappa)}(t)|g^{(\kappa)}|\varphi_l^{(\kappa)}(t)\rangle \tag{3.110}$$

where g^κ is a constraint operator. These constraints keep orthonormal SPFs orthogonal. From here, one can derive the MCTDH EOMs by applying the Dirac-Frenkel variational principle to the *ansatz* of equation (3.108), resulting in two coupled EOMs, one for the expansion coefficients and one for the SPFs:

$$iA_j = \sum_L \langle\Phi_J|H|\Phi_L\rangle A_L, \tag{3.111}$$

$$i\dot{\varphi}_j^{(\kappa)} = \left(1 - P^{(\kappa)}\right) \sum_{\kappa,l} \rho_{j,\kappa}^{(\kappa)^{-1}} \left\langle \hat{H} \right\rangle_{\kappa,l}^{(\kappa)} \varphi_l^{(\kappa)} \tag{3.112}$$

For the EOM for the SPFs, P is the projector onto the space spanned over by the SPFs for each degree of freedom:

$$P^{(\kappa)} = \sum_J |\varphi_j^{(\kappa)}\rangle\langle\varphi_j^{(\kappa)}| \tag{3.113}$$

ρ is the density matrix and $\langle\hat{H}\rangle_{\kappa,l}^{(\kappa)}$ the matrix of mean-field operators.

The MCTDH equations ensure that the norm is conserved and, when using a time-independent Hamiltonian, the total energy is also conserved.

3.11.3 Discrete Variable Representation

In order to solve the EOMs derived for the expansion coefficients, A, and the SPFs, one is required to determine the matrix elements of $\langle\Phi_J|H|\Phi_L\rangle$:

$$\left\langle \varphi_{j_1}^{(1)} \cdots \varphi_{j_p}^{(p)} \left| H \right| \varphi_{k_1}^{(1)} \cdots \varphi_{k_p}^{(p)} \right\rangle = \left\langle \varphi_{j_1}^{(1)} \cdots \varphi_{j_p}^{(p)} \left| T + V \right| \varphi_{k_1}^{(1)} \cdots \varphi_{k_p}^{(p)} \right\rangle \tag{3.114}$$

This integral is less challenging when the basis functions are a discrete variable representation (DVR). DVRs are typically time-independent basis sets used throughout wavepacket dynamics [211–214]. Expanding the SPFs through a DVR results in a set of primitive basis functions. These primitive basis functions are based upon a set of orthogonal polynomials. For example, a set of DVR functions along the coordinate $q_v\{\chi_i^{(v)}(q_v)\}$ has the property that the matrix representation of the position operator $\hat{q_v}$ is diagonal, hence:

$$\langle\chi_i^{(v)}|q_v|\chi_j^{(v)}\rangle = q_j^{(v)}\delta_{ij} \tag{3.115}$$

where q_v is a grid of points related to the DVR functions. Given enough functions (*i.e.* grid points) the potential energy operator can be assumed to be diagonal and one can obtain the integral by calculating the potential energy only at grid points $q_{j_1}^{(1)} \ldots q_{j_f}^{(f)}$.

Similarly for the kinetic energy operator, the matrix elements can be determined in a finite basis representation (FBR), and then a FBR-DVR transformation can be used to obtain $\{\phi^{(v)}\}$. DVR representations have been derived for the Harmonic oscillator, Legendre, sine and exponentials [210]. In the application of MCTDH, the potential energy matrix elements are determined by transforming from a SPF basis to DVR via:

$$\left\langle \varphi_{i_1}^{(1)} \cdots \varphi_{i_p}^{(p)} \left| V \right| \varphi_{j_1}^{(1)} \cdots \varphi_{j_p}^{(p)} \right\rangle = \sum_{i_1 \ldots i_p} \sum_{j_1 \ldots j_p} a_{k_1 i_1}^{(1)*} \ldots a_{k_p i_1}^{(p*)} a_{k_1 j_1}^{(1)} \ldots a_{k_p j_1}^{(p)} V(Q_{k_1}^{(1)} \ldots Q_{k_p}^{(p)}) \tag{3.116}$$

This equation though will transform the SPF basis to the full direct-product primitive grid, the dimensionality of which is significantly large and a hurdle one wants to avoid. Writing the Hamiltonian as a product of functions, with the same coordinates as particles in the MCTDH wavefunction, ensures one takes advantage of the DVR without such excessive scaling:

$$H(q_1 \ldots q_f) = \sum_{r=1}^{s} c_r h_r^{(1)}(Q_1) \ldots h_r^{(p)}(Q_p) \tag{3.117}$$

This beneficial approach reduces the integrals of equation (3.116) to lower dimensional ones:

$$\left\langle \varphi_{j_1}^{(1)} \cdots \varphi_{j_p}^{(p)} \left| H \right| \varphi_{k_1}^{(1)} \cdots \varphi_{k_p}^{(p)} \right\rangle = \sum_{r=1}^{n_s} c_r \left\langle \varphi_{j_1}^{(1)} | h^{(1)} | \varphi_{k_1}^{(1)} \right\rangle \cdots \left\langle \varphi_{j_p}^{(p)} | h^{(p)} | \varphi_{k_p}^{(p)} \right\rangle \tag{3.118}$$

The formulism outlined here applies only to a single state, thus for treatment of multi-states, an inherent feature in non-adiabatic dynamics, different electronic states need to be included. Inclusion of electronic states has been successfully implemented into the MCTDH equations, further details of which are outlined in Appendix E and references [215, 216].

3.11.4 Memory and Efficiency

For standard wavepacket dynamics, such as equation (3.108), if N is the number of basis functions for each DOF, f, then the wavefunction is described by N^f expansion coefficients; an exponential scaling prohibiting the size of the system these methods can realistically be used for.

In contrast, the MCTDH wavefunction scales as:

$$\text{memory} \quad \sim \quad n^p + pnN^d \tag{3.119}$$

where n is the number of SPFs for particles p and d the number of degrees of freedom.

One can consider two main limits: firstly, when all the particles are one-dimensional *i.e.* $p = f$ and $d = 1$. At this limit the first term in equation (3.119) contributes most and an exponential scaling occurs so that even at $f = 10$ each wavefunction requires ∼150 GB of storage.

The other limit occurs when all the degrees of freedom are combined, ergo $d = f$ and only a single particle is present ($p = 1$). As the first term now always equals one, it is the second term that contributes most, simply becoming the size of the full primitive grid N^f.

It should therefore be evident that for optimal efficiency a balance is needed between the memory for the A coefficients and those for the SPFs.

3.11.5 Analysis and Spectra

From the propagated wavefunction one can extract a range of useful information to analyse a property of interest such as photoelectron [217, 218] and photoabsorption spectra [219]. All of these were essential to the work undertaken in this thesis. The extraction of such properties from MCTDH is complicated by virtue of two MCTDH wavefunctions being formed in different basis sets, not only preventing simple summation, but making the Fourier transform of the wavefunction very challenging.

When the matrix elements of operators are in product form, evaluation becomes simpler. Letting:

$$\Psi = \sum_J A_J \Phi_J \tag{3.120}$$

$$\tilde{\Psi} = \sum_L \tilde{A}_L \tilde{\Phi}_L \tag{3.121}$$

where the wavefunction at time zero is in a different basis to the wavefunction at a different time, and:

$$\hat{\Omega} = \sum_r^M c_r \hat{\omega}_r^{(1)} \cdots \hat{\omega}_r^{(f)} \tag{3.122}$$

is an operator given in product form, then the result:

$$\begin{aligned} \langle \Psi | \hat{\Omega} | \tilde{\Psi} \rangle = & \sum_{r=1}^M c_r \sum_{j_1} \cdots \sum_{j_f} A^*_{j_1 \cdots j_f} \\ & \times \sum_{l_1} \langle \varphi_{j_1}^{(1)} | \hat{\omega}_r^{(1)} | \tilde{\varphi}_{j_1}^{(1)} \rangle \cdots \sum_{l_f} \langle \varphi_{j_f}^{(f)} | \tilde{\varphi}_{l_f}^{(f)} \rangle \tilde{A}_{l_1 \ldots l_f} \end{aligned} \tag{3.123}$$

requires only one dimensional integrals [210].

One can therefore easily evaluate the simple overlap between wavefunctions for auto-correlation functions using equation (3.123) and setting $\hat{\Omega} = 1$. The auto-correlation function, c(t), is then defined as overlap between the initial and propagated wavefunction:

$$c(t) = \langle \Psi(0) | \Psi(t) \rangle \tag{3.124}$$

If the Hamiltonian is Hermitian then:

$$c(-t) = c^*(t) \tag{3.125}$$

and since:

$$\langle \Psi(0) | \exp(-Ht) | \Psi(0) \rangle = \langle (\exp(-iH^{\dagger *} t/2) \Psi^*(0)) | \exp(-iHt/2) \Psi(0) \rangle \tag{3.126}$$

then if $\Psi(0)$ is real and the Hamiltonian symmetric then one obtains [220, 221]:

$$c(t) = \langle \Psi^*(t/2) | \Psi(t/2) \rangle \tag{3.127}$$

hence, one need only propagate Ψ over half the time for which the auto-correlation is needed.

For computing spectra, one can make use of the auto-correlation function. Defining $\Psi_i(Q,0)$ as the nuclear wavefunction of an initial electronic state and:

$$\Psi_f(Q,0) = \mathbf{e}.\mathbf{u}_{fi}(Q)\Psi_i(Q,0) \tag{3.128}$$

as the nuclear wavefunction of an excited electronic state within the Condon approximation (where $\mathbf{e}$ is the vector of the electric field and $\mathbf{u_f}$ is the transition dipole moment vector). Propagation of $\Psi_f(Q,0)$ to $\Psi_f(Q,t)$ results in an auto-correlation function (c(t)) for which the total absorption cross-section is given by the Fourier transform [222–224]:

$$\sigma(E) \sim E \int_{-\infty}^{+\infty} c(t)\mathrm{e}^{i(E+E_i)t}\mathrm{d}t = 2E \int_{0}^{\infty} \mathrm{Re}(c(t)\mathrm{e}^{i(E+E_i)t})\mathrm{d}t \tag{3.129}$$

where E_i is the energy of the initial state.

For unbound states, c(t) gradually vanishes as t increases but for bound states the upper limit of integration has to become some finite time, T. This reduction to finite time introduces spurious structures (Gibbs phenomenon) into the spectrum. These errors can be minimised by multiplying c(t) by a damping function:

$$g(t) = \cos\left(\frac{\pi t}{2T}\right) \underbrace{\Theta\left(1 - \frac{|t|}{T}\right)}_{\text{Heaviside Function}} \tag{3.130}$$

The introduction of the Heaviside function forces c(t) to become zero at T. If desired c(t) can also be multiplied further by:

$$f(t) = \exp\left(\frac{-t}{\tau}\right) \tag{3.131}$$

which produces results analogous to convoluting spectral lines with Lorentzian functions.

3.12 Direct Dynamics - Variational Multi-configurational Gaussian

One of the limiting and constraining features of the MCTDH method is the grid construct used for the SPFs. Naturally, one may consider whether this dependence on the use of a grid can be reduced or removed altogether.

Early developments in this approach were undertaken by Burghardt *et al.* through the G-MCTDH method whereby some SPFs are replaced by Gaussian functions. In this form the *ansatz* is:

$$\Psi(x,t) = \sum_{j_1,\ldots j_f} A_{j_1,\ldots j_f} \varphi_{j_1}^{(1)}(x_1,t)\ldots\varphi_{j_d}^{(d)}(x_d,t) g_{j_{d+1}}^{(d+1)}(x_{d+1},t)\ldots g_{j_f}^{(f)}(x_f,t) \quad (3.132)$$

By removing all grid-based SPFs one arrives at a Gaussian wavepacket (GWP) method, in this instance the variational multi-configurational Gaussian (vMCG) method [225–230]. In the vMCG method, the approximate nuclear wavefunction is a sum of TD basis functions multiplied by TD coefficients:

$$\Psi(x,t) = \sum_{j=1}^{n} A_j(t) g_j(x,t) \quad (3.133)$$

Here $g_j(x,t)$ are the basis functions; multi-dimensional Gaussian functions. These multi-dimensional Gaussians have the form:

$$g_j(x,t) = \exp(x^T.\zeta_j.x + \xi_j.x + \eta_j) \quad (3.134)$$

The parameters associated with these Gaussians can be collected into a square matrix, $\mathbf{\Lambda}$:

$$\mathbf{\Lambda}_j = \{\zeta_j, \xi_j, \eta_j\} \quad (3.135)$$

The choice given to the parameter ζ_j determines the type of Gaussians used.

Thawed Gaussians: Contains both diagonal and off-diagonal elements.

Separable Gaussians: Contains only diagonal elements.

Frozen Gaussians: The diagonal elements are frozen.

From this approach, the form for the multi-dimensional Gaussians can be reformulated and expressed into Heller form:

$$g_j(x,t) = exp\left(\frac{1}{\hbar}\sum -a_{j\kappa}(x_\kappa - q_{j\kappa})^2 + ip_{j\kappa}(x_\kappa - q_{j\kappa}) + i\gamma_j\right) \tag{3.136}$$

From this, one can assign the following properties to the parameters in $\mathbf{\Lambda}_j$:

ζ_j**:** Width of the Gaussian function.

ξ**:** Linear parameters specifying the momentum and centre of the Gaussian.

η**:** The sum of remaining scalar parameters.

Applying the Dirac-Frenkel variational principle to the wavefunction, equation (3.133), yields two EOMs. One for the TD coefficients, $A_j(t)$:

$$i\dot{A}_j = \sum_{lm} [S_{jl}]^{-1} (H_{lm} - i\tau_{lm}) A_m \tag{3.137}$$

where $\mathbf{S}$ is the overlap matrix, $S_{jl} = \langle g_j | g_l \rangle$, $\mathbf{H}$ is the Hamiltonian matrix, $H_{jl} = \langle g_j | \hat{H} | g_j \rangle$ and τ is an overlap time-derivative matrix. Ensuring the diagonal matrix elements of τ are zero keeps the propagated Gaussians normalised.

The other EOM for the Gaussian parameters, using compacted notation, has the form [231]:

$$i\dot{\mathbf{\Lambda}} = [\mathbf{C}]^{-1}\mathbf{Y} \tag{3.138}$$

Here the matrices C and Y are defined as:

$$C_{j\alpha,l\beta} = \rho_{jl}\left(S_{jl}^{(\alpha\beta)} - \left[\mathbf{S}^{(\alpha 0)}\mathbf{S}^{-1}\mathbf{S}^{(0\beta)}\right]_{jl}\right) \tag{3.139a}$$

$$Y_{j\alpha} = \sum_l \rho_{jl}\left(H_{jl}^{(\alpha\beta)} - \left[\mathbf{S}^{(\alpha 0)}\mathbf{S}^{-1}\mathbf{H}\right]_{jl}\right) \tag{3.139b}$$

Within these matrices, ρ_{jl} is simply an element of the density matrix. The differing terms for the overlap and Hamiltonian matrix can be further defined as:

$$S_{jl}^{(\alpha\beta)} = \left\langle \frac{\partial g_j}{\partial \lambda_{j\alpha}} \middle| \frac{\partial g_l}{\partial \lambda_{l\beta}} \right\rangle \tag{3.140a}$$

$$S_{jl}^{(\alpha 0)} = \left\langle \frac{\partial g_j}{\partial \lambda_{j\alpha}} \middle| g_l \right\rangle \tag{3.140b}$$

$$H_{jl}^{(\alpha\beta)} = \left\langle \frac{\partial g_j}{\partial \lambda_{j\alpha}} \middle| H \middle| g_l \right\rangle \tag{3.140c}$$

Employing the CX formulism allows the Y-vector to be separated into:

$$\mathbf{Y} = \mathbf{Y}_0 + \mathbf{Y}_R \tag{3.141}$$

In this partition, $\mathbf{Y}_0$ depends upon the Hamiltonian that can be expressed in terms of $\mathbf{S}^{0\alpha}$, whilst $\mathbf{Y}_R$ is a "residual" term, containing the remaining portion of the Hamiltonian. This allows equation (3.141) to be recast as:

$$Y_{j\alpha} = \sum_{l\beta} C_{j\alpha,l\beta} X_l^{(\beta)} + Y_{R,j\alpha} \tag{3.142}$$

From here a simplification of the EOM for the Gaussian parameters can be obtained:

$$i\dot{\mathbf{\Lambda}} = X + \mathbf{C}^{-1}\mathbf{Y}_R \tag{3.143}$$

This formulism allows one to separate the EOM into classical and non-classical components. When utilising this separation, terms pertaining to the classical propagation of Gaussians are incorporated into the X-term, whilst quantum terms are placed into $\mathbf{Y}_R$.

3.12.1 Singularities and Matrix Inversion

It is clear from inspecting the EOMs that one is required to calculate the inverse of matrices $\mathbf{S}$ and $\mathbf{C}$. This can create problems if the matrix becomes singular.

C matrix

For the **C** matrix, singularities can occur from two sources: the density matrix, ρ, becomes singular or the basis set tends towards completeness, the result of which are the parameter derivatives can no longer be projected out the space spanned by the Gaussians. Different ways have been proposed to address this problem.

The first uses a "dynamic coupling" approach, allowing one to neglect the coupling between GWPs when needed [232]. For large integration steps, the matrix is diagonalised and the corresponding eigenvalues compared with a pre-defined threshold (typically $\approx 10^{-6}$). For any inverse eigenvalues lower than this threshold, these functions are projected out of the matrix. The now uncoupled GWPs follow classical trajectories. For smaller integration steps, a regularisation technique is adopted. In this approach a scaling is applied to the lowest eigenvalue inverses and the inverse matrix is then reformed. This standard regularisation, however, still requires diagonalisation of the full C-matrix, creating severe bottlenecks for systems with many DOFs. Alternative regularisation schemes include Tikhonov regularisation [233], where the inverse is given by:

$$\tilde{\mathbf{A}}^{-1} = \left(\mathbf{A}^T\mathbf{A} + \Gamma^T\Gamma\right)^{-1}\mathbf{A}^T \tag{3.144}$$

Here Γ is a unit matrix multiplied by a factor that dictates the level of regularisation.

One can remove regularisation altogether (quite often feasible if unwanted parameters have been projected out through "dynamic coupling") and use a simple Cholesky or LU decomposition. This approach can result in very small integration steps and unstable propagation.

S matrix

When considering the **S** matrix, singularities arise either as the Gaussian overlap approaches one or, again, for a complete basis set which leads to an overlap matrix

with small eigenvalues. One can deal with these singularities in a similar way to those for the **C**-matrix. At each step, **S** is diagonalised and a threshold is chosen. If n eigenvalues are below this threshold then n are removed from the propagation and the wavepacket is re-expressed. Caution must be taken in this approach as it can lead to instabilities.

Despite the various techniques available, matrix inversion scales as $(n \times d)^3$ with n being the number of Gaussian basis functions and d with number of DOFs. It is this inversion that creates the major bottleneck in the computation.

Combatting this bottleneck can be achieved through a reformulation of the G-MCTDH or through a multi-layer approach, similar to ML-MCTDH [234], for which a two-layer system has been published [235].

3.12.2 Direct Dynamics

An extension to the vMCG model is the direct dynamics variant, DD-vMCG. One of the most promising applications of DD-vMCG is its ability to calculate the PES "on-the-fly". This avoids the need for a pre-fitted, pre-calculated PES, which is not only a time-consuming process but can also lead to complicated expressions for the kinetic energy operator. This recent development forms the basis for the methodology used to study the GFP proton mechanism in Chapter 7. It also serves the highlight a different way to construct PESs than were used in previous Chapters. As such, a range of different coordinates - Cartesian [236], Jacobi [227] and normal modes [237, 238] - have been used with DD-vMCG. These still suffer from issues, particularly separating out the translation, rotation and vibration motion.

By using a local Harmonic approximation, LHA:

$$V_j(\mathbf{r}) = V_{j0} + \sum_{\kappa} V'_{j,\kappa}(r_\kappa - q_{j\kappa}) + \frac{1}{2}\sum_{\kappa\mu} V''_{j,\kappa\mu}(r_\kappa - q_{j\kappa})(r_\mu - q_{j\mu}) \tag{3.145}$$

a simple form for the potential energy can be obtained and all that is required are the

energies, gradients and Hessians at the centre of each Gaussian basis function. These can be determined via an electronic structure package interfaced to the DD-vMCG algorithm. Nonetheless, electronic structure calculations can be computationally intense, especially for gradients and Hessians.

The DD-vMCG algorithm has been set up to allow for the creation of a database containing information about electronic energies, gradients, Hessians and even dipole moments and derivative couplings [236]. Using this data, the PES can be expanded in a Taylor series, truncated at second-order, around a particular geometry:

$$\mathbf{V}(\mathrm{x}) = (\mathbf{V}_0) + \mathbf{g}(\mathrm{x}_0).(\mathrm{x} - \mathrm{x}_0) + \frac{1}{2}(\mathrm{x} - \mathrm{x}_0).\mathbf{H}(\mathrm{x}_0).(\mathrm{x} - \mathrm{x}_0) \tag{3.146}$$

where $\mathbf{g}(\mathrm{x}_0)$ is the gradient and $\mathbf{H}(\mathrm{x}_0)$ the Hessian.

When constructing the nuclear wavepacket, each GWP is centred at a particular geometry (*i.e.* some point in configuration space). During the dynamics a GWP may reach a new geometry that has not been considered and hence is not already the database. This therefore requires the potential at this point to be determined. Whether this is through an electronic structure calculation or a weighted expansion, based on previous energies, is decided by the parameter *dbmin*.

When a new geometry is reached, the difference between it and those already in the database is measured through taking the Euclidean norm of the difference vector between all atomic coordinates. If the minimum value of this norm is greater than *dbmin* then a new point is calculated. The calculation of Hessians can however become a bottleneck. Proposed ways to avoid this include a Hessian update algorithm or a Hessian approximation using the Powell update algorithm [239].

Should the minimum value of the norm be less than *dbmin* then an expansion of the potential can be performed using a Shepard interpolation [240] to obtain the energies, gradients and Hessians. From the LHA data, the Shepard weighted

interpolated formula is as follows:

$$V(\mathbf{q}) = \sum_i \omega_i(\mathbf{q}) T_i(\mathbf{q}) \tag{3.147}$$

where:

$$\omega_i(\mathbf{q}) = \frac{\nu_i(\mathbf{q})}{\sum_j \nu_j(\mathbf{q})} \tag{3.148}$$

$$\nu_i(\mathbf{q}) = \frac{1}{|\mathbf{q} - \mathbf{q}_i|^{2p}} \tag{3.149}$$

and $T_i(\mathbf{q})$ is a Taylor series expansion of the energy.

Examples using the DD-vMCG have been outlined in a recent review [241].

Chapter 4

Components of the HBDI chromophore

Theoretical and experimental studies of the chromophore HBDI have highlighted inconsistencies between the relative energies of the ionisation threshold and excited states. One approach to examining the electronic structure and photoelectron spectrum of HBDI is to understand its chemical make up. This chapter aims to describe HBDI in terms of its individual components, phenoxide and imidazolide, by calculating their photoelectron spectra and energies of the S_1 and D_0 states. To achieve this, model Hamiltonians were used, through which the potential energy surfaces were obtained by fitting to a series of *ab initio* points. The results show that the electronic structure and photoelectron spectrum of HBDI can be attributed to effects from each component. The fine structure results from the imidazolide moiety and also emphasises the importance the bridge plays in the photodynamics. The location of S_1 below the detachment energy was attributed to the phenoxide moiety.

4.1 Introduction

The chromophore responsible for the eponymous green fluorescence in GFP was identified as *p*-hydroxybenzylidene-2,3-dimethylimidazolinone (HBDI) [49, 50]. It has also been established that only in its anionic form will HBDI emit green light, undergoing an ESPT to move from the neutral to the anionic form [242] . This makes

the electronic and photophysics of the HBDI anion of primary interest as a model to gain insight into GFP. From the outset, it is important to note differences between the HBDI anion in isolation and GFP itself. One major difference is the stabilisation that results from the protein environment in GFP, a mixture of amino acid residues and water. The location and determination of the detachment energy, whereby the neutral radical species is formed, is therefore of great interest. The energy of the ground state of the neutral radical (D_0) is not the only important electronic state. The location and possible interaction between excited radical states, D_1 and excited anion states (S_1, S_2 and S_3) is also essential. Figure 4.1 shows the location, relative energy differences and interaction between the anionic and neutral radical electronic states of HBDI.

Photoelectron spectroscopy is an important tool for providing information on the valence orbitals and electronic structure of a molecule. Data such as binding energies and ionisation potentials can be extracted. Analysis of the fine structure of the spectrum allows vibrational motion of the molecule, upon ionisation, to be resolved. The tunability of laser input energies means ionisation from different, higher energy orbitals can be readily explored. The photoelectron spectrum of the HBDI anion is useful for providing information on both the photodynamics and the stability of the anion. Such spectra have been measured and analysed extensively by both experimentalists and theoreticians. A contentious issue has been location of the excited S_1 state relative to the ionised D_0 state and as to whether such a state is bound at the FC region or adiabatically.

Using a combination of laser induced fluorescence and ion trapping, the photoelectron spectrum of the HBDI anion was recorded by Forbes *et al.* at 470 nm (2.64 eV) [243]. They observed no fluorescence in their ion trap and noted the major routes of ion deactivation was electron detachment and photo-fragmentation of the methyl group. Following this, photoelectron spectra from three different groups

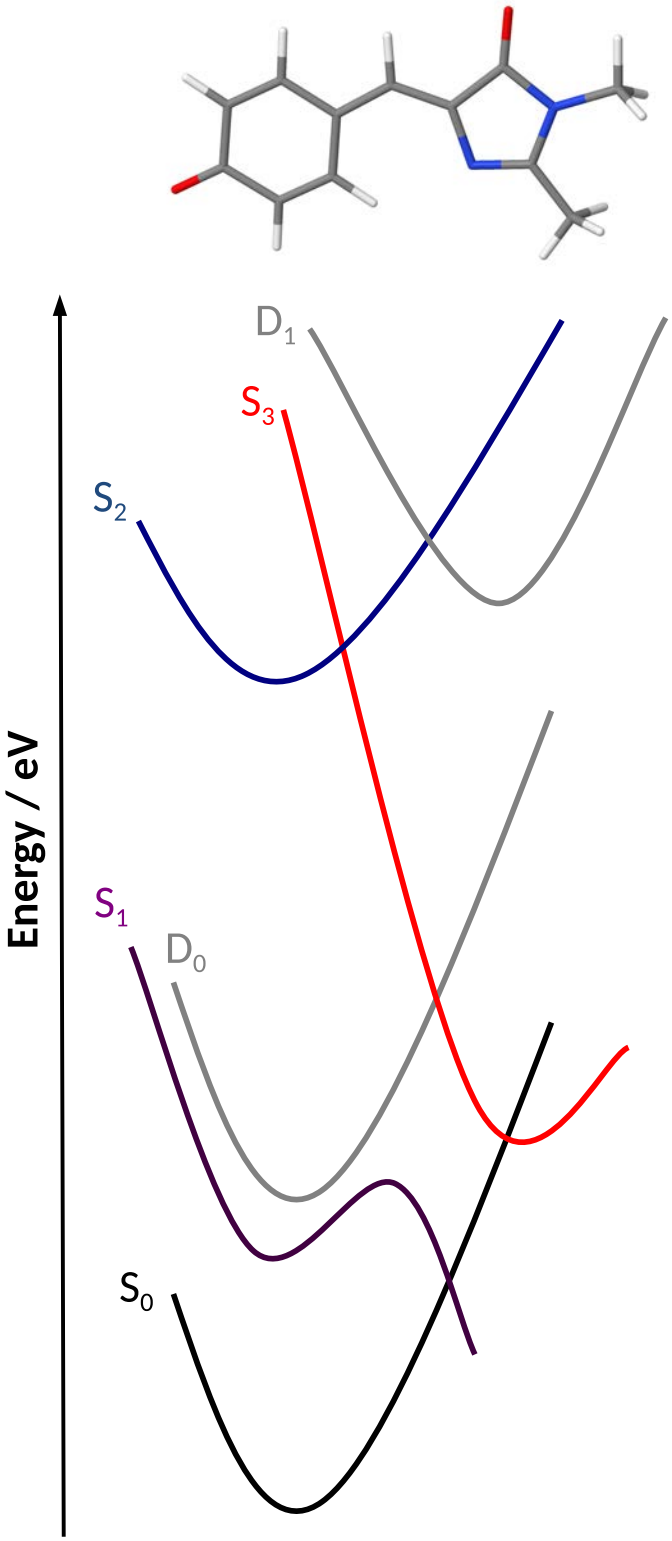

Fig. 4.1: Schematic diagram showing the relative energies and positions of the ground state (S_0) and excited states (S_1, S_2 and S_3) of the HBDI anion in relation to the detachment energy forming the ground state of the neutral radical species (D_0). Shown also is the first excited state of the neutral radical species (D_1). The closeness in energies and crossing between states lead to the variety of different photodynamic processes described in the text. The barrier in the S_1 state is also shown. Figure adapted from several references [246–248].

were published within the same year. Each also focussed on the electron detachment energy against the excited S_1 energy. Toker *et al.* determined from their measured photoelectron spectroscopy a vertical detachment energy of 2.68 eV and showed the S_1 state was bound in the FC region [244]. They also reported indirect resonant electron emission through the S_1 state. Horke and Verlet likewise agreed the S_1 state is bound and lies below the vertical detachment energy in the FC region [245], although their vertical detachment energy was 2.80 eV. This detachment energy was found to be higher than the S_1 absorption maximum at 2.57 eV. The adiabatic detachment energy was also reported as 2.60 eV. From this, they concluded that following excitation to S_1, the dominant channel in the FC region is not autodetachment, with there being evidence for a deactivation channel through internal conversion back to the ground state as illustrated in Figure 4.1.

Finally, using photoelectron imaging spectroscopy, Mooney *et al.* observed evidence of competition between direct photodetachment and autoionisation [249]. Upon excitation, these channels are accessed through IVR and IC of vibrational and electronic excited states that reside above the photodetachment energy. This points to anionic excited states higher than S_1 playing an important role in the ionisation dynamics. From the photoelectron spectrum, a vertical detachment energy of 2.85 eV was reported. The appearance of a second peak at 4.08 eV was assigned to ionisation via the first excited state of the neutral radical, shown as D_1 in Figure 4.1.

Theoretical values using an electronic propagator theory with an aug-cc-pVDZ basis returned a vertical detachment of 2.6 eV, showing reasonable agreement with experiment. As the GFP chromophore can be considered as being composed of two moieties: an imidazolinone and phenol unit, the authors suggest that the photodetachment of these individual components could provide useful insights into the photophysics of the HBDI anion. By examining the phenol anion only, it was noted

the vertical detachment energy of the HBDI anion is higher than the phenol anion. The higher energy of HBDI was explained as increased conjugation and delocalisation introduced by the imidazolinone unit, with the effect of stabilising the negative charge of the anion.

High-level *ab initio* calculations of the electron detachment energies and photoelectron spectrum have been reported by Bravaya and Krylov [250]. A variety of quantum chemical calculations and basis sets resulted in vertical detachment energies ranging from 2.50 to 2.80 eV, in good agreement with experimental data. In calculating the photoelectron spectrum, they also attributed the vibrational fine structure to bending modes predominantly involving the imidazolinone unit and bridge region. The photoelectron spectrum of the phenol anion was also calculated, following a similar approach to Mooney *et al.*, in examining of the moieties of HBDI. The phenoxide anion provides an ideal model system as the absence of any low-lying excited states removes the possibility of competing autodetachment.

One outstanding issue is whether the S_1 state is adiabatically bound. Work by Deng *et al.* supported the S_1 state to be bound in the FC region. They reported adiabatic and vertical detachment energies to be 2.73 eV and therefore the S_1 state to be bound adiabatically. This is shown in Figure 4.1, where the S_1 state clearly lies below D_0. In their recorded photoelectron spectrum, they also observed fine structure consistent with the vibrations of the radical species. Here again, it is important to stress these studies contained the HBDI anion in isolation, quite often in gaseous conditions.

Usually fluorescence is not observed when removing the chromophore from the protein environment. Recent work has, however, shown it to be possible to trap the isolated HBDI anion in the first excited state long enough for fluorescence to be recorded [247]. Of greatest intrigue was the presence of an energetic barrier in the S_1 state, highlighted in Figure 4.1, preventing fast radiationless IC back to the

ground state. This barrier succeeds at preventing relaxation in the gas phase only at temperatures under 100 K. In the protein, coupling between the chromophore and the environment raises this barrier to the extent that fluorescence is more readily observed.

Since the energies of S_1 and D_0 in the HBDI anion are close, a variety of competing deactivation channels have been reported. So far this includes: radiationless relaxation to S_0, photofragmentation, direct detachment, resonance autodetachment with S_1 and thermionic emission. Further work has explored the involvement of anionic excited states above the ionisation energy. Photoelectron spectra measured between 350 and 315 nm, identified a significant amount of detachment from $D_0 \leftarrow S_1$, but also identified resonant excitation of $2^1\pi\pi^*$ (S_1), which results in autodetachment to D_0 [248]. At high energies (315 nm, 3.94 eV) the D_1 detachment channel becomes available, allowing both direct and indirect electron detachment. The observed spectral broadening was proposed to occur from rapid vibration decoherence and ultrafast IVR.

Recent work by West *et al.* showed that for excitation energies greater than 3.7 eV there is population of the bright S_3 excited state [246]. The decay pathways can either be through autodetachment to D_0 or IC to S_2. For the latter, there is competition between autodetachment and rapid vibrational motion. For energies greater than 4.10 eV, there is also evidence for the $D_1 \leftarrow S_2$ channel becoming accessible. This channel is shown in Figure 4.1 where the two states cross each other.

The ionisation of the HBDI anion results in the removal of a π-electron from the HOMO to leave a singly-occupied orbital [251]. TD-DFT calculations show the first excited state of the neutral radical to be removal of an electron from the HOMO-2. The subsequent excited states are formed from removing an electron from the HOMO-1, HOMO-3 and HOMO-4 [245]. The S_1 and S_2 excited states of the anion

are formed from $\pi \rightarrow \pi^*$ transitions [248]. These orbitals are shown in Figure 4.2. The HOMO and LUMO are clearly π-orbitals and are delocalised across the entire molecule. The same is also true for the HOMO-2, from which removal of an electron forms the first excited radical state. The remaining orbitals are localised on one of the chromophore moieties and gives rise to higher energy radical excited states.

Discrepancies between theoretical and experiment studies, particularly between the vertical detachment energy relative to the S_1 energy have been reported [245]. This disparity brought to attention a need for greater understanding of the relative energies of the excited anion and ionised states. Moreover, a thorough understanding of the electronic structure of HBDI and its photoelectron spectrum was also desired. This formed the main motivation behind the work carried out here.

A bottom-up approach, considering firstly the individual components of HBDI and then the analogous totally symmetric "bis" versions of these components, can provide information on which moiety within the chromophore stabilises the anion and possibly gives rise to the fine structure in the photoelectron spectrum. Using this approach, the considered molecules were: imidazolide, phenoxide, bis-imidazoloxy and bis-phenoxide. Structures of these molecules are shown in Figure 4.3. The

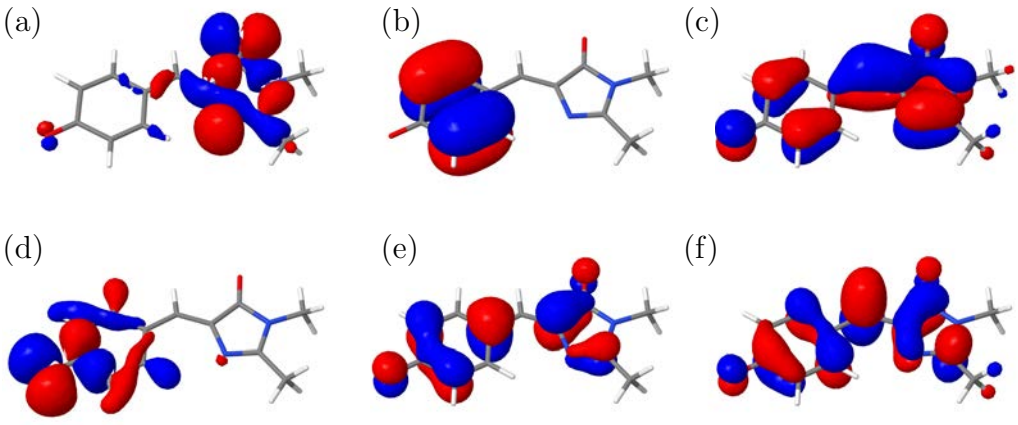

Fig. 4.2: Molecular orbitals for the HBDI anion from which an electron is either removed or excited to form the anion and neutral radical excited states. Shown are the (a) HOMO-4 (b) HOMO-3 (c) HOMO-2 (d) HOMO-1 (e) HOMO and (f) LUMO orbitals, calculated at the CCSD/6-31+G* level of theory.

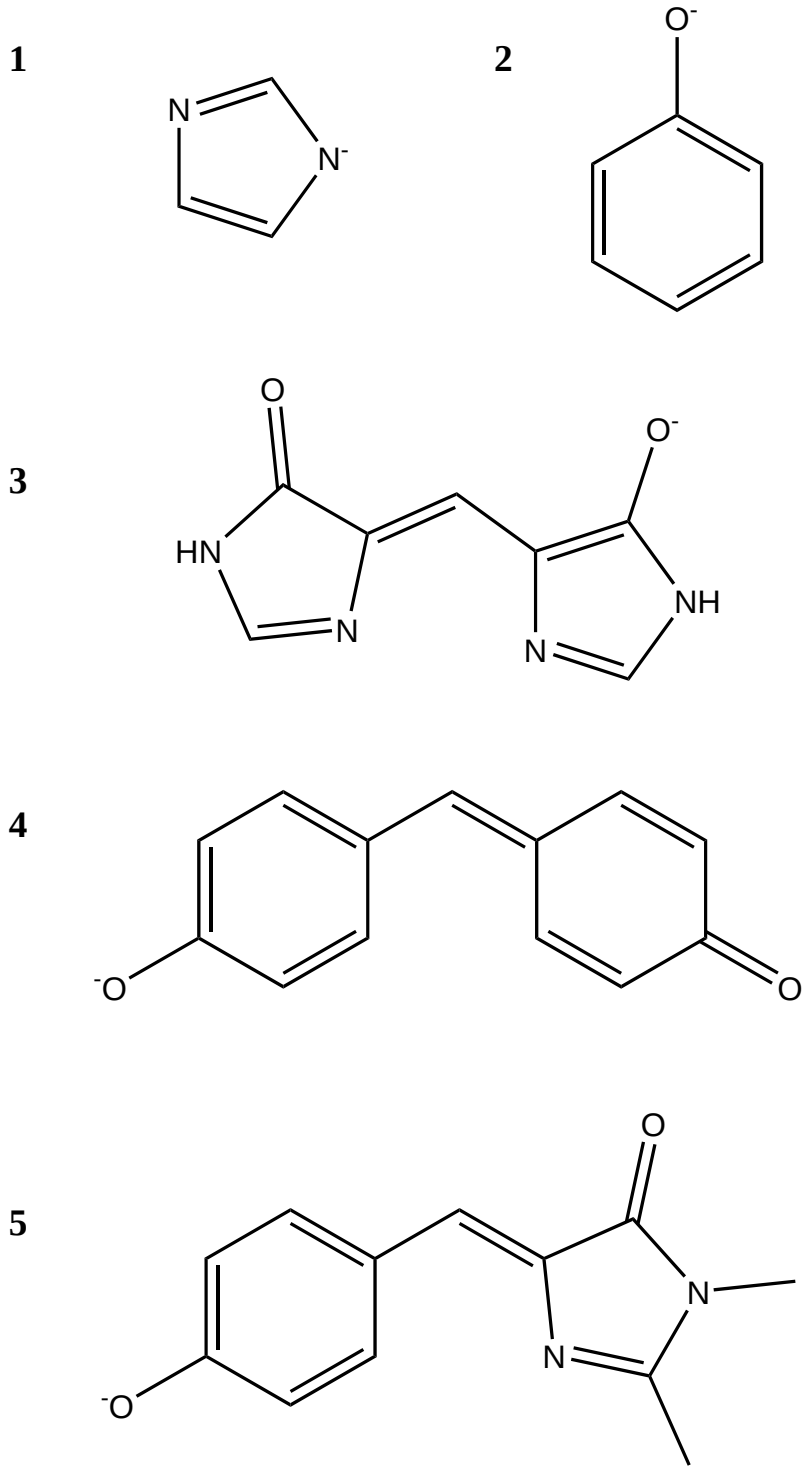

Fig. 4.3: Chemical structures of the molecules investigated in this chapter. **1** Imidazolide, **2** Phenoxide, **3** Bis-imidazoloxy, **4** Bis-phenoxy and **5** *p*-hydroxybenzylidene-2,3-dimethylimidazolinone (HBDI) the chromophore found in GFP. All molecules are in their deprotonated, anionic form.

idea of relating the electronic structure of HBDI to the individual components has already been discussed, although so far the focus has been on the phenoxide anion. The examination of the corresponding totally symmetric bis-systems has only been undertaken by Olsen and McKenzie, who considered the HBDI chromophore as a Brooker dye [252]. Their approach was more focussed on the electronic structure of the chromophore through simple molecular orbital theories and not on calculating photoelectron spectra.

4.2 The model Hamiltonian

In order to run quantum dynamics to calculate the photoelectron spectrum, a model Hamiltonian was constructed using the vibronic coupling Hamiltonian (VCHAM) model as outlined in Section 2.6. A model containing two states, the ground state of the anion and neutral radical, was sufficient for calculating the photoelectron spectrum, although the first excited state of the radical did require consideration for some of the molecules.

Symmetry will again play an important role as the majority of vibrational fine structure corresponds to totally-symmetric modes. It also provides a useful indicator of the modes coupling electronic states. Together, these reduce the number of parameters that are non-zero in the vibronic coupling Hamiltonian. The parameters are obtained by fitting adiabatic surfaces to a series of *ab initio* points.

Optimisation and frequencies of each structure were calculated at the DFT level of theory, using the B3LYP functional [193] and 6-31+G* basis set [167]. The use of DFT rather than wavefunction based methods was necessary for optimising the larger bis-systems, due to the low computational cost. The ionisation energies were obtained using the IP-EOM-CCSD [152] method as implemented in QChem [253]. It was also important to locate the energies of anionic excited states that may lie below the ionisation threshold. These were calculated using the EE-EOM-CCSD

Table 4.1: Computational details for the quantum dynamic simulations. The DVR type HO corresponds to Harmonic oscillator DVR, N_i are the number of primitive DVR functions used to describe each mode and n_i are the number of single particle functions used for the wavepacket on each state.

	Mode	DVR Type	N_i	n_1, n_2
	Imidazolide			
Excitation to $^2B_1$	Q_2	HO	31	6,4
	Q_5	HO	31	6,4
	Q_8	HO	31	6,4
	Phenoxide			
Excitation to $^2B_1$	Q_1	HO	31	6,1
	Q_{22}	HO	31	6,1
	Bis-imidazoloxy			
Excitation to $^2A_2$	Q_1	HO	31	6,1
	Q_2	HO	31	6,1
	Q_3	HO	31	6,1
	Q_6	HO	31	6,1
	Q_9	HO	31	6,1
	Q_{13}	HO	31	6,1
	Q_{14}	HO	31	6,1
	Bis-phenoxy			
Excitation to ^2A	Q_7	HO	31	6,1
	Q_8	HO	31	6,1
	Q_{19}	HO	31	6,1
	Q_{40}	HO	31	6,1
	Q_{57}	HO	31	6,1

method [254], also implemented in QChem. The choice of theory for the vertical energies was made by comparing values calculated using EOM-CCSD, ADC(2) and TDDFT with experimental data.

For calculating the photoelectron spectrum, the wavepacket was excited to the FC point on the ground state of the neutral radical (D_0) and allowed to propagate for 300 fs. Each wavepacket was prepared as a Gaussian with a width defined by the ground state Harmonic frequencies and centred on the FC point. A Harmonic oscillator DVR was used to describe each mode. Full details of the basis sets used in each simulation are given in Table 4.1.

4.3 Imidazolide

Imidazole is a five-membered heterocyclic aromatic compound. It contains two, non-adjacent nitrogens making it an azole. Deprotonation of the nitrogen bound hydrogen yields its anionic form, imidazolide (Figure 4.3(**1**)). Imidazolide possesses 18 vibrational modes and has C_{2v} symmetry. The first two ionisations involve removal of an electron from a π-orbital. The first ionisation is removal from the HOMO and the second from the HOMO-1. These valence orbitals are shown in Figure 4.4.

There has been little work reported on the imidazolyl radical and those there are utilised low level computational methods, although both agree the ground state of the radical to be $^2B_1$ [255, 256]. Calculations determined the first excited state

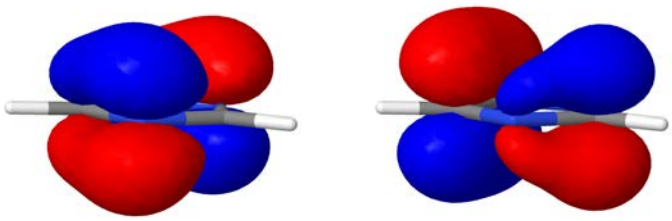

Fig. 4.4: The molecular orbitals for the valence electrons of imidazolide. Shown from left to right are the HOMO-1 and HOMO π-orbitals, calculated at the CCSD/6-31+G* level of theory.

Table 4.2: Vertical excited and ionisation energies of the imidazolide anion, calculated from the equilibrium geometry of the S_0 state, with different levels of theory and a 6-31+G* basis. All values in eV.

State	EOM-CCSD	ADC(2)	ωB97X-D	Experimental
$1^1B_2(S_1)$	4.14	4.12	4.41	-
$2^1B_2(S_2)$	4.65	4.61	4.96	-
$^2B_1(D_0)$	2.57	3.06	2.76	2.61 [257]
$^2A_2(D_1)$	3.50	4.49	4.09	-

of the neutral radical to lie between 0.40 and 0.90 eV above the ground state and to have $^2A_2$ symmetry. More recent work by Lineberger *et al.* has provided a detailed analysis of the electronic structure of the imidazolyl radical along with experimental and computational photoelectron spectra of imidazolide [257]. From the photoelectron spectra the electron affinity was determined to be 2.61 eV. The ground and first excited state of the radical was also confirmed to be $^2B_1$ and $^2A_2$. The energy of the excited D_1 state was determined to be between 0.90 and 1.00 eV above D_0. Detailed analysis of the photoelectron spectrum showed the presence of coupling between the $^2B_1$ and $^2A_2$ states [258].

To assess the quality of electronic structure methods and locate the relative energies of the anion excited states and ionisation threshold, a variety of methods were initially employed to provide a comparison. The results are shown in Table 4.2. From Table 4.2, it is evident that the ionisation threshold lies below the first excited state of the anion, thus any electronic transition into these excited states is likely to result in autodetachment. This is in contrast to HBDI in which, as shown in Figure 4.1, the S_1 state is below D_0. The calculated ionisation energy predicted by EOM-CCSD and TDDFT is in good agreement with values obtained from experimental photoelectron studies. The ADC(2) method overestimates the ionisation energy but predicts excited state energies of the anion consistent with EOM-CCSD. For TDDFT, the calculated energies of the S_1 and S_2 state are much higher. With

experimental data only available for the ionisation energy, the EOM-CCSD method performs best and was the chosen method for calculating the adiabatic surfaces and energies for all molecules. From the values calculated at EOM-CCSD, the excited radical state lies less than 1 eV above the ground state, a difference small enough for coupling between states to occur. The ionisation energy is close, but lower than the range of values given for the HBDI anion. This lower detachment energy reflects the smaller conjugation and delocalisation present for imidazolide.

The symmetry of the radical ground state was determined to be $^2B_1$ and the first excited radical state $^2A_2$, thus any coupling between these states will occur via b_2 modes. The vibrational frequencies of imidazolide calculated at the B3LYP/6-31+G* level are shown in Table 4.3. The calculated frequencies show good agreement with available experimental data.

Even with its low number of vibrational modes, a quantum dynamics model including all 18 is unfeasible, so only those important to the photodynamics are considered. This includes the totally-symmetric a_1 modes and the coupling b_2 modes. From the 18 vibrational modes there are seven totally-symmetric a_1 and six b_2 modes. Of these, three are important to the model: two a_1 modes, ν_2 a C-C stretch/C-H bend and ν_5 a C-C ring stretch/H-C-N deformation and the lowest frequency b_2 mode, ν_8, a ring distortion. Figure 4.5 illustrates these normal modes.

Parameters were obtained from fitting the vibronic coupling Hamiltonian to the adiabatic surfaces. The quality of fitting is evident from the low root mean square displacement (RMSD) value of 0.013 eV. This implies the fitted potentials pass through the majority of the calculated points, especially around the minima and any crossing points.

The on-diagonal, κ_α, and off-diagonal, λ_α, linear coupling constants are shown in Table 4.4. For the totally symmetric a_1 modes the values of κ_α are all non-zero. The two highest frequency modes as well as ν_3 were fitted as Morse potentials to

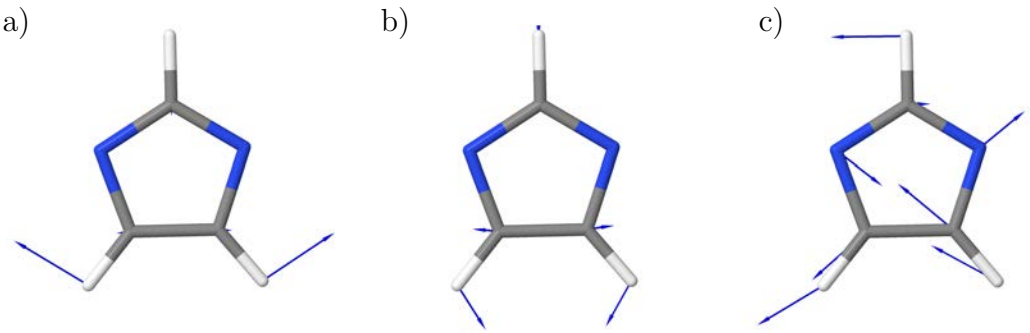

Fig. 4.5: The normal modes of imidazolide important in describing its photoelectron spectrum: (a) ν_2 C-C stretch/C-H bend, (b) ν_5 C-C ring stretch/H-C-N deformation and (c) ν_8 ring distortion. Calculated at the B3LYP/6-31+G* level of theory.

Table 4.3: Theoretically calculated frequencies of vibrational modes, in cm^{-1} and electron volts, for $\tilde{X}^1A_1$ state of the imidazolide anion calculated at the B3LYP/6-31+G* level of theory and ordered by their C_{2v} symmetries.

	Frequency		Symmetry	Exp.	Description
Mode	/ cm^{-1}	/ eV		[259, 260]	
1	933	0.116	a_1	971	Ring distortion
2	1095	0.136	a_1	1079	C-C stretch/C-H bend
3	1190	0.147	a_1	1146	Ring breathing
4	1264	0.157	a_1	1237	N-C stretch/C-N-C def.
5	1457	0.181	a_1	1489	C-C stretch/H-C-N def.
6	3168	0.393	a_1		C-H stretch
7	3188	0.395	a_1		C-H stretch
8	927	0.115	b_2	923	Ring distortion
9	1109	0.137	b_2	1106	C-H wagging
10	1245	0.154	b_2	1276	C-H bend
11	1321	0.164	b_2	1313	C-N stretch/C-H bend
12	1482	0.184	b_2	1459	C-N stretch/C-H bend
13	3161	0.392	b_2		C-H stretch
14	662	0.095	a_2		out of plane ring torsion
15	768	0.082	a_2		out of plane C-H bend
16	696	0.086	b_1		out of plane H-C-N bend
17	734	0.091	b_1		out of plane C-H bend
18	803	0.100	b_1		out of plane C-H bend

Table 4.4: On-diagonal linear coupling constants, κ_α for the normal modes of the imidazolide anion, as determined from fitting the vibronic coupling model Hamiltonian to adiabatic surfaces calculated at the IP-EOM-CCSD/6-31+G* level. All values in eV.

	κ_α				λ_α
Mode	$^2B_1$	κ/ω	$^2A_2$	κ/ω	
ν_1	-0.062	0.534	0.083	0.716	-
ν_2	-0.104	0.765	0.073	0.537	-
ν_3	-	-	-	-	-
ν_4	0.195	1.240	-0.110	0.701	-
ν_5	-0.204	1.130	0.117	0.646	-
ν_8	-		-		0.009
ν_{10}	-		-		0.213
ν_{11}	-		-		0.201

account for anharmonicity. The table also shows the ratio κ/ω, a value that provides information on how displaced the ground state radical minima are from the ground state anion minimum. The ratio values are large for modes ν_4, a N-C stretch/C-N-C deformation, ν_5, a C-C ring stretch/H-C-N deformation and ν_2, a C-C stretch/C-H bend. It was found that ν_4 did not contribute significantly to the photoelectron spectrum despite its large ratio value and was not included in the model. Larger displacements occur in the $^2B_1$ state compared with the excited $^2A_2$ state. The values of the κ_α parameters for modes ν_2 and ν_5 needed adjusting to improve the simulated photoelectron spectrum.

The λ_α parameters coupling electronic states are also shown in Table 4.4. Based on the symmetries of the two radical states, non-zero values are expected for b_2 modes. The values obtained indicate there to be strong coupling through ν_{10} and ν_{11}, with a very small amount occurring via the lowest frequency mode, ν_8. It was found, however, that modes ν_{10} and ν_{11} do not contribute to the photoelectron spectrum whilst ν_8 is important, although a small adjustment to the parameter is required. This adjustment was necessary to ensure the experimental spectrum was accurately replicated.

The on-diagonal second order quadratic parameters $\gamma_{\alpha\alpha}$ and the bilinear param-

Table 4.5: On-diagonal second-order coupling constants, γ_α, for the normal modes of the imidazolide anion, as determined from fitting the vibronic coupling model Hamiltonian to adiabatic surfaces calculated at the IP-EOM-CCSD/6-31+G* level. All values in eV.

Mode	$^2B_1$	$^2A_2$
ν_1	0.006	0.000
ν_2	0.017	0.016
ν_3	-	-
ν_4	0.003	0.027
ν_5	0.021	0.004
ν_6	-	-
ν_7	-	-
ν_8	-0.014	0.017
ν_9	0.007	0.010
ν_{10}	0.028	0.015
ν_{11}	0.021	0.033
ν_{12}	0.002	0.010
ν_{13}	0.052	0.051

Table 4.6: Off-diagonal second-order bilinear coupling constants, $\gamma_{\alpha\beta}$, for the normal modes of the imidazolide anion, as determined from fitting the vibronic coupling model Hamiltonian to adiabatic surfaces calculated at the IP-EOM-CCSD/6-31+G* level. All values in eV.

Mode	$^2B_1$	$^2A_2$
ν_{1-2}	-	0.0002
ν_{1-4}	-	0.0001
ν_{1-5}	-	-0.0001
ν_{2-3}	-	0.0001
ν_{2-4}	-0.0001	-
ν_{2-4}	-	-0.0002
ν_{3-5}	0.0002	-
ν_{3-5}	-	0.0003
ν_{4-5}	-0.0004	-
ν_{4-7}	-	0.0001
ν_{10-11}	-0.0001	-
ν_{11-13}	0.0001	-

Table 4.7: Parameters for the Morse functions used to fit the potential energy curves along the ring breathing mode ν_3 and the C-H stretch modes ν_6 and ν_7. The values of D_0 and E_0 have units of eV.

	D_0				D_1			
Mode	D_0	α	X_0	E_0	D_0	α	X_0	E_0
ν_3	98.931	-0.028	0.553	-0.024	98.979	-0.027	-1.350	-0.131
ν_6	5.838	-0.191	0.019	0.000	5.988	-0.191	-0.056	-0.001
ν_7	8.682	0.159	-0.102	-0.002	8.715	0.159	-0.117	-0.003

eters $\gamma_{\alpha\beta}$ are shown in Tables 4.5 and 4.6. The parameters $\gamma_{\alpha\alpha}$ govern changes in frequency from the ground state to the ionised states, whilst the $\gamma_{\alpha\beta}$ parameters correspond to IVR. All values for both parameters are small, with the largest indicating a small change in frequency for the ionised states of ν_{13}, the b_2 C-H stretch mode.

Some of the modes exhibited significant anharmonicity and needed fitting as Morse potentials, for which the parameters are listed in Table 4.7. This is typically true for high frequency modes and was so for modes ν_6 and ν_7, both C-H stretches. It was also found that the lower frequency, ring breathing mode, ν_3, required a Morse potential for the ionised states. Inspection of the cut along this mode showed the D_1 and D_0 states to cross. None of these modes were found to be important to the photodynamics and so were not included in the model. Based on the parameters, a model Hamiltonian consisting of the three modes expected to contribute to the spectrum were used.

Cuts through the PES along the important modes are shown in Figure 4.6. Being a totally-symmetric mode, a non-zero on-diagonal linear coupling value and hence a large shift is observed for the C-C stretch/C-H bend mode (Figure 4.6(a)). A greater shift is noted for the $^2B_1$ ground state. Another interesting feature seen along this mode, is the near crossing of these states. This suggests the possible presence of a conical intersection.

The totally symmetric C-C ring stretch/HCN deformation mode (Figure 4.6(b)) shows an even greater displacement for the $^2B_1$ state and clearly shows a crossing to occur with the $^2A_2$ state. The intersection is positioned near the FC point but is relatively high energy from the $^2B_1$ state and is unlikely to be significant to the photoelectron spectrum. Its position relative to the FC point on the upper $^2A_2$ state is more significant given the lower energy difference. It is likely that ionisation into this state will result in population transfer back to the neutral radical ground state. For calculating the photoelectron spectrum, only ionisation to the $^2B_1$ state was considered, however the prospect of an intersection existing between these states warrants further investigation, as does the photoelectron spectrum of the second ionisation band. Such an intersection is not surprising and has been seen for phenol, as will be discussed in Chapter 5.

As expected, the cut along the non-totally symmetric mode ν_8 shows no shift away from Q_0, although a small change in frequency is observed.

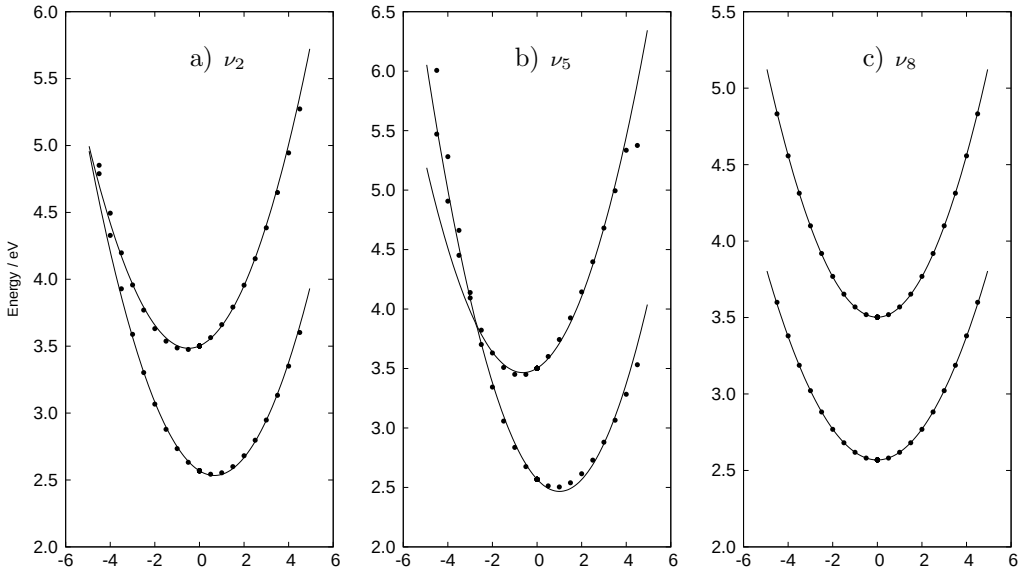

Fig. 4.6: Cuts through the adiabatic potential energy surfaces along select normal modes for the ionised states, which in order of energy at Q_0 are $^2B_1$ and $^2A_2$. The points are obtained from *ab initio* calculations at the IP-EOM-CCSD/6-31+G* level. The normal modes included are: (a) ν_2 C-C stretch/C-H bend, (b) ν_5 C-C ring stretch/H-C-N deformation and (c) ν_8 ring distortion.

Table 4.8: Values of selected coupling parameters adjusted from those obtained from the fitting procedure in order to reproduce the experimental spectra. All values in eV.

	κ_α	
Mode	$^2B_1$	κ/ω
$\nu_2^{(1)}$	-0.170	1.250
$\nu_5^{(1)}$	-0.230	1.270

The photoelectron spectrum calculated from the parameters obtained directly from the fitting was found to inadequately reproduce the experimental spectrum. The main difference were the intensities of the progressions, which were too weak. Adjustments to the on-diagonal linear coupling constants, κ_α, changed the gradients and so shifted the displacement of that mode's minimum. It was found that increasing the κ_α value for modes ν_2 and ν_5 increased the intensities in these modes' progressions. Table 4.8 lists the parameters where an adjustment to the fitted value was required. Only small amendments to the values were required. This implies the IP-EOM-CCSD surfaces are generally good.

The calculated photoelectron spectrum is shown in Figure 4.7(b and c) alongside experiment (a). The spectrum was calculated using the Quantics package with a two state, three mode model Hamiltonian. The spectrum in (b) has a damping time of 75 fs to match experimental broadening, whilst (c) has a damping time of 150 fs to emphasise the fine structure present and allow clear assignment. The electronic origin 0_0^0 of the resulting spectrum was at 2.35 eV due to errors in the electronic structure calculation. Agreement with experiment was only obtained when increasing the D_0 state energy to 2.83 eV. After correcting for the S_0 zero point energy, the vertical ionisation potential was 2.61 eV, in agreement with the experimental value.

The photoelectron spectrum is structured and shows good agreement with experiment. The intensities of the progressions relative to the origin are not as strong despite the adjustments made to the κ_α parameters. The progressions and peak spacings do however conform well with experiment. In their combined experimental

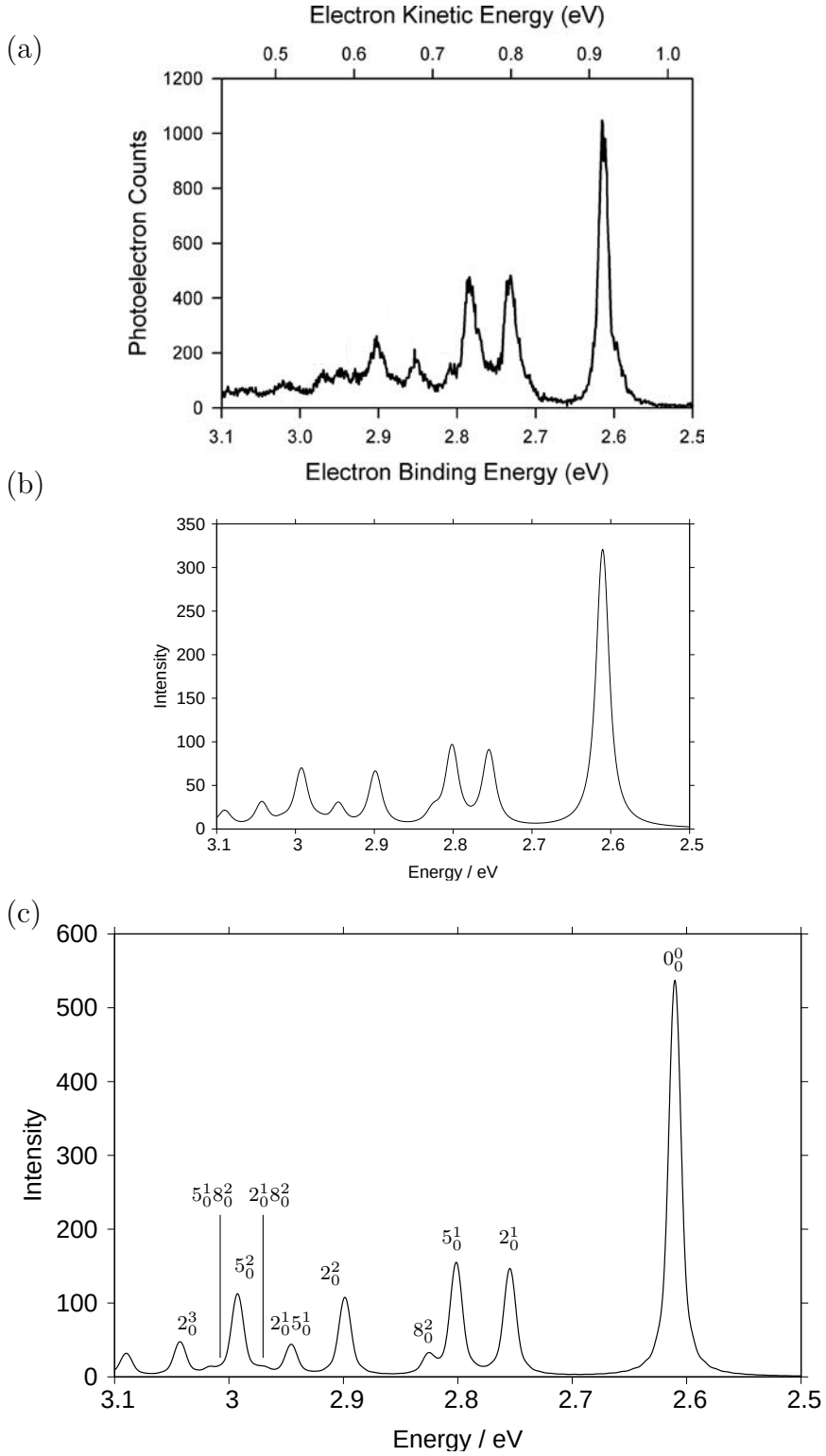

Fig. 4.7: The $^2B_1 \longleftarrow \tilde{X}^1A_1$ photoelectron spectrum. (a) the experimental spectrum measured by Lineberger *et al.* and reproduced with permission [258]. (b) the calculated spectrum using the Quantics program and a three mode model with a damping time of 75 fs and (c) the calculated spectrum with a damping of 150 fs to highlight the fine structure present, which has been assigned to the corresponding vibrational modes of the anion.

and simulated spectrum, Lineberger *et al.* assign the vibrational structure, based on the normal modes of the radical, to an a_1 C-C stretch mode (982 cm^{-1}), an a_1 N-C stretch mode (1436 cm^{-1}) and a b_2 N-C-N asymmetric stretch (780 cm^{-1}) [258]. These correspond to modes ν_2, ν_5 and ν_8 in the vibronic coupling model and show excellent agreement.

Initially, the peak appearing at 2.85 eV in the experimental spectrum seems to be absent from the simulated spectrum. This peak corresponds to 2_0^2, which in the simulated spectrum is seen to occur at 2.90 eV. This discrepancy originates from the differences in frequencies between the ν_2 mode in the anion and radical species. The spacings between peaks in the experimental spectrum correspond to the imidazolide radical frequencies, whereas the simulation uses the imidazolide anion frequencies. Normally, such changes in frequencies are small and included in the model through the γ_α terms. Further evidence can be seen from the 2_0^1 peak, which in the simulation occurs at slightly higher energy than in the experimental spectrum. Consequently, the peak that appears at 2.9 eV in the experimental spectrum, the combination mode $2_0^1 5_0^1$, also occurs at higher energy in the simulated spectrum. For ν_8 and ν_5, the peak spacings relative to the origin are in good agreement with the experiment.

Coupling between the $^2B_1$ and $^2A_2$ state results in a progression and combination peaks in the spectrum associated with ν_8, a b_2 mode. These peaks are very small, but nonetheless significant and do not appear in the spectrum if this mode is excluded from the model. This mode, however, only appears as the overtone 8_0^2. In the experimental spectrum, the absence of large changes in vibrational frequencies between the electronic states for this mode, lead the authors to conclude the overtone peaks gain intensity from a Fermi resonance with the 5_0^1 peak [258]. An alternative suggestion for this overtone peak was mode ν_{17}, a b_1 out of plane C-H bend mode. The exclusion of this mode from the model and presence of the 8_0^2 confirms the assignment of this peak as corresponding to ν_8.

4.4 Phenoxide

Phenoxide, Figure 4.3 (**2**), a six-membered aromatic cyclic compound, is the deprotonated form of phenol. It contains 30 vibrational modes and possesses C_{2v} symmetry. The molecular orbitals for the valence π electrons are shown in Figure 4.8. As an aromatic system, the HOMO is a π-orbital, as is the HOMO-1. The next lowest energy orbital comprises the oxygen lone pair and is similar to the HOMO-1 seen for the HBDI anion.

The first ionisation results from removal of a π-electron from the HOMO orbital, whilst the second ionisation is the removal of an electron from the oxygen lone pair, corresponding to the HOMO-2. Experimental photoelectron spectra have been measured for phenoxide. Gunion *et al.* determined an electron affinity of 2.25 eV from the photoelectron spectrum [261]. In the spectrum recorded at 3.50 eV, a small feature observed at high energy ($\sim$3.3 eV) was assigned as being the first excited state of the neutral radical species. From this, they predicted this excited state to reside about 1 eV above the radical ground state. The photoelectron spectrum at this energy also showed fine structure that could not be assigned, a finding attributed to autoionisation from a metastable anion state located 3.5 eV above the anion ground state. The photoelectron spectrum recorded at a lower energy (3.4 eV) showed the spectrum to contain a single FC progression corresponding to an a_1 ring breathing

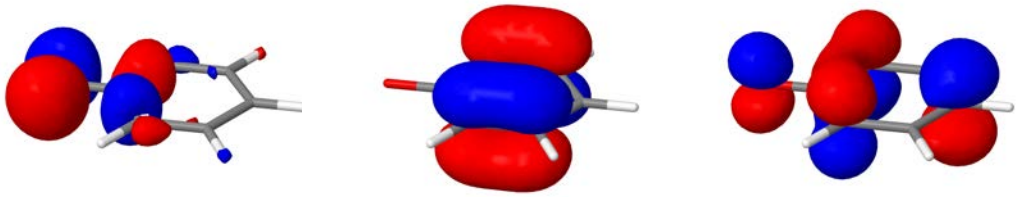

Fig. 4.8: The molecular orbitals for the valence electrons of the phenoxide anion. Shown from left to right are the HOMO-2, oxygen lone pair orbital and the HOMO-1 and HOMO π-orbitals, calculated at the CCSD/6-31+G* level of theory.

mode at (515 cm^{-1}). Further analysis suggested the presence of a second FC active mode at 1476 cm^{-1} corresponding to a C-O stretching mode.

More recently, Kim *et al.* used slow photoelectron velocity-map imaging (SEVI) spectroscopy to study the phenoxide anion [262]. From the spectrum, their electron affinity value of 2.25 eV is in excellent agreement with Gunion. At low resolution, the spectrum also showed a single progression corresponding to the low frequency a_1 ring breathing mode reported previously. At high resolution, however, a doublet structure was observed in the spectrum. This second progression was assigned as being a combination of the ring breathing a_1 mode with the hot band of the lowest frequency a_2 mode, an out of plane ring distortion. The spectrum also showed the C-O stretch mode, previously reported as being observed, to not be FC active. Both studies did agree on the symmetry of the ground state neutral radical to be $^2B_1$.

The theoretical photoelectron spectrum calculated by Mooney *et al.* and Krylov predicted ionisation values between 1.97 and 2.37 eV, depending on the quantum chemical method employed [249, 250]. Studies of the excited states of the neutral radical have shown the first excited state to lie 1 eV above the ground state and to be of $^2B_2$ symmetry [263–265].

Table 4.9 shows the vertical excitation and ionisation energies calculated using different levels of theory. The ionisation energy predicted by EOM-CCSD, which showed excellent agreement for imidazolide, is underestimated. The first excited state of the radical does, however, show good agreement. The TDDFT ionisation energy is in good agreement, but the excited state of the anion is overestimated. ADC(2) is the only method to predict the ionisation energy to lie above the first excited state of the anion. This method, however, calculates the ground state radical to have $^2B_2$ symmetry as opposed to $^2B_1$. This is why the predicted value of 3.23 eV for the D_0 state is consistent with the values predicted by EOM-CCSD and TDDFT for the D_1. The ADC(2) method therefore either misses this state or predicts its

Table 4.9: Vertical excited and ionisation energies of the phenoxide anion, calculated from the equilibrium geometry of the S_0 state, with different levels of theory and a 6-31+G* basis. All values in eV.

State	EOM-CCSD	ADC(2)	ωB97X-D	Experimental [262]
$^1B_2(S_1)$	3.37	3.14	3.94	3.31
$^1A_2(S_2)$	3.73	3.49	4.13	-
$^2B_1(D_0)$	1.89	3.23	2.18	2.25
$^2B_2(D_1)$	3.12	4.64	3.30	3.31

energy to be much higher. Despite predicting a lower ionisation energy compared with experiment, the EOM-CCSD method was retained, having been successful in calculating the photoelectron spectrum of imidazole.

The energy needed to remove an electron is lower than for imidazolide, implying the phenoxide anion is less stable. Similarly to imidazolide, the ionisation energy is below any anion excited states. This ordering of states differs to those seen in Figure 4.1 for HBDI. The energy of the first excited state of the anion shows good agreement with the feature Gunion *et al.* observed in their high energy spectrum and assigned to a metastable excited state of the anion. However, the presence of a metastable anion state above the the ionisation threshold is similar to HBDI.

The excited state of the radical (D_1) was considered, as given it lies close in energy to the D_0 state, coupling between states may occur. The symmetry of the electronic states were determined to be $^2B_1$ and $^2B_2$ for the ground and first excited state of the radical. Any coupling between these states will therefore be via a_2 vibrational modes.

The vibrational frequencies calculated at the B3LYP/6-31+G* level of theory are shown in Table 4.10. There are eleven totally-symmetric a_1 modes, with similar vibrations to those for phenol and three a_2 modes that are responsible for any coupling between the states. The calculated values show good agreement for modes where experimental data could be obtained.

Table 4.10: Theoretically calculated frequencies of vibrational modes, in cm^{-1} and electron volts, for $\tilde{X}^1A_1$ state of the phenoxide anion calculated at the B3LYP/6-31+G* level of theory and ordered by their C_{2v} symmetries.

	Frequency		Symmetry	Exp.	Description
Mode	/ cm^{-1}	/ eV		[266, 267]	
1	531	0.066	a_1		Ring deformation/C-O stretch
2	823	0.102	a_1	820	Ring breathing
3	980	0.122	a_1	992	Trigonal ring breathing
4	1027	0.127	a_1	1020	C-C-H bend
5	1177	0.146	a_1	1168	C-H bend
6	1408	0.175	a_1	1264	C-O stretch/C-H bend
7	1548	0.192	a_1	1534	C-C-H bend/C-O stretch
8	1628	0.202	a_1	1585	C-C ring stretch
9	3100	0.384	a_1		C-H stretch
10	3149	0.391	a_1		C-H stretch
11	3162	0.392	a_1		C-H stretch
12	446	0.055	b_2		C-C-O bend
13	616	0.076	b_2		Ring deformation
14	1075	0.133	b_2		C-H bend
15	1160	0.144	b_2		C-H bend
16	1260	0.156	b_2		C-H bend/C-C stretch
17	1351	0.168	b_2	1324	C-H bend/C-C stretch
18	1484	0.184	b_2	1447	C-C stretch
19	1555	0.193	b_2	1569	C-C stretch
20	3104	0.385	b_2		C-H stretch
21	3149	0.391	b_2		C-H stretch
22	428	0.053	a_2		Out of plane ring distortion
23	795	0.099	a_2		Out of plane assym. C-H bend
24	929	0.115	a_2		Out of plane assym. C-H bend
25	189	0.024	b_1		Out of plane ring bend/C-O bend
26	500	0.062	b_1		Out of plane C-H bend
27	680	0.084	b_1		Out of plane C-H bend
28	696	0.086	b_1		Out of plane C-H bend
29	838	0.104	b_1		Out of plane C-H bend/O-C-C bend
30	931	0.116	b_1		Out of plane C-H bend

For the construction of a vibronic coupling Hamiltonian only the totally symmetric a_1 and the a_2 modes contained non-zero parameters and are therefore important in the photochemistry of the phenoxide anion. From this subset of normal modes, only two are important to the model, the lowest frequency a_1 mode, a ring deformation with C-O stretch and the lowest frequency a_2 mode, an out of plane ring distortion. From previous experimental studies, the a_1 mode ν_7, a C-C-H bend plus C-O stretch mode, was suggested as being active and so was considered for inclusion in the model. The three modes: ν_1, ν_7 and ν_{22} are illustrated in Figure 4.9

The parameters obtained from fitting the vibronic coupling model Hamiltonian to the adiabatic surfaces are shown in Tables 4.11-4.14 and the cuts along the important normal modes are illustrated in Figure 4.10.

The on-diagonal linear coupling constants, κ_α, for the two lowest ionised states are listed in Table 4.11. It was necessary to fit the three highest frequencies, ν_9, ν_{10} and ν_{11} as Morse potentials to account for anharmonicity. Shown also is the ratio κ/ω, an important parameter for determining how displaced the ionised state minima are from the ground state minimum. Such a ratio becomes important for lower frequency modes and is therefore large for ν_1, the ring deformation/C-O stretch mode. The remaining ratios for the D_0 state are small and so only the ν_1 mode was

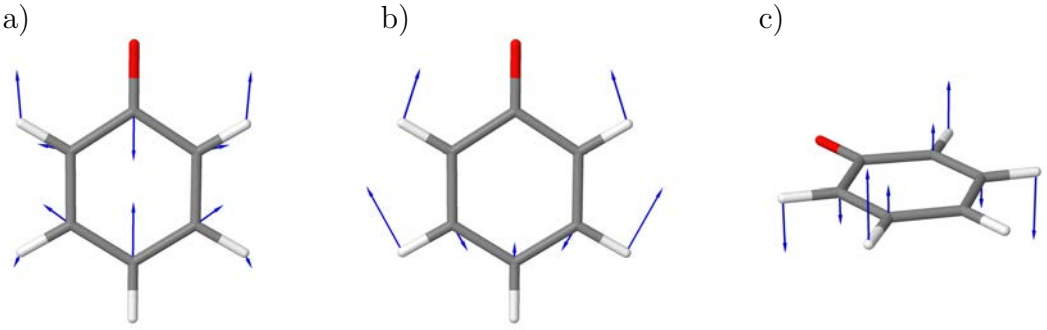

Fig. 4.9: The normal modes of phenoxide important in describing its photoelectron spectrum: (a) ν_1 ring deformation/C-O stretch, (b) ν_7 C-C-H bend/C-O stretch and (c) ν_{22} out of plane ring distortion. Calculated at the B3LYP/6-31+G* level of theory.

Table 4.11: On-diagonal linear coupling constants, κ_α for the normal modes of the phenoxide anion, as determined from fitting the vibronic coupling model Hamiltonian to adiabatic surfaces calculated at the IP-EOM-CCSD/6-31+G* level. All values in eV.

Mode	$^2B_1$	κ/ω	$^2B_2$	κ/ω
ν_1	-0.092	1.396	-0.055	0.835
ν_2	-0.032	0.314	0.044	0.431
ν_3	-0.021	0.172	0.002	0.016
ν_4	0.029	0.228	0.016	0.126
ν_5	-0.011	0.075	0.040	0.274
ν_6	0.016	0.091	0.111	0.636
ν_7	0.041	0.214	0.136	0.709
ν_8	-0.022	0.109	-0.187	0.926

Table 4.12: On-diagonal second-order coupling constants, γ_α, for the normal modes of the phenoxide anion, as determined from fitting the vibronic coupling model Hamiltonian to adiabatic surfaces calculated at the IP-EOM-CCSD/6-31+G* level. All values in eV.

Mode	$^2B_1$	$^2B_2$
ν_1	0.001	-0.000
ν_2	0.005	0.004
ν_3	0.005	-0.002
ν_4	0.009	0.012
ν_5	0.016	0.024
ν_6	0.009	0.014
ν_7	0.003	-0.017
ν_8	-0.013	-0.016
ν_{22}	-0.007	0.002
ν_{23}	0.041	0.048
ν_{24}	0.037	0.029

included in the model. The C-C-H bend/C-O stretch mode, ν_7, has previously been suggested as a possible transition in the photoelectron spectrum. The κ_α value for this mode is small, as is the ratio κ/ω. This makes it unlikely to be important in the photoelectron spectrum.

The absence of any off-diagonal linear coupling constants, λ_α, shows there is no coupling between the electronic states through the a_2 modes. The calculated energy difference between the $^2B_1$ and $^2B_2$ state is large enough for there to be no significant coupling. Despite this, the lowest frequency a_2 mode has been reported as a combination peak in the photoelectron spectrum. As such, it was decided to include this mode in the model.

Table 4.12 shows the on-diagonal second order coupling constants, γ_α and Table 4.13 the bilinear coupling constants, $\gamma_{\alpha\beta}$. The values are all small, with the largest occurring in the γ_α values for modes ν_{23} and ν_{24}, the a_2 modes.

The parameters for the Morse potentials needed to fit the high frequency a_1 modes are shown in Table 4.13. These modes are all C-H stretches and were not deemed important, so were excluded from the model.

Based on the fitted parameters, a model was constructed comprising three normal modes deemed to be important to the photodynamics. These modes are ν_{22}, ν_1 and ν_7.

The cuts through the PES along the three normal modes are shown in Figure 4.10. Being a non-totally symmetric mode, the cut for ν_{22}, as shown in Figure 4.10(a), shows there to be no displacement of the minima away from Q_0. The change in frequency, represented by the larger value for γ_α, can also be observed. The energy gap between the $^2B_1$ and $^2B_2$ state is sufficient that no coupling λ_α parameters for this mode were obtained.

Figure 4.10(b) shows the cut along ν_1, the ring deformation/C-O stretch mode. As a totally symmetric mode, the on-diagonal linear coupling constant is non-zero

Table 4.13: Off-diagonal second-order bilinear coupling constants, $\gamma_{\alpha\beta}$, for the normal modes of the phenoxide anion, as determined from fitting the vibronic coupling model Hamiltonian to adiabatic surfaces calculated at the IOP-EOM-CCSD/6-31+G* level. All values in eV.

Mode	$^2B_1$	$^2A_2$
ν_{22-23}	0.001	0.001
ν_{1-10}	0.001	0.001
ν_{1-11}	0.003	0.003
ν_{2-9}	-0.001	-0.001
ν_{2-11}	-0.005	-0.005
ν_{3-9}	-0.002	-0.002
ν_{3-10}	-0.001	-0.001
ν_{3-11}	0.003	0.003
ν_{4-9}	0.001	0.001
ν_{4-10}	0.001	0.001
ν_{4-11}	0.005	0.005
ν_{5-8}	-0.001	-
ν_{5-9}	0.001	0.001
ν_{5-10}	-0.001	-0.001
ν_{5-11}	0.001	0.001
ν_{6-7}	0.001	0.001
ν_{6-10}	0.001	0.001
ν_{6-11}	-0.002	-0.002
ν_{7-8}	-0.000	-
ν_{7-9}	-0.002	-0.002
ν_{7-10}	0.001	0.001
ν_{7-11}	0.002	0.002
ν_{8-9}	-0.001	-0.001
ν_{8-11}	-0.004	-0.004
ν_{9-10}	0.001	0.001
ν_{9-11}	0.002	0.002
ν_{10-11}	-0.002	-0.002

Table 4.14: Parameters for the Morse functions used to fit the potential energy curves along the C-H stretch modes ν_9, ν_{10} and ν_{11}. The values of D_0 and E_0 have units of eV.

	D_0				D_1			
Mode	D_0	α	X_0	E_0	D_0	α	X_0	E_0
ν_9	16.928	0.112	-0.031	-0.0002	17.003	0.113	-0.040	-0.0003
ν_{10}	44.462	0.072	-0.108	-0.003	44.141	0.072	-0.108	-0.003
ν_{11}	83.778	-0.052	-0.455	-0.047	83.812	-0.052	-0.463	-0.048

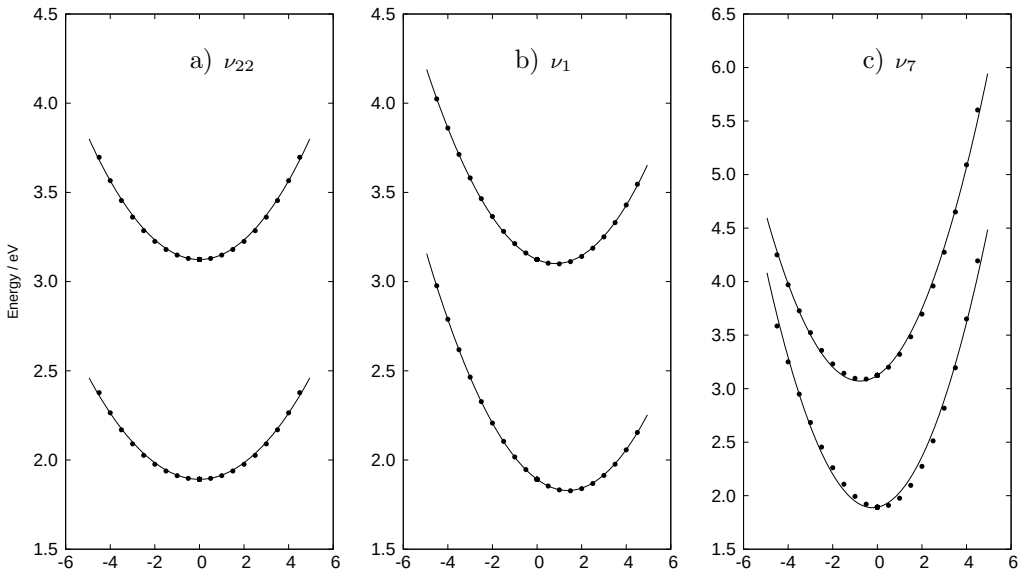

Fig. 4.10: Cuts through the adiabatic potential energy surfaces along select normal modes for the ionised states of phenoxide, which in order of energy at Q_0 are $^2B_1$ and $^2B_2$. The points are obtained from *ab initio* calculations at the IP-EOM-CCSD/6-31+G* level. The normal modes included are: (a) ν_{22} out of plane ring deformation, (b) ν_1 ring deformation/C-O stretch and (c) ν_7 C-C-H bend/C-O stretch.

and a large shift in the $^2B_1$ state is observed. For ν_7, the C-C-H bend/C-O stretch mode, no displacement in the $^2B_1$ is observed, reflecting the small κ_α value. The cut along this mode shows it is insignificant and unlikely to contribute to the spectrum. This leaves a two mode model consisting of modes ν_1 and ν_{22}.

The calculated photoelectron spectrum with a damping of 100 fs is shown in Figure 4.11(b) alongside the spectrum measured by Kim *et al.*, Figure 4.11(a). The top panel of (a) shows the experimental spectrum at low resolution, below which are selected regions of high-resolution scans. The bottom panel is a FC simulation. To fully replicate the intensities of the progression, it was necessary to adjust the parameter $\kappa_1^{(1)}$ to a value of -0.12 eV.

The overall shape of the simulated spectrum matches well with experiment. The electronic origin 0_0^0 of the simulated spectrum was at 1.78 eV as a result of errors from the electronic structure calculation. In order to obtain good agreement with experiment, the energy of the D_0 state was increased to 2.35 eV. After again cor-

(a)

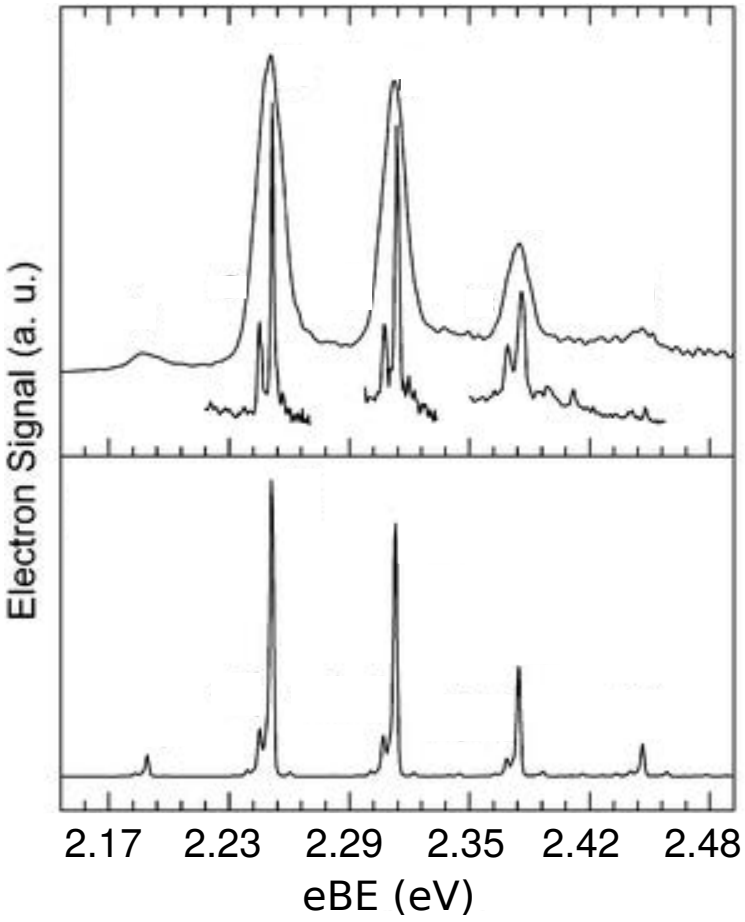

(b)

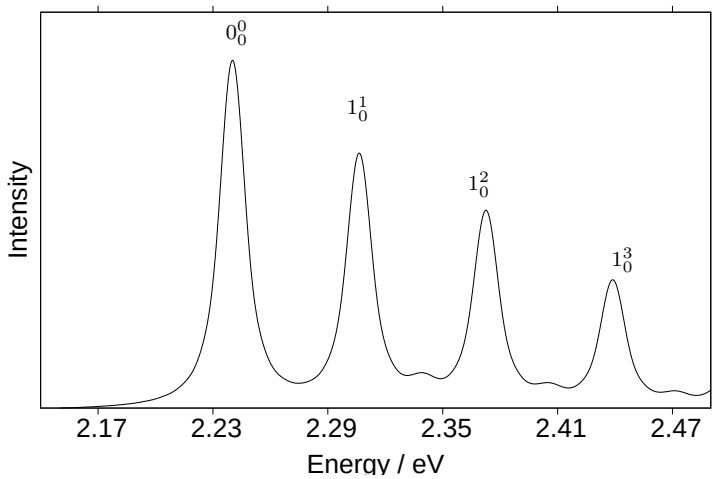

Fig. 4.11: The $^2B_1 \longleftarrow \tilde{X}^1A_1$ photoelectron spectrum of phenoxide. (a) the experimental spectrum as measured by Kim *et al.* and reproduced with permission [262]. (b) the calculated spectrum using the Quantics program and a two mode model with a damping time of 100 fs.

recting for the S_0 zero point energy, a vertical ionisation potential of 2.25 eV was obtained.

A single progression is observed corresponding to ν_1, the a_1 ring distortion / C-O stretch mode. This assignment agrees with both Gunion and Kim. A small feature observed between the progression, starting from the 1_0^1 peak is likely the $1_0^n 22_0^1$ combination peak. This feature is not observed in the low resolution experimental spectrum, although a very small feature can be observed in the high resolution and FC simulated spectrum. The very low intensity however makes it difficult to confidently assign against background noise. The doublet structure formed from the $1_0^n 22_1^1$ combination progression was not observed, likewise the hotband peak corresponding to 1_1^0 is also absent. The MCTDH framework is capable of calculating hotband features, but all attempts to reproduce these in the simulated spectrum were unsuccessful.

The photoelectron spectrum of phenoxide is much simpler compared with imidazolide. The structure of the phenoxide spectrum consists of a progression arising from a single mode, whilst imidazolide contains two progressions, in addition to combination peaks and overtones. Coupling also plays a role in the imidazolide spectrum, whereas none is observed for phenoxide. It is difficult to compare these spectra to that of the HBDI anion, which is often observed to be broad and lacking clear fine structure. However, there are experimental and theoretical photoelectron spectra that clearly show the fine structure, [244, 250, 251], with a comparison between them shown in Figure S3 of [251]. The fine structure shows similarities to the phenoxide and imidazolide spectra. A main progression, similar to phenoxide is evident, but also present are numerous features resembling the more complicated structure seen for imidazolide. Bavara and Krylov identified the fine structure as resulting mainly from bending vibrations [250], whereas stretching modes, particularly ring distortions, are responsible for the structure in both phenoxide and imidazolide.

4.5 Bis-imidazoloxy

Having examined the ionisation energy and photoelectron spectrum of the individual components of the HBDI chromophore, the next step was to investigate the totally symmetric analogues of the chromophore. This entails having both moieties on the chromophore being the same *e.g.* two phenoxide groups. This approach leads to the molecules bis-imidazoloxy (Figure 4.3 (**3**)) and bis-phenoxy (Figure 4.3 (**4**)). It was anticipated that comparing these molecules with the HBDI anion would provide insights as to which component contributes most (or equally) to the electronic structure and stability of the chromophore. The relative energies of the ion and excited states with respect to HBDI (shown in Figure 4.1) was also of great interest.

Bis-imidazoloxy is the totally-symmetric analogue containing the imidazolinone derivative. Unlike imidazole, deprotonation now occurs by removal of a proton from an oxygen and not the nitrogen. The optimised structure remains planar and keeps the C_{2v} molecular symmetry. It possesses 46 vibrational modes, but the retention of symmetry reduces the number of normal modes that need to be considered. The

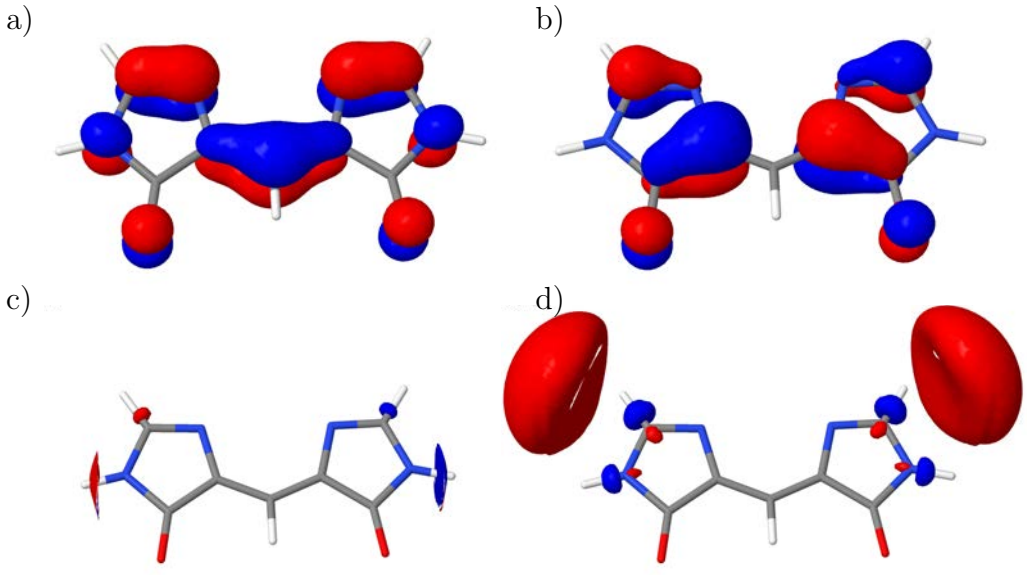

Fig. 4.12: The frontier molecular orbitals for the valence electrons of bis-imidazoloxy. Shown are the (a) HOMO-1, (b) HOMO, (c) LUMO and (d) LUMO+1. The HOMO-1 and HOMO are π-orbitals whilst the LUMO and LUMO+1 are diffuse orbitals, calculated at the CCSD/6-31+G* level of theory.

Table 4.15: Vertical excited and ionisation energies of the bis-imidazoloxy anion, calculated from the equilibrium geometry of the S_0 state, with EOM-CCSD level of theory and a 6-31+G* basis. All values in eV.

State	EOM-CCSD
$^1A_2(S_1)$	3.49
$^1B_2(S_2)$	3.54
$^2A_2(D_0)$	2.39
$^2B_2(D_1)$	4.57

frontier molecular orbitals for the valence electrons are shown in Figure 4.12. The HOMO-1 and HOMO are π-orbitals, as expected for a conjugated system. The LUMO and LUMO+1 do not show significant valence character, with the majority of the density residing away from the molecular structure. The lowest π^*-orbital is the LUMO+5.

There is very little work in the literature on bis-imidazoloxy. One theoretical study by Olsen and McKenzie, using state averaged CAS(4,3) calculations, predicted the S_1 energy as 2.91 eV and the S_2 energy as 4.01 eV [252]. This was found to be higher than the HBDI chromophore, which itself was higher than the bis-phenoxy energies.

From IP-EOM-CCSD calculations, the first and second ionisations are removal of a π-electron from the HOMO and HOMO-1. The calculated ionisation energies, alongside the excited state energies of the anion, are shown in Table 4.15. The vertical ionisation energy was calculated to be 2.39 eV, lower than imidazolide and the HBDI anion. This indicates the bis-imidazoloxy anion is less stable and removal of an electron easier. The value is, however, higher than for the phenoxide anion. The calculated energy for the first excited state of the neutral radical is much higher than imidazolide or phenoxide, with a value over 2 eV above the ground state. This difference in energy is large enough for coupling between the states to be negligible.

The symmetry of the radical ground state was determined to be $^2A_2$ and for the first excited radical state to be $^2B_2$. The first excited state of the anion results from a HOMO $\rightarrow$ LUMO+1 transition. The value of S_1 is higher than the detachment energy. This is similar to the other molecules studied so far, but different from the HBDI pictured illustrated in Figure 4.1.

The vibrational frequencies calculated at the B3LYP/6-31+G* level of theory are listed in Table 4.16. Only the in plane a_1 and b_2 vibrations are shown, of which there are 17 a_1 modes.

For building the vibronic coupling Hamiltonian only the totally symmetric a_1 modes were considered. Any coupling between the D_0 and D_1 states occurs via the out of plane b_1 modes, however given the large energy gap between these states, any coupling is likely to be very small and therefore these modes were not considered.

From the fitted parameters, seven a_1 modes were deemed important in the photoelectron spectrum and were included in the model. These were: ν_1, a C-C(H)-C bridge bending mode; ν_2, a C-C bridge stretching mode; ν_3, a C-O, N-H and C-H bending mode; ν_6, a N-C-N ring bend mode; ν_9, a C-C ring stretch mode; ν_{13}, a C-N stretch with C-H bending mode and ν_{14}, a C-O stretching mode. These are illustrated in Figure 4.13. Similar to that observed for HBDI, the important modes consist mainly of bending modes, with the low frequency modes involving motion of the bridging methine group.

The parameters obtained from fitting the vibronic coupling Hamiltonian to the adiabatic surfaces are shown in Table 4.17-4.19. The RMSD value of 0.012 indicates good quality fitting is achieved, with the fitted curve passing through most of the calculated points.

The on-diagonal linear coupling constants, κ_α, are shown in Table 4.17. Again, the values are only non-zero for totally symmetric modes. The three highest frequency modes were fitted as Morse potentials to account for anharmonicity. Refer-

Table 4.16: Theoretically calculated frequencies of the in plane vibrational modes (a_1 and b_2), in cm^{-1} and electron volts, for $\tilde{X}^1A_1$ state of the bis-imidazoloxy anion calculated at the B3LYP/6-31+G* level of theory and ordered by their C_{2v} symmetries.

	Frequency		Symmetry	Description
Mode	/ cm^{-1}	/ eV		
1	94	0.012	a_1	C-C(H)-C bridge bend
2	245	0.030	a_1	C-C bridge stretch
3	549	0.068	a_1	C-O bend / N-H bend / C-H bend
4	678	0.084	a_1	C-H bridge stretch / C-O stretch / N-H bend
5	833	0.103	a_1	C-H bridge stretch
6	910	0.113	a_1	N-C-N ring bend
7	1053	0.131	a_1	N-H bend
8	1087	0.135	a_1	H-N-C-H bend
9	1241	0.154	a_1	C-C ring stretch
10	1324	0.164	a_1	C-H ring bend
11	1390	0.172	a_1	N-H bend
12	1473	0.183	a_1	C-C bridge stretch
13	1581	0.196	a_1	C-N stretch / C-H bend
14	1718	0.213	a_1	C-O stretch
15	3160	0.392	a_1	C-H bridge stretch
16	3208	0.398	a_1	C-H ring stretch
17	3651	0.453	a_1	N-H stretch
18	220	0.027	b_2	C(H)-C-C(O) assym. bend
19	508	0.063	b_2	O-C-N-H assym. bend
20	694	0.086	b_2	C-H bridge bend / C-O stretch
21	837	0.104	b_2	C-H bridge bend / ring distortion
22	903	0.112	b_2	N-C-N bend
23	1061	0.132	b_2	N-H bend / C-H bridge bend
24	1064	0.132	b_2	H-N-C-H bend
25	1182	0.147	b_2	C-C ring stretch / C-H bend
26	1321	0.164	b_2	C-H bend bridge and ring
27	1364	0.169	b_2	C-H bend bridge
28	1390	0.172	b_2	N-H bend
29	1564	0.194	b_2	C-N stretch / C-H bend
30	1621	0.201	b_2	C-C ring stretch / C-C bridge stretch
31	1710	0.212	b_2	C-O stretch
32	3207	0.398	b_2	C-H stretch
33	3651	0.453	b_2	N-H stretch

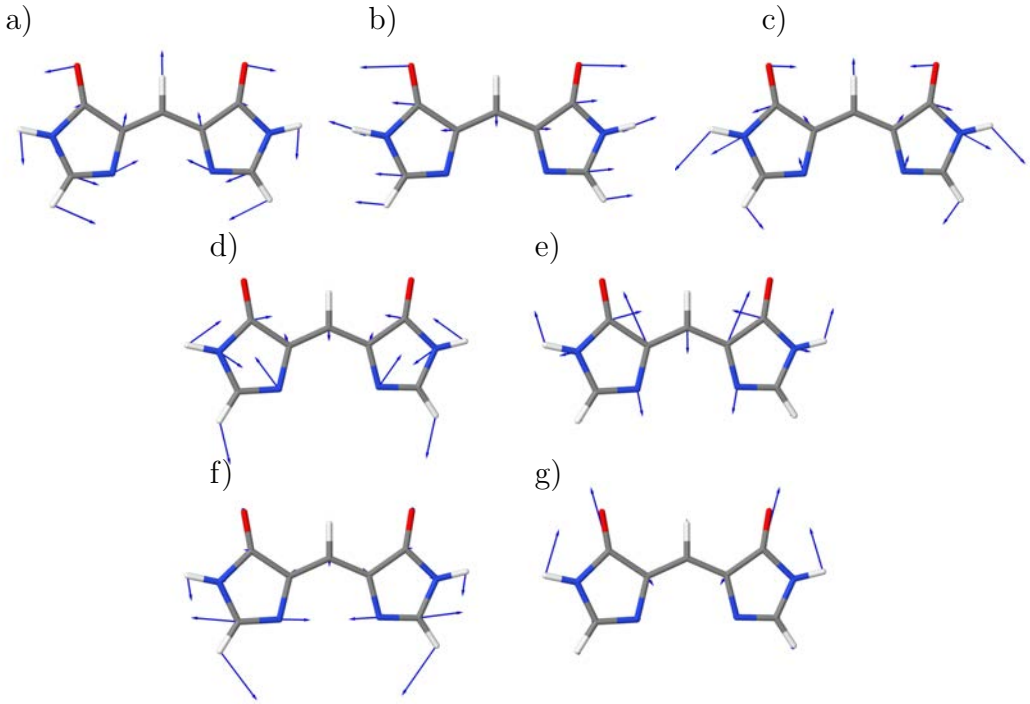

Fig. 4.13: The normal modes of bis-imidazoloxy important in describing its photoelectron spectrum: (a) ν_1, C-C(H)-C bridge bend (b) ν_2, C-C bridge stretch (c) ν_3, C-O, N-H and C-H bend (d) ν_6, N-C-N ring bend (e) ν_9, C-C ring stretch (f) ν_{13}, C-N stretch with C-H bend and (g) ν_{14}, C-O stretch. Calculated at the B3LYP/6-31+G* level of theory.

ring to the ratio κ/ω shows there is large displacement of the ionised minima from the ground state minimum for modes ν_1, ν_2, ν_3, ν_6, ν_9, ν_{13} and ν_{14}. From these, the largest values were obtained for the second lowest frequency mode ν_2, a C-C bridge stretch and ν_6 a N-C-N ring bend mode. The inclusion of ν_2, in addition to ν_1, emphasises the importance motion of the bridge plays in the dynamics. Despite its very small κ_α value, the ratio is large for ν_1 mainly as a result of its very low frequency. A large κ_α value is found in the $^2A_2$ state for mode ν_{13}, a C-N stretch with C-H bend.

Modes similar to those important in the photoelectron spectrum of imidazolide are observed here. This is true for modes ν_9, a C-C ring stretch and ν_6, the N-C-N ring bend, although for the latter the imidazolide vibration was an asymmetric b_2 mode. No off-diagonal linear coupling constants, λ_α, were obtained since cuts along

Table 4.17: On-diagonal linear coupling constants, κ_α for the normal modes of the bis-imidazoloxy anion, as determined from fitting the vibronic coupling model Hamiltonian to adiabatic surfaces calculated at the IP-EOM-CCSD/6-31+G* level. All values in eV.

	κ_α			
Mode	$^2A_2$	κ/ω	$^2B_2$	κ/ω
ν_1	-0.006	0.517	-0.007	0.603
ν_2	0.027	0.889	0.013	0.428
ν_3	-0.031	0.455	-0.021	0.308
ν_4	-0.024	0.285	-0.026	0.309
ν_5	0.016	0.155	0.005	0.048
ν_6	0.090	0.797	-0.003	0.027
ν_7	-0.006	0.046	-0.032	0.245
ν_8	0.012	0.089	0.019	0.141
ν_9	0.087	0.566	0.026	0.169
ν_{10}	0.003	0.018	-0.030	0.183
ν_{11}	-0.003	0.017	0.013	0.075
ν_{12}	0.010	0.055	-0.098	0.537
ν_{13}	-0.089	0.454	-0.132	0.673
ν_{14}	-0.077	0.362	0.031	0.146

Table 4.18: On-diagonal second-order coupling constants, γ_α, for the normal modes of the bis-imidazoloxy anion, as determined from fitting the vibronic coupling model Hamiltonian to adiabatic surfaces calculated at the IP-EOM-CCSD/6-31+G* level. All values in eV.

Mode	$^2A_2$	$^2B_2$
ν_1	0.007	0.006
ν_2	0.001	0.000
ν_3	0.004	0.000
ν_4	0.001	0.001
ν_5	0.002	0.001
ν_6	0.002	-0.002
ν_7	0.008	0.006
ν_8	0.009	0.007
ν_9	0.025	0.010
ν_{10}	0.006	0.008
ν_{11}	0.012	0.007
ν_{12}	0.006	0.005
ν_{13}	0.005	-0.006
ν_{14}	0.005	-0.016

Table 4.19: Parameters for the Morse functions used to fit the potential energy curves along modes ν_{15}, ν_{16} and ν_{17}. The values of D_0 and E_0 have units of eV.

	D_0				D_1			
Mode	D_0	α	X_0	E_0	D_0	α	X_0	E_0
ν_{15}	3.577	0.241	-0.033	0.000	3.573	0.241	-0.023	0.000
ν_{16}	7.473	0.168	-0.030	0.000	7.617	0.168	-0.057	-0.001
ν_{17}	8.342	0.167	0.026	0.000	8.078	0.168	0.063	-0.001

the b_2 modes were not calculated. The large energy separation between the D_0 and D_1 state makes coupling unlikely.

Table 4.18 shows the on-diagonal second order coupling constants γ_α. All the values are small indicating no change in frequency between the anion ground state and the ionised states. No bi-linear parameters $\gamma_{\alpha\beta}$ were obtained.

For several of the high frequency a_1 modes, a Morse potential was required, for which the parameters can be found in Table 4.19. These modes correspond to ν_{15} and ν_{16}, both C-H stretches, and ν_{17}, an N-H stretch. These modes were found not to contribute to the photoelectron spectrum and were neglected from the model Hamiltonian. This resulted in a seven mode model.

Cuts through the PES along each of the seven normal modes used in the model are shown in Figure 4.14. The cut along the C-C(H)-C bridge bending mode is shown in Figure 4.14(a). As a totally symmetric mode, the on-diagonal linear coupling value is non-zero, although the value is small enough that no clear shift in the minima of both ionised states is observed. Being a low frequency mode, the potentials are shallow.

Similar shallow potentials can be observed for ν_2, the C-C bridge stretch mode (Figure 4.14(b)). The larger on-diagonal linear coupling constant for the $^2A_2$ state can be seen in displacement of the minimum away from the equilibrium geometry. The totally symmetric C-O, N-H and C-H bend (Figure 4.14(c)), N-C-N ring bend (Figure 4.14(d)) and C-C ring stretch (Figure 4.14(e)) show the expected shift away

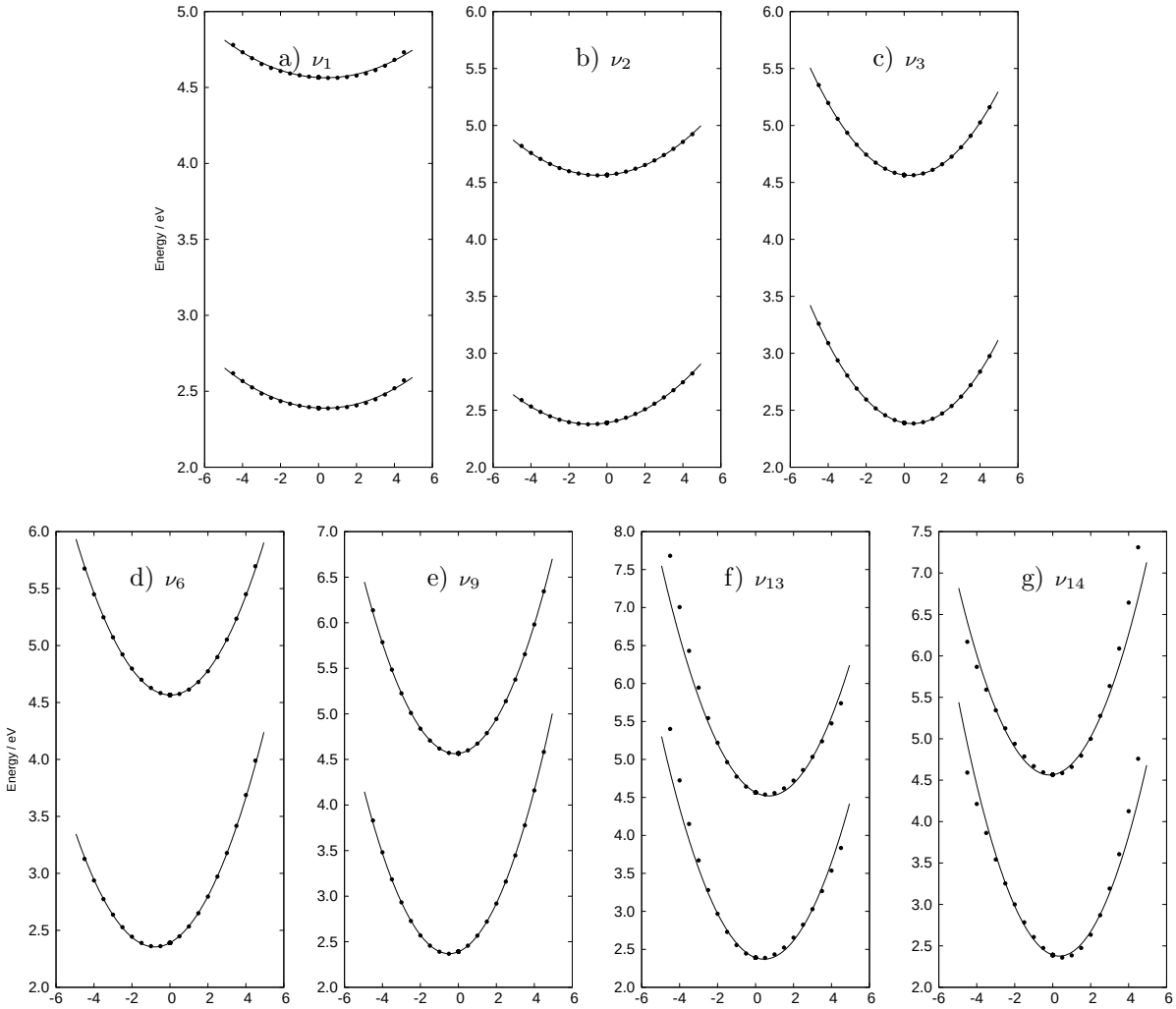

Fig. 4.14: Cuts through the adiabatic potential energy surfaces along select normal modes for the ionised states of bis-imidazoloxy, which in order of energy at Q_0 are $^2A_2$ and $^2B_2$. The points are obtained from *ab initio* calculations at the IP-EOM-CCSD/6-31+G* level. The normal modes included are: (a) ν_1, C-C(H)-C bridge bend (b) ν_2, C-C bridge stretch (c) ν_3, C-O, N-H and C-H bend (d) ν_6, N-C-N ring bend (e) ν_9, C-C ring stretch (f) ν_{13}, C-N stretch with C-H bend and (g) ν_{14}, C-O stretch.

from the equilibrium geometry and are much deeper potentials. These cuts otherwise show little significance. The small values of γ_α, reflecting the lack of change in frequency, can also be seen by no change in the shape of the potentials between states.

The cuts along ν_{13}, a C-N stretch with C-H bend and ν_{14}, C-O stretch, again shows displacement of the minima away from the anion ground state minimum. Both cuts exhibit calculated points in the $^2A_2$ and $^2B_2$ states that lie away from the fitted curves. A better fit was achieved by introducing third order parameters or fitting as a Morse potential, but since the fitting is good around the FC point, then these awry points will have little impact on the calculated photoelectron spectrum.

The large gap in energy between the $^2A_2$ and $^2B_2$ state is evident from the cuts and clearly shows that any coupling through the b_1 modes is expected to be negligible. Inspection of the coupling constants and cuts along the modes shows there to be no dominant mode. Instead, there are several modes that exhibit significant displacement of the minima and values of the ratio κ/ω. The effect of this is likely to be a spectrum with fine structure composed of a series of short, low intensity progressions, similar to the imidazolide anion.

The calculated photoelectron spectrum for transition to the ground state of the neutral radical is shown in Figure 4.15(a). The spectrum has been shifted to account for the zero point energy of the anion. The top spectrum (a) shows a broad, low resolution spectrum with a damping time of 60 fs. For assigning the vibrational structure, a higher resolution spectrum was obtained (b), where a damping time of 200 fs has been applied. The assignment of the vibrational structure is listed in Table 4.20.

Inspection of the spectrum shows it is well structured with progressions from several vibrational modes, but with peaks of low intensity. This is similar to the photoelectron spectrum of imidazolide, although more structure is observed in bis-

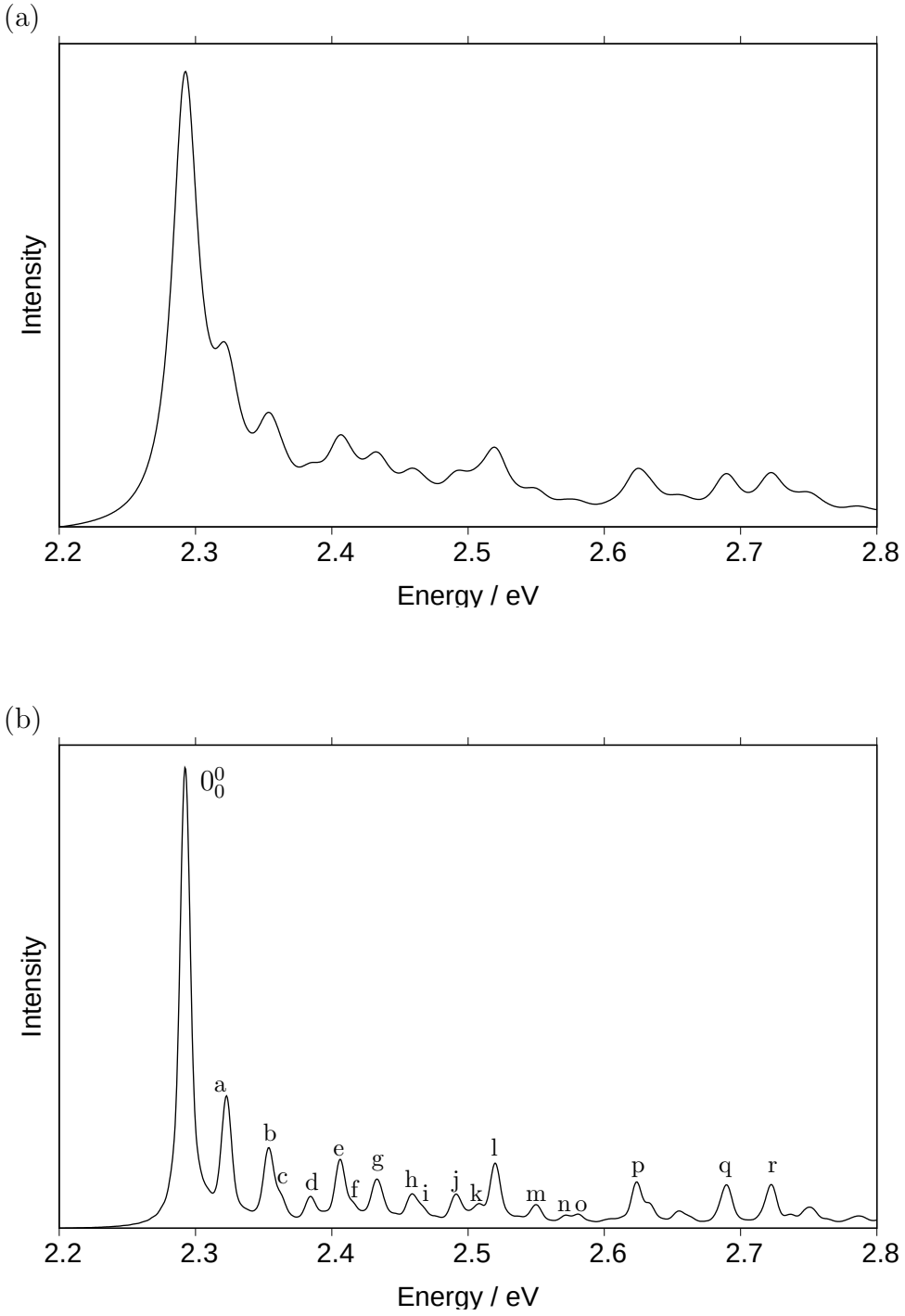

Fig. 4.15: The $^2A_2 \longleftarrow \tilde{X}^1A_1$ photoelectron spectrum of bis-imidazoloxy calculated using the Quantics program and a seven mode model. Shown is (a) a low resolution spectrum with a damping time of 60 fs and (b) a high resolution spectrum with a damping time of 200fs, allowing for assignment of the fine structure, shown in Table 4.20.

Table 4.20: Assignment of the vibrational structure for the photoelectron spectrum of the bis-imidazoloxy anion corresponding to vibrational modes of the anion. Values in parentheses are possible alternative assignments.

Peak	Energy from 0_0^0 / eV	Assignment(s)
a	0.03	2_0^1
b	0.06	2_0^2
c	0.07	3_0^1
d	0.09	2_0^3
e	0.11	6_0^1
f	0.12	$6_0^1 1_0^1$
g	0.14	$6_0^1 2_0^1$
h	0.16	9_0^1
i	0.17	$9_0^1 1_0^1$
j	0.20	13_0^1
k	0.21	14_0^1
l	0.23	$9_0^1 3_0^1$ $(13_0^1 2_0^1)$ $(14_0^1 1_0^1)$
m	0.26	$6_0^2 2_0^1$ $(13_0^1 3_0^1)$
n	0.28	$9_0^1 6_0^1$ $(14_0^1 3_0^1)$
o	0.29	$9_0^1 3_0^2$ $(14_0^1 3_0^1)$
p	0.33	$9_0^2 1_0^2$ $(14_0^1 6_0^1)$
q	0.40	$6_0^3 2_0^2$
r	0.43	$9_0^2 6_0^1$

imidazoloxy. The electronic origin, 0_0^0, is located at 2.29 eV and is lower than the energy for imidazolide and phenoxide.

From Figure 4.15(b), the fine structure was analysed and the assignments are listed in Table 4.20. Only ν_2, a C-C bridge stretch, shows a progression of any great length. Even then, this progression has low intensity. All other modes, except ν_1, exhibit a progression in the spectrum, although only the fundamental transition is observed. For the highest frequency modes in the model, ν_{13} and ν_{14}, the progressions observed around 2.50 eV, are very weak. No progression from the C-C(H)-C bridge bend, ν_1, is observed in the spectrum, but is present in combination peaks with modes ν_6 and ν_9.

Beyond 2.50 eV, the fine structure becomes more difficult to assign, with peaks

l to r resulting from a series of combinations between modes. Given the rapid decrease in intensities observed, it is unlikely any of these peaks form part of an expanded progression. In particular, peaks l, p, q and r have high intensities. Possible assignments for these peaks are given in Table 4.20. For many of these peaks, an alternative assignment involving modes ν_{13} and ν_{14} are given. These peaks, however, remained when the photoelectron spectrum was calculated without modes ν_{13} and ν_{14}. This suggests these modes are not responsible for the observed peaks.

The photoelectron spectrum for bis-imidazoloxy looks similar to that for the HBDI anion. Both have the electronic transition 0_0^0 as the most intense peak, with weaker vibrational structure. This highlights the importance the imidazolinone component plays in the photoelectron spectrum of HBDI. Moreover, motion of the methine bridge that connects the two rings, also has a strong affect on the spectrum.

4.6 Bis-phenoxide

The other totally symmetric analogue of the HBDI chromophore is bis-phenoxy (Figure 4.3 (**5**)) where both of the rings are phenoxide. Similar to HBDI, the oxygens are located in the *para* position from the bridge. There is very little in the literature regarding this molecule except the theoretical study by Olsen and McKenzie that also involved the bis-imidazoloxy anion [252]. The structure of bisphenoxy is, however, similar to the series of bisphenols, especially bisphenol F, which is fully protonated and contains a CH_2 group in the bridge.

The optimised structure was initially found to be fully planar with C_{2v} symmetry, consistent with imidazolide, phenoxide and bis-imidazoloxy. This structure is shown in Figure 4.16(a). Frequency calculations on this optimised structure, however, returned a single, imaginary (shown as negative in the calculation) vibrational frequency indicating this structure is not a minimum. This imaginary vibrational

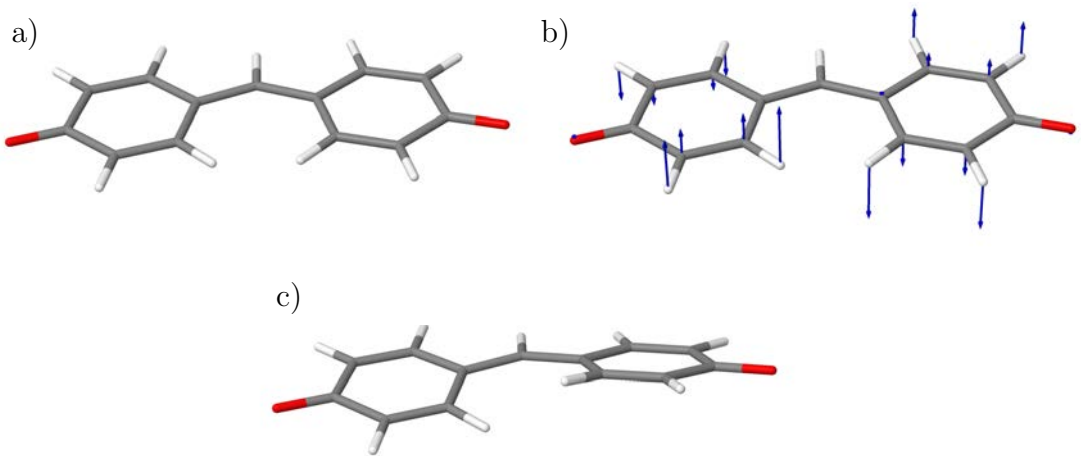

Fig. 4.16: Optimised structures for the bis-phenoxy anion, calculated at the B3LYP/6-31+G* level of theory. The planar optimised structure is shown in (a). Subsequent frequency calculations showed this structure to possess a single negative frequency, shown in (b). A lower energy non-planar structure deemed to be the global minimum is shown in (c).

mode corresponded to an out of plane twist whereby the rings are no longer planar with respect to each other, as shown in Figure 4.16(b). Re-optimising the structure, moving one ring out of the plane, leads to the structure seen in Figure 4.16(c). This structure returned no imaginary frequencies. The two structures are very similar in energy, with a calculated difference of only 0.07 eV.

The reason for the totally planar structure not being a minimum is attributed to interaction between the hydrogens in the *ortho* position on either side of the ring. This is removed when the rings are no longer forced to be planar with each other. Such an interaction is not a problem for bis-imidazoloxy as there are no hydrogens bonded to the nitrogen atom in a similar position. The optimised structure reported by Olsen and McKenzie was also non-planar. Crystal structures reported for the similar molecule, bisphenol F, again showed the structure to be non-planar and the rings twisted [268].

The frontier molecular orbitals for the valence electrons are shown in Figure 4.17. The HOMO and HOMO-1 are π-orbitals localised across the entire molecule, consistent with the previous molecules studied. The LUMO is a π^*-orbital, however,

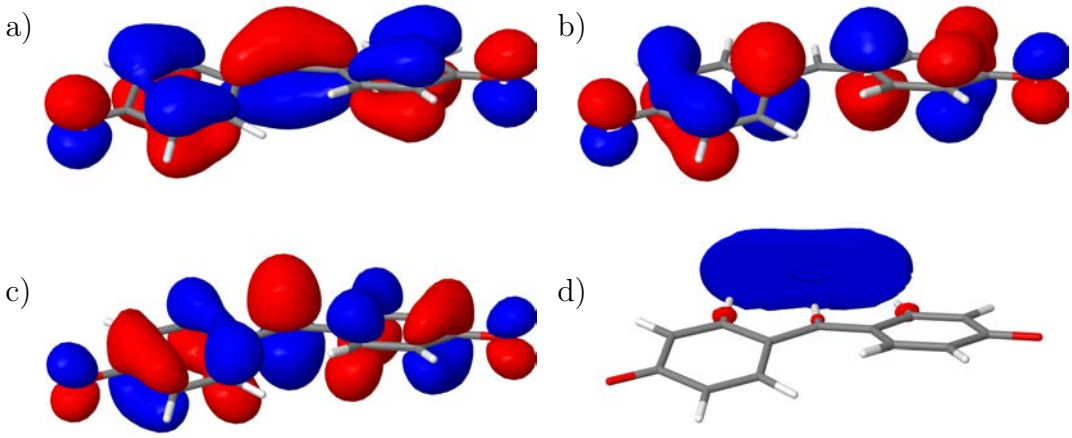

Fig. 4.17: The frontier molecular orbitals for the valence electrons of bis-phenoxy. Shown are the (a) HOMO-1, (b) HOMO, (c) LUMO and (d) LUMO+1. The HOMO-1 and HOMO are π-orbitals, the LUMO is π^* orbital and the LUMO+1 is a diffuse orbital, calculated at the CCSD/6-31+G* level of theory.

the LUMO+1 shows diffuse character, with a small portion of density on the C-H, but the majority occurring away from the structure. The HOMO and LUMO show that delocalisation is across the entire structure and the non-planarity of the structure does not disrupt the conjugation.

The vertical excitation and ionisation energies are shown in Table 4.21. From the IP-EOM-CCSD calculations the ionisation energy was predicted as 2.99 eV, the highest of all four molecules studied, and higher than the HBDI anion. This implies the bis-phenoxy anion is more stable than bis-imidazoloxy and the HBDI anion, a consequence of the increased conjugation. The first ionisation results from removal of a π-electron from the HOMO. The second ionisation energy is predicted to be 5.23 eV and correspond to removal of the π-electron from the HOMO-1.

Crucially, the first excited state of the anion is predicted to be 2.66 eV, lower than the ionisation threshold, and similar to the HBDI anion. This suggests S_1 to be bound, at least in the FC region. This is similar to the relative energies shown in Figure 4.1 where the S_1 is shown to be bound at the FC point. The S_1 state results

Table 4.21: Vertical excited and ionisation energies of the bis-phenoxy anion, calculated from the equilibrium geometry of the S_0 state, with EOM-CCSD level of theory and a 6-31+G* basis. All values in eV.

State	EOM-CCSD
S_1	2.66
S_2	3.77
D_0	2.99
D_1	5.23

from a HOMO to LUMO transition. The energy difference between the S_1 and D_0 states of ∼0.3 eV is small enough that crossing may occur. The second excited state of the anion, S_2, was calculated to be 3.77 eV, higher than the detachment energy. The energies calculated by Olsen and McKenzie were 2.25 eV for S_1 and 2.84 eV for S_2 [252]. The calculation of these energies employed a small CAS of orbitals situated on the methine bridge only. This CAS space is inadequate to obtain reliable energies, hence the discrepancy in values.

The twisted structure for bis-phenoxy results in a loss of symmetry and hence has C_1 molecular symmetry. Such symmetry means all 66 vibrational modes have a symmetry and therefore need to be considered. A quantum dynamics model encompassing all of these modes is unfeasible, as is calculating *ab initio* points along each of them. To decide which modes are important, it was necessary to express, in normal modes, the change in geometry between the anion and radical equilibrium structures. From this, 12 normal modes were determined to be important, for which the vibrational frequencies calculated at the B3LYP/6-31+G* level of theory are shown in Table 4.22. The modes listed consist mainly of low frequency modes, with many being out of plane vibrations. Unlike bis-imidazoloxy, there are few vibrations that involve the bridge component.

For constructing the vibronic coupling Hamiltonian, the ground state of the neutral radical as well as the first excited state of the anion were included. It

Table 4.22: Theoretically calculated frequencies of selected vibrational modes, in cm^{-1} and electron volts, for $\tilde{X}^1A$ state of the bis-phenoxy anion calculated at the B3LYP/6-31+G* level of theory.

	Frequency		Symmetry	Description
Mode	/ cm^{-1}	/ eV		
1	38	0.005	a	out of plane ring twist
3	84	0.010	a	out of plane ring distortion
4	128	0.016	a	out of plane ring distortion
7	260	0.032	a	ring stretch and C-H bend
8	283	0.035	a	out of plane ring distortion
12	452	0.056	a	C-O bend / ring bending
19	640	0.079	a	C-C ring stretch
22	784	0.097	a	asymm. out of plane C-H bend
24	796	0.099	a	assym. out of plane C-H bend
40	1206	0.150	a	C-H bend
55	1617	0.201	a	C-O stretch / C-H bend
57	1675	0.208	a	C-C ring stretch

is possible these two states couple or even cross, although dealing with couplings between states involving different number of electrons has not been accomplished. Parameters were obtained for the first and second excited states of the anion and the ground and first excited state of the radical. Since, however, the only states of interest are the anion S_1 state and the radical ground state (D_0), then parameters are shown for these states only. The cuts through the PES along these modes show all the states.

From the 12 normal modes of interest, five were found to be important for the photoelectron spectrum. These were ν_7, a ring stretch and C-H bend, ν_8, an out of plane ring distortion, ν_{19}, a C-C stretch/ring distortion, ν_{40}, a C-H bend and ν_{57}, a C-C ring stretch. These modes are illustrated in Figure 4.18. As the molecule has C_1 symmetry, then both in plane and out of plane vibrations are included. Unlike bis-imidazoloxy and HBDI, the important modes for bis-phenoxy involve distortion of the rings and not the bridging group.

The parameters obtained from fitting the vibronic coupling Hamiltonian to the adiabatic surfaces are shown in Tables 4.23 - 4.25. Performing a full fit for all 66

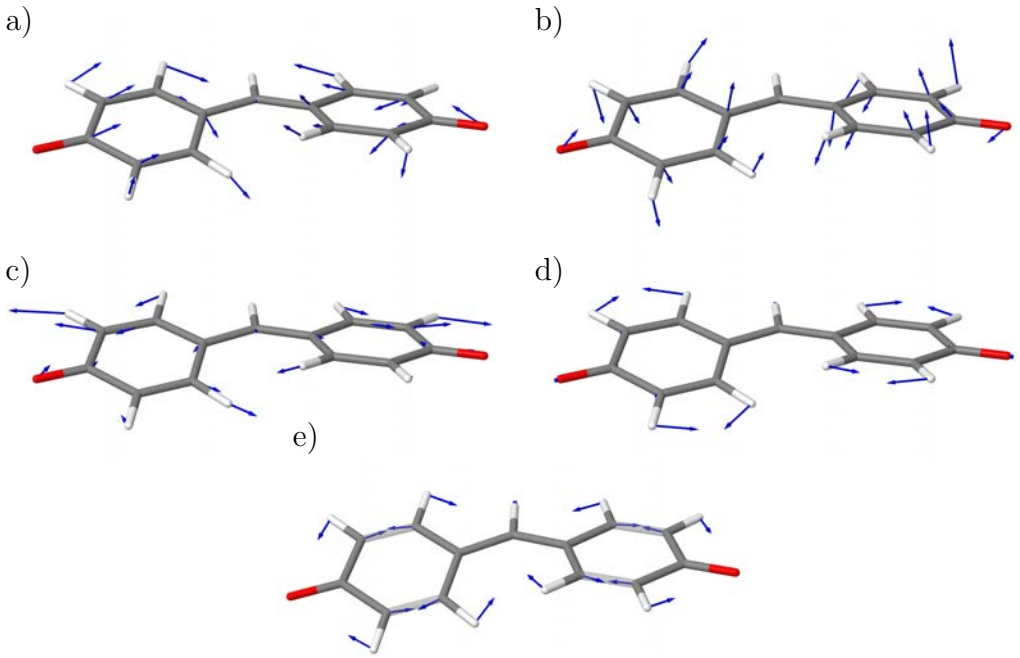

Fig. 4.18: The normal modes of bis-phenoxy important in describing its photoelectron spectrum: (a) ν_7, ring stretch and C-H bend (b) ν_8, an out of plane ring distortion (c) ν_{19}, C-C stretch/ring distortion (d) ν_{40}, C-H bend and (e) ν_{57}, C-C ring stretch. Calculated at the B3LYP/6-31+G* level of theory.

normal modes and four electronic states was very demanding computationally, and so was only undertaken for the 12 normal modes of interest. A value of 0.014 was obtained for the RMSD, showing the fitting to be good and passing through the majority of the calculated points.

The on-diagonal linear coupling constants are shown in Table 4.23. The low molecular symmetry means that non-zero values are expected for all modes. The lowest frequency mode, ν_1, was fitted as a quartic potential to account for the double well potential observed for this mode. The ratio κ/ω indicates large displacement in the D_0 state for ν_7, a ring stretch with C-H bend. Significant displacement also occurs for ν_8, an out of plane ring distortion. The majority of modes for both the S_1 and D_0 state have small κ and κ/ω values. In addition to ν_7 and ν_8, modes ν_{19}, ν_{40} and ν_{57} were also considered important to the model since they have the next largest values of κ and the ratio for the radical ground state.

No off-diagonal linear coupling constants, λ_α, were obtained. Given the small

Table 4.23: On-diagonal linear coupling constants, κ_α for the normal modes of the bis-phenoxy anion, as determined from fitting the vibronic coupling model Hamiltonian to adiabatic surfaces calculated at the EOM-CCSD/6-31+G* level. All values in eV.

	κ_α			
Mode	S_1	κ/ω	D_0	κ/ω
ν_3	-0.002	0.191	0.002	0.211
ν_4	-0.007	0.447	0.000	0.027
ν_7	0.014	0.441	-0.034	1.069
ν_8	-0.006	0.168	-0.025	0.703
ν_{12}	0.017	0.295	-0.007	0.128
ν_{19}	-0.005	0.061	-0.033	0.413
ν_{22}	-0.027	0.277	-0.016	0.163
ν_{24}	0.026	0.259	0.031	0.319
ν_{40}	0.020	0.131	-0.048	0.318
ν_{55}	0.033	0.163	-0.019	0.096
ν_{57}	0.065	0.311	-0.052	0.248

Table 4.24: On-diagonal second-order coupling constants, γ_α, for the normal modes of the bis-phenoxy anion, as determined from fitting the vibronic coupling model Hamiltonian to adiabatic surfaces calculated at the EOM-CCSD/6-31+G* level. All values in eV.

Mode	S_1	D_0
ν_3	-0.002	0.006
ν_4	-0.002	0.003
ν_7	-0.002	-0.001
ν_8	-0.010	-0.001
ν_{12}	-0.003	0.003
ν_{19}	-0.000	-0.001
ν_{22}	-0.002	0.002
ν_{24}	-0.003	0.001
ν_{40}	0.006	0.010
ν_{55}	0.002	0.006
ν_{57}	-0.006	-0.006

Table 4.25: Parameters for the quartic potentials used to fit the potential energy curves along mode ν_1. All values have units of eV.

	S_1			D_0		
Mode	k_1	k_2	k_3	k_1	k_2	k_3
ν_1	0.022	-0.005	0.023	0.016	-0.015	0.024

energy gap between the S_1 and D_0 state, it is highly probable there is coupling between these states. Calculating such coupling has not been fully established yet. The main difficulty being the two states contain different number of electrons.

The on-diagonal second order terms, γ_α are shown in Table 4.24. The small values for all modes show there is little change in frequency from the anion ground state to the S_1 and D_0 states. No bi-linear $\gamma_{\alpha\beta}$ terms were obtained.

The lowest frequency mode, ν_1, the out of plane ring rocking, was fitted as a quartic potential of the form:

$$\frac{1}{2}\omega^2 Q^2 + k_1 Q + \frac{1}{2}k_2 Q^2 + \frac{1}{24}k_3 Q^4 \tag{4.1}$$

The fitted parameters are shown in Table 4.25. The need to use such a potential suggests the cut along this mode contains a double well. The out of plane vibration for this mode is similar to the imaginary frequency observed for the planar geometry. As this mode made no contribution to the photoelectron spectrum it was neglected from the model. This left a five mode model consisting of modes ν_7, ν_8, ν_{19}, ν_{40} and ν_{57}.

Figure 4.19 shows the cuts through the PES along each of the five normal modes used in the model. The cuts show the S_1 and S_2 states for the anion and the D_0 and D_1 states of the radical. For the model, only the S_1 and D_0 state were included, but given the small energy gap between the anion and radical states, it was important to assess the cuts for each state.

From the cuts, it is clear that the S_1 and D_0 states lie close in energy. The S_2 and D_1 states are much higher in energy and do not significantly interact with each other or the lower states. The relative energies of these states reflects those shown in Figure 4.1 for HBDI. This suggests the photodynamics of bis-phenoxy will closely reflect those of HBDI. The shallow potentials seen for modes ν_7 and ν_8 (Figures

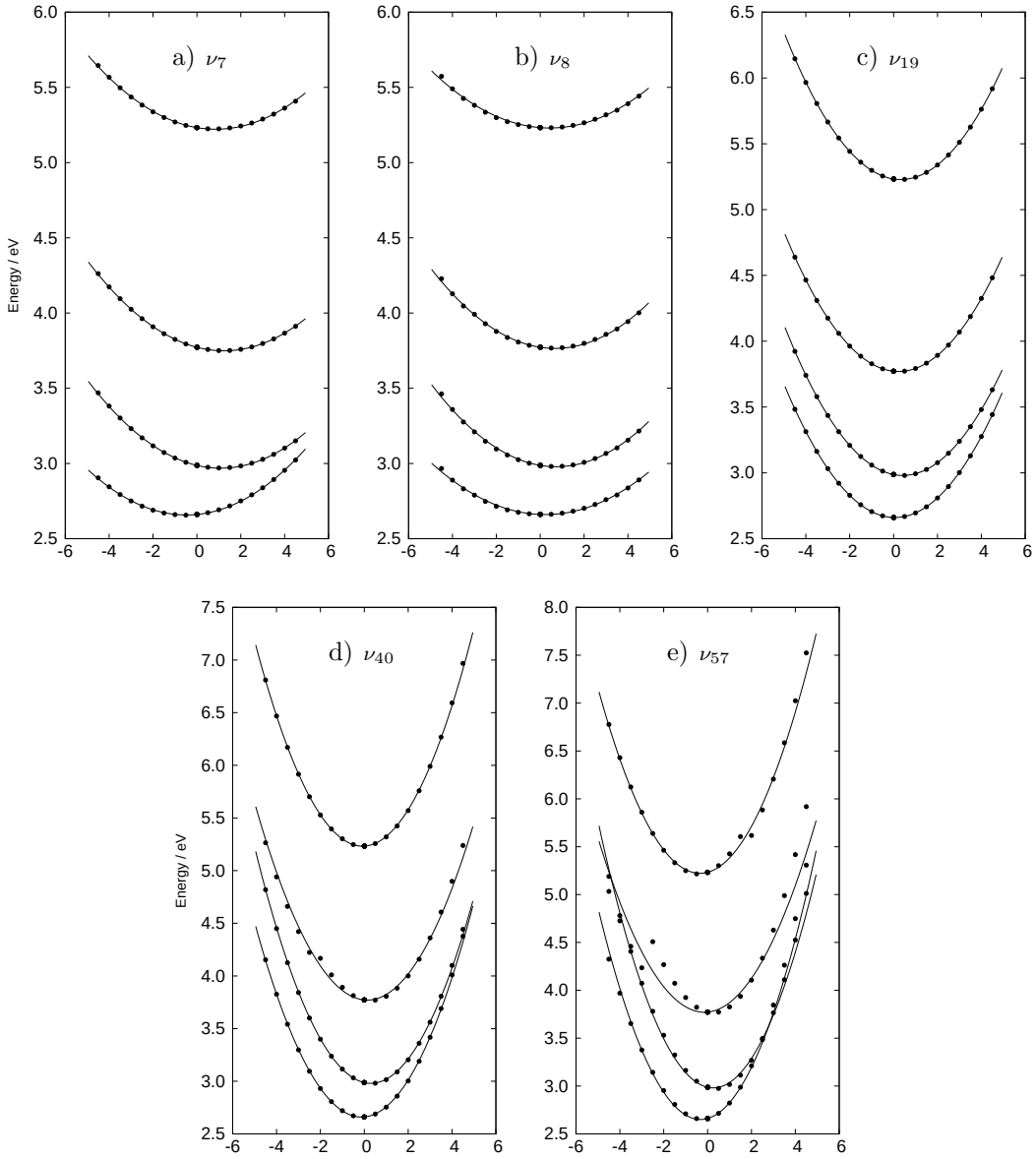

Fig. 4.19: Cuts through the adiabatic potential energy surfaces along select normal modes for the excited anion and radical states of bis-phenoxy, which in order of energy at Q_0 are S_1, D_0, S_2 and D_1. The points are obtained from *ab initio* calculations at the IP/EE-EOM-CCSD/6-31+G* level. The normal modes included are: (a) ν_7, ring stretch and C-H bend (b) ν_8, an out of plane ring distortion (c) ν_{19}, C-C stretch/ring distortion (d) ν_{40}, C-H bend and (e) ν_{57}, C-C ring stretch .

4.19(a,b)) are expected for low frequency modes. For the ring stretch/C-H bend mode, ν_7, the large value for the ratio κ/ω can be seen as the minimum is greatly shifted away from the equilibrium geometry for D_0. There is a smaller displacement for S_1. This cut also clearly shows the two states approach each other, although the actual crossing point is located far from the FC point. Similar displacement of the D_0 minimum is evident for mode ν_8, the out of plane ring distortion. For this mode, S_1 and D_0 remain separate with no indication of coming together.

The cut along ν_{19}, (Figure 4.19(c)), a C-C stretch/ring distortion mode shows little significance except for a small displacement in the S_1 and D_0 minima away from the equilibrium geometry. Figures 4.19(d,e) show little displacement of the minima in the S_1 and D_0 states for modes ν_{40}, a C-H bend and ν_{57} a C-C ring stretch. Significantly, however, these modes show the S_1 and D_0 states to cross. This is particularly apparent for mode ν_{57}, where the crossing occurs close to the FC point of the D_0 state. Crossing from D_0 to S_1 implies, however, the detached electron somehow returning to the molecule, which is very improbable. This does suggest though that excitation to the S_1 state leads to indirect electron emission through vibrational autodetachment. Another interesting feature in the cuts along both these modes are a series of awry points in the S_2 state. The energy of the calculated points differs substantially in mode ν_{57} to the extent that the fitted curve is poor. This is attributed to failings in the EE-EOM-CCSD calculations and crossing from a higher excited state. As the calculated points and fitting for the S_1 and D_0 states are good, then these awry points will not impact the photoelectron spectrum.

The calculated photoelectron spectrum is shown in Figure 4.20. The spectrum has been shifted to account for the zero point energy of the anion. Figure 4.20(a) shows the photoelectron spectrum with a damping time of 40 fs. Vibrational structure is clearly present in the spectrum, although the peaks are all of low intensity. The electronic origin, 0_0^0, is the most intense peak in the spectrum and is located at

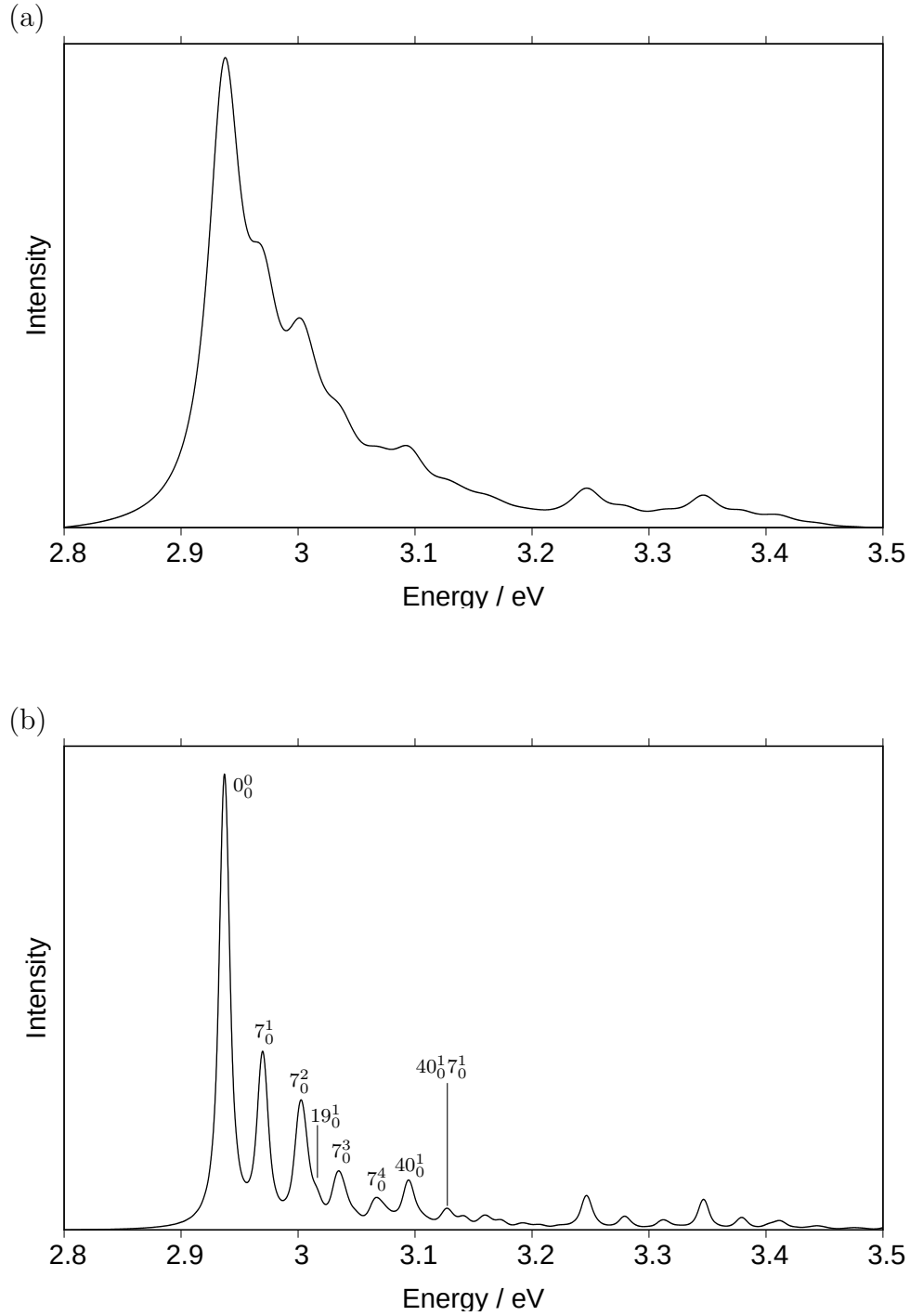

Fig. 4.20: The D_0 photoelectron spectrum of bis-phenoxy calculated using the Quantics program and a seven mode model. Shown is (a) a low resolution spectrum with a damping time of 40 fs and (b) a high resolution spectrum with a damping time of 150fs, allowing for assignment of the fine structure.

2.94 eV, higher than bis-imidazoloxy and the HBDI anion. The spectrum has less fine structure than bis-imidazoloxy, but looks similar to the HBDI anion, especially the calculated spectrum by Toker and Bravaya [244, 250].

A higher resolution photoelectron spectrum, using a damping time of 150 fs, is shown in Figure 4.20(b). This allowed assignment of the major features in the fine structure. The main progression is formed from ν_7, the ring stretch/C-H bend mode. This long progression is responsible for most of the fine structure present. The only other mode to show a progression with any appreciable intensity was ν_{40}, the C-H bend mode. A small shoulder peak on the 7_0^2 peak is assigned as the fundamental peak for mode ν_{19}, the C-C stretch/ring distortion mode. The peaks that appear at energies higher than 3.10 eV are attributed to combination modes, although only the $40_0^1 7_0^1$ peak was assigned with certainty. The more intense peaks located at 3.25 and 3.35 eV disappeared when ν_{40} was excluded from the model suggesting this mode to be involved in these combination peaks.

Comparison of the photoelectron spectrum for the two totally-symmetric bis analogues with HBDI provides valuable insights into the photoelectron spectrum of the latter. The photoelectron spectrum for both bis-imidazoloxy and bis-phenoxy are similar to HBDI, as evident in Figure 4.1. From assigning the fine structure, it was found the modes important to bis-phenoxy involved stretches and out of plane motion of the rings. Alternatively, the important modes for bis-imidazoloxy involved more bending modes and motion of the methine bridge, similar to the modes assigned in the HBDI spectrum. Motion of the bridge becomes more important when the molecule is completely planar and so contributions to the HBDI spectrum arise from it being able to adopt a planar conformation.

From the calculated detachment and excitation energies, the first excited state of the anion lies below the detachment energy only for bis-phenoxy. This molecule also had the highest detachment energy. The increased stability of the bis-phenoxy

anion and location of S_1 relative to D_0 is similar to HBDI. The stability of the HBDI anion and close energy of the S_1 and D_0 vertical energies therefore result from the phenoxide moiety, whereas the imidazolinone moiety contributes the fine structure observed in the photoelectron spectrum. The smaller ring system of the imidazole allows HBDI to remain planar and prevents it adopting a twisted structure. The broadening seen in the HBDI spectrum results from interaction with the close lying S_1 state. Similar broadening would therefore be expected for experimental measurements of bis-phenoxy.

4.7 Conclusion

The photophysics of the GFP chromophore, HBDI, has long attracted a great amount of interest. Much focus has been given to the detachment energy of the HBDI anion and corresponding photoelectron spectrum. As illustrated in Figure 4.1, the first excited state of the anion resides close to the detachment energy, but has been shown to be bound at the FC point and adiabatically. Indirect emission through vibrational autodetachment has been observed and has the effect of broadening the photoelectron spectrum. Further work has also established resonant excitation to higher excited states of the anion, followed by autodetachment from the D_0 and D_1 states. Insights into the HBDI anion can be achieved from a bottom-up approach, considering first the individual ring components, phenoxide and imidazolide, before moving onto the totally-symmetric analogues, bis-imidazoloxy and bis-phenoxy.

Using a simple linear vibronic coupling Hamiltonian, the photoelectron spectra of the four HBDI related molecules were calculated. This model required calculation of the PESs for which the IP-EOM-CCSD method performed reasonably well. The calculated vertical excitation and ionisation energies showed the first excited state of the anion to lie above the detachment energies for all molecules except bis-phenoxy.

Here, the S_1 state lies just below the detachment energy, similar to the HBDI anion.

For imidazolide, a three mode model was sufficient to replicate the experimental photoelectron spectrum. The first excited state of the radical, D_1 was found to couple to the radical ground state through b_2 modes. These modes, along with the totally-symmetric modes were considered. A cut along the totally-symmetric C-C ring stretch/HCN deformation mode showed the D_0 and D_1 state to cross, suggesting the presence of an intersection that warrants further investigation. Adjustments to the fitted parameters were necessary to ensure the calculated spectrum fully reproduced experiment.

The photoelectron spectrum for phenoxide was much simpler and required only a two mode model to obtain good agreement with experiment. Unlike imidazolide, no coupling was found between the D_0 and D_1 states. The predicted vertical ionisation energy was not in good agreement with experiment and so it was necessary to increase the energy of the D_0 state. The lower detachment energy indicates the phenoxide anion is less stable than imidazolide. The calculated photoelectron spectrum consists of a single progression from the ring deformation/C-O stretch mode. A small series of shoulder peaks on this main progression from the out of plane, a_2 ring deformation mode were not replicated by the model despite their inclusion.

The main insights into the HBDI anion came from the two bis-systems. The photoelectron spectrum for both show the electronic origin, 0_0^0, to be the most intense peak followed by low intensity fine structure, similar to HBDI. For bis-imidazoloxy, a seven mode model was used consisting only of the radical ground state, with there being no coupling to the D_1 state. These modes were found to mainly involve the bridging group and in-plane bends, consistent with those for HBDI.

Initially, bis-phenoxy was optimised to a planar structure, consistent with bis-imidazoloxy and HBDI. The presence of a single, imaginary frequency showed this was not the true ground state. Instead, the molecule adopted a twisted structure

to relieve the interaction between the two *ortho* protons. The difference in energy between these structures was extremely small. The loss of symmetry meant that all normal modes could be important to the photoelectron spectrum. However, by expressing the geometric changes between the minima of the anion and radical ground state in terms of normal modes, only 12 modes needed considering. From these, six were found to be important to the photoelectron spectrum. Several of the cuts along the normal modes showed the S_1 and D_0 states to cross. Further work is needed to calculate the absorption spectrum and the coupling between the S_1 and D_0 state.

By relating the HBDI anion to bis-phenoxy and bis-imidazoloxy, it was concluded that the imidazolinone component contributes more to the fine structure of the photoelectron spectrum, particularly the bending vibrations. The combination of the imidazolinone and phenoxide ring keeps the structure planar and allows vibrations involving the bridge to become important. The phenoxide group contributes more to the relative energies of the S_1 and D_0 state.

Chapter 5

Photodynamics of Phenol

The contents of this chapter are an extended version of published work and therefore taken in part directly from Reference [269]. I performed all calculations and analyses within this work.

This chapter details the photoelectron spectrum of phenol, with emphasis on the two lowest ion states. The study here aims to provide a thorough and detailed analysis of these ion states and the calculated photoelectron spectrum absent from the literature. From the vibronic coupling model Hamiltonian, a previously undiscovered CoI was found to exist between the D_0 and D_1 states. Diabatic state populations show the CoI to affect the photodynamics, with population transfer of 30% from the upper D_1 state observed. Another main outcome of the model is a new assignment of the vibrational structure in the photoelectron spectrum. This assignment is described and differences with previous work noted. Combining the ion surfaces with those for the excited states provides a full model for future work calculating time-resolved spectra. The quality of the S_1 surface is confirmed by calculating the absorption spectrum, which is in good agreement with experiment.

5.1 Introduction

Like benzene, phenol and its derivatives are abundant in compounds found naturally and synthesised industrially. A phenolic group is one of the constituents of the GFP

chromophore, HBDI. Its deprotonation forms the final step in an excited state proton transfer through which the anionic chromophore fluoresces its eponymous green. As a result, phenol has been extensively studied through theoretical and experimental means. In recent decades, much attention has been given to the photochemistry and photodissociation of phenol [270–275].

The dynamics along the O-H stretching mode involving different electronic states provide examples of non-adiabaticity and CoIs. The PES along this mode and the C-O-H angle are shown in Figure 5.1. The two lowest lying excited states ($^1\pi\pi^*$ and $^1\pi\sigma^*$) have been shown to contain a CoI seam [270, 276]. This enables ultrafast internal conversion from the bright $^1\pi\pi^*$ state to the $^1\pi\sigma^*$ state, which leads to the dissociation of hydrogen to form the phenoxyl radical. There is also evidence to suggest the O-H dissociation bypasses the CoI through hydrogen tunnelling [272, 277]. There also exists another CoI between the $^1\pi\sigma^*$ and S_0 state, which provides an alternative pathway of rapid relaxation to the electronic ground state.

Following the seminal work of Sobolewski and Domcke [278], the existence of dissociative $^1\pi\sigma^*$ states has been shown for a range of aromatic molecules. They are dark states, characterised at the FC point as a 3s Rydberg state, that forms a CoI with the ground state. Moreover, their repulsive nature is responsible for hydrogen transfer or dissociation in many bioaromatic molecules [279] and is thought to provide photostability. Whilst this state cannot be directly accessed, its position relative to the $^1\pi\pi^*$ state dictates the dynamics that occurs and the location of the crossing points. This has been observed in a variety of planar organic molecules [278, 280]. The difference in positions of these two states and the effect becomes apparent when comparing the photodissociation of phenol with pyrrole [279, 281, 282]. The shift in relative energy of the $^1\pi\sigma^*$ with respect to the $^1\pi\pi^*$ state in phenol has also been investigated when complexed with water and ammonia clusters [283].

The absorption spectrum of phenol has been determined experimentally and

a)

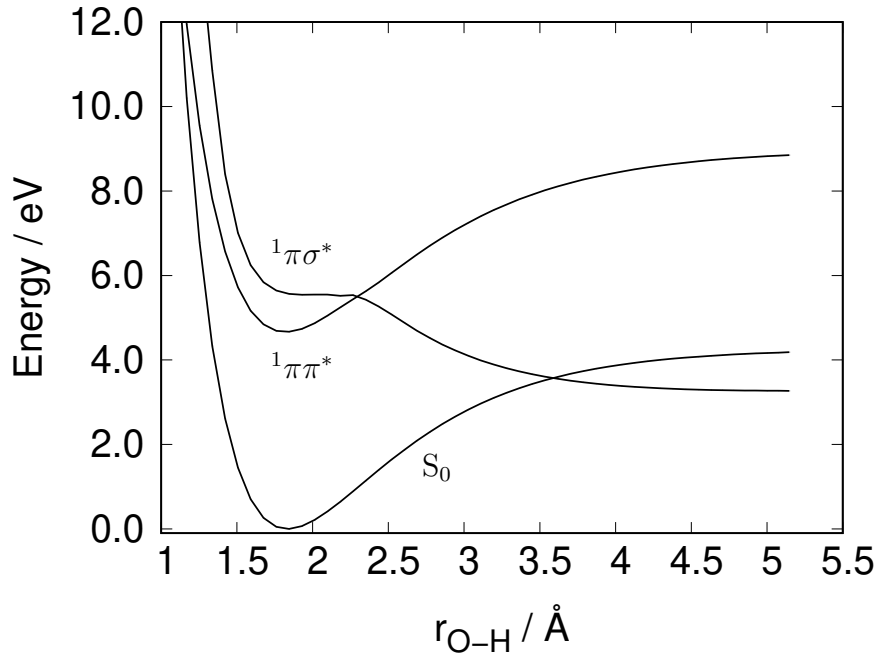

b)

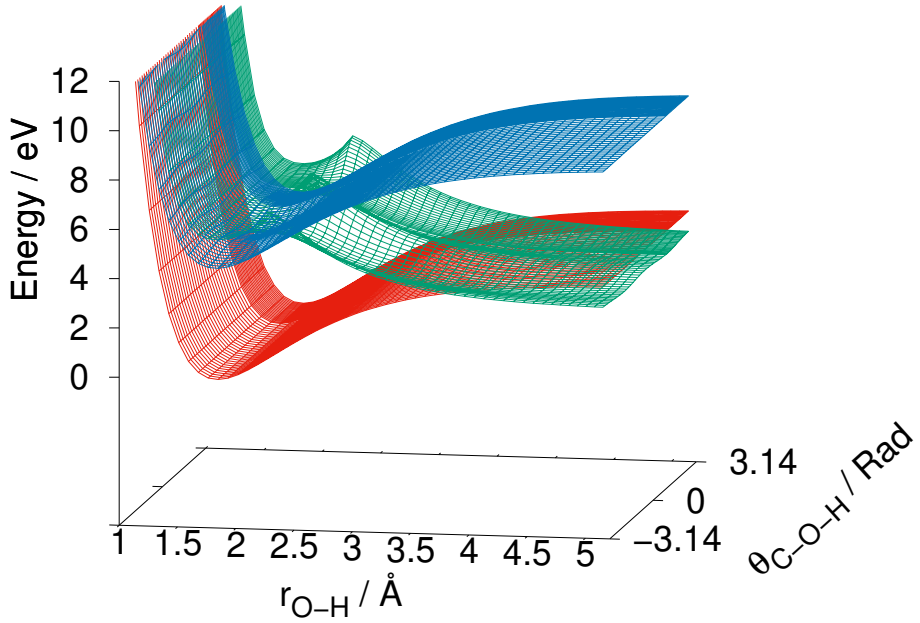

Fig. 5.1: (a) Potential energy curve for the ground and excited singlet states as a function of **r**, the O-H bond distance. (b) Potential energy surfaces for the ground and excited singlet states as a function of **r**, the O-H bond distance and θ, the C-O-H bond angle. The surface in red denotes the S_0 ground state, blue the $^1\pi\pi^*(S_1)$ state and green the $^1\pi\sigma^*(S_2)$ state.

theoretically. Gerrard *et al.* showed the absorption spectrum to exhibit strong solvation effects, possibly due to H-bonding between phenol molecules and with the solute molecules [284]. As such, reported spectra in the literature can often appear as broad and featureless. In certain solvents and gas phase the vibrational fine structure in the absorption spectrum becomes apparent [285].

More recently, the ultraviolet absorption cross-section of phenol at different temperatures has been measured [286]. This highlighted the detailed fine structure present but did not comment on the modes responsible. Assignment of the fine structure has been undertaken theoretically. A FC simulation of the $S_1 \rightarrow S_0$ transition provided not only vibrational frequencies in the S_0 and S_1 states, but also assigned the intense peaks in the spectrum [287]. These assignments were a_1 vibrations corresponding to two ring deformation/C-O stretch modes, a ring breathing mode, an in plane C-H bend mode and a C-O stretch/C-C stretch mode. Present also were peaks corresponding to vibrations from all possible symmetries. The most intense of these was from the b_1 out of plane C-O bend/ring torsion mode.

The role of non-adiabaticity has been investigated. Karmakar *et al.* measured the absorption spectrum of phenol in the vapour phase [288]. This showed a broader spectrum still rich in fine structure and the presence of vibrational progressions, with peaks at 268, 275 and 282 nm. Again, further broadening of the spectrum in various solvents was recorded. Building upon this work, Rajak *et al.* reported vibronic coupling in the absorption of phenol [289]. Through construction of their own vibronic coupling Hamiltonian, they assigned the vibronic structure to be similar to that reported in the FC model. They also concluded there to be weak coupling between the $\pi\pi^*(S_1)$ and $\pi\sigma^*(S_2)$ states, finding a population transfer of around 10% over 200 fs.

While the photo-excited dynamics of neutral phenol has been extensively studied, the photo-ionisation and subsequent dynamics have received little attention and the

ion states are usually only included as a continuum for the theoretical description of pump-probe measurements on the excited states [290, 291]. Recent work has also recorded the effect of aqueous solvation on the ionisation and excited states of phenol [292]. It was found that in aqueous solution the vertical ionisation energy was lowered by around 0.8 eV.

The photoelectron spectrum has been measured and the ionisation potentials determined to be 8.508 and 9.280 eV for the first two ion states [293–296]. The symmetry of these ion states have been determined to be $^2B_1$ and $^2A_2$ and result from the removal of a π-electron. The full He(I)/He(II) spectra were measured with the aim of obtaining all the valence ionisation potentials and the vibrational fine structure of the photoelectron spectrum has been largely overlooked. The possibility of non-adiabaticity and coupling associated with the ionised states has also not been explored.

Quantum dynamics simulations, which solve the time-dependent Schrödinger equation, are a powerful way to probe the photodynamics of a system and provide rationale behind experimental observables [297]. Examples are the use of simulated spectra and population dynamics to support pump-probe time-resolved photoelectron spectra (TR-PES) [22, 298]. These calculations require a potential energy function in the form of a set of coupled surfaces to model the excited-state dynamics. In some studies, the time-resolved signal from a TR-PES experiment has been directly modelled [299–301] and in this case the potential surfaces of the ion are also required.

Coupled potential surfaces are impossible to obtain accurately for more than a few atoms due to the large number of high level quantum chemistry calculations required and the difficulty of fitting these points using multi-dimensional functions. For this reason, model Hamiltonians are a useful approach to capture the essential physics in a simple way. For the coupled surfaces involved in photo-excited systems

the vibronic coupling model Hamiltonian [119,302] has become a standard approach. This involves a low-order Taylor expansion of diabatic potentials and couplings with parameters obtained by fitting to quantum chemistry calculations and experimental data. Making use of the vibronic coupling Hamiltonian thus allows for explicit consideration of vibronic couplings and non-adiabatic photochemistry. The vibronic coupling Hamiltonian has already been applied to a range of aromatic systems [303–307].

Here, a simple vibronic linear coupling model is constructed to simulate the absorption spectrum of the $S_1(^1B_2)$ state and the photoelectron spectrum of the two lowest ionisation bands of phenol, $D_0(^2B_1)$ and $D_1(^2A_2)$. This model allows the dynamics to be elucidated in terms of normal modes and couplings between the diabatic electronic states. It was found that two separate but modest seven mode models were sufficient to replicate the necessary photodynamic behaviour. The vibrational structure of the obtained absorption and photoelectron spectra has been assigned and compared with previous studies. Differences between the assignments for the photoelectron spectrum have been noted and discussed. The possibility of a conical intersection between the first two ion states is investigated, and its affect on the dynamics can be observed by following the relative diabatic state populations. These surfaces can be used, together with potential surfaces for phenol [270, 275] to help support the TR-PES of phenol measured in recent work by Riley *et al.* [292], which requires ionisation to two closely lying ion states. Accurate potentials are crucial for theoretical TR-PES calculations and therefore an important pre-requisite are surfaces that reliably reproduce the experimental absorption and photoelectron spectra.

5.2 Methodology

By making use of the vibronic coupling Hamiltonian [119], the diabatic potentials can be expressed through a Taylor series in terms of dimensionless normal modes around a particular point, Q_0, usually taken as the equilibrium geometry. At this point, the diabatic electronic wavefunction is assumed to be equal to the adiabatic. The Hamiltonian can therefore be written:

$$\mathbf{H} = \mathbf{H}^{(0)} + \mathbf{W}^{(0)} + \mathbf{W}^{(1)} + \dots \tag{5.1}$$

with the zeroth-order Hamiltonian expressed as the ground state Hamiltonian in the Harmonic approximation:

$$H^{(0)} = \sum_{\alpha} \frac{\omega_\alpha}{2} \left(\frac{\partial^2}{\partial Q_\alpha^2} + Q_\alpha^2 \right) \tag{5.2}$$

and ω representing the frequency of mode Q. The set of diabatic coupling matrices, W describe the changes in excited state surfaces compared with the ground state. $W^{(0)}$ is the ground state Harmonic oscillator displaced to excitation energy, E_i. The first order matrix elements are expressed as:

$$W_{ii}^{(1)} = \sum_{\alpha} \kappa_\alpha^{(i)} Q_\alpha \tag{5.3}$$

$$W_{ij}^{(1)} = \sum_{\alpha} \lambda_\alpha^{(i,j)} Q_\alpha \quad ; \quad i \neq j \tag{5.4}$$

Here, the κ parameters are related to the gradients of the adiabatic potential at Q_0 with respect to nuclear coordinates and the λ parameters are the non-adiabatic elements, again at Q_0, which provide coupling between the electronic states:

$$\kappa_\alpha^{(i)} = \left\langle \phi_i \left| \frac{\partial H}{\partial Q_\alpha} \right| \phi_i \right\rangle \tag{5.5}$$

$$\lambda_{\alpha}^{(ij)} = \left\langle \phi_i \left| \frac{\partial H}{\partial Q_\alpha} \right| \phi_j \right\rangle \tag{5.6}$$

Included also were the on-diagonal second order matrix elements:

$$W_{ii}^{(2)} = \sum_{\alpha} \frac{1}{2} \gamma_{\alpha}^{(i)} Q_{\alpha}^2 + \sum_{\alpha<\beta} \gamma_{\alpha\beta}^{(i)} Q_\alpha Q_\beta \tag{5.7}$$

where γ are the second derivatives of the adiabatic potentials at Q_0. These parameters provide changes in the frequencies and Duschinsky rotation by coupling the modes.

For modes exhibiting strong anharmonicity it becomes necessary to express the diabatic potentials as Morse potentials in place of the harmonic form above. These have the following form:

$$V = D_0 \left[\exp(\alpha(Q - Q_0) - 1)\right]^2 + E_0 \tag{5.8}$$

with parameters D_0 for the dissociation energy, Q_0 for the equilibrium geometry, and E_0 an energy shift.

Consideration of molecular symmetry is important as many of the matrix elements vanish due to symmetry arguments:

$$\kappa_{\alpha}^{(i)} \neq 0 \quad \text{if} \quad \Gamma_\alpha \supset \Gamma_A \tag{5.9}$$

$$\lambda_{\alpha}^{(i,j)} \neq 0, \quad \text{if} \quad \Gamma_\alpha \otimes \Gamma_i \otimes \Gamma_j \supset \Gamma_A \tag{5.10}$$

$$\gamma_{\alpha\beta}^{(i)} \neq 0, \quad \text{if} \quad \Gamma_\alpha \otimes \Gamma_\beta \otimes \Gamma_i \supset \Gamma_A \tag{5.11}$$

where $\Gamma_\alpha, \Gamma_\beta$ are the symmetry irreps of the vibrations, Γ_i, Γ_j the irreps of the electronic states and Γ_A the totally symmetric irrep. Phenol possesses C_s symmetry, however for determining the modes that couple the electronic states and give rise to

vibrational fine structure, the symmetry was ascended to C_{2v}. From the symmetry arguments only the totally symmetric a_1 modes need to be considered for both the absorption and photoelectron spectrum, with coupling from the a_2 modes for the absorption and b_2 for the photoelectron.

The PES and parameters are obtained through a least-squares fitting procedure to a series of *ab initio* points calculated along each normal mode. This is done using the VCHAM program [308] within the Quantics package [309]. Energies at each of these points were calculated at the CASSCF level of theory, (described in Section 3.7), employing an (8,8) active space for the singlet excited states and a (7,8) active space for the ion states with a 6-31+G* basis. The active space comprises the oxygen lone pair, $\pi\pi$, $\pi\pi^*$ and $\pi\sigma^*$ orbitals as shown in Figure 5.2. The choice of CASSCF was based on several criteria. Firstly, the need to be able to calculate energies at ground and excited states, and be applicable to scans along normal modes to create PESs. Given the non-adiabaticity observed in the excited states, then for these and the ion states a method with multireference description is desirable. This is even more essential should the surfaces cross. The analytical energy gradients available for CASSCF allows crossing points to be located and derivative couplings calculated. CASSCF provides qualitatively correct energies and allows a reasonable model to be built without the need to resort to more demanding levels of theory.

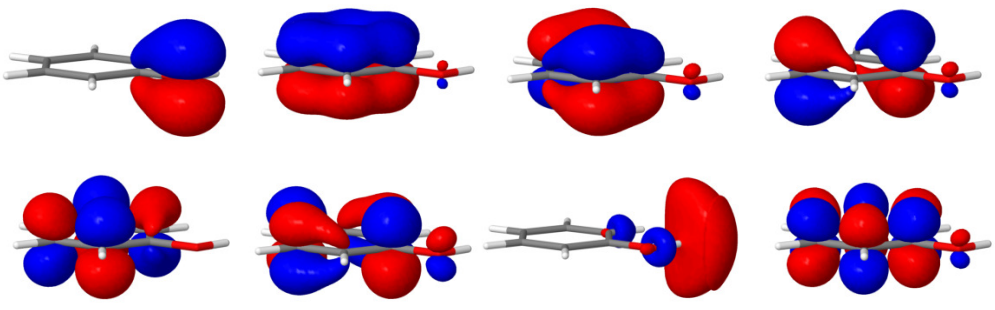

Fig. 5.2: Hartree-Fock molecular orbitals of phenol used in CASSCF calculations. The active space comprises the $\pi\pi$, oxygen lone pair, $\pi\pi^*$ and $\pi\sigma^*$ orbitals.

All electronic structure calculations were run using the Gaussian 09 program [310]. Vertical energies calculated at the EOM-CCSD level of theory used the QChem program [253].

The spectra are obtained by taking the Fourier transform:

$$I(\omega) \propto \omega \int_{-\infty}^{\infty} \mathrm{d}t C(t) \mathrm{e}^{i\omega t} \tag{5.12}$$

of the autocorrelation function

$$C(t) = \langle \Psi(0) | \Psi(t) \rangle \tag{5.13}$$

$$= \langle \Psi(t/2)^* | \Psi(t/2) \rangle \tag{5.14}$$

To reduce spurious structures (Gibbs phenomenon) that result from the finite propagation time in the Fourier transform, the autocorrelation function is multiplied by a weight function $\cos(\pi t/2T)$. The broadening seen in experimental spectra can then be simulated by further multiplying with a damping function $\exp(-t/\tau)$. By altering the damping function, broad spectra that replicate experiment can be obtained. Increasing the damping results in higher resolved spectra that allow the fine structure to be examined and then assigned.

The quantum dynamics were performed with the Quantics package which uses the MCTDH method, a highly efficient algorithm for the propagation of wavepackets [210]. Details on the theory and use of MCTDH can be found in Section 3.11.2. The wavepacket propagations were initiated from separate excitations to the $^1B_2$, $^2B_1$ and $^2A_2$ states and were performed using two different seven mode models. Initially, each wavepacket was prepared as a Gaussian with a defined width and centred on the FC point. Each propagation was performed for 200 fs. Every mode in the simulation was described using a Harmonic oscillator DVR [210]. Details of the basis sets used are given in Table 5.1.

Table 5.1: Computational details for the quantum dynamic simulations. The DVR type HO corresponds to Harmonic oscillator DVR, N_i are the number of primitive DVR functions used to describe each mode and n_i are the number of single particle functions used for the wavepacket on each state.

	Mode	DVR Type	N_i	n_1, n_2
Excitation to $^1B_2$	Q_1	HO	31	6,3
	Q_2	HO	31	6,3
	Q_3	HO	31	6,3
	Q_4	HO	31	6,3
	Q_7	HO	31	6,3
	Q_{24}	HO	31	6,6
	Q_{25}	HO	31	6,6
Excitation to $^2B_1$	Q_1	HO	31	6,7
	Q_6	HO	31	6,7
	Q_7	HO	31	6,7
	Q_9	HO	31	6,7
	Q_{12}	HO	31	6,7
	Q_{13}	HO	31	6,7
	Q_{14}	HO	31	6,7
Excitation to $^2A_2$	Q_1	HO	31	6,7
	Q_6	HO	31	6,7
	Q_7	HO	31	6,7
	Q_9	HO	31	6,7
	Q_{12}	HO	31	6,7
	Q_{13}	HO	31	10,7
	Q_{14}	HO	31	10,7

5.3 Photoelectron Spectrum

The calculated vertical ionisation energies using CASSCF and IP-EOM-CCSD are shown in Table 5.2. Compared with experimental data, the IP-EOM-CSSD energies are in good agreement, but are computationally intensive and not suitable for use when calculating cuts, in addition this method is unable to search for conical intersections. The CASSCF energies are underestimated but the relative energetic difference between all three states is in good agreement with experimental values. The first two ionised states result from removal of a π-electron from the benzene e_{1g}(S) and e_{1g}(A) orbitals, forming two $^2\Pi$ states. The third ionised state is much higher in energy and has been assigned as an n-state, with the electron being removed from the oxygen lone pair.

For use in the model Hamiltonian, only the energies of the $^2B_1$ and $^2A_2$ states needed consideration. To ensure accuracy in the spectrum, these energies were shifted to match those experimentally measured [296, 311].

The vibrational frequencies, evaluated at the MP2/aug-cc-pVDZ level of theory are listed in Table 5.3. The assignments of these frequencies to C_{2v} symmetry followed those outlined by Evans [312] and correspond well to other reported values [313–316]. It is important to note, however, that here phenol has been defined along a plane such that the b_2 modes are in plane vibrations and the b_1 modes are out of plane. Vibrational modes with significant motion of the phenyl ring and C-O

Table 5.2: Vertical ionisation energies of phenol, calculated from the equilibrium geometry, using different levels of theory. The CAS(7,8) calculations used a 6-31+G* basis. All values in eV.

State	CAS(7,8)	IP-EOM-CCSD	Experimental
$^2B_1$	7.986	8.333	8.508 [311]
$^2A_2$	8.670	9.164	9.280 [296]
n	10.950	11.966	11.560 [293]

Table 5.3: Theoretically calculated frequencies of vibrational modes, in cm^{-1} and electron volts, for $\tilde{X}^1A_1$ state of phenol calculated at the MP2/aug-cc-pVDZ level of theory and ordered by their C_{2v} symmetries.

	Frequency		Symmetry		Description
Mode	/ cm^{-1}	/ eV	(C_s)	(C_{2v}) [312]	
1	520	0.065	a'	a_1	Ring deformation + C-O stretch
2	812	0.101	a'	a_1	Ring deformation + C-O stretch
3	998	0.124	a'	a_1	Breathing mode
4	1035	0.128	a'	a_1	C-H bend in plane
5	1176	0.146	a'	a_1	C-H bend
6	1194	0.148	a'	a_1	OH bend
7	1267	0.157	a'	a_1	C-O stretch + C-C stretch
8	1501	0.186	a'	a_1	C-C ring stretch
9	1646	0.204	a'	a_1	C-C ring stretch
10	3192	0.396	a'	a_1	C-H stretch
11	3236	0.401	a'	a_1	C-H stretch
12	3806	0.472	a'	a_1	O-H stretch
13	397	0.049	a'	b_2	In plane C-O-H bend
14	612	0.076	a'	b_2	Ring deformation
15	1083	0.134	a'	b_2	C-H bend in plane
16	1161	0.144	a'	b_2	C-H bend in plane
17	1332	0.165	a'	b_2	C-H bend
18	1471	0.182	a'	b_2	C-C ring stretch
19	1482	0.184	a'	b_2	C-C ring stretch
20	1635	0.203	a'	b_2	C-C ring stretch
21	3207	0.398	a'	b_2	C-H stretch
22	3217	0.399	a'	b_2	C-H stretch
23	3230	0.400	a'	b_2	C-H stretch
24	406	0.050	a''	a_2	C-C twist
25	817	0.101	a''	a_2	C-H bend
26	910	0.113	a''	a_2	C-H bend out of plane
27	223	0.028	a''	b_1	Out of plane C-O bend + ring torsion
28	332	0.041	a''	b_1	Out of plane O-H bend
29	496	0.062	a''	b_1	Out of plane C-O bend + ring torsion
30	613	0.076	a''	b_1	Ring deformation
31	742	0.092	a''	b_1	C-H bend out of plane
32	864	0.107	a''	b_1	C-H bend out of plane
33	926	0.115	a''	b_1	C-H bend out of plane

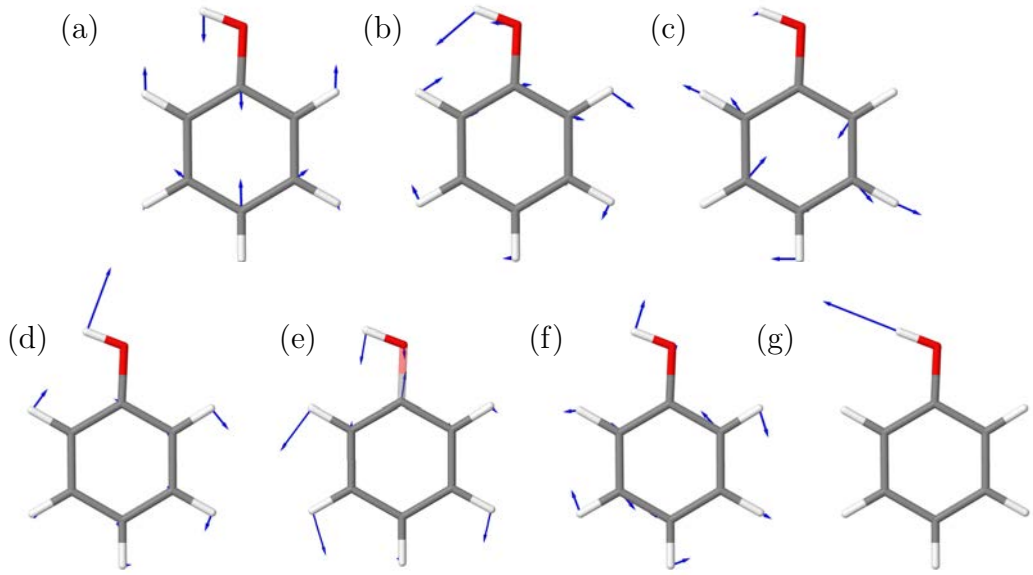

Fig. 5.3: The normal modes of phenol important in describing its photoelectron spectrum: (a) ν_1 ring deformation and C-O stretch, (b) ν_{13} in plane C-O-H bend mode, (c) ν_{14} ring deformation mode, (d) ν_6 O-H bend mode, (e) ν_7 C-O stretch and ring distortion mode, (f) ν_9 C-C ring stretch mode and (g) ν_{12} O-H stretch.

moiety are described as X-sensitive modes and are greatly affected by the substituent X [312,317], which in this case is oxygen. These modes are $Q_1, Q_2, Q_7, Q_{13}, Q_{27}$ and Q_{29}.

A quantum dynamics model containing all 33 normal modes of phenol would be prohibitively demanding and so only those important in describing the photochemistry of phenol were included. From symmetry arguments, the a_1 and b_2 modes are likely to contribute most to the dynamics. From these, seven modes are important to the phenol model. They are the low frequency b_2 in plane C-O-H bend and ring deformation modes, the lowest frequency a_1 ring deformation/C-O stretch mode and the a_1 modes corresponding to the O-H bend, C-O and C-C stretch, C-C ring stretch and the O-H stretch. These are illustrated in Figure 5.3. Previous models to study the excited states of phenol considered two nuclear degrees of freedom, r and θ, corresponding to the O-H bond length and C-C-O-H torsion [270,273,318]. These degrees of freedom are present in the model described here as vibrational normal modes.

Table 5.4: On-diagonal linear coupling constants, κ_α and off-diagonal linear coupling constants, λ_α, for the select normal modes of phenol, as determined from fitting the vibronic coupling model Hamiltonian to adiabatic surfaces calculated at the CASSCF(7,8)/6-31+G* level. All values in eV.

	κ_α				λ_α	
Mode	$^2B_1$	κ/ω	$^2A_2$	κ/ω	$^2B_1/^2A_2$	λ/ω
ν_1	-0.118	1.829	0.051	0.790	-	
ν_2	-0.070	0.695	-0.074	0.735	-	
ν_3	0.001	0.008	-0.011	0.089	-	
ν_4	0.012	0.093	0.017	0.132	-	
ν_5	-0.089	0.611	0.044	0.302	-	
ν_6	-0.126	0.851	-0.122	0.824	-	
ν_7	-0.129	0.821	-0.138	0.879	-	
ν_8	-0.045	0.242	-0.083	0.446	-	
ν_9	0.111	0.544	-0.070	0.343	-	
ν_{10}	-0.003	0.008	-0.012	0.030	-	
ν_{11}	-0.008	0.020	-0.034	0.085	-	
ν_{12}	-0.035	0.074	-0.159	0.337	-	
ν_{13}	-		-		-0.0002	0.004
ν_{14}	-		-		0.0011	0.015
ν_{17}	-		-		0.0001	0.001
ν_{18}	-		-		-0.0001	0.001
ν_{19}	-		-		0.0004	0.002

The parameters obtained from fitting the vibronic coupling model Hamiltonian to the adiabatic surfaces are shown in Table 5.4 and in Table 5.5. Cuts along the seven important normal modes are shown in Figure 5.5. The quality of the fitting is evident by how well the curves pass through the calculated points, particularly around points of interest such as the minimum or crossing points. Quantitatively the quality of fitting can be assessed by the root mean square displacement (RMSD) between the fitted surfaces and the *ab initio* points. A RMSD of 0.022 eV shows that the fitted surfaces in the model Hamiltonian are very good.

The on-diagonal linear coupling constants, κ_α, are shown in Table 5.4. For the totally symmetric a_1 modes the values are all non-zero. The three highest frequency modes were subsequently fitted as Morse potentials to account for anharmonicity. Details of these parameters are shown in Table 5.7. Consideration of the parameter

ratio $\kappa_\alpha/\omega_\alpha$ is important for determining how displaced the ionised state minima are from the ground state minimum. This parameter becomes important for lower frequency modes and thus is largest for ν_1 with important contributions coming from ν_6 and ν_7. The C-C ring stretch mode, ν_9 was also chosen as being important. Despite having a lower parameter ratio, the size of the displacement from the equilibrium geometry was significant. An adjustment to the value of this mode improved the simulated spectrum and also increased the parameter ratio. The new value is listed in Table 5.8.

Table 5.4 also lists the off-diagonal linear coupling constants, λ_α, the coupling between electronic states. Based on the symmetries of the two ionised states, non-zero values are expected for the b_2 modes. Out of the eleven b_2 modes, only five were determined to have non-zero values for the coupling constant. Making use of the ratio $\lambda_\alpha/\omega_\alpha$ again indicates only the low frequency modes to be of most importance. The only modes to exhibit significant coupling therefore are the two lowest frequency b_2 modes, ν_{13} and ν_{14}. On inspection, it was found the initial

Table 5.5: On-diagonal second-order coupling constants, γ_α, for the normal modes of phenol, as determined from fitting the vibronic coupling model Hamiltonian to adiabatic surfaces calculated at the CASSCF(7,8)/6-31+G* level. All values in eV.

Mode	$^2B_1$	$^2A_2$
ν_1	0.006	0.012
ν_2	0.007	0.014
ν_3	0.018	0.015
ν_4	0.018	0.015
ν_5	0.045	0.045
ν_6	0.049	0.067
ν_7	0.030	0.047
ν_8	0.040	0.059
ν_9	-0.011	0.075
ν_{13}	0.029	0.023
ν_{14}	-0.003	0.026
ν_{18}	-0.004	-0.008
ν_{19}	0.009	0.034
ν_{20}	-0.103	0.076

values for these modes to be insufficient to reproduce the experimental spectrum. The values have been adjusted, as shown in Table 5.8, such that good agreement with experiment is achieved.

The on-diagonal second order quadratic parameters $\gamma_{\alpha\alpha}$ are shown in Table 5.5. These parameters correspond to changes in frequency from the ground state to the ionised states. The majority of the values are small indicating little change to the shape of the potentials from the ground state to the ionised states.

One exception is the parameter for ν_{20}, a b_2 C-C ring stretch mode, which possesses a large value for the $^2B_1$ state. The cut through the PES along this mode is shown in Figure 5.4 alongside an illustration of this normal mode. From the cut, the change in frequency between the lower and upper ionised state is clear, with the $^2A_2$ potential narrower than the $^2B_1$ state. Despite the intrigue in this mode and its large γ_α, no significant coupling was found to exist between this mode and so it was excluded from the final model. It is, however, worth noting its similarity to ν_9, which is evident when comparing cuts (Figures 5.5(f)) and the normal modes

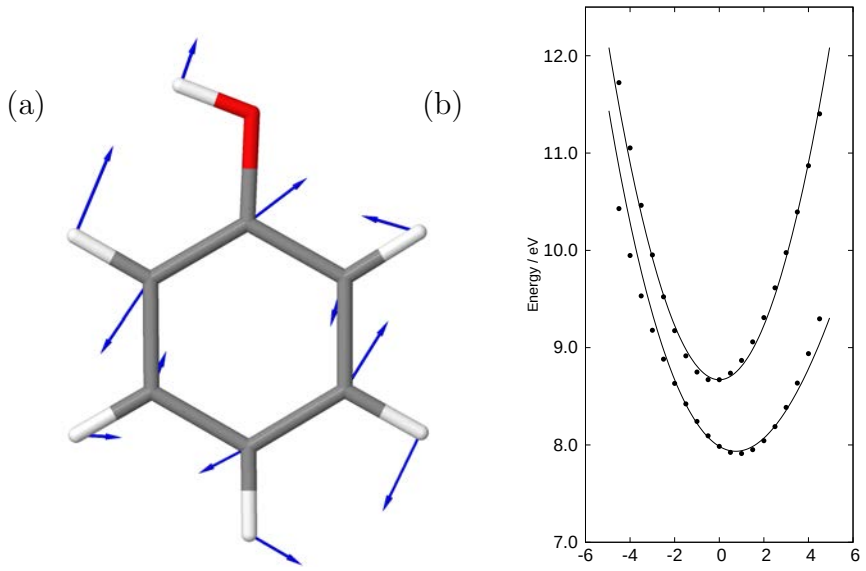

Fig. 5.4: (a) Graphical illustration for the normal mode, ν_{20} an in plane C-C ring stretch (b) shows the cut through the potential energy surface along this mode

Table 5.6: Off-diagonal second-order bilinear coupling constants, $\gamma_{\alpha\beta}$, for the normal modes of phenol, as determined from fitting the vibronic coupling model Hamiltonian to adiabatic surfaces calculated at the CASSCF(7,8)/6-31+G* level. All values in eV.

Mode	$^2B_1$	$^2A_2$	Mode	$^2B_1$	$^2A_2$
ν_{13-14}	-0.019	-0.052	ν_{2-9}	-0.010	-0.038
ν_{13-15}	-0.002	-0.003	ν_{3-5}	0.002	0.004
ν_{13-18}	-0.016	-0.039	ν_{3-6}	-0.003	-0.010
ν_{13-19}	0.011	0.025	ν_{3-7}	-0.003	-0.004
ν_{1-2}	0.019	0.061	ν_{3-9}	-0.003	-0.008
ν_{1-3}	0.004	0.010	ν_{4-5}	-0.001	-0.004
ν_{1-4}	-0.005	-0.010	ν_{4-6}	0.004	0.010
ν_{1-5}	-0.016	-0.038	ν_{4-7}	-	0.002
ν_{1-6}	-0.048	0.134	ν_{4-9}	0.003	0.006
ν_{1-7}	0.013	0.033	ν_{15-19}	-0.002	-
ν_{1-8}	-	0.004	ν_{5-6}	0.017	0.045
ν_{1-9}	0.005	0.082	ν_{5-7}	0.005	0.014
ν_{14-15}	-	-0.002	ν_{5-9}	0.010	0.027
ν_{14-18}	-0.008	-0.017	ν_{6-7}	-0.014	-0.037
ν_{14-19}	0.005	0.012	ν_{6-8}	-	-0.003
ν_{2-3}	-0.003	-0.007	ν_{6-9}	-0.016	-0.083
ν_{2-4}	0.003	0.007	ν_{7-8}	-	-0.001
ν_{2-5}	0.010	0.024	ν_{7-9}	-0.010	-0.023
ν_{2-6}	-0.008	-0.083	ν_{18-19}	0.008	-0.013
ν_{2-7}	-0.007	-0.019	ν_{8-9}	-	-0.004

(Figure 5.3(f)). In C_s symmetry, these two modes are both a′ vibrations and occur sequentially, hence the similarity.

The bi-linear parameters, $\gamma_{\alpha\beta}$, are listed in Table 5.6. These parameters are responsible for intramolecular vibrational relaxation (IVR). The majority of the parameters are very small, however several of the bi-linear parameters exhibited large values, particularly for the $^2A_2$ state. It was therefore necessary to adjust some of these parameters to obtain spectra with good experimental agreement.

A Morse potential was required to fit several of the high frequency a_1 modes, parameters of which can be found in Table 5.7. These modes were the C-H stretches, ν_{10} and ν_{11} and the O-H stretch, ν_{12}. The linear coupling constants (gradient at the FC point) obtained from the fitting are again useful indicators of the importance of

Table 5.7: Parameters for the Morse functions used to fit the potential energy curves along modes ν_{10}, ν_{11} (both C-H stretches) and ν_{12} (O-H stretch). The values of D_0 and E_0 have units of eV.

	D_0				D_1			
Mode	D_0	α	X_0	E_0	D_0	α	X_0	E_0
ν_{10}	10.932	-0.140	0.119	-0.003	11.147	-0.139	0.122	-0.003
ν_{11}	26.927	-0.091	0.369	-0.032	22.064	-0.102	0.383	-0.035
ν_{12}	7.203	0.187	-0.071	-0.001	6.085	0.214	0.196	-0.010

these modes. All the values are very small except for the upper ionised state of ν_{12} and only this mode, the O-H stretch, was included in the model. Based on these arguments, the remaining modes were neglected from the model Hamiltonian as they exhibit little coupling and would not be expected to contribute to the spectrum.

Figure 5.5(a) shows the cut along the ring deformation/C-O stretch ν_1 mode. As expected for a totally symmetric mode, the on-diagonal linear coupling value is non-zero and a large shift is observed in the $^2B_1$ state. Another significant feature seen along this mode is the crossing of the states suggesting a conical intersection to be present. The existence and location of such a crossing is discussed later. The two b_2 coupling modes are shown in Figure 5.5(b,c). Being non totally symmetric modes there is no shift away from Q_0, however a small change in frequency is noted for both modes.

The totally symmetric O-H bend mode (Figure 5.5(d)) and C-O stretch (Figure 5.5(e)) show little significance aside from the expected shift away from the equilibrium geometry. Both cuts, particularly mode ν_7, contain calculated points in the $^2A_2$ state that lie away from the fitted curve. Calculated points along the next ionised state energetically present no crossing or interaction between states and these awry points are attributed to minor failings of the low level CASSCF calculations. As these points are located far from the equilibrium geometry, they are expected to have little effect.

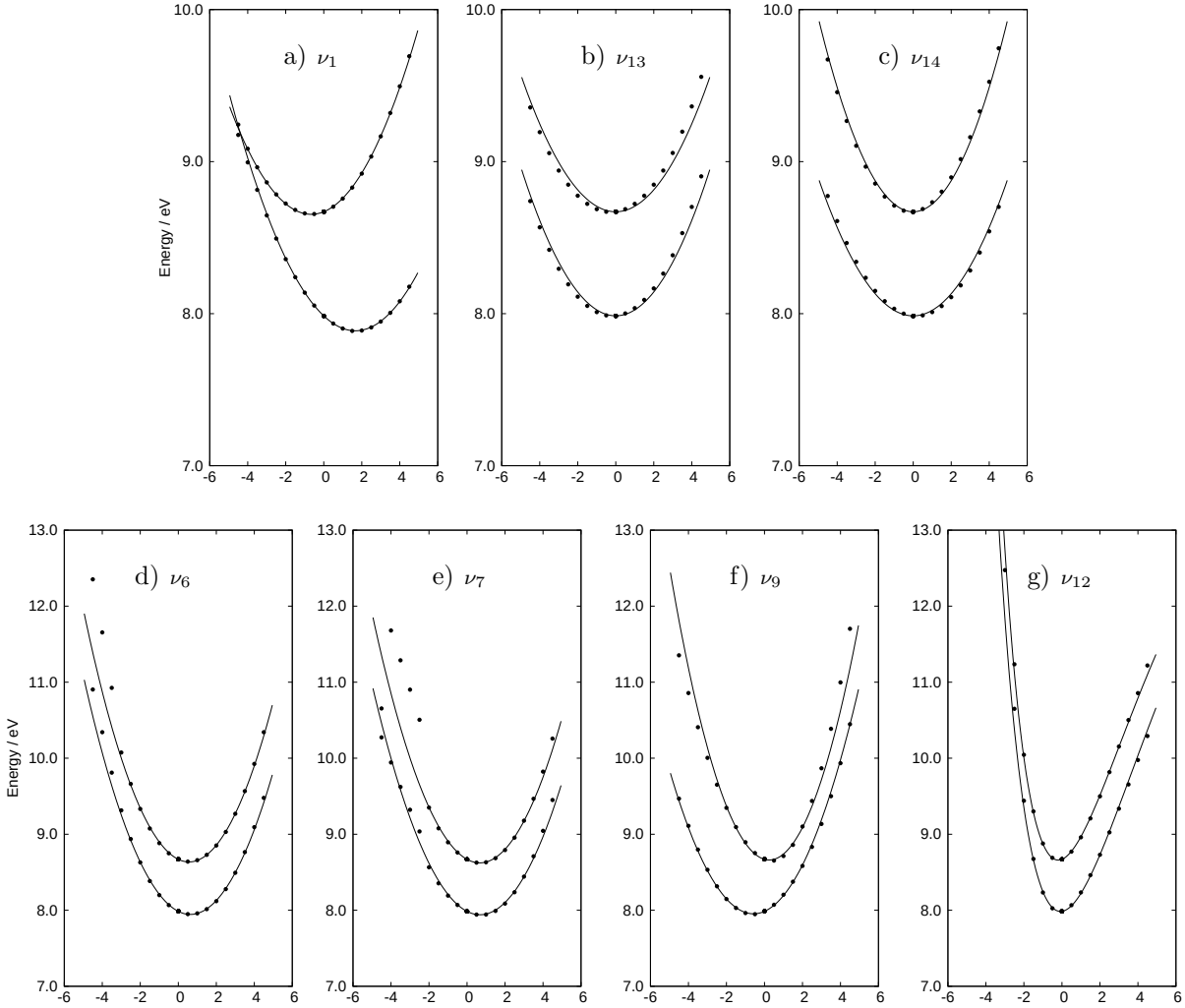

Fig. 5.5: Cuts through the adiabatic potential energy surfaces along select normal modes for the ionised states, which in order of energy at Q_0 are $^2B_1$ and $^2A_2$. The points are obtained from *ab initio* calculations at the CASSCF(7,8)/6-31+G* level. The normal modes included are: (a) ν_1 ring deformation and C-O stretch, (b) ν_{13} in plane C-O-H bend mode, (c) ν_{14} ring deformation mode, (d) ν_6 O-H bend mode, (e) ν_7 C-O stretch mode, (f) ν_9 C-C ring stretch mode and (g) ν_{12} O-H stretch.

Table 5.8: Values of selected coupling parameters adjusted from those obtained from the fitting procedure in order to reproduce the experimental spectra. All values in eV.

λ_{13}	-0.100
λ_{14}	0.080
$\kappa_9^{(1)}$	-0.200
$\gamma_{1-6}^{(1)}$	-0.010
$\gamma_{1-6}^{(2)}$	0.005
$\gamma_{1-9}^{(2)}$	-0.010
$\gamma_{6-7}^{(2)}$	-0.020
$\gamma_{6-9}^{(2)}$	-0.020

Of particular interest was the cut along the C-C ring stretch mode, ν_9, Figure 5.5(f). A significant shift in equilibrium geometry is seen for the $^2B_1$ state whilst a smaller shift in the opposite direction for the $^2A_2$ causes the two states to become close. As expected, the cut along the O-H stretch (Figure 5.5(g)) is anharmonic for each state and best fitted as a Morse potential. Unlike in the S_1, S_2 and S_3 excited states of neutral phenol, the ionised states show no evidence of crossing or photodissociation of the phenolic hydrogen.

It is evident that for the totally symmetric modes large shifts are present only for the lower $^1B_2$ states and this is reflected in the values of on-diagonal linear coupling parameters. The consequence of this is likely to appear in a spectrum containing significant vibrational structure from several progressions, whilst the $^2A_2$ spectrum may lack structure.

The photoelectron spectrum calculated using the parameters obtained directly from the fitting is shown in Figure 5.6. When compared with experiment (reproduced in Figure 5.11(a)) it is clear the simulation does not accurately reproduce the spectrum. The likely causes for this are inadequacies in the fitted values, which therefore require adjustments. Table 5.8 lists the parameters where an adjustment from the fitted values was necessary in order to successfully reproduce the experimental spectra.

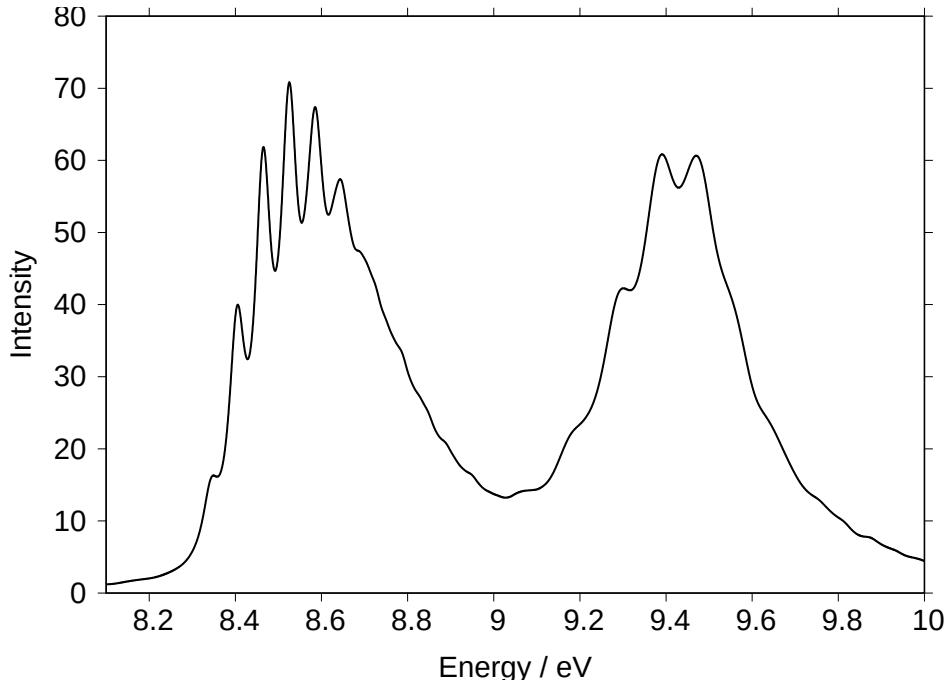

Fig. 5.6: The $^2B_1 \longleftarrow \tilde{X}^1A_1$ and $^2A_2 \longleftarrow \tilde{X}^1A_1$ photoelectron spectrum calculated using parameters obtained from the fitting procedure without any adjustments. The spectrum was calculated using the Quantics program and a seven mode model with a damping time of 30 fs for the first band and 14 fs for the second band.

Examination of the $^2B_1(D_0)$ band shows the simulated spectrum to be dominated by a progression from a single mode, ν_1. In contrast, the experimental spectrum shows there to be several different progressions present. The general shape and range of this band in the simulated spectrum matches well with experiment, but the correct fine structure is lacking. This indicates adjustments are needed to the on-diagonal linear coupling constants of the other totally-symmetric modes to incorporate the fine structure. A change to the on-diagonal linear coupling constant for ν_9 for the $^2B_1$ state ensured the first peak in this progression conformed correctly to being the most intense peak in this band. This change, whilst retaining a similar value to the fitted value, is particularly notable as a change in sign was required.

The effect of changing the parameter for ν_9 for the $^2B_1$ state can seen in Figure 5.7. In these spectra all other parameter changes have been implemented. The spectrum in Figure 5.7(a) contains a κ value similar to that obtained from the fitting procedure and replicates the spectrum shown in Figure 5.6. Increasing the parameter to 0.2 eV has little effect and the spectrum still shows a progression from a single mode. It is not until the sign is changed that a more pronounced effect is seen, with the introduction of a second progression (Figure 5.7(c)), although even at -0.1 eV the fine structure is still not properly reproduced. Finally, altering the parameter to -0.2 eV provides the correct fine structure observed experimentally.

In altering the sign of $\kappa_9^{(1)}$, the implication is a change in the displacement of the gradient and a large shift in the minimum along this mode. This alludes to a failing in the CASSCF PESs. It is however a necessary change as simulations performed with a positive value of 0.2 eV produce the spectrum seen in Figure 5.7(b), devoid of any additional fine structure except a single progression from ν_1. Support for this change is given by calculations at the MP2/6-31+G* level of theory. By using gradients and second derivatives from Hessians calculated at the neutral equilibrium geometry and the FC point on the $^2B_1$ state, on-diagonal linear coupling constants

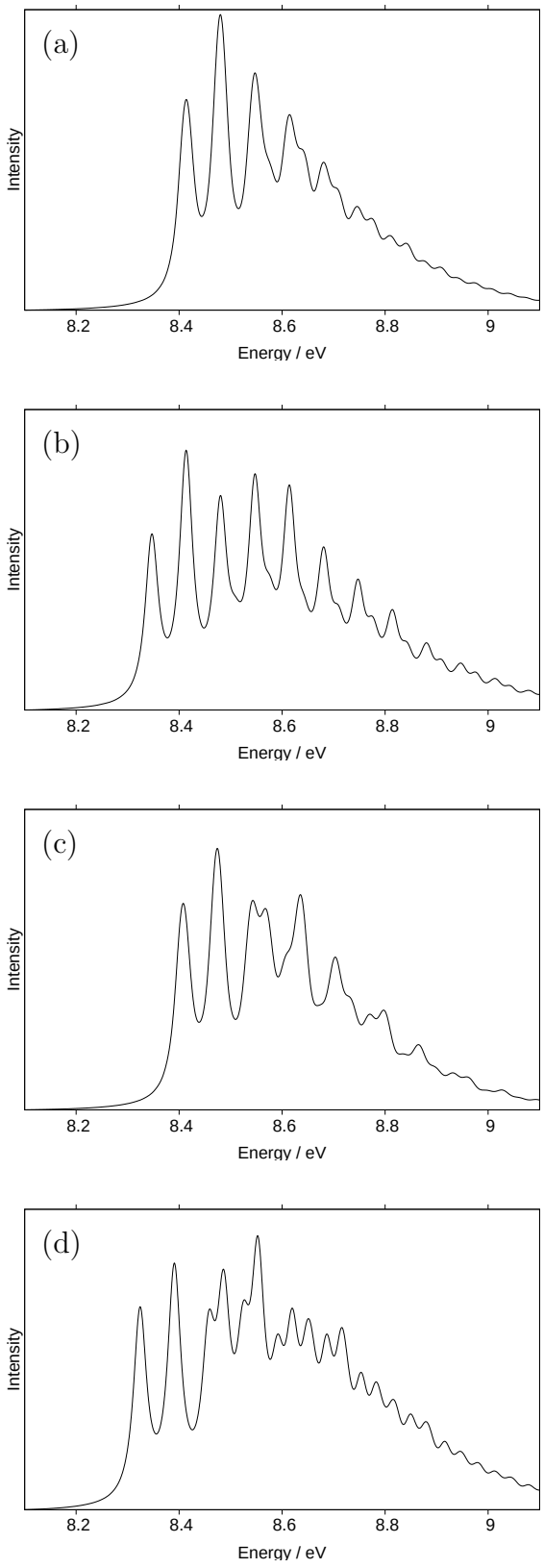

Fig. 5.7: The $^2B_1 \longleftarrow \tilde{X}^1A_1$ photoelectron spectrum calculated with different values of the parameter $\kappa_9^{(1)}$. (a) $\kappa_9^{(1)} = 0.1$ eV (b) $\kappa_9^{(1)} = 0.2$ eV (c) $\kappa_9^{(1)} = -0.1$ eV (d) $\kappa_9^{(1)} = -0.2$ eV.

Table 5.9: On-diagonal linear coupling constants, κ_α for the select normal modes of phenol, comparing those determined from fitting the vibronic coupling model Hamiltonian to adiabatic surfaces calculated at the CASSCF(7,8) / 6-31+G* level and those obtained from a Franck-Condon model calculated at the MP2/6-31+G* level. All values in eV.

Mode	CASSCF	MP2
ν_1	-0.118	0.110
ν_2	-0.070	0.008
ν_3	0.001	0.020
ν_4	0.012	0.028
ν_5	-0.089	0.046
ν_6	-0.126	0.127
ν_7	-0.129	0.010
ν_8	-0.045	0.021
ν_9	0.111	0.246
ν_{10}	-0.003	0.001
ν_{11}	-0.008	0.003
ν_{12}	-0.035	0.046

can be obtained without fitting to a series of *ab initio* points. This procedure treats the potential as Harmonic oscillators only and so ignores anharmonicity but nevertheless can provide the necessary gradients along each mode. Table 5.9 shows the on-diagonal linear coupling constants obtained at the MP2 level of theory with comparison to those obtained from fitting to CASSCF calculated points.

The values obtained at the MP2 level of theory show good agreement with the fitted parameters, particularly along the important a_1 modes. Exceptions to this are ν_7 the C-O stretching mode, for which the κ value determined from the fitting is larger. This mode however is not resolved as a separate peak in the fine structure of the photoelectron spectrum. The other significant difference is seen for ν_9. Here, the gradient along ν_9 for the $^2B_1(D_0)$ state at the neutral equilibrium geometry calculated gives a value of $\kappa_9^{(1)} = 0.246$ eV. It is notable that all the gradients from the MP2 calculations are the same, hence the gradient of ν_9 is the same as the other modes. This, therefore, means the adjusted value of -0.2 eV is close to the MP2 value for this parameter. This points to the potential importance of electron

correlation for this mode.

The change in this parameter also serves to change the ν_1 progression, preventing it from dominating the fine structure and moving the position of the most intense peak. As such, the emergence of other peaks, from different vibrational progressions, without changing any other on-diagonal linear coupling constants supports the need to change the ν_9 parameter in such a way.

The $^2A_2(D_1)$ band simulated using the unaltered parameters is vastly different to experiment. Instead of a featureless spectrum comprising two peaks, the simulation incorrectly produces additional peaks of differing intensities. It was found that no adjustments to the κ values were required to reproduce experiment, rather alterations to the off-diagonal linear, λ_α and bi-linear, $\gamma_{\alpha\beta}$ coupling constants, which were shown to contain large values for this state, were needed.

The changes to the off-diagonal bi-linear parameters prevented the spurious progressions from occurring and ensured the relative peak heights were in good agreement. The presence of large values in these parameters would often result in too much broadening to the $^2A_2$ band and loss of the little structure present. Furthermore, these adjustments make certain the origin is the most intense peak in the band and occurs at the correct energy. These changes, despite being successful in reproducing the correct structure, were often well resolved and lacked broadness.

As discussed above, an increase in the coupling between the electronic states from the low frequency b_2 modes was needed to broaden the spectrum. This increase in coupling had no effect on the the $^2B_1(D_0)$ band but was required for the $^2A_2(D_1)$ band, although the effect on the spectrum is small, but important. Since the strength of the coupling corresponds to the square of the parameter, increasing the parameter by a magnitude is needed in order to increase the coupling sufficiently.

To check whether a conical intersection exists between the $^2B_1$ and $^2A_2$ states, a CAS(7,8) conical intersection minimisation was performed using Gaussian09. This

Table 5.10: Cartesian coordinates corresponding to the geometry at the minimum energy conical intersection, calculated using a conical geometry optimisation at the CASSCF(7,8)/6-31+G* level.

	x	y	z
C	-1.178513	-1.183481	0.000000
C	-1.176800	0.278007	0.000000
C	0.000000	0.994535	0.000000
C	1.173837	0.265507	0.000000
C	1.170690	-1.209377	0.000000
C	0.000542	-1.919208	0.000000
H	-2.133038	-1.676628	0.000000
H	-2.116231	0.798974	0.000000
H	2.129437	0.758630	0.000000
H	2.123930	-1.703953	0.000000
H	-0.012120	-2.991037	0.000000
O	-0.085839	2.335889	0.000000
H	-0.756208	2.771005	0.000000

confirmed the existence of an intersection. The point in normal mode space corresponding to the intersection is denoted Q_{CI}. As a function of the normal modes coordinates, the conical intersection energy minimum can be expressed as: $Q_1 = -1.31$, $Q_2 = 0.88$, $Q_3 = 0.15$, $Q_4 = -0.14$, $Q_5 = -0.59$, $Q_6 = 1.52$, $Q_7 = 0.51$, $Q_9 = 0.96$, $Q_{10} = 0.14$, $Q_{11} = 0.40$, $Q_{12} = -1.86$, $Q_{13} = 1.33$, $Q_{14} = 0.61$, $Q_{17} = -0.54$, $Q_{18} = 0.58$, $Q_{19} = -0.41$, $Q_{20} = -0.66$, $Q_{21} = -0.11$, $Q_{22} = 0.13$. Cartesian coordinates for the geometry of the minimum energy conical intersection are shown in Table 5.10.

The conical intersection was calculated to be 0.54 eV above the FC point of the $^2B_1$ state. The geometry is distorted away from the FC point but remains planar. The distortion is similar to the quinoid-type vibration observed for benzene and phenyl derivatives. As shown in Figure 5.8, there is a lengthening of all the C-C bonds. The *ortho* to *meta* C-C bonds increase the most, with the remaining C-C bonds lengthening slightly. The C-O and the O-H bonds both contract and the C-O-H angle increases. This geometric change conforms with the position of the

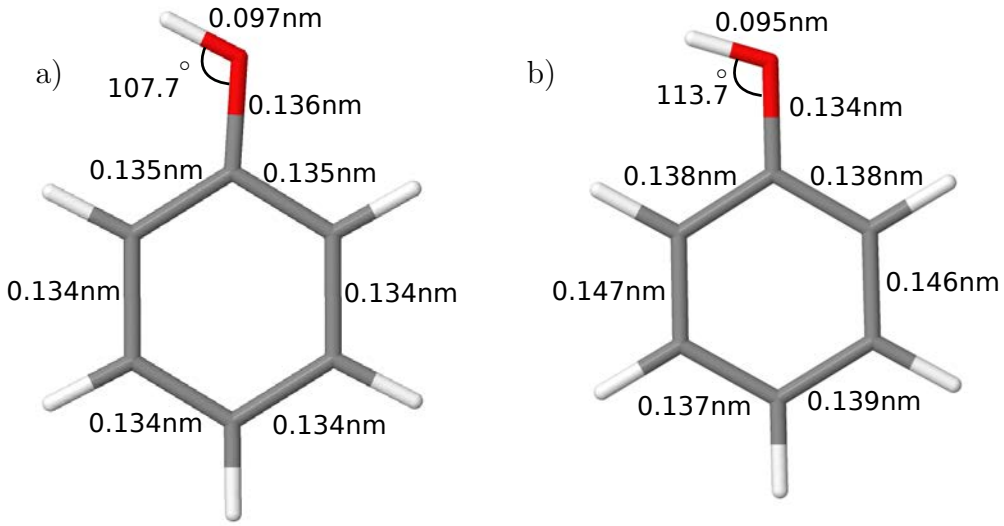

Fig. 5.8: Bond lengths and angles for phenol, comparing the geometry at (a) the neutral equilibrium and Franck-Condon geometry with (b) the conical intersection geometry. Structures calculated at the CASSCF(7,8)/6-31+G* level of theory.

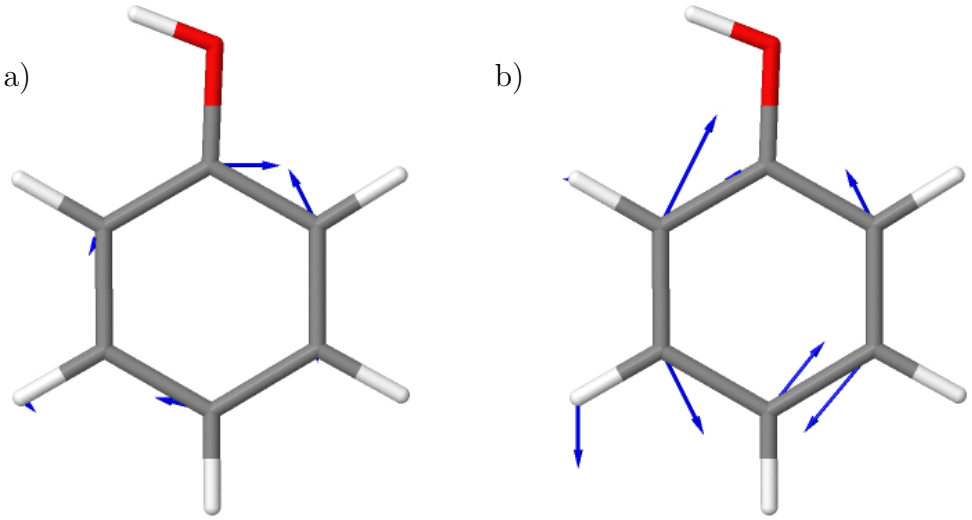

Fig. 5.9: The vectors leading from the FC point to the conical intersection: (a) the derivative coupling vector and (b) the gradient difference vector, calculated at the CASSCF(7,8)/6-31+G* level of theory.

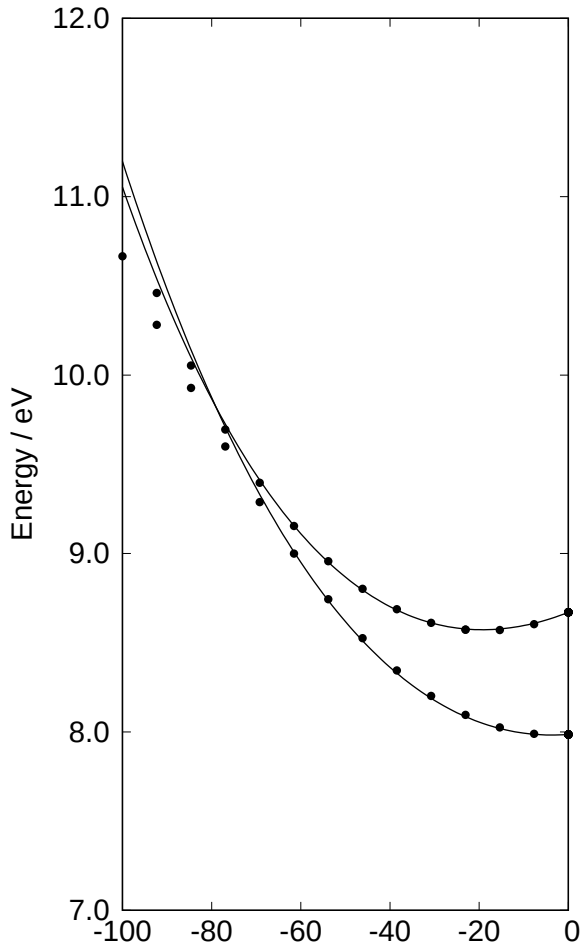

Fig. 5.10: Cut along the vector leading to the ${}^2B_1/{}^2A_2$ conical intersection. The points are obtained from *ab initio* calculations at the CASSCF(7,8)/6-31+G* level.

intersection in normal mode space, where the largest shift occurs for modes ν_{12}, the O-H stretch, ν_6, the OH bend, ν_{13}, the in plane C-O-H bend, ν_1, the ring deformation plus C-O stretch and ν_9, the C-C ring stretch. The derivative coupling and gradient difference vectors, showing the direction of the distortion by which the degeneracy is lifted, are illustrated in Figure 5.9.

A series of equal step points were generated from the FC point (Q_0) to Q_{CI} and the energies at each point calculated using CASSCF(7,8). The fitted points along the vector to the intersection are shown in Figure 5.10. The fitting was up to second order only. This is the first reported observation of a conical intersection between these two states. The intersection is high energy relative to the minima of the $^2B_1$ and $^2A_2$ states and is shifted far from Q_0, nevertheless a small amount of population transfer between states is possible.

Figure 5.11 shows the calculated photoelectron spectrum (b and c) for transitions to the lowest ionised states with comparison to experiment (a). The band between 8.20 and 9.00 eV is the transition to the $^2B_1$ state and between 9.20 and 10.00 eV to the $^2A_2$ state. The spectrum was calculated using the Quantics package, with the parameters describing the PESs obtained from the fitting using VCHAM as described previously. For calculating the spectrum, a two state, seven mode model Hamiltonian was required including the D_0 ($^2B_1$) and D_1 ($^2A_2$) ionised states. Both spectral bands have been shifted to account for the zero point energy of the neutral molecule.

The simulated spectrum shows good agreement with experiment. The electronic origins, 0_0^0, for each band, located at 8.33 and 9.31 eV, also show good agreement. For the $^2B_1$ spectrum in Figure 5.11(b), a damping time of 30 fs was used, whereas 14 fs was used for the $^2A_2$ spectrum. The differences in damping times indicate that the modes ignored from the model contribute less broadening to the $^2B_1$ portion of the spectrum. In other words, those modes excluded from the model would likely

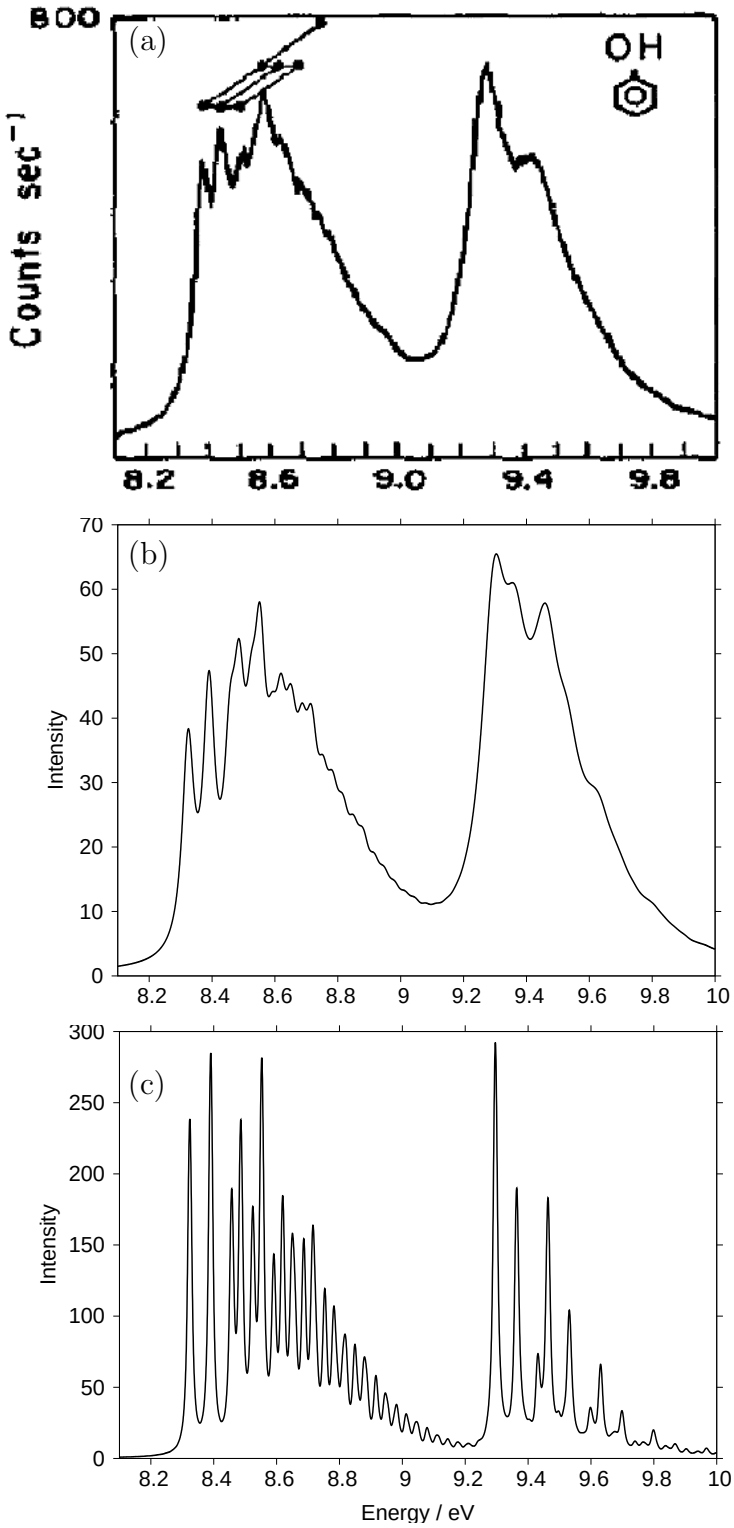

Fig. 5.11: The ${}^2B_1 \longleftarrow \tilde{X}^1A_1$ and ${}^2A_2 \longleftarrow \tilde{X}^1A_1$ photoelectron spectrum. (a) the experimental as measured by Debais and Rabalais and reproduced with permission [293]. (b) the calculated spectrum using the Quantics program and a seven mode model with a damping time of 30 fs for the first band and 14 fs for the second band. (c) the calculated spectrum with a damping of 100 fs to highlight the fine structure present.

have broadened the $^2A_2$ band. This means that the low damping time used here would not have been needed to obtain the broad spectrum observed experimentally. The presence of the conical intersection also adds broadening to the $^2A_2$ band.

The $^2B_1 \longleftarrow \tilde{X}^1A_1$ spectrum (left band in Figure 5.11) is well structured with progressions from several vibrational modes. Figure 5.12(a) shows this band with an applied damping of 150 fs. This provides higher resolution to the spectrum and allows analysis of the peak progressions. In their assignment for this band, Debies and Rabalais attributed the structure to the symmetric ring deformation/C-O stretch and ring stretching modes with frequencies 530 cm^{-1} and 1608 cm^{-1}, respectively [293]. In this work these correspond to modes ν_1 and ν_9, however only including these modes is not sufficient to fully assign, or indeed reproduce, the spectrum.

The band origin 0_0^0 is located at 8.33 eV with the ν_1 progression 1_0^n immediately following, replicating well both the spacing and relative peak height. The most intense peak in the spectrum forms from the C-C ring stretch progression 9_0^1. These modes on their own, however, are insufficient to explain the vibrational structure of the band and so a peak is assigned to the C-O stretch progression, 7_0^1. Observed on

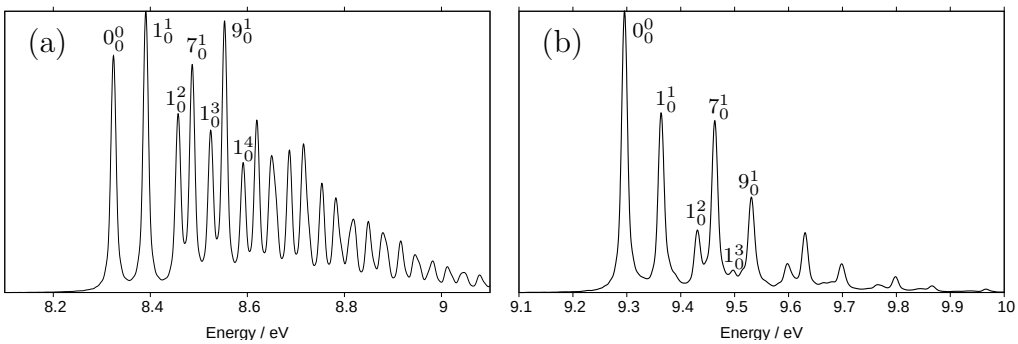

Fig. 5.12: High resolution photoelectron spectra for (a) $^2B_1 \longleftarrow \tilde{X}^1A_1$ and (b) $^2A_2 \longleftarrow \tilde{X}^1A_1$ transition. Assignments of the structure corresponding to the ground state vibrational modes are also shown. The higher resolution is achieved by setting the damping time to 150 fs.

both the 7_0^1 and 9_0^1 peak, is a shoulder peak forming part of the long 1_0^n progression.

The $^2A_2 \longleftarrow \tilde{X}^1A_1$ spectrum (right band in Figure 5.11) is broader and lacks structure. In the original assignment, what little vibrational structure is present was assigned to another ring deformation/C-O stretch mode with a frequency of 814 cm^{-1}. In our model this corresponds to mode ν_2. From the cut along this mode and subsequent fitted parameters, it seems unlikely that ν_2 is responsible for the observed structure, in disagreement with the previous assignment of Debies and Rabalais. Instead, the peak at ~ 9.47 eV is attributed to the C-O stretch, 7_0^1. The shoulder peak on the 0_0^0 transition, which can be observed in the experimental spectrum, results from the 1_0^1 progression. Figure 5.12(b) shows there to be underlying vibrational structure, however both the ν_1 and ν_7 progressions rapidly decrease in intensity and are obscured in the broadness of the spectrum. The high resolution spectrum also show the presence of a peak corresponding to the 9_0^1, which is not observable in the experimental or lower resolution simulated spectrum.

Dynamical information and the effect of the conical intersection were also investigated. Figure 5.13 shows the diabatic state populations of the $^2B_1$ and $^2A_2$ states during the simulation time of 200 fs, following separate ionisations to the $^2B_1$ and $^2A_2$ state. For ionisation into the $^2B_1$ state, no population transfer is observed as the intersection is too high in energy compared with the FC point. When ionised to the $^2A_2$ state significant population transfer occurs within 10 fs, indicating transfer of the wavepacket onto the lower state. Following this initial burst, the population of the $^2B_1$ state increases gradually during the simulation, reaching a final population value of approximately 0.3 at 200 fs. This supports the involvement of the conical intersection in the dynamics of phenol ionisation.

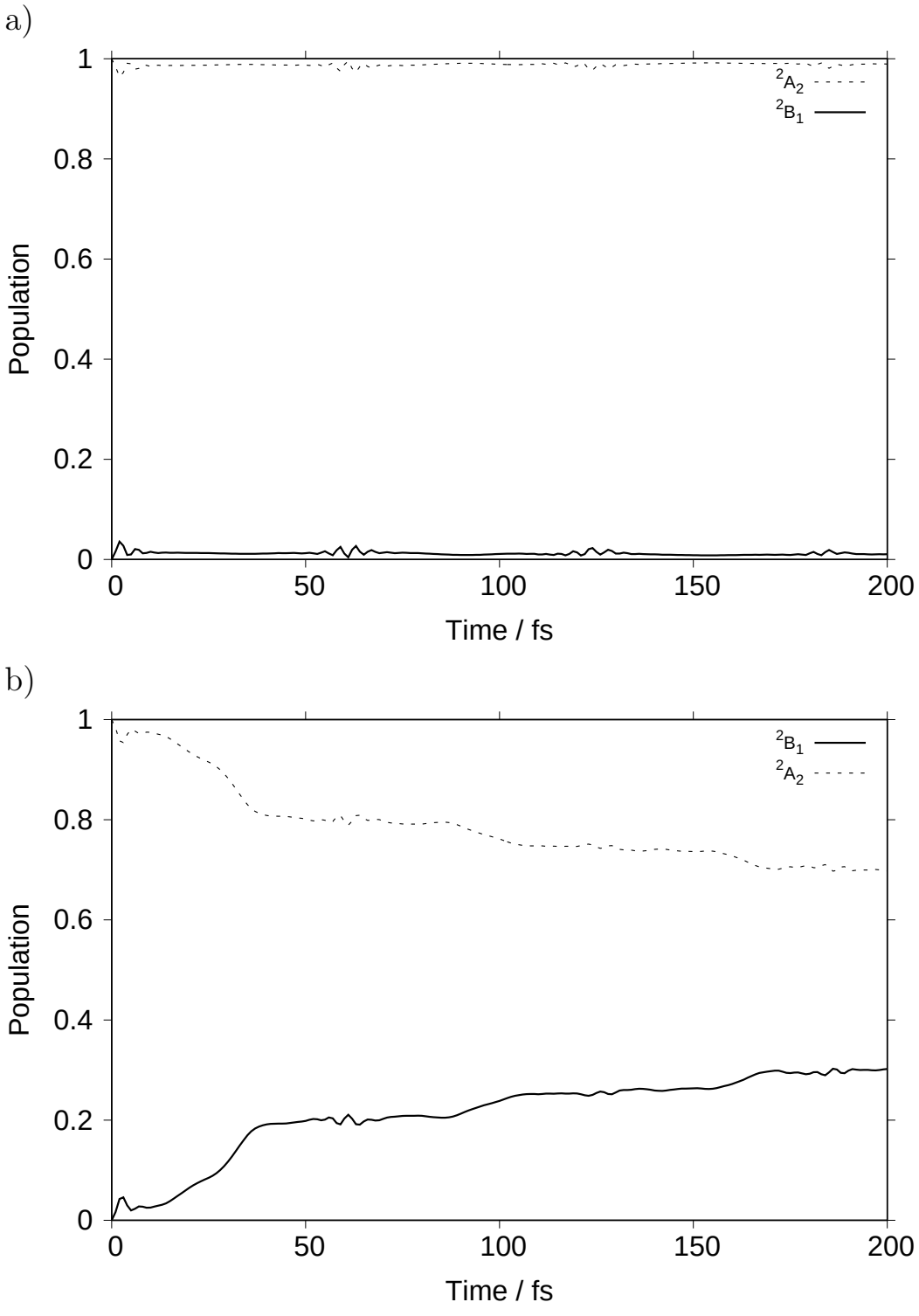

Fig. 5.13: State populations and transfer between the $^2B_1$ and $^2A_2$ states following a vertical ionisation into (a) the $^2B_1$ state which shows there to be no population transfer and (b) the $^2A_2$ state which at the end of the simulation shows the population of $^2A_2$ and $^2B_1$ to be approximately 0.7 and 0.3, respectively.

5.4 Absorption Spectrum

The calculated vertical excitation energies using CASSCF and EOM-CCSD alongside experimental values, are shown in Table 5.11. Both levels of theory overestimate the total energies of the states and the relative difference between them. Previous calculations using a larger CAS and bigger basis set show very good agreement with experiment for the S_1 state but still overestimate the S_2 state [272]. Indeed, numerous theoretical studies using a range of methods all fail to accurately reproduce the excitation energies [272]. As before, when constructing the model Hamiltonian the vertical excitation energies were shifted to match those determined experimentally [317, 319, 320].

The vibrational frequencies shown in Table 5.3 were retained, as was the ascension of symmetry to C_{2v}. From symmetry arguments only, the a_1 and a_2 modes are likely to contribute to the dynamics. Unlike for the photoelectron spectrum, the a_2 modes coupling the S_1 and S_2 states are out of plane vibrations, of which there are only three, all low frequency modes. Given the large energetic separation between the S_0 and S_2 state no coupling is observed [270].

For the S_1 absorption spectrum seven modes are important to the phenol model. These are the low frequency a_2 out of plane C-C twisting mode and C-H bending mode, the two lowest frequency a_1 ring deformation/C-O stretching modes and the a_1 modes corresponding to the ring breathing mode, C-H bending mode and the

Table 5.11: Vertical excitation energies of phenol, calculated from the equilibrium geometry, using different levels of theory. The CAS(8,8) calculations used a 6-31+G* basis. All values in eV.

State	CAS(8,8)	EOM-CCSD	Experimental [317, 319, 320]
$^1B_2$	4.82	4.93	4.51
$^1B_1$	5.94	5.75	5.12

C-O/C-C stretching mode. These are shown in Figure 5.14. The nuclear degree of freedom r, the O-H bond length (corresponding to the O-H stretching normal mode), was shown not to be important in the S_1 dynamics despite the conical intersections that exist along it. As evident in Figure 5.1, at the FC point this state is bound and at low excess energies is unlikely to reach the conical intersection with the S_2 state. For models probing the dynamics of the S_2 however it is critical this mode is included in the model.

Compared with the photoelectron spectrum, the only totally symmetric modes found to be important to both models is ν_1, the ring deformation/C-O stretch, and ν_7 the C-O stretch mode. The modes important to the S_1 dynamics are the lower frequency a_1 modes.

Parameters are obtained from fitting the vibronic coupling Hamiltonian to the adiabatic surfaces for the seven important normal modes. Cuts along these normal

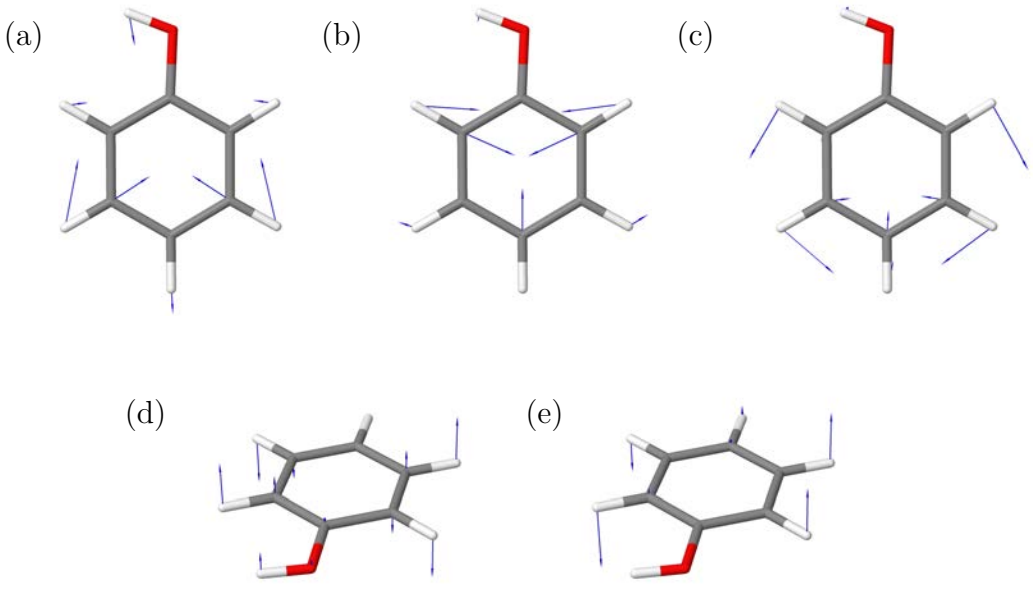

Fig. 5.14: The normal modes of phenol important in describing its absorption spectrum: (a) ν_2 ring deformation and C-O stretch mode, (b) ν_3 ring breathing mode, (c) ν_4 C-H bend mode, (d) ν_{24} out of plane C-C twist and (e) ν_{25} out of plane C-H bend. Modes ν_1 and ν_7 have been illustrated already in Figure 5.3.

modes are shown in Figure 5.15. An RMSD value of 0.032 eV signifies the fittings to be of high quality, with the curves extremely close to the majority of the calculated points. This is especially important around the minima and other points of interest such as crossings.

The on-diagonal linear coupling constants, κ_α are shown in Table 5.12. For the totally symmetric a_1 modes the values are all non-zero. The high frequency modes ν_{10} and ν_{11} were fitted as Morse potentials. The potentials for the highest frequency mode ν_{12}, the O-H stretch, were constructed using the surfaces of Domcke, using the nuclear degree of freedom r instead of the normal mode [270].

The ratio $\kappa_\alpha/\omega_\alpha$ is informative for how displaced the excited state minima are from the ground state minimum. For the $^1B_2(S_1)$ state, this ratio is largest for ν_4, the in plane C-H bend mode. In addition, ν_2, the ring deformation/C-O stretch mode and ν_3, the breathing mode, also possess a large ratio, thus were also included

Table 5.12: On-diagonal linear coupling constants, κ_α and off-diagonal linear coupling constants, λ_α, for the S_1 and S_2 electronic states for the select normal modes of phenol, as determined from fitting the vibronic coupling model Hamiltonian to adiabatic surfaces calculated at the CASSCF(8,8)/6-31+G* level. All values in eV.

	κ_α				λ_α	
Mode	$^1B_2$	κ/ω	$^1B_1$	κ/ω	$^1B_2/^1B_1$	λ/ω
ν_1	-0.024	0.372	-0.106	1.643	-	
ν_2	0.069	0.685	-0.090	0.894	-	
ν_3	0.084	0.679	0.010	0.081	-	
ν_4	0.101	0.787	0.011	0.086	-	
ν_5	-0.006	0.041	-0.069	0.473	-	
ν_6	-0.076	0.513	-0.181	1.223	-	
ν_7	-0.064	0.407	-0.150	0.955	-	
ν_8	-0.005	0.027	-0.116	0.623	-	
ν_9	0.013	0.064	0.139	0.681	-	
ν_{10}	0.455	1.150	0.464	1.173	-	
ν_{11}	0.122	0.304	0.140	0.349	-	
ν_{24}	-		-		0.085	1.688
ν_{25}	-		-		0.140	1.382
ν_{26}	-		-		0.099	0.877

in the model. Low frequency modes usually have a large ratio due to the low value of ω, although this is not true for ν_1. Despite this, ν_1 was also included in the model, having been shown as important for the photoelectron spectrum and also having a large ratio in the $^1B_1(S_2)$ state. Finally, ν_7 was also included in the model.

Whilst the S_2 absorption spectrum is not of primary interest, it is worth examining the κ_α parameters for this state. Immediately, it is evident the parameters for all the totally-symmetric modes are much larger than the S_1 state, hence the minima are more shifted. Whether such a larger shift results in the surfaces crossing will be seen in the cuts through the PES.

Again, it became necessary to adjust several of the κ_α values to accurately reproduce the experimental spectrum. These changes are listed in Table 5.16.

Table 5.12 also shows the off-diagonal linear coupling constants, λ_α, the coupling between the S_1 and S_2 electronic states. From the symmetry of the electronic states non-zero values are expected for a_2 modes. From the frequency calculation there are only three a_2 modes, all of which have non-zero λ values. The parameters for all three modes are reasonably large, showing there to be definite coupling between the states. Referring to the ratio $\lambda_\alpha/\omega_\alpha$ indicates the two lowest frequency modes to be the most important, both possessing large ratios. These modes are ν_{24}, an out of plane C-C twist and ν_{25}, an out of plane C-H bend. Only a minor adjustment was required to the ν_{24} parameter to ensure good replication of the experimental spectrum, as shown in Table 5.16.

Table 5.13 shows the on-diagonal second order quadratic parameters γ_α. These parameters relate to changes in frequencies between the ground and excited states. The values for the a_1 modes are small for both excited states with the exception of ν_6 for the $^1B_2$ state. The slightly larger value indicates some change to the shape of the potential. Significant values are also noted for modes ν_{25} and ν_{26} in the $^1B_1$ state.

Table 5.13: On-diagonal second-order coupling constants, γ_α, for the S_1 and S_2 electronic states for the normal modes of phenol, as determined from fitting the vibronic coupling model Hamiltonian to adiabatic surfaces calculated at the CASSCF(8,8)/6-31+G* level. All values in eV.

Mode	$^1B_2$	$^1B_1$
ν_1	-0.001	0.004
ν_2	0.009	0.008
ν_3	0.016	0.016
ν_4	0.010	0.019
ν_5	0.046	0.044
ν_6	0.072	0.018
ν_7	0.031	0.011
ν_8	0.029	0.026
ν_9	0.030	0.000
ν_{24}	-0.028	0.010
ν_{25}	0.009	0.070
ν_{26}	0.015	0.072

The bi-linear parameters, $\gamma_{\alpha\beta}$, shown in Table 5.14, are also very small. These parameters account for IVR. The only significant values occur between modes ν_{10} and ν_{11}, high frequency a_1 modes corresponding to C-H stretches. Neither of these modes were included in the model and with the largest value occurring in the S_2 state, it is unlikely to be important to the S_1 band in the absorption spectrum.

As before, a Morse potential was needed to fit the high frequency a_1 C-H stretch modes, parameters for which are listed in Table 5.15. The importance of these modes can be assessed from the linear coupling constants obtained during the fitting. The fitting procedure, however, returns no values for the modes, in either state, suggesting them to be insignificant in the S_1 dynamics and so were excluded from the model.

Cuts through the PES along the seven normal modes considered important are shown in Figure 5.15. All the potentials shown are relatively harmonic. The cut along ν_1, the ring deformation/C-O stretch, is shown in Figure 5.15(a). Here, the non-zero value of the on-diagonal linear coupling constant is reflected by the dis-

Table 5.14: Off-diagonal second-order coupling constants, $\gamma_{\alpha\beta}$ for the singlet excited states for the normal modes of phenol, as determined from fitting the vibronic coupling model Hamiltonian to adiabatic surfaces calculated at the CASSCF(8,8)/6-31+G* level. All values in eV. The omission of data indicate these values to be zero.

Mode	$^1B_2$	$^1B_1$
ν_{1-9}	0.0001	-0.0001
ν_{1-10}	0.0001	-
ν_{2-6}	0.0002	0.0001
ν_{2-9}	-0.0001	-
ν_{3-7}	0.0003	0.0003
ν_{3-9}	0.0001	-
ν_{4-5}	0.0001	0.0001
ν_{4-9}	-0.0001	0.0001
ν_{4-10}	-0.0001	-
ν_{5-6}	-	-0.0001
ν_{5-10}	0.0002	-
ν_{6-7}	0.0002	0.0001
ν_{6-8}	0.0002	-
ν_{6-9}	0.0002	-
ν_{7-9}	-0.0002	-0.0004
ν_{7-10}	0.0001	-0.0002
ν_{8-9}	-0.0001	-
ν_{8-11}	0.0001	0.0001
ν_{9-10}	-0.0002	-
ν_{10-11}	-0.0532	-0.1021
ν_{11-12}	0.0002	0.0002
ν_{25-26}	-0.0002	-0.0002

Table 5.15: Parameters for the Morse functions used to fit the potential energy curves along modes ν_{10} and ν_{11} (both C-H stretches) for the S_1 and S_2 states

	S_1				S_2			
Mode	D_0	α	X_0	E_0	D_0	α	X_0	E_0
ν_{10}	7.595	-0.176	0.257	-0.016	6.321	-0.189	0.292	-0.020
ν_{11}	24.038	-0.098	0.386	-0.036	24.364	-0.097	0.342	-0.028

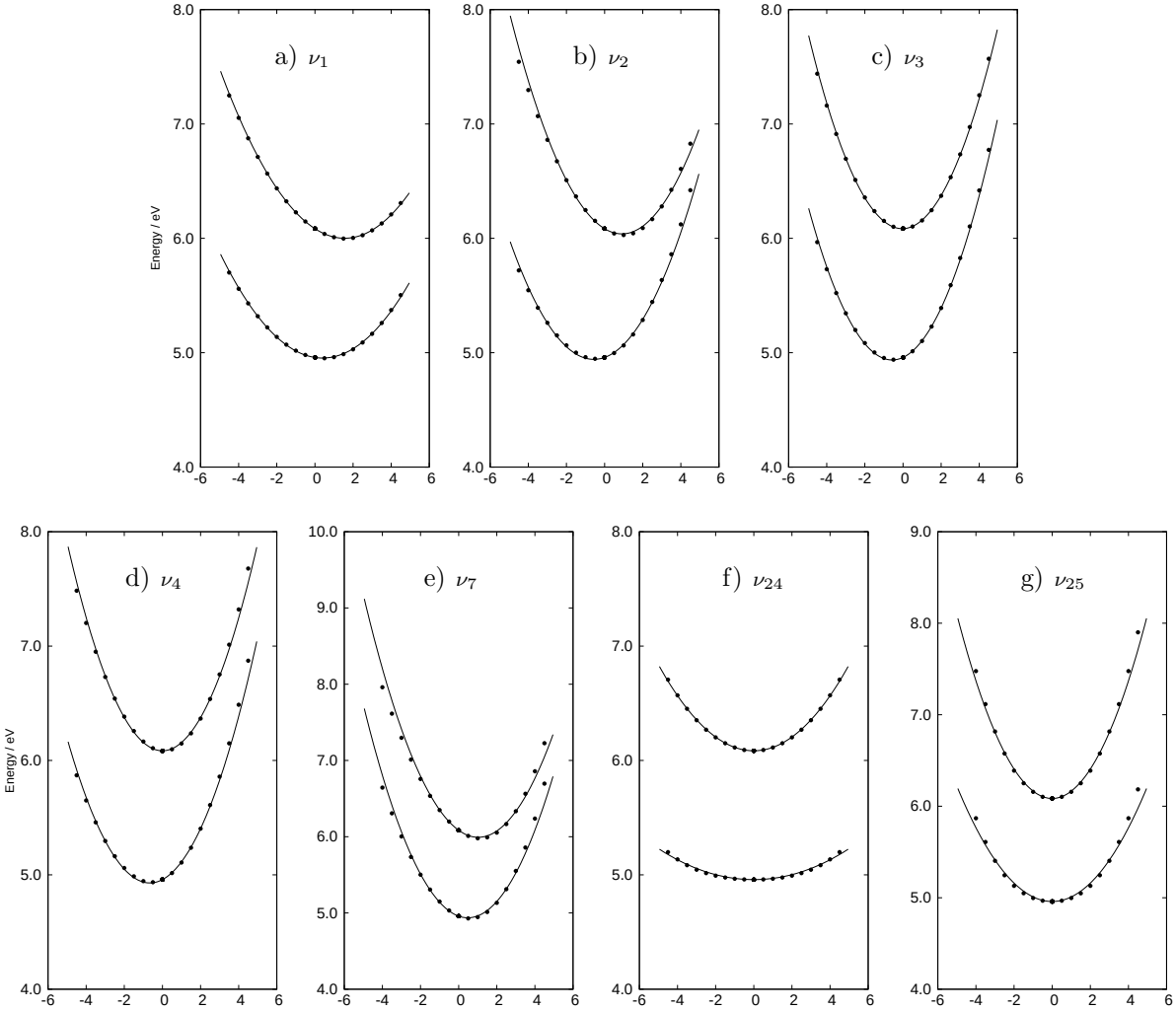

Fig. 5.15: Cuts through the adiabatic potential energy surfaces along select normal modes for the singlet excited states, which in order of energy at Q_0 are $^1B_2$ and $^1B_1$. The points are obtained from *ab initio* calculations at the CASSCF(8,8)/6-31+G* level. The normal modes included are: (a) ν_1 ring deformation/C-O stretch, (b) ν_2 ring deformation and C-O stretch mode, (c) ν_3 ring breathing mode, (d) ν_4 C-H bend mode, (e) ν_7 C-O/C-C ring stretch, (f) ν_{24} out of plane C-C twist and (g) ν_{25} out of plane C-H bend.

placement of the minima away from $\mathbf{Q}_0$. A more pronounced shift occurs for the $^1B_1$ state. The cut along ν_2, another ring deformation/C-O stretch mode shows the minima of the excited states to be displaced in opposite directions, *i.e.* the gradients are of opposite sign. The effect of this is that the two states become close together, although such a feature would occur far from the FC geometry.

Figure 5.15(c), the ring breathing mode, shows nothing significant except for a large shift away from the equilibrium geometry in the S_1 state. An almost negligible displacement occurs for the upper state. Similar features are seen for ν_4 (Figure 5.15(d)), the C-H bending mode, which contains the largest displacement in the S_1 of the normal modes.

The cut along ν_7, the C-O/C-C stretch mode exhibits displacement of the minima, particularly for the S_2 state. Similarly to ν_2, the curves become close at points far from the equilibrium geometry and is unlikely to impact the spectrum.

Figures 5.15(f,g) show the cuts along the a_2 coupling modes, ν_{24}, the out of plane C-C twist and ν_{25}, the out of plane C-H bend. Being non-totally symmetric modes, there is no shift away from $\mathbf{Q_0}$, however the more significant values noted for the on-diagonal quadratic parameter, γ_α, corresponding to a change in frequency, is obvious. The S_1 potential for ν_{24} is very shallow, to the point of nearly being flat.

Using the parameters obtained directly from fitting, the absorption spectrum was calculated and is shown in Figure 5.16. A damping time of 26 fs was applied to view the broader spectrum and 100 fs to produce a higher resolution spectrum. Compared with the experimental absorption spectrum (shown in Figure 5.17(a)), the simulation does not adequately reproduce the spectrum. This disparity suggests amendments to the fitted values are necessary to ensure good agreement between simulated and experimental spectra. Such adjustments are outlined in Table 5.16.

Upon inspection, the obvious discrepancy in the simulated spectra is the relative peak intensities and small amount of fine structure present. Effecting such

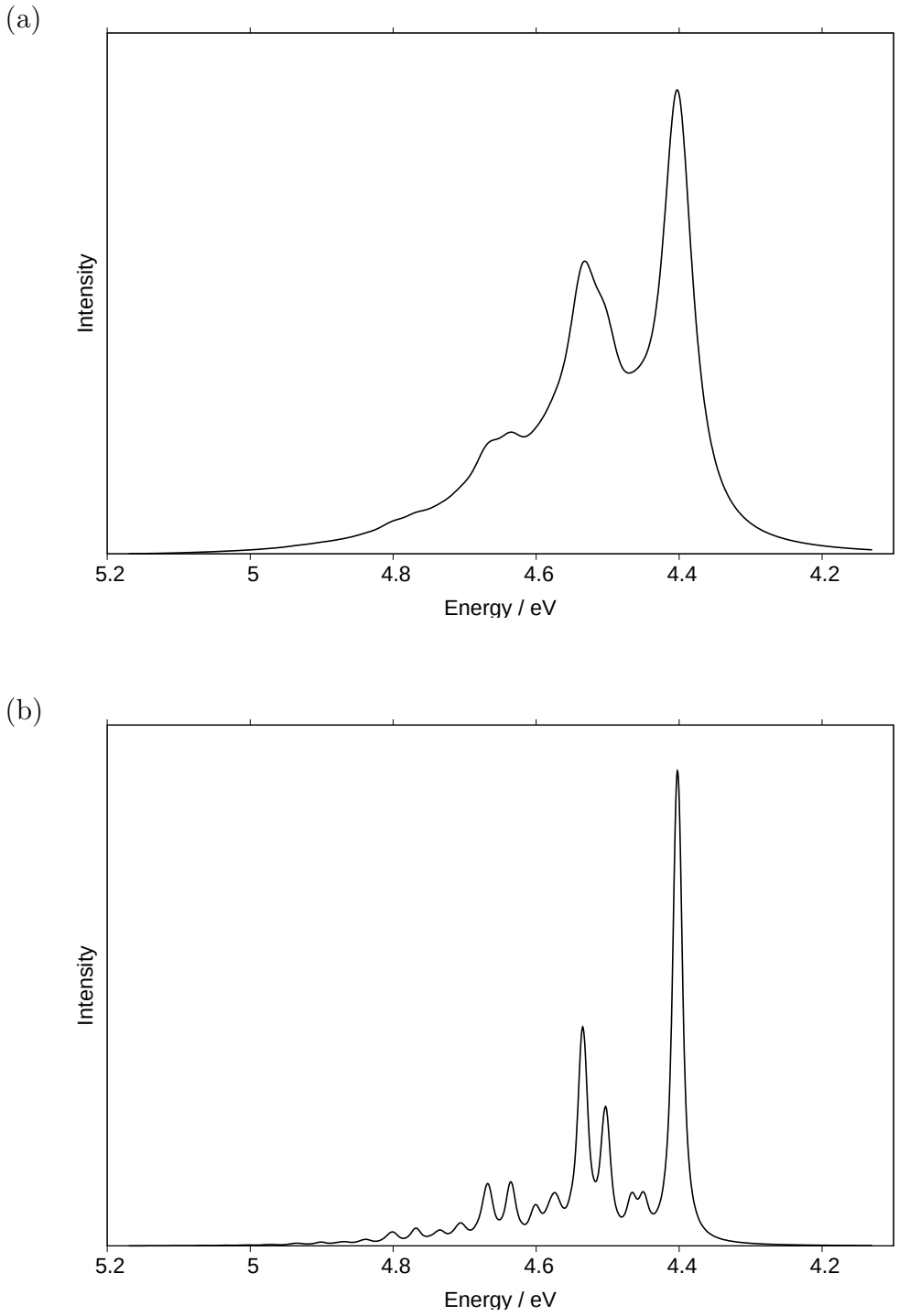

Fig. 5.16: The ${}^1B_2 \longleftarrow \tilde{X}^1A_1$ absorption spectrum calculated using parameters obtained from the fitting procedure without any adjustments. The spectrum was calculated using the Quantics program and a seven mode model. The spectra have damping times of (a) 26 fs and (b) 100 fs.

Table 5.16: Values of selected coupling parameters adjusted from those obtained from the fitting procedure in order to reproduce the experimental spectra. All values in eV.

λ_{24}	0.100
$\kappa_1^{(1)}$	-0.035
$\kappa_3^{(1)}$	0.120
$\kappa_4^{(1)}$	0.120
$\kappa_7^{(1)}$	-0.120

a change will mean adjusting the on-diagonal linear coupling constants for certain modes. Increasing these parameters will alter the intensity to ensure the first peak in the progression has an intensity that matches the origin. These changes will also introduce more progressions and combination modes into the spectrum, increasing the fine structure.

The changes listed in Table 5.16 show only small changes were necessary to the κ values. The largest increase was for mode ν_7, the C-O/C-C ring stretch. This was also the mode that required the largest increase in parameters for simulating the photoelectron spectrum, although a change in sign was necessary, attributable to failings in the CASSCF PESs. Increasing the parameter κ_7 introduces an additional peak of noticeable intensity, important in the observable fine structure. The increase in κ_3 and κ_4 ensures the intensity of the first band is similar to the electronic origin, which given the similar energies of those modes, is likely to form from their combined intensities. Missing also from the unaltered spectrum is a small shoulder peak occurring between the origin and the first progression band, corresponding to the lowest frequency ν_1 mode. As such, a small increase to the parameter κ_1 was required.

The λ_α parameters coupling the S_1 and S_2 states obtained from the fitting were already significant, unlike for the photoelectron spectrum which were near negligible. To induce additional broadness to the spectrum, a small change to the coupling parameter for the lowest frequency a_2 mode, ν_{24}, was implemented.

No changes were needed to the on-diagonal second order terms, γ_α, or the bilinear, $\gamma_{\alpha\beta}$, coupling constants. The majority of these already contained small values and had no impact on the absorption spectrum.

The values for the adjusted parameters conform also with the vibronic coupling model of Rajak [289], which shows overall good agreement between the CASSCF potentials obtained here and the EOM-CCSD potentials achieved in their work.

The calculated absorption spectrum for transition to the $S_1(\pi\pi^*)$ state is shown in Figure 5.17(b and c). The spectrum was calculated with the Quantics package using the parameters for the PESs determined through fitting using the VCHAM program. A two state, seven mode Hamiltonian model was set up, incorporating the S_1 and S_2 state. A damping time of 26 fs was used in Figure 5.17(b) and 150 fs for Figure 5.17(c). The general shape of the simulated spectrum is in good agreement with experiment. In the original simulated spectrum the electronic origin, 0_0^0, was at 4.33 eV, lower than experiment by approximately 0.2 eV. This is due to errors in the CASSCF energies for this state. It was therefore necessary to shift the energy of the S_1 state to 4.69 eV to obtain good agreement with experiment. Removing the S_0 zero point energy, gives a vertical excitation energy of 4.51 eV.

The absorption spectrum is structured, with progressions and combination modes occurring throughout. The lower resolved simulated spectrum shows good agreement for peak intensity and fine structure with experiment. The range of the spectra and relative positioning of the peaks also show good agreement. Figure 5.18 shows the absorption spectrum with an applied damping of 150 fs. Such a large damping provides a very high resolution spectrum that allows the assignment of the vibrational fine structure.

From the electronic origin peak, are located two peaks of small intensity corresponding to the lowest frequency a_1 modes, ν_1 and ν_2, both of which correspond to ring deformation/C-O stretch vibrations. These peaks only appear in higher re-

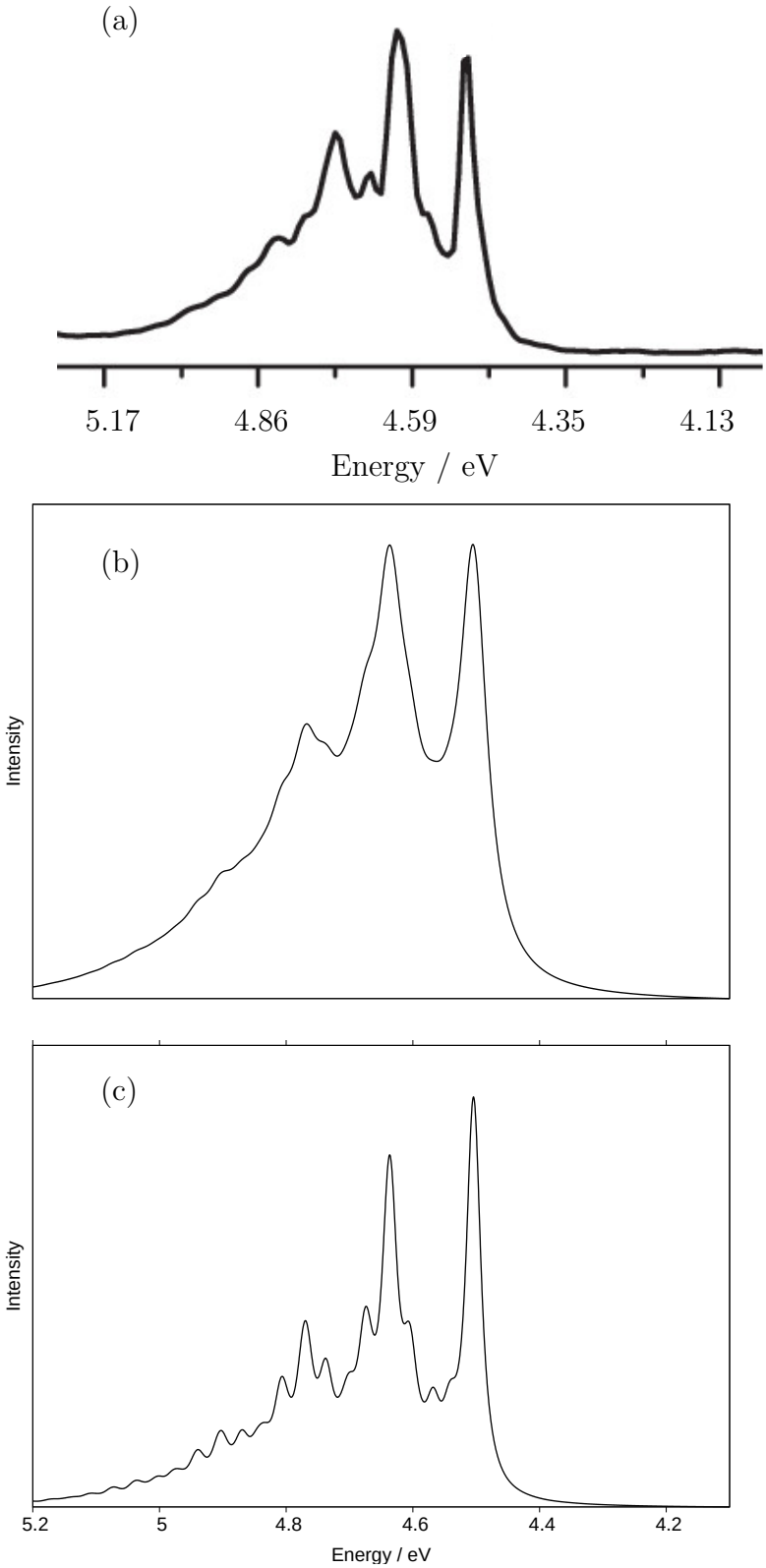

Fig. 5.17: The ${}^1B_2 \longleftarrow \tilde{X}^1A_1$ absorption spectrum. (a) the experimental as measured by Karmakar *et al.* and reproduced with permission [288]. (b) the calculated spectrum using the Quantics program and a seven mode model with a damping time of 26 fs to reproduce the broadness of experiment. (c) the calculated spectrum with a damping of 150 fs to highlight the fine structure present.

solved spectra and are lost in the low resolution spectra obtained from simulations and experiment. Assignment of the main peak in the progression, which in the experimental and low resolution spectra corresponds to the most intense peak, is difficult. Its location at $\tilde{0}.13$ eV from the origin is similar to the vibrational energies of ν_3, a breathing mode and ν_4,an in-plane C-H bend mode. The intensity of this peak may result from the progression of both modes and combination of their intensities. It is possible for there to be a small contribution from the second progression, 1_0^2. In their simulations, Rajak *et al.* assign the same modes to this peak [289].

The next peak along occurs 0.17 eV from the origin and corresponds to the first peak in the 7_0^1 progression, the C-O/C-C ring stretch mode. This peak was absent from the spectrum simulated using the unaltered parameters and its appearance supports the adjustments that were needed to the κ_7 value. The presence of this peak is also evident in the low resolution spectrum. The remaining peaks can be assigned

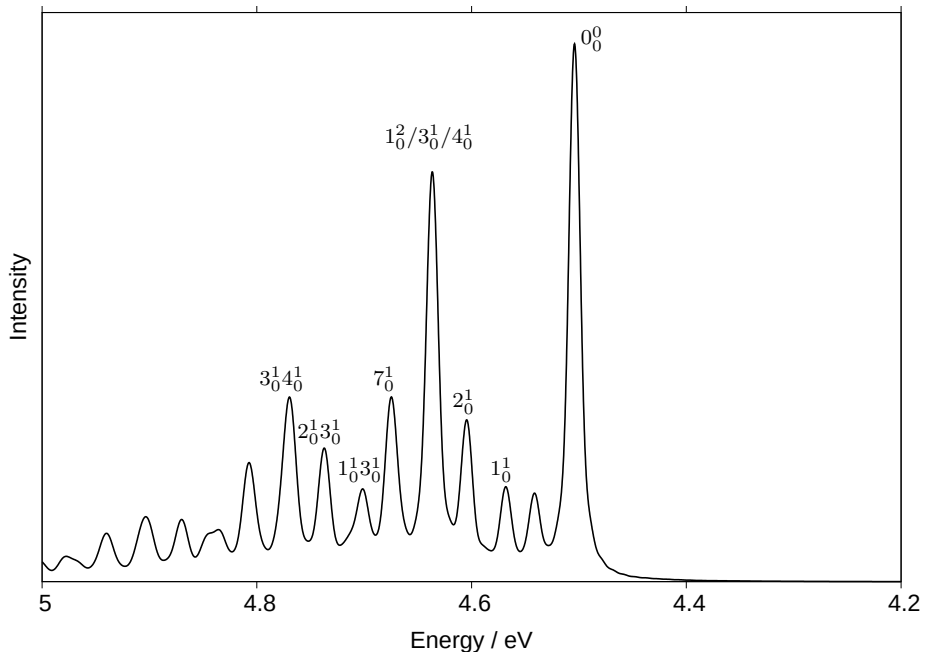

Fig. 5.18: High resolution absorption spectrum for ${}^1B_2 \longleftarrow \tilde{X}^1A_1$ transition. Assignments of the structure corresponding to the ground state vibrational modes are also shown. The higher resolution is achieved by setting the damping time to 150 fs.

as combination modes between ν_1, ν_2, ν_3 and ν_4. Whilst the majority of these are weak, a more intense peak can be observed corresponding to the combination $\nu_3 + \nu_4$. From the assignments it can be seen that the vibrational progressions are short, comprising the fundamental and little else.

5.5 Conclusion

The study and rationalisation of molecular photodynamics can be explained through the topology of the PESs. Consideration of these surfaces are especially critical for non-adiabaticity and where vibronic coupling plays an important role. Accurately calculating PESs is crucial for determining the correct coupling. Despite lacking dynamic electron correlation, the CASSCF method performs reasonably well in reproducing the surfaces. Even though there are discrepancies between the calculated energies and those determined from experiments, the method correctly predicts the ordering of states and relative energetic differences.

A full multi-dimensional PES encompassing all the vibrational modes of a molecule is computationally demanding for all but the smallest systems. For phenol this means that explicit consideration of all 33 vibrational modes is unfeasible. Taking a smaller, select number of modes containing all the totally symmetric modes and modes coupling the states, creates a more tractable model. The two lowest ionised states are coupled through b_2 modes whilst the singlet excited S_1 and S_2 states are coupled by a_2 modes. The automatic fitting procedure is able to provide all the necessary parameters, but the linear optimisation used in the fitting does not guarantee the parameters obtained are optimal and a different set of parameters may be better. This is evident by the need to adjust parameters to accurately reproduce the experimental spectrum. In general, such adjustments are small, although the change in sign required for one of the κ parameters highlights the importance of electron correlation.

In addition to the coupling between states, a CoI was found to exist between the two lowest ion states. Whilst a cut along the lowest frequency totally symmetric mode showed the states to cross, the actual intersection was located along a vector comprising a large number of normal modes. Diabatic state populations during the simulation showed that ionisation into the $^2A_2$ state leads to transfer and population of the lower ionised state, hence the crossing point plays an important role in the dynamics.

The two models described here, both consisting of seven modes, are sufficient to reproduce the experimental photoelectron and absorption spectrum. This implies the model describes the regions around the FC point well. Analysis of the vibrational fine structure for the photoelectron spectrum differs to that proposed alongside the experimental data. An extra mode is needed to fully assign the first ionisation band. The little structure observed in the second ionisation band was suggested to correspond to the second lowest totally-symmetric vibrational mode. From the linear coupling parameters and cuts along the PES, an alternative assignment is suggested. In the absence of experimental data, there is little to compare the assignment of the absorption vibrational fine structure with. Those proposed here, however, agree with other theoretical work. The fine structure is composed of the fundamental transitions for the the lowest totally symmetric modes and peaks formed from combination between these modes.

Good agreement between the simulated photoelectron and absorption spectrum with experiment is strongly indicative of accurate PESs for the excited and ionised states of phenol. The construction of a model containing parameters for these potentials is important in allowing theoretical time-resolved photoelectron spectra (TR-PES) to be simulated and compared with experiment. To fully confirm the accuracy of the potentials, it will be necessary to incorporate the O-H stretch, as nuclear degree of freedom r into the model as well as calculating the S_2 absorption spectrum.

Chapter 6

Anthracene and related derivatives

This chapter details the development of new methodology, based on the model Hamiltonians seen in previous chapters, to calculate absorption and emission spectra. Motivated by a desire for the method to be efficient and rapid, the PESs can be quickly obtained, without the need for fitting to a series of calculated points, and allow much larger systems to be studied. To test the method, the absorption and emission spectra for a series of polycyclic compounds are calculated and compared with experiment. The model is shown to successfully calculate the spectra and reproduce experimental data reasonably well. This makes it the ideal tool for predicting such spectra, particularly in the absence of experimental data. Furthermore, it is also able to capture Stokes shift. The model has its limitations, such as for naphthalene, but even then quickly shows when more complicated processes are present and a different model needed.

6.1 Introduction

It has been well established so far in this thesis that the construction of PESs are a mandatory pre-requisite for quantum dynamic studies. Calculating these PESs can become time intensive, particularly if many degrees of freedom are considered. Methods that can generate PESs more efficiently are much sought after, not only to reduce the need to employ electronic structure calculations for a vast number

of points, but also to enable many more degrees of freedom to be considered. One such method is to use information at the FC point only to generate PESs for all normal modes as displaced Harmonic oscillators. This forms the basis for the model described in this Chapter. Another method, the DD-vMCG, is outlined in Chapter 7.

To test the utility of such a model, the electronic transitions to and from the S_1 state, *i.e.* absorption and emission, were explored. Other possible relaxation pathways were ignored, unless direct evidence from the spectra indicated otherwise. Obtaining electronic spectra can also provide other useful information such as Stokes shift. This shift is defined as the difference between the positions of the maxima in the absorption and emission spectra and usually results from fluorescence at longer wavelengths than the absorption. This difference in wavelength can result from vibrational relaxation, but is most strongly affected by the solvent, particularly the solvent reorganisation energy. In the gas phase, the 0-0 transition for absorption and emission will occur at the same wavelength and it is only in the presence of a solvent that a Stokes shift is observed.

Often absorption and emission profiles appear as mirror images of each other. This usually happens when the vibrational energy level spacings in the S_0 and S_1 are similar and the potential energy surfaces are quasi-harmonic. A simple FC framework will therefore likely produce such mirror-imaged spectra. For strongly anharmonic potentials, this mirror image principle breaks down and the emission spectrum can look vastly different to the absorption. This is especially true where torsional motion is present, but can also be affected by vibronic coupling and non-adiabaticity.

The series of molecules for which the absorption and emission spectra were calculated are shown in Figure 6.1. The main components are anthracene based derivatives, although a range of polyacenes are also included. The aim is to pro-

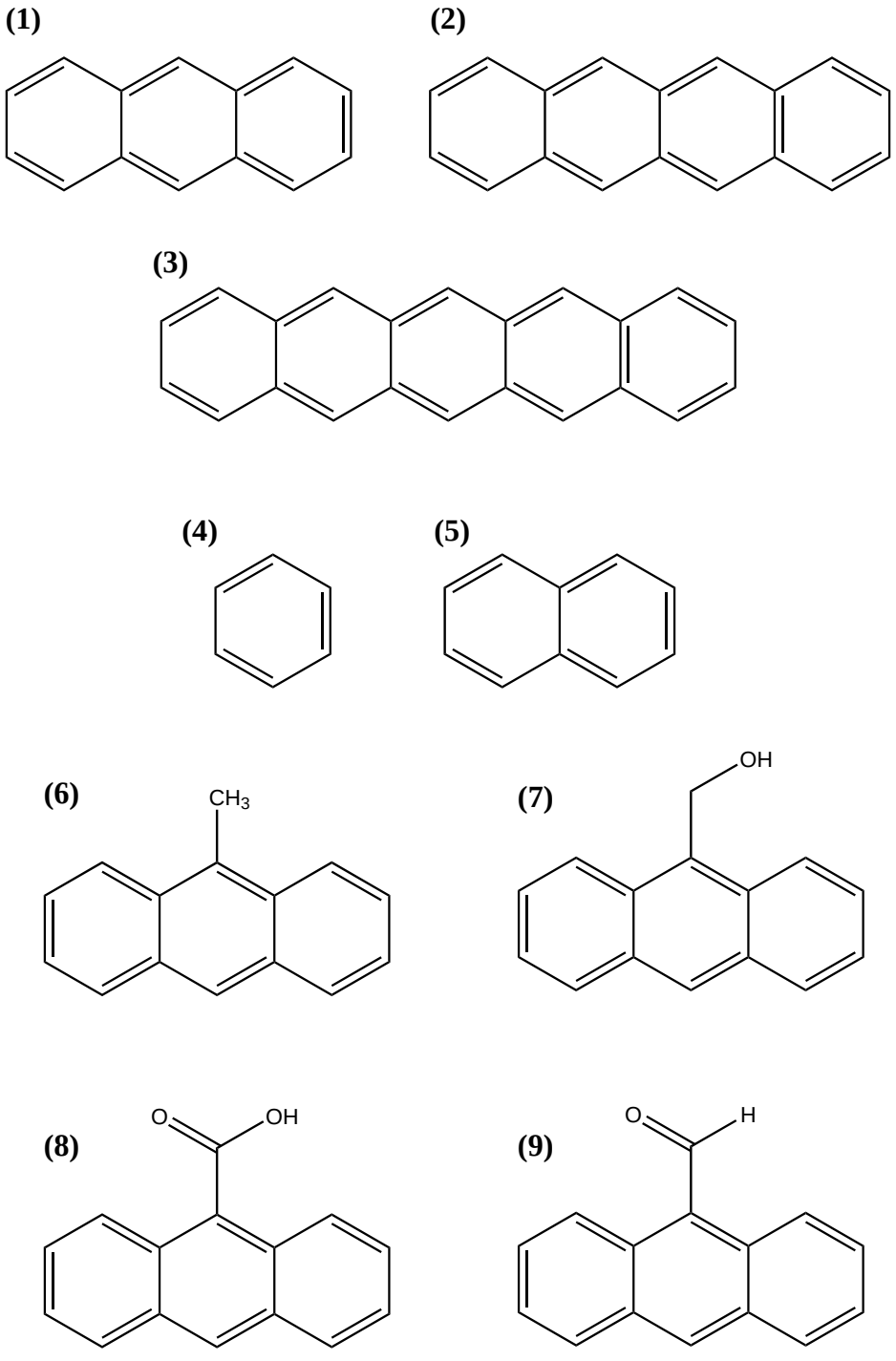

Fig. 6.1: Molecular structures of the different linear polyacenes and anthracene derivatives for which the absorption and emission spectra were calculated. **(1)** anthracene, **(2)** tetracene, **(3)** pentacene, **(4)** benzene, **(5)** naphthalene, **(6)** 9-methyl anthracene, **(7)** 9-hydroxymethyl anthracene, **(8)** anthracene-9-carboxylic acid and **(9)** anthracene-9 -carbaldehyde.

vide methodology for the rapid and accurate prediction of absorption and emission spectra. This also allows prediction of spectra for larger molecules and those with no experimental data. Alternatively, cataloging the absorption and emission profiles provides a database against which spectra of an unknown molecule could be checked against, aiding its identification. Such an application makes it a valuable tool for molecular identification in the interstellar medium. Likewise comparison of spectral profiles of very large molecules against their individual components, provides insights on the moieties responsible for photochemical behaviour.

Electronic Structure of Polyacenes

The electronic properties of polyacenes are of considerable interest and numerous studies have revealed an emerging pattern in their excited states. The linear progression of fused benzene rings to form polyacenes also exhibits a notable crossover in character between naphthalene (n=2) and tetracene (n=4). These studies tend to ignore the parent molecule benzene due to its higher symmetry.

All the linear polyacenes from naphthalene onwards possess D_{2h} symmetry. The lowest two singlet excited states, as denoted in the literature [321], are either L_a (short axis polarised) or L_b (long axis polarised). Within the constraints of D_{2h} symmetry, these states correspond to B_{2u} and B_{3u} respectively. The $L_a(B_{2u})$ state is a bright state resulting from a HOMO $\rightarrow$ LUMO transition, whilst the $L_b(B_{3u})$ state is dark, arising from a mixture of HOMO $-1 \rightarrow$ LUMO and HOMO $\rightarrow$ LUMO $+1$ transitions. Valence-bond theory predicts the L_a state to be more ionic in character, while the L_b state is covalent and similar to the ground state. A study using a semi-empirical approach yielded similar results [322].

In naphthalene, $L_b(B_{3u})$ is the lowest excited state (S_1) followed by the $L_a(B_{2u})$ state. The same is also true for benzene, although its D_{6h} symmetry confusingly makes the L_b state B_{2u} in symmetry, however descending symmetry to D_{2h} converts B_{2u} to B_{3u}, thus agreeing with naphthalene.

In tetracene, a crossover in these states occurs, with the lowest excited state (S_1) now being the $L_a(B_{2u})$ state, followed by the $L_b(B_{3u})$ state. In anthracene the two states become very close in energy, the $L_a(B_{2u})$ state being marginally lower. Numerous theoretical studies have examined the accuracy of electronic structure methods for reproducing the correct ordering and energies of these states. It was reported that EOM-CCSD performed reasonably well; discrepancies were observed between the calculated and experimental energies, but the correct ordering in the states was achieved [323]. Similar findings were reported for ADC(2) calculations [324]. Both studies, in addition to work by Grimme and Parac [325, 326], noted issues with TDDFT in calculating the L_a state, which was attributed to the ionic character of the state. This is demonstrated best by its wrong prediction in the ordering of states for naphthalene, although it correctly orders the states for the larger polyacenes, showing increasing accuracy for the large systems.

6.2 The model

The model Hamiltonian makes use of the vibronic coupling Hamiltonian described in Section 2.6. The model presented here differs in that the only information required are the Hessians at the optimised ground state structure and at the FC point for each state of interest. This removes the need for *ab initio* calculations to be carried out on a series of points. For large systems, such as anthracene, such calculations can become computationally intensive due to its size and number of vibrational modes that may need to be considered. From the Hessian, the gradients and second-derivatives are readily available. These correspond to the on-diagonal first-order, κ_α, and second-order, γ_α and $\gamma_{\alpha\beta}$, terms:

$$\kappa_{\alpha}^{(i)} = \left\langle \phi_i \left| \frac{\delta H_{el}}{\delta Q_{\alpha}} \right| \phi_i \right\rangle \tag{6.1a}$$

$$\gamma_{\alpha\beta}^{(i)} = \left\langle \phi_i \left| \frac{\delta^2 H_{el}}{\delta Q_{\alpha} \delta Q_{\beta}} \right| \phi_i \right\rangle \tag{6.1b}$$

Within this simplified vibronic coupling Hamiltonian the potentials are expressed only as Harmonic oscillators around the FC point in terms of ground state normal modes. These potentials are then shifted from the equilibrium geometry, $\mathbf{Q}_0$ as per the κ_{α} values.

The constructed Hamiltonian is then used for quantum dynamic calculations, using the MCTDH method, as implemented in the Quantics package. The full details of the MCTDH algorithm are outlined in Chapter 3 and in a recent review [210]. Each mode included in the simulation was described by a Harmonic oscillator discrete variable representation (DVR), with 21 primitive DVR functions used. Each wavepacket was described with six single particle functions (SPFs). The same basis set was employed for absorption and emission calculations of each molecule. The simulation was initiated by preparing a Gaussian wavepacket, of defined width, centred on the FC point. The wavepacket was then allowed to propagate along the S_1 surface for 300 fs.

The absorption spectrum is obtained by taking the Fourier transform of the autocorrelation function. Each spectrum is then shifted to account for the zero point energy. In order to match experimental spectra, the autocorrelation function is multiplied by a damping function:

$$f(t) = \exp\left(\frac{-t}{\tau}\right) \tag{6.2}$$

which has the effect of broadening the spectrum.

For simulating the emission spectrum the wavepacket is firstly relaxed on the

excited state surface to create the ground state vibrational wavefunction in the excited state. In the MCTDH method, wavepacket relaxation is realised through propagation in imaginary time, $t = -i\tau$, with the wavefunction now expressed as:

$$\Psi(\tau) = \sum_j a_j \mathrm{e}^{-E_j\tau}\phi_j \tag{6.3}$$

Improvements to the relaxation scheme by modifying the working equations for the A-vectors, and constraining the SPFs such that $g^{(\kappa)} = 0$, ensures the wavefunction remains normalised as the lowest energy eigenfunction of the Hamiltonian is sought [210]. Once the wavefunction has converged and the relaxation is complete, a vertical de-excitation places the wavepacket on the ground state FC point from the S_1 minimum. The wavepacket is then allowed to propagate on the ground state surface before taking the Fourier transform of the autocorrelation function to give the spectrum. This spectrum is not yet the true emission spectrum as the energy will be too low, representative of the energy of the ground state itself and not of the transition. To account for this, the final energy obtained from relaxing the wavepacket on the excited state surface is subtracted from the Fourier transformed autocorrelation function. This results in the final emission spectrum.

To account for the Stokes shift, two geometry optimisations on the excited state are performed: one optimisation in the gas-phase and the second including implicit solvation. The difference between the energies of these optimised structures reflects the change in energy of the state due to the solvent. This difference is then subtracted from the energy obtained from relaxing the wavepacket on the excited state surface. This ensures the final emission spectrum is shifted to lower energy and reveals any differences between the two λ_{max} values corresponding to a Stokes shift.

The choice of electronic structure method is vital for ensuring accurate vertical excitation energies and vibrational frequencies and, therefore, an accurate PES. The method therefore needs to be able to calculate excited states and also Hessians at

the FC point. EOM-CCSD methods provide accurate excited state energies but involve expensive numerical frequency calculations. The size of the molecules being studied also restrict the use of high scaling methods such as coupled cluster (CC). This also prevents the use of complete active space (CAS) methods, for which the large number of orbitals and electrons needed exceeds the limitations for which CAS can be efficiently utilised. Other possible methods include Grimme's DFT-MRCI method [327], that has been shown to accurately determine excited state energies [328, 329] at low computational cost, but for which Hessians are not available. One method that has reasonable scaling with molecule size, is able to compute excited state energies and has analytical Hessians is TDDFT, as described in Section 3.10. The use of TDDFT raises two major points. Firstly, the accuracy of the excited state values obtained and secondly which functional is best to use. Comparison of TDDFT energies against other levels of theory and experiment will be informative as to the reliability of the method. The choice of best functional is highly contentious, with no universal "black-box" functional and a multitude of variants available. The choice of B3LYP is somewhat arbitrary, but has been shown in numerous studies to provide reliable structures, frequencies and excited state energies [330–333].

The choice of basis set also balances accuracy against efficiency. For the systems under investigation, it was found that a 6-31G(d) basis was adequate, although for the aldehyde derivative the addition of polarised functions on the hydrogen, to give a 6-31G(d,p) basis, was used. Both these basis sets are described in Section 3.8.

All calculations were run using Gaussian 09 [310], except for certain vertical excitation calculations. EOM-CCSD and ADC(2) calculations were run using QChem [253] and DFT-MRCI calculations were run as implemented in Turbomole [334]. It is important note that the definition of the plane in which the molecule lies will change the symmetry of the states. In all calculations the plane is defined such that for D_{2h} the electronic symmetry changes from B_{3u} to B_{1u}.

6.3 Anthracene, Tetracene and Pentacene

To test the utility of the methodology outlined above, the absorption and emission spectra of anthracene, tetracene and pentacene (Figure 6.1**(1,2,3)**) were simulated. This sequential progression of adding a ring provides information on the changes in the transition energy and electronic state symmetries. The vibrational modes excited in each molecule and the fine structure in the spectra were also examined to elucidate any features prevalent in aromatic systems. The experimental spectra for all molecules were recorded by Oliver Daubney at the University of Birmingham.

6.3.1 Anthracene

Anthracene is a linear polyacene formed from three fused benzene rings. It was first isolated from coal tar in 1832 and was important in the synthesis of anthraquionone, a precursor in the manufacture of many dyes. Anthracene's flat shape and large π-surface area makes it ideal for use in optoelectronics. Organic electro-luminescence was first observed in anthracene in the 1980s [335] and has found widespread use in supramolecular chemistry [336]. One major application is as a fluorescence chemosensor [337, 338] and fluorescent probe capable of binding to DNA [339–341]. Its ability to fluoresce blue light makes it highly attractive for use in organic light emitting diodes [342]. Its existence in the interstellar medium has also been reported [343].

Given the size of the molecules under investigation, it was important that the electronic structure method employed had the right balance of accuracy in predicting the vertical excited energies but with low computational cost, particularly since Hessian calculations can be very demanding. To assess the quality of using TDDFT with a B3LYP functional, excited state calculations using a range of different methods were performed to compare amongst and with experiment. These are shown in Table 6.1.

Table 6.1: First five excited states of anthracene calculated at different levels of theory. All calculations used a 6-31G(d) basis.

	TD-DFT	ADC(2)	CASPT2	EOM-CCSD	DFT-MRCI	Exp. [344]
S_1	3.28	3.89	3.14	3.95	3.54	3.31/3.43
S_2	3.91	3.98	3.36	4.27	3.57	3.84/3.45
S_3	4.59	5.40	4.30	5.76	4.52	4.12/4.44
S_4	4.99	5.60	-	5.79	4.55	-
S_5	5.31	5.62	-	5.93	5.05	4.66/4.83

The experimental value for S_1 is not fully certain with two possible values being assigned. The value predicted by TDDFT agrees with the lower energy, whilst DFT-MRCI agrees with the higher. Surprisingly, the more accurate levels of theory, EOM-CCSD and CASPT2, perform poorly. Predictions of the energetic difference between S_1 and S_2 vary, with some studies calculating very small differences and others showing greater separation. DFT-MRCI calculates the two excited states to be close in energy, whilst the TDDFT gives a large gap. Overall, the performance of TDDFT is good and justifies its use for calculating the S_1 state of anthracene. This also provides strong support in using it for other molecules.

TDDFT correctly establishes the S_1 state as being a HOMO $\rightarrow$ LUMO transition and therefore the L_a state. The symmetry of this state is determined to be B_{1u}, although this difference simply results from the different axis labelling. This disparity however should have little effect, given the correct orbital transition is obtained.

The ground state vibrational frequencies calculated for optimised anthracene are shown in Table 6.2 and are listed by their symmetry. The calculated frequencies show good agreement to experiment with any discrepancies usually highlighting uncertainties in the experimental assignment.

A full quantum dynamic model including all 66 normal modes would be challenging. The model presented here allows all modes to be included, although the number is dramatically reduced through symmetry arguments that require consideration of totally-symmetric modes only. From these modes, only six are important in reproducing the absorption spectrum of anthracene. These include ν_1, the lowest

Table 6.2: Theoretical frequencies (cm^{-1}) for ground state anthracene ordered by its D_{2h} symmetry and compared against experimental data [345]. Question marks refer to either possible typos or queries as discussed in reference text. Values in parentheses are uncertain assignments.

Mode	Symmetry	B3LYP	Exp.	Mode	Symmetry	B3LYP	Exp.
Q_1	A_g	399	397	Q_{34}	A_u	124	(137)
Q_2		642	625	Q_{35}		508	(552)
Q_3		766	754	Q_{36}		759	743
Q_4		1040	1007	Q_{37}		871	858
Q_5		1199	1164	Q_{38}		989	988
Q_6		1304	1264	Q_{39}	B_{1u}	235	234
Q_7		1445	1412	Q_{40}		661	653
Q_8		1535	1480	Q_{41}		917	906
Q_9		1610	1556	Q_{42}		1181	1147
Q_{10}		3174	3027	Q_{43}		1298	1272
Q_{11}		3182	3048	Q_{44}		1348	1317
Q_{12}		3208	3072	Q_{45}		1501	1460
Q_{13}	B_{1g}	238	244	Q_{46}		1688	1627
Q_{14}		488	479	Q_{47}		3172	3022
Q_{15}		776	760	Q_{48}		3178	3032
Q_{16}		957	956	Q_{49}		3195	3062
Q_{17}	B_{2g}	273	287	Q_{50}	B_{2u}	618	601
Q_{18}		591	580	Q_{51}		826	809
Q_{19}		783	773	Q_{52}		1036	998
Q_{20}		850	896?	Q_{53}		1175	-
Q_{21}		919	916	Q_{54}		1200	1169
Q_{22}		991	977	Q_{55}		1394	1346
Q_{23}	B_{3g}	394	397?	Q_{56}		1433	1397
Q_{24}		534	521	Q_{57}		1501	-
Q_{25}		927	903	Q_{58}		1597	1534
Q_{26}		1134	1102??	Q_{59}		3181	3048
Q_{27}		1223	1187	Q_{60}		3208	3084
Q_{28}		1308	1273	Q_{61}	B_{3u}	92	106
Q_{29}		1428	1433	Q_{62}		388	380
Q_{30}		1640	1574	Q_{63}		485	474
Q_{31}		1685	1632/1627	Q_{64}		746	737
Q_{32}		3177	3017/3005	Q_{65}		892	883
Q_{33}		3195	3054	Q_{66}		962	956

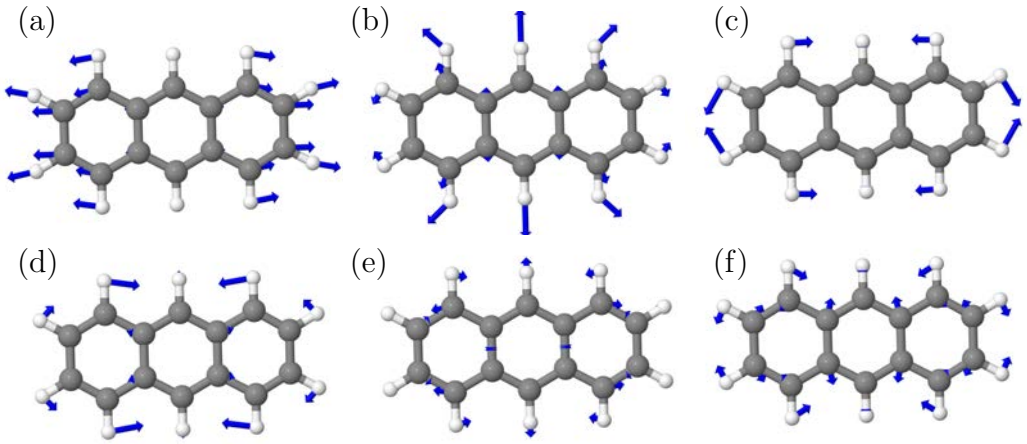

Fig. 6.2: The normal modes of anthracene important in describing its absorption spectrum: (a) ν_1 ring breathing mode, (b) ν_3 in-plane ring distortion, (c) ν_5 C-H bending mode, (d) ν_6 C-H bending mode + inner ring breathing mode (e) ν_7 ring distortion and (f) ν_9 C-C ring stretch.

frequency totally-symmetric ring breathing mode, ν_3, the in-plane ring distortion, ν_5, C-H bending mode, ν_6, the C-H bending of the outer rings and breathing mode of the inner ring, ν_7, another in-plane ring distortion and ν_9, a C-C ring stretch. These are illustrated in Figure 6.2.

Table 6.3 shows the on-diagonal linear coupling constants, κ. As previously discussed these are only non-zero for the totally-symmetric modes. The ratio κ/ω is informative of the displacement of the excited state minima from the ground state minimum. Inspection of these ratios show modes ν_1, ν_7 and ν_9 are important to the photodynamics in the S_1 state of anthracene and confirm that they should be included in the model. In order to ensure all features of the spectrum are captured, modes ν_6, ν_5 and ν_3 were also included in the model. The coupling constants and κ/ω ratio of these three modes exhibit enough significance to justify their inclusion. All of the remaining modes were excluded from the model used in the dynamic calculations.

Tables 6.4 and 6.5 show the on-diagonal second order and bilinear coupling constants. The former correspond to changes in frequency from the ground to excited

Table 6.3: Vibrational energies, ω, and on-diagonal linear coupling constants, κ, for the S_1 state of anthracene. All values are in eV.

Mode	ω	κ	κ/ω
$\nu 1$	0.049	0.043	0.863
$\nu 2$	0.080	0.016	0.207
$\nu 3$	0.095	−0.023	0.244
$\nu 4$	0.129	0.018	0.140
$\nu 5$	0.149	0.061	0.411
$\nu 6$	0.162	0.089	0.550
$\nu 7$	0.179	−0.168	0.935
$\nu 8$	0.190	−0.018	0.097
$\nu 9$	0.200	−0.180	0.904
$\nu 10$	0.393	0.002	0.006
$\nu 11$	0.395	−0.004	0.011
$\nu 12$	0.398	0.012	0.030

Table 6.4: Second order on-diagonal, $\gamma_{\alpha\alpha}$, coupling constants for the S_1 state of anthracene. All values are in eV.

Mode	$\gamma_{\alpha\alpha}$	Mode	$\gamma_{\alpha\alpha}$
ν_1	−0.007	ν_{24}	−0.004
ν_2	0.003	ν_{25}	−0.006
ν_3	−0.001	ν_{27}	−0.005
ν_4	−0.008	ν_{29}	−0.009
ν_6	−0.010	ν_{30}	−0.008
ν_7	−0.002	ν_{31}	−0.007
ν_9	−0.007	ν_{32}	−0.007
ν_{10}	−0.005	ν_{36}	0.007
ν_{13}	−0.007	ν_{45}	0.013
ν_{14}	−0.003	ν_{47}	−0.003
ν_{15}	−0.005	ν_{51}	−0.002
ν_{17}	−0.003	ν_{52}	−0.007
ν_{18}	−0.006	ν_{53}	0.002
ν_{19}	−0.003	ν_{54}	−0.002
ν_{20}	−0.006	ν_{55}	−0.012
ν_{21}	−0.007	ν_{56}	−0.002
ν_{23}	−0.008		

Table 6.5: Second order on-diagonal bilinear, $\gamma_{\alpha\beta}$, coupling constants for the S_1 state of anthracene. All values are in eV.

Mode	$\gamma_{\alpha\beta}$	Mode	$\gamma_{\alpha\beta}$
ν_{6-7}	−0.002	ν_{37-38}	0.002
ν_{6-9}	−0.002	ν_{39-41}	0.002
ν_{7-8}	0.002	ν_{50-51}	0.002
ν_{7-9}	0.003	ν_{50-53}	−0.002
ν_{8-9}	0.002	ν_{50-55}	0.003
ν_{13-14}	0.003	ν_{51-53}	0.002
ν_{13-16}	−0.002	ν_{51-55}	−0.002
ν_{14-15}	−0.005	ν_{52-55}	0.002
ν_{14-16}	−0.002	ν_{53-54}	−0.003
ν_{15-16}	−0.003	ν_{53-54}	−0.010
ν_{17-18}	−0.005	ν_{54-55}	0.004
ν_{17-19}	0.005	ν_{54-58}	0.002
ν_{17-21}	0.002	ν_{55-56}	0.002
ν_{18-20}	0.006	ν_{55-57}	0.002
ν_{19-20}	−0.002	ν_{56-58}	−0.004
ν_{20-21}	−0.004	ν_{61-62}	0.004
ν_{20-22}	−0.003	ν_{61-63}	−0.005
ν_{25-31}	−0.002	ν_{61-66}	0.003
ν_{27-31}	−0.005	ν_{62-64}	−0.005
ν_{30-31}	−0.003	ν_{63-66}	−0.003
ν_{34-35}	−0.005	ν_{64-65}	−0.002
ν_{35-36}	0.004	ν_{64-66}	0.002
ν_{35-37}	−0.003		
ν_{36-38}	−0.002		

state. Unsurprisingly, with the potentials all being expressed as Harmonic oscillators around the FC point and no points being calculated along each normal mode then any anharmonicity will be neglected, thus the values obtained are small. The bilinear coupling constants relate to IVR and are typically small.

Figure 6.3 shows the cuts through the potential energy surface along the six modes used in the model. These cuts again emphasise the potentials being expressed as displaced Harmonic oscillators and also serve to illustrate the small $\gamma_{\alpha\alpha}$ values. A large displacement from the equilibrium geometry is shown along ν_7, the in-plane ring distortion and ν_9, the C-C ring stretch in the S_1 excited state (Figures 6.3(e,f)).

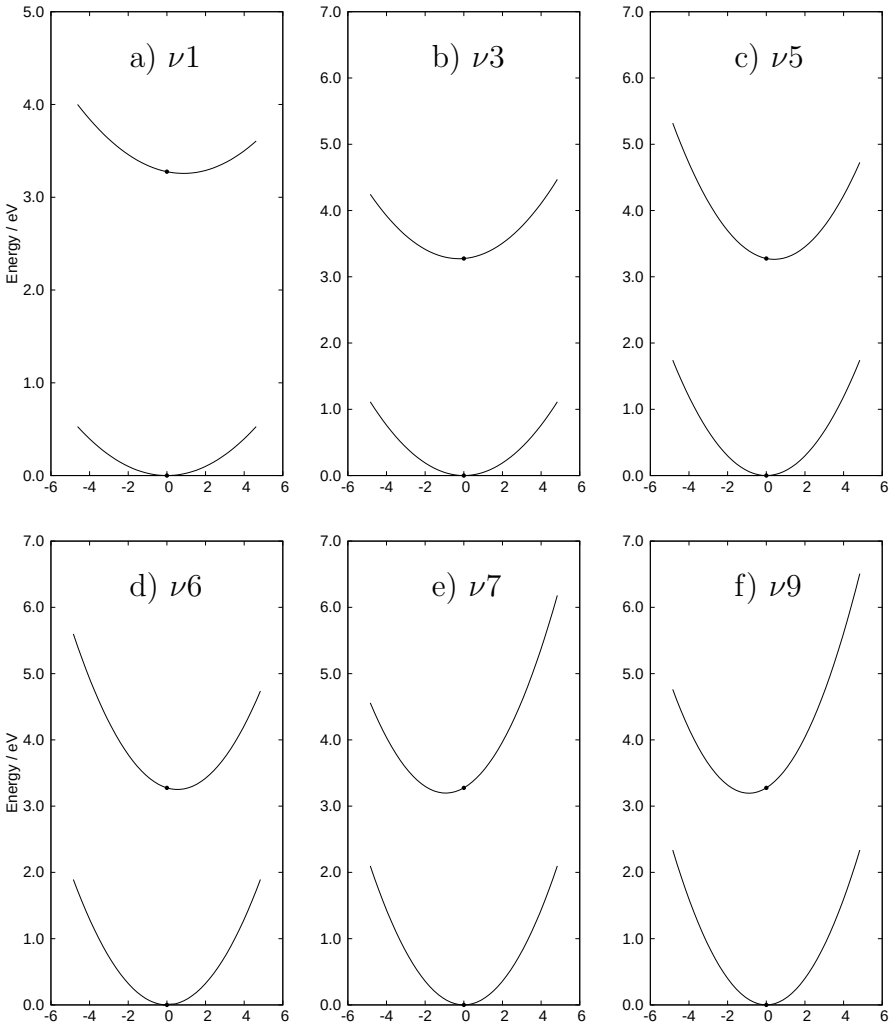

Fig. 6.3: Cuts through the adiabatic potential energy surfaces along select totally-symmetric normal modes for the ground state and first excited state of anthracene. The solitary point is the FC point obtained at the TDDFT/6-31G(d) level. The normal modes include are (a) ν_1 ring breathing mode, (b) ν_3 in-plane ring distortion, (c) ν_5 C-H bending mode, (d) ν_6 C-H bending mode + inner ring breathing mode (e) ν_7 ring distortion and (f) ν_9 C-C ring stretch.

The simulated absorption and emission spectra are shown together in Figure 6.4a. The absorption spectrum has been shifted to account for the S_0 zero point energy. The simulated spectra have a damping time of 50 fs. This allows sufficient broadening to reproduce experimental data but retains any vibrational fine structure. The emission spectrum is a mirror image of the absorption, however small differences in peak intensity, and hence shape of the spectrum, indicate the critical role the second-order on-diagonal $\gamma_{\alpha\alpha}$ terms play, despite their small values. The main progression in both spectra is attributed to the ν_7 and ν_9 modes. With frequencies close in energy of 0.200 and 0.179 eV, their progressions are close to each other and form the broad peaks observed in the experimental spectra. It is only with the higher resolution simulated spectra that this becomes apparent. The ν_7 mode is the in-plane ring distortion and ν_9 the C-C ring stretch. The main shoulder peak present on the 0-0 transition can be attributed to the ring breathing, ν_1 mode, whilst the smaller shoulder peak could either be part of the 1_0^n progression or result from the in-plane ring distortion, ν_3 mode.

The comparison of the simulated absorption spectrum with experiment is shown in Figure 6.4(b). The intensities of both spectra have been normalised to allow for accurate comparison. It is immediately evident that the simulated absorption spectrum occurs at lower energy than experiment. The exact difference was determined from the 0-0 transition, which from experiment is 3.31 eV and from simulation is 3.06 eV. This difference of 0.25 eV reflects the accuracy of the TDDFT calculation and this shift between simulation and experiment was consistent throughout this chapter. The main peak progression is in good agreement and, despite the broadening, small shoulder peaks can be observed in the experimental absorption spectrum that are clearly reproduced in the simulated spectrum. The relative intensities of the peaks are not well reproduced, with $\lambda_{\max}$ being the second peak in the experimental spectrum and the 0-0 transition in the simulated one. This difference shows

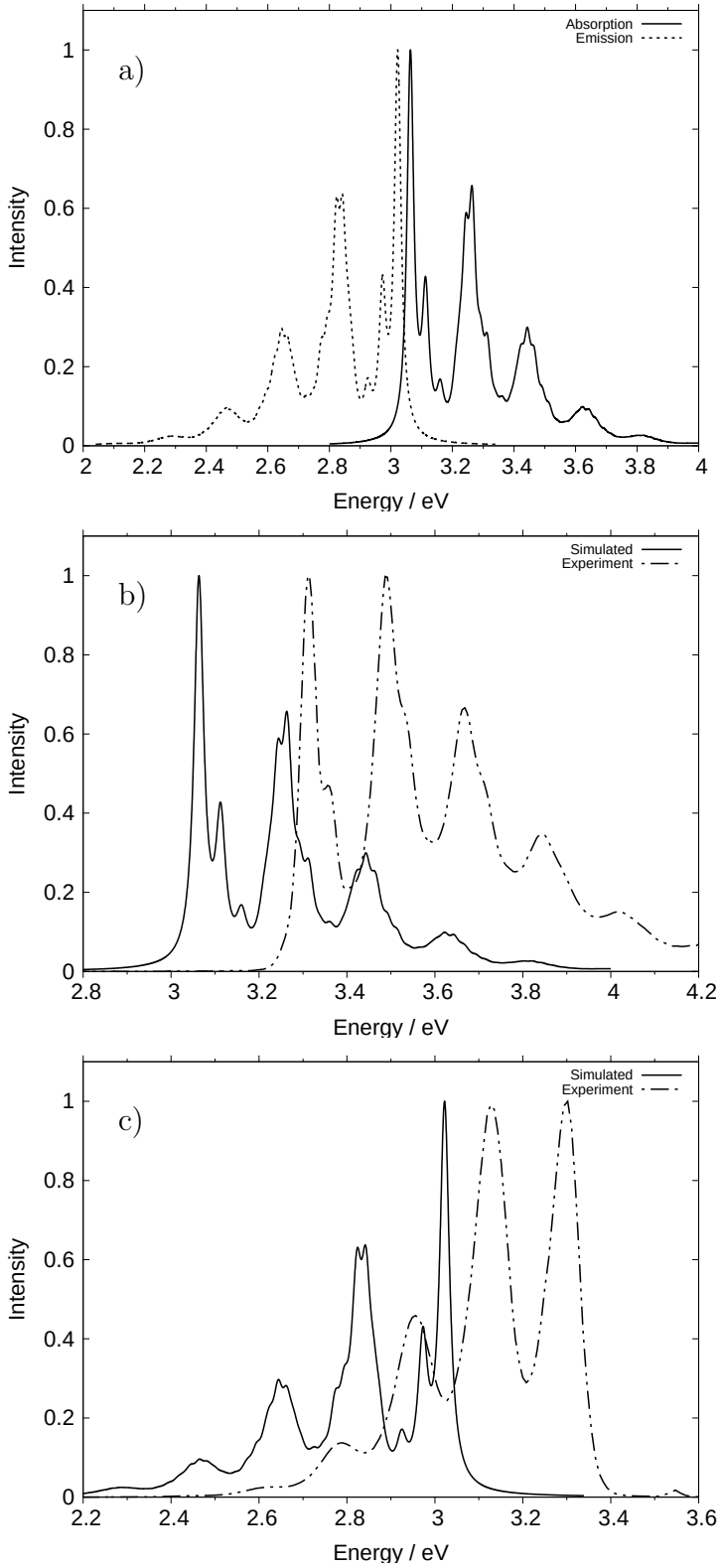

Fig. 6.4: The S_1 absorption and emission spectra of anthracene calculated using a six mode model with comparison to experiment. (a) The simulated absorption and emission spectra. (b) The S_1 absorption spectrum showing comparison of experiment with theory and (c) the S_1 emission spectrum showing comparison of experiment with theory. All simulated spectra have a damping time of 50 fs.

the gradient (κ value) for the mode is underestimated by TDDFT. Despite discrepancies in the energy and peak intensities, the simulated spectrum shows very good agreement with experiment, capturing the main features.

The emission spectra (Figure 6.4(c)) shows the same characteristics as the absorption when comparing experiment with simulation: the discrepancy between the energies and the relative peak intensities. The experimental emission shows a shorter progression with no additional fine structure aside from the main progression. By contrast, the simulated emission spectrum retains the fine structure seen in the simulated absorption, with the progressions being the same as elucidated for the absorption.

To further confirm the validity of the model, the Stokes shift for anthracene was determined for both sets of spectra. The experimental solvent used was n-hexane and this was applied implicitly in the calculation to determine the shift in minimum of the S_1 state. For the simulated spectra the shift was calculated to be 0.04 eV and from experiment 0.01 eV. These values show good agreement and further supports the model. This also justifies the methodology of computing the S_1 minima in gas and condensed phase to calculate energetic shifts of the electronic states and the use of implicit solvation models to represent the solvent.

Comparison to explicit fitting

It is worthwhile comparing the potentials and spectra calculated using this simplified model with those obtained from the explicit fitting of parameters to a series of *ab initio* points. The potentials calculated using the explicit fitting will include any anharmonicity. The main significance, however, will be if there is strong agreement with potentials around the equilibrium point and the main features in both spectra. A series of *ab initio* points were calculated along each the normal modes used in the original model. Parameters were then obtained by fitting a vibronic coupling Hamiltonian to the adiabatic surfaces.

Table 6.6: Vibrational energies, ω, and on-diagonal linear coupling constants, κ, for the S_1 state of anthracene obtained by fitting to a series of *ab initio* points. Comparison with the on-diagonal linear coupling constants obtained from the simplified Harmonic model is shown. All values are in eV.

		Explicit Fits		Harmonic Fits	
Mode	ω	κ	κ/ω	κ	κ/ω
$\nu 1$	0.049	−0.046	0.939	0.043	0.863
$\nu 3$	0.095	0.011	0.116	−0.023	0.244
$\nu 5$	0.149	−0.062	0.416	0.061	0.411
$\nu 6$	0.162	−0.085	0.525	0.089	0.550
$\nu 7$	0.179	0.178	0.994	−0.168	0.935
$\nu 9$	0.200	0.178	0.890	−0.180	0.904

Table 6.7: Second order on-diagonal, $\gamma_{\alpha\alpha}$, coupling constants for the S_1 state of anthracene obtained by fitting to a series of *ab initio* points. Comparison with the second order on-diagonal terms obtained from the simplified Harmonic model is shown All values are in eV.

	Explicit Fits	Harmonic Fits
Mode	$\gamma_{\alpha\alpha}$	
ν_1	0.000	−0.007
ν_3	−0.005	−0.001
ν_5	0.007	0.000
ν_6	0.002	−0.010
ν_7	−0.005	−0.002
ν_9	0.005	−0.007

Table 6.6 shows the on-diagonal linear coupling constants, κ_α, obtained from the fitting. Inspection of Table 6.6 shows the values obtained from the simplified FC model concur very well with those from the fitted points.

Similarly, comparing the second order on-diagonal terms between the simplified model and those from the explicit fitting (Table 6.7) show little discrepancy; no on-diagonal bilinear terms were obtained.

Cuts through the potential energy surface along the normal modes are shown in Figure 6.5. The cuts shown are along the same six normal modes that were used in the FC Harmonic oscillator model. As all these modes are totally-symmetric then the on-diagonal linear coupling values are non-zero, which is seen as displacement

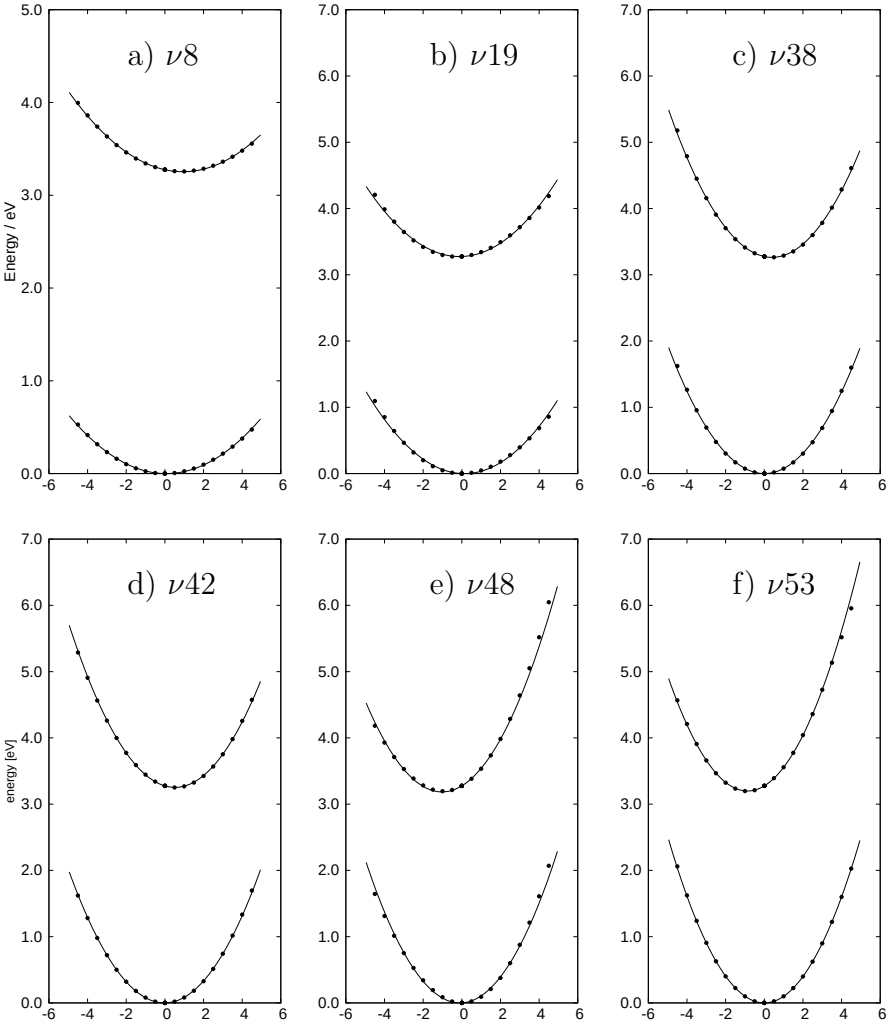

Fig. 6.5: Cuts through the adiabatic potential energy surfaces along select totally-symmetric normal modes for the ground state and first excited state of anthracene. The points are obtained from *ab initio* calculations at the TDDFT/6-31G(d) level. The normal modes include are (a) ν_1 ring breathing mode, (b) ν_3 in-plane ring distortion, (c) ν_5 C-H bending mode, (d) ν_6 C-H bending mode + inner ring breathing mode (e) ν_7 ring distortion and (f) C-C ring stretch.

of the S_1 minima away from Q_0. Comparison of Figure 6.5 with Figure 6.3 show there to be very good agreement between the potential energy surfaces. This strong agreement benefits from the harmonic nature of the potentials around the minima and serves to illustrate the strength of the simplified model when the potentials are harmonic and there is little vibronic coupling present.

With the two cuts through the PES showing close similarity, it is therefore unsurprising that the simulated absorption and emission from the simplified model shows excellent agreement with the spectra simulated from the explicitly calculated adiabatic surfaces. Figure 6.6 shows the calculated spectra using the explicitly fitted surfaces. Shown also is an overlay of the absorption and emission spectra simulated using both models. Figure 6.6(b) shows the absorption spectrum comparing the explicitly fitted model with the harmonic potential. The two spectra are nearly identical, matching in both peak intensities and fine structure. The only difference is a small shift in energy and the relative intensities between the peaks in the first progressions at ≈ 3.25 eV.

The agreement between the simulated emission spectra from both models is better than the absorption. The overlap of the spectra is identical with only minor differences in peak intensities.

The excellent agreement between the simulated absorption and emission spectra highlights the success of the simplified model using only information at the FC and expressing the potentials as Harmonic oscillators. The ability of this model to reproduce spectra without generating potentials by fitting a series of *ab initio* points, allows larger molecules with many degrees of freedom to be investigated. Following the success of anthracene, the model was then used on the larger aromatic molecule tetracene, moving from three fused aromatic rings to four.

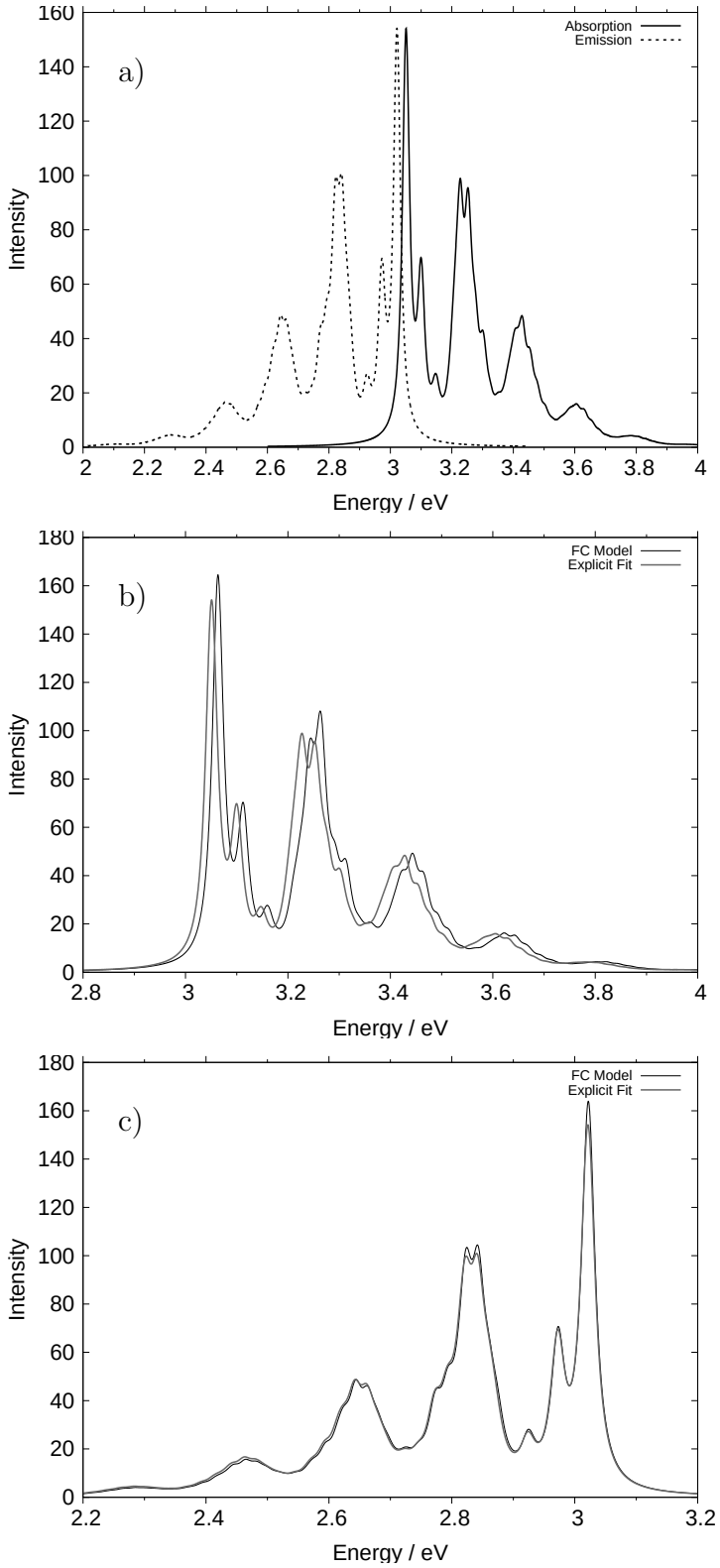

Fig. 6.6: The S_1 absorption and emission spectra of anthracene calculated using a six mode model with potential energy surfaces generated from fitting to a series of *ab initio* points and compared with the simplified model. (a) The simulated absorption and emission spectra. (b) The S_1 absorption spectrum showing comparison of explicitly fitted surfaces with the FC model (c) the S_1 emission spectrum showing comparison of explicitly fitted surfaces with the FC model. All simulated spectra have a damping time of 50 fs.

6.3.2 Tetracene

Tetracene is the next molecule in the linear acenes after anthracene, consisting of four fused benzene rings. Like anthracene the molecule remains planar and retains the D_{2h} molecular symmetry.

The use of tetracene in organic photovoltaics has been explored in great detail. The small HOMO-LUMO gap makes it an ideal candidate for exciton formation and its planar structure allows for the formation of thin-films [346]. This ability to form excitons also allows tetracene is undergo singlet fission, whereby a prepared singlet state can dissociate into two triplet excitons [347]. This makes tetracene rich with different photodynamic processes. Tailoring these excited state pathways offers promising routes to organic photovoltaics and similar applications [347, 348].

The $S_1 \leftarrow S_0$ transition is allowed and corresponds to a HOMO $\rightarrow$ LUMO transition. As shown previously, the lowest excited state for linear acenes for $n \geq 3$ is the bright $^1B_{2u}$ state and the forbidden $^1B_{3u}$ state is the next electronic state, S_2. From TDDFT calculations, the S_1 vertical excitation energy was determined to be 2.49 eV, with the transition correctly corresponding to a HOMO $\rightarrow$ LUMO transition. Again, like anthracene the S_1 electronic symmetry is predicted to be B_{1u} due to different axis labels. The lower energy of the S_1 state compared with anthracene is to be expected with the increase in conjugation from the addition of another benzene ring. This value is however lower than the experimental value, measured in a benzene solution, of 2.62 eV [349] and lower than other theoretical calculations [344].

Tetracene has 84 vibrational modes comprising 15 totally-symmetric modes. Again, the utility of the simplified model is exemplified here, dramatically reducing the number of modes to be considered. The vibronic coupling constants and cuts through the PES along the important normal modes are found in section F.1 of Appendix F.

The simulated absorption and emission spectra are shown in Figure 6.7(a) and compared with experimental spectra, measured in toluene solution (Figures 6.7(b and c)).

The absorption spectra shown in Figure 6.7(b) differ in energy. The 0-0 transition for the simulated spectrum is 2.39 eV and from experiment 2.61 eV. The shift between the spectra of 0.22 eV is similar to that observed for anthracene and highlights the systematic difference in S_1 energy from TDDFT calculations. Regardless of the shift to lower energy, the peak spacings and progressions of the simulated spectrum agree well with experiment.

Analysis of the fine structure indicates each peak to be composed of several progressions with similar energy. The overlap from each of these progressions result in the broad peaks observed experimentally. The small shoulder peak seen on the left side of the first progressive band is attributed to the C-H rocking and ring distortion mode, ν_{52}. Assignment of the main progression is difficult with the possibility of two vibrational modes being responsible. These modes are the C-C ring stretch, ν_{59} and the C-H rocking/C-C ring stretch mode, ν_{61}. The similarity in energy of these vibrational modes makes it difficult to distinguish whether the progression is formed of a single mode, or the overlap of both. The slight asymmetry of the first peak in the progression and the broader appearance of the second peak suggests both modes are involved. From the on-diagonal linear coupling constants, both of these modes have similar values and ratios further suggesting both modes are involved in the progression.

Despite the similarity in peak spacings, it is evident that the length of the progression is not correctly reproduced. The experimental absorption spectrum contains a long progression with peak intensities that gradually decrease. This indicates a large change in molecular geometry, especially along one normal mode. The inability to reproduce this is likely to be found in the on-diagonal coupling constants.

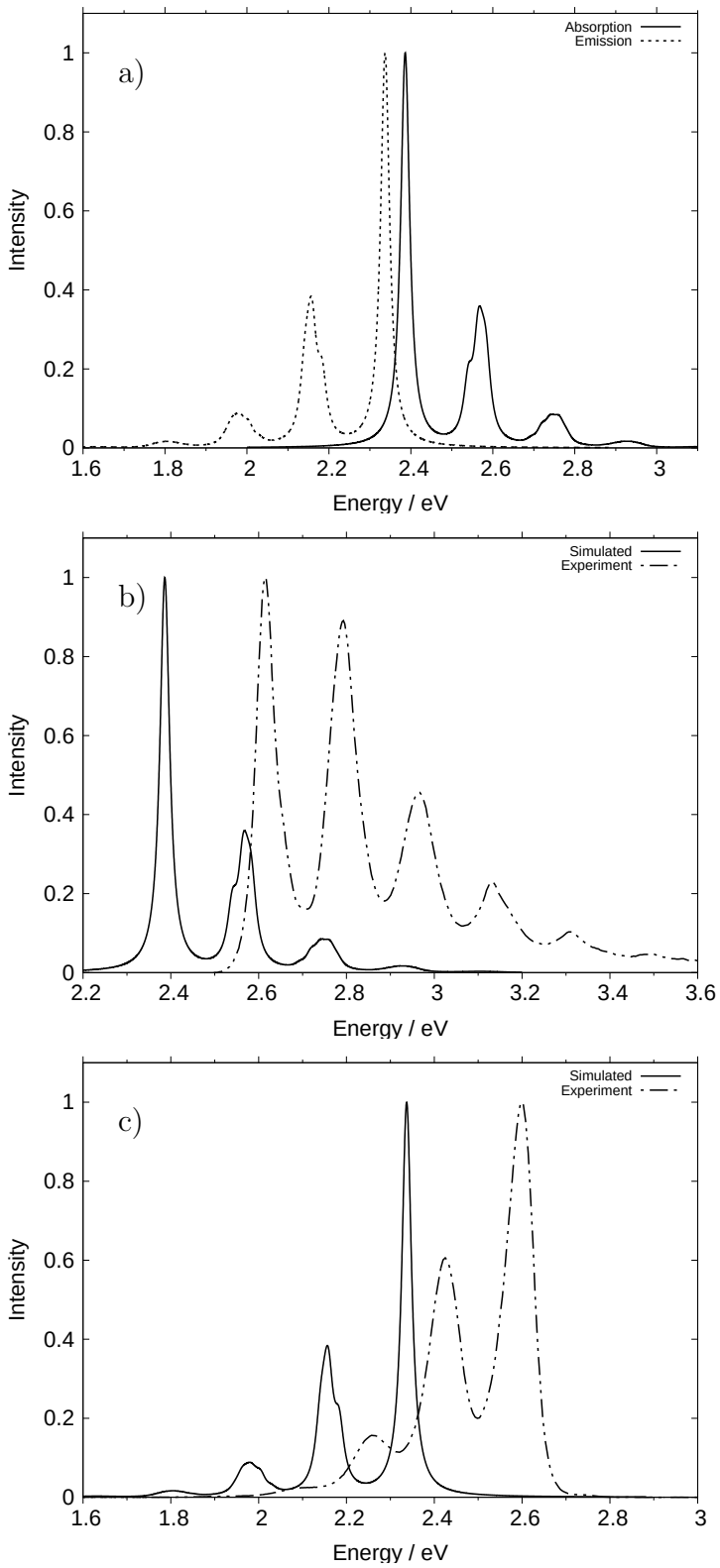

Fig. 6.7: The S_1 absorption and emission spectra of tetracene calculated using a six mode model with comparison to experiment. (a) The simulated absorption and emission spectra. (b) The S_1 absorption spectrum showing comparison of experiment with theory and (c) the S_1 emission spectrum showing comparison of experiment with theory. All simulated spectra have a damping time of 50 fs.

Large values of κ, particularly a large ratio of κ/ω, will increase the length of the progression and also increase the peak intensities.

The emission spectra are shown in Figure 6.7(c). The agreement here is much better with the shorter progression seen experimentally reproduced well by the simulation. The fine structure in the simulated spectrum is still retained, whilst the measured spectrum is still broad. The assignment of the vibrational structure is identical to that of the absorption.

The Stokes shift from the experimental data was determined to be 0.02 eV in toluene and 0.05 eV in the simulations, again showing good agreement. The small value of the shift indicates that little energy from excitement is lost due to vibrational relaxation or solvent reorganisation.

Comparison with explicit fits

To investigate whether the failure to reproduce the length of the progression in the absorption spectrum was a failure of the model itself, explicit fits were undertaken along several of the totally-symmetric normal modes. By obtaining parameters through fitting to a series of *ab initio* points, differences in the κ_α terms were determined. Re-running the simulations with different κ values to reproduce the absorption spectrum with the correct progression length, will detail which modes in the simplified model were not optimal. The parameters obtained from fitting the surfaces to the vibronic coupling Hamiltonian are detailed in section F.1.1 of Appendix F.

The simulated absorption and emission spectra were obtained, using the amended κ values calculated from the explicit fits. These new spectra are shown in Figure 6.8 alongside the original simulated spectra and experimental data.

The absorption spectrum from the explicitly fitted three mode model has an energy shift away from the experiment data similar to the simplified model. The effect of the larger κ value is evident from the greater peak intensities and the

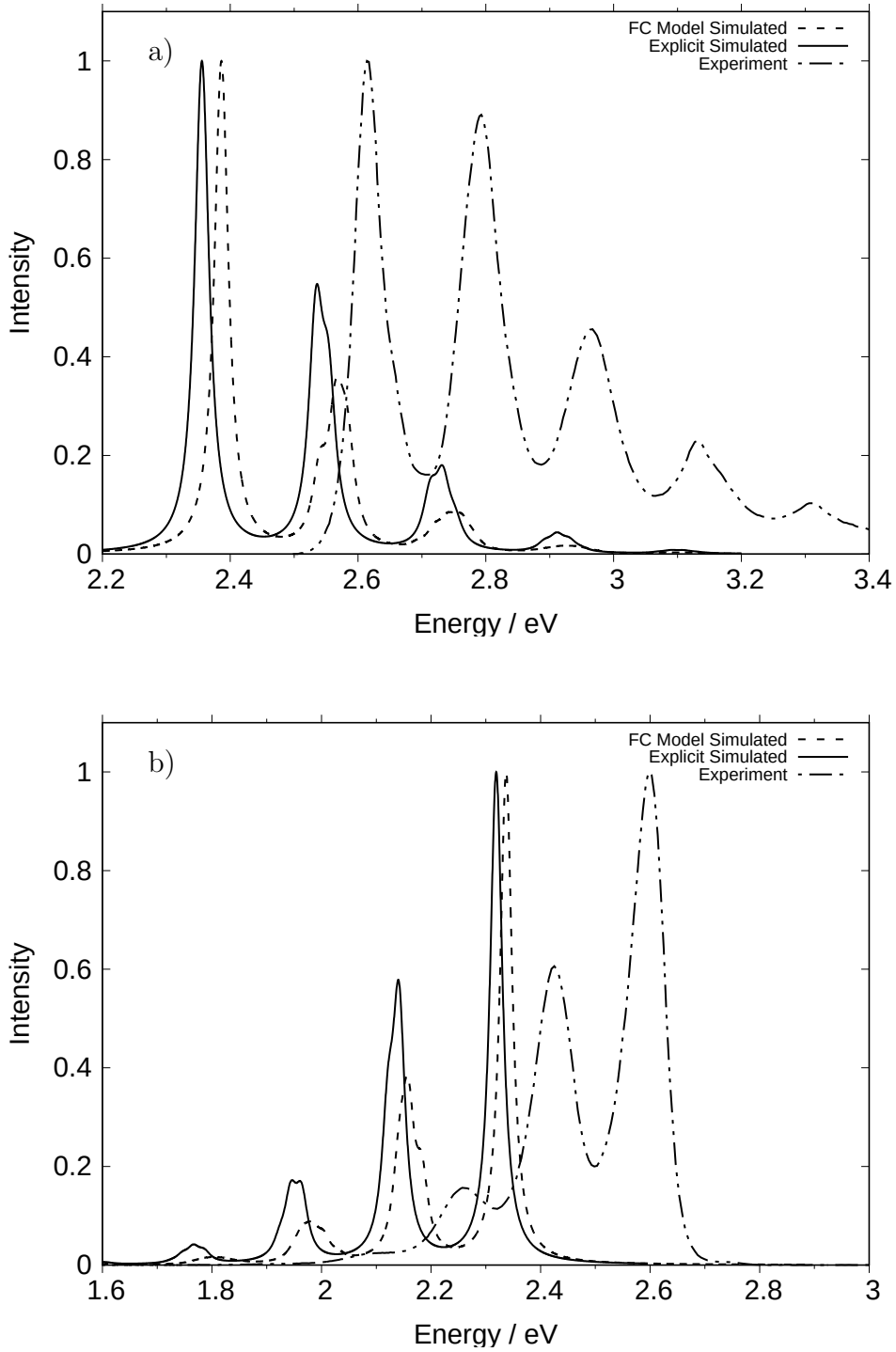

Fig. 6.8: The S_1 absorption and emission spectra of tetracene calculated with potential energy surfaces of four normal modes generated from fitting to a series of *ab initio* points and compared with the simplified model and experiment. (a) The S_1 absorption spectrum showing comparison of explicitly fitted surfaces with the FC model and experiment (b) the S_1 emission spectrum showing comparison of explicitly fitted surfaces with the FC model and experiment. All simulated spectra have a damping time of 50 fs.

occurrence of a large progression. This progression is still not as intense or long as experiment, but is definitely an improvement. It is expected that inclusion of the other normal modes used in the simplified model, but excluded here, would further improve the absorption spectrum. Moreover, making use of surfaces obtained from the explicit fittings would likely yield larger κ values for these remaining modes *e.g.* ν_{59}.

Analysis of the absorption spectrum from the explicitly fitted model, shows the fine structure to comprise modes ν_{61} and ν_{67}. The simplified model showed the fine structure to have contributions from ν_{52} and ν_{59}, so inclusion of these modes could provide intensities to match experiment.

Likewise, the emission spectrum from the explicitly fitted simulation has higher intensities than the previous model. This increase in relative peak intensity results in good agreement with experiment.

The simplified model using only information of the FC point has been extended to successfully reproduce the absorption and emission spectra for tetracene, the next linear polyacene. Differences, however, in the length of intensities of the progression between the simulated and experimental spectra prompted the PESs of the important totally-symmetric modes to be fitted through a series of explicit points. This led to larger on-diagonal linear coupling constants not obtained from the simplified model and which resulted in simulated spectra matching better the progression and peak intensity from experiment. This minor discrepancy in the model does highlight its simplicity and inability to provide highly accurate potential energy surfaces. Nonetheless, the agreement between the spectra still shows the model to be reasonable, especially for larger molecules where calculating a series of points along many modes can be computationally expensive.

6.3.3 Pentacene

The next molecule in the series of linear acenes is pentacene, comprising five fused benzene rings. This molecule is highly conjugated but, as it has a low HOMO-LUMO gap, it has been shown to readily generate excitons [350]. Its sensitivity to oxidation makes it easily functionalisable. This has made it promising in the development and application of organic electronics, particularly as a semiconductor in photovoltaic devices or organic light emitting diodes (OLEDs) [351, 352]. This is further strengthened by its planar structure allowing the growth of uniform thin-films [353]. Pentacene also came to the fore in 2009, when researchers at IBM used atomic-force microscopy to image it as a single molecule [354]. Further work in 2011 allowed the shapes of the HOMO and LUMO to be determined [355].

From TDDFT, the vertical energy of the S_1 state was calculated to be 1.94 eV and result from a HOMO $\rightarrow$ LUMO transition. This is in good agreement with previous literature [356]. The symmetry of the S_1 state is yet again determined to be B_{1u}. The transition energy is lower than for tetracene, continuing the trend of decreasing energy for the first excited state when moving along the linear polyacenes. Pentacene has 102 normal modes and making use of its D_{2h} molecular symmetry returns 17 totally-symmetric, a_g modes.

As before, a simplified vibronic coupling Hamiltonian, using information only from the Hessian at the equilibrium geometry and the FC point on the S_1 state, yielded the adiabatic surfaces, expressed as Harmonic oscillators. The obtained parameters and cuts through the PES are shown in section F.2 of Appendix F.

The simulated absorption and emission spectra are shown in Figure 6.9 and compared with experimental data run in toluene. The simulations were run for 300 fs and the energy shifted to account for the zero point energy.

The experimental absorption spectrum is similar to that obtained for anthracene and tetracene. A progression of broad peaks is observed, although it is evident this

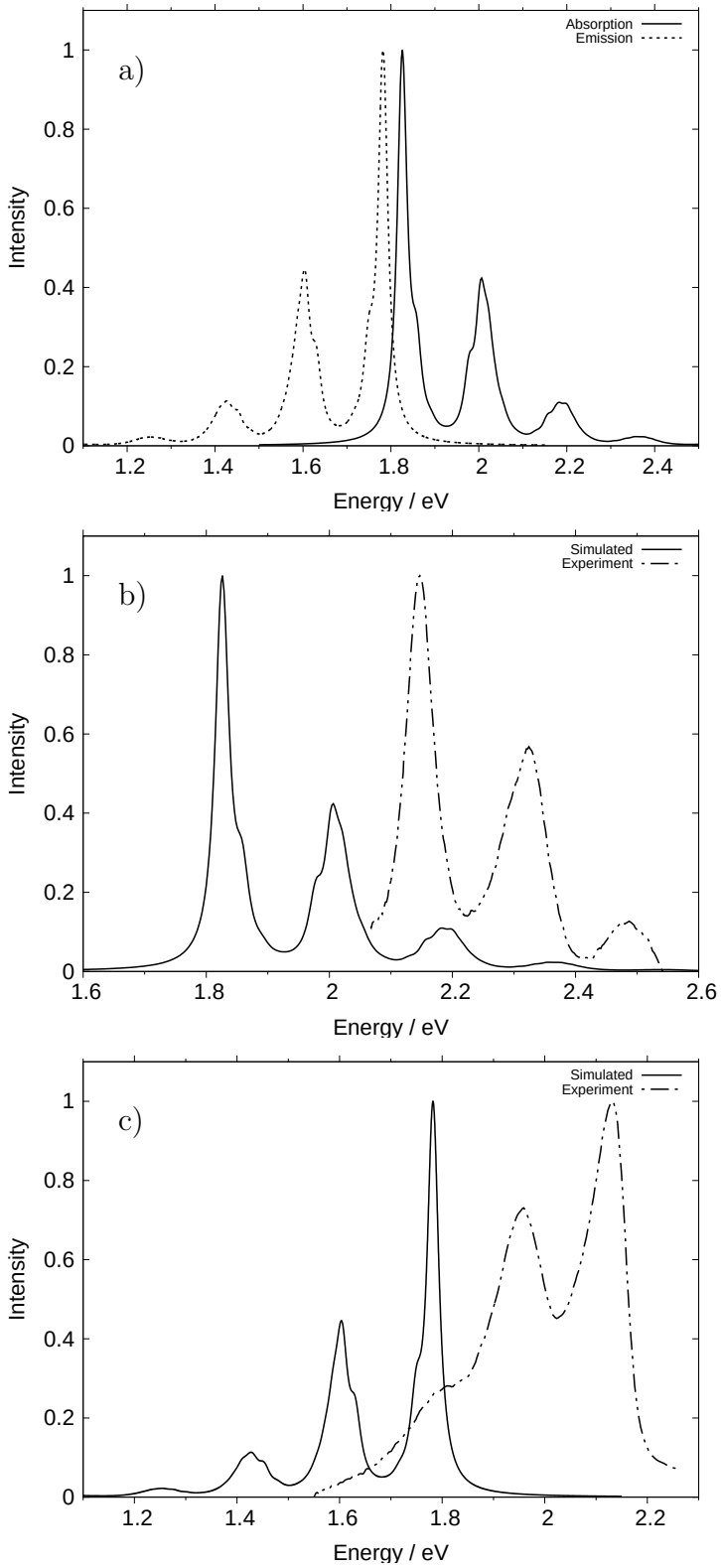

Fig. 6.9: The S_1 absorption and emission spectra of pentacene calculated using a five mode model with comparison to experiment. (a) The simulated absorption and emission spectra. (b) The S_1 absorption spectrum showing comparison of experiment with theory and (c) the S_1 emission spectrum showing comparison of experiment with theory. All simulated spectra have a damping time of 50 fs.

progression is much shorter than for tetracene. The first peak in the progression at $\approx$ 2.3 eV, shows the presence of some vibrational structure with a small shoulder peak on the left side. The simulated absorption spectrum again occurs at lower energy than experiment. The 0-0 transition is located at 1.83 eV for the simulated spectrum and 2.15 eV from experiment. This difference of 0.32 eV is similar to the differences in the anthracene and tetracene spectra. The progression and peak intensities also show good agreement with experiment. The fine structure in the spectrum is resolved better in the simulated spectrum and assignment to the underlying vibrational modes was made.

A small series of shoulder peaks can be observed on the 0-0 transition. These peaks are a progression formed from the lowest frequency, ring breathing mode, ν_9. The main progression observed is a combination of several progressions. The shoulder peak on the left side, evident in both simulated and experimental spectra, corresponds to the C-H bending ν_{62} mode. The asymmetry in this band suggests there are at least two vibrational modes, of similar energy, which overlap to form a broader peak. Based on the modes included in the model, two modes are likely responsible, the ν_{72} C-C ring stretch and ν_{81} in plane ring distortion mode. The second band in the overall progression clearly shows that three peaks are present.

Figure 6.9(c) shows the simulated and experimental emission spectra. Similar to the absorption, the simulated spectrum is at lower energy than experiment. The progressions are similar to that seen in the absorption spectrum and are well reproduced by simulation. The same modes are responsible for the fine structure.

The Stokes shift for pentacene was determined experimentally to be 0.02 eV in toluene. This follows the similar small values seen for anthracene and tetracene, suggesting little loss in energy to the solvent or during relaxation. The calculated Stokes shift from the simulated spectrum of 0.05 eV agrees well with the experimental value.

Summary of linear polyacenes $n = 3$ to 5

The simplified model introduced here, using only the Hessian at the equilibrium geometry and the FC point, and expressing the PES as harmonic potentials, provides reasonable emission and absorption spectra. Differences in energy, however, are apparent, but depend on the level of theory (and to some extent the basis set) used, although such energy differences are usually small, around 0.30 eV. The vibrational progressions and structure observed experimentally are also captured by this model. The utility of this model is best when there is little vibronic coupling and non-adiabaticity. The first excited state of linear polyacenes where $n \geq 3$ are expected to have B_{2u} symmetry and thus are short axis polarised L_a states . This symmetry makes transitions to these states allowed based on electronic dipole selection rules. These bright states are HOMO $\rightarrow$ LUMO, $\pi \rightarrow \pi^*$, transitions. TDDFT calculations determine the correct transitions although the axis labelling means the symmetry of this state is B_{1u}.

Increasing the size of the linear polyacene increases the conjugation and decreases the energy of the S_1 state. This trend can be seen experimentally and is matched by theoretical calculations. A pattern in the vibrational modes most significant to the photodynamics in the S_1 state is also noted. For all three molecules it was found that the C-H bending mode, C-C ring stretching (of those carbons not bound to hydrogens) mode and a ring breathing mode of the inner-most ring were all important in describing the S_1 dynamics.

Moving forward, the ability to provide rapid and reliable absorption and emission spectra should also apply to derivatives and capture any deviations in energy or structure that may occur. To this end, a range of functionalised derivatives of anthracene were selected and the absorption and emission spectra simulated. Again, comparison with experiment and against anthracene itself highlights changes resulting from the functionalisation.

6.4 Benzene and Naphthalene

The quick and simple model presented here reasonably reproduced the electronic spectra of anthracene, tetracene and pentacene. Its application to the smaller linear acenes, benzene and naphthalene, should therefore also be successful.

6.4.1 Benzene

Benzene (Figure 6.1(**4**)), the smallest and simplest acene, has been studied and applied throughout chemistry. Its importance as a precursor renders it ever-present in synthetic chemistry, whilst its rich photochemistry has provided numerous experimental and theoretical studies. In the ground state electronic structure of benzene, the highest occupied molecular orbital comprises four electrons in doubly degenerate $1e_{1g}$ orbitals. Unlike the other polyacenes, benzene contains greater symmetry, possessing D_{6h} molecular symmetry. Compared with anthracene, this higher symmetry changes the symmetry labels applied to both the vibrational modes and the electronic states and gives rise to orbital and vibrational degeneracies. Now, the totally-symmetric modes are of a_{1g} symmetry, as is the electronic ground state, S_0.

The initial $\pi \rightarrow \pi^*$ transition promotes an electron from the e_{1g} HOMO into the e_{2u} LUMOs, giving an electron configuration of $(1e_{1g})^3(e_{2u})^1$. This produces three excited singlet states: $\tilde{A}^1B_{2u}$, $\tilde{B}^1B_{1u}$ and $\tilde{C}^1E_{1u}$. The transition to S_1,$\tilde{A}^1B_{2u} \leftarrow \tilde{X}^1A_{1g}$ is electronically forbidden, however it can be observed experimentally [16,357] due to Herzberg-Teller excitation (see Section 2.5.4). The spectrum shows a clear progression resulting from the ring breathing a_{1g} mode with a series of shoulder peaks from the degenerate e_{2g} modes. The fluorescence spectrum of benzene can also be observed at low excess energy, competing alongside intersystem crossing to the triplet states [14, 15].

Despite the complex photochemistry of benzene, the simplified model introduced here should be able to reproduce the experimental absorption and emission spectra.

Even though the transition to the S_1 state is electronically forbidden, theoretically the transition can be simulated to produce a spectrum similar to experiment. No attempt, however, was made to incorporate vibronic coupling into the model, simulating only the fine structure occurring from the totally-symmetric modes and ignoring peaks arising from the e_{2g} modes. It should be noted that extensive work on calculating benzene photochemistry using surfaces generated from fitting to a series of points, including also vibronic coupling and non-adiabaticity, has already been achieved [23, 303, 304, 358].

Again, the coupling constants and cuts through the PES are described in section F.3 of Appendix F. The simulated absorption and emission spectra are shown in Figure 6.10. As experimental data for benzene is prevalent throughout the literature, comparisons were made with data found there.

Compared with experimental data, as measured by Pantos *et al.* [357] and Callomon *et al.* [16], the simulated absorption spectrum shows good agreement in shape and peak intensity. The much higher energy at which the simulation spectrum occurs reflects the higher S_1 vertical energy as calculated with TDDFT. It is important to stress that experimentally the 0-0 origin transition is not observed due to the forbidden nature of the transition. The apparent origin in the experimental absorption spectrum corresponds to the 6_0^1 transition. The simulated spectrum includes the electronic origin transition, which is situated at 5.42 eV. Likewise the progression observed experimentally is actually formed from $6_0^1 1_0^n$, with the coupled e_{2g} mode providing the intensity to the ring breathing progression. The simulated spectrum however only included the ring breathing mode to provide good agreement with experiment. The additional structure seen experimentally results from two different hotbands, a feature not calculated in the simulation.

The simulated fluorescence spectrum of benzene shows good agreement with experiment. The experimental spectrum seen in literature shows a much larger

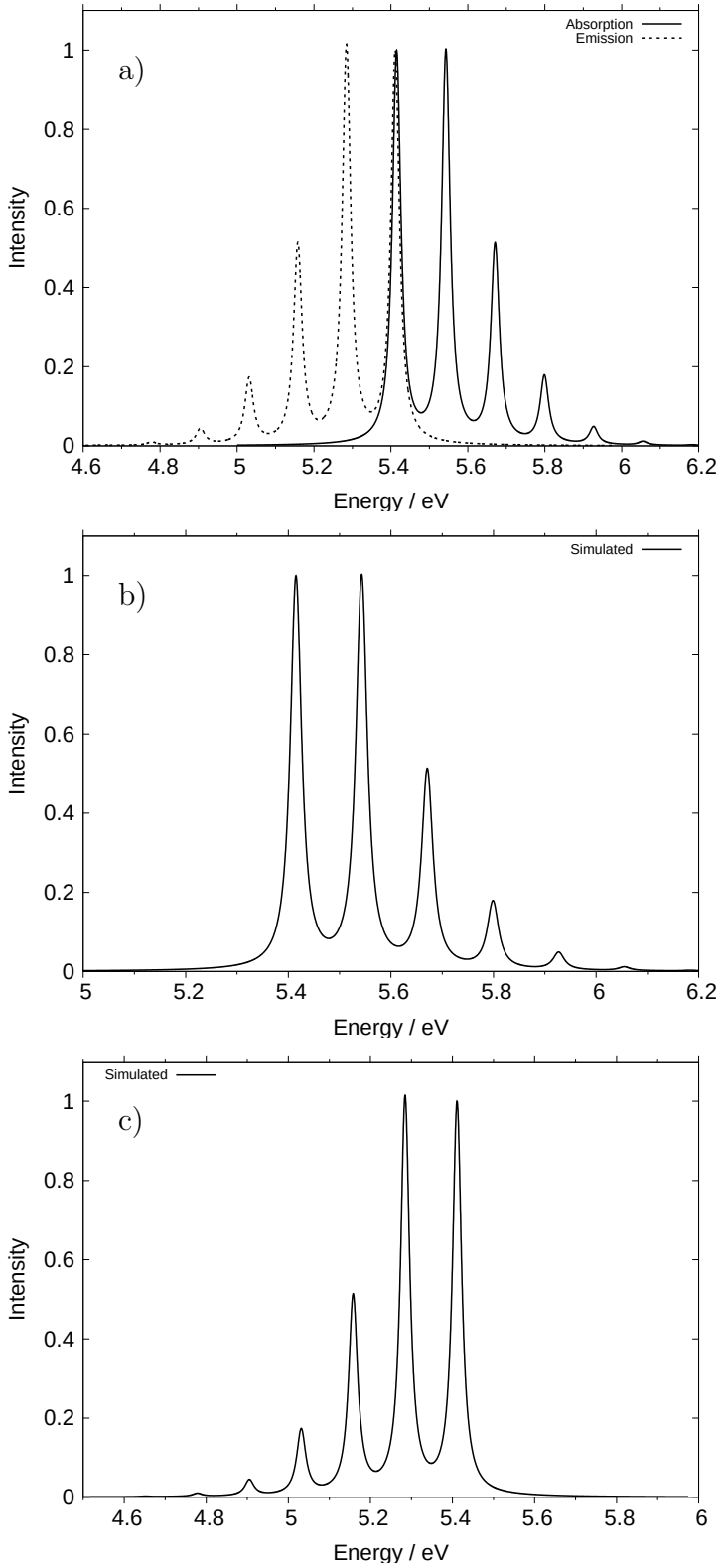

Fig. 6.10: The S_1 absorption and emission spectra of benzene calculated using a single mode model. (a) The simulated absorption and emission spectra. (b) The S_1 simulated absorption spectrum and (c) the S_1 simulated emission spectrum. All simulated spectra have a damping time of 50 fs.

Stokes shift than predicted from the simulation [359]. The predicted value of 0.004 eV in n-hexane is somewhat distorted by the presence of the 0-0 transition that is absent from experiment. In addition, the spectra from the literature were recorded using water as the solvent, whereas the predicted shift was with n-hexane.

Overall, despite the S_1 transition in benzene being electronically forbidden, the simplified model has been successful in reproducing the absorption and emission spectra. To fully replicate the experiment, Herzberg-Teller excitation would need to be included, but nevertheless the main progression from the ring breathing mode is captured within the model. The presence of the experimentally absent 0-0 transition is unavoidable within the framework of the model.

To fully complete the linear progression of acenes, the absorption and emission spectra for naphthalene were simulated using the model.

6.4.2 Naphthalene

Naphthalene (Figure 6.1(**5**)) consists of two fused benzene rings and is the next molecule in the linear polyacenes after benzene. As previously discussed, naphthalene is the only linear polyacene where the L_b state is lower than the L_a. This therefore makes the S_1 a dark L_b state of B_{3u} symmetry, corresponding to HOMO $-1 \rightarrow$ LUMO and HOMO $\rightarrow$ LUMO $+1$ transitions. The S_2 is then a bright L_a state with B_{2u} symmetry resulting from a HOMO $\rightarrow$ LUMO transition.

It is well known that the transition to the S_1 is very weak with an oscillator strength of 0.002, whilst the S_2 strength is much stronger [360]. Explanations for this low oscillator strength propose the transition being pseudo-parity forbidden. This is based upon alternacy symmetry which assigns the ground state and the first excited state as being *minus* states, thus the transition ${}^1B_{3u}^- \leftarrow {}^1A_g^-$ involves going from a minus to minus state [322, 361]. The 0-0 transition is followed by strong vibronic coupling with the S_2 state. This same method predicts the S_1 state in anthracene to be a plus state and therefore the transition allowed.

Measurements of naphthalene emission have ascertained the fluorescence quantum yield to be around 0.3 at low excess energy, with intersystem crossing to the triplet state outcompeting internal conversion [362].

Naphthalene is perhaps most renowned for being the primary component in mothballs and other similar deterrents. Similar to other linear polyacenes, its use in organic light emitting diodes (OLEDs) and other optoelectronic applications is of great interest, principally as a base for a diverse range of derivatives [363].

Theoretical studies calculating the L_a and L_b states of naphthalene show varying results. Disparities occur not only in the excited state energies but also the ordering of the states. TDDFT in particular has been reported as failing to predict the states in the correct order [326]. The calculated vertical excitation energies for the first two states of naphthalene are shown in Table 6.8.

The chosen theory, DFT using the B3LYP functional, performs poorly. The energy of the S_1 state is overestimated to the extent of lying just below the S_2 energy. The S_2 energy is, however, more reasonable. The B3LYP functional correctly identifies the symmetry of the S_1 state but predicts the wrong transition and hence ordering of the L_a and L_b states. Given the difficulties in calculating these states in naphthalene, a range of different functionals and quantum chemical methods were also tested. The performance of the different functionals varies, sometimes predicting the correct transitions but failing in their energies. Values in good agreement with the S_1 energy often suffer from underestimation of the S_2 energy. Even higher levels of wavefunction based methods are far from successful. Methods such as EOM-CCSD and ADC(2) determine the correct transitions and symmetries but have poor excitation energies. The best values are provided by the DFT-MRCI hybrid, a method that sadly cannot be used in the model due to its inability to calculate Hessians.

Table 6.8: Vertical excitations, electronic state symmetries and transitions for the S_1 and S_2 states of naphthalene as calculated using a range of DFT functionals and quantum chemical methods. All calculations used a 6-31G(d) basis.

	S_1	Transition			Symmetry	S_2	Transition			Symmetry
B3LYP	4.46	HOMO	→	LUMO	B_{1u}	4.53	HOMO-1	→	LUMO	B_{2u}
							HOMO	→	LUMO+1	
BP86	4.17	HOMO	→	LUMO	B_{1u}	4.34	HOMO-1	→	LUMO	B_{2u}
							HOMO	→	LUMO+1	
CAM-B3LYP	4.69	HOMO-1	→	LUMO	B_{2u}	4.78	HOMO	→	LUMO	B_{1u}
		HOMO	→	LUMO+1						
OLYP	4.18	HOMO	→	LUMO	B_{1u}	4.37	HOMO-1	→	LUMO	B_{2u}
							HOMO	→	LUMO+1	
PBEO	4.56	HOMO	→	LUMO	B_{1u}	4.61	HOMO-1	→	LUMO	B_{2u}
							HOMO	→	LUMO+1	
ωB97XD	4.69	HOMO-1	→	LUMO	B_{2u}	4.78	HOMO	→	LUMO	B_{1u}
		HOMO	→	LUMO+1						
MRCI-DFT	4.15	HOMO-1	→	LUMO	B_{3u}	4.72	HOMO	→	LUMO	B_{2u}
		HOMO	→	LUMO+1						
ADC(2)	4.55	HOMO-1	→	LUMO	B_{3u}	5.10	HOMO	→	LUMO	B_{2u}
		HOMO	→	LUMO+1						
EOM-CCSD	4.49	HOMO-1	→	LUMO	B_{3u}	5.40	HOMO	→	LUMO	B_{2u}
		HOMO	→	LUMO+1						
Exp. [326]	4.13	HOMO-1	→	LUMO	B_{3u}	4.66	HOMO	→	LUMO	B_{2u}
		HOMO	→	LUMO+1						

Retaining the B3LYP functional, the Hessians at the ground state equilibrium geometry and the FC point on the S_1 and S_2 state were calculated and the on-diagonal first order and second order terms obtained. The on-diagonal linear coupling constants, κ_α are shown in Table F.9. These correspond to modes of a_g symmetry, the only ones expected to have non-zero values. The coupling constants and cuts through the PES, alongside discussions are found in section F.4 of Appendix F.

Figure 6.11 shows the simulated S_1 and S_2 absorptions and the S_1 emission alongside experimental data. It is immediately obvious from the absorption spectra, Figure 6.11(b), that the simulation has drastically failed to reproduce experiment. The aforementioned failings of TDDFT in calculating the excited state energies contributes to the S_1 and S_2 band overlapping each other.

The experimental absorption spectrum shows the weak S_1 band starting around 4 eV and progressing up to 4.2 eV. Even if the simulated S_1 band had been at the correct energy, it is difficult to tell whether it successfully reproduces experiment. Experimentally, the weak intensities make observing the vibrational structure present challenging and the presence of the more dominant S_2 band hide the full range of the S_1 progression. It is therefore not certain whether the simulated S_1 band agrees with the structure. The inset shows this portion of the spectrum magnified to try to observe the fine structure.

The lower intensity of this simulated band as compared with the S_2 does agree though. The vibrational structure in the simulated S_1 band results from a long progression of the ring breathing, ν_1 mode. A similar assignment based on theoretically obtained spectra has also been made [364].

The simulated S_2 band is vastly different from experiment. The fine structure and length of the progression show no agreement to the experimental band. This suggests a failing in the on-diagonal linear coupling constants, which for the S_2 state were relatively small. Such a failing results from the TDDFT calculation,

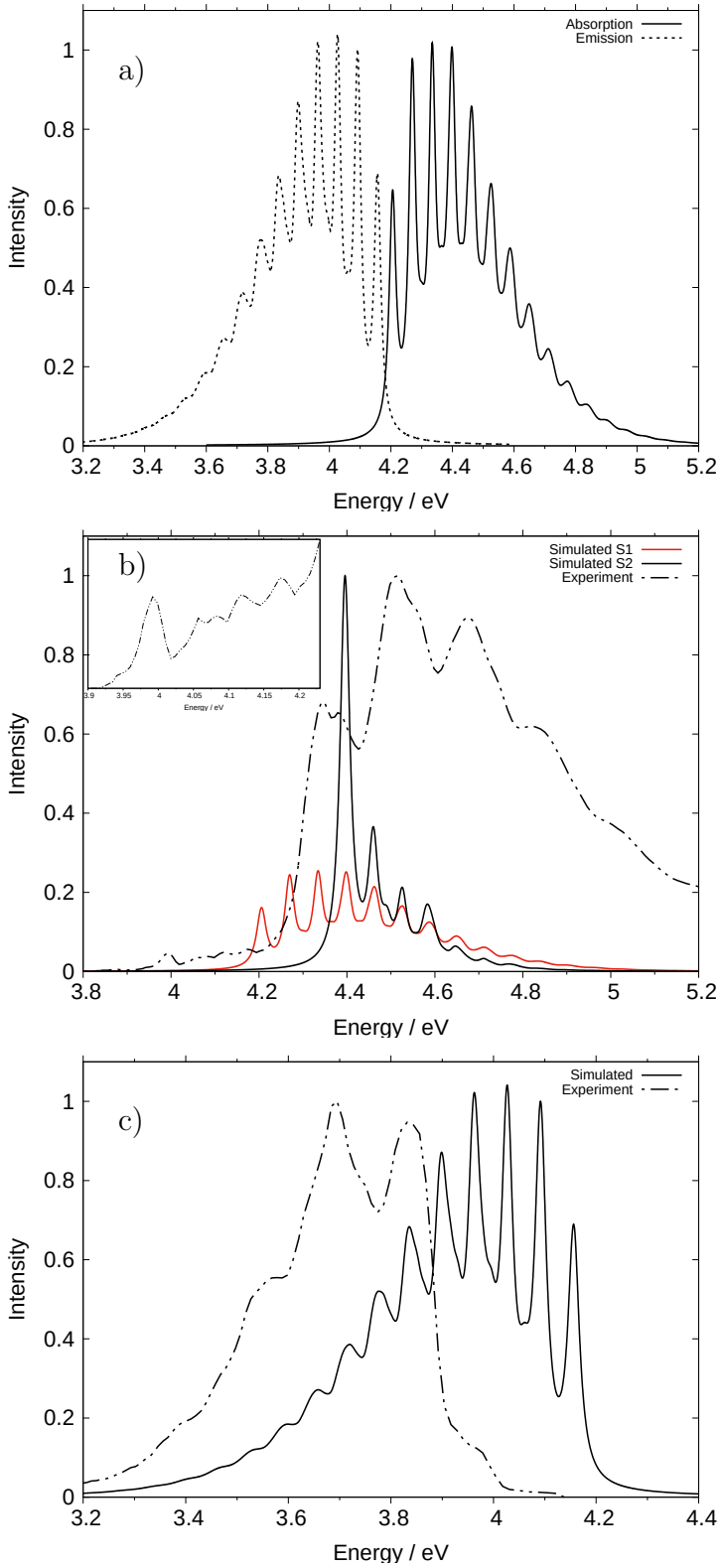

Fig. 6.11: The S_1 and S_2 absorption and S_1 emission spectra of naphthalene calculated using a six mode model with comparison to experiment. (a) The simulated absorption and emission spectra. (b) The S_1 (shown in red) and S_2 absorption spectrum showing comparison of experiment with theory, the inset shows the S_1 band zoomed in, and (c) the S_1 emission spectrum showing comparison of experiment with theory. All simulated spectra have a damping time of 50 fs.

which has already been shown to be inadequate for describing the L_a and L_b states of naphthalene. The calculated S_2 vertical energy agreed well with experiment but the differing fine structure can either be attributed to anharmonicity absent in this Harmonic model, or non-adiabaticity between the S_1 and S_2 states.

The emission spectrum however, Figure 6.11(c), shows better agreement to experiment. Such agreement suggests the S_1 surfaces at the FC point and minima are well described and the issues in the absorption spectrum result from phenomena not included in this model or problems with the S_2 surfaces. The higher energy of the simulated emission spectrum is not surprising considering the overestimation in the S_1 energy by TDDFT. The range of the simulated spectrum matches well with experiment, although the progression, formed from the ring breathing ν_1 mode, has peak widths much narrower than experiment, suggesting a different mode to be primarily responsible. Broadening due to coupling between the S_1 and S_2 states would have the effect of altering the simulated spectra as well as changing the intensities of the peaks.

Obtaining Better Spectra

As seen and discussed throughout this section, TDDFT does not perform well in calculating the L_a and L_b states. The major issue is the overestimation in the S_1 energy, bringing it close to the S_2, and the incorrect ordering of the states. The inability to reproduce the experimental spectra may also arise from the exclusion of vibronic coupling and non-adiabaticity between the states.

To investigate whether the problem lies with the electronic structure method or the simplified model presented here, attempts to accurately reproduce the absorption spectra were undertaken by amending the model. Re-examination of Table 6.8 shows that none of the DFT functionals perform reasonably well, however the decision was made to calculate the potentials using the CAM-B3LYP functional. The calculated vertical energies using this functional are also greatly overestimated but, crucially,

Table 6.9: Vibrational energies, ω and on-diagonal linear coupling constants, κ for the S_1 and S_2 state of naphthalene calculated using CAM-B3LYP level of theory. All values are in eV.

Mode	ω	$\kappa^{(1)}$	κ/ω	$\kappa^{(2)}$	κ/ω
ν_1	0.065	−0.046	0.708	−0.099	1.523
ν_2	0.098	0.041	0.418	0.069	0.704
ν_3	0.133	−0.070	0.526	−0.126	0.947
ν_4	0.149	−0.014	0.094	−0.028	0.188
ν_5	0.179	0.074	0.413	0.134	0.749
ν_6	0.189	0.074	0.392	0.139	0.735
ν_7	0.208	0.054	0.260	0.099	0.476
ν_8	0.398	−0.008	0.020	−0.012	0.030
ν_9	0.401	−0.020	0.050	−0.031	0.077

predict the correct transitions for the S_1 and S_2. To focus solely on reproducing the profile of the spectrum, the vertical energies were shifted to match experimental data. Whilst this devalues the model as a predictive tool, it serves to ensure the absorption bands are located at the correct energy.

The on-diagonal linear coupling constants obtained from the CAM-B3LYP calculations are shown in Table 6.9. The swap in orbital transitions in the S_1 and S_2 state determined by CAM-B3LYP is evident by the larger κ values and κ/ω ratio now occurring for modes in the S_2 state. Overall the values obtained differ little between the two functionals, but critically the larger shift in minima is now in the S_2 state, a change likely to manifest as an S_2 band with more fine structure and larger progressions.

Previous studies have commented on the low oscillator strength of the transition to the $S_1(B_{3u})$ state and suggested the intensity to derive from vibronic coupling. The majority of these studies assign the b_{1g} vibrations as coupling S_1 and S_2 [365], although it has also been been proposed that the coupling is with b_{3g} vibrations, with the S_1 intensity borrowed from the S_5, via a_g modes, and from the S_2 and S_6 states through b_{3g} modes [364]. The existence of a conical intersection between these states has also been offered [366]. With regards to which of the b_{1g} modes couple

the states, Zgierski [367] and Robey [368] determined modes with frequencies of 506 cm^{-1} and 938 cm^{-1} to be responsible.

Given the importance vibronic coupling between S_1 and S_2 may have on the photodynamics of the molecule, attempts were made to incorporate it into the model. It has been established that this model works best when there is little coupling between states and indeed a rigorous treatment of this coupling would involve calculating a series of points along each of the b_{1g} modes and fitting these modes to obtain the coupling parameters. By choosing the lowest frequency b_{1g} mode, a parameter that couples the states through this mode can arbitrarily be included.

The lowest frequency b_{1g} mode as calculated by the CAM-B3LYP functional, is an out-of-plane ring distortion with a frequency of 403 cm^{-1}. This mode was selected to couple the S_1 and S_2 states and a value of 0.2 eV was chosen. Since the coupling is proportional to the square of the parameter, then a large parameter ensures sufficient coupling is present. This mode is illustrated in Figure 6.12 alongside the cut through the PES along it.

Using the new κ parameters and the coupling term, the absorption spectrum of naphthalene was simulated. To try and ensure all features were captured a nine mode model was used. This included the same six modes as previous but also

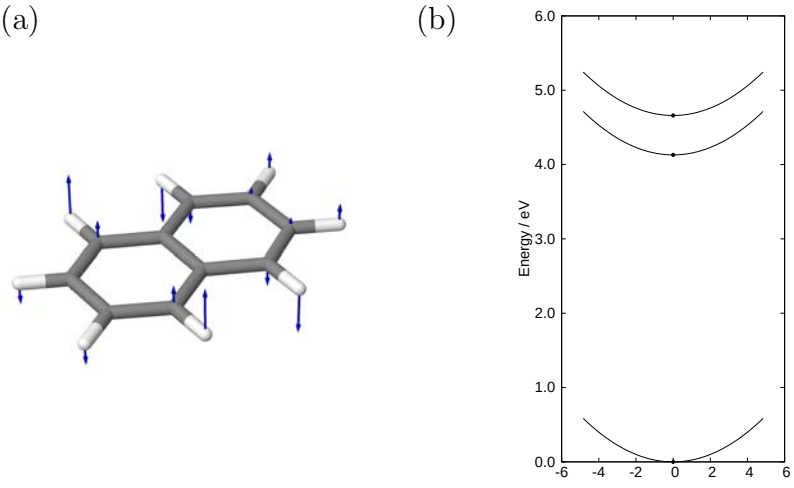

Fig. 6.12: (a) Graphical illustration for the normal mode, ν_{10} an out of plane ring distortion. (b) shows the cut through the potential energy surface along this mode

included ν_4, a C-H bending mode and ν_8, a C-H stretching mode, in addition to the coupling mode, ν_{10}.

The simulated S_1 absorption spectrum is shown in Figure 6.13(a). The spectrum shows there is vibrational structure equating to progression of the ν_1 mode. The difference in the S_1 κ values, determined using the CAM-B3LYP, is clearly visible with a much shorter progression of varying intensities unlike the S_1 band calculated using the B3LYP functional.

The spectrum resulting from transition to the S_2 state is shown in Figure 6.13(b). Here, the effect of introducing coupling via the b_{1g} mode is pronounced. The 0-0 transition for the S_2 band is situated around 4.4 eV, however the emergence of a series of peaks between 3.9 eV and 4.2 eV, the same energy range as the S_1 band, can be observed. This shows the coupling to be crucial in the naphthalene spectra and supports work indicating the intensity of the S_1 spectrum is borrowed from the S_2 state. As for the S_2 band itself, the range is much greater than previously simulated, with a long progression mainly resulting from the ν_1 ring breathing mode.

The success of this new simulated absorption spectrum can be evaluated by comparison with the experimental spectrum. This is shown in Figure 6.13(c). The simulated spectrum was obtained by summing together the S_1 and S_2 spectra. To achieve a similar intensity ratio between the two bands, it was necessary to scale the intensities of the simulated S_1 spectrum. The simulated spectrum replicates experiment much better than before. Whilst shifting the energies prevents the two bands from overlapping, the change in the coupling constants causes the vibrational structure of the bands to reproduce the experiment. The energy of the S_2 band is still slightly higher in energy than the experiment and the gap between peaks still shows divergence, indicating contribution from a second progression. The intensities of the S_1 band are too high in the simulation, but retain the correct trend in the ratio between the bands.

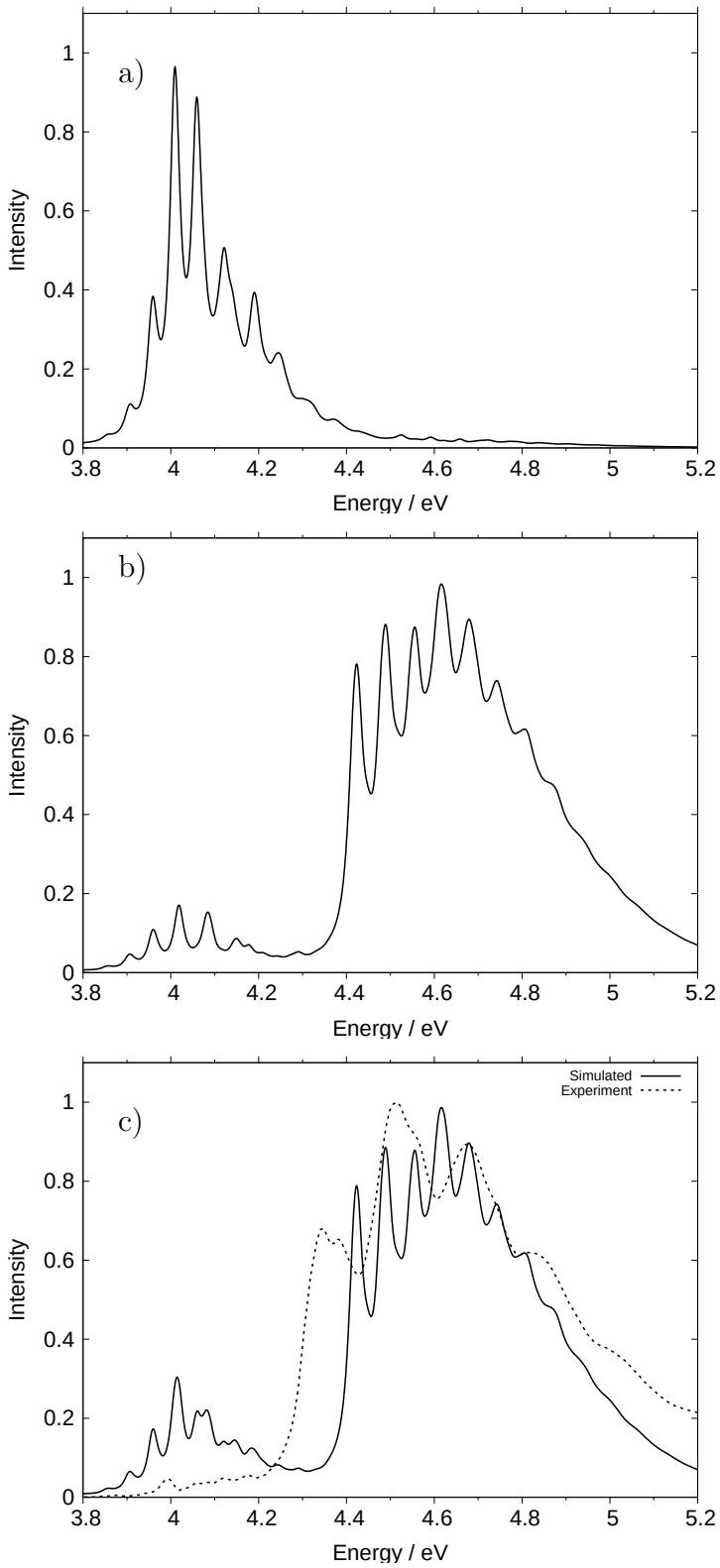

Fig. 6.13: The S_1 and S_2 absorption of naphthalene calculated using a nine mode model with comparison to experiment. This model was calculated using CAM-B3LYP. (a) The simulated S_1 absorption spectrum. (b) The simulated S_2 absorption spectrum, and (c) the combined S_1 and S_2 spectra to provide the overall spectrum alongside experimental data. All simulated spectra have a damping time of 50 fs.

Summary

The application of the simplified model to benzene and naphthalene have shown increased complexity. In benzene, the transition to the S_1 state is electronically forbidden and is observed experimentally due to Herzberg-Teller excitation of the e_{2g} modes. The model is, however, successfully able to reproduce the absorption and emission and capture the main features. The major progression resulting from the ring breathing mode still shows good agreement with experiment.

Naphthalene, however, proved to be more challenging. The failure of electronic structure methods, particularly TDDFT, to calculate the correct ordering of the L_a and L_b states has already been reported. It was therefore unsurprising that the calculations using the B3LYP functional overestimate the S_1 vertical energy and predict orbital transitions with different ordering to experiment. This produced absorption and emission spectra containing very little agreement to experiment.

Analysis of these discrepancies presented three issues to be addressed: the incorrect vertical excitation energies, the on-diagonal linear coupling constants and vibronic coupling between the S_1 and S_2 states via b_{1g} modes. The first two of these originated from the TDDFT/B3LYP calculations. Changing the functional to CAM-B3LYP produced L_a and L_b states in the correct order, although the energies were shifted to match experiment. This correct ordering of states also leads to κ_α values more consistent with spectral features, namely larger values for the S_2 state, where greater vibrational structure occurs. The final issue, the coupling between the states, was included by assigning a parameter to the lowest frequency b_{1g} mode. The value of this parameter was arbitrarily chosen, but the re-simulated absorption spectrum showed much better agreement with the experiment, highlighting the importance the vibronic coupling plays.

These alterations emphasise the limitations of this model, in particular for systems with strong coupling between states or where anharmonicity is prevalent. De-

spite this, it is possible to extend the model to integrate coupling, albeit in a qualitative manner. For methods where gradient differences and derivative couplings can be calculated, such as CASSCF, then using the model to determine values for the couplings should be possible.

6.5 Methyl and Hydroxymethyl Anthracene

To begin the investigation of the effect of functional groups, the methyl and hydroxymethyl (Figure 6.1 **(6,7)**) derivatives of anthracene were chosen. These are shown in Figure 6.1. Recent interest in 9-methyl anthracene (AnMe) has focussed on investigations into the internal rotation of the methyl group, attempting to quantify the energetic barrier to this rotation [369]. 9-hydroxymethyl anthracene (AnMeOH), also known as 9-anthracene methanol, is a useful intermediate in the synthesis of pharmaceutical molecules. It has also been shown that its presence aids in the efficient ring-opening polymerisation of certain lactones [370].

Figure 6.14 shows the experimental spectra for both derivatives alongside that for anthracene, as measured by Oliver Daubney at the University of Birmingham. Spectra for all three molecules were recorded in n-hexane solution.

The experimental data show the absorption and emission spectra of the two derivatives to have shifted to lower energy compared with anthracene. The methyl derivative is slightly lower in energy than the hydroxymethyl. The vibrational fine structure for all three molecules is very similar, with similar progressions and peak intensities. This suggests the substituent to have little effect on the photodynamics of the S_1 state, except lowering its energy.

Simulation of the spectra proceeded as before with the optimisation of the ground state structure before calculating the Hessian at both the equilibrium geometry and the FC point on the S_1 state. It has been well established that the geometry of anthracene is planar, though the position the substituents adopt differs. The opti-

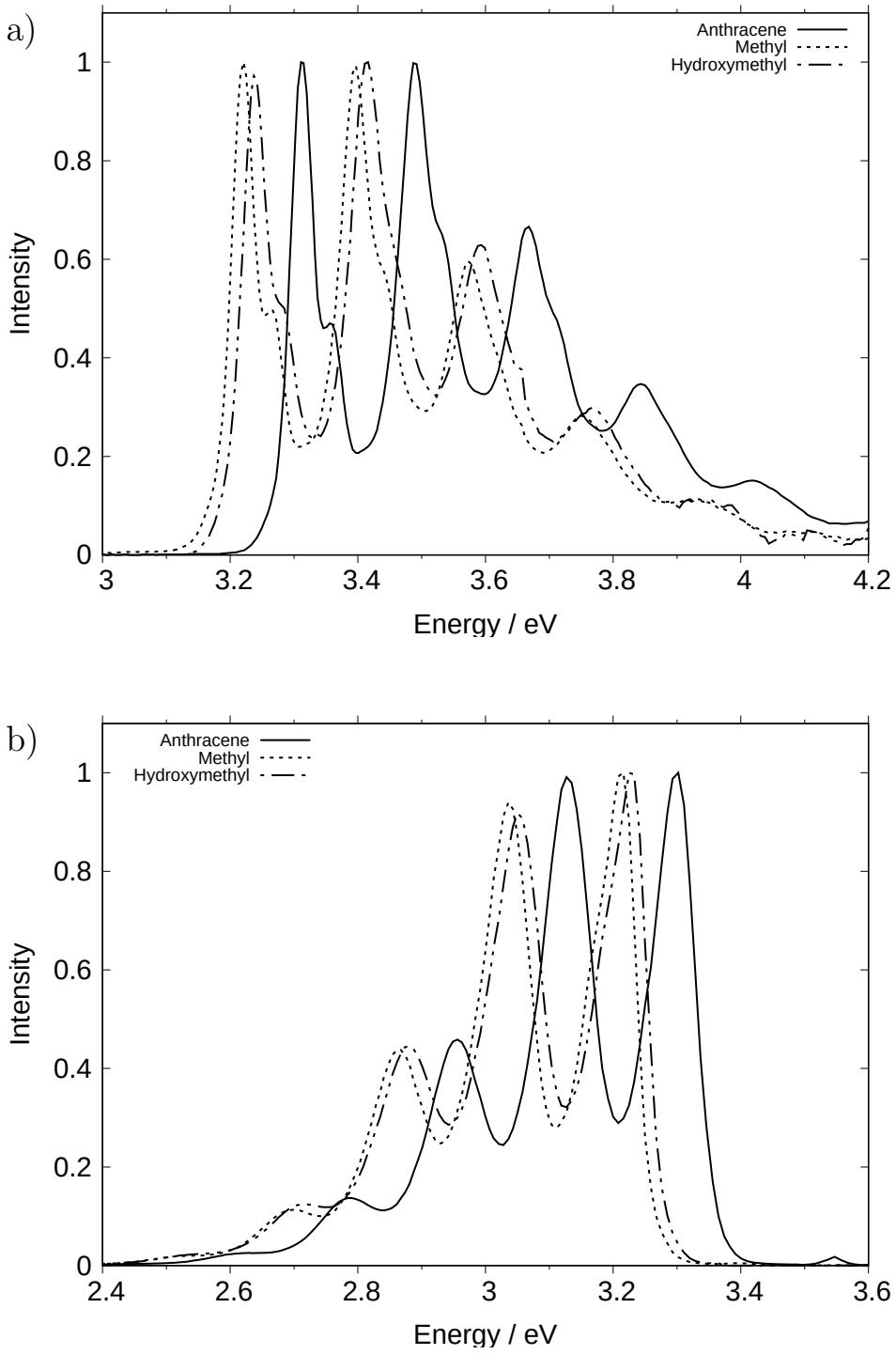

Fig. 6.14: Experimental absorption (a) and emission (b) spectra for 9-methyl anthracene and 9-hydroxymethyl anthracene. Included also for comparison are the experimental spectra for anthracene.

Table 6.10: Calculated vertical excitation energy of 9-methyl anthracene, 9-hydroxy methyl anthracene and anthracene, calculated using TDDFT (B3LYP functional) and a 6-31G(d) basis. All values in eV.

	B3LYP/6-31G	Exp.	
Anthracene	3.28	3.31/3.43	
9-methyl anthracene	3.20	3.18	[369]
9-hydroxymethyl anthracene	3.21	3.23	[375]

mised structure of AnMe showed the methyl substituent to have only one hydrogen in the plane. The position of the two remaining hydrogens results in the molecule possessing C_s symmetry. This has also been seen experimentally [371–373]. The optimised structure of AnMeOH showed the substituent was out of plane by 78°, similar to that seen experimentally [374, 375]. In adopting this conformation, all molecular symmetry is lost, leaving it with C_1 symmetry.

The calculated vertical excitation energies are shown in Table 6.10 and shows the two derivatives to be lower in energy than anthracene. Furthermore, the 9-methyl derivative is predicted to be slightly lower in energy than the 9-hydroxymethyl, matching the pattern seen in the experimental spectra. This is encouraging, and suggested the model would be able to predict the shifts in energy for the absorption and emission spectra. Details on the frequencies, parameters for the vibronic coupling Hamiltonian and cuts through the PES are detailed in section F.5 of Appendix F.

Figures 6.15(a,b and c) show the electronic spectra for AnMe. The electronic origins, 0-0 transitions, are located experimentally at 3.22 eV and from the simulation at 3.00 eV, the difference of 0.22 eV reflecting similar energy differences seen for the other molecules. The peak progressions between the two spectra are well matched, although a slight narrowing of the peak width for the simulated absorption spectrum is noted. From the vibrational fine structure, it was determined that the peak progression is formed from three vibrational modes. These generate three progressions that overlap so as to create a broader series of peaks. These are ν_{40},

the C-H bending/ring distortion mode, ν_{30}, the methyl bending/para C-H bending mode and ν_{51}, C-H bending of the outer rings. One feature missing from the simulated structure, is the series of shoulder peaks on the electronic origin. These peaks can be observed in the experimental spectrum and have been a feature of all the linear polyacenes, and are also present in AnMeOH. The absence of this peak results from neglecting a low frequency mode, typically the ring breathing mode, from the model. This corresponds to ν_9 and is shown in Figure F.6(c), the same mode is also shown in (d) for AnMeOH.

The emission spectrum of AnMe again shows the simulation to be shifted to lower energy, but agrees well with the progression and relative intensities observed in experiment. The experimental emission spectrum is more featureless than the absorption, whereas the simulation retains the same vibrational fine structure as the absorption.

The Stokes shift in n-hexane was determined from the experimental data to be 0.005 eV, and from the simulation, 0.043 eV. Whilst this value is a magnitude higher than experiment, it is still a very small shift.

For AnMeOH, the experimental and simulated spectra are very similar to AnMe. Again, the simulated spectra are shifted by 0.22 eV, with 0-0 transitions located at 3.24 eV in the experiment and 3.02 eV in the simulation. The vibrational fine structure in the simulation matches the experiment well. Unlike in AnMe, the inclusion of the ring breathing ν_{11} mode manifests as shoulder peaks on the electronic origin peak. The main progression comprises the overlap of two vibrational modes, ν_{63}, a C-C ring stretch mode and ν_{56}, a C-C ring stretch with methylene rocking.

The simulated emission spectrum, Figure 6.15(f), shows good agreement to experiment, aside from the usual shift to lower energy.

In addition to successfully being able to reproduce experimental data, the simulated spectra also captured the change in energy compared with anthracene. More-

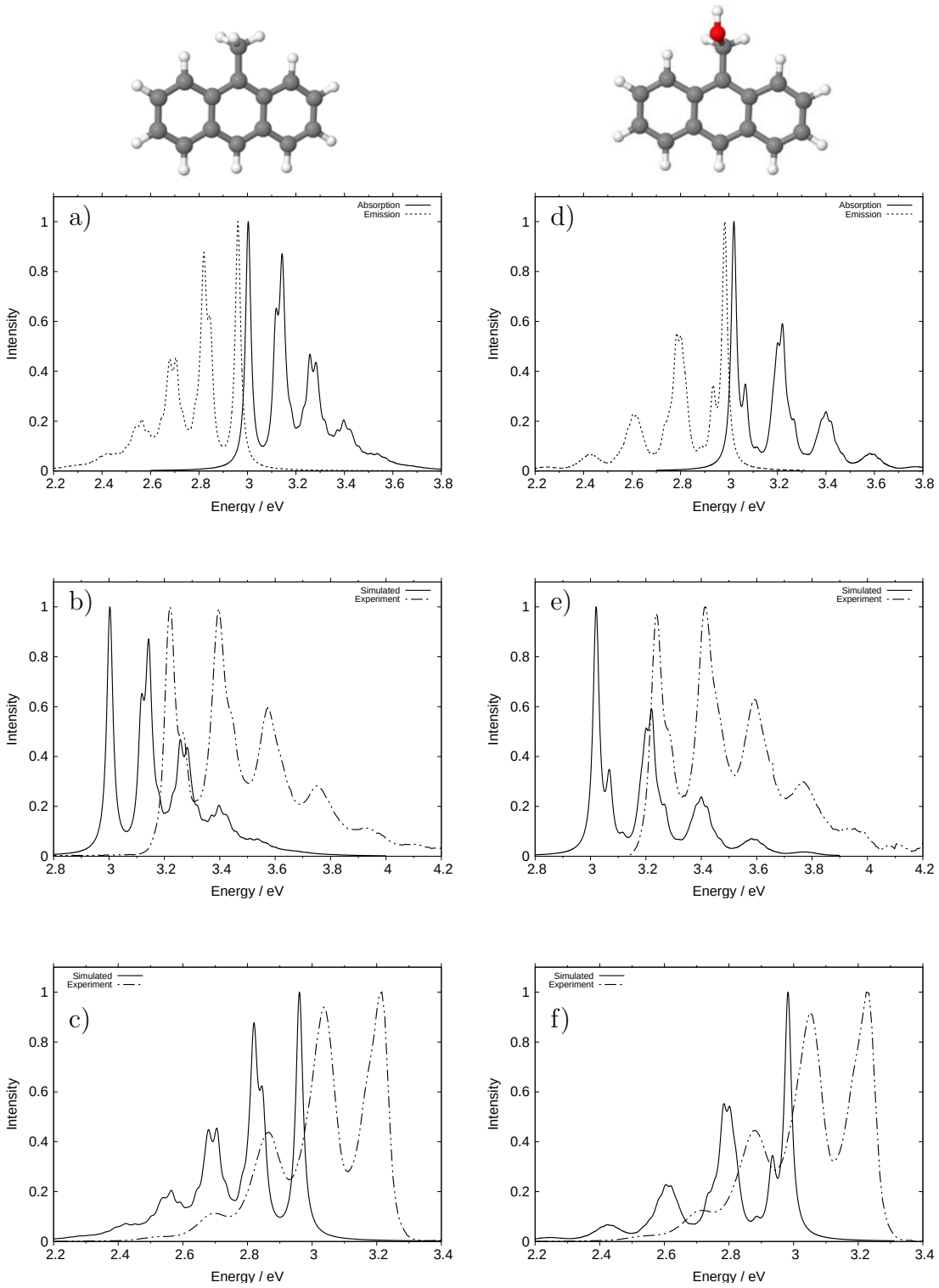

Fig. 6.15: The absorption and emission spectra for 9-methyl anthracene and 9-hydroxymethyl anthracene using an eight mode model with comparison to experiment. (a,d) The simulated absorption and emission spectra. (b,e) The S_1 absorption spectrum showing comparison of experiment with theory and (c,f) The S_1 emission spectrum showing comparison of experiment with theory. All simulated spectra have a damping time of 50 fs.

over, the slightly lower energy of the methyl derivative is reproduced. It is crucial that the model is able to replicate the change in energies, as with the structure of the spectra being very similar, distinguishing anthracene from the two derivatives relies upon these energy differences. Distinguishing between the methyl and hydroxymethyl derivatives themselves, however, is a challenge given that they lie very close in energy.

The Stokes shift, measured in n-hexane, for both 9-methyl and 9-hydroxymethyl anthracene is small. Experimental data provides a shift of 0.015 eV, whilst the simulated shift was calculated to be 0.040 eV.

Summary

The study of the derivatives 9-methyl and 9-hydroxymethyl anthracene show these substituents to have little affect on the absorption and emission spectra of anthracene. The vibrational fine structure is very similar, reflecting the similar vibrational modes involved in the photochemistry of the S_1 state. A shift to lower energy is observed for both derivatives. The simplified model presented here is successfully able to reproduce the spectra and the associated changes in energy. The C_s and C_1 symmetry in these derivatives greatly increases the number of modes containing non-zero on-diagonal linear coupling constants. Despite this, taking the largest values of κ and the ratio κ/ω, alongside modes similar to those used in the anthracene model, resulted in two models, each with eight modes, that provided reliable spectra.

To really test the model, a range of different derivatives were also investigated, particularly with substituents known to be electron donating or electron withdrawing.

6.6 Carboxylic Acid and Aldehyde

The final set of functionalities investigated were the carbonyl derivatives, anthracene-9-carboxylic acid (AnCA) and anthracene-9-carbaldehyde (AnCHO) shown in Figure 6.1**(8,9)**. These molecules provide a good test for the model presented here in dealing with additional complexities. The carboxylic acid and aldehyde derivatives demonstrate solvent effects that greatly influence the shape and structure of the electronic spectra. These molecules contain functional groups that are able to freely rotate. This torsional motion can lead to the breakdown in the mirror-image relationship between the absorption and emission profiles. Such motion, particularly of the carboxylic moiety, has also been shown to involve a conical intersection to the ground state, allowing for rapid relaxation [376–379].

These molecules show promise as photomechanical materials [380] and possibly in the formation of complexes with antimicrobial activity [381].

The experimental electronic spectra for the carboxylic acid and aldehyde derivatives, as measured by Oliver Daubney at the University of Birmingham, are shown in Figure 6.16.

The absorption spectrum for AnCA shows structure similar to anthracene, indicating the anthracene core to be responsible. The 0-0 transition at around 3.2 eV is consistent with the other anthryl derivatives and slightly lower in energy than anthracene itself.

The emission spectra however shows a clear solvent dependence, which greatly affects the profile of the spectrum and the emission energy. In basic water, the fluorescence of AnCA is sharp and retains the anthracene like structure, keeping the mirror-image property. Upon changing to the aprotic solvent acetonitrile, the emission profile becomes broad and lower in energy. The fine structure disappears leaving only one prominent peak at 2.8 eV.

This solvent effect has been noted and investigated throughout the literature.

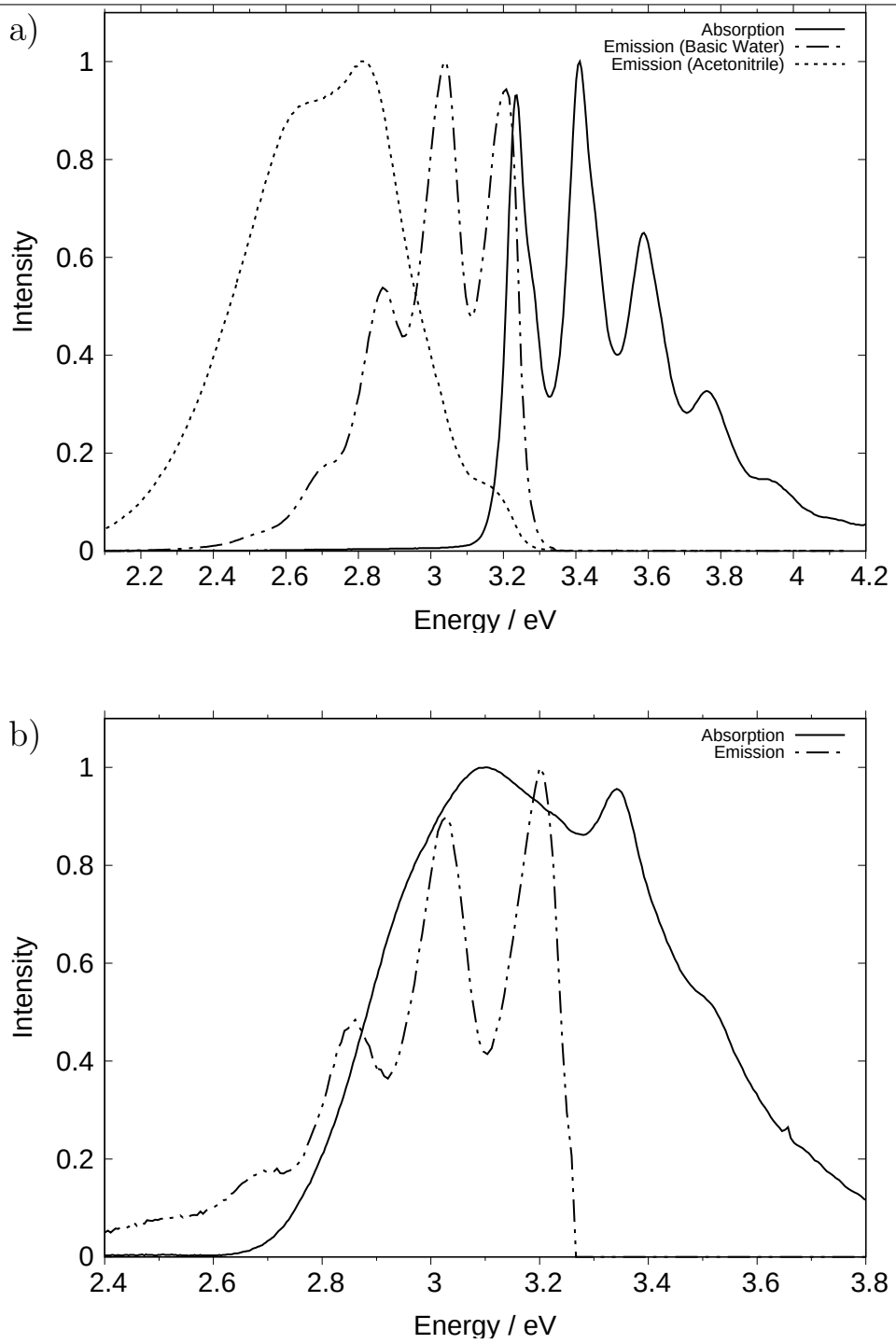

Fig. 6.16: Experimental S_1 absorption and emission spectra for (a) anthracene-9-carboxylic acid and (b) anthracene-9-carbaldehyde. The emission spectrum for anthracene-9-carboxylic acid was recorded in different solvents to observe differences in the spectral features and the solvation effects. For anthracene-9-carbaldehyde, an ethanol solvent was used.

Abdel-Mottaleb *et al.* studied the fluorescence and photostability of AnCA and showed the emission profile in water to be sharp, whilst in ethanol a broad band centred at 470 nm (2.64 eV) was observed [382]. This broadness was found to persist when using cyclohexane and acetonitrile solvents. The absorption spectrum, however, exhibited little solvent sensitivity.

This behaviour has been attributed to various equilibria: acid-base [383], monomer-dimer [384] and dimer-tetramer [385]. The sharp fluorescence seen in water, and to some extent a few alcohols, emanates from solvation and H-bonding between the solvent molecules and the COO^- and COOH moieties. This interaction serves to inhibit the free rotation of these groups [386].

Based on this, Abdel-Mottaleb *et al.* suggested these hydrophilic carboxyl groups prevent neutral AnCA molecules from dissolving in hydrocarbon solvents but form the anionic anthracene-9-carboxylate (AnC) when dissolved in water and some alcohols. When placed in hydrophobic solvents, it has been suggested the molecules aggregate into H-bonded dimers. In the excited state, the two carboxyl groups are able to rotate into the plane, consequently causing the broad fluorescence [385,387].

The assignment of the emission spectra can therefore be broken down into several components. Peaks between 3.20 and 3.00 eV correspond to emission from anionic AnC, shoulder peaks situated around 2.82 eV are from the neutral AnCA and the presence of a broad band at 2.64 eV is due to the H-bonded dimers.

In contrast, the emission spectrum of AnCHO is sharp and well resolved, whilst its absorption spectrum is unusual; a broad band with a prominent shoulder peak emerging around 3.4 eV. There has been little work on the electronic spectra of AnCHO, but Hirayama showed this broad absorption spectrum to occur in a variety of solvents, implying a lack of solvent dependence [388]. Instead, it was proposed to result from the torsional motion of the carbonyl group. Transitions from numerous ground states with different torsional angles leads to a broad spectrum, unaffected

by solvent. This work also identified a small shoulder peak at 420 nm (2.95 eV) that was assigned to the 0-0 electronic origin. The absorption peak shown in Figure 6.16 also shows a very weak feature at this energy, which is therefore denoted as the 0-0 transition.

Both molecules also show contrasting Stokes shifts. Depending on the solvent used, AnCA can exhibit a very small or a larger shift, although this may be attributed to dissociation of the carboxylic acid to form the corresponding anion. Conversely, an anti-Stokes shift is observed for AnCHO, where the emission energy is higher than the absorption. These two molecules will likely provide a serious test of the model here, particularly in reproducing solvent effects and the anti-Stokes shift.

It was necessary to increase the basis set size for the electronic structure calculations on AnCHO. The original basis, 6-31G(d), was found to be inadequate, failing to converge during the optimisation. The addition of an extra set of p-functions on the hydrogens, to give a 6-31G(d,p) basis, resolved these problems.

The optimised structures for AnCA and AnCHO showed that they are not perfectly planar. The anthracene core lies in the plane but the carbonyl group is rotated out of the plane. For AnCA, the optimised structure has a C-C-C-O dihedral angle of $-45°$ and a C-C-C-O(H) angle of 132°. This shows good agreement with experimental crystal structures that determined the C-C-C-O dihedral angle to be 54.87° [389]. Dimers were also found to form in the crystal. The dihedral angle formed by the aldehyde was found to be smaller, with the optimised structure predicting an angle of 11°, which is in reasonable agreement with the crystal structure value of 27° [390].

The calculated vertical excitation energies are shown in Table 6.11. Compared with experimental data, the calculated S_1 energies show good agreement and this state is correctly predicted to be the bright L_a state resulting from the HOMO to

Table 6.11: Calculated vertical excitation energies for the first two excited states of anthracene-9-carboxylic acid and anthracene-9-carbaldehyde calculated using TDDFT (B3LYP functional). All values in eV.

		S_1	
	Transition	Calculated	Exp.
anthracene-9-carboxylic acid	HOMO→LUMO	3.14	3.24 [382]
anthracene-9-carbaldehyde	HOMO→LUMO	2.97	2.95 [388]
		S_2	
	Transition	Calculated	Exp.
anthracene-9-carboxylic acid	HOMO−1 →LUMO	3.85	-
anthracene-9-carbaldehyde	HOMO−1 →LUMO	3.08	-

LUMO transition. The S_2 state for both is shown to resemble the dark L_b, with the transition from the HOMO−1 to the LUMO. Interestingly, the energies of the S_1 and S_2 states for AnCHO are shown to be close, possibly alluding to coupling between these states.

Frequency calculations yield 75 normal modes for AnCA and 72 for AnCHO. The positioning of the carbonyl group outside of the plane removes all symmetry elements from the molecules, leaving them possessing C_1 symmetry. This causes all vibrations to have a symmetry and therefore all normal modes to have non-zero on-diagonal linear coupling constants. The vibronic coupling constants and cuts through the PES are found in section F.6 of Appendix F. For both AnCA and AnCHO a four mode model was used to calculated the spectra. These modes exhibited the largest κ values, except for ν_1 of AnCHO, which had a large ratio of κ/ω.

The simulated and experimental spectra for both AnCA and AnCHO are shown in Figure 6.17. For AnCA, the simulated absorption spectrum is lower in energy than experiment but it reproduces the vibrational fine structure. The fine structure present results from either ν_{56}, a C-C ring stretching mode, or ν_{59}, a C-H bending mode. A small shoulder present on the 0-0 peak arises from the low frequency out

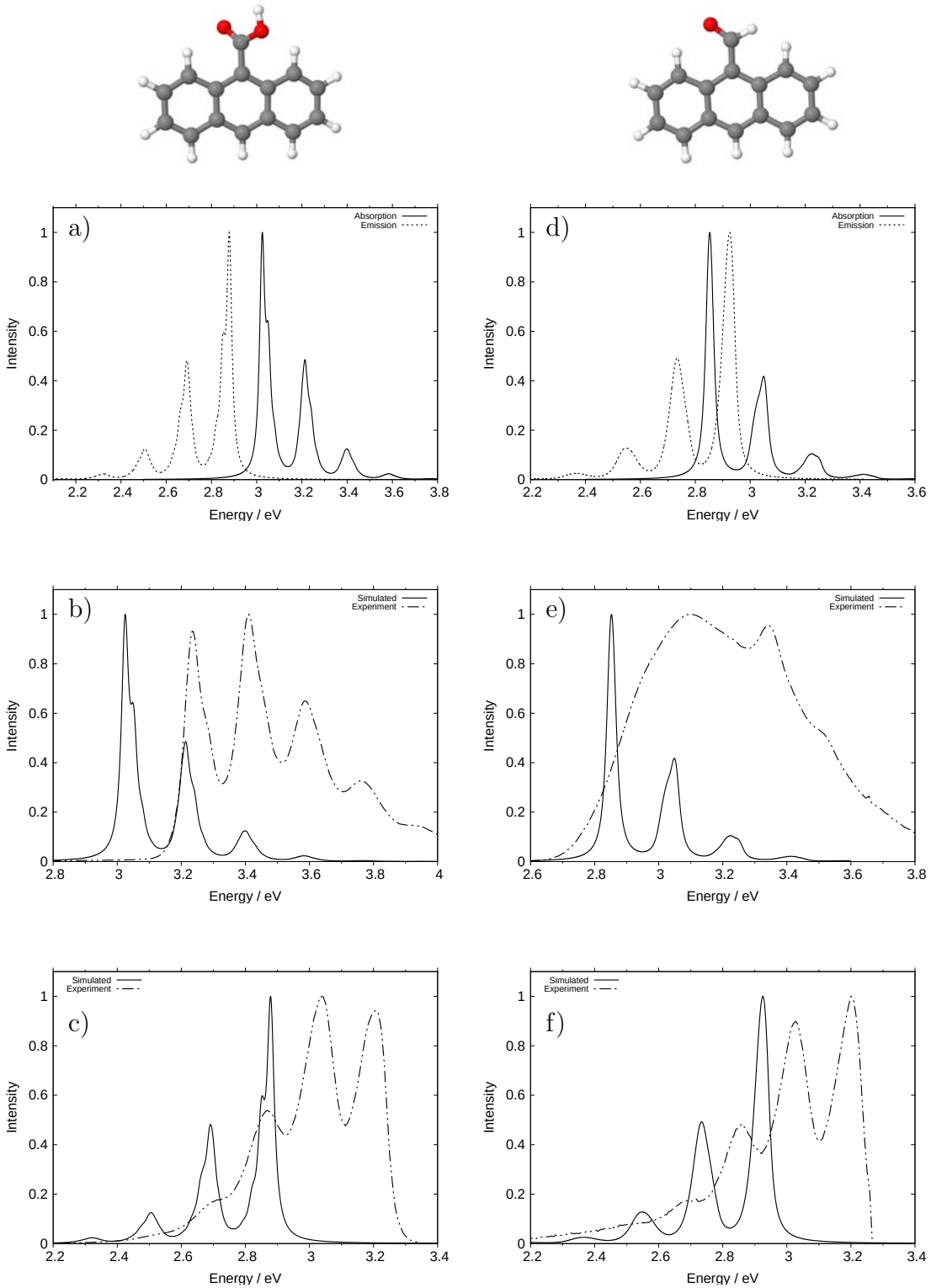

Fig. 6.17: The absorption and emission spectra for anthracene-9-carboxylic acid and anthracene-9-carbaldehyde using a four mode model with comparison to experiment. (a,d) The simulated absorption and emission spectra. (b,e) The S_1 absorption spectrum showing comparison of experiment with theory and (c,f) The S_1 emission spectrum showing comparison of experiment with theory. All simulated spectra have a damping time of 50 fs.

of plane bending mode, ν_6. The experimental emission spectrum of AnCA is sharp and structured due to the solvent, which here was basic water (pH = 10). The simulated spectrum is again at lower energy, although the difference is greater than seen in absorption. This is further reflected in the Stokes shift. In basic water the shift was determined to be 0.38 eV. This larger shift is brought about by $\lambda_{\max}$ not being the 0-0 transition. The simulations, however, predict a shift of 0.15 eV. This lower value is explained due to the simulation always having the 0-0 transition as $\lambda_{\max}$. Furthermore, the simulated shift is manifested as a large gap between the 0-0 transitions and worsens the agreement with experiment. It is also important to note that the emission spectrum in basic water is likely to be due to the deprotonated carboxylate and not the acid, unlike in the simulation. The experimental Stokes shift in acetonitrile is even larger with a value of $\sim$0.6 eV.

For AnCHO, the experimental absorption spectrum has the expected broad shape, whereas the simulation predicts a well resolved spectrum. Assuming the electronic origin in the experimental spectrum occurs at around 3.1 eV, then the simulated spectrum is lower in energy. The difficulty in reproducing the broadness in the spectrum depends on its cause. If, as reported in literature, the broad spectrum is caused by electronic transitions from ground states with different dihedral angles, then building a model is possible. This would require numerous optimisations for structures each with a different dihedral angle. Having to run so many calculations depreciates the model as a quick and simple method. The possibility that the broad structure results from solvent effects are also difficult to include within this model, particularly through the use of implicit solvation. The fine structure present in the simulation is assigned to two modes, ν_{52} and ν_{58}, two C-C ring stretch modes. The closeness in energies of these modes, gives rise to the wider peaks observed along the progressions.

The experimental emission spectrum is much sharper, with well resolved peaks

in good agreement with the simulated spectrum. Again, the simulated spectrum is shifted to lower energy, but provides the correct vibrational structure, with only a minor discrepancy in the peak heights. The simulated absorption and emission spectra (Figure 6.17(d)) show a negative Stokes shift of roughly -0.075 eV. This is also true for the experimental spectra, where the broad absorption spectrum has a λ_{max} around 3.1 eV, with an emission value of 3.2 eV, leading to a Stokes shift of -0.1 eV.

Summary

Anthracene derivatives containing a carboxylic acid and an aldehyde show a distinct change in the electronic spectra. This change is brought about by interaction with the solvent and motion of the substituent itself.

For AnCA the absorption spectrum is unchanged from that of anthracene. The emission spectrum, however, is influenced by the solvent via interaction between the hydrophilic carboxylic group and the solvent molecules. The formation of H-bonded dimers in hydrophobic solvents and rotation of the carboxylic groups broadens the spectrum, whilst water and some alcohols retain the sharp structure seen in the absorption. Deprotonation in solvent to form the carboxylate anion gives rise to the sharper emission spectrum. The simulated absorption spectra agrees well with experiment, and correctly reproduces the fine structure. The simulated emission spectra, retains the fine structure, with the model unable to incorporate the solvent effects observed experimentally, especially the broadening.

Problems were encountered along the lowest frequency torsional modes of the COOH group, ν_1 and ν_2, where cuts through the PES along these modes were unbound in the S_1 state. Expanding the range of these cuts showed minima to exist that were vastly shifted and the formation of a crossing point to the ground state. Calculations reported in the literature revealed the potential energy curve along the dihedral O-C-C-C to form a double well potential in the ground state with a

small barrier to rotation. In the S_1 state, this barrier was much larger to the extent that the FC point occurred on this barrier and likely explains the shape of the cuts obtained from the model.

The other molecule, AnCHO, at first appeared to show a similar solvent effect in its absorption spectrum. Studies in the literature, however, showed it to have little sensitivity to solvent and propose the broadness to result from a number of different ground states with the aldehyde group at different angles. The simplified model is not able to reproduce this, instead calculating a well resolved spectrum, although at a lower energy than experiment.

The emission spectrum is well structured, returning to the familiar progressions observed for anthracene. The simulated emission agrees well with experiment, although the energy is again lower, and replicates the fine structure. Notably, the Stokes shift for this molecule is shown in be negative in experiment and simulation. This is unusual and warrants further investigation but nevertheless the ability of the model to correctly predict this shift is pleasing.

For both models, similar modes to those seen previously were found to be important for the S_1 dynamics. These comprise a C-C ring stretch mode and a C-H bending mode. The lack of symmetry (C_1 point group) for both molecules leads to all vibrational modes having a_1 symmetry and non-zero on-diagonal linear coupling constants. As a result there were out of plane modes that possessed large κ/ω ratios in both models. Whilst these modes did not provide progressions in the spectrum, they are likely to influence the broadening of the peaks.

6.7 Conclusion

The construction of the PES is vital for quantum dynamic studies. Accurately capturing their topology is crucial for investigating a variety of photodynamic behaviour. Building these potentials involves calculating numerous points using electronic struc-

ture calculations, which quickly becomes time-intensive if a large number of normal modes need to be considered and for large systems.

The newly developed methodology presented here provides an efficient way to produce potentials for all normal modes in a molecule. This requires the Hessian only at the equilibrium ground state structure and the FC point on each excited state. By using the gradients and second derivatives from these Hessians, the potentials along each normal mode can be expressed as shifted harmonic potentials. Such an approach is only useful for systems where the potentials are strongly harmonic, particularly around the equilibrium point, and when there is little coupling between states.

To test the utility and validity of this model, the absorption and emission spectra of a series of anthracene derivatives and polyacenes of increasing size were simulated. This also provided an additional study on the performance of quantum chemical methods for calculating the bright L_a and dark L_b states. As experimental studies were conducted in solvent, the Stokes shift and solvent effects were studied. Throughout the calculations, the energies obtained by TDDFT were always lower than experiment, leading to spectra shifted to lower energy.

For anthracene, simulated spectra produced by the model showed excellent agreement with experiment, replicating the fine structure. Comparison with potentials obtained by fitting to a series of *ab initio* points demonstrated the harmonic potentials to be in good agreement and confirm the validity of the model. For tetracene and pentacene, the simulated spectra conform well with experiment, although the length and intensity of the progression for tetracene showed some disparity. It was determined that the κ values for the important modes in tetracene were smaller than in the explicit fit, giving rise to the shorter, weaker progression.

Benzene and naphthalene provided the first real challenge to the model. Despite the S_1 transition being forbidden for benzene, the model accurately reproduced the

absorption spectrum without needing to include vibronic coupling. The simulated spectrum does, however, not reproduce the shoulder progression from the vibronic coupling mode and also includes the 0-0 transition not observed experimentally. Naphthalene proved to be complex, with a very weak transition to S_1 and domination by the strong S_2 transition. Failure of TDDFT to calculate the correct energies and transitions results in spectra which are significantly different to experiment. Only by adjusting the energies to match experiment, changing functionals and arbitrarily introducing a coupling term between the S_1 and S_2 states were reasonable spectra obtained. This failure of the model was attributed to problems with the electronic structure theory and the unusual behaviour of naphthalene itself.

For the methyl and hydroxymethyl anthracene derivatives, the experimental spectra showed little difference compared with anthracene, except a shift to lower energy. The simplified model was able to reproduce the change in energy and the fine structure. The lower symmetry meant more modes needed to be considered, however a pattern was found in the important normal modes across all the molecules. It was found that a C-C ring stretch and a C-H bending mode were prevalent and responsible for the observed progression. Often a low frequency ring breathing mode was also present, causing a small progression, which appeared as shoulder peaks on the 0-0 transition.

Finally, the carboxylic acid and carbaldehyde derivatives were investigated. These show unusual behaviour and broader spectra. It was necessary to slightly increase the basis set to 6-31G(d,p) to converge all calculations. Anthracene-9-carboxylic acid was shown to be solvent dependent. In hydrophobic solvents, hydrogen-bonded dimers form, with rotation of the COOH groups into the plane leading to a broad emission. In water, the emission spectrum is much sharper, which is attributed to deprotonation and formation of the carboxylate anion. The model successfully reproduces the absorption spectrum but was unable to capture the solvent effects in

the emission spectrum. The inherent difficulty in modelling solvation is not unique to this model but is likely best achieved through more rigorous explicit fitting of potentials. In the case of anthracene-9-carbaldehyde, the broad absorption spectrum was reported as not being solvent sensitive. Again, the simulated spectrum was well resolved but was able to reproduce the negative Stokes shift observed.

Overall, the methodology presented here provides a rapid and efficient model for calculating the absorption and emission spectra for large simple polyaromatic molecules. It is also able to quickly show when more complicated processes must be invoked to explain spectra.

Chapter 7

Direct Dynamics Study of Proton Transfer in GFP

The previous chapters have developed and used model Hamiltonians to study photo-excited systems. While these are very useful, they are limited by being based on short expansions of the potential surfaces around the FC point, which means they are unsuited for studying long-time reactive processes. To address this problem, in recent years the use of direct dynamics methods have shown much promise in the study of photodynamics. In this Chapter, the recently developed Direct dynamics variational multiconfigurational Gaussian (DD-vMCG) method is tested on the ESPT mechanism in GFP. The model representing the chromophore and protein matrix is large and provides a rigorous test for the method. The use of Cartesian coordinates also demonstrates the flexibility of the method. A range of accompanying analysis tools allows changes in the geometry during the simulation to be viewed. The individual trajectories taken by each GWP can be followed and the expectation value calculated, giving a simple visualisation of the process in terms of molecular structures. The DD-vMCG method was successfully applied to the large model system and provided insights into the proton transfer. The simulation indicated the first step in the mechanism was transfer of a proton from the methanol group to the acetate moiety, agreeing with experiment. Large motion was also observed for the protons involved in subsequent steps of the mechanism. Having shown the

DD-vMCG can be used, further refinements to the model are needed. However, the method itself was demonstrated to be viable for large systems and can therefore be applied to studying other large models.

7.1 Introduction

The construction of potential energy surfaces (PES) is a vital component upon which quantum dynamic simulations can be performed. To reduce time and computational demands, alternative methods have been devised, aimed at providing efficient, yet reliable, potentials.

One such method, outlined in Chapter 6, requires only information at the equilibrium geometry and the Franck-Condon point. This allows approximate potentials to be generated as displaced Harmonic oscillators for all normal modes. This approach, however, still requires Hessian calculations that can be equally demanding, particularly as the system size increases. Modes that exhibit anharmonicity are not properly accounted for using this approach. The model is also only reliable for short time dynamics.

Another method showing much promise is the calculation of the PES "on-the-fly", running in tandem alongside the dynamics. This is achieved here through the DD-vMCG method outlined in Section 3.12. The development of such a method is aimed towards the study of large systems. For large systems, the construction of fitted surfaces, as was done in Chapters 4 and 5, is difficult due to the number of demanding electronic structure calculations needed. For using the DD-vMCG method, the system studied was chosen as the HBDI chromophore and the protein matrix enveloping it. Such a system is not only large, but contains several molecules held together through a hydrogen bonded network. This is makes it an ideal test for direct dynamics simulations. This chapter explores this approach and its application to the study of the proton transfer mechanism in GFP.

The general model explaining the photophysics of wt-GFP is shown in Figure 7.1. Within this model, excitation of the anionic chromophore, HBDI, leads directly to green fluorescence. Excitation of the neutral species (A) to an excited state (A*), results in proton transfer, which rapidly converts this excited neutral state to an excited anionic state, denoted I*. This species is responsible for the emission of green fluorescence. Spectroscopic studies have shown this conversion to occur on a timescale of picoseconds [391, 392].

Further studies looking at the kinetics of this conversion from A* to I* noted any emission of blue light from the excited A* state, which was observed on a picosecond scale [393] and seen as a very weak band in the emission spectrum [394]. Furthermore, an inverse relationship between the decay kinetics of the A* state and the green fluorescence from I* was also observed. The kinetics of both the decay and rise in green emission was seen to slow when the protons were exchanged with the corresponding deuterated equivalents [391]. Additional work, comparing the structure of wt-GFP and the variant S65T, showed the latter did not contain the 395 nm absorption peak [242]. The only structural differences between the two was

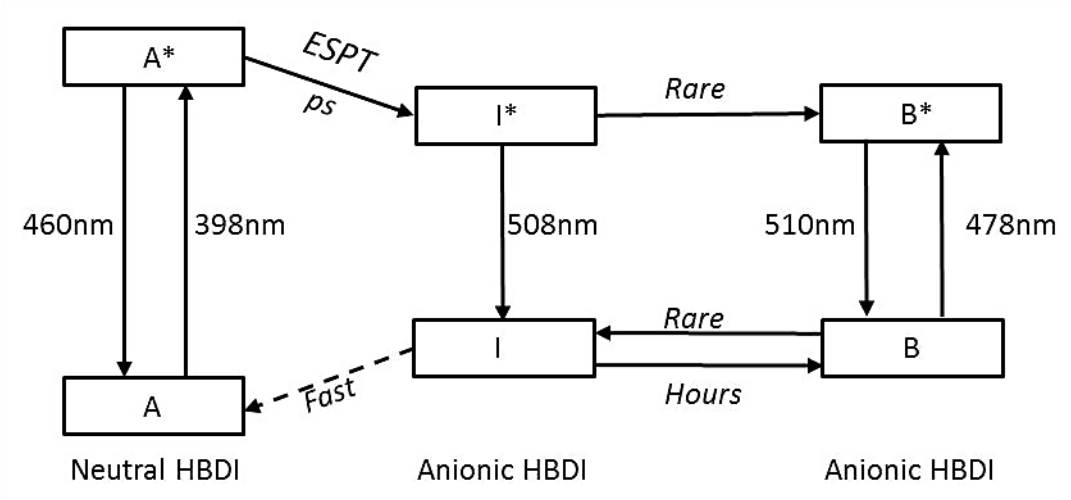

Fig. 7.1: Model of the photophysics thought to occur in GFP, as originally proposed by Chattoraj [391].

the replacement of a hydrogen by a methyl group. From this, it was concluded that the connection between the A* and I* states, and hence green fluorescence occurring when exciting the neutral HBDI species, was the result of an excited-state-proton transfer (ESPT). When the hydrogen was replaced with a methyl group the hydrogen-bonding was de-stabilised, making the anionic form exclusively favoured instead. Whilst this type of process is well known in chemical systems it is, at present, the only observed example of ESPT taking place in a biological molecule.

The proposed mechanism, suggested by Brejc *et al.*, is shown in Figure 7.2 [242]. In the excited state of the neutral chromophore (A*), a proton transfer involving three different protons leads to formation of the anionic chromophore in its excited state (I*). Emission from this state results in green fluorescence.

Studies have also shown that the recovery of state A is facilitated by a ground state inverse proton transfer from one of the nearby amino acid residues to the chromophore [391]. Furthermore, conversion from the excited I* state to the B* is slow due to the necessary rotation of Thr203 [242,391]. Ultrafast dynamics probing this inverse proton transfer in the conversion from I to A showed it to be in agreement with a proton tunneling mechanism [395]. Subsequent ground state conversion from A to I was observed to be very slow [391]. There is also a large barrier in the conversion of the B ground state to the A ground state, consistent with the observed relaxation time being several hours [52].

Other factors that may influence the ESPT have also been investigated. One issue is the possible photo-induced *cis-trans* isomerism of the chromophore, which may be attributed as the mechanism for the radiationless conversion of HBDI. Such behaviour is well known in similar molecules, and often the *trans* state is non-fluorescent [52]. This *cis-trans* isomerism also leads to wider discussion about the role the protein matrix plays. Whilst the ground state of the GFP chromophore is defined as planar, studies have shown that in the excited state a twisting can

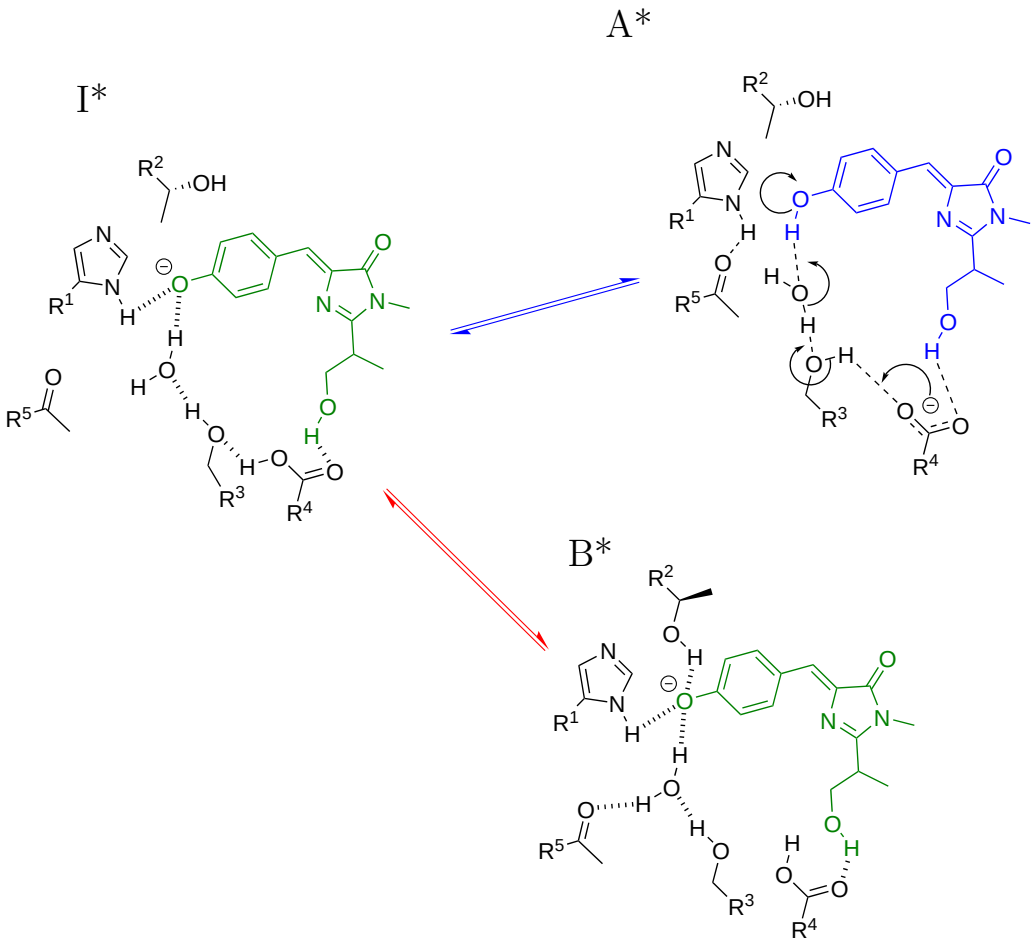

Fig. 7.2: The proposed mechanism by which deprotonation of the chromophore occurs forming the anion. A* is the neutral chromophore, I* is the deprotonated intermediate state and B* is another anionic structure formed by rotation of the amino acid side chains. In each conformation the chromophore is in its S_1excited state. Adapted from [242].

occur, to the point at which the two rings are perpendicular to each other [396]. A review by Tonge and Meech [58] has summarised the work that has been carried out in trying to elucidate the mechanism of this isomerism and importantly the location at which it occurs. The general consensus, presently, is that this internal conversion between states stems from a single bond rotation, with a small barrier, likely to be coordinated around the bridging carbon atom. The intersection point at which the ground and excited states interact is also thought to be at a 90° twist angle. There is still much debate, however, about which single bond rotation has the largest effect [397–399].

Further work to analyse and understand this ESPT has been the subject of much research and several groups have reported more detailed steps, including the photocyclic process, hidden excited states, intermediate states and single crystal spectroscopy [395, 400–403]. It should be noted that, whilst model systems of the GFP protein matrix provide a decent general view of the process, it is far from perfect. There are still unanswered issues to be addressed in order to provide a complete understanding of the ESPT and the mechanism of fluorescence in GFP. This is where computational models have been sought after to complement experiments.

Theoretical models have attempted to determine if the proton transfer is concerted or sequential and provide the potential energy landscape for this reaction. One of the first theoretical studies used molecular dynamics simulations to study the proton shuttle [404]. Their proposed mechanism initially involved forcing the proton to move from the phenol moiety on the chromophore to a nearby, trapped water molecule. The next two steps were proton transfer from the water to serine residue and then from the serine residue to an anionic glutamate residue. These last two steps were found to occur rapidly, 10 fs for each. By forcing the initial movement of the proton, the proposed mechanism was still debatable. The emergence of studies employing quantum calculations added further doubt to this mechanism.

From their quantum study, Wang disagreed with the proposed mechanism and reported it to be the reverse, *i.e.* the proton on the chromophore is the final one to move. Instead, the mechanism begins with proton movement from the serine residue to the glutamate, followed by a proton from the water moving to the serine and finally from the chromophore to the water [405, 406]. The mechanism was concerted and fast, along a single barrier with no intermediates. This study strongly supported the work of Zhang *et al.* who, using TDDFT, observed a concerted proton transfer mechanism, consisting of low barrier hydrogen bonds [407]. The histidine group, despite not being directly involved, was found to be important in stabilising the transition state.

As to whether the three proton transfers are concerted or sequential is still the subject of much research. Vendrell *et al.* performed quantum dynamic simulations using MCTDH on a proton-wire model. The simulations showed the proton shuffle along the wire to be very fast, leading the authors to conclude the mechanism is concerted and synchronous [408]. The timescale of a couple of hundred femtoseconds was determined for the dynamics. Zhang *et al.* also concluded the mechanism to be concerted, with a single barrier, however potentials calculated along each proton transfer step showed the presence of small barriers. The smallest barrier initially was seen for proton transfer from methanol (acting as the serine residue) to an acetate group (acting as the glutamate) and therefore this proton moves first [409]. Kang *et al.* suggested the ground state proton transfer (GSPT) and ESPT could be considered as both concerted and asynchronous [410]. They argued that without stable intermediates the process must be concerted, but state that the movement of the protons shows asynchronous character.

The use of a proton-wire model for studying the mechanism has been extensively used by Vendrell and co-workers. One study performed molecular mechanics simulations on the solvated GFP and further determined the photoactive state to be a

$\pi\pi^*$ state [411]. Another study reached the same conclusion as Kang *et al.* that the proton transfer mechanism is concerted, yet asynchronous [412].

Recently, Zhou and Han have discussed the latest theoretical methods they have employed to study the ESPT in GFP [80]. Crucially, they emphasised that studying the time-evolution of the ESPT requires "on-the-fly" dynamic simulations to be performed. This statement, in addition to elucidating the mechanism, was the motivation in choosing to study this system with direct dynamics.

7.2 The model

For investigating the proton transfer mechanism in GFP using DD-vMCG, a suitable model is required. Such a model should include all the important components to represent the real protein matrix, but be small enough to prevent the calculations becoming too demanding. The chosen model is shown in Figure 7.3 and is based upon previous models used to study the proton transfer [405–407, 409]. The model contains the full, protonated chromophore with a Ser65 residue connected to the imidazolinone component. The protein matrix around the chromophore consists of an acetate accepting group (representing the Glu222 residue), a methanol group (representing the Ser205 residue) and a water molecule. To prevent the model becoming too large, the histidine (His148) residue, seen to stabilise the water, was excluded.

Figure 7.3 shows the numbering scheme for each atom in the model and is useful when referring to specific clusters and atoms. Using this numbering scheme, the proposed proton shuttle mechanism is as follows: step 1, movement of H32 to the acetate oxygen (O40); step 2, transfer of H44, the proton water to the (now deprotonated) methanol oxygen (O31) and step 3 movement of the chromophore phenolic hydrogen (H24) to the water oxygen (O42).

The potential energy curves (PECs) were calculated along each step in the

a)

b)

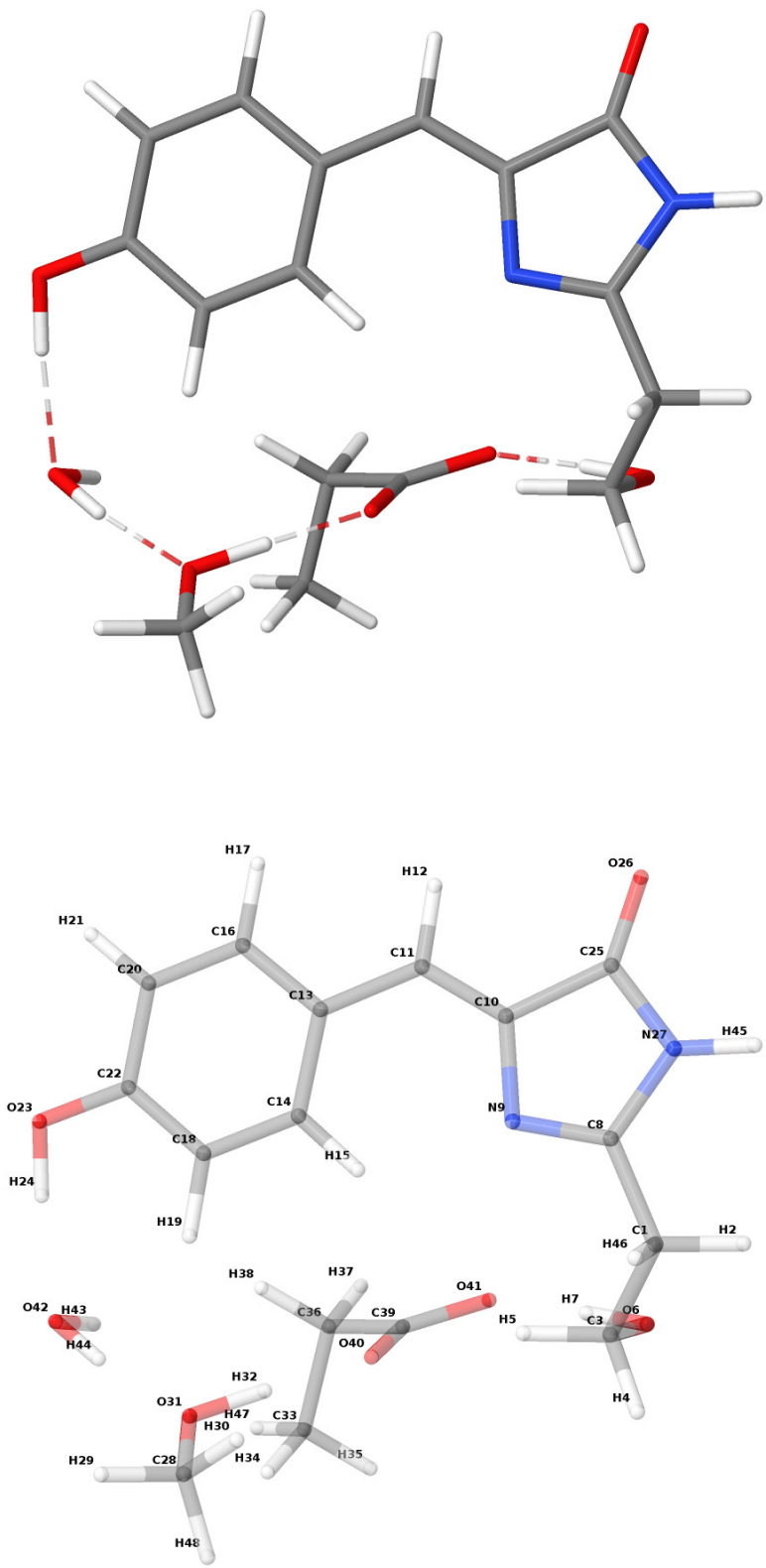

Fig. 7.3: The model system used to represent the protein environment surrounding the chromophore, including the important residues in the proton shuttle mechanism. (a) shows the overall structure and (b) shows the numeric labelling for each atom.

mechanism. Whilst not essential for the DD-vMCG simulations, it provided an insight into each individual proton transfer. Following a geometry optimisation, a scan was performed along step 1 of the mechanism. The bond distance between the proton (H32) and the receiving oxygen (O40) was decreased in increments of 0.05 Å to simulate the transfer of this proton. The energies of the ground and excited states were calculated at each step during this scan and the results plotted. From the plotted curves, the bond length corresponding the lowest energy structure with H32, now bonded to O40, was determined. This bond length was then assumed to correspond to the optimised structure and fixed prior to performing the scan for step 2. The procedure was then repeated for step 2 and step 3 to give three PECs for transfer of each proton in the proposed mechanism.

These calculations were performed using DFT and TDDFT for the excited state. Given the large size of the system, the choice of DFT is sensible, especially when optimising the structure and calculating excited state energies. The choice of functional, however, then becomes a decisive factor. For all calculations, the functional ωB97X-D was used. This hybrid functional is a re-development of a long-range corrected functional to include empirical atom-atom dispersion corrections. The functional contains 100% long-range exchange and around 22% short-range exchange [413]. The inclusion of long-range corrections and dispersion makes this functional ideal for studying the proton transfer mechanism, especially for a large system, where hydrogen-bonding and dispersion interactions are important [414]. The cc-pVDZ basis set of Dunning was chosen [168]. As the focus of this study is proton movement, a large basis set ensures accurate description of the molecular orbitals, but not so large as to make the calculations too computationally intensive. All calculations were run using QChem [253].

For the direct dynamic simulations, the DD-vMCG method, as implemented in the Quantics package, was used [309]. The calculations were performed using

Cartesian coordinates and so included all 43 atoms in the model. Propagations allowing all atoms to move would be prohibitively expensive and so only a small selection were allowed to move, with the rest remaining frozen. Two states, the ground state and the first excited state, were used in the calculation. The basis set was reduced to the more modest 6-31G* to decrease the time taken for electronic structure calculations. Each Gaussian wavepacket (GWP) was placed on the S_1 state, where the proton transfer occurs.

The use of a database allowed geometries and energies from previous calculations to be stored and called upon, reducing the number of electronic structure calculations needed. The database is vital for systems of this size, where quantum chemical calculations are demanding. Multiple runs were performed, with the propagation time varying from 400 to 600 fs. This timescale was chosen from a combination of computational limits found by testing the direct dynamics, but also previous studies showing there to be significant dynamics within the first few hundred femtoseconds [408].

7.3 Results

7.3.1 Potential Energy Curves

The PECs calculated along each of the proton transfer steps at the ωB97X-D/cc-pVDZ level of theory are shown in Figure 7.4. The first step, movement of the proton from the methanol (H32) to the acetate (O40) is shown in Figure 7.4(a). The longer bond lengths correspond to the proton still being bonded to the methanol, whilst the shorter bond lengths show the proton transfer to have occurred, with the proton now bonded to the acetate. The PES shows there to be a barrier to transfer in both the ground and excited states. The barrier is very small and there is no discernible minimum following movement of the proton. This suggests that, even if the proton successfully moves to the acetate group, there exists a barrierless pathway for it to

(a)

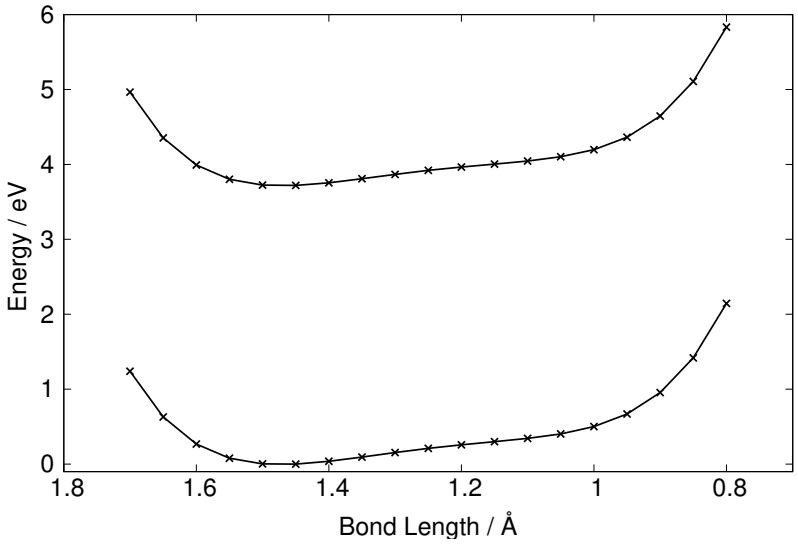

(b)

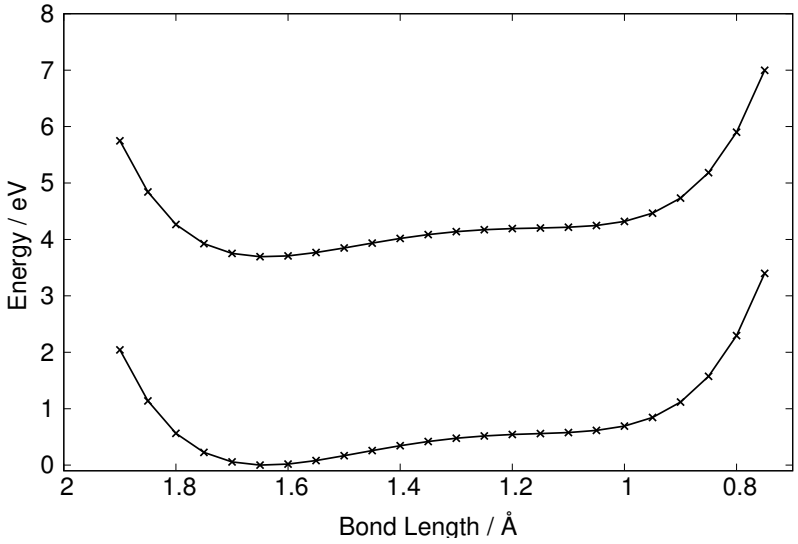

(c)

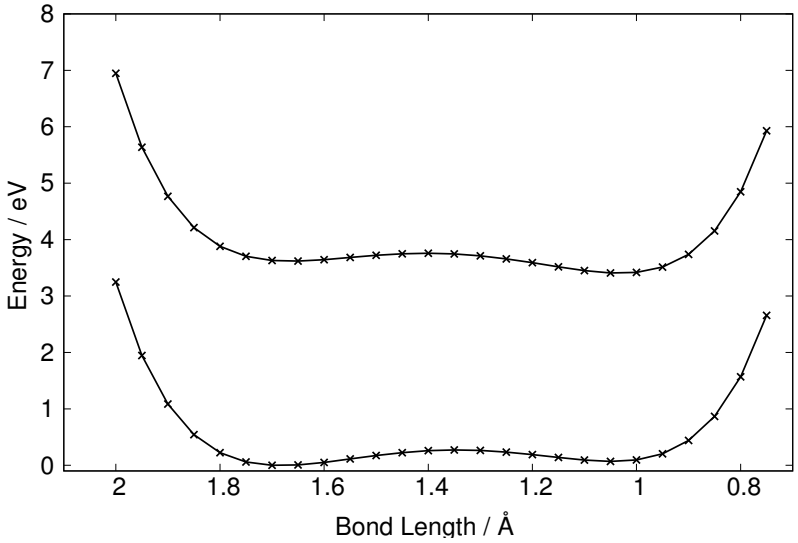

Fig. 7.4: Potential energy curves for each proton transfer in the HBDI deprotonation mechanism. The bond length is between the proton that is moving and the receiving oxygen atom. (a) is step 1: methanol to acetate transfer (b) is step 2: water to methanol transfer and (c) is step 3: chromophore to water transfer.

return to the methanol. Similar features are seen in Figure 7.4(b) for step 2, the water proton (H44) moving to the deprotonated methanol (O31). This PEC was calculated after the completion of step 1, movement of H32 to O40. Again, a small barrier is observed when moving this proton, although the barrier is lower in the excited stated compared with the ground state. Again, no minimum exists on the product side of the proton transfer, indicating a barrierless return of the proton to the water. The presence of a barrier here is not surprising since the step essentially involves deprotonation of water to form hydroxide. This assumes, however, that the mechanism occurs in a step-wise fashion. The lack of minima may result from the system not being allowed to relax along each scan. Optimising the system once each step has completed may indicate the presence of a minimum.

The final step, deprotonation of the chromophore (H24) to re-form water (O42), after completion of steps 1 and 2, is shown in Figure 7.4(c). Notably, the PEC for this step looks different to the previous two steps. The ground state shows a symmetric double well potential separated by a barrier. Furthermore, the minimum on the right is higher in energy. In the excited state, the double well is asymmetric and the right hand minimum, corresponding to the deprotonated chromophore and reformation of water, is lower in energy. The potential is nearly barrierless, suggesting this final step occurs readily.

The results from the PECs at first seem contradictory to the literature, which states the proton transfer mechanism is concerted, with only a single barrier. Analysis, however, shows the results to be consistent with previous studies. The lack of minima in the PECs for step 1 and 2 show there to be no stable intermediates. This supports a concerted process, in agreement with work by Kang *et al.* [410]. The calculated PECs support similar work undertaken by Zhang *et al.* [409]. The lack of any stable intermediates suggests that steps 1 and 2 are concerted and correlated. It is likely that the initial movement of the proton from methanol to the acetate

induces the water proton to move towards the methanol. The lack of barrier in step 3 means this proton will move as soon as the proton in step 2 begins to move.

The PECs are useful indicators for probing each step in the proton transfer mechanism. It is important to note that the model used here does not contain the full protein matrix that surrounds the chromophore and excludes residues that may be important. One example is a histidine residue, which hydrogen bonds to the water and likely stabilises it. Indeed, this stabilisation effect may alter the PEC for step 2, reducing, or even removing, the barrier.

7.3.2 Direct Dynamic Simulations

Moving forward from calculating the PECs along each step of the proton transfer, direct dynamic simulations were then performed. Initially, only one Gaussian wavepacket was used, with the aim of providing a quick calculation to test the dynamics and provide geometries and energies for the database. Subsequently, several direct dynamic calculations were run, varying the number of wavepackets, length of the simulation time and which atoms were selected to be frozen/unfrozen. From the direct dynamic calculations, the most promising results have come from calculations using 16 GWPs, running for 500 fs. In this particular simulation atoms 23, 24, 28, 31-44 and 47 were allowed to move. This corresponds to the O-H phenolic group of the chromophore, the C-O-H group of the methanol, the entire acetate group and the water. The need to unfreeze the entire acetate group, as opposed to just the O-H, was justified because free rotation of this molecule may facilitate encouraging the initial proton to move across.

From the direct dynamic simulations, changes in the geometry of the model system over time can be viewed. This takes into account the trajectory of the GWP and shows the overall movement of the model system. Figure 7.5(a) shows the molecular structure at 130 fs along the trajectory of one of the GWPs. This clearly shows the O-H bond of the methanol to have increased to the extent that

a)

b)

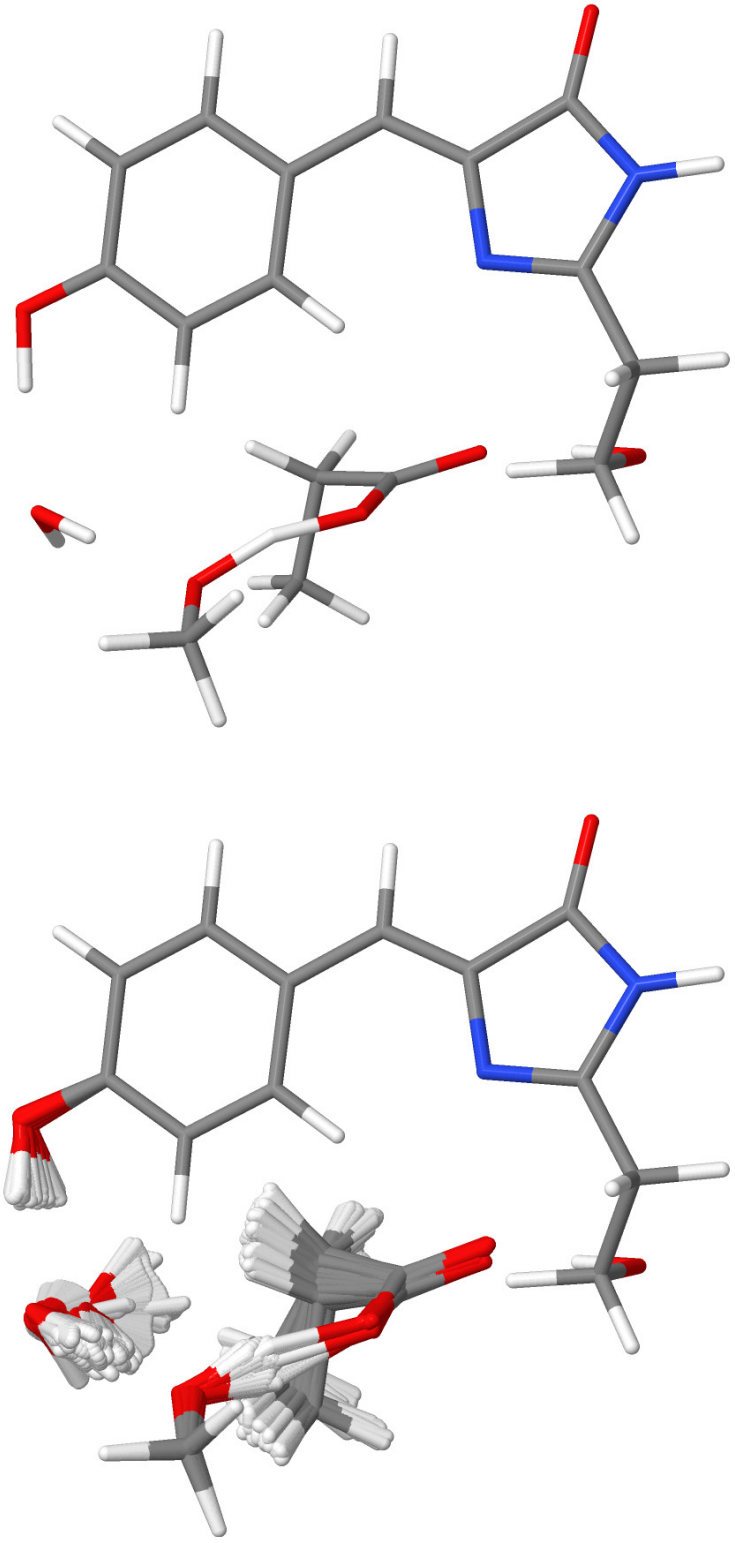

Fig. 7.5: A snapshot of the molecular structure along a GWP trajectory during the direct dynamic simulation. (a) is the structure at 130 fs and clearly shows the formation of a bond between the acetate oxygen and th methanol hydrogen. (b) shows the molecular structures overlaid for all timesteps and illustrates the motion of each atom throughout the simulation.

bond formation between the acetate oxygen and the proton occurs, indicative of step 1 in the mechanism. This exciting feature highlights the promise of direct dynamic simulations. The direct dynamics shows no simultaneous bond formation between the water proton and the methanol oxygen - step 2. Referring back to the PECs for step 1, this is perhaps not surprising, given that no minimum was seen following transfer of the proton to the acetate. The PES constructed during the direct dynamics is likely to be similar to the PEC for step 1.

It is possible that steps 2 and 3 will only occur once the methanol proton has moved closer to the acetate group, and the O-H methanol bond breaks. If this occurs, then whether steps 2 and 3 are concerted and synchronous, or if initial movement of the water proton encourages the phenolic proton to move, will be of great interest.

The overall movement of the structure along the trajectory during the entire simulation is shown in Figure 7.5(b). As expected, large amplitude motions are seen for the molecules for which all atoms were allowed to move; the water and acetate group. It is also clear that the formation of a bond between the acetate occurred numerous times and was long lasting. The water molecule shows large motion, but this is mostly rotation and translation; little change to the O-H bond lengths is observed. The phenolic O-H bond bends during the course of the simulation, but no bond-lengthening is observed. Large amplitude motions are also observed for the methyl and methylene groups of the acetate. It is unclear, however, whether allowing this motion is beneficial to the proton transfer.

In addition to the changes in geometry, the trajectories each GWP follows can also be viewed. These are shown in Figure 7.6 for the atoms important to step 1, H32, O31 and C28. The majority of trajectories (illustrated as grey lines in Figure 7.6) are bunched together, indicating that they follow similar pathways. The non-grey lines are evidence of trajectories where the wavepacket has become spread out and

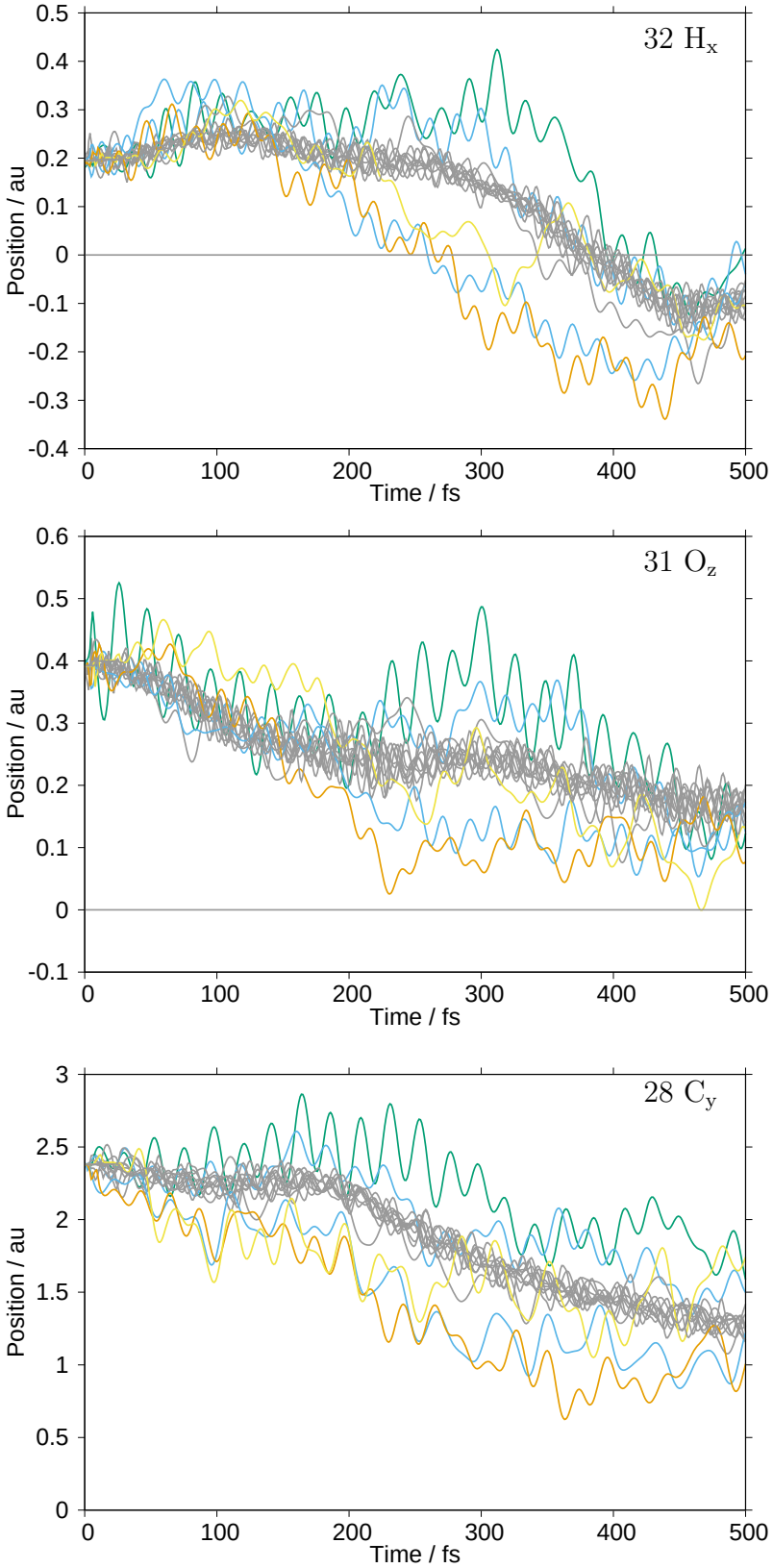

Fig. 7.6: Trajectories of the GWPs for selected atoms along a specific Cartesian axis. The numbers for each atom relate to the model structure shown in 7.3. Grey lines shown GWPs with similar trajectories and non-grey lines correspond to GWPs exhibiting interesting behaviour where the wavepacket has become more spread out and exploring different geometries.

is exploring more different geometries. These trajectories are more interesting and show the wavepacket exploring different areas of the PES. None of these trajectories correspond to the geometry changes for the GWP shown in Figure 7.5. Viewing the geometry changes for these more dispersed trajectories also shows the formation of a bond between the methanol proton (32H) and the acetate oxygen at different times during the simulation. In addition, one of these trajectories results in large motion of the water molecule. The gross Gaussian population (GGP) [238, 415], weighted for each of the GWPs, was evaluated for the five disperse trajectories. The GGPs were found to be large for several of these trajectories, with values of 0.095 (light blue line), 0.076 (dark green line) and 0.016 (yellow line).

The expectation values for the O-H distances between the receiving oxygen and transferring proton for each step in the mechanism is shown in Figure 7.7. Extracting this information from the simulation allows correlation between the movements each

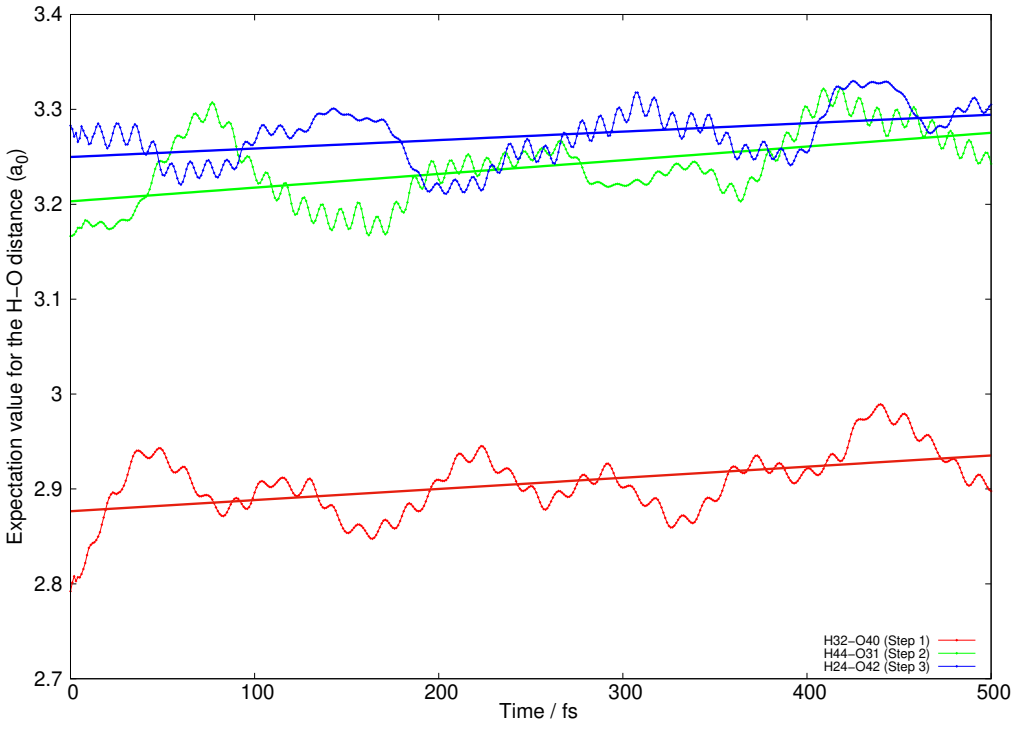

Fig. 7.7: Expectation values for the H-O distance for each of the three proton transfers in the GFP model system during the simulation.

proton to be examined. In agreement with the optimised structure, the initial O-H distance is smaller between H32 and O40 (methanol to acetate, step 1) than the succeeding two proton transfers. The expectation values for all three O-H bond distances oscillate throughout the simulation. A decrease in the expectation value is indicative of the proton moving towards its receiving oxygen. The line of best fit for each step shows a positive gradient, indicating the protons were moving further away from the receiving oxygen. The oscillations relate to the large bending motion of the O-H bond as observed in Figure 7.5(b).

A clear correlation is observed between proton transfer steps 2 and 3, which shows an out of phase relationship. This relationships occurs for 400 fs before the oscillations become in phase. Such a relationship suggests that, as the O-H bond length increases for step 2 (water to methanol transfer), the phenolic O-H bond length decreases. After 400 fs, the in-phase correlation between these steps indicates concerted bending motion, shown in Figure 7.7 as both the O-H bond lengths in step 2 and 3 simultaneously increase. The timestep at which steps 2 and 3 become in-phase corresponds to the downward motion in position observed in the GWP trajectories (Figure 7.6), consistent with movement of the proton in step 1.

The O-H distance expectation value for step 1 shows more frequent oscillations than in the other two steps. This is consistent with the observed changes in geometry (Figure 7.5), which during the simulation showed the large bending of the O-H bond. Clearly, the H32 to O40 distance decreases sufficiently for bond formation to occur as evident in Figure 7.5. This change in geometry is shown occurring for a single trajectory whereas the expectation values in Figure 7.7 consider all the trajectories. There is some correlation between the bending motion in this step and step 2, although the more frequent oscillations in step 1 show that the relationship is not strong.

The expectation values presented here support previous studies that propose

the proton transfer mechanism is asynchronous. This is evident from the weak correlation between step 1 and step 2 and the strong correlation between step 2 and step 3. The change in O-H bond distance for all three steps after 400 fs relates to all three protons moving together, although from the changes in geometry only the proton in step 1 comes close to fully transferring across. Longer simulation times may be required to observe the full proton transfer mechanism.

7.3.3 Further work

The direct dynamic simulations performed so far have shown promise and demonstrate the applicability of the method to large molecular systems. When applied to the ESPT in GFP, the results show there is strong motion of the methanol proton towards the acetate oxygen replicating step 1. This demonstrates the effectiveness of using the DD-vMCG method and supports its use for modelling this system. The next steps are to improve and further refine the model. Further simulations will allow the full proton transfer to be observed, leading to important insights into the mechanism. There are various approaches to implement in the direct dynamic simulations to refine the model. Increasing the length of the dynamics is one option, since the timescale for the full proton transfer occurs over picoseconds. Running the dynamics for this amount of time substantially increases the running time of the calculation and may not be useful given studies have shown the greatest dynamic activity to occur over hundreds of femtoseconds. Another option is increasing the number of GWPs in the simulation. Again, this will increase the computational cost but allows more variation in the PESs explored by the GWPs.

The key to realising the full proton transfer mechanism, however, depends upon which atoms are frozen and which are allowed to move. Initial studies, where only the protons and oxygen atoms involved in the mechanism were allowed to move, were too restrictive. Allowing more of the system to move by unfreezing atoms showed more promise and encouraged greater proton motion towards the receiving

oxygen. Further direct dynamic simulations must address the balance between which atoms must be allowed to move and those that should remain frozen. Based on the results described here, two approaches immediately become obvious. The first is to completely unfreeze the methanol group and the second is to freeze the methyl group of the acetate.

In all simulations the majority of atoms in the chromophore are frozen and the planar structure retained. Allowing the chromophore itself to move may be important, especially as studies have suggested twisting occurs in the excited state as well as *cis-trans* isomerism. Movement of the chromophore may also cause the molecules involved in the proton wire to contract. This will decrease the distances between the protons and receiving oxygens. Such changes as easy to implement within the model and direct dynamics calculations.

The addition of extra residues into the model may also need to be considered, particularly the histidine residue, which has been seen to stabilise the water molecule. This is undesirable however, as including new molecules into the model will require re-calculating the Hessian, which was already intensive given the size of the system.

7.4 Conclusion

Direct dynamic methods, where the PES is calculated "on-the-fly", offer alternative and efficient ways for performing quantum dynamic calculations. These methods offer more flexibility and are practical in the study of larger systems. Of greatest benefit is the removal of the need to pre-calculate and fit PESs. The DD-vMCG method outlined in this chapter shows much promise and has been applied to a large system involving multiple molecules. This system is a model for the GFP matrix and has been used to investigate the excited state proton transfer that gives rise to the observed green fluorescence. The proposed mechanism involves three steps, all involving the transfer of protons, ending ultimately in deprotonation of

the chromophoric phenol.

Prior to running direct dynamic calculations, PECs were calculated along each of the proton transfer steps. A small barrier to transfer was observed for each step. For steps 1 and 2, no minimum on the product side of the PEC, corresponding to full transfer of the proton, was observed. A minimum was present in step 3, forming an asymmetric double well potential in the excited state, for which the products (resulting in deprotonation of the phenol) are lower in energy. Without performing the direct dynamic simulations, these PECs already show evidence for a concerted, yet asynchronous mechanism.

Even though PECs were calculated along each step of the mechanism, obtaining fitted surfaces for this model would be very demanding. These demands stem from the size of the system and the large number of normal modes present. This makes direct dynamics simulations suitable for studying this system. Conversely, the size of the system and multiple steps in the mechanism provide the ideal test for using the direct dynamics.

From the simulations large oscillations, corresponding to lengthening of the methanol O-H bond, were repeatedly observed, and inspection of the geometries showed the formation of a bond between the methanol proton and the acetate oxygen. This is promising, as the direct dynamics is given no instruction for which proton to move, except for freezing certain atoms the system and yet this proton shows significant motion and starts to transfer across. From expectation values of the O-H bond length, there is some correlation between the steps in the mechanism, particularly steps 2 and 3. Overall, the distance between the receiving oxygen and transferring H for each step increases during the simulation and by 400 fs the oscillations of all three steps are in phase.

For future direct dynamic simulations to achieve full proton transfer, several options need to be considered. Increasing the duration of the simulation and the

number of GWPs is one possibility, although initial results suggest this will make little difference. The choice of which atoms to freeze and which to allow to move is vital. Addressing this is key to achieving full proton transfer, from which further details regarding the mechanism can be elucidated.

Nevertheless, the work undertaken here shows the applicability of direct dynamic methods, especially for large molecules or systems. The success of the DD-vMCG method in studying HBDI and the corresponding protein matrix is highly encouraging and makes it suitable for studying other systems.

Chapter 8

Conclusions

The interaction of light with molecules is critical to numerous fundamental processes and plays a vital role in daily life. Understanding these processes and the features involved is, therefore, essential and justifiably the subject of extensive research. Absorption of photons excites molecules to higher energy electronic states from which a cascade of relaxation pathways are possible. Some of these are radiative, where the emission of a photon results in fluorescence of phosphorescence. Non-radiative pathways can quickly dissipate excess energy through vibrational motion and relax the molecule to lower energy states. Intersystem crossing transits the molecule between states of different multiplicity. Points at which electronic states cross are also possible, leading to topological features such as conical intersections. Here, nuclear and electronic motion become coupled leading to breakdown of the BOA. Theoretical models examining excited states and conical intersections are challenging, but provide the required understanding of the system's photodynamics.

In this thesis, the photodynamics of a range of different aromatic molecules have been studied using quantum dynamics. The key component of any quantum dynamic calculation is the potential energy surface (PES) upon which the wavepacket propagates. Generating these surfaces requires the use of electronic structure methods. The work presented here has also examined various ways by which these PES can be obtained and the intricate balance of accuracy against efficiency.

Aromatic molecules are often found in highly conjugated systems such as fluorescent proteins and much focus has also been dedicated to the photophysics of the green fluorescent protein (GFP). The photoelectron spectrum of the anionic GFP chromophore, HBDI has been measured and observed to contain low intensity vibrational structure. The spectrum is complicated by the presence of the nearby S_1 state that lies just below the detachment threshold. This can result in vibrational autodetachment, causing the spectrum to broaden. To better understand the stability and electronic structure of the HBDI anion, its components were studied: imidazolide, phenoxide, bis-imidazoloxy and bis-phenoxy.

In Chapter 3, a simple linear vibronic coupling Hamiltonian was constructed for each molecule to calculate the photoelectron spectrum. Here, the PES were obtained by calculating a series of *ab initio* points along important normal modes. These points were then fitted to give a vibronic coupling Hamiltonian. The calculations were performed using IP-EOM-CCSD with a 6-31+G* basis set. As the molecular symmetry of imidazolide, phenoxide and bis-imidazoloxy was C_{2v} only the totally-symmetric a_1 modes were important. To investigate possible coupling with the D_1 state, cuts along the b_2 modes of imidazolide and the a_2 modes of phenoxide were also calculated. The most stable conformation of bis-phenoxy was found not to be planar, instead having the rings twisted out of the plane. This lowered the symmetry to C_1 and so all normal modes needed to be considered.

As experimental data was available for the photoelectron spectrum of imidazolide and phenoxide, the accuracy of the model Hamiltonian could be tested. The $^2B_1 \longleftarrow \tilde{X}^1A_1$ spectrum for imidazolide and $^2B_1 \longleftarrow \tilde{X}^1A_1$ spectrum of phenoxide showed good agreement with experiment, reproducing the main features. For both, however, it was necessary to increase the energy of the D_0 state and adjust the values of several on-diagonal linear coupling constants. Despite this, the parameters obtained from IP-EOM-CCSD calculations provide reasonably good surfaces. The

$^2B_1 \longleftarrow \tilde{X}^1A_1$ spectrum for imidazolide contains two progressions from C-C and N-C stretching modes as well as coupling with the b_2 N-C-N asymmetric stretch mode. The photoelectron spectrum for phenoxide is dominated by a ring deformation/C-O stretch mode. A secondary series of shoulder peaks formed from the hot band of an a_2 vibration were not reproduced by the model. The detachment energies showed phenoxide to be less stable than imidazolide, with the HBDI anion being more stable than both.

The $^2A_2 \longleftarrow \tilde{X}^1A_1$ photoelectron spectrum of bis-imidazoloxy showed an increase in fine structure, although all at low intensity. The main progression was from a C-C stretch, with numerous combination peaks present. No coupling to the D_1 state was found. Like the HBDI anion, the important normal modes were found to involve bending vibrations and motion of the bridge. The bis-phenoxy spectrum was similar to bis-imidazoloxy, however the important normal modes were found to be out of plane vibrations and distortion of the ring. Bis-phenoxy was also the only molecule where the S_1 state lay below the detachment energy, resembling the electronic states for HBDI. It is proposed that vibrational autodetachment would occur upon excitation to this state.

The results presented suggest the fine structure of the HBDI spectrum can be attributed to vibrational motion of the bridge, which becomes more important when the molecule is planar. The photoelectron spectrum and electronic states of HBDI can be attributed to its constituents. The fine structure is largely due to the imidazolinone group and bridge, whereas the phenoxide moiety influences the position of the S_1 state relative to D_0.

Like benzene, the photochemistry of phenol has been extensively studied. The main interest has been the O-H stretching mode, along which conical intersections between several electronic states have been found. These interactions can populate an unbound state leading to dissociation of the hydroxy proton. TR-PES is a useful

technique for probing the photodynamics of a system. Theoretical models to simulate experimental TR-PES require PES for the excited states as well as the ionised states. The quality of these PES are evident from the agreement with experimental photoelectron and absorption spectra. Chapter 5 outlines a linear vibronic coupling Hamiltonian for the photoelectron and absorption spectra of phenol.

The vibronic coupling Hamiltonian was calculated by fitting a series of *ab initio* points along the important normal modes. From symmetry arguments, cuts were calculated along the totally symmetric a_1 modes, b_2 modes and a_2 modes. The calculations utilised CASSCF with a 6-31+G* basis and were found to provide good surfaces. The lack of electron correlation was, however, highlighted for one mode by the change in sign required for the κ parameter. The existence of a CI was found between the two lowest energy ion surfaces and a cut along the vector leading to this intersection was included in the model.

Using a Hamiltonian consisting of two states and seven modes, the $^2B_1 \longleftarrow \tilde{X}^1A_1$ and $^2A_2 \longleftarrow \tilde{X}^1A_1$ photoelectron spectra were calculated. For each transition, the calculated spectra reproduced the main features seen in the experimental spectra. The assignment of the fine structure, however, differed to that previously reported and a new assignment is proposed. The assignment for the $^2B_1 \longleftarrow \tilde{X}^1A_1$ transition also includes a C-O stretch mode. The $^2A_2 \longleftarrow \tilde{X}^1A_1$ transition was found to involve the same normal modes as the transition to D_0 and not from a separate mode as previously suggested. As for the conical intersection, diabatic state populations showed that excitation to the $^2A_2(D_1)$ state leads to 30% population transfer to the lower state within 200 fs.

For the $^1B_2 \longleftarrow \tilde{X}^1A_1$ absorption spectrum, a two state, seven mode Hamiltonian was used. There was coupling between S_1 and S_2, however the O-H mode containing the CI was found not to be needed to reproduce the S_1 absorption spectrum. Assignment of the fine structure showed there to be no dominant mode,

consisting of a mixture of fundamental and combination bands.

Future work will make use of these surfaces for calculating the TR-PES of phenol. Inclusion of the pre-fitted diabatic states, using the nuclear degrees of freedom r (O-H stretch) and θ (C-C-O-H torsion), are necessary for the S_0, S_1 and S_2 states.

Chapter 6 introduced an automated way for constructing simple models of PESs. Using only the gradients and second derivatives from Hessians calculated at the ground state equilibrium geometry and FC point, PESs for all normal modes can be obtained. These potentials are then expressed as shifted Harmonic potentials. The utility of this approach is to provide rapid and efficient methodology for calculating absorption and emission spectra.

To test the model, the absorption and emission spectra for a series of anthracene derivatives and linear polyacenes of increasing size were calculated. Additionally, the performance of quantum chemical methods for calculating the bright L_a and dark L_b states can be assessed. The chosen level of theory, TDDFT, systematically predicted S_1 energies which were lower than experimental data and showed severe deviations for the case of naphthalene.

The model was successfully able to replicate the absorption and emission spectra for benzene, anthracene, pentacene, 9-methyl anthracene and 9-hydroxymethyl anthracene. Comparison between the anthracene spectra obtained using the model and from explicit fittings showed them to be very similar. The progression in the tetracene absorption was shorter than experiment, but was successfully obtained through explicit fitting along the normal mode. The methyl and hydroxymethyl derivative were shown experimentally to look similar to anthracene but occur at lower energies. The model was able to successfully reproduce the spectra, but, crucially, was also able to determine to differences in energy. The fine structure present in these molecules was found to originate from similar vibrational modes involving C-H bending and ring distortion. A low frequency ring breathing mode was also in-

volved. In general, the harmonic character for the PES along the important normal modes lends itself to the success of the model.

Naphthalene proved to be complex, with a very weak transition to S_1 and domination by the strong S_2 transition. TDDFT failed to calculate the correct S_1 energy and predicted it to reside close to S_2. This resulted in an absorption spectrum vastly different to experiment. Only by adjusting the energies to match experiment and arbitrarily introducing a coupling term between the S_1 and S_2 states were reasonable spectra obtained. This failure of the model was attributed to problems with the electronic structure theory, but did highlight its limitations when strong non-adiabaticity is involved.

The model was also unable to calculate spectra where solvent effects were strong. This was the case for anthracene-9-carboxylic acid and anthracene-9-carbaldehyde. Experimentally, these spectra were broad due to interaction with the solvent, whilst the calculated spectra remained well resolved, showing clear vibrational fine structure. Eventually, a sharper emission spectrum for AnCA was obtained by changing the solvent to basic water, for which the calculated spectrum showed good agreement. Rotation of the COOH groups and the formation of dimers were responsible for the effect of solvent on the spectrum. Difficulty in calculating the absorption spectrum for AnCHO again highlighted the limits of this model and also where anharmonicity become important.

Using this methodology, the Stokes shift for each molecule was also calculated and whilst discrepancies with experimental data did occur, the overall agreement was good. The model was largely successful in showing the relative differences in Stokes shift between the molecules and correctly predicted the inverse shift observed for AnCHO. For efficient prediction of the electronic spectra of large aromatic polyacenes, the model presented here performs well. Even though amendments can be made to the model to incorporate non-adiabatic behaviour, it is best suited for

molecules with relatively harmonic potentials and small coupling to other states.

The models detailed in Chapters 3-5 all required the PES to be constructed prior to running quantum dynamic calculations. Such an approach is restrictive and realistically is best suited for the study of small molecules only. In Chapter 7 the DD-vMCG method was introduced where the PES is calculated "on-the-fly", removing the need for pre-fitted surfaces. Direct dynamics provides increased flexibility and also allows larger systems to be studied. To demonstrate this, the method was applied to study the ESPT in GFP, an important mechanism for the fluorescence of green light. A proton wire model including the HBDI chromophore, amino acid residues and water was built to represent the protein matrix that is vital in facilitating the proton shuttle. The large size of the model was ideal for showing the DD-vMCG method can be successfully for quantum dynamic simulations.

PECs calculated for the movement of each proton in the proposed mechanism showed steps 1 and 2 to have small barriers and no discernible minimum on the product side of the transfer. For step 3, an asymmetric double well potential, with no barrier, was obtained. The PEC for this step had a minimum for the products that was lower in energy than the starting conformation. The PECs obtained are indicative of a concerted, but asynchronous proton transfer mechanism, supporting conclusions from previous studies.

The direct dynamics simulations were shown to be suitable to study this system. Limitations in the model itself indicated the key is finding the right balance between which atoms to freeze and which to allow to move. Increasing the number of GWPs is another option. The calculations exhibited significant motion of the transferring proton in step 1. Lengthening of the O-H bond was observed, to the extent that bond formation occurs with the receiving oxygen, although complete transfer is not accomplished. From the trajectories of the GWPs, significant movement occurs after 300 fs, similar to the timescale for proton transfer reported in the literature.

The expectation values for the three O-H bonds involved in the mechanism oscillate throughout the simulation, indicating correlated O-H bending motion. Towards the end of the simulation, all three O-H bond lengths oscillate in-phase, suggesting concerted motion for all three protons.

The results from the DD-vMCG are encouraging and show much promise for larger, more complex systems comprising multiple molecules. This also allows reaction dynamics to be studied and mechanisms elucidated.

Appendix A

Gauge Transformation and Diabatic States

A.1 Example of a Gauge Transformation

A standard gauge transformation is:

$$\mathbf{S^g}(\mathbf{R}) = \begin{pmatrix} \cos\theta(\mathbf{R}) & \sin\theta(\mathbf{R}) \\ -\sin\theta(\mathbf{R}) & \cos\theta(\mathbf{R}) \end{pmatrix} \tag{A.1}$$

from which $\tilde{\tau} = \nabla\theta + \tau$, with $\tilde{\tau} = \langle\tilde{\Psi}_1|\nabla\tilde{\Psi}_2\rangle$ being the derivative coupling in the transformed electronic basis.

For example, one can consider a two state system, where the set of states, (g), contains two electronic states, Φ_1 and Φ_2 both of which are real. Here, the matrix of derivative couplings has the following form:

$$\mathbf{F}^g = \begin{pmatrix} 0 & \tau \\ -\tau & 0 \end{pmatrix} \tag{A.2}$$

where $\tau = \langle\Psi_1|\nabla\Psi_2\rangle$.

A.2 Constructing Diabatic States

A simple approach to construct diabatic states begins by introducing a gauge field tensor with the quantities:

$$A_{\alpha\beta,ij} = \left\langle \Phi_i \left| \frac{\partial^2}{\partial R_\alpha \partial R_\beta} \Phi_j \right. \right\rangle - \left\langle \Phi_i \left| \frac{\partial^2}{\partial R_\beta \partial R_\alpha} \Phi_j \right. \right\rangle \tag{A.3}$$

A necessary condition for equation (2.25) to have a solution is the following equality for the second derivative of the adiabatic-diabatic transformation matrix:

$$\frac{\partial^2}{\partial R_\alpha \partial R_\beta} \mathbf{S} = \frac{\partial^2}{\partial R_\beta \partial R_\alpha} \mathbf{S} \tag{A.4}$$

This equality implies that the components of the gauge field tensor are equal to zero and so the tensor becomes:

$$A_{\alpha\beta,ij} = \sum_{k \notin g} F_{\alpha,ik} F_{\beta,jk} - F_{\beta,ik} F_{\alpha,jk} \tag{A.5}$$

hence, strictly diabatic states are possible so long as the derivative coupling between states inside the group to those outside can be ignored.

Appendix B

Character Tables

Character table for C_s

	E	σ_h	linear, rotations	quadratic
A'	1	1	x, y, R_z	x^2, y^2, z^2, xy
A"	1	-1	z, R_x, R_y	yz, xz

Character table for C_{2v}

	E	$C_2(z)$	$\sigma_v(xz)$	$\sigma_v(yz)$	linear, rotations	quadratic
A_1	1	1	1	1	z	x^2, y^2, z^2
A_2	1	1	-1	-1	R_z	xy
B_1	1	-1	1	-1	x,R_y	xz
B_2	1	-1	-1	1	y,R_x	yz

Product table for C_{2v}

	A_1	A_2	B_1	B_2
A_1	A_1	A_2	B_1	B_2
A_2	A_2	A_1	B_2	B_1
B_1	B_1	B_2	A_1	A_2
B_2	B_2	B_1	A_2	A_1

Character table for D_{2h}

	E	$C_2(z)$	$C_2(y)$	$C_2(x)$	i	$\sigma(xy)$	$\sigma(xz)$	$\sigma(yz)$	linear, rotations	quadratic
A_g	1	1	1	1	1	1	1	1		x^2, y^2, z^2
B_{1g}	1	1	-1	-1	1	1	-1	-1	R_z	xy
B_{2g}	1	-1	1	-1	1	-1	1	-1	R_y	xz
B_{3g}	1	-1	-1	1	1	-1	-1	1	R_x	yz
A_u	1	1	1	-1	-1	-1	-1	-1		
B_{1u}	1	1	-1	-1	-1	-1	1	1	z	
B_{2u}	1	-1	1	1	-1	1	-1	1	y	
B_{3u}	1	-1	-1	1	-1	1	1	-1	x	

Product table for D_{2h}

	A_g	B_{1g}	B_{2g}	B_{3g}	A_u	B_{1u}	B_{2u}	B_{3u}
A_g	A_g	B_{1g}	B_{2g}	B_{3g}	A_u	B_{1u}	B_{2u}	B_{3u}
B_{1g}	B_{1g}	A_g	B_{3g}	B_{2g}	B_{1u}	A_u	B_{3u}	B_{2u}
B_{2g}	B_{2g}	B_{3g}	A_g	B_{1g}	B_{2u}	B_{3u}	A_u	B_{1u}
B_{3g}	B_{3g}	B_{2g}	B_{1g}	A_g	B_{3u}	B_{2u}	B_{1u}	A_u
A_u	A_u	B_{1u}	B_{2u}	B_{3u}	A_g	B_{1g}	B_{2g}	B_{3g}
B_{1u}	B_{1u}	A_u	B_{3u}	B_{2u}	B_{1g}	A_g	B_{3g}	B_{2g}
B_{2u}	B_{2u}	B_{3u}	A_u	B_{1u}	B_{2g}	B_{3g}	A_g	B_{1g}
B_{3u}	B_{3u}	B_{2u}	B_{1u}	A_u	B_{3g}	B_{2g}	B_{1g}	A_g

Appendix C

Additional theory for electronic structure methods

C.1 Many-Body Perturbation Theory

In perturbation theory the Hamiltonian is partitioned into a zeroth-order term, $\hat{H}_0$, a small parameter, λ, and a perturbation, $\hat{V}$:

$$\hat{H} = \hat{H}_0 + \lambda\hat{V} \tag{C.1}$$

The zeroth-order Hamiltonian is selected such that the eigenstates Φ_n and corresponding eigenvalues, E_n, are known and thus satisfy the eigenvalue equation:

$$H^0|\Phi_n\rangle = E_n^{(0)}|\Phi_n\rangle \tag{C.2}$$

A similar partition can also be done for the wavefunction and the energy:

$$\Psi = \Psi_0 + \lambda\Psi_1 + \lambda^2\Psi_2 + \lambda^3\Psi_3 + \ldots \tag{C.3a}$$

$$E = E_0 + \lambda E_1 + \lambda^2 E_2 + \lambda^3 E_3 + \ldots \tag{C.3b}$$

Substitution of equation (C.3a) and equation (C.3b) into the Schrödinger equation

yields:

$$\begin{aligned}&(\hat{H}^{(0)} + \lambda\hat{V})(|\Phi_0\rangle + \lambda|\Psi_0^{(1)}\rangle + \lambda^2|\Psi_0^{(2)}\rangle + \cdots) \\ &= (E_0^{(0)} + \lambda E_0^{(1)} + \lambda E_0^{(2)} + \cdots)(|\Phi_0\rangle + \lambda|\Psi_0^{(1)}\rangle + \lambda^2|\Psi_0^{(2)}\rangle + \cdots)\end{aligned} \tag{C.4}$$

Introducing the following condition, $\langle\Phi_0|\Psi_0^{\lambda}\rangle = 1$, known as intermediate normalisation, and collecting terms in equation (C.4) by order in λ provides the following.

Zeroth-Order

The zeroth-order energy is identical to that defined by equation (C.2):

$$H^0|\Phi_0\rangle = E_0^0|\Phi_0\rangle \tag{C.5a}$$

$$E_n^0 = \langle\Psi_n^0|\hat{H}_0|\Psi_n^{(0)}\rangle \tag{C.5b}$$

First-Order

Collecting the terms that are first-order with respect to λ gives the following:

$$\hat{H}^0|\Psi_0^{(1)} + \hat{V}|\Phi_0\rangle = E_0^{(0)}|\Psi_0^{(1)}\rangle + E_0^{(1)}|\Phi_0\rangle \tag{C.6}$$

Multiplying through by Ψ_n^{0*} and imposing that $\langle\Phi_0|\Psi_0^{(1)}\rangle = 0$ provides the first-order correction to the energy:

$$E_0^{(1)} = \langle\Phi_0|\hat{V}|\Phi_0\rangle \tag{C.7}$$

One can also determine the first-order correction to the wavefunction. Starting again from equation (C.6) but now multiplying through on the left by $\Psi_n^{(0)*}$ and integrating gives:

$$E_n^{(0)}\langle\Phi_n|\Psi_0^{(1)}\rangle + \langle\Phi_n|\hat{V}|\Phi_0\rangle = E_0^{(0)}\langle\Phi_n|\Psi_0^{(1)}\rangle \tag{C.8}$$

Expanding $|\Psi_n^{(1)}\rangle$ in a basis such as: $|\Psi_n^{(1)}\rangle = \sum_m a_m|\Phi_n\rangle$ leads to the first-order wavefunction correction:

$$|\Psi_0^{(1)}\rangle = -\sum_{n\neq 0} \frac{\langle\Phi_0|\hat{V}|\Phi_0\rangle}{E_n^{(0)} - E_0^{(0)}}|\Phi_n\rangle \tag{C.9}$$

Second-Order

Proceeding as before, but now collecting terms that are second-order with respect to λ gives:

$$\hat{H}^0|\Psi_0^{(2)} + \hat{V}|\Phi_0^{(1)}\rangle = E_0^{(0)}|\Psi_0^{(2)}\rangle + E_0^{(1)}|\Phi_0^{(1)}\rangle + E_0^{(2)}|\Phi_0\rangle \tag{C.10}$$

Using the same approach as for first-order results in the second-order energy correction:

$$E_0^{(2)} = \langle\Phi_0|\hat{V}|\Psi_0^{(1)}\rangle \tag{C.11}$$

Inspection of the above equations shows the need to utilise the first-order correction to the wavefunction as determined previously, equation (C.9). Substituting this into the second-order energy correction provides:

$$E_0^{(2)} = -\sum_{n\neq 0} \frac{|\langle\Phi_0|\hat{V}|\Phi_n\rangle|^2}{E_n^{(0)} - E_0^{(0)}} \tag{C.12}$$

In principle one could continue and extend this to third, fourth, fifth and n-order corrections to the energy.

C.2 CASPT2

The formulation as outlined for perturbation theory in Section 3.4 can be applied to a multiconfiguration case, specifically the CAS.

Here, the reference function is chosen to be the CAS wavefunction and the fol-

lowing notation is presented,

$$\Psi_0 = |\text{CASSCF}\rangle = |0\rangle$$

$$|K\rangle = \text{Rest of the CAS configuration space}$$

$$|SD\rangle = \text{Singly and Doubly excited CSFs with respect to the CAS reference}$$

$$|X\rangle = \text{Remaining configuration space}$$

Implementing the above leads to an expression for the zeroth-order Hamiltonian of the multireference system:

$$\hat{H}_0 = \hat{P}_0\hat{F}\hat{P}_0 + \hat{P}_K\hat{F}\hat{P}_K + \hat{P}_{SD}\hat{F}\hat{P}_{SD} + \hat{P}_X\hat{F}\hat{P}_X \tag{C.13}$$

with the assumption that the operator $\hat{F}$ can be written as a Fock-type one-electron operator:

$$\hat{F} = \sum_{p,q} f_{pq}\hat{E}_{pq} \tag{C.14a}$$

$$f_{pq} = h_{pq} + \sum_{r,s} D_{rs}[(pq|rs) - \frac{1}{2}(pq|rs)] \tag{C.14b}$$

From the zeroth-order Hamiltonian, the first-order wavefunction includes contributions from single and double configurations, which interact directly with the CAS reference wavefunction, and so can be written as:

$$\Psi_1 = \sum_{pqrs} c_{pqrs}\hat{E}_{pq}\hat{E}_{rs}\Psi_0 \tag{C.15}$$

where p,q,r and s cannot be active. The above *ansatz* is also referred to as 'internally contracted'. The first-order equation for the coefficients can take the more general form:

$$(\boldsymbol{F} - E_0\boldsymbol{S})\boldsymbol{C} = -\boldsymbol{W} \tag{C.16}$$

where **F** is the Fock Matrix in the function space V_{SD} and **S** the corresponding overlap matrix. **C** refers to the vector coefficients of the first-order wavefunction, equation (C.15)) and **W** a vector representing the interaction between V_{SD} and the reference function. The elements of **F**, shown in equation (C.17) require up to fourth order density matrices and is a major segment of the computational time in CASPT2 calculations:

$$\langle pqrs|\hat{F}|p'q'r's'\rangle = \sum_{mn} f_{mn}\langle\Psi_0|\hat{E}_{sr}\hat{E}_{qp}\hat{E}_{mn}\hat{E}_{p'q'}\hat{E}_{r's'}|\Psi_0\rangle \tag{C.17}$$

From this formulation, a summary of the steps taken during a CASPT2 calculation can be given. The first step requires a CASSCF calculation to be performed. From this, the Fock matrix is transformed into a pseudo-diagonal form. Further transformations are then applied to the two-electron integrals with at least two indices which relate to the occupied orbitals. The **S** matrix is computed and diagonalised and the second-order energy is calculated. This leaves a large system of linear equations to solve, which incorporates the coupling arising from the non-diagonal blocks of the Fock matrix [416, 417].

C.2.1 Intruder States - The level shift solution

A potential problem that can arise in CASPT2 calculations are the emergence of intruder states. These occur when the electronic configurations in V_{SD} space have a zeroth-order energy close to that of the reference energy *i.e.* $E_\mu \approx E_0$. Intruder states can be removed by using the level-shifting technique introduced by Roos *et al.* [418]. The theory behind this technique involves rewriting the zeroth-order Hamiltonian by including a level shift operator, $\hat{P}_i$, and a small positive number, ε:

$$\hat{H} = \hat{H}_0 + \varepsilon\hat{P}_i \tag{C.18}$$

From this, one can obtain a first-order equation with a shifted Hamiltonian:

$$(\hat{H}_0 - E_0 + \varepsilon)\tilde{\Psi}_1 = -(\hat{H}_1 - E_1)\Psi_0 \tag{C.19}$$

from which the second-order energy is reformulated as:

$$\tilde{E}_2 = -\sum_{i=1}^{M} \frac{|\langle \phi_i | \hat{H}_1 | \Psi_0 \rangle|^2}{\epsilon_i - E_0 + \varepsilon} \tag{C.20}$$

This removes intruder states, but results in an second-order energy that depends upon ε. Since the value of ε is chosen arbitrarily without any real conviction then the quality of the resulting calculation is called into question. The second-order energy can though be back transformed to an unshifted value, E_2^{LS}, the level-shifted corrected second-order energy:

$$\tilde{E}_2 = E_2 + \varepsilon \sum_{i=1}^{M} |\tilde{C}_i|^2 \left(1 + \frac{\varepsilon}{\epsilon_i - E_0}\right) \tag{C.21}$$

Assuming $\epsilon_i - E_0 \gg \varepsilon$,

$$E_2 \approx \tilde{E}_2 - \varepsilon \left(\frac{1}{\omega} - 1\right) \equiv E_2^{LS}. \tag{C.22}$$

Appendix D

Additional theory on DFT and TDDFT

D.1 The Hohenberg-Kohn Theorem

The proof of the first HK theorem is based upon a *reductio ad absurdum* argument where one considers two external potentials, V_{ext} and V'_{ext}, which are different, but provide the same electron density. These external potentials form two differing Hamiltonians and hence provide two different ground state wavefunction with energies, E_0 and $E_0^{'}$, respectively. This can be illustrated as:

$$V_{\text{ext}} \Rightarrow \hat{H} \Rightarrow \Psi \Rightarrow \rho(\mathbf{r}) \Leftarrow \Psi' \Leftarrow \hat{H}' \Leftarrow V'_{\text{ext}} \tag{D.1}$$

After making the assumption that both wavefunctions give the same electron density, Ψ' can be used as a guess for the Hamiltonian $\hat{H}$. Invoking the variational principle yields:

$$E_0 < \langle \Psi' | \hat{H} | \Psi' \rangle = \langle \Psi' | \hat{H}' | \Psi' \rangle + \langle \Psi' | \hat{H} - \hat{H}' | \Psi' \rangle \tag{D.2}$$

Repeating the procedure with the primed and unprimed terms swapped leads to two variational expressions for E_0 and E'_0:

$$E_0 < E'_0 + \int \rho(\mathbf{r}) \left\{ V_{\text{ext}} - V'_{\text{ext}} \right\} \mathrm{d}\mathbf{r} \tag{D.3a}$$

$$E'_0 < E_0 - \int \rho(\mathbf{r}) \left\{ V_{\text{ext}} - V'_{\text{ext}} \right\} \mathrm{d}\mathbf{r} \tag{D.3b}$$

Addition of these two expressions gives the nonsensical result:

$$E_0 + E_0' < E_0' + E_0, \qquad i.e. \qquad 0 < 0 \tag{D.4}$$

From this, it is clear that two different external potentials cannot output the same ground state electron density. This proves *the external potential uniquely determines that ground state electron density and hence the energy.* The implications from this are that the individual components that define the energy must also be a functional of the electron density, such that:

$$E_0[\rho_0] = T[\rho_0] + E_{\text{ee}}[\rho_0] + E_{\text{Ne}}[\rho_0] \tag{D.5}$$

This expression can be re-formulated to split the components into those that depend on the system, specifically the potential energy due to the attraction of nuclei and electrons, and those deemed system independent. The latter, known as the HK functional, contains the kinetic energy and the electron-electron repulsions:

$$E_0[\rho_0] = \int \rho_0(\mathbf{r}) V_{\text{Ne}} \mathrm{d}\mathbf{r} + \mathrm{F}_{\text{HK}}[\rho_0] \tag{D.6}$$

where

$$\mathrm{F}_{\text{HK}}[\rho] = T[\rho] + E_{\text{ee}}[\rho] \tag{D.7}$$

The consequence of this is remarkable; if $\mathrm{F}_{\text{HK}}[\rho]$ is known exactly then the Schrödinger equation could be solved exactly. Whilst tantalising, the explicit forms of both $T[\rho]$ and $E_{\text{ee}}[\rho]$ are, regrettably, unknown. The Coulomb interaction, $J[\rho]$ can be withdrawn from the electron-electron functional leaving forms for the kinetic energy and the remaining non-classical contributions to be determined.

D.2 Points regarding the Kohn-Sham approach to DFT

The Kohn Sham approach as outlined in Section 3.9.3 shares many similarities with the derivation of Hartree-Fock theory. There are, however, important physical and theoretical differences between the two. Some of the major contentious issues are briefly commented on below.

Exchange Correlation: HF vs. KS

The theoretical frameworks of HF and DFT both contain components referred to as exchange, correlation or the combinatorial exchange-correlation. The context of these terms, whilst similar between the different *ab initio* methods here, do not have the same meaning. In the HF regime, the correlation energy is defined as the difference between the exact energy and the HF energy. In the KS approach, the energy of the correlation hole is the difference between the total exchange-correlation hole and the exchange part,

$$h_c^{\mathrm{KS}}(\mathbf{r}_1;\mathbf{r}_2) = h_{xc}^{\mathrm{KS}}(\mathbf{r}_1;\mathbf{r}_2) - h_x^{\mathrm{KS}}(\mathbf{r}_1;\mathbf{r}_2) \tag{D.8}$$

Do the KS Orbitals mean anything?

The use of orbitals in the KS equations is a necessary requirement to construct the ground state density. It is has also been explicitly stated that there is categorically no wavefunction in DFT. Taken together, these two statements lead to an obvious and contentious question: Do the Kohn-Sham orbitals mean anything? Or perhaps more formally, do they have any physical meaning whatsoever? This is a question that has caused strong debate amongst theoreticians, physicists and chemists, with arguments given for both 'yes' and 'no' [419–421].

Basis Sets in DFT

The employment of basis sets, especially in wavefunction based methods, is used to construct molecular orbitals. Larger basis sets result in a higher quality wavefunction. There is a strong dependence on basis set size of both the accuracy of the calculated result and the computational expense. It was, and still is, assumed the basis set dependency is not as strong for DFT and that accuracy is affected more by the functional used. Even so, atomisation energies were found to differ between basis sets, with the larger sets, such as aug-cc-pVTZ, found to perform worse than Pople's 6-311+G(3df,2p) [422]. Lynch *et al.* showed the addition of diffuse functions to be more important is DFT energy calculations than standard wavefunction theories [423].

Boese *et al.* studied the role of basis sets in DFT. They found Pople basis sets to perform best. They also concluded, that the need to reach the basis set limit in DFT was not necessary as the overall error from DFT itself is larger [424]. Whilst developing basis sets for DFT could be a solution, the major issue then becomes which functional is best to use..

A recent overview on the situation regarding basis sets and DFT have addressed the issue and arguments on both sides, with a particular focus on Dunning's correlation-consistent bases [425].

D.3 Adiabatic Connection

The adiabatic connection formula, used as a starting point for consideration of hybrid functionals, can be summarised as the following [426]. The well known Hellmann-Feynman theorem can be expressed in the following form:

$$\frac{\partial}{\partial\lambda}\langle\Psi_\lambda\left|H_\lambda\right|\Psi_\lambda\rangle = \left\langle\Psi_\lambda\left|\frac{\partial H_\lambda}{\partial\lambda}\right|\Psi_\lambda\right\rangle \tag{D.9}$$

Assuming the Hamiltonian operator can be take the form:

$$\mathbf{H}_\lambda = \mathbf{T} + \mathbf{V}_{\text{ext}}(\lambda) + \lambda \mathbf{V}_{\text{ee}} \tag{D.10}$$

then inputting this Hamiltonian into the Hellmann-Feynman equation leads to:

$$H_\lambda = T + V_{\text{ext}}(\lambda) + \lambda V_{\text{ee}} \tag{D.11a}$$

$$\frac{\partial}{\partial \lambda} \langle \Psi_\lambda | H_\lambda | \Psi_\lambda \rangle = \left\langle \Psi_\lambda \left| \frac{\partial V_{\text{ext}}(\lambda)}{\partial \lambda} + V_{\text{ee}} \right| \Psi_\lambda \right\rangle \tag{D.11b}$$

Integrating between the limits of 0 and 1 represents the transition from a non-interacting reference system to a real, fully interacting system. Performing the integration, with the assumption the density remains constant, leads to:

$$\int_0^1 \frac{\partial}{\partial \lambda} \langle \Psi_\lambda | H_\lambda | \Psi_\lambda \rangle = \int_0^1 \left\langle \Psi_\lambda \left| \frac{\partial V_{\text{ext}}(\lambda)}{\partial \lambda} + V_{\text{ee}} \right| \Psi_\lambda \right\rangle \mathrm{d}\lambda \tag{D.12a}$$

$$\langle \Psi_1 | H_1 | \Psi_1 \rangle - \langle \Psi_0 | H_0 | \Psi_0 \rangle = E_1 - E_0 = \int_0^1 \left\langle \Psi_0 \left| \frac{\partial V_{\text{ext}}(\lambda)}{\partial \lambda} + V_{\text{ee}} \right| \Psi_\lambda \right\rangle \mathrm{d}\lambda \tag{D.12b}$$

From here, the integration for just the external potential term can be expressed as the two limits:

$$\int_0^1 \left\langle \Psi_\lambda \left| \frac{\partial V_{\text{ext}}(\lambda)}{\partial \lambda} + V_{\text{ee}} \right| \Psi_\lambda \right\rangle \mathrm{d}\lambda = \int \rho(\mathbf{r}) \left(\int_0^1 \frac{\partial V_{\text{ext}}(\mathbf{r}, \lambda)}{\partial \lambda} \mathrm{d}\lambda \right) \mathrm{d}\mathbf{r} \tag{D.13}$$

$$= \int \rho(\mathbf{r}) \left(V_{\text{ext}}(1) - V_{\text{ext}}(0) \right) \mathrm{d}\mathbf{r} \tag{D.14}$$

$$= \int \rho(\mathbf{r}) V_{\text{ext}}(1) \mathrm{d}\mathbf{r} - \int \rho(\mathbf{r}) V_{\text{ext}}(0) \mathrm{d}\mathbf{r} \tag{D.15}$$

Since for the non-interacting system, *i.e.* at the integral limit of 0, there will no contribution to the electron-electron interaction, V_{ee}, then the energy for this system is given by:

$$E_0 = \langle \Psi_0 | T | \Psi_0 \rangle + \int \rho(\mathbf{r}) V_{\text{ext}}(0) \mathrm{d}\mathbf{r} \tag{D.16}$$

From equations (D.12), (D.13) and (D.16) emerges an equation for E_1:

$$E_1 = \langle\Psi_0|T|\Psi_0\rangle + \int \rho(\mathbf{r})V_{\text{ext}}(1)\mathrm{d}\mathbf{r} + \int_0^1 \langle\Psi_\lambda|V_{\text{ee}}|\Psi_\lambda\rangle\,\mathrm{d}\lambda \tag{D.17}$$

Setting $V_{\text{ext}}(1) = V_{\text{ne}}$ and making use of equation (3.79a) implies that:

$$J[\rho] + E_{\text{xc}}[\rho] = \int_0^1 \langle\Psi_\lambda|V_{\text{ee}}|\Psi_\lambda\rangle\mathrm{d}\lambda \tag{D.18}$$

hence by integrating the electron-electron term and subtracting the Coulombic term, one arrives at the exchange-correlation energy. Making use of reduced density matrices and the definition of the exchange-correlation hole, the right hand side of the above equation can be expressed as:

$$\langle\Psi_\lambda|V_{\text{ee}}|\Psi_\lambda\rangle = \frac{1}{2}\int \frac{\rho_2(\lambda,\mathbf{r}_1,\mathbf{r}_2)}{|\mathbf{r}_1-\mathbf{r}_2|}\mathrm{d}\mathbf{r}_1\mathrm{d}\mathbf{r}_2 \tag{D.19}$$

$$= \frac{1}{2}\int \frac{\rho_1(\mathbf{r}_1)\rho_2(\mathbf{r}_2)}{|\mathbf{r}_1-\mathbf{r}_2|}\mathrm{d}\mathbf{r}_1\mathrm{d}\mathbf{r}_2 + \frac{1}{2}\int \frac{\rho_1(\mathbf{r}_1)h_{\text{xc}}(\lambda,\mathbf{r}_1,\mathbf{r}_2)}{|\mathbf{r}_1-\mathbf{r}_2|}\mathrm{d}\mathbf{r}_1\mathrm{d}\mathbf{r}_2 \tag{D.20}$$

$$= J[\rho] + \frac{1}{2}\int \frac{\rho_1(\mathbf{r}_1)h_{\text{xc}}(\lambda,\mathbf{r}_1,\mathbf{r}_2)}{|\mathbf{r}_1-\mathbf{r}_2|}\mathrm{d}\mathbf{r}_1\mathrm{d}\mathbf{r}_2 \tag{D.21}$$

where the exchange-correlation hole, V_{xc}^{HOLE} is defined as:

$$V_{\text{xc}}^{\text{HOLE}}(\lambda,\mathbf{r}_1) = \frac{1}{2}\frac{h_{\text{xc}}(\lambda,\mathbf{r}_1,\mathbf{r}_2)}{|\mathbf{r}_1-\mathbf{r}_2|}\mathrm{d}\mathbf{r}_2 \tag{D.22}$$

$$E_{\text{xc}} = \int_0^1 \langle\Psi_\lambda|V_{\text{xc}}^{\text{HOLE}}(\lambda)|\Psi_\lambda\rangle\mathrm{d}\lambda \tag{D.23}$$

$$E_{\text{xc}} = \int \rho(\mathbf{r})\left(\int_0^1 V_{\text{xc}}^{\text{HOLE}}(\lambda,\mathbf{r})\mathrm{d}\lambda\right)\mathrm{d}\mathbf{r} \tag{D.24}$$

from which one arrives at the adiabatic connection formula:

$$E_{\text{xc}} \approx \frac{1}{2}\left(\langle\Psi_0|V_{\text{xc}}^{\text{HOLE}}(0)|\Psi_0\rangle + \langle\Psi_1|V_{\text{xc}}^{\text{HOLE}}(1)|\Psi_1\rangle\right) \tag{D.25}$$

which taken in its crudest form shows $V_{\mathrm{xc}}^{\mathrm{HOLE}}$ to be linear with respect to λ with the integral given as average values of the end points.

D.4 Time Dependent Density Functional Theory Framework

As was done with standard DFT, one can refer to the Schrödinger equation in its TD many-body form:

$$i\hbar\frac{\partial\Psi(\mathbf{x},t)}{\partial t} = \hat{H}\Psi(\mathbf{x},t) \tag{D.26}$$

with a Hamiltonian expressed as:

$$\hat{H}(t) = \hat{T} + \hat{V}(t) + \hat{W} \tag{D.27}$$

The kinetic energy operator retains the same form as the static, however the potential operator is now time dependent:

$$\hat{V} = \sum_{j=1}^{N} \nu(\mathbf{r},t) \tag{D.28}$$

whilst $\hat{W}$ is the particle-particle interaction:

$$\hat{W} = \frac{1}{2}\sum_{\substack{j,k \\ j\neq k}}^{N} \omega(|r_1 - r_k|) \tag{D.29}$$

From a practical viewpoint, it is useful to consider a system evolving from its ground state when subject to a time dependent external potential being switched on a t_0, such that:

$$v(\mathbf{r},t) = v_0(\mathbf{r}) + v_1(\mathbf{r},t)\theta(t-t_0) \tag{D.30}$$

The density operator of an N-electron system can be defined as:

$$\hat{n}(\mathbf{r}) = \sum_{l=1}^{N} \delta(\mathbf{r} - \mathbf{r}_l) \tag{D.31}$$

and the current-density operator as:

$$\hat{\mathbf{j}}(\mathbf{r}) = \frac{1}{2i}\sum_{l=1}^{N}[\nabla_l \delta(\mathbf{r}-\mathbf{r}_l) + \delta(\mathbf{r}-\mathbf{r}_l)\nabla_l] \tag{D.32}$$

Taking the expectation values of equation (D.31) and (D.32) gives the time-dependent versions of the density and current density[a]:

$$n(\mathbf{r},t) = \langle\Psi(t)|\hat{n}(\mathbf{r})|\Psi(t)\rangle \tag{D.33a}$$

$$\mathbf{j}(\mathbf{r},t) = \langle\Psi(t)|\hat{\mathbf{j}}(\mathbf{r})|\Psi(t)\rangle \tag{D.33b}$$

Taking the equation of motion of the expectation value for the density operator yields:

$$i\frac{\partial}{\partial t}n(\mathbf{r},t) = \langle\Psi(t)|[\hat{n}(\mathbf{r}),\hat{H}(t)]|\Psi(t)\rangle \tag{D.34}$$

Computing the commutator between $\hat{n}(\mathbf{r})$ and $\hat{H}(t)$ results in the continuity equation:

$$\frac{\partial}{\partial t}n(\mathbf{r},t) = -\nabla.\mathbf{j}(\mathbf{r},t) \tag{D.35}$$

The continuity equation indicates that the rate of change of the number of particles in a given volume is the result of the flux of the particle current across the volume boundary. Applying the same procedure to the current density gives the the analogous equation:

$$i\frac{\partial}{\partial t}j(\mathbf{r},t) = \langle\Psi(t)|[\hat{j}(\mathbf{r}),\hat{H}(t)]|\Psi(t)\rangle \tag{D.36}$$

from which the commutator is:

$$\frac{\partial}{\partial t}j_\mu(\mathbf{r},t) = -n(\mathbf{r},t)\frac{\partial}{\partial r_\mu}\nu(\mathbf{r},t) - \mathrm{F}_\mu^{\mathrm{KIN}}(\mathbf{r},t) - \mathrm{F}_\mu^{\mathrm{INT}}(\mathbf{r},t) \tag{D.37}$$

Here, vectors $\mathrm{F}_\mu^{\mathrm{KIN}}$ and $\mathrm{F}_\mu^{\mathrm{INT}}$ are the kinetic and interaction effects due to the internal force densities of the many-body system.

[a]The equation of motion of the expectation value of a generic operator $\hat{O}(t)$ is: $i\frac{\partial}{\partial t}\langle\Psi(t)|\hat{O}(t)|\Psi(t)\rangle = \langle\Psi(t)|i\frac{\partial}{\partial t}\hat{O}(t) + [\hat{O}(t),\hat{H}(t)]|\Psi(t)\rangle$

By defining the momentum of the system as:

$$\mathbf{P}(t) = \int \mathrm{d}^3 r \; \mathbf{j}(\mathbf{r}, t) \tag{D.38}$$

then integration of equation (D.37) provides:

$$\frac{\partial}{\partial t}\mathbf{P}(t) = -\int \mathrm{d}^3 r \; n(\mathbf{r}, t)\nabla\nu(\mathbf{r}, t) \tag{D.39}$$

This shows that the rate of change of the total momentum is equal to the total external force acting upon it.

D.5 The Runge-Gross Theorem

The proof of the Runge-Gross theorem proceeds from the equation of motion for the current density, equation (D.36). As $\Psi(t)$ and $\Psi'(t)$ evolve from the same initial state, Ψ_0 then:

$$\begin{aligned} \frac{\partial}{\partial t}\left\{\mathbf{j}(\mathbf{r}, t) - \mathbf{j}'(\mathbf{r}, t)\right\}\Big|_{t=t_o} &= -i\langle\Psi_0|[\hat{\mathbf{j}}(\mathbf{r}), \hat{H}(t_0) - \hat{H}'(t_0)]|\Psi_0\rangle \\ &= -n(\mathbf{r}, t_0)\nabla\left\{\nu(\mathbf{r}, t_0) - \nu'(\mathbf{r}, t_0)\right\} \end{aligned} \tag{D.40}$$

Invoking the earlier condition that the smallest integer of k for which equation (3.96) holds is greater than 0, then the first time derivative currents are equal. More importantly, however, differences do appear between $\mathbf{j}$ and $\mathbf{j}'$ in the higher order time derivatives. Proceeding from here, applying the equation of motion k times yields:

$$\frac{\partial^{k+1}}{\partial t^{k+1}}\left\{\mathbf{j}(\mathbf{r}, t) - \mathbf{j}'(\mathbf{r}, t)\right\}\Big|_{t=t_o} = -n(\mathbf{r}, t_0)\nabla\left\{\nu_k(\mathbf{r}) - \nu'_k(\mathbf{r})\right\} \tag{D.41}$$

From this, one can conclude that $\mathbf{j}(\mathbf{r}, t) \neq \mathbf{j}'(\mathbf{r}, t)$.

The following step now proceeds by demonstrating that different current densities result in the densities themselves being different. From the continuity equation

(D.35), the $(k+1)$ time derivative can be expressed as:

$$\left.\frac{\partial^{k+2}}{\partial t^{k+2}}\left\{\mathbf{n}(\mathbf{r},t)-\mathbf{n}'(\mathbf{r},t)\right\}\right|_{t=t_o} = -\nabla.\frac{\partial^{k+1}}{\partial t^{k+1}}\left\{\mathbf{j}(\mathbf{r},t)-\mathbf{j}'(\mathbf{r},t)\right\}|_{t=t_o} = -\nabla.(\eta_0(\mathbf{r})\nabla_{\omega_k}(\mathbf{r})) \tag{D.42}$$

where: $\omega_k(\mathbf{r}) = \nu_k(\mathbf{r}) - \nu'_k(\mathbf{r})$ and $\eta_0(\mathbf{r}) = \eta(\mathbf{r}, t_0)$.

The proof that different current densities give rise to different densities comes from showing that the right hand side of equation (D.42) does not finish identically.

Making use of Green's integral formulation, a relation can be derived such that:

$$\int \mathrm{d}^3r\; n_0(\mathbf{r})(\nabla\omega_k(\mathbf{r}))^2 = -\int d^3r\omega_k(\mathbf{r})\nabla.(n_0(\mathbf{r})\nabla\omega_k(\mathbf{r})) + \oint \mathrm{d}\mathbf{S}.(n_0(\mathbf{r})\omega_k(\mathbf{r})\nabla\omega_k(\mathbf{r})) \tag{D.43}$$

The crux of the Runge-Gross theorem is that for all physically real potentials, the surface integral on the right hand side of equation (D.43) disappears [427]. Making the assumption that $\omega_k \neq 0$ prevents the left hand side from vanishing, a consequence of which is a non-negative integrand. This result also causes the remaining term on the right hand side to be non-vanishing and thus suggests that $\nabla.(n_0(\mathbf{r})\nabla\omega_k(\mathbf{r})) \neq 0$.

The Runge-Gross theorem therefore shows that two densities, $n(\mathbf{r}, t)$ and $n'(\mathbf{r}, t)$ being subjected to two different potentials, $\nu(\mathbf{r}, t)$ and $\nu'(\mathbf{r}, t)$ will differ infinitesimally after t_0. This confirms the existence of a one-to-one mapping between the TD densities and TD potentials. From here, it can also be inferred that the external potential is a unique functional of the TD density. It therefore follows that the many-body Hamiltonian and wavefunction too are unique functionals of the density:

$$v(\mathbf{r},t) = v[n,\Psi_0](\mathbf{r},t) \Longrightarrow \hat{H}(t) = \hat{H}[n,\Psi_0](t) \Longrightarrow \Psi(t) = \Psi[n,\Psi_0](t) \tag{D.44}$$

D.6 Adiabatic Connection in TDDFT

As described in section 3.9.4, the major underpinning in the utility of static DFT are approximations to the exchange-correlation $v^0_{\mathrm{xc}}[n_0](\mathbf{r})$. Likewise, a crucial com-

ponent in TDDFT is determining the form for the TD exchange-correlation. The simplest method is to utilise the exchange-correlation functional for static DFT in its TD counterpart. This approach is known as the adiabatic connection:

$$v_{\mathrm{xc}}^{A}(\mathbf{r},t) = v_{\mathrm{xc}}^{0}[n_0](\mathbf{r})|_{n_0(\mathbf{r})\to n(\mathbf{r},t)} \tag{D.45}$$

In general, the adiabatic approximation holds, even for systems containing a certain proportion of non-adiabaticity. Choosing one of the many functional forms available for static DFT leads to a corresponding adiabatic approximation defined as:

$$v_{\mathrm{xc}}^{A,\mathrm{approx}}(\mathbf{r},t) = v_{\mathrm{xc}}^{0,\mathrm{approx}}[n_0](\mathbf{r})|_{n_0(\mathbf{r})\to n(\mathbf{r},t)} \tag{D.46}$$

A commonly used variant for the TD exchange-correlation potentials is the adiabatic local density approximation, ALDA, with the form:

$$v_{\mathrm{xc}}^{\mathrm{ALDA}}(\mathbf{r},t) = \left.\frac{\mathrm{d}e_{\mathrm{xc}}^{h}(\bar{n})}{\mathrm{d}\bar{n}}\right|_{\bar{n}=n(\mathbf{r},t)} \tag{D.47}$$

where $e_{\mathrm{xc}}^{h}(\bar{n})$ is the exchange-correlation energy density of the homogeneous electron liquid of partical density $\bar{n}$.

D.7 Linear Response Theory

This is a brief formulism of linear response theory as outlined by Ullrich [428].

For any quantum mechanical observable *e.g.*, $\hat{\alpha}$, the ground state expectation value is given by:

$$\alpha_0 = \langle\Psi_0|\hat{\alpha}|\Psi_0\rangle \tag{D.48}$$

Assuming the system is acted upon by a time-dependent perturbation, such as:

$$\hat{H}_1(t) = F(t)\hat{\beta} \qquad\qquad t \geqslant t_0 \tag{D.49}$$

where $F(t)$ is an external field, turned on at t, associated with an observable $\hat{\beta}$, then

the expectation value of the observable $\hat{\alpha}$ becomes:

$$\alpha(t) = \langle \Psi_0(t) | \hat{\alpha} | \Psi_0(t) \rangle \tag{D.50}$$

hence, $\hat{\alpha}$ is now time-dependent. The *response* of $\hat{\alpha}$ to the perturbation is defined as the difference between the initial static value and time-dependent expectation value of $\hat{\alpha}$. Expanding this response in powers of the field, $F(t)$ results in:

$$\alpha(t) - \alpha_0 = \underbrace{\alpha_1(t)}_{\text{linear response}} + \underbrace{\alpha_2(t)}_{\text{quadratic response}} + \alpha_3(t) + \ldots \tag{D.51}$$

From here, as shown by Bruus and Flensberg, the linear response can be obtained as [429]:

$$\alpha_1(t) = -i \int_{t_0}^{t} \mathrm{d}t' F(t') \left\langle \Psi_0 \middle| \left[\hat{\alpha}(t), \hat{\beta}(t') \right] \middle| \Psi_0 \right\rangle \tag{D.52}$$

Making use of the time-independent Hamiltonian for the initial state, the commutator in equation (D.52) can be reformulated as [429]:

$$\left[\hat{\alpha}(t), \hat{\beta}(t') \right] = \left[\hat{\alpha}(t)(t - t'), \hat{\beta} \right] \tag{D.53}$$

allowing the retarded response function to be defined as:

$$\chi_{\alpha\beta}(t - t') = -i\theta(t - t') \left\langle \Psi_0 \middle| \left[\hat{\alpha}(t)(t - t'), \hat{\beta} \right] \middle| \Psi_0 \right\rangle \tag{D.54}$$

Finally, one can obtain the linear response of $\alpha_1(t)$ as:

$$\alpha_1(t) = \int_{-\infty}^{\infty} \mathrm{d}t' \chi_{\alpha\beta}(t - t') F(t') \tag{D.55}$$

D.7.1 Application to TDDFT

The total potential of the ground state of a system of interacting particles, with a perturbation switch on at $t = 0$, is expressed as:

$$v(\mathbf{r}, t) = v_0(\mathbf{r}) + \theta(t - t_0)v_1(\mathbf{r}, t) \tag{D.56}$$

As there exists a unique mapping between the TD external potential and the TD density then the latter becomes a functional of the external potential, $n(\mathbf{r}, t) = n[\nu](\mathbf{r}, t)$ which when expanded out in terms of the density response leads to:

$$n(\mathbf{r}, t) = n_0(\mathbf{r}) + n_1(\mathbf{r}, t) + n_2(\mathbf{r}, t) \dots \tag{D.57a}$$

$$n(\mathbf{r}, t) - n_0(\mathbf{r}) = n_1(\mathbf{r}, t) + n_2(\mathbf{r}, t) + n_3(\mathbf{r}, t) \dots \tag{D.57b}$$

From here the linear response of the density is given by:

$$n_1(\mathbf{r}, t) = \int_{-\infty}^{\infty} \mathrm{d}t' \int \mathrm{d}^3 r' \chi(r, r', t - t')v_1(\mathbf{r}', t') \tag{D.58}$$

where χ is the linear density-density response:

$$\chi(r, r', t - t') = -i\theta(t - t') \langle \Psi_0 | [\hat{n}(\mathbf{r}, t - t'), \hat{n}(\mathbf{r}')] | \Psi_0 \rangle \tag{D.59}$$

Transforming to frequency space, *i.e.* replacing time, t, with frequency, ω, yields the frequency-dependent density response:

$$n_1(\mathbf{r}, \omega) = \int \mathrm{d}^3 r' \chi(r, r', \omega)v_1(\mathbf{r}', \omega) \tag{D.60}$$

By considering a complete set of eigenfunctions, $\{\Psi_n\}$, with the completeness relation $1 = \sum_{n=0}^{\infty} |\Psi_n\rangle\langle\Psi_n|$ one arrives at the Lehmann representation for the density-

density response function, in the limit $\eta \longrightarrow 0_+$:

$$\chi(r, r', \omega) = \sum_{n=1}^{\infty} \left\{ \frac{\langle \Psi_0 | \hat{n}(\mathbf{r}) | \Psi_n \rangle \langle \Psi_n | \hat{n}(\mathbf{r}') | \Psi_0 \rangle}{\omega - \Omega_n + i\eta} - \frac{\langle \Psi_0 | \hat{n}(\mathbf{r}') | \Psi_n \rangle \langle \Psi_n | \hat{n}(\mathbf{r}) | \Psi_0 \rangle}{\omega + \Omega_n + i\eta} \right\} \tag{D.61}$$

Here the n^{th} excitation state is defined by:

$$\Omega_n = E_n - E_0 \tag{D.62}$$

From the above it becomes apparent that linear response function has poles (becomes singular) at the exact excitation energies. The major result in this derivation is that knowledge of the response function χ would enable one to calculate the density response by simply solving the integral in equation (D.60). It is unfortunate therefore that calculating the response function, χ is extremely difficult. The alternative is once again provided through the Kohn-Sham system, whereby the linear response is calculated exactly in response to an effective perturbation acting upon the non-interacting Kohn-Sham system. This linear response has the form:

$$n_1(\mathbf{r}, t) = \int \mathrm{d}t' \int \mathrm{d}^3 r' \underbrace{\chi_s(r, r', t - t')}_{\substack{\text{density-density} \\ \text{response}}} \underbrace{v_{1s}(\mathbf{r}', t')}_{\substack{\text{effective} \\ \text{perturbation}}} \tag{D.63}$$

As before the density-density response is provided through the Lehmann representation:

$$\chi_s(r, r', \omega) = \sum_{j,k=1}^{\infty} (f_k - f_j) \frac{\varphi_j(\mathbf{r}) \varphi_k^*(\mathbf{r}) \varphi_j^*(\mathbf{r}') \varphi_k(\mathbf{r}')}{\omega - \omega_{jk} + i\eta} \tag{D.64}$$

where the f terms refer to the configurational occupation of the Kohn-Sham ground state; 1 for occupied and 0 for unoccupied. Similarly to equation (D.62) the excitation states are defined as:

$$\omega_{jk} = \varepsilon_j - \varepsilon_k \tag{D.65}$$

and the Kohn-Sham linear response has poles at the exact excitation energies of the Kohn-Sham system. Inspection of equation (D.62) and (D.65) reveals an apparent

contradiction. From equation (D.61) and hence equation (D.62), it can be seen that the density response diverges at the exact excitation energies Ω_n, which themselves are poles of the full-many body response function χ. It had also been shown, however, through equations (D.64) and (D.65) that the poles of χ_s are located at the frequencies ω_{jk} of the Kohn-Sham system, which are different from Ω_n.

The resolution here is replacing the poles ω_{jk} with the many-body poles at the true excitation energy Ω_n. There are two important components within LR-TDDFT that guarantees the poles at Ω_n are correct: the self-consistency and the structure of f_{xc}.

Expanding the effective potential of the TD Kohn-Sham, equation (3.102), in terms of the density response $n_1(\mathbf{r}, t)$ yields the first-order perturbation of the Kohn-Sham potential:

$$v_{s1}(\mathbf{r}, t) = v_1(\mathbf{r}, t) + \int \mathrm{d}^3 r' \frac{n_1(\mathbf{r}', t)}{|r - r'|} + \int \mathrm{d}t' \int \mathrm{d}^3 r' f_{\mathrm{xc}}(\mathbf{r}, t, \mathbf{r}', t') n_1(\mathbf{r}', t') \quad \text{(D.66)}$$

Here, f_{xc}, known as the xc kernel is an expression of the derivative of the xc potential with respect to the density and has the form:

$$f_{\mathrm{xc}}(\mathbf{r}, t, \mathbf{r}', t') = \left. \frac{\delta V_{\mathrm{xc}}[n](\mathbf{r}, t)}{\delta n(\mathbf{r}', t')} \right|_{n_0(\mathbf{r})} \quad \text{(D.67)}$$

Determining the form for xc kernel suffers from the same problems as for the exchange-correlation function. There are numerous approximations to the xc kernel, but the simplest involves simply setting it to zero. This is known as the random phase approximation, RPA:

$$f_{\mathrm{xc}}^{\mathrm{RPA}}(\mathbf{r}, t, \mathbf{r}', t') = 0 \quad \text{(D.68)}$$

Insertion of equation (D.66) into (D.63) results in:

$$n_1(\mathbf{r},t) = \int \mathrm{d}t' \int \mathrm{d}^3r' \chi_s(\mathbf{r},\mathbf{r}',t-t') \left[v_1(\mathbf{r},t) + \int \mathrm{d}^3r' \frac{n_1(\mathbf{r}',t)}{|r-r'|} + \int \mathrm{d}t' \int \mathrm{d}^3r' f_{\mathrm{xc}}(\mathbf{r},t,\mathbf{r}',t') n_1(\mathbf{r}',t') \right] \tag{D.69}$$

with $n_1(\mathbf{r},t)$ on both sides. Solving this self-consistent equation allows calculation of the excitation energies. Recasting equation (D.69) into the Lehmann representation by Fourier transforming and factorising yields:

$$n_1(\mathbf{r},\omega) = \int \mathrm{d}^3r' \chi_s(\mathbf{r},\mathbf{r}',\omega) \left[v_1(\mathbf{r}',\omega) + \int \mathrm{d}^3r'' \left\{ \frac{1}{|r'-r''|} + f_{\mathrm{xc}}(\mathbf{r}',t,\mathbf{r}'',\omega) \right\} n_1(\mathbf{r}',\omega) \right] \tag{D.70}$$

The next major step is to move to a spin-dependent formulation; a common practice for LR-TDDFT. Now, the linear spin-density response (analogous to equation (D.60)) is:

$$n_{1\sigma}(\mathbf{r},\omega) = \sum_{\sigma} \int \mathrm{d}^3r' \chi_{s,\sigma,\sigma'}(\mathbf{r},\mathbf{r}',\omega) v_{s1\sigma}(\mathbf{r}',\omega) \tag{D.71}$$

where the spin-dependent linearised effective potential is given by:

$$v_{s1\sigma}(\mathbf{r},t) = v_{1\sigma}(\mathbf{r},\omega) + \sum_{\omega'} \int \mathrm{d}^3r' \left\{ \frac{1}{|r-r'|} + f_{\mathrm{xc},\sigma,\sigma'}(\mathbf{r},\mathbf{r}',\omega) \right\} n_{1\sigma'}(\mathbf{r}',\omega) \tag{D.72}$$

and the non-interacting KS response is:

$$\chi_{s,\sigma,\sigma'}(\mathbf{r},\mathbf{r}',\omega) = \delta_{\sigma,\sigma'} \sum_{j,k=1}^{\infty} (f_{k\sigma} - f_{j\sigma}) \frac{\varphi^0_{j\sigma}(\mathbf{r}) \varphi^{0*}_{k\sigma}(\mathbf{r}) \varphi^{0*}_{j\sigma}(\mathbf{r}') \varphi^0_{k\sigma}(\mathbf{r}')}{\omega - \omega_{jk\sigma} + i\eta} \tag{D.73}$$

As before, the Kohn-Sham excitation energies are given as: $\omega_{jk\sigma} = \varepsilon_{j\sigma} - \varepsilon_{k\sigma}$.

Despite the formulation, the overall outcomes of these equations are the same, namely the exact excitation energies, Ω_n are given by the poles of the density-density response function and hence this response will diverge if subjected to any external

perturbation at that exact frequency. One can even dispense with the need for an external perturbation altogether as the system will still elicit a response at the exact excitation frequency. Calculating the eigenvalues/eigenfrequencies in this way requires the linear response equation to exclude the external perturbation:

$$n_{1\sigma}(\mathbf{r},\Omega) = \sum_{\sigma',\sigma''} \int \mathrm{d}r' \chi_{s,\sigma,\sigma'}(\mathbf{r},\mathbf{f}',\Omega) \int \mathrm{d}r'' f_{Hxc,\sigma'\sigma''}(\mathbf{r}',\mathbf{r}'',\Omega) n_{1\sigma''}(\mathbf{r}'',\Omega) \quad \text{(D.74)}$$

Where the eigenvalue at the exact excitation energy equals one. Equation (D.74) can be compacted into matrix notation as:

$$\begin{pmatrix} A & B \\ B & A \end{pmatrix} \begin{pmatrix} X \\ Y \end{pmatrix} = \Omega \begin{pmatrix} -I & 0 \\ 0 & -I \end{pmatrix} \begin{pmatrix} X \\ Y \end{pmatrix} \quad \text{(D.75)}$$

This is known as the Casida equation [430]. Here the matrix elements A and B, known as orbital rotation Hessians [431], are given as:

$$A_{ia\sigma,i'a'\sigma'}(\Omega) = \delta_{ii'}\delta aa'\delta_{\sigma\sigma'}\omega_{a'i'\sigma'} + K_{ia\sigma,i'a'\sigma'}(\Omega) \quad \text{(D.76)}$$

$$B_{ia\sigma,i'a'\sigma'}(\Omega) = K_{ia\sigma,i'a'\sigma'}(\Omega) \quad \text{(D.77)}$$

In principle this formulation yields the exact excitation energies, however this assumes knowledge of the exact ground state, thus knowledge of the exact form of $V_{\mathrm{xc}}^0[n_0]$, in addition to all the occupied and unoccupied Kohn-Sham orbitals and energies. The Casida equation is therefore applied alternatively as:

$$CZ = \Omega^2 Z \quad \text{(D.78)}$$

In this form the Kohn-Sham orbitals are assumed to be real and f_{xc} is now frequency dependent causing matrices A and B to also be real. Under these conditions the

following matrices can be defined:

$$C = (A-B)^{\frac{1}{2}}(A+B)(A-B)^{\frac{1}{2}} \tag{D.79}$$

$$Z = (A-B)^{\frac{1}{2}}(X-Y) \tag{D.80}$$

Making use of equations (D.79) provides the following:

$$\sum_{i'a'\sigma'} \left[\delta_{ii'}\delta aa'\delta_{\sigma\sigma'}\omega^2_{a'i'\sigma'} + 2\sqrt{\omega_{ai\sigma}\omega_{a'i'\sigma'}}K_{ia\sigma,i'a'\sigma'}\right] Z_{i'a'\sigma'} = \Omega^2 Z_{ia\sigma} \tag{D.81}$$

This approximate form for the Casida equation is executed in most TDDFT codes. One final point addresses the inclusion in equation (D.78) of the square of the excitation energies, Ω^2. This suggests that for each value of Ω exists a corresponding negative equivalent $-\Omega$. This is indeed the case, with the negative value being attributed as a de-excitation. If, when using equation (D.75), all the de-excitations are ignored, one arrives at the Tamm-Dancoff approximation, TDA. Incorporating this approximation within TDDFT has been achieved [432] and leads to a simplification of the eigenvalue problem.

Appendix E

MCTDH on multiple electronic states

The extension of the MCTDH method to include more than one state can be done in two ways. The first approach, known as *single-set*, takes equation (3.108) and appends an additional degree of freedom for the electronic degree of freedom, α:

$$\Psi(q_1, \ldots, q_f, \alpha, t) = \sum_{j_1=1}^{n_1} \cdots \sum_{j_p=1}^{n_f} A_{j_1 \ldots j_p}(t) \varphi_{j_1}^{(1)}(Q_1, t) \cdots \varphi_{j_{p-1}}^{(p-1)}(Q_{p-1}, t) \varphi_{j_p}^{(p)}(\alpha, t) \tag{E.1}$$

Assigning σ to the number of electronic states, then this formulation uses a complete set of electronic SPFs such that $n_p = \sigma$. These SPFs are time-independent and selected so $\varphi_{j_p}^{(p)}(\alpha, t) = \delta_{\alpha, j_p}$. This allows equation (E.1) to be rewritten in the following form where $|\alpha\rangle$ are electronic state functions:

$$\Psi = \sum_{j_1=1}^{n_1} \cdots \sum_{j_p=1}^{n_f} \sum_{\alpha=1}^{\sigma} A_{j_1 \ldots j_{p-1}, \alpha} \varphi_{j_1}^{(1)} \cdots \varphi_{j_{p-1}}^{(p-1)} |\alpha\rangle \tag{E.2}$$

The alternative approach, know as *multi-set*, provides a different set of SPFs per state. This allows the wavefunction to be written as:

$$\Psi = \sum_{\alpha=1}^{\sigma} \Psi^{\alpha} |\alpha\rangle \tag{E.3}$$

In this formulation, each function Ψ^α is expanded in MCTDH form as:

$$\Psi^\alpha(q_1,\ldots,q_f,t) = \sum_{j_1^\alpha=1}^{n_1^\alpha} \cdots \sum_{j_p^\alpha=1}^{n_p^\alpha} A^\alpha_{j_1^\alpha \ldots j_p^\alpha}(t)\varphi^{1,\alpha}_{j_1^\alpha}(Q_1,t)\cdots\varphi^{p,\alpha}_{j_p^\alpha}(Q_p,t) \tag{E.4}$$

One can apply the equations of motion as before but now the resulting equations must include state symbols. Setting the constraint $\mathbf{g}^{(\kappa)}$ yields:

$$i\dot{\mathbf{A}} = \sum_{\beta=1}^{\sigma} \mathcal{K}^{(\alpha,\beta)}\mathbf{A}^{(\beta)} \tag{E.5}$$

$$i\dot{\boldsymbol{\varphi}}^{(\kappa,\alpha)} = (1-P^{\kappa,\alpha})(\rho^{\kappa,\alpha})^{-1}\sum_{\beta=1}^{\sigma}\mathcal{H}^{(\kappa,\alpha\beta)}\boldsymbol{\varphi}^{\kappa,\beta} \tag{E.6}$$

Appendix F

Parameters and cuts through PES for anthracene derivatives

Here follows the parameters for the vibronic coupling model Hamiltonian and cuts through the PES along the important normal modes for the molecules studied in Chapter 6.

F.1 Tetracene

Making use of the vibronic coupling Hamiltonian provides the on-diagonal linear coupling constants κ, shown in Table F.1. In contrast to anthracene, the κ values for tetracene show that no modes are greatly displaced from the S_0 minima. Several modes exhibit higher κ values and these are ν_{52}, a C-H rocking/ring distortion mode, ν_{59}, C-C ring stretching mode, ν_{61}, C-H rocking/C-C ring stretching mode, ν_{64}, C-H rocking mode and ν_{67} C-C ring stretching mode. Even the ratio κ/ω provides little information on which are the important modes. By taking the modes with the highest κ values and assuming that the important vibrations will likely to similar to those for anthracene, the six modes described above were selected for use in the model. The second order parameters are shown in Table F.2. Like anthracene, these values are very small, reflecting little change in frequency between states.

Table F.1: Vibrational energies, ω and on-diagonal linear coupling constants, κ for the S_1 state of tetracene. All values are in eV.

Mode	ω	κ	κ/ω
$\nu 8$	0.039	0.034	0.871
$\nu 20$	0.079	−0.011	0.139
$\nu 26$	0.095	−0.036	0.379
$\nu 33$	0.108	−0.010	0.093
$\nu 44$	0.128	0.053	0.414
$\nu 48$	0.148	0.017	0.115
$\nu 52$	0.154	0.083	0.539
$\nu 59$	0.177	−0.085	0.480
$\nu 61$	0.179	0.089	0.497
$\nu 64$	0.186	−0.075	0.403
$\nu 66$	0.195	−0.084	0.431
$\nu 67$	0.198	−0.063	0.318
$\nu 76$	0.394	−0.002	0.005
$\nu 80$	0.395	−0.005	0.013
$\nu 84$	0.398	0.014	0.035

Table F.2: Second order on-diagonal, $\gamma_{\alpha\alpha}$ and bilinear, $\gamma_{\alpha\beta}$, coupling constants for the S_1 state of tetracene. All values are in eV.

Mode (All a_g)	$\gamma_{\alpha\alpha}$	Modes	$\gamma_{\alpha\beta}$
$\nu 52$	0.000	$\nu 52 - 59$	−0.001
$\nu 59$	0.002	$\nu 52 - 66$	0.000
$\nu 61$	−0.003	$\nu 52 - 67$	−0.002
$\nu 64$	−0.001	$\nu 59 - 61$	−0.001
$\nu 66$	−0.001	$\nu 59 - 64$	0.001
$\nu 67$	0.001	$\nu 59 - 66$	0.001
		$\nu 59 - 67$	0.003
		$\nu 61 - 64$	0.001
		$\nu 61 - 66$	−0.003
		$\nu 61 - 67$	−0.001
		$\nu 64 - 66$	0.001
		$\nu 64 - 67$	0.001
		$\nu 66 - 67$	0.002

F.1.1 Comparison with explicit fits

To prevent having to calculate points along all the totally-symmetric modes, the VCTRANS sub-program within the VCHAM package was used to propose which modes are important to the S_1 photochemistry. By taking the optimised geometry in the ground S_0 state, and the S_1 state, the change in geometry as expressed through the normal modes can be obtained. From this, the four largest values were modes $\nu_8, \nu_{67}, \nu_{59}$ and ν_{61}. Cuts through the potential energy surface were calculated along these normal points and adiabatic surfaces obtained by fitting to a series of *ab initio* points. These points were calculated using Grimme's DFT/MRCI method, as implemented in Turbomole, utilising the BH-LYP [188] functional and an aug-cc-pVDZ basis. This method has been shown to provide accurate excited state energies, but at much lower computational cost then standard MRCI methods. Unfortunately, its use is limited to single-point energy calculations otherwise it would likely have been the preferred quantum chemical method used in this model.

Differences in the on-diagonal linear coupling constants and the cuts through the potential energy surface are shown in Table F.3 and Figure F.1.

It is immediately evident from the parameters obtained from fits to explicit points and from the cuts, that the displacement of the S_1 minima from the ground state minimum has been underestimated by the simplified model. The exception being ν_8 which was displaced too much by the simplified model. In turn, these large

Table F.3: Comparison of the ω and on-diagonal linear coupling constants, κ obtained through the simplified FC model with those obtained through fitting to a series of *ab initio* points for the S_1 state of tetracene. All values are in eV.

Mode		FC Model		Explicit Fits	
	ω	κ	κ/ω	κ	κ/ω
$\nu 8$	0.039	0.034	0.871	0.013	0.300
$\nu 59$	0.177	−0.085	0.480	−0.140	0.791
$\nu 61$	0.179	0.089	0.497	0.114	0.637
$\nu 67$	0.198	−0.063	0.318	−0.140	0.700

a) ν67

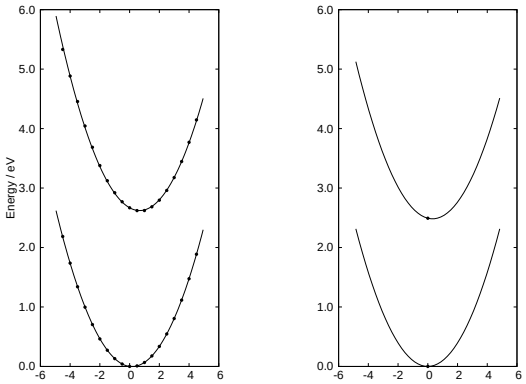

b) ν61

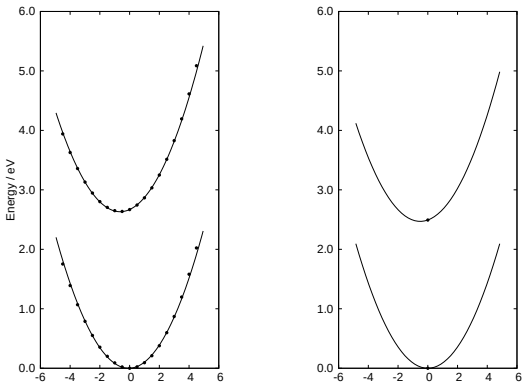

c) ν59

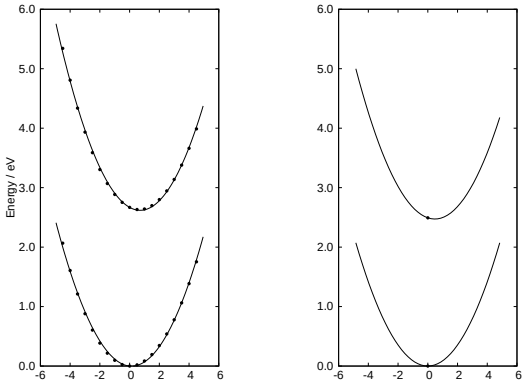

d) ν8

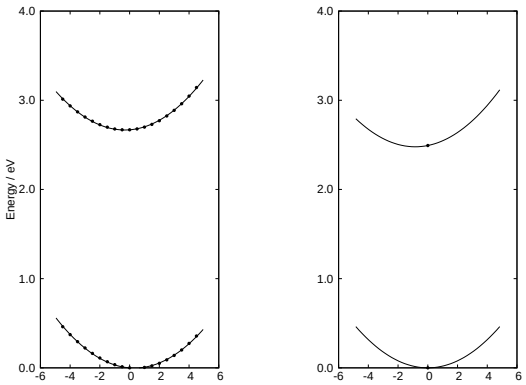

Fig. F.1: Cuts through the adiabatic potential energy surfaces along select totally symmetric modes for the ground and first excited state of tetracene. The cuts on the left are the surfaces obtained from fitting to a series of calculated *ab initio* points (DFT-MRCI/aug-cc-pVDZ) and those on the right are Harmonic potentials formed from information at the FC point only.

parameters increase the ratio κ/ω and should therefore provide a longer progression in the spectrum. Despite the differences in the magnitude of displacement of the S_1 minima, Figure F.1 does illustrate that the general shape of the surfaces are reproduced well by the FC, simplified model. It should be noted that the slight shift in energy results from the different level of theory being used to calculate the points. The model Hamiltonian was constructed using only three normal modes, ν_{59}, ν_{61} and ν_{67}. This illustrates not only the small number of modes needed to replicate the spectra, but also the importance of the three modes with the new parameters.

F.2 Pentacene

The on-diagonal linear coupling constants for the totally-symmetric modes are shown in Table F.4. Examining the κ values and the ratio κ/ω suggests the modes important to the S_1 photodynamics of pentacene. From the modes, five were deemed significant enough to be selected for the model. These were the modes with the largest four κ values, ν_{72}, a C-C ring stretch, ν_{81}, a in-plane ring distortion, ν_{62}, a C-H rocking and ν_{76}, a C-C ring stretch. The lowest frequency a_g mode, the ring breathing mode, ν_9, was also selected due to its large κ/ω ratio.

The second order on-diagonal $\gamma_{\alpha\alpha}$ and bilinear $\gamma_{\alpha\beta}$ terms are shown in Table F.5. As seen with the previous molecules, these values are very small, indicating little change in frequency in the upper state and insignificant coupling between the modes. Given the large number of normal modes of pentacene, only the values associated with the five totally symmetric modes used in the model are shown.

The vibrational motion of these modes, as well as cuts through the potential energy surface along them, are shown in Figures F.2 and F.3. The important normal modes in pentacene are similar to those used for simulating the anthracene spectra. The lowest frequency totally-symmetric mode is present in all three of the linear acenes studied so far. This mode, as seen in Figure F.2(a) is best described as

Table F.4: Vibrational energies, ω and on-diagonal linear coupling constants, κ for the S_1 state of pentacene. All values are in eV.

Mode	ω	κ	κ/ω
ν_9	0.033	0.021	0.626
ν_{24}	0.076	−0.018	0.232
ν_{26}	0.080	−0.003	0.041
ν_{33}	0.095	−0.032	0.335
ν_{36}	0.099	−0.018	0.182
ν_{54}	0.128	−0.025	0.193
ν_{58}	0.148	−0.042	0.284
ν_{62}	0.152	−0.087	0.576
ν_{69}	0.167	0.014	0.084
ν_{72}	0.177	0.131	0.740
ν_{76}	0.180	0.067	0.373
ν_{79}	0.187	0.022	0.119
ν_{81}	0.195	−0.107	0.549
ν_{82}	0.198	−0.048	0.245
ν_{90}	0.393	0.001	0.002
ν_{96}	0.394	−0.001	0.003
ν_{102}	0.398	−0.004	0.009

Table F.5: Second order on-diagonal, $\gamma_{\alpha\alpha}$ and off-diagonal, $\gamma_{\alpha\beta}$, coupling constants for the S_1 state of pentacene. All values are in eV.

Mode	$\gamma_{\alpha\alpha}$	Modes	$\gamma_{\alpha\beta}$
$\nu 62$	0.000 71	$\nu 9-62$	0.000
$\nu 72$	0.002 04	$\nu 9-72$	0.000
$\nu 76$	−0.004 23	$\nu 9-76$	0.000
$\nu 81$	0.001 33	$\nu 9-81$	0.000
		$\nu 62-72$	−0.002
		$\nu 62-76$	0.001
		$\nu 62-81$	0.002
		$\nu 72-76$	0.001
		$\nu 72-81$	−0.003
		$\nu 76-81$	−0.002

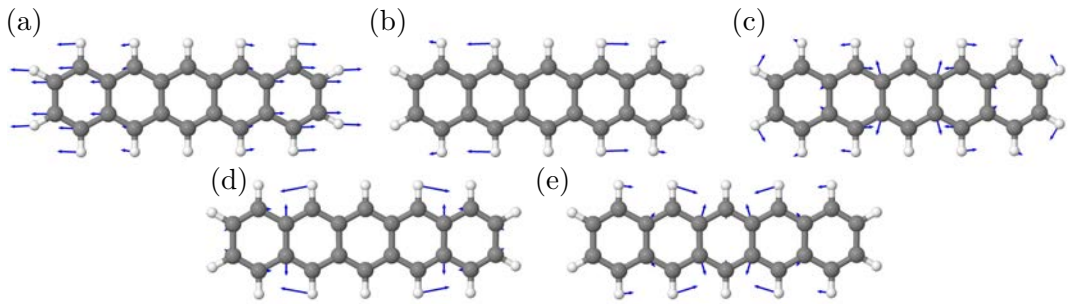

Fig. F.2: The normal modes of pentacene important in describing its absorption spectrum: (a) ν_9 ring breathing, (b) ν_{62} C-H rocking, (c) ν_{72} C-C ring stretch, (d) ν_{76} C-C ring stretch and (e) ν_{81} in-plane ring distortion.

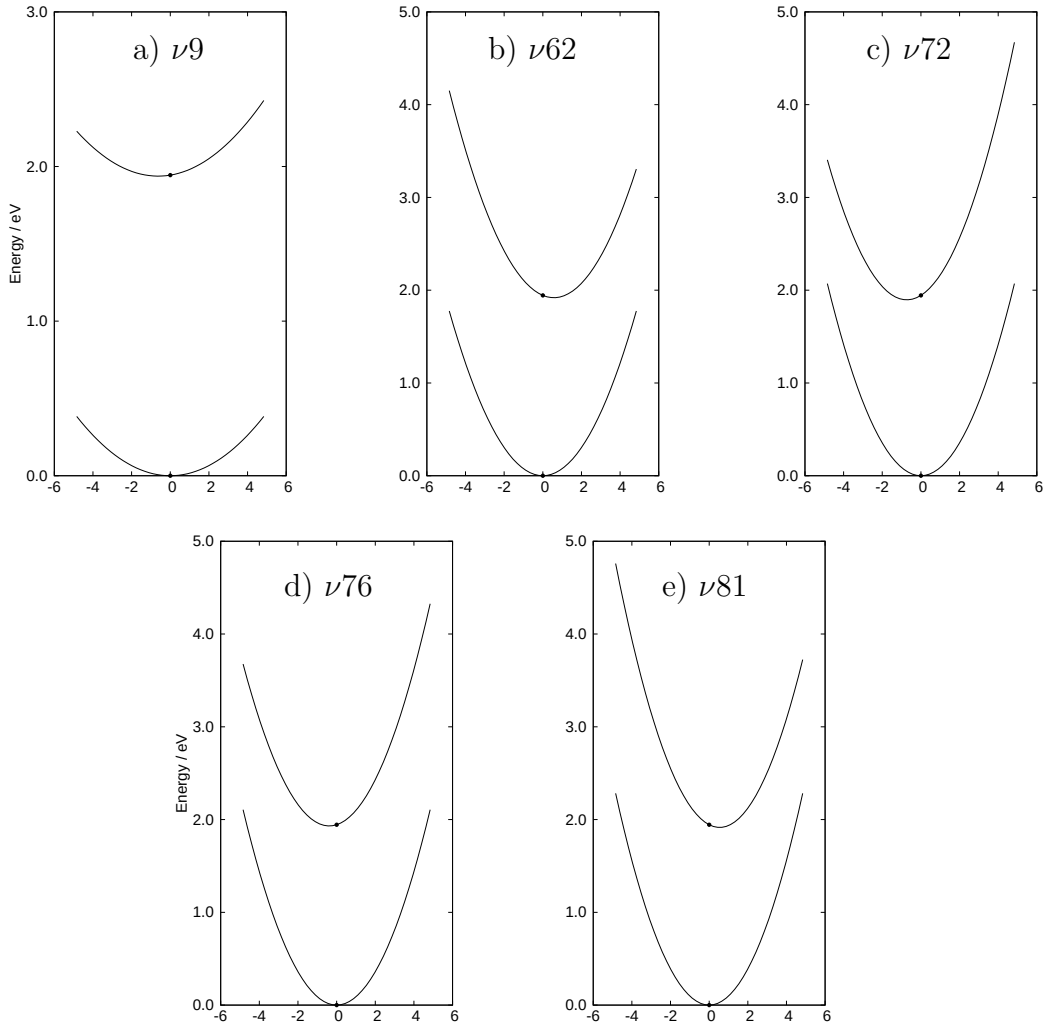

Fig. F.3: Cuts through the adiabatic potential energy surfaces along select totally-symmetric normal modes for the ground state and first excited state of pentacene. The solitary point is the FC point obtained at the TDDFT/6-31G(d) level. The normal modes include are (a) ν_9 ring breathing, (b) ν_{62} C-H rocking, (c) ν_{72} C-C ring stretch, (d) ν_{76} C-C ring stretch and (e) ν_{81} in-plane ring distortion.

ring breathing of the inner-most ring and outward displacement of the outer atoms. Given the low frequency associated with this mode, the ratio κ/ω is large. Present also are C-H bending modes involving all C-H bonds except those on the central ring. The largest values of κ corresponds to modes involving C-C stretching of the central rings, between those sp^2 carbons not bonded to any hydrogens.

The cuts through the PES highlight the large displacement of the S_1 minima from the equilibrium point for modes ν_{72} and ν_{81}. The small second order on-diagonal values are also illustrated by the lack of change in shape of the potentials between the states. The surfaces are well separated and no crossing is seen. The large separation in energy means any coupling between the states is weak. This provides good justification for the rationale behind the utility of this model.

F.3 Benzene

As expected, geometry optimisation and frequency calculations lead to a planar geometry with 30 normal modes, containing only two totally symmetric modes. These two modes consist of the symmetric ring breathing and C-H stretch a_{1g} modes. The vertical excitation energies calculated using TDDFT and compared with experiment and other levels of theory are shown in Table F.6. The accuracy of the calculated vertical excitation energies varies between methods with the most reliable being the CASPT2(6,6). As stated earlier the calculation of the Hessian, particularly at the FC point, is an intensive and demanding calculation. This makes TDDFT the ideal choice of method. The S_1 energy calculated using TDDFT is higher than experiment, although the subsequent excited states are in relative good agreement.

From the Hessians calculated at the ground state equilibrium geometry and the FC point, the vibronic coupling Hamiltonian was constructed and the on-diagonal linear and second order coupling constants obtained. These are shown in Tables F.7 and F.8.

Table F.6: First five excited states of benzene calculated at different levels of theory. All calculations used a 6-31G(d) basis.

	TD-DFT	ADC(2)	CASPT2	EOM-CCSD	DFT-MRCI	Exp. [433]
S_1	5.54	5.41	4.91	5.30	5.09	4.90
S_2	6.31	6.90	6.28	7.02	6.47	6.20
S_3	7.38	7.77	6.92	8.00	7.35	6.94
S_4	7.38	7.77	6.92	8.00	7.41	6.94
S_5	7.87	9.04	-	9.01	7.76	7.80

Table F.7: Vibrational energies, ω and on-diagonal linear coupling constants, κ for the S_1 state of benzene. All values are in eV.

Mode	ω	κ	κ/ω
$\nu 1$	0.127	0.183	1.441
$\nu 2$	0.398	0.046	0.116

Table F.8: Second order on-diagonal, $\gamma_{\alpha\alpha}$ and bi-linear $\gamma_{\alpha\beta}$ coupling constants for the S_1 state of benzene. All values are in eV.

Mode	$\gamma_{\alpha\alpha}$	Mode	$\gamma_{\alpha\beta}$
ν_1	−0.022	ν_{1-9}	0.002
ν_2	−0.022	ν_{2-10}	0.002
ν_3	−0.010	ν_{3-23}	−0.004
ν_4	−0.010	ν_{3-26}	−0.002
ν_5	−0.014	ν_{4-24}	0.004
ν_6	−0.035	ν_{4-27}	0.002
ν_7	−0.030	ν_{6-11}	0.012
ν_8	−0.030	ν_{14-22}	0.004
ν_9	−0.028	ν_{15-21}	−0.004
ν_{10}	−0.028	ν_{16-19}	−0.013
ν_{11}	−0.029	ν_{17-24}	−0.002
ν_{13}	0.003	ν_{18-23}	−0.002
ν_{14}	−0.004		
ν_{15}	−0.004		
ν_{16}	0.006		
ν_{17}	0.002		
ν_{18}	0.002		
ν_{19}	0.037		
ν_{21}	−0.003		
ν_{22}	−0.003		
ν_{23}	0.005		
ν_{24}	0.005		

Table F.7 shows that only one of these modes, ν_1, the ring breathing mode exhibits a large displacement away from the ground state minimum. This leads to a very small model containing this solitary mode. The second order $\gamma_{\alpha\alpha}$ and bilinear $\gamma_{\alpha\beta}$ coupling constants shown in Table F.8 are all very small, having a negligible effect on the spectrum.

F.4 Naphthalene

Table F.9 shows large differences in the on-diagonal linear parameters between the first and second excited states. Greater shifts in the S_1 minima compared with the S_2 are noted for nearly all the vibrational modes. Inspection of the ratio κ/ω show the lowest frequency totally symmetric mode to be important in the photodynamics of both states. In addition, ν_3, the C-H bending mode exhibits a large ratio, warranting its inclusion the model. The high frequency C-H stretching modes however all possess small κ values, rendering them unlikely to be important.

No second order on diagonal, γ, parameters were obtained, although since the majority of these values have been smaller for the previously studied systems, their absence is not too surprising.

Table F.9: Vibrational energies, ω and on-diagonal linear coupling constants, κ for the S_1 and S_2 state of naphthalene. All values are in eV.

Mode	ω	$\kappa^{(1)}$	κ/ω	$\kappa^{(2)}$	κ/ω
ν_1	0.065	−0.105	1.615	−0.049	0.754
ν_2	0.096	0.055	0.573	0.033	0.344
ν_3	0.131	−0.116	0.885	−0.063	0.481
ν_4	0.148	−0.021	0.142	−0.009	0.061
ν_5	0.176	0.122	0.693	0.066	0.375
ν_6	0.187	0.114	0.610	0.060	0.321
ν_7	0.202	0.088	0.436	0.048	0.238
ν_8	0.395	−0.011	0.028	−0.007	0.018
ν_9	0.398	−0.029	0.073	−0.018	0.045

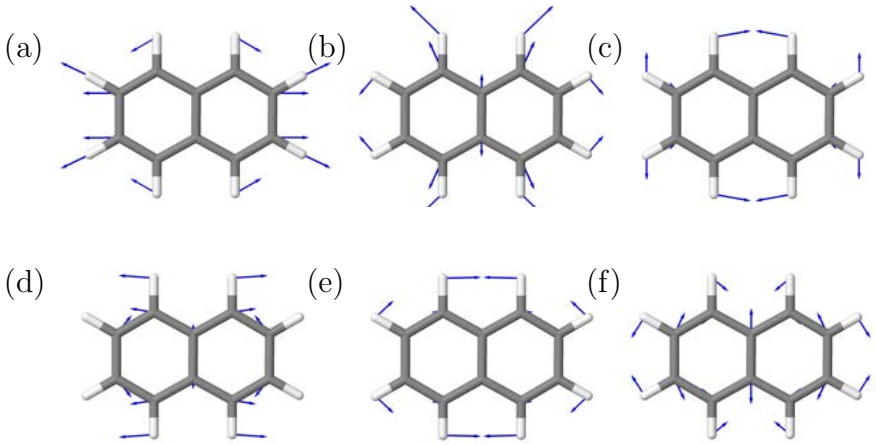

Fig. F.4: The normal modes of naphthalene important in describing its absorption spectrum: (a) ν_1, ring breathing (b) ν_2, ring distortion (c) ν_3, C-H bending (d) ν_5, C-C ring stretch (e) ν_6, C-H bending and (f) ν_7, C-C ring stretch.

Based on these values six modes were determined to be important for both excited states. They are: ν_1, the lowest frequency totally symmetric mode corresponding to a ring breathing mode; ν_2, a ring distortion mode; ν_3, C-H bending model; ν_5, C-C ring stretching mode; ν_6, C-H bending mode and ν_7, C-C ring stretch mode. These modes are illustrated in Figure F.4 and are consistent with similar modes deemed important in the photodynamics of the higher polyacenes studied previously. The lowest frequency ring breathing mode again shows itself to be significant, as well as C-H bending and C-C ring stretching modes.

Cuts through the PES, along each of these six modes, are shown in Figure F.5. Initially, the cuts appear to show the S_1 and S_2 states crossing or approaching each other. This is unlikely to be a true reflection of the potential energy surfaces and is presumably an artifact of the TDDFT energies predicting the two states to be too close in energy. Given that experimentally the S_1 vertical excitation energy was determined to be around 4 eV, then more accurate electronic structure calculations would see the S_1 potentials shifted downwards and away from the S_2 curves. As a result, the convergence and crossing of the curves would be removed. This exemplifies the need for accurate quantum chemical calculations to ensure false

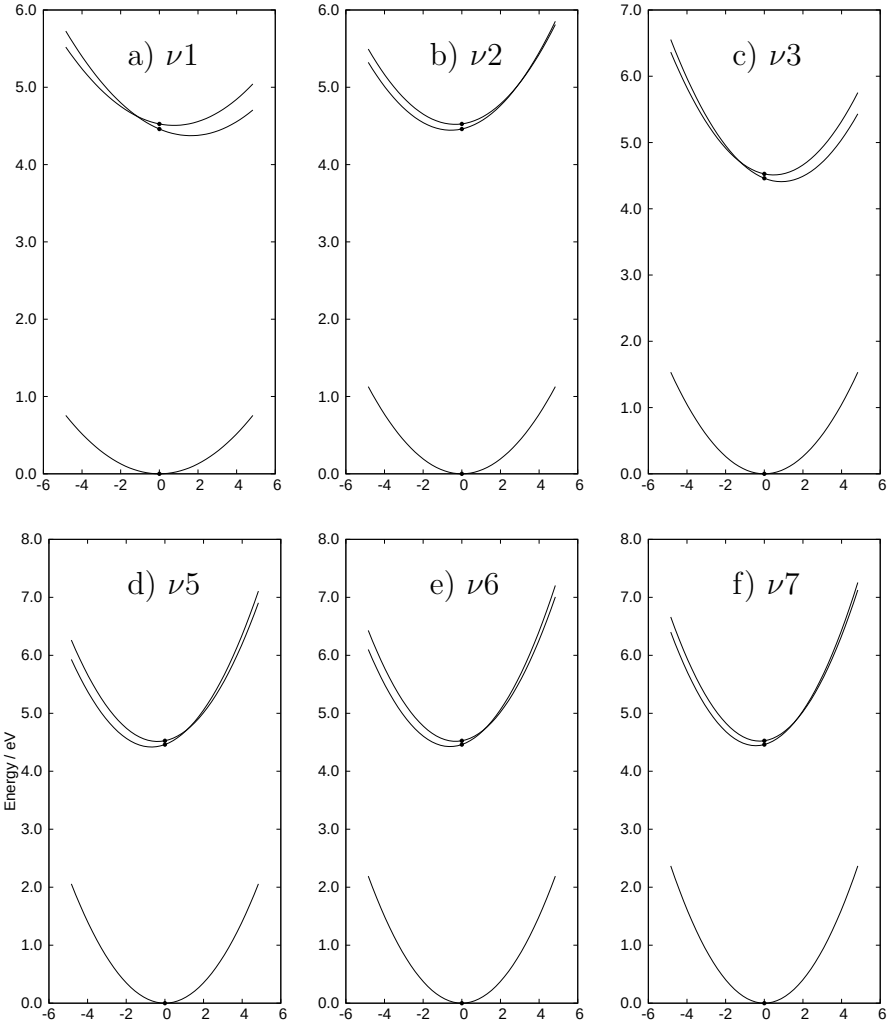

Fig. F.5: Cuts through the adiabatic potential energy surfaces along select totally-symmetric normal modes for the ground state, first and second excited state of naphthalene. The two points are the FC point obtained at the TDDFT/6-31G(d) level. The normal modes include are (a) ν_1, ring breathing (b) ν_2, ring distortion (c) ν_3, C-H bending (d) ν_5, C-C ring stretch (e) ν_6, C-H bending and (f) ν_7, C-C ring stretch.

features do not emerge. These potential energy surfaces are highly likely to affect the simulations.

The surfaces do however highlight the large displacement in the S_1 minima and relatively small shift in the S_2, especially in the ring breathing ν_1 mode. The absence of any second-order γ terms is also apparent, with no change in the width of the potentials between the ground and excited states.

The exclusion of modes that possibly couple the S_1 and S_2 states may be a notable omission. Although this simplified model neglects coupling terms, and has been shown to perform best when there is little coupling between states, it is possible to be incorporated to provide at least qualitative results.

F.5 Methyl and Hydroxmethyl

Vibrational frequency calculations yield 78 and 75 normal modes for 9-hydroxymethyl- and 9-methyl anthracene, respectively. An issue encountered is the low molecular symmetry each derivative possesses as mentioned early. This lack of symmetry reduces the number of matrix-elements that become zero in the vibronic-coupling Hamiltonian. In the case of 9-hydroxymethyl anthracene, its C_1 symmetry leads to all vibrations having a symmetry and hence all 78 normal modes having non-zero on-diagonal linear coupling constants. The C_s symmetry of 9-methyl anthracene does at least offer two different vibrational symmetry labels, the totally-symmetric a' mode and the a'' mode. Even then, there exist 49 non-zero values for the on-diagonal linear coupling constants. These values are shown in Tables F.11 and F.10.

Immediately, it becomes apparent that selecting the significant modes from this large number of non-zero parameters is challenging. Whilst the model is efficient in rapidly providing the coupling constants for the Harmonic potentials, the wavepacket propagation through the MCTDH method is still computationally restrictive on the number of modes included in the calculation. Picking out the largest κ values and

Table F.10: Vibrational energies, ω and on-diagonal linear coupling constants, κ for the S_1 state of 9-hydroxymethyl anthracene. All values are in eV.

Mode	ω	κ	κ/ω	Mode	ω	κ	κ/ω
ν_1	0.005	0.004	0.800	ν_{40}	0.133		0.000
ν_2	0.010	−0.005	0.500	ν_{41}	0.134	−0.001	0.006
ν_3	0.013	0.004	0.308	ν_{42}	0.141	−0.009	0.064
ν_4	0.014	0.000	0.000	ν_{43}	0.147	−0.001	0.007
ν_5	0.027	−0.005	0.185	ν_{44}	0.148	0.034	0.226
ν_6	0.029	0.001	0.034	ν_{45}	0.150	−0.042	0.278
ν_7	0.034	−0.015	0.441	ν_{46}	0.151	0.000	0.000
ν_8	0.037	0.003	0.081	ν_{47}	0.156	−0.021	0.134
ν_9	0.043	−0.017	0.395	ν_{48}	0.156	−0.005	0.032
ν_{10}	0.045	0.005	0.111	ν_{49}	0.157	0.001	0.004
ν_{11}	0.049	0.036	0.735	ν_{50}	0.161	0.075	0.463
ν_{12}	0.053	−0.002	0.038	ν_{51}	0.163	0.063	0.385
ν_{13}	0.053	−0.018	0.340	ν_{52}	0.171	0.021	0.123
ν_{14}	0.060	−0.003	0.050	ν_{53}	0.171	0.040	0.233
ν_{15}	0.063	−0.001	0.016	ν_{54}	0.176	0.001	0.006
ν_{16}	0.066	0.001	0.015	ν_{55}	0.177	0.000	0.000
ν_{17}	0.070	−0.001	0.014	ν_{56}	0.180	−0.140	0.778
ν_{18}	0.072	−0.030	0.417	ν_{57}	0.183	0.051	0.279
ν_{19}	0.077	0.002	0.026	ν_{58}	0.186	0.001	0.005
ν_{20}	0.081	−0.012	0.148	ν_{59}	0.189	−0.006	0.032
ν_{21}	0.083	−0.004	0.048	ν_{60}	0.191	0.013	0.068
ν_{22}	0.088	−0.025	0.284	ν_{61}	0.195	0.013	0.067
ν_{23}	0.093	0.000	0.000	ν_{62}	0.196	−0.013	0.066
ν_{24}	0.094		0.000	ν_{63}	0.200	0.176	0.880
ν_{25}	0.096	0.000	0.000	ν_{64}	0.203		0.000
ν_{26}	0.100	0.005	0.050	ν_{65}	0.208	0.005	0.024
ν_{27}	0.104	0.001	0.010	ν_{66}	0.209	−0.002	0.010
ν_{28}	0.107	0.009	0.084	ν_{67}	0.374	0.005	0.013
ν_{29}	0.108	−0.004	0.037	ν_{68}	0.380	−0.001	0.003
ν_{30}	0.109	0.010	0.092	ν_{69}	0.393	0.001	0.003
ν_{31}	0.112	−0.004	0.036	ν_{70}	0.394	0.003	0.007
ν_{32}	0.114	0.017	0.149	ν_{71}	0.394	0.003	0.008
ν_{33}	0.118	0.001	0.008	ν_{72}	0.395	0.001	0.003
ν_{34}	0.119	−0.004	0.034	ν_{73}	0.395	0.001	0.002
ν_{35}	0.122	−0.003	0.025	ν_{74}	0.397	0.003	0.008
ν_{36}	0.123	−0.004	0.033	ν_{75}	0.397	−0.008	0.020
ν_{37}	0.127	−0.012	0.094	ν_{76}	0.400	−0.005	0.013
ν_{38}	0.128	0.002	0.016	ν_{77}	0.400	−0.004	0.010
ν_{39}	0.130	−0.020	0.154	ν_{78}	0.462	−0.004	0.009

Table F.11: Vibrational energies, ω and on-diagonal linear coupling constants, κ for the S_1 state of 9-methyl anthracene. All values are in eV.

Mode	ω	κ	κ/ω
ν_6	0.031	−0.001	0.032
ν_8	0.043	0.021	0.488
ν_9	0.049	−0.003	0.061
ν_{11}	0.053	0.013	0.245
ν_{14}	0.066	0.001	0.015
ν_{16}	0.070	0.009	0.129
ν_{18}	0.077	0.001	0.013
ν_{19}	0.081	0.001	0.012
ν_{20}	0.087	−0.001	0.011
ν_{25}	0.104	−0.005	0.048
ν_{28}	0.108	0.004	0.037
ν_{30}	0.114	0.104	0.912
ν_{35}	0.128	−0.031	0.242
ν_{36}	0.130	0.002	0.015
ν_{37}	0.131	0.011	0.084
ν_{39}	0.135	0.028	0.207
ν_{40}	0.141	−0.166	1.177
ν_{41}	0.147	−0.001	0.007
ν_{42}	0.148	−0.004	0.027
ν_{43}	0.150	0.002	0.013
ν_{44}	0.152	0.032	0.211
ν_{45}	0.157	0.057	0.363
ν_{46}	0.161	−0.005	0.031
ν_{47}	0.163	0.002	0.012
ν_{48}	0.169	−0.031	0.183
ν_{49}	0.171	−0.008	0.047
ν_{50}	0.176	0.002	0.011
ν_{51}	0.177	0.080	0.452
ν_{52}	0.179	−0.010	0.056
ν_{53}	0.180	0.003	0.017
ν_{54}	0.185	−0.003	0.016
ν_{55}	0.186	−0.007	0.038
ν_{57}	0.189	−0.002	0.011
ν_{58}	0.192	−0.005	0.026
ν_{59}	0.196	0.011	0.056
ν_{60}	0.200	−0.004	0.020
ν_{61}	0.203	−0.034	0.167
ν_{62}	0.208	0.048	0.231
ν_{63}	0.209	0.006	0.029
ν_{64}	0.378	−0.004	0.011
ν_{66}	0.393	0.005	0.013
ν_{68}	0.394	−0.022	0.056
ν_{69}	0.394	0.002	0.005
ν_{70}	0.395	−0.002	0.005
ν_{71}	0.395	0.001	0.003
ν_{72}	0.397	−0.007	0.018
ν_{73}	0.397	0.004	0.010
ν_{74}	0.400	−0.011	0.028
ν_{75}	0.400	0.011	0.028

κ/ω ratio will greatly reduce the number of modes that may be important. Given also that the experimental spectra shows no change in the vibrational fine structure from that of anthracene, then picking out the vibrational modes similar to those important in anthracene should be a useful approach.

From analysing Table F.11, eight vibrational modes were deemed to be important in the S_1 photochemistry of the methyl derivative and were included in the model. These were ν_{30}, methyl bending/para C-H bending, ν_{35}, C-H bending and methyl rocking, ν_{40}, C-H bending and ring distortion, ν_{44} and ν_{45}, C-H bending, ν_{51}, C-H bending of the outer rings, ν_{61}, methyl bending/para C-H bending and ν_{62}, C-H bending and C-C ring stretch. Mode ν_{40}, which possesses the largest value of κ and of the ratio κ/ω and is shown in Figure F.6(a) is very similar to the normal modes selected for the anthracene model.

For the hydroxymethyl derivative, eight modes were also chosen for use in the

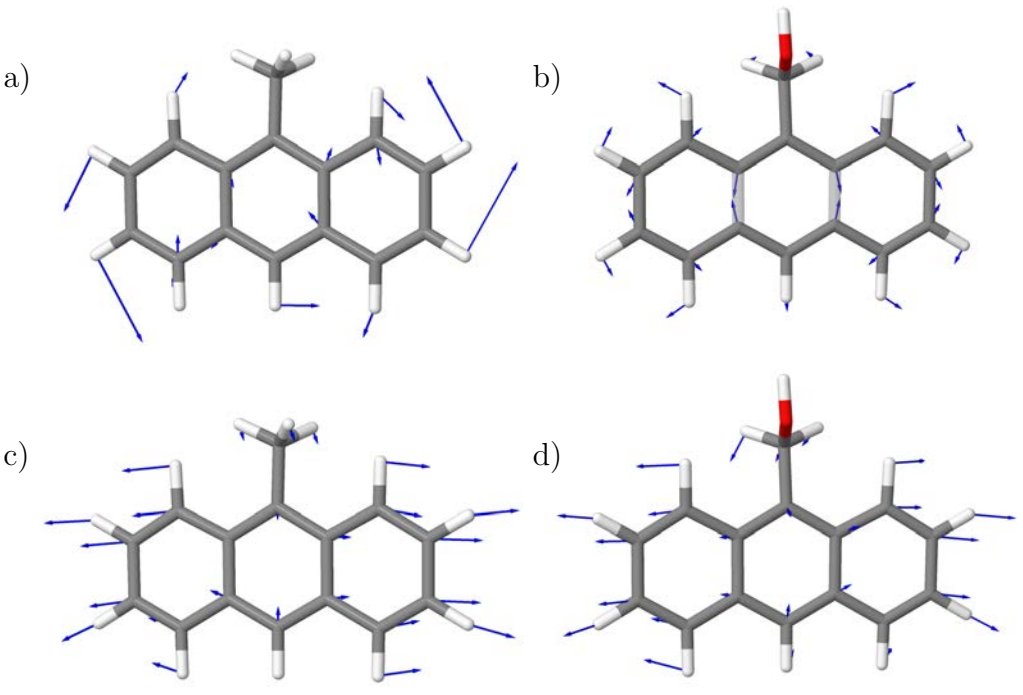

Fig. F.6: Select normal modes of 9-methyl and 9-hydroxymethyl anthracene. (a) and (b) show the modes with the highest κ values whilst (c) and (d) show the ring breathing mode.

model. These were ν_{11}, ring breathing mode, ν_{45}, C-H rocking, ν_{50}, C-H rocking/middle ring distortion, ν_{51}, C-H rocking/ring distortion, ν_{53}, C-H rocking, ν_{56}, C-C and methylene rocking, ν_{57}, methylene rocking and ν_{63}, C-C ring stretch mode. Again, the mode with the largest κ value and ratio, ν_{63}, the C-C ring stretch mode, was also observed to be important for anthracene, tetracene and pentacene. This mode is shown in Figure F.6(b) and is very similar to the ν_9 mode seen in anthracene.

F.6 Carboxylic Acid and Aldehyde

The on-diagonal linear coupling constants for AnCA and AnCHO are shown in Tables F.12 and Tables F.13. Analysis of Table F.12 shows there to be four modes with large κ values. These are ν_{40}, a C-H bending mode, ν_{49}, a ring breathing/C-H bending mode, ν_{56}, a C-C ring stretch mode and ν_{59}, a C-H bending mode. Again, these modes resemble those shown to be important for anthracene and the other derivatives studied so far. Based on high values of the ratio κ/ω, a further three modes were considered: these were the two lowest frequency modes, ν_1 and ν_2, both of which involve torsional motion of the carbonyl group and out of plane motion of the anthracene core ring system, and ν_6, an out of plane ring wiggle mode. Out of these modes, four were regarded as being important for the S_1 photodynamics of AnCA, $\nu_6, \nu_{49}, \nu_{56}$ and ν_{59}, these are shown in Figure F.7. Despite its large κ value, it was found that ν_{40} introduces progressions in the spectrum which are not observed experimentally. The omission of modes ν_1 and ν_2 is discussed later.

For AnCHO, there are three normal modes that display large κ values. These are ν_{46}, a C-H bending/skeletal distortion mode, ν_{52}, C-C stretch mode and ν_{58}, another C-C stretch mode. Based on the ratio κ/ω, mode ν_1, an out of plane ring bend, is also likely to contribute to the photodynamics. Combining these creates the four mode model used in simulating the absorption and emission spectra. These modes are illustrated in Figure F.8.

Table F.12: Vibrational energies, ω and on-diagonal linear coupling constants, κ for the S_1 state of anthracene-9-carboxylic acid. All values are in eV.

Mode	ω	κ	κ/ω	Mode	ω	κ	κ/ω
ν_1	0.008	0.043	5.375	ν_{40}	0.131	0.170	1.298
ν_2	0.009	−0.041	4.556	ν_{41}	0.131	0.002	0.015
ν_3	0.013	0.004	0.308	ν_{42}	0.141	0.003	0.021
ν_4	0.015	0.007	0.467	ν_{43}	0.145	−0.016	0.110
ν_5	0.024	−0.005	0.208	ν_{44}	0.147	0.001	0.007
ν_6	0.029	−0.024	0.828	ν_{45}	0.148	−0.017	0.115
ν_7	0.030	−0.004	0.133	ν_{46}	0.151	0.014	0.093
ν_8	0.033	0.008	0.242	ν_{47}	0.152	−0.004	0.026
ν_9	0.044	−0.023	0.523	ν_{48}	0.158	−0.001	0.006
ν_{10}	0.045	−0.036	0.800	ν_{49}	0.161	0.058	0.360
ν_{11}	0.051	−0.020	0.392	ν_{50}	0.162	0.015	0.093
ν_{12}	0.051	0.045	0.882	ν_{51}	0.166	−0.002	0.012
ν_{13}	0.054	0.006	0.111	ν_{52}	0.169	−0.003	0.018
ν_{14}	0.060	0.008	0.133	ν_{53}	0.173	0.008	0.046
ν_{15}	0.063	−0.003	0.048	ν_{54}	0.176	−0.001	0.006
ν_{16}	0.064	0.012	0.188	ν_{55}	0.178	−0.007	0.039
ν_{17}	0.071	0.000	0.000	ν_{56}	0.180	0.117	0.650
ν_{18}	0.074	0.005	0.068	ν_{57}	0.186	0.014	0.075
ν_{19}	0.078	−0.005	0.064	ν_{58}	0.186	0.010	0.054
ν_{20}	0.080	0.010	0.125	ν_{59}	0.191	−0.142	0.743
ν_{21}	0.082	0.004	0.049	ν_{60}	0.195	−0.003	0.015
ν_{22}	0.082	0.006	0.073	ν_{61}	0.200	−0.016	0.080
ν_{23}	0.088	−0.029	0.330	ν_{62}	0.202	0.001	0.005
ν_{24}	0.093	−0.004	0.043	ν_{63}	0.208	0.000	0.000
ν_{25}	0.094	−0.008	0.085	ν_{64}	0.209	−0.005	0.024
ν_{26}	0.095	0.010	0.105	ν_{65}	0.224	0.017	0.076
ν_{27}	0.096	−0.005	0.052	ν_{66}	0.394	−0.002	0.005
ν_{28}	0.101	0.001	0.010	ν_{67}	0.394	−0.001	0.003
ν_{29}	0.107	0.059	0.551	ν_{68}	0.395	−0.007	0.018
ν_{30}	0.108	0.003	0.028	ν_{69}	0.396	0.007	0.018
ν_{31}	0.108	0.001	0.009	ν_{70}	0.396	0.012	0.030
ν_{32}	0.109	−0.001	0.009	ν_{71}	0.398	0.010	0.025
ν_{33}	0.114	−0.001	0.009	ν_{72}	0.398	−0.026	0.065
ν_{34}	0.117	−0.003	0.026	ν_{73}	0.403	0.001	0.002
ν_{35}	0.120	−0.003	0.025	ν_{74}	0.404	−0.002	0.005
ν_{36}	0.120	0.002	0.017	ν_{75}	0.455	0.001	0.002
ν_{37}	0.123	−0.028	0.228				
ν_{38}	0.123	0.019	0.154				
ν_{39}	0.124	0.007	0.056				

Table F.13: Vibrational energies, ω and on-diagonal linear coupling constants, κ for the S_1 state of anthracene-9-carbaldehyde. All values are in eV.

Mode	ω	κ	κ/ω	Mode	ω	κ	κ/ω
ν_1	0.007	0.010	1.351	ν_{40}	0.141	0.007	0.050
ν_2	0.011	−0.007	0.642	ν_{41}	0.147	0.012	0.082
ν_3	0.013	0.001	0.075	ν_{42}	0.147	0.024	0.163
ν_4	0.015	0.002	0.130	ν_{43}	0.150	−0.053	0.353
ν_5	0.029	−0.001	0.034	ν_{44}	0.151	0.008	0.053
ν_6	0.031	−0.012	0.385	ν_{45}	0.157	−0.004	0.025
ν_7	0.034	−0.006	0.179	ν_{46}	0.159	−0.080	0.503
ν_8	0.037	−0.003	0.081	ν_{47}	0.163	0.034	0.209
ν_9	0.046	−0.010	0.216	ν_{48}	0.168	−0.009	0.054
ν_{10}	0.049	−0.005	0.101	ν_{49}	0.170	0.020	0.118
ν_{11}	0.050	−0.019	0.377	ν_{50}	0.175	−0.001	0.006
ν_{12}	0.053	0.025	0.469	ν_{51}	0.177	−0.001	0.006
ν_{13}	0.060	0.001	0.017	ν_{52}	0.179	−0.104	0.581
ν_{14}	0.063		0.000	ν_{53}	0.183	−0.039	0.213
ν_{15}	0.065	−0.007	0.108	ν_{54}	0.184	−0.010	0.054
ν_{16}	0.066	0.014	0.211	ν_{55}	0.185	−0.002	0.011
ν_{17}	0.074	0.012	0.162	ν_{56}	0.190	−0.019	0.100
ν_{18}	0.076	−0.006	0.079	ν_{57}	0.195	−0.003	0.015
ν_{19}	0.081	0.039	0.481	ν_{58}	0.199	0.160	0.804
ν_{20}	0.083	0.003	0.036	ν_{59}	0.202	0.001	0.005
ν_{21}	0.089	−0.019	0.213	ν_{60}	0.207	−0.002	0.010
ν_{22}	0.093	−0.002	0.021	ν_{61}	0.209	−0.006	0.029
ν_{23}	0.094	−0.002	0.021	ν_{62}	0.218	0.030	0.138
ν_{24}	0.096	0.000	0.000	ν_{63}	0.369	0.002	0.005
ν_{25}	0.098	−0.003	0.031	ν_{64}	0.393	0.006	0.015
ν_{26}	0.107	0.002	0.019	ν_{65}	0.394	0.002	0.005
ν_{27}	0.107	−0.008	0.075	ν_{66}	0.394	−0.004	0.010
ν_{28}	0.110	0.004	0.036	ν_{67}	0.395	0.003	0.008
ν_{29}	0.110		0.000	ν_{68}	0.395	0.003	0.008
ν_{30}	0.115	−0.002	0.017	ν_{69}	0.397	0.006	0.015
ν_{31}	0.117	0.001	0.009	ν_{70}	0.398	−0.005	0.013
ν_{32}	0.120	0.000	0.000	ν_{71}	0.401	−0.002	0.005
ν_{33}	0.121	0.000	0.000	ν_{72}	0.405	0.004	0.010
ν_{34}	0.123	−0.002	0.016				
ν_{35}	0.125	0.006	0.048				
ν_{36}	0.126	0.004	0.032				
ν_{37}	0.130	0.002	0.015				
ν_{38}	0.131	0.014	0.107				
ν_{39}	0.133	0.005	0.038				

The cuts through the potential energy surfaces along the selected modes are shown in Figure F.9. The cuts shown on the left are for AnCA. As expected, the non-zero value for the linear coupling constant manifests itself in the displacement of the S_1 minima away from the equilibrium geometry. The cut along the ν_6 mode is shallow, reflecting the low frequency of the mode. Similarly the cuts for AnCHO show the displacement of the S_1 minima away from the equilibrium geometry. Interestingly, the cut along the lowest frequency ν_1 mode is nearly flat for the S_1 state. Such a flat surface is indicative of an unbound surface, although the slight gradient suggests the minimum may be displaced much further from the ground state minimum.

The two lowest modes for AnCA, ν_1 and ν_2, were previously mentioned as being omitted from the model, despite their high κ/ω ratios. This is because the cuts along these modes exhibit similar behaviour to that seen for ν_1 in AnCHO. Namely, the S_1 potential for these modes is not bound, instead forming a negative gradient. This creates problems with the dynamics, as the wavepacket will either rapidly disperse as it reaches the end of the potential, or rebound against the grid on which the potentials are constructed. The easiest way to avoid these problems is simply to exclude these modes from the model. It is unlikely these modes contribute to the absorption spectrum, although it has been established that the torsional motion of the group has an impact on the dynamics. Increasing the length of the cut along these modes show there is a conical intersection with the ground state. In addition, both show a minimum, although its location is shifted far from the ground state minimum. The cuts through the potential energy surface along these modes are shown in Figure F.10.

In their study of the fluorescence of AnCA, Rodriquez-Cordoba *et al.* calculated potential energy curves for the dihedral angle O-C-C-C in the ground and S_1 state employing a PCM model to replicate condensed phase behaviour [434]. The results

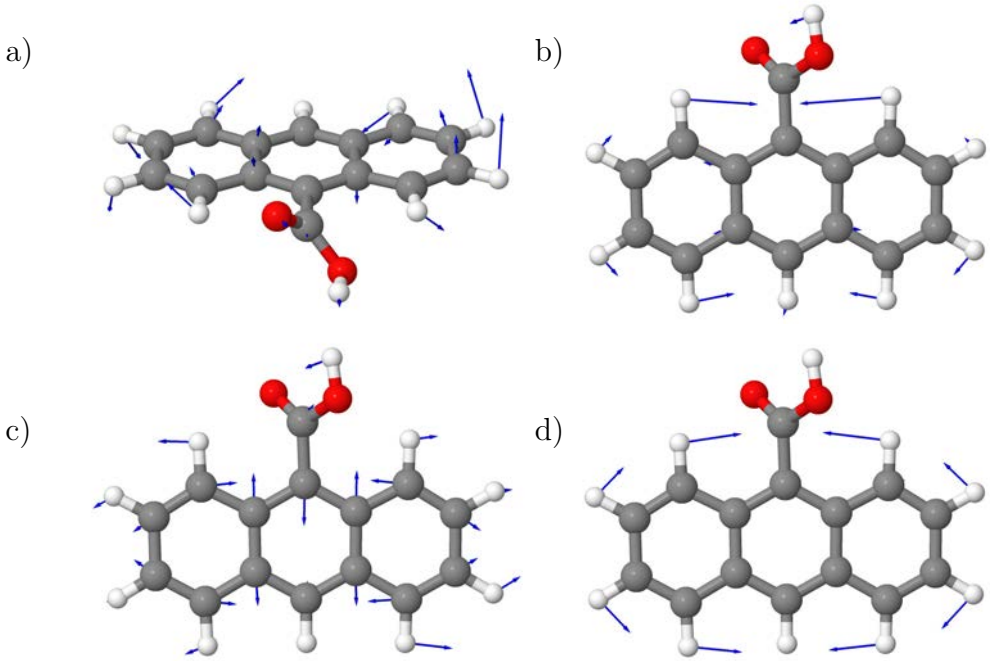

Fig. F.7: The normal modes that are important in the S_1 photodynamics of anthracene-9-carboxylic acid. (a) ν_6 out of plane wiggle (b) ν_{49} a ring breathing/C-H bending mode (c) ν_{56}, a C-C ring stretch mode and (d) ν_{59}, a C-H bending mode.

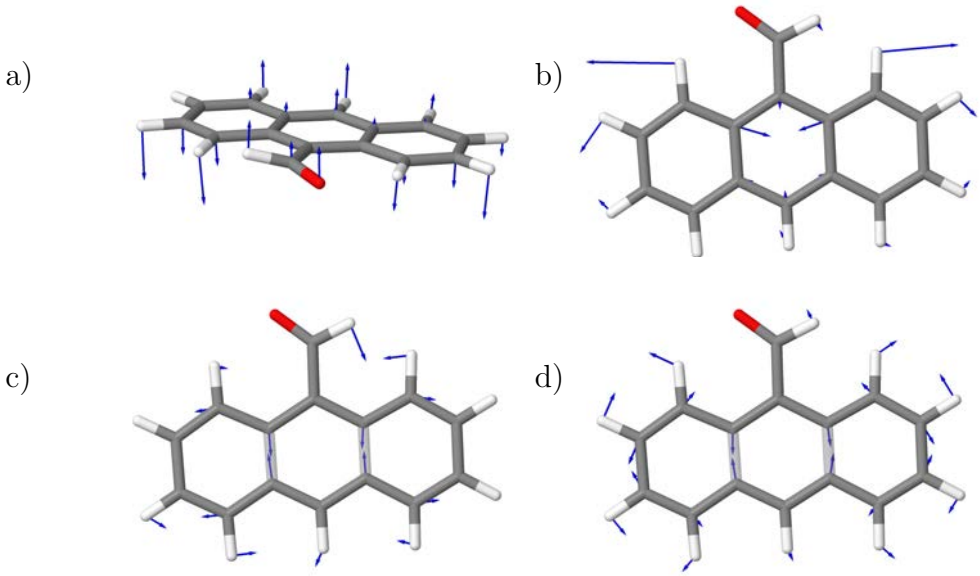

Fig. F.8: The normal modes that are important in the S_1 photodynamics of anthracene-9-carboxylic acid. (a) ν_1, an out of plane ring bend (b) ν_{46}, a C-H bending/skeletal distortion mode (c) ν_{52}, C-C stretch mode and (d) ν_{58}, another C-C stretch mode.

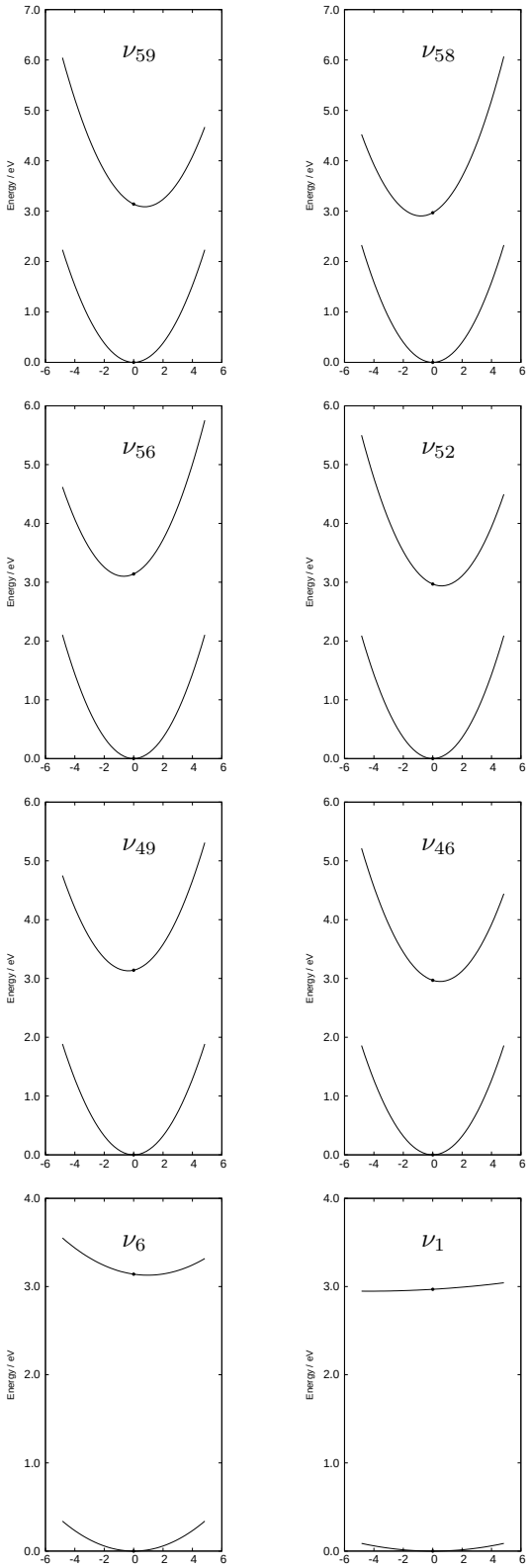

Fig. F.9: Cuts through the adiabatic potential energy surfaces along select totally symmetric modes for the ground and first excited state of (left) anthracene-9-carboxylic acid and (right) anthracene-9-carbaldehyde.

a)

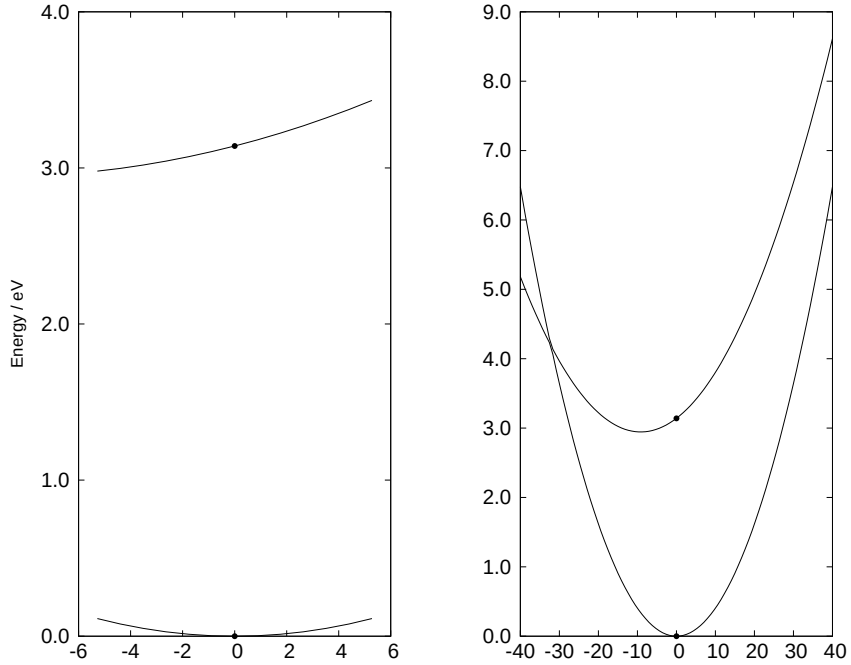

b)

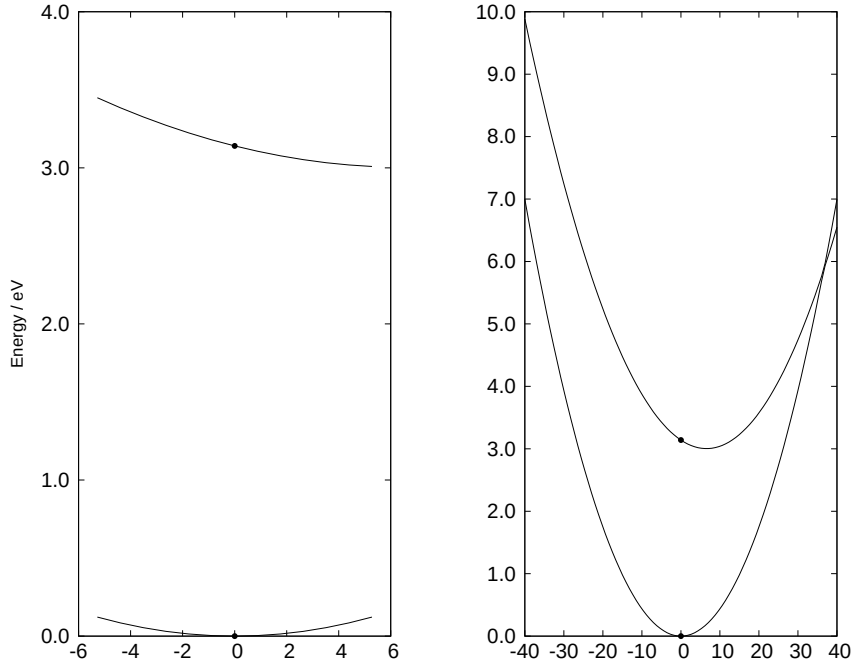

Fig. F.10: Cuts through the adiabatic potential energy surfaces along (a) ν_1 and (b) ν_2 for the ground and first excited state of anthracene-9-carboxylic acid. The cuts on the right show these modes along a greater number of points and the intersection made with the ground state.

showed the ground state to be formed of a double well potential with a small rotational barrier, whilst in the excited state a much large barrier was encountered. The implications of this are that the FC points on the S_1 possess a large gradient with respect to the nuclear coordinates. Since the simplified model here only constructs potentials harmonically, then it is unable to produce such a topology. This supports the shape of the cuts along modes ν_1 and ν_2, both of which correspond to this torsional motion. In the dissociated carboxylate salt, however, the potentials along this dihedral angle are much more harmonic in both states, with the S_1 minimum hardly shifted.

Bibliography

[1] J. Hellot, *Mem. Acad. Roy. Sci.*, 1737, (54-58), 101–120.

[2] H. Trommsdorff, *Ann. der Pharm.*, 1834, **11**(2), 190–207.

[3] T. von Grotthuss, *Schweiggers J. Chem. Phys.*, 1815, **14**(163), 174.

[4] J. Draper, *London, Edinburgh, Dublin Philos. Mag. 3rd. Ser.*, 1841, **19**(3), 195–210.

[5] J. J. Balmer, *Ann. Phys.*, 1885, **261**(5), 80–87.

[6] M. Planck, *Ann. Phys.*, 1901, **309**(3), 553–563.

[7] A. Einstein, *Ann. Phys.*, 1905, **322**(6), 132–148.

[8] G. N. Lewis, *Nature*, 1926, **118**(2981), 874.

[9] M. Kasha, *Discuss. Faraday Soc.*, 1950, **9**(c), 14.

[10] M. A. El-Sayed, *J. Chem. Phys.*, 1963, **38**(12), 2834–2838.

[11] M. A. El-Sayed, *Acc. Chem. Res.*, 1968, **1**(1), 8–16.

[12] M. N. Ashfold, D. Murdock, and T. A. Oliver, *Annu. Rev. Phys. Chem.*, 2017, **68**(1), 63–82.

[13] J. von Neuman and E. Wigner, *Phys. Zeitschrift*, 1929, **30**(1), 467–470.

[14] K. G. Spears and S. A. Rice, *J. Chem. Phys.*, 1971, **55**(12), 5561–5581.

[15] T. A. Stephenson and S. A. Rice, *J. Chem. Phys.*, 1984, **81**(3), 1083–1101.

[16] J. H. Callomon, T. M. Dunn, and I. M. Mills, *Philos. Trans. R. Soc. A Math. Phys. Eng. Sci.*, 1966, **259**(1104), 499–532.

[17] L. Kaplan, S. P. Walch, and K. E. Wilzbach, *J. Am. Chem. Soc.*, 1968, **90**(20), 5646–5647.

[18] I. J. Palmer, I. N. Ragazos, F. Bernardi, M. Olivucci, and M. A. Robb, *J. Am. Chem. Soc.*, 1993, **115**(2), 673–682.

[19] L. T. Scott and M. Jones, *Chem. Rev.*, 1972, **72**(2), 181–202.

[20] D. Bryce-Smith and A. Gilbert, *Tetrahedron*, 1976, **32**(12), 1309–1326.

[21] W. Radloff, T. Freudenberg, H.-H. Ritze, V. Stert, K. Weyers, and F. Noack, *Chem. Phys. Lett.*, 1995, **245**(4-5), 400–406.

[22] R. S. Minns, D. S. N. Parker, T. J. Penfold, G. A. Worth, and H. H. Fielding, *Phys. Chem. Chem. Phys.*, 2010, **12**(48), 15607.

[23] T. J. Penfold, R. Spesyvtsev, O. M. Kirkby, R. S. Minns, D. S. N. Parker, H. H. Fielding, and G. A. Worth, *J. Chem. Phys.*, 2012, **137**(20), 15607–15615.

[24] M. Beer and H. C. Longuet-Higgins, *J. Chem. Phys.*, 1955, **23**(8), 1390–1391.

[25] P. Rentzepis, *Chem. Phys. Lett.*, 1969, **3**(9), 717–720.

[26] J. P. Heritage and A. Penzkofer, *Chem. Phys. Lett.*, 1976, **44**(1), 76–81.

[27] B. D. Wagner, M. Szymanski, and R. P. Steer, *J. Chem. Phys.*, 1993, **98**(1), 301.

[28] A. J. Wurzer, T. Wilhelm, J. Piel, and E. Riedle, *Chem. Phys. Lett.*, 1999, **299**(3-4), 296–302.

[29] M. J. Bearpark, F. Bernardi, S. Clifford, M. Olivucci, M. A. Robb, B. R. Smith, and T. Vreven, *J. Am. Chem. Soc.*, 1996, **118**(1), 169–175.

[30] Y. Amatatsu and Y. Komura, *J. Chem. Phys.*, 2006, **125**(17), 174311.

[31] T. Itoh, *Chem. Rev.*, 2012, **112**(8), 4541–4568.

[32] D. Polli, P. Altoè, O. Weingart, K. M. Spillane, C. Manzoni, D. Brida, G. Tomasello, G. Orlandi, P. Kukura, R. A. Mathies, M. Garavelli, and G. Cerullo, *Nature*, 2010, **467**(7314), 440–443.

[33] T. Yoshizawa and G. Wald, *Nature*, 1963, **197**(4874), 1279–1286.

[34] M. Garavelli, P. Celani, F. Bernardi, M. A. Robb, and M. Olivucci, *J. Am. Chem. Soc.*, 1997, **119**(29), 6891–6901.

[35] R. Gonzalez-Luque, M. Garavelli, F. Bernardi, M. Merchan, M. A. Robb, and M. Olivucci, *Proc. Natl. Acad. Sci.*, 2000, **97**(17), 9379–9384.

[36] P. Kukura, D. W. McCamant, S. Yoon, D. B. Wandschneider, and R. A. Mathies, *Science*, 2005, **310**(5750), 1006–1009.

[37] O. Shimomura, F. H. Johnson, and Y. Saiga, *J. Cell. Comp. Physiol.*, 1962, **59**(3), 223–239.

[38] F. H. Johnson, O. Shimomura, Y. Saiga, L. C. Gershman, G. T. Reynolds, and J. R. Waters, *J. Cell. Comp. Physiol.*, 1962, **60**(1), 85–103.

[39] O. Shimomura and F. H. Johnson, *Biochemistry*, 1969, **8**(10), 3991–3997.

[40] H. Morise, O. Shimomura, F. H. Johnson, and J. Winant, *Biochemistry*, 1974, **13**(12), 2656–2662.

[41] J. G. Morin and J. W. Hastings, *J. Cell. Physiol.*, 1971, **77**(3), 313–318.

[42] M. Chalfie, Y. Tu, G. Euskirchen, W. Ward, and D. Prasher, *Science*, 1994, **263**(5148), 802–805.

[43] S. Inouye and F. I. Tsuji, *FEBS Lett.*, 1994, **351**(2), 211–214.

[44] D. Prasher, R. O. McCann, and M. J. Cormier, *Biochem. Biophys. Res. Commun.*, 1985, **126**(3), 1259–1268.

[45] D. C. Prasher, V. K. Eckenrode, W. W. Ward, F. G. Prendergast, and M. J. Cormier, *Gene*, 1992, **111**(2), 229–233.

[46] M. Ormo, A. B. Cubitt, K. Kallio, L. A. Gross, R. Y. Tsien, and S. J. Remington, *Science*, 1996, **273**(5280), 1392–1395.

[47] X. W. Yang, P. Model, and N. Heintz, *Nat. Biotechnol.*, 1997, **15**(9), 859–865.

[48] M. Zimmer, *Chem. Soc. Rev.*, 2009, **38**(10), 2823.

[49] O. Shimomura, *FEBS Lett.*, 1979, **104**(2), 220–222.

[50] C. W. Cody, D. C. Prasher, W. M. Westler, F. G. Prendergast, and W. W. Ward, *Biochemistry*, 1993, **32**(5), 1212–1218.

[51] R. Heim, D. C. Prasher, and R. Y. Tsien, *Proc. Natl. Acad. Sci.*, 1994, **91**(26), 12501–12504.

[52] T. D. Craggs, *Chem. Soc. Rev.*, 2009, **38**(10), 2865–2875.

[53] A. F. Bell, X. He, R. M. Wachter, and P. J. Tonge, *Biochemistry*, 2000, **39**(15), 4423–4431.

[54] V. Helms, T. P. Straatsma, and J. A. McCammon, *J. Phys. Chem. B*, 1999, **103**(16), 3263–3269.

[55] S. S. Patnaik, S. Trohalaki, and R. Pachter, *Biopolymers*, 2004, **75**(6), 441–452.

[56] J. J. Van Thor, G. Zanetti, K. L. Ronayne, and M. Towrie, *J. Phys. Chem. B*, 2005, **109**(33), 16099–16108.

[57] J. J. Van Thor, *Chem. Soc. Rev.*, 2009, **38**(10), 2935–2950.

[58] P. J. Tonge and S. R. Meech, *J. Photochem. Photobiol. A Chem.*, 2009, **205**(1), 1–11.

[59] C. C. Hsieh, P. T. Chou, C. W. Shih, W. T. Chuang, M. W. Chung, J. Lee, and T. Joo, *J. Am. Chem. Soc.*, 2011, **133**(9), 2932–2943.

[60] H. Niwa, S. Inouye, T. Hirano, T. Matsuno, S. Kojima, M. Kubota, M. Ohashi, and F. I. Tsuji, *Proc. Natl. Acad. Sci.*, 1996, **93**(24), 13617–13622.

[61] F. McCapra, Z. Razavi, and A. P. Neary, *J. Chem. Soc. Chem. Commun.*, 1988, **5**(12), 790.

[62] S. Kojima, H. Ohkawa, T. Hirano, S. Maki, H. Niwa, M. Ohashi, S. Inouye, and F. I. Tsuji, *Tetrahedron Lett.*, 1998, **39**(29), 5239–5242.

[63] L. Wu and K. Burgess, *J. Am. Chem. Soc.*, 2008, **130**(12), 4089–4096.

[64] K. A. Lukyanov, A. F. Fradkov, N. G. Gurskaya, M. V. Matz, Y. A. Labas, A. P. Savitsky, M. L. Markelov, A. G. Zaraisky, X. Zhao, Y. Fang, W. Tan, and S. A. Lukyanov, *J. Biol. Chem.*, 2000, **275**(34), 25879–25882.

[65] M. C. Chan, S. Karasawa, H. Mizuno, I. Bosanac, D. Ho, G. G. Privé, A. Miyawaki, and M. Ikura, *J. Biol. Chem.*, 2006, **281**(49), 37813–37819.

[66] Y. A. Labas, N. G. Gurskaya, Y. G. Yanushevich, A. F. Fradkov, K. A. Lukyanov, S. A. Lukyanov, and M. V. Matz, *Proc. Natl. Acad. Sci. U. S. A.*, 2002, **99**(7), 4256–61.

[67] G. H. Patterson, S. M. Knobel, W. D. Sharif, S. R. Kain, and D. W. Piston, *Biophys. J.*, 1997, **73**(5), 2782–2790.

[68] D. Wu, W. W. Guo, X. Y. Liu, and G. Cui, *ChemPhysChem*, 2016, **17**(15), 2340–2347.

[69] F. Chen, Q. Zeng, W. Zhuang, and W. Liang, *J. Phys. Chem. B*, 2016, **120**(37), 9833–9842.

[70] J. Wierzchowski, *Nucleosides, Nucleotides and Nucleic Acids*, 2014, **33**(9), 626–644.

[71] D. A. Horke, H. M. Watts, A. D. Smith, E. Jager, E. Springate, O. Alexander, C. Cacho, R. T. Chapman, and R. S. Minns, *Phys. Rev. Lett.*, 2016, **117**(16), 1–5.

[72] I. Georgieva, N. Trendafilova, A. J. Aquino, and H. Lischka, *J. Phys. Chem. A*, 2007, **111**(1), 127–135.

[73] Y. H. Liu, M. S. Mehata, and J. Y. Liu, *J. Phys. Chem. A*, 2011, **115**(1), 19–24.

[74] Z. Tang, Y. Qi, Y. Wang, P. Zhou, J. Tian, and X. Fei, *J. Phys. Chem. B*, 2018, **122**(14), 3988–3995.

[75] N. Agmon, *J. Phys. Chem. A*, 2005, **109**(1), 13–35.

[76] P. Chou, D. McMorrow, T. J. Aartsma, and M. Kasha, *J. Phys. Chem.*, 1984, **88**(20), 4596–4599.

[77] J. E. Kwon and S. Y. Park, *Adv. Mater.*, 2011, **23**(32), 3615–3642.

[78] J. Zhao, S. Ji, Y. Chen, H. Guo, and P. Yang, *Phys. Chem. Chem. Phys.*, 2012, **14**(25), 8803–8817.

[79] H. W. Tseng, J. Q. Liu, Y. A. Chen, C. M. Chao, K. M. Liu, C. L. Chen, T. C. Lin, C. H. Hung, Y. L. Chou, T. C. Lin, T. L. Wang, and P. T. Chou, *J. Phys. Chem. Lett.*, 2015, **6**(8), 1477–1486.

[80] P. Zhou and K. Han, *Acc. Chem. Res.*, 2018, **51**(7), 1681–1690.

[81] M. Born and H. Kuang, *Dynamical Theory of Crystal Lattices*, Oxford University Press, 1962.

[82] C. J. Ballhausen and A. E. Hansen, *Annu. Rev. Phys. Chem.*, 1972, **23**(1), 15–38.

[83] T. Pacher, L. S. Cederbaum, and H. Koppel in *Adv. Chem. Phys.;* John Wiley & Sons, Inc., 1993; pp. 293–391.

[84] M. Born and R. Oppenheimer, *Ann. Phys.*, 1927, **389**(20), 457–484.

[85] C. Zener, *Proc. R. Soc. A Math. Phys. Eng. Sci.*, 1932, **137**(833), 696–702.

[86] L. D. Landau, *Phys. Z. Sowjetunion*, 1932, **2**(46), 1–13.

[87] E. C. G. Stueckelberg, *Helv. Phys. Acta*, 1932, **5**(6), 369.

[88] W. Lichten, *Phys. Rev.*, 1967, **164**(1), 131–142.

[89] F. T. Smith, *Phys. Rev.*, 1969, **179**(1), 111–123.

[90] C. A. Mead and D. G. Truhlar, *J. Chem. Phys.*, 1982, **77**(12), 6090–6098.

[91] W. Domcke, D. R. Yarkony, and H. Koppel, *Conical Intersections - Electronic structure, dynamics & spectroscopy*, World Scientific Publishing Co., Singapore, 2004.

[92] E. Teller, *J. Phys. Chem.*, 1937, **41**(1), 109–116.

[93] R. F. Frey and E. R. Davidson, *The von Neumann-Wigner and Jahn-Teller theorems and their consequences*, Vol. 1, Wiley, New York, USA, 1990.

[94] H. A. Jahn and E. Teller, *Proc. R. Soc. A Math. Phys. Eng. Sci.*, 1937, **161**(905), 220–235.

[95] H. A. Jahn, *Proc. R. Soc. A Math. Phys. Eng. Sci.*, 1938, **164**(916), 117–131.

[96] R. Englman, *The Jahn-Teller Effect in Molecules and Crystals*, Wiley, New York, NY, USA, 1972.

[97] I. Bersuker, *Vibronic interactions in molecules and crystals*, Springer-Verlag, Berlin, Germany, 1989.

[98] I. B. Bersuker, *Chem. Rev.*, 2001, **101**(4), 1067–1114.

[99] B. Heumann, R. Düren, and R. Schinke, *Chem. Phys. Lett.*, 1991, **180**(6), 583–588.

[100] N. Matsunaga and D. R. Yarkony, *J. Chem. Phys.*, 1997, **107**(19), 7825–7838.

[101] H. C. Longuet-Higgins, *Proc. R. Soc. A Math. Phys. Eng. Sci.*, 1975, **344**(1637), 147–156.

[102] C. A. Mead, *J. Chem. Phys.*, 1979, **70**(5), 2276–2283.

[103] C. A. Mead and D. G. Truhlar, *J. Chem. Phys.*, 1986, **84**(2), 1055–1056.

[104] D. R. Yarkony, *J. Chem. Phys.*, 1996, **104**(20), 7866–7881.

[105] G. Herzberg, *Molecular spectra and molecular structure. Vol. 1: Spectra of Diatomic Molecules*, Prentice-Hall, New York, NY, USA, 1939.

[106] G. Herzberg, *Molecular spectra and molecular structure. Vol. 2: Infrared and Raman spectra of polyatomic molecules*, Van Nostrand, Princeton, US, 1945.

[107] G. Herzberg, *Electronic Spectra and Electronic Structure of Polyatomic Molecules*, Van Nostrand Reinhold, New York, NY, USA, 1966.

[108] J. Franck and E. G. Dymond, *Trans. Faraday Soc.*, 1926, **21**(1), 536.

[109] E. U. Condon, *Phys. Rev.*, 1926, **28**(6), 1182–1201.

[110] E. U. Condon, *Phys. Rev.*, 1928, **32**(6), 858–872.

[111] J. Brand and D. Williamson in *Adv. Phys. Org. Chem.*, Vol. 1; Elsevier B.V., 1963; pp. 365–423.

[112] S. J. Strickler and R. J. Barnhart, *J. Phys. Chem.*, 1982, **86**(4), 448–455.

[113] T. Cvitaš and J. Hollas, *Mol. Phys.*, 1970, **18**(1), 101–111.

[114] Y. Jain and H. Bist, *J. Mol. Spectrosc.*, 1973, **47**(1), 126–133.

[115] T. G. Wright, S. I. Panov, and T. A. Miller, *J. Chem. Phys.*, 1995, **102**(12), 4793.

[116] G. Herzberg and E. Teller, *Zeitschrift für Phys. Chemie*, 1933, **27**(1), 410–446.

[117] J. J. Davenport, J. Hodgkinson, J. R. Saffell, and R. P. Tatam, *Meas. Sci. Technol.*, 2016, **27**(1), 015802.

[118] J. H. Callomon and K. K. Innes, *J. Mol. Spectrosc.*, 1963, **10**(1-6), 166–181.

[119] H. Koppel, W. Domcke, and L. S. Cederbaum in *Adv. Chem. Phys.;* John Wiley & Sons, Inc., 1984; pp. 59–246.

[120] L. S. Cederbaum, H. Köppel, and W. Domcke, *Int. J. Quantum Chem.*, 1981, **20**(15), 251–267.

[121] J. C. Slater, *Phys. Rev.*, 1929, **34**(10), 1293–1322.

[122] C. C. J. Roothaan, *Rev. Mod. Phys.*, 1951, **23**(2), 69–89.

[123] L. Brillouin, *J. Phys. le Radium*, 1932, **3**(9), 373–389.

[124] E. Schrödinger, *Ann. Phys.*, 1926, **385**(13), 437–490.

[125] J. Rayleigh, *The Theory of Sound*, number v. 1 in The Theory of Sound, Macmillan, 1894.

[126] C. Møller and M. S. Plesset, *Phys. Rev.*, 1934, **46**(7), 618–622.

[127] J. A. Pople, J. S. Binkley, and R. Seeger, *Int. J. Quantum Chem.*, 1976, **10**(10 S), 1–19.

[128] R. Krishnan and J. A. Pople, *Int. J. Quantum Chem.*, 1978, **14**(1), 91–100.

[129] D. Cremer, *Wiley Interdiscip. Rev. Comput. Mol. Sci.*, 2011, **1**(4), 509–530.

[130] F. Coester, *Nucl. Phys.*, 1958, **7**(1), 421–424.

[131] F. Coester and H. Kümmel, *Nucl. Phys.*, 1960, **17**(1), 477–485.

[132] J. Čížek, *J. Chem. Phys.*, 1966, **45**(11), 4256–4266.

[133] J. Čížek and J. Paldus, *Int. J. Quantum Chem.*, 1971, **5**(4), 359–379.

[134] J. Paldus, J. Cizek, and I. Shavitt, *Phys. Rev. A*, 1972, **5**(1), 50–67.

[135] R. J. Bartlett and G. D. Purvis, *Int. J. Quantum Chem.*, 1978, **14**(5), 561–581.

[136] J. A. Pople, R. Krishnan, H. B. Schlegel, and J. S. Binkley, *Int. J. Quantum Chem.*, 1978, **14**(5), 545–560.

[137] R. J. Bartlett and G. D. Purvis, *Phys. Scr.*, 1980, **21**(3-4), 255–265.

[138] M. J. Frisch, R. Krishnan, and J. A. Pople, *Chem. Phys. Lett.*, 1980, **75**(1), 66–68.

[139] R. Krishnan, M. J. Frisch, and J. A. Pople, *J. Chem. Phys.*, 1980, **72**(7), 4244–4245.

[140] R. J. Bartlett, *Annu. Rev. Phys. Chem.*, 1981, **32**(1), 359–401.

[141] T. Van Voorhis and M. Head-Gordon, *J. Chem. Phys.*, 2000, **113**(20), 8873–8879.

[142] G. D. Purvis and R. J. Bartlett, *J. Chem. Phys.*, 1982, **76**(4), 1910–1918.

[143] Y. S. Lee, S. A. Kucharski, and R. J. Bartlett, *J. Chem. Phys.*, 1984, **81**(12), 5906–5912.

[144] Y. S. Lee, S. A. Kucharski, and R. J. Bartlett, *J. Chem. Phys.*, 1985, **82**(12), 5761–5761.

[145] Y. S. Lee and R. J. Bartlett, *J. Chem. Phys.*, 1984, **80**(9), 4371–4377.

[146] J. Noga and R. J. Bartlett, *J. Chem. Phys.*, 1987, **86**(12), 7041–7050.

[147] J. D. Watts and R. J. Bartlett, *Int. J. Quantum Chem.*, 1993, **48**(S27), 51–66.

[148] J. F. Stanton and R. J. Bartlett, *J. Chem. Phys.*, 1993, **98**(9), 7029–7039.

[149] T. Kuś, V. F. Lotrich, and R. J. Bartlett, *J. Chem. Phys.*, 2009, **130**(12), 124122.

[150] S. R. Gwaltney, M. Nooijen, and R. J. Bartlett, *Chem. Phys. Lett.*, 1996, **248**(3-4), 189–198.

[151] D. Sinha, S. Mukhopadhyay, R. Chaudhuri, and D. Mukherjee, *Chem. Phys. Lett.*, 1989, **154**(6), 544–549.

[152] J. F. Stanton and J. Gauss, *J. Chem. Phys.*, 1994, **101**(10), 8938–8944.

[153] M. Musiał, S. A. Kucharski, and R. J. Bartlett, *J. Chem. Phys.*, 2003, **118**(3), 1128–1136.

[154] M. Nooijen and R. J. Bartlett, *J. Chem. Phys.*, 1995, **102**(9), 3629–3647.

[155] J. Hinze, *J. Chem. Phys.*, 1973, **59**(12), 6424–6432.

[156] B. O. Roos in *Adv. Chem. Physics, v. 69 ab initio Methods Quantum Chem. part II*, ed. K. P. Lawley, Vol. 69 of *Advances in Chemical Physics;* John Wiley & Sons, Inc., Hoboken, NJ, USA, 1987; pp. 399–445.

[157] B. O. Roos, P. R. Taylor, and P. E. M. Siegbahn, *Chem. Phys.*, 1980, **48**(2), 157–173.

[158] D. Roca-Sanjuán, F. Aquilante, and R. Lindh, *Wiley Interdiscip. Rev. Comput. Mol. Sci.*, 2012, **2**(4), 585–603.

[159] J. G. Hill, *Int. J. Quantum Chem.*, 2013, **113**(1), 21–34.

[160] J. C. Slater, *Phys. Rev.*, 1930, **36**(1), 57–64.

[161] S. F. Boys, *Proc. R. Soc. London A*, 1950, **200**(1063), 542–554.

[162] W. J. Hehre, R. F. Stewart, and J. A. Pople, *J. Chem. Phys.*, 1969, **51**(6), 2657–2664.

[163] R. Ditchfield, W. J. Hehre, and J. A. Pople, *J. Chem. Phys.*, 1971, **54**(2), 724–728.

[164] W. J. Hehre, R. Ditchfield, and J. A. Pople, *J. Chem. Phys.*, 1972, **56**(5), 2257–2261.

[165] P. C. Hariharan and J. A. Pople, *Theor. Chim. Acta*, 1973, **28**(3), 213–222.

[166] M. M. Francl, W. J. Pietro, W. J. Hehre, J. S. Binkley, M. S. Gordon, D. J. DeFrees, and J. A. Pople, *J. Chem. Phys.*, 1982, **77**(7), 3654–3665.

[167] M. J. Frisch, J. A. Pople, and J. S. Binkley, *J. Chem. Phys.*, 1984, **80**(7), 3265–3269.

[168] T. H. Dunning, *J. Chem. Phys.*, 1989, **90**(2), 1007–1023.

[169] R. A. Kendall, T. H. Dunning, and R. J. Harrison, *J. Chem. Phys.*, 1992, **96**(9), 6796–6806.

[170] R. Mcweeny, *Int. J. Quantum Chem.*, 1967, **1**(1 S), 351–359.

[171] P. Hohenberg and W. Kohn, *Phys. Rev.*, 1964, **136**(3B), B864–B871.

[172] L. H. Thomas, *Math. Proc. Cambridge Philos. Soc.*, 1927, **23**(05), 542–548.

[173] E. Fermi, *Rend. Accad. Naz. Lincei*, 1927, **6**(32), 602–607.

[174] W. Kohn and L. J. Sham, *Phys. Rev.*, 1965, **140**(4A), A1133–A1138.

[175] P. A. M. Dirac, *Math. Proc. Cambridge Philos. Soc.*, 1930, **26**(03), 376.

[176] F. Bloch, *Zeitschrift für Phys.*, 1929, **57**(7-8), 545–555.

[177] D. M. Ceperley and B. J. Alder, *Phys. Rev. Lett.*, 1980, **45**(7), 566–569.

[178] A. D. Becke, *Phys. Rev. A*, 1988, **38**(6), 3098–3100.

[179] N. C. Handy and A. J. Cohen, *Mol. Phys.*, 2001, **99**(5), 403–412.

[180] A. D. Becke, *J. Chem. Phys.*, 1986, **84**(8), 4524–4529.

[181] J. P. Perdew, K. Burke, and M. Ernzerhof, *Phys. Rev. Lett.*, 1996, **77**(18), 3865–3868.

[182] J. P. Perdew, *Phys. Rev. B*, 1986, **33**(12), 8822–8824.

[183] C. Lee, W. Yang, and R. G. Parr, *Phys. Rev. B*, 1988, **37**(2), 785–789.

[184] B. Miehlich, A. Savin, H. Stoll, and H. Preuss, *Chem. Phys. Lett.*, 1989, **157**(3), 200–206.

[185] J. P. Perdew, S. Kurth, A. Zupan, and P. Blaha, *Phys. Rev. Lett.*, 1999, **82**(12), 2544–2547.

[186] O. Gunnarsson and B. I. Lundqvist, *Phys. Rev. B*, 1976, **13**(10), 4274–4298.

[187] J. Harris, *Phys. Rev. A*, 1984, **29**(4), 1648–1659.

[188] A. D. Becke, *J. Chem. Phys.*, 1993, **98**(2), 1372–1377.

[189] A. D. Becke, *J. Chem. Phys.*, 1993, **98**(7), 5648–5652.

[190] A. J. Cohen and N. C. Handy, *Mol. Phys.*, 2001, **99**(7), 607–615.

[191] S. Grimme, *J. Chem. Phys.*, 2006, **124**(3), 034108.

[192] Y.-S. Lin, G.-D. Li, S.-P. Mao, and J.-D. Chai, *J. Chem. Theory Comput.*, 2013, **9**(1), 263–272.

[193] P. J. Stephens, F. J. Devlin, C. F. Chabalowski, and M. J. Frisch, *J. Phys. Chem.*, 1994, **98**(45), 11623–11627.

[194] E. Runge and E. K. U. Gross, *Phys. Rev. Lett.*, 1984, **52**(12), 997–1000.

[195] R. van Leeuwen, *Phys. Rev. Lett.*, 1998, **80**(6), 1280–1283.

[196] G. Giuliani and G. Vignale, *Quantum theory of the electron liquid*, Vol. 117, Cambridge University Press, New York, NY, USA, 1 ed., 2005.

[197] E. J. Heller, *J. Chem. Phys.*, 1975, **62**(4), 1544–1555.

[198] M. Feit, J. Fleck, and A. Steiger, *J. Comput. Phys.*, 1982, **47**(3), 412–433.

[199] H. Tal-Ezer and R. Kosloff, *J. Chem. Phys.*, 1984, **81**(9), 3967–3971.

[200] T. J. Park and J. C. Light, *J. Chem. Phys.*, 1986, **85**(10), 5870–5876.

[201] J. Frenkel, *Wave Mechanics*, Clarendon Press, Oxford, 1934.

[202] A. McLachlan, *Mol. Phys.*, 1964, **8**(1), 39–44.

[203] P. Jungwirth and R. B. Gerber, *J. Chem. Phys.*, 1995, **102**(15), 6046–6056.

[204] P. Jungwirth and R. B. Gerber, *J. Chem. Phys.*, 1995, **102**(22), 8855–8864.

[205] P. Jungwirth, E. Fredj, and R. B. Gerber, *J. Chem. Phys.*, 1996, **104**(23), 9332–9339.

[206] H.-D. Meyer, U. Manthe, and L. S. Cederbaum, *Chem. Phys. Lett.*, 1990, **165**(1), 73–78.

[207] U. Manthe, H. Meyer, and L. S. Cederbaum, *J. Chem. Phys.*, 1992, **97**(5), 3199–3213.

[208] M. Beck and H.-D. Meyer, *Zeitschrift für Phys. D Atoms, Mol. Clust.*, 1997, **42**(2), 113–129.

[209] G. A. Worth, H.-D. Meyer, and L. S. Cederbaum, *J. Chem. Phys.*, 1998, **109**(9), 3518–3529.

[210] M. Beck, A. Jackle, G. A. Worth, and H. Meyer, *Phys. Rep.*, 2000, **324**(1), 1–105.

[211] D. O. Harris, G. G. Engerholm, and W. D. Gwinn, *J. Chem. Phys.*, 1965, **43**(5), 1515–1517.

[212] A. S. Dickinson and P. R. Certain, *J. Chem. Phys.*, 1968, **49**(9), 4209–4211.

[213] J. C. Light, I. P. Hamilton, and J. V. Lill, *J. Chem. Phys.*, 1985, **82**(3), 1400–1409.

[214] J. C. Light, in *Time-Dependent Quantum Mol. Dyn.*, ed. J. Broeckhove and L. Lathouwers, Springer US, Boston, MA, 1992; pp. 185–199.

[215] J. Fang and H. Guo, *J. Chem. Phys.*, 1994, **101**(7), 5831–5840.

[216] G. A. Worth, H.-D. Meyer, and L. S. Cederbaum, *J. Chem. Phys.*, 1996, **105**(11), 4412–4426.

[217] S. Mahapatra, G. A. Worth, H.-D. Meyer, L. S. Cederbaum, and H. Köppel, *J. Phys. Chem. A*, 2001, **105**(23), 5567–5576.

[218] C. Cattarius, G. A. Worth, H.-D. Meyer, and L. S. Cederbaum, *J. Chem. Phys.*, 2001, **115**(5), 2088–2100.

[219] A. Raab, I. Burghardt, and H. Meyer, *J. Chem. Phys.*, 1999, **111**(19), 8759–8772.

[220] V. Engel, *Chem. Phys. Lett.*, 1992, **189**(1), 76–78.

[221] U. Manthe, H.-D. Meyer, and L. S. Cederbaum, *J. Chem. Phys.*, 1992, **97**(12), 9062–9071.

[222] R. Schinke, *Photodissociation Dynamics*, Cambridge University Press, Cambridge, 1993.

[223] G. G. Balint-Kurti, R. N. Dixon, and C. C. Marston, *J. Chem. Soc. Faraday Trans.*, 1990, **86**(10), 1741.

[224] O. Vendrell, F. Gatti, and H.-D. Meyer, *J. Chem. Phys.*, 2007, **127**(18), 184303.

[225] G. A. Worth and I. Burghardt, *Chem. Phys. Lett.*, 2003, **368**(3-4), 502–508.

[226] G. A. Worth, M. A. Robb, and I. Burghardt, *Faraday Discuss.*, 2004, **127**, 307.

[227] B. Lasorne, M. A. Robb, and G. A. Worth, *Phys. Chem. Chem. Phys.*, 2007, **9**(25), 3210.

[228] G. A. Worth, M. A. Robb, and B. Lasorne, *Mol. Phys.*, 2008, **106**(16-18), 2077–2091.

[229] I. Burghardt, K. Giri, and G. A. Worth, *J. Chem. Phys.*, 2008, **129**(17), 174104.

[230] D. Mendive-Tapia, B. Lasorne, G. A. Worth, M. A. Robb, and M. J. Bearpark, *J. Chem. Phys.*, 2012, **137**(22), 22A548.

[231] I. Burghardt, H.-D. Meyer, and L. S. Cederbaum, *J. Chem. Phys.*, 1999, **111**(7), 2927–2939.

[232] I. Polyak, C. S. M. Allan, and G. A. Worth, *J. Chem. Phys.*, 2015, **143**(8), 084121.

[233] N. A. Tikhonov, *Dokl. Akad. Nauk SSSR*, 1943, **39**, 195–198.

[234] H. Wang and M. Thoss, *J. Chem. Phys.*, 2003, **119**(3), 1289–1299.

[235] S. Römer, M. Ruckenbauer, and I. Burghardt, *J. Chem. Phys.*, 2013, **138**(6), 064106.

[236] B. Lasorne, M. J. Bearpark, M. A. Robb, and G. A. Worth, *Chem. Phys. Lett.*, 2006, **432**(4-6), 604–609.

[237] D. Asturiol, B. Lasorne, G. A. Worth, M. A. Robb, and L. Blancafort, *Phys. Chem. Chem. Phys.*, 2010, **12**(19), 4949–4958.

[238] C. S. M. Allan, B. Lasorne, G. A. Worth, and M. A. Robb, *J. Phys. Chem. A*, 2010, **114**(33), 8713–8729.

[239] T. J. Frankcombe, *J. Chem. Phys.*, 2014, **140**(11), 114108.

[240] T. J. Frankcombe, M. A. Collins, and G. A. Worth, *Chem. Phys. Lett.*, 2010, **489**(4-6), 242–247.

[241] G. W. Richings, I. Polyak, K. Spinlove, G. A. Worth, I. Burghardt, and B. Lasorne, *Int. Rev. Phys. Chem.*, 2015, **34**(2), 269–308.

[242] K. Brejc, T. K. Sixma, P. A. Kitts, S. R. Kain, R. Y. Tsien, M. Ormo, and S. J. Remington, *Proc. Natl. Acad. Sci.*, 1997, **94**(6), 2306–2311.

[243] M. W. Forbes and R. A. Jockusch, *J. Am. Chem. Soc.*, 2009, **131**(47), 17038–17039.

[244] Y. Toker, D. B. Rahbek, B. Klærke, A. V. Bochenkova, and L. H. Andersen, *Phys. Rev. Lett.*, 2012, **109**(12), 128101.

[245] D. A. Horke and J. R. Verlet, *Phys. Chem. Chem. Phys.*, 2012, **14**(24), 8511–8515.

[246] C. W. West, J. N. Bull, A. S. Hudson, S. L. Cobb, and J. R. Verlet, *J. Phys. Chem. B*, 2015, **119**(10), 3982–3987.

[247] A. Svendsen, H. V. Kiefer, H. B. Pedersen, A. V. Bochenkova, and L. H. Andersen, *J. Am. Chem. Soc.*, 2017, **139**(25), 8766–8771.

[248] C. R. S. Mooney, M. A. Parkes, L. Zhang, H. C. Hailes, A. Simperler, M. J. Bearpark, and H. H. Fielding, *J. Chem. Phys.*, 2014, **140**(20), 205103.

[249] C. R. S. Mooney, M. E. Sanz, A. R. McKay, R. J. Fitzmaurice, A. E. Aliev, S. Caddick, and H. H. Fielding, *J. Phys. Chem. A*, 2012, **116**(30), 7943–7949.

[250] K. B. Bravaya and A. I. Krylov, *J. Phys. Chem. A*, 2013, **117**(46), 11815–11822.

[251] S. H. Deng, X. Y. Kong, G. Zhang, Y. Yang, W. J. Zheng, Z. R. Sun, D. Q. Zhang, and X. B. Wang, *J. Phys. Chem. Lett.*, 2014, **5**(12), 2155–2159.

[252] S. Olsen and R. H. McKenzie, *Chem. Phys. Lett.*, 2010, **492**(1-3), 150–156.

[253] Y. Shao, Z. Gan, E. Epifanovsky, A. T. B. Gilbert, M. Wormit, J. Kussmann, A. W. Lange, A. Behn, J. Deng, X. Feng, D. Ghosh, M. Goldey, P. R. Horn, L. D. Jacobson, I. Kaliman, R. Z. Khaliullin, T. Kuś, A. Landau, J. Liu, E. I. Proynov, Y. M. Rhee, R. M. Richard, M. A. Rohrdanz, R. P. Steele, E. J. Sundstrom, H. L. W. III, P. M. Zimmerman, D. Zuev, B. Albrecht, E. Alguire, B. Austin, G. J. O. Beran, Y. A. Bernard, E. Berquist, K. Brandhorst, K. B. Bravaya, S. T. Brown, D. Casanova, C.-M. Chang, Y. Chen, S. H. Chien, K. D. Closser, D. L. Crittenden, M. Diedenhofen, R. A. D. Jr., H. Do, A. D. Dutoi, R. G. Edgar, S. Fatehi, L. Fusti-Molnar, A. Ghysels, A. Golubeva-Zadorozhnaya, J. Gomes, M. W. D. Hanson-Heine, P. H. P. Harbach, A. W. Hauser, E. G. Hohenstein, Z. C. Holden, T.-C. Jagau, H. Ji, B. Kaduk, K. Khistyaev, J. Kim, J. Kim, R. A. King, P. Klunzinger, D. Kosenkov, T. Kowalczyk, C. M. Krauter, K. U. Lao, A. D. Laurent, K. V. Lawler, S. V. Levchenko, C. Y. Lin, F. Liu, E. Livshits, R. C. Lochan, A. Luenser, P. Manohar, S. F. Manzer, S.-P. Mao, N. Mardirossian, A. V. Marenich, S. A. Maurer, N. J. Mayhall, E. Neuscamman, C. M. Oana, R. Olivares-Amaya, D. P. O'Neill, J. A. Parkhill, T. M. Perrine, R. Peverati, A. Prociuk, D. R. Rehn, E. Rosta, N. J. Russ, S. M. Sharada, S. Sharma, D. W. Small, A. Sodt, T. Stein, D. Stück, Y.-C. Su, A. J. W. Thom, T. Tsuchimochi, V. Vanovschi, L. Vogt, O. Vydrov, T. Wang, M. A. Watson, J. Wenzel, A. White, C. F. Williams, J. Yang, S. Yeganeh, S. R. Yost, Z.-Q. You, I. Y. Zhang, X. Zhang, Y. Zhao, B. R. Brooks, G. K. L. Chan, D. M. Chipman, C. J. Cramer, W. A. G. III, M. S. Gordon, W. J. Hehre, A. Klamt, H. F. S. III, M. W. Schmidt, C. D. Sherrill, D. G. Truhlar, A. Warshel, X. Xu, A. Aspuru-Guzik, R. Baer, A. T.

Bell, N. A. Besley, J.-D. Chai, A. Dreuw, B. D. Dunietz, T. R. Furlani, S. R. Gwaltney, C.-P. Hsu, Y. Jung, J. Kong, D. S. Lambrecht, W. Liang, C. Ochsenfeld, V. A. Rassolov, L. V. Slipchenko, J. E. Subotnik, T. V. Voorhis, J. M. Herbert, A. I. Krylov, P. M. W. Gill, and M. Head-Gordon, *Mol. Phys.*, 2015, **113**(2), 184–215.

[254] H. Sekino and R. J. Bartlett, *Int. J. Quantum Chem.*, 1984, **26**(S18), 255–265.

[255] K. van der Meer and J. Mulder, *Chem. Phys. Lett.*, 1975, **34**(1), 189–191.

[256] J. M. Bofill, S. Olivella, and A. Sole, *J. Am. Chem. Soc.*, 1989, **111**(20), 7740–7746.

[257] A. J. Gianola, T. Ichino, R. L. Hoenigman, S. Kato, V. M. Bierbaum, and W. C. Lineberger, *J. Phys. Chem. A*, 2005, **109**(50), 11504–11514.

[258] T. Ichino, A. J. Gianola, W. C. Lineberger, and J. F. Stanton, *J. Chem. Phys.*, 2006, **125**(8), 084312.

[259] J. Sadlej and W. D. Edwards, *Int. J. Quantum Chem.*, 1992, **44**(26 S), 409–420.

[260] M. A. Walters and T. G. Spiro, *Inorg. Chem.*, 1983, **22**(26), 4014–4017.

[261] R. F. Gunion, M. K. Gilles, M. L. Polak, and W. C. Lineberger, *Int. J. Mass Spectrom. Ion Process.*, 1992, **117**(1-3), 601–620.

[262] J. B. Kim, T. I. Yacovitch, C. Hock, and D. M. Neumark, *Phys. Chem. Chem. Phys.*, 2011, **13**(38), 17378.

[263] S. Hirata and M. Head-Gordon, *Chem. Phys. Lett.*, 1999, **302**(5-6), 375–382.

[264] J. G. Radziszewski, M. Gil, A. Gorski, J. Spanget-Larsen, J. Waluk, and B. J. Mróz, *J. Chem. Phys.*, 2001, **115**(21), 9733–9738.

[265] C.-W. Cheng, Y.-P. Lee, and H. A. Witek, *J. Phys. Chem. A*, 2008, **112**(47), 11998–12006.

[266] L. A. Kotorlenko and V. S. Aleksandrova, *Theor. Exp. Chem.*, 1982, **18**(1), 97–99.

[267] A. Mukherjee, M. L. McGlashen, and T. G. Spiro, *J. Phys. Chem.*, 1995, **99**(14), 4912–4917.

[268] C. F. Lim and J. M. Tanski, *J. Chem. Crystallogr.*, 2007, **37**(9), 587–595.

[269] M. Taylor and G. Worth, *Chem. Phys.*, 2018, **515**, 719–727.

[270] Z. Lan, W. Domcke, V. Vallet, A. L. Sobolewski, and S. Mahapatra, *J. Chem. Phys.*, 2005, **122**(22), 224315.

[271] M. L. Hause, Y. Heidi Yoon, A. S. Case, and F. F. Crim, *J. Chem. Phys.*, 2008, **128**(10), 104307.

[272] R. N. Dixon, T. A. A. Oliver, and M. N. R. Ashfold, *J. Chem. Phys.*, 2011, **134**(19), 194303.

[273] X. Xu, K. R. Yang, and D. G. Truhlar, *J. Chem. Theory Comput.*, 2013, **9**(8), 3612–3625.

[274] X. Xu, J. Zheng, K. R. Yang, and D. G. Truhlar, *J. Am. Chem. Soc.*, 2014, **136**(46), 16378–16386.

[275] X. Zhu and D. R. Yarkony, *J. Chem. Phys.*, 2014, **140**(2), 024112.

[276] M. N. R. Ashfold, *Science*, 2006, **312**(5780), 1637–1640.

[277] G. M. Roberts, A. S. Chatterley, J. D. Young, and V. G. Stavros, *J. Phys. Chem. Lett.*, 2012, **3**(3), 348–352.

[278] A. L. Sobolewski and W. Domcke, *Chem. Phys.*, 2000, **259**(2-3), 181–191.

[279] A. L. Sobolewski, W. Domcke, C. Dedonder-Lardeux, and C. Jouvet, *Phys. Chem. Chem. Phys.*, 2002, **4**(7), 1093–1100.

[280] A. L. Sobolewski and W. Domcke, *Chem. Phys. Lett.*, 1999, **315**(3-4), 293–298.

[281] V. Vallet, Z. Lan, S. Mahapatra, A. L. Sobolewski, and W. Domcke, *Faraday Discuss.*, 2004, **127**, 283–293.

[282] V. Vallet, Z. Lan, S. Mahapatra, A. L. Sobolewski, and W. Domcke, *J. Chem. Phys.*, 2005, **123**(14), 144307.

[283] A. L. Sobolewski and W. Domcke, *J. Phys. Chem. A*, 2001, **105**(40), 9275–9283.

[284] D. Gerrard and W. Maddams, *Spectrochim. Acta Part A Mol. Spectrosc.*, 1978, **34**(12), 1205–1211.

[285] D. L. Gerrard and W. F. Maddams, *Spectrochim. Acta Part A Mol. Spectrosc.*, 1978, **34**(12), 1219–1223.

[286] H. Grosch, Z. Sárossy, H. Egsgaard, and A. Fateev, *J. Quant. Spectrosc. Radiat. Transf.*, 2015, **156**(1), 17–23.

[287] S. Schumm, M. Gerhards, and K. Kleinermanns, *J. Phys. Chem. A*, 2000, **104**(46), 10648–10655.

[288] S. Karmakar, D. P. Mukhopadhyay, and T. Chakraborty, *J. Chem. Phys.*, 2015, **142**(18), 184303.

[289] K. Rajak, A. Ghosh, and S. Mahapatra, *J. Chem. Phys.*, 2018, **148**(5), 054301.

[290] C. P. Schick, S. D. Carpenter, and P. M. Weber, *J. Phys. Chem. A*, 1999, **103**(49), 10470–10476.

[291] R. A. Livingstone, J. O. F. Thompson, M. Iljina, R. J. Donaldson, B. J. Sussman, M. J. Paterson, and D. Townsend, *J. Chem. Phys.*, 2012, **137**(18), 184304.

[292] J. W. Riley, B. Wang, J. L. Woodhouse, M. Assmann, G. A. Worth, and H. H. Fielding, *J. Phys. Chem. Lett.*, 2018, **9**(4), 678–682.

[293] T. Debies and J. Rabalais, *J. Electron Spectros. Relat. Phenomena*, 1972, **1**(4), 355–370.

[294] J. P. Maier and D. W. Turner, *J. Chem. Soc., Faraday Trans. 2*, 1973, **69**, 521–531.

[295] T. Kobayashi and S. Nagakura, *Bull. Chem. Soc. Jpn.*, 1974, **47**(10), 2563–2572.

[296] M. H. Palmer, W. Moyes, M. Speirs, and J. A. Ridyard, *J. Mol. Struct.*, 1979, **52**, 293–307.

[297] W. Domcke and G. Stock, in *Adv. Chem. Phys.*, Wiley-Blackwell, 2007; pp. 1–169.

[298] G. Wu, S. P. Neville, O. Schalk, T. Sekikawa, M. N. R. Ashfold, G. A. Worth, and A. Stolow, *J. Chem. Phys.*, 2015, **142**(7), 074302.

[299] M. Seel and W. Domcke, *Chem. Phys.*, 1991, **151**(1), 59–72.

[300] M. Seel and W. Domcke, *J. Chem. Phys.*, 1991, **95**(11), 7806–7822.

[301] G. A. Worth, R. Carley, and H. H. Fielding, *Chem. Phys.*, 2007, **338**(2-3), 220–227.

[302] G. A. Worth, H.-D. Meyer, H. Köppel, L. S. Cederbaum, and I. Burghardt, *Int. Rev. Phys. Chem.*, 2008, **27**(3), 569–606.

[303] G. A. Worth, *J. Photochem. Photobiol. A Chem.*, 2007, **190**(2-3), 190–199.

[304] T. J. Penfold and G. A. Worth, *J. Chem. Phys.*, 2009, **131**(6), 064303.

[305] F. Wang, S. P. Neville, R. Wang, and G. A. Worth, *J. Phys. Chem. A*, 2013, **117**(32), 7298–7307.

[306] S. P. Neville and G. A. Worth, *J. Chem. Phys.*, 2014, **140**(3), 034317.

[307] G. W. Richings and G. A. Worth, *J. Chem. Phys.*, 2014, **141**(24), 244115.

[308] C. Cattarius, A. Markmann, and G. A. Worth, The VCHAM program, 2007.

[309] G. A. Worth, K. Giri, G. W. Richings, I. M. Burghardt, H. Beck, A. Jäckle, and H.-D. Meyer, The Quantics Package, 2015.

[310] M. J. Frisch, G. W. Trucks, H. B. Schlegel, G. E. Scuseria, M. A. Robb, J. R. Cheeseman, G. Scalmani, V. Barone, G. A. Petersson, H. Nakatsuji, X. Li, M. Caricato, A. V. Marenich, J. Bloino, B. G. Janesko, R. Gomperts, B. Mennucci, H. P. Hratchian, J. V. Ortiz, A. F. Izmaylov, J. L. Sonnenberg, D. Williams-Young, F. Ding, F. Lipparini, F. Egidi, J. Goings, B. Peng, A. Petrone, T. Henderson, D. Ranasinghe, V. G. Zakrzewski, J. Gao, N. Rega, G. Zheng, W. Liang, M. Hada, M. Ehara, K. Toyota, R. Fukuda, J. Hasegawa, M. Ishida, T. Nakajima, Y. Honda, O. Kitao, H. Nakai, T. Vreven, K. Throssell, J. A. Montgomery Jr., J. E. Peralta, F. Ogliaro, M. J. Bearpark, J. J. Heyd, E. N. Brothers, K. N. Kudin, V. N. Staroverov, T. A. Keith, R. Kobayashi, J. Normand, K. Raghavachari, A. P. Rendell, J. C. Burant, S. S. Iyengar, J. Tomasi, M. Cossi, J. M. Millam, M. Klene, C. Adamo, R. Cammi, J. W. Ochterski, R. L. Martin, K. Morokuma, O. Farkas, J. B. Foresman, and D. J. Fox, Gaussian 09, 2009.

[311] R. J. Lipert and S. D. Colson, *J. Chem. Phys.*, 1990, **92**(5), 3240–3241.

[312] J. Evans, *Spectrochim. Acta*, 1960, **16**(11-12), 1382–1392.

[313] S. Schumm, M. Gerhards, W. Roth, H. Gier, and K. Kleinermanns, *Chem. Phys. Lett.*, 1996, **263**(1-2), 126–132.

[314] P. J. O'Malley, *J. Mol. Struct.*, 2005, **755**(1-3), 147–150.

[315] H. Lampert, W. Mikenda, and A. Karpfen, *J. Phys. Chem. A*, 1997, **101**(12), 2254–2263.

[316] D. Michalska, D. C. Bieńko, A. J. Abkowicz-Bieńko, and Z. Latajka, *J. Phys. Chem.*, 1996, **100**(45), 17786–17790.

[317] H. Bist, J. Brand, and D. Williams, *J. Mol. Spectrosc.*, 1967, **24**(1-4), 402–412.

[318] K. R. Yang, X. Xu, J. Zheng, and D. G. Truhlar, *Chem. Sci.*, 2014, **5**(12), 4661–4680.

[319] H. Bist, J. Brand, and D. Williams, *J. Mol. Spectrosc.*, 1966, **21**(1-4), 76–98.

[320] H. Bist, J. Brand, and D. Williams, *J. Mol. Spectrosc.*, 1967, **24**(1-4), 413–467.

[321] J. R. Platt, *J. Chem. Phys.*, 1949, **17**(5), 484–495.

[322] R. Pariser, *J. Chem. Phys.*, 1956, **24**(2), 250–268.

[323] K. Lopata, R. Reslan, M. Kowalska, D. Neuhauser, N. Govind, and K. Kowalski, *J. Chem. Theory Comput.*, 2011, **7**(11), 3686–3693.

[324] S. Knippenberg, J. H. Starcke, M. Wormit, and A. Dreuw, *Mol. Phys.*, 2010, **108**(19-20), 2801–2813.

[325] M. Parac and S. Grimme, *Chem. Phys.*, 2003, **292**(1), 11–21.

[326] S. Grimme and M. Parac, *Chemphyschem*, 2003, **4**(3), 292–295.

[327] S. Grimme and M. Waletzke, *J. Chem. Phys.*, 1999, **111**(13), 5645–5655.

[328] A. B. J. Parusel and S. Grimme, *J. Porphyrins Phthalocyanines*, 2001, **05**(03), 225–232.

[329] C. M. Marian and N. Gilka, *J. Chem. Theory Comput.*, 2008, **4**(9), 1501–1515.

[330] A. P. Scott and L. Radom, *J. Phys. Chem.*, 1996, **100**(41), 16502–16513.

[331] A. Dreuw and M. Head-Gordon, *Chem. Rev.*, 2005, **105**(11), 4009–4037.

[332] K. E. Riley, B. T. Op't Holt, and K. M. Merz, *J. Chem. Theory Comput.*, 2007, **3**(2), 407–433.

[333] J. Tirado-Rives and W. L. Jorgensen, *J. Chem. Theory Comput.*, 2008, **4**(2), 297–306.

[334] R. Ahlrichs, S. Bäcker, M. Ehrig, K. Eichkorn, S. Elliott, F. Haase, M. Hoser, H. Horn, C. Huber, U. Huniar, M. Kattannek, C. Kolmel, M. Kollwitz, C. Ochsenfeld, H. Öhm, A. Schäfer, U. Schneider, O. Treutler, M. von Arnim, F. Weigend, P. Weis, and H. Weiss, TURBOMOLE V6.2 2010, a development of University of Karlsruhe and Forschungszentrum Karlsruhe GmbH, 1989-2007, TURBOMOLE GmbH, since 2007; available from http://www.turbomole.com., 2008.

[335] M. Pope, H. P. Kallmann, and P. Magnante, *J. Chem. Phys.*, 1963, **38**(8), 2042–2043.

[336] M. Yoshizawa and J. K. Klosterman, *Chem. Soc. Rev.*, 2014, **43**(6), 1885–1898.

[337] J. P. Konopelski, F. Kotzyba-Hibert, J.-M. Lehn, J.-P. Desvergne, F. Fagès, A. Castellan, and H. Bouas-Laurent, *J. Chem. Soc., Chem. Commun.*, 1985, (7), 433–436.

[338] A. P. de Silva and S. A. de Silva, *J. Chem. Soc., Chem. Commun.*, 1986, (23), 1709–1710.

[339] C. V. Kumar and E. H. Asuncion, *J. Am. Chem. Soc.*, 1993, **115**(19), 8547–8553.

[340] J.-L. H. A. Duprey, G. A. Bullen, Z.-y. Zhao, D. M. Bassani, A. F. A. Peacock, J. Wilkie, and J. H. R. Tucker, *ACS Chem. Biol.*, 2016, **11**(3), 717–721.

[341] J. Manchester, D. M. Bassani, J.-L. H. A. Duprey, L. Giordano, J. S. Vyle, Z.-y. Zhao, and J. H. R. Tucker, *J. Am. Chem. Soc.*, 2012, **134**(26), 10791–10794.

[342] M.-H. Ho, B. Balaganesan, and C. H. F. Chen, *Isr. J. Chem.*, 2012, **52**(6), 484–495.

[343] S. Iglesias-Groth, A. Manchado, R. Rebolo, J. I. González Hernández, D. A. García-Hernández, and D. L. Lambert, *Mon. Not. R. Astron. Soc.*, 2010, **407**(4), 2157–2165.

[344] Y. Kawashima, T. Hashimoto, H. Nakano, and K. Hirao, *Theor. Chim. Acta*, 1999, **102**(1-6), 49–64.

[345] J. M. L. Martin, J. El-Yazal, and J.-P. François, *J. Phys. Chem.*, 1996, **100**(38), 15358–15367.

[346] G. M. Akselrod, P. B. Deotare, N. J. Thompson, J. Lee, W. A. Tisdale, M. A. Baldo, V. M. Menon, and V. Bulović, *Nat. Commun.*, 2014, **5**(1), 3646.

[347] J. J. Burdett and C. J. Bardeen, *Acc. Chem. Res.*, 2013, **46**(6), 1312–1320.

[348] J. J. Burdett, A. M. Müller, D. Gosztola, and C. J. Bardeen, *J. Chem. Phys.*, 2010, **133**(14), 144506.

[349] A. Bree and L. E. Lyons, *J. Chem. Soc.*, 1960, (5206), 5206.

[350] R. G. Endres, C. Y. Fong, L. H. Yang, G. Witte, and C. Wöll, *Comput. Mater. Sci.*, 2004, **29**(3), 362–370.

[351] S. Shi and D. Ma, *Semicond. Sci. Technol.*, 2005, **20**(12), 1213–1216.

[352] M. V. Madhava Rao, T.-S. Huang, Y.-K. Su, and Y.-T. Huang, *J. Electrochem. Soc.*, 2010, **157**(1), H69–H71.

[353] R. Ruiz, D. Choudhary, B. Nickel, T. Toccoli, K. C. Chang, A. C. Mayer, P. Clancy, J. M. Blakely, R. L. Headrick, S. Iannotta, and G. G. Malliaras, *Chem. Mater.*, 2004, **16**(23), 4497–4508.

[354] L. Gross, F. Mohn, N. Moll, P. Liljeroth, and G. Meyer, *Science*, 2009, **325**(5944), 1110–1114.

[355] L. Gross, N. Moll, F. Mohn, A. Curioni, G. Meyer, F. Hanke, and M. Persson, *Phys. Rev. Lett.*, 2011, **107**(8), 086101.

[356] L. Z. Khatymova, R. R. Kinzyabulatov, and O. G. Khvostenko, *High Energy Chem.*, 2018, **52**(1), 38–44.

[357] E. Pantos, J. Philis, and A. Bolovinos, *J. Mol. Spectrosc.*, 1978, **72**(1), 36–43.

[358] D. S. N. Parker, R. S. Minns, T. J. Penfold, G. A. Worth, and H. H. Fielding, *Chem. Phys. Lett.*, 2009, **469**(1-3), 43–47.

[359] F. P. Schwarz and S. P. Wasik, *Anal. Chem.*, 1976, **48**(3), 524–528.

[360] G. George and G. Morris, *J. Mol. Spectrosc.*, 1968, **26**(1), 67–71.

[361] T. Hashimoto, H. Nakano, and K. Hirao, *J. Chem. Phys.*, 1996, **104**(16), 6244–6258.

[362] F. M. Behlen and S. A. Rice, *J. Chem. Phys.*, 1981, **75**(12), 5672–5684.

[363] J. Li, Y.-H. Li, Y. Zhao, X.-Y. Liu, M.-K. Fung, and J. Fan, *Org. Electron.*, 2018, **54**, 140–147.

[364] F. Negri and M. Z. Zgierski, *J. Chem. Phys.*, 1996, **104**(10), 3486–3500.

[365] K. Yoshida, Y. Semba, S. Kasahara, T. Yamanaka, and M. Baba, *J. Chem. Phys.*, 2009, **130**(19), 194304.

[366] R. Montero, A. Longarte, R. Martínez, M. N. Sánchez Rayo, and F. Castaño, *Chem. Phys. Lett.*, 2009, **468**(4-6), 134–137.

[367] M. Z. Zgierski, *Chem. Phys. Lett.*, 1977, **47**(3), 499–502.

[368] M. Robey, I. Ross, R. V. Southwood-Jones, and S. J. Strickler, *Chem. Phys.*, 1977, **23**(2), 207–216.

[369] A. Mordziński, A. Leś, Y. Stepanenko, J. Rycombel, and L. Adamowicz, *J. Mol. Spectrosc.*, 2005, **233**(1), 98–109.

[370] C. Y. Tsai, C. Y. Li, C. H. Lin, B. H. Huang, and B. T. Ko, *Inorg. Chem. Commun.*, 2011, **14**(1), 271–275.

[371] P. J. Cox and G. A. Sim, *Acta Crystallogr. Sect. B Struct. Crystallogr. Cryst. Chem.*, 1979, **35**(2), 404–410.

[372] A. Bach, J. Hewel, and S. Leutwyler, *J. Phys. Chem. A*, 1998, **102**(51), 10476–10485.

[373] M. Nakagaki, E. Nishi, K. Sakota, H. Nakano, and H. Sekiya, *Chem. Phys.*, 2006, **328**(1-3), 190–196.

[374] D. Barraza-Jimenez, A. Flores-Hidalgo, and D. Glossman-Mitnik, *J. Mol. Struct. THEOCHEM*, 2009, **894**(1-3), 64–70.

[375] S. Kou, H. Zhou, G. Tang, R. Li, Y. Zhang, J. Zhao, and C. Wei, *Spectrochim. Acta - Part A Mol. Biomol. Spectrosc.*, 2012, **96**(1), 768–775.

[376] S. Yamazaki and S. Kato, *J. Am. Chem. Soc.*, 2007, **129**(10), 2901–2909.

[377] A. L. Sobolewski and W. Domcke, *Phys. Chem. Chem. Phys.*, 2006, **8**(29), 3410–3417.

[378] O. Dmitrenko, W. Reischl, R. D. Bach, and J. Spanget-Larsen, *J. Phys. Chem. A*, 2004, **108**(26), 5662–5669.

[379] T. Raeker and B. Hartke, *J. Phys. Chem. A*, 2017, **121**(32), 5967–5977.

[380] L. Zhu, R. O. Al-Kaysi, R. J. Dillon, F. S. Tham, and C. J. Bardeen, *Cryst. Growth Des.*, 2011, **11**(11), 4975–4983.

[381] M. McCann, R. Curran, M. Ben-Shoshan, V. McKee, A. A. Tahir, M. Devereux, K. Kavanagh, B. S. Creaven, and A. Kellett, *Dalt. Trans.*, 2012, **41**(21), 6516.

[382] M. S. A. Abdel-Mottaleb, H. R. Galal, A. F. M. Dessouky, M. El-Naggar, D. Mekkawi, S. S. Ali, and G. M. Attya, *Int. J. Photoenergy*, 2000, **2**(1), 47–53.

[383] N. S. Bazilevskaya and A. S. Cherkasov, *J. Appl. Spectrosc.*, 1965, **3**(6), 412–416.

[384] I. Momiji, C. Yoza, and K. Matsui, *J. Phys. Chem. B*, 2000, **104**(7), 1552–1555.

[385] S. Suzuki, T. Fujii, N. Yoshiike, S. Komatsu, and T. Iida, *Bull. Chem. Soc. Jpn.*, 1978, **51**(9), 2460–2466.

[386] T. C. Werner and D. M. Hercules, *J. Phys. Chem.*, 1969, **73**(6), 2005–2011.

[387] V. Swayambunathan and E. C. Lim, *J. Phys. Chem.*, 1987, **91**(25), 6359–6364.

[388] S. Hirayama, *Bull. Chem. Soc. Jpn.*, 1975, **48**(4), 1127–1132.

[389] L. J. Fitzgerald and R. E. Gerkin, *Acta Crystallogr. Sect. C Cryst. Struct. Commun.*, 1997, **53**(1), 71–73.

[390] J. Trotter, *Acta Crystallogr.*, 1959, **12**(11), 922–928.

[391] M. Chattoraj, B. A. King, G. U. Bublitz, and S. G. Boxer, *Proc. Natl. Acad. Sci. USA*, 1996, **93**(16), 8362–7.

[392] T. M. Creemers, A. J. Lock, V. Subramaniam, T. M. Jovin, and S. Volker, *Nat. Struct. Biol.*, 1999, **6**(6), 557–560.

[393] X. Shi, P. Abbyad, X. Shu, K. Kallio, P. Kanchanawong, W. Childs, S. J. Remington, and S. G. Boxer, *Biochemistry*, 2007, **46**(43), 12014–12025.

[394] M. Kondo, I. A. Heisler, D. Stoner-Ma, P. J. Tonge, and S. R. Meech, *J. Photochem. Photobiol. A Chem.*, 2012, **234**(1), 21–26.

[395] J. T. M. Kennis, D. S. Larsen, I. H. M. van Stokkum, M. Vengris, J. J. van Thor, and R. van Grondelle, *Proc. Natl. Acad. Sci. U. S. A.*, 2004, **101**(52), 17988–93.

[396] S. L. Maddalo and M. Zimmer, *Photochem. Photobiol.*, 2006, **82**(2), 367.

[397] A. Toniolo, G. Granucci, and T. J. Martínez, *J. Phys. Chem. A*, 2003, **107**(19), 3822–3830.

[398] M. E. Martin, F. Negri, and M. Olivucci, *J. Am. Chem. Soc.*, 2004, **126**(17), 5452–5464.

[399] P. Altoe, F. Bernardi, M. Garavelli, G. Orlandi, and F. Negri, *J. Am. Chem. Soc.*, 2005, **127**(11), 3952–3963.

[400] J. J. Van Thor, C. N. Lincoln, B. Kellner, K. N. Bourdakos, L. M. Thompson, M. J. Bearpark, P. M. Champion, and J. T. Sage, *Vib. Spectrosc.*, 2012, **62**(1), 1–6.

[401] D. Stoner-Ma, A. A. Jaye, P. Matousek, M. Towrie, S. R. Meech, and P. J. Tonge, *J. Am. Chem. Soc.*, 2005, **127**(9), 2864–2865.

[402] J. J. Van Thor, K. L. Ronayne, M. Towrie, and J. T. Sage, *Biophys. J.*, 2008, **95**(4), 1902–1912.

[403] S. Bettati, E. Pasqualetto, G. Lolli, B. Campanini, and R. Battistutta, *Biochim. Biophys. Acta - Proteins Proteomics*, 2011, **1814**(6), 824–833.

[404] M. A. Lill and V. Helms, *Proc. Natl. Acad. Sci. U. S. A.*, 2002, **99**(5), 2778–81.

[405] S. Wang and S. C. Smith, *J. Phys. Chem. B*, 2006, **110**(10), 5084–5093.

[406] S. Wang and S. C. Smith, *Phys. Chem. Chem. Phys.*, 2007, **9**(4), 452–458.

[407] R. Zhang, M. T. Nguyen, and A. Ceulemans, *Chem. Phys. Lett.*, 2005, **404**(4-6), 250–256.

[408] O. Vendrell, R. Gelabert, M. Moreno, and J. M. Lluch, *J. Phys. Chem. B*, 2008, **112**(17), 5500–5511.

[409] H. Zhang, Q. Sun, Z. Li, S. Nanbu, and S. S. Smith, *Comput. Theor. Chem.*, 2012, **990**(1), 185–193.

[410] B. Kang, S. Karthikeyan, D. J. Jang, H. Kim, and J. Y. Lee, *Bull. Korean Chem. Soc.*, 2013, **34**(7), 1961–1966.

[411] O. Vendrell, R. Gelabert, M. Moreno, and J. M. Lluch, *J. Chem. Theory Comput.*, 2008, **4**(7), 1138–1150.

[412] O. Vendrell, R. Gelabert, M. Moreno, and J. M. Lluch, *J. Am. Chem. Soc.*, 2006, **128**(11), 3564–3574.

[413] J.-D. Chai and M. Head-Gordon, *Phys. Chem. Chem. Phys.*, 2008, **10**(44), 6615.

[414] S. Grimme, *Wiley Interdiscip. Rev. Comput. Mol. Sci.*, 2011, **1**(2), 211–228.

[415] K. E. Spinlove, G. W. Richings, M. A. Robb, and G. A. Worth, *Faraday Discuss.*, 2018, **157**, 243.

[416] K. Andersson, P. A. Malmqvist, B. O. Roos, A. J. Sadlej, and K. Wolinski, *J. Phys. Chem.*, 1990, **94**(14), 5483–5488.

[417] K. Andersson, P. Malmqvist, and B. O. Roos, *J. Chem. Phys.*, 1992, **96**(2), 1218–1226.

[418] B. O. Roos and K. Andersson, *Chem. Phys. Lett.*, 1995, **245**(2-3), 215–223.

[419] R. Stowasser and R. Hoffmann, *J. Am. Chem. Soc.*, 1999, **121**(14), 3414–3420.

[420] S. Hamel, P. Duffy, M. E. Casida, and D. R. Salahub, *J. Electron Spectros. Relat. Phenomena*, 2002, **123**(2-3), 345–363.

[421] R. Van Meer, O. V. Gritsenko, and E. J. Baerends, *J. Chem. Theory Comput.*, 2014, **10**(10), 4432–4441.

[422] C. W. Bauschlicher and H. Partridge, *Chem. Phys. Lett.*, 1995, **240**(5-6), 533–540.

[423] B. J. Lynch, Y. Zhao, and D. G. Truhlar, *J. Phys. Chem. A*, 2003, **107**(9), 1384–1388.

[424] A. D. Boese, J. M. L. Martin, and N. C. Handy, *J. Chem. Phys.*, 2003, **119**(6), 3005–3014.

[425] D. Feller and D. A. Dixon, *J. Phys. Chem. A*, 2018, **122**(9), 2598–2603.

[426] F. Jensen, *Introduction to Computational Chemistry*, John Wiley & Sons, Inc., Hoboken, NJ, USA, 2nd ed., 2007.

[427] E. K. U. Gross and W. Kohn in *Adv. Quantum Chem.*, ed. P.-O. Lowdin, Vol. 21; Academic Press, 1990; pp. 255–291.

[428] C. A. Ullrich, *Time-Dependent Density-Functional Theory: Concepts and Applications*, Oxford University Press, 2011.

[429] H. Bruus and K. Flensberg, *Many-Body Quantum Theory in Condensed Matter Physics: An Introduction*, Oxford University Press, 2004.

[430] M. E. Casida in *Recent Adv. Density Funct. Methods, Part I*, Vol. 1; Cambridge University Press, Cambridge, 1995; pp. 155–92.

[431] F. Furche and R. Ahlrichs, *J. Chem. Phys.*, 2002, **117**(16), 7433–7447.

[432] S. Hirata and M. Head-Gordon, *Chem. Phys. Lett.*, 1999, **314**(3-4), 291–299.

[433] J. Lorentzon, P.-A. Malmqvist, M. Fulscher, and B. O. Roos, *Theor. Chim. Acta*, 1995, **91**(1-2), 91–108.

[434] W. Rodríguez-Córdoba, R. Noria-Moreno, P. Navarro, and J. Peon, *J. Lumin.*, 2014, **145**(1), 697–707.